# Identification and Fate of Bioactive Transformation Products of Pharmaceuticals and Industrial Antioxidants

Haoqi (Nina) Zhao

A dissertation
submitted in partial fulfillment of the
requirements for the degree of

Doctor of Philosophy

University of Washington
2021

Reading Committee:
Edward P. Kolodziej, Chair
Michael C. Dodd
Joel E. Baker

Civil and Environmental Engineering

University of Washington

## Abstract

Identification and Fate of Bioactive Transformation Products of
Pharmaceuticals and Industrial Antioxidants

Haoqi (Nina) Zhao

Chair of the Supervisory Committee:
Edward P. Kolodziej
Department of Civil and Environmental Engineering

Human society discharges complex chemical mixtures into the aquatic environment that cause various adverse effects to aquatic organisms and humans. Upon discharge, organic chemicals typically form multiple transformation products (TPs) during abiotic and biotic environmental transformations. While many TPs are likely benign and unable to interact with biological pathways, some TPs can contribute significantly to the environmental risks of complex mixtures. There is a pressing need to identify stable and/or toxic TPs, to study their environmental fate and transport, and to evaluate the potential for TP toxicity in comprehensive risk assessments of environmental contaminants.

In this thesis, we focused on the environmental transformations of two classes of organic contaminants: steroid hormone pharmaceuticals and industrial antiozonants used in tire rubbers. Specifically, project analytes include the photoproducts of trenbolone (TBOH) and altrenogest (ALT), compounds that occur in agricultural environments, and two synthetic progestins, dienogest (DIE) and drospirenone (DRO), that are contaminants of municipal wastewaters. These analytes represented novel steroid hormone pharmaceuticals that are potent and used

widely but are less well characterized in the scientific literature. In addition, we focused on understanding the fate and transformation of 6PPD (*N*-(1,3-dimethylbutyl)-*N*′-phenyl-*p*-phenylenediamine) and its structural analogues, which are globally ubiquitous antioxidants used in tire rubber and other consumer products. Our group recently identified 6PPD as a pre-toxicant responsible for the massive coho salmon (*Oncorhynchus kisutch*) mortality observed in the Pacific Northwest. For the above analytes, laboratory experiments were used to simulate environmentally relevant abiotic (e.g., photolysis, ozonation) and biotic transformation processes to (i) quantitatively analyze known TPs with liquid chromatography-tandem mass spectrometry (LC-MS/MS), (ii) determine the rate and extent of contaminant transformations, (iii) identify unknown TPs with high-resolution mass spectrometry (HRMS) based suspect screening and non-target analysis, and (iv) evaluate TPs bioactivity and environmental occurrence.

Chapter 2 discussed a novel and sensitive analytical method for the detection and quantification of metastable TBOH and ALT photoproducts in agricultural receiving waters. The developed method employed solid phase extraction and LC-MS/MS analysis. Because commercial analytical standards are not available, reference standards for photoproducts were generated from TBOH or ALT with a solar simulator. With cold and pH neutral conditions, rapid sample processing, minimal extract storage, and reduction of cationic artifacts, we achieved efficient detection of the metastable photoproducts with method detection limits at the low ng/L ranges. The analytical method was then employed to evaluate the sorption of the steroid photoproducts in batch soil-water systems. We showed that the photoproducts exhibited reduced sorption affinity ($\log K_{oc}$ of 1.92-2.57) relative to the more hydrophobic parent structures ($\log K_{oc}$ of 2.46-2.76). Therefore, traditional runoff management practices in agroecosystems would be expected to exhibit reduced treatment effectiveness when the photoproducts were considered.

Chapter 3 evaluated the biotransformation of ALT and its primary photo-cycloaddition product (ALT-CAP) in agricultural receiving waters and identified the TPs with HRMS. We showed that ALT-CAP (half-life, 1.6 days) demonstrated ~2-fold faster biotransformation than ALT (half-life, 3.5 days). However, the absolute abundance (based on electrospray ionization (ESI) HRMS peak areas) of the major ALT-CAP TPs, including dehydrogenation TPs, hydroxylation TPs, and isomerization TPs, was often an order of magnitude higher than that of ALT TPs. This indicated that biotransformation of ALT seemed to produce less abundant and less stable TPs, while ALT-CAP biotransformation tended to produce larger, and more stable TPs with higher potential for retained steroid structures. Therefore, the exposure risks of ALT are prone to underestimation if the formation and subsequent biotransformation products of ALT-CAP are not considered as part of the environmental fate of these compounds.

In Chapter 4, we investigated the biotransformation of DIE and DRO with representative activated sludge batch incubations and identified relevant TPs using HRMS. We showed that DIE exhibited slow biotransformation (16-30 hr half-life), and proceeded through a quantitative aromatic dehydrogenation (molar yields ~55%) to form an aromatic TP ~30% estrogenic as 17β-estradiol. DRO experienced more rapid biotransformation (<0.5 hr half-life), and 1,2-dehydrogenation formed the major product (molar yields ~40%) as an anti-mineralocorticoid drug candidate named spirorenone. Lactone ring hydrolysis was another important biotransformation pathway for DRO (molar yields ~20%) and generated a pharmacologically inactive TP. Other minor pathways for DIE and DRO included hydroxylation, methoxylation, and 3-keto and C4(5) double bond hydrogenation; distinct bioactivities are plausible for such TPs, including anti-gestagenic activity, anti-gonadotropic activity, and pregnancy inhibition effects. These results demonstrated that biotransformation of DIE and DRO formed bioactive

TPs in large quantities during wastewater treatment, which should be considered in future risk assessments of synthetic progestins.

Chapter 5 focused on the identification and environmental fate of tire rubber-derived chemicals acutely toxic to coho salmon. Firstly, this chapter described the contribution of Nina Zhao to a large collaborative research project, led by Dr. Zhenyu Tian (postdoc scientist of our group), to identify the causal toxicant(s) for the coho salmon mortality from aqueous leachates of tire tread wear particles (TWPs). After initial purification of the TWP leachate by Dr. Tian, Zhao and Tian developed orthogonal HPLC fractionation steps that effectively separated the pure toxicant from ~600 chemicals in the purified TWP leachate. Thereafter, the coho toxicant was identified to be a highly toxic quinone TP of 6PPD formed during ozonation (i.e., 6PPD-quinone). This chapter then expanded this reaction pathway to analogue substituted-PPD antioxidants, and confirmed the formation of PPD-quinones in ozonation of four other substituted-PPDs with synthetic PPD-quinone standards (from Dr. Kelly Kim at UWT). Furthermore, this chapter explored the ozonation TPs of 6PPD beyond 6PPD-quinone with HRMS screening. Twenty-one potential TPs were identified, with five confirmed through reference standards and eleven with likely or probable structures proposed based on MS/MS spectra and literature information. The major 6PPD TPs were then retrospectively screened in archived sample extracts of TWP, TWP leachate, roadway runoff, and creek stormwater. We revealed widespread presence of 6PPD TPs in these sample matrices (ΣTPs: TWP methanolic extracts, 110 ± 7 μg/g; TWP leachate (0.25 g TWP/L water), 11 ± 2.7 μg/L; roadway runoff, 40 ± 15 μg/L; creek stormwater, 59 ± 20 μg/L).

Overall, the results presented in this thesis confirmed our overall hypothesis that environmental transformations produced TPs that could contribute to residual biological activity

in the aquatic environments. These TPs are discharged in large quantities and should be evaluated in future environmental risk assessments of the synthetic steroids and rubber antioxidants. More generally, holistic assessments of the environmental transformation processes are needed for future risk assessment of high potency environmental chemicals, in order to accurately assess the fate and exposure risks of these contaminants of emerging concerns.

# Acknowledgements

It took me awhile to save enough courage for writing this acknowledgement. There are so many people and things I am grateful of during my PhD journey, and it is so hard for me to accept that this thesis is coming to an end. I am so grateful that my advisor Prof. Edward Kolodziej admitted me and took me from the airport five years ago. Thank you, Ed, for trusting me and always giving me the freedom to explore. It was hard in the middle, as you know, but I am so grateful of such training in the end because it turned me into a much better researcher scientifically and mentally. The discussion and chats with you were the fondest experiences during my PhD, no matter they happened in Zoom, in your UW/UWT/CUW offices, on the 586 bus, in the backseats of Runbang's car, or when I walked you out of More Hall/CUW. During those conversations, you taught me the way to look at data critically, the need to always assess their validity, yet the necessity to sometimes acknowledge the variable nature of the environmental systems and our experimental data. I will carry such scientific integrity learned from the Kolodziej lab, and I will always remember your advice to save some of my courage for interesting, hardcore science.

I am grateful to my committee members, Prof. Michael Dodd, Prof. Joel Baker, and Prof. Frank Turecek for their guidance and tremendous support during my graduate career. Thanks for the hard questions during my defense; they really helped me realize the strengths and weaknesses of my knowledge and reminded me that a PhD is not the end of learning but just a start. I am so fortunate to have Prof. Dodd as the co-advisor for the second half of my PhD (although we never officially say so). Prof. Dodd, the last chapter of my thesis is not possible without your expertise, dedication, availability, support, and understanding. I am so amazed by your knowledge in environmental organic chemistry and your familiarity with the literature. I still do not fully

understand how you remembered/searched for all those informative research papers from the 1950s-1990s, but I will always think of you as setting a standard for how much I should understand about my research field. I must also thank you for your openness in our conversation; I really liked getting alone with you personally. Prof. Baker, thank you for providing us with such wonderful research labs at CUW. It is a huge privilege for me to work at CUW enjoying the advanced lab and office spaces and interacting with the scientists, employees, and interns. A normal on-campus student will never have access to so many resources. Thank you also for always checking on us and bringing us your knowledge and humor! Prof. Turecek, thank you for the informative Analytical Mass Spectrometry Class in my first year and reminding me of the gas phase basicity knowledge during my defense! You brought more chemistry viewpoints into my defense; it is my honor to have you on my committee.

I am very grateful to learn from the brilliant postdoc scientists in the Kolodziej Group: Dr. Zhenyu Tian, Dr. Kathy Peter, and Dr. Bowen Du. Zhenyu and Kathy, thank you for answering all the silly questions I asked. Beyond your scientific expertise, I was always motivated by the dedication and professionalism of you two – to be frank, you two are my role models. I am especially thankful to Zhenyu for discussing the research frontiers with me, for teaching me all the professional skillsets (the use of Twitter!), and for all the food we bought and ate together. Bowen, thank you for your huge support to me professionally and personally. There are a lot of things I would not have thought of without your advice. Beyond the postdoc mentors, I also enjoyed working with my peer PhD students, Ximin Hu, Rui Wang, Ting Tang, Fan Hou, and Xingjian Yang. Thank you all for being good friends with me! Especially Ximin, huge thanks for the experimental support at the end of my PhD. I am also very fortunate to receive the experimental help from the assistants at UW CEE and CUW, including Melissa Gonzalez

(thanks for your dedication), Craig Rideout (for your jokes), David Wark (for rescuing me in hail), Christopher Wu (for your rice cooker), Alex Gipe, Kenji Lam, Hengyu Liu, and Yunsi Mou. Wish you all the best in your future career!

Beyond the CUW crew, I was also fortunate to receive the education and professional support from professors at UW CEE, especially Prof. Steve Burges, Prof. Gregory Korshin, Prof. Jess Ray, and Prof. Mike Brett. I would also like to thank my peers for the experimental and life support, including Dr. Huan He, Dr. Tess Young, Sin-Yi Liou, Stephany Wei, Bao Nguyen Quoc, Bolun Wang, Dr. Yuemei Ye, and Yasmin Farhat. Also thank Sean Yeung and Songlin Wang for supporting us in the lab!

Lastly, I would like to thank my families and my boyfriend. It is your tremendous understanding, care, and love that give me the courage to always move forward.

# Table of Contents

**Chapter 1 Introduction** ..... 1

1.1 Environmental Transformations Can Form Bioactive Products ..... 1

1.2 Identification of Transformation Products with Liquid Chromatography Coupled to Mass Spectrometry ..... 4

1.2.1 Targeted Analysis ..... 5

1.2.2 Suspect Screening ..... 6

1.2.3 Non-Targeted Analysis ..... 9

1.2.4 Effect-Directed Analysis ..... 12

1.3 Specific Aims and Rationale ..... 13

References ..... 18

**Chapter 2 A Quantification Method for Metastable Photoproducts of Trenbolone and Altrenogest Using Liquid Chromatography-Tandem Mass Spectrometry and Method Application in a Sorption Study** ..... 24

2.0 Publication and Contribution Statement ..... 24

2.1 Introduction ..... 24

2.2 Materials and Methods ..... 30

2.2.1 Reagents and Materials ..... 30

2.2.2 Sample Collection ..... 31

2.2.3 Calibration Standards ..... 32

2.2.4 Solid Phase Extraction ..... 33

2.2.5 LC-MS/MS Detection ..... 33

2.2.6 LC-MS/MS Method Validation ..... 34

2.2.7 Solvent-Water Partitioning Coefficients ..... 35

2.2.8 Batch Experiments ..... 36

2.2.9 Batch Sorption Isotherms ..... 38

2.3 Results and Discussion ..... 38

2.3.1 LC-MS/MS Method Optimization ..... 38

2.3.2 LC-MS/MS Method Validation ..... 46

2.3.3 Solvent Partition and Sorption ..... 54

2.4 Environmental Implications ..... 62

References ..... 66
Supplementary Materials ..... 71
**Chapter 3 Biotransformation of Altrenogest and its Primary Photo-Transformation Product** ..... 82
3.1 Introduction ..... 82
3.2 Materials and Methods ..... 85
3.2.1 Reagents and Materials ..... 85
3.2.2 Inocula Collection ..... 85
3.2.3 Microcosm Design ..... 86
3.2.4 Cell Viability Assessment ..... 87
3.2.5 Analytical Mass Spectrometry ..... 88
3.3 Results and Discussion ..... 89
3.3.1 Biotransformation Kinetics ..... 89
3.3.2 Biotransformation Products ..... 92
3.3.3 Biotransformation Pathways ..... 103
References ..... 106
Supplementary Materials ..... 109
**Chapter 4 Biotransformation of Current-Use Progestins Dienogest and Drospirenone in Laboratory-Scale Activated Sludge Systems Forms High-Yield Products with Altered Endocrine Activity** ..... 117
4.0 Publication Statement ..... 117
4.1 Introduction ..... 117
4.2 Materials and Methods ..... 120
4.3 Results and Discussion ..... 123
4.3.1 Biotransformation Kinetics ..... 123
4.3.2 Product Identification ..... 126
4.3.3 Transformation Pathways ..... 131
4.4 Environmental Implications ..... 139
Reference ..... 142
Supplementary Materials ..... 147
**Chapter 5 Identification and Environmental Fate of Tire Rubber-Derived Chemicals Acutely Toxic to Coho Salmon** ..... 218
5.0 Publication and Contribution Statement ..... 218

5.1 Introduction ..... 218
5.2 Materials and Methods ..... 221
5.2.1 Chemicals and Reagents ..... 221
5.2.2 TWP Leachate Fractionation ..... 222
5.2.3 Ozonation of Substituted-PPDs ..... 224
5.3 Results and Discussion ..... 230
5.3.1 Fractionation of the TWP Leachate and Identification of 6PPD-quinone ..... 230
5.3.2 PPD-quinones Formation in Ozonation of Substituted-PPDs ..... 235
5.3.3 Identification of 6PPD Ozonation TPs ..... 245
5.3.4 Environmental Occurrence of 6PPD TPs ..... 256
Reference ..... 264
Supplementary Materials ..... 268
**Chapter 6 General Conclusions** ..... 307

# Chapter 1 Introduction

## 1.1 Environmental Transformations Can Form Bioactive Products

Human society has been discharging complex chemical mixtures into the aquatic environment since beginning commercial production of organic chemicals (Hollender et al., 2017). The Chemical Abstract Services (CAS) registration now contains over 175 million unique chemical substances, including at least 30,000 - 70,000 compounds such as pharmaceuticals, biocides, surfactants, and industrial chemicals that are currently used commercially (Howard and Muir, 2010; Schwarzenbach et al., 2006). These chemicals pose the potential for adverse effects to aquatic organisms or humans upon exposure, although such risks have not been characterized rigorously for most of these compounds. Compounding the problem, organic chemicals typically form multiple transformation products (TPs) during the manufacture and use phases. After disposal into the natural and engineered environments, reactive attenuation processes such as biodegradation, chemical oxidation or reduction, photolysis, and hydrolysis further produce substantial quantities of TPs (Bletsou et al., 2015; Boxall et al., 2004; Picó and Barceló, 2015). While industrial TPs and other manufacturing "impurities" are sometimes reported, most environmental TPs have not been identified yet and pose a substantial current data gap (Bletsou et al., 2015; Picó and Barceló, 2015).

While many TPs are likely benign and unable to interact with biological pathways, some TPs can contribute significantly to the environmental risks of complex mixtures if they are: (a) formed with a high yield; (b) more persistent, mobile, or bioavailable; or (c) more toxic than the parent compounds (Escher and Fenner, 2011; Hübner et al., 2015; Picó and Barceló, 2015). Decades of research have demonstrated examples of structural conservation (conserved "pharmacophores") or conservation or even creation of bioactive properties in TPs across many

chemical classes (Boxall et al., 2004; Cwiertny et al., 2014). Accordingly, the research community has a pressing need to identify stable and/or toxic TPs, to study their environmental fate and transport, and to evaluate the potential for TP toxicity in comprehensive risk assessments of environmental contaminants (Escher and Fenner, 2011; Richardson, 2012). All of the above topics represent extensive data gaps and areas of uncertainty with respect to environmental hazard assessments of organic contaminants.

In this thesis, we focused on environmental transformations of two classes of organic contaminants: steroid hormone pharmaceuticals and industrial antiozonants used in tire rubbers. First, the environmental fate and effects of endocrine active steroid hormones represent high priority research areas because of their very high potency, structural stability, widespread use, and their potential to affect endocrine function (e.g., reproductive dysfunction after chronic exposure to estrogens) (Cwiertny et al., 2014; Kidd et al., 2007; Runnalls et al., 2010). In particular, steroid hormones are highly potent pollutants that are demonstrated to be capable of adverse effects down to and below 1 ng/L exposures (Ankley et al., 2018; Kidd et al., 2014, 2007; Lai et al., 2002; Lee et al., 2007; Oberdörster and Cheek, 2001; Zhao et al., 2016). Subsequently, their environmental transformations are of special concern because these processes often do not alter the tetracyclic backbone (i.e. the structural basis of their "pharmacophore") of steroid contaminants, and minor structural modifications often result in alterations in biological activity rather than removal (Bhatti and Khera, 2012; Cwiertny et al., 2014; Ma and Yates, 2018). For example, conjugated estrogens, which are naturally excreted by all mammals and lack direct bioactivity, can undergo hydrolytic deconjugation in the presence of fecal bacteria (e.g., *Escherichia coli*) to regenerate free, bioactive parent steroid (Khanal et al., 2006). Aqueous chlorination of 17β-estradiol removed parent compound effectively, but

produced 4-chloro-17β-estradiol, which is ~30% estrogenic as 17β-estradiol (Hu et al., 2003). Testosterone degradation by manure-derived bacteria generated boldenone (i.e., 1-dehydrotestosterone), an anabolic steroid 56% more androgenic than testosterone, as the major TP (Bauer et al., 2000; Yang et al., 2011). Progesterone "degradation" by freshwater microalgae formed androstenedione, which is a weak endogenous androgen (Peng et al., 2014). Glucocorticoids chlorination converted endogenous glucocorticoids into more potent synthetic analogs (e.g. cortisol to prednisolone), to chlororinated glucocorticoids with ~4X increased glucocorticoid activity, or to androgens (e.g. cortisone to adrenosterone) (Pflug et al., 2017). Many other examples exist across all major classes of steroid hormones and throughout many diverse types of reactive systems where contaminant "degradation" or "attenuation" is expected. Such examples illustrate conservation of bioactivity upon transformation, formation of potent products, and complex environmental hazard assessment.

These examples, and many others, highlight the need to characterize transformation processes of high-potency steroid hormones and environmental fate of the generated TPs to accurately assess their potential for environmental hazard. In this thesis, we investigated novel steroid hormone pharmaceuticals that are potent and often used widely, but also are less well characterized in the scientific literature. Specifically, project analytes include the photoproducts of trenbolone and altrenogest, compounds that occur in agricultural environments, (Chapter 2 and 3) and two synthetic progestins, dienogest and drospirenone, that are contaminants of municipal wastewaters (Chapter 4).

In addition to examining the above pharmaceutical contaminants present in agricultural runoff or wastewater effluent, we focused on understanding the fate and transformation of industrial chemicals present in roadway runoff. Particularly in the Pacific Northwest,

environmental pollution caused by urban stormwater runoff has been of high interest in recent years. Stormwater runoff transports complex mixtures of contaminants to receiving waters (Carpenter et al., 2019; Peter et al., 2020; Zgheib et al., 2012) and induces a range of lethal and sublethal impacts in invertebrates and fish, although the chemical causation of many such effects remains unknown (Kayhanian et al., 2008; Mayer et al., 2011; McIntyre et al., 2014). For example, in U.S. Pacific Northwest coho salmon (*Oncorhynchus kisutch*), stormwater exposure annually causes unexplained acute mortality when adult salmon migrate to urban creeks to reproduce, which subsequently hampers the long-term conservation of this species. In an effort to understand this phenomenon, we recently discovered that an environmental ozonation TP of *N*-(1,3-dimethylbutyl)-*N*′-phenyl-*p*-phenylenediamine (6PPD), a globally ubiquitous tire rubber antioxidant, was primarily responsible for coho salmon mortality (Chapter 5). Considering such significant potential for ecological impacts of designed reactive, and also toxic, industrial antioxidants, it is then critical to also understand the environmental transformations of other analogous antioxidants.

## 1.2 Identification of Transformation Products with Liquid Chromatography Coupled to Mass Spectrometry

Although our analytes of interest are diverse in structure and source, they are unified analytically by the common use of liquid chromatography-mass spectrometry techniques to evaluate their environmental fate and transformations. Since the development of electrospray ionization (ESI) techniques, liquid chromatography coupled to mass spectrometry (LC-MS) has expanded its popularity and become one of the most important tools for qualitative and quantitative study of environmental transformation products. Compared with gas

chromatography, LC is especially suitable for many small-molecule environmental TPs due to the frequent polar and non-volatile characteristics of many environmental contaminant classes. The analytical approaches for TP determination by environmental mass spectrometry can generally be divided into three categories: targeted analysis, suspect screening, and non-targeted analysis (Bletsou et al., 2015). **Figure 1.1** presented a flow chart of the screening procedures under these three categories, summarized by Bletsou et al (Bletsou et al., 2015).

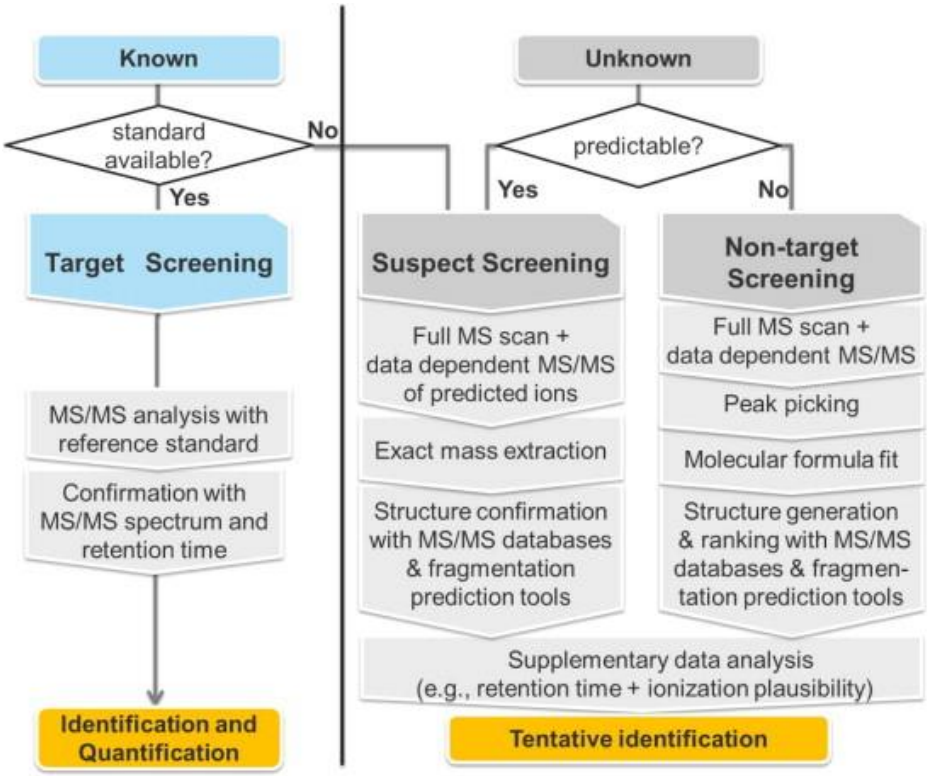


**Figure 1.1** Workflow for transformation product characterization using targeted, suspect, and non-targeted screening methodologies, produced by Bletsou et al (2015).

### 1.2.1 Targeted Analysis

Targeted analysis refers to an analytical scheme where highly specific and accurate analyses are built for a limited number of compounds with reference standards that are selected in advance; their specific transitions are monitored and their concentrations quantified based on

standard calibration, often with isotopic surrogate standards. Targeted analysis was commonly performed with low resolution (unit resolutions of ~1 Da, mass resolving factors <5000) tandem mass spectrometry instruments such as triple quadrupole (QqQ) MS, and when instrumentation is available, with high-resolution (~0.001 Da resolution, mss resolving factors >10,000) mass spectrometry (HRMS) via full scan-based methods (Bletsou et al., 2015; Evgenidou et al., 2015). The advantage of using low-resolution tandem mass spectrometry is its especially high sensitivity for targeted transition monitoring along with a broad instrumental linear response range, parameters which are crucial for quantitative trace analysis of emerging environmental contaminants and their TPs. For example, Evgenidou et al. reviewed the presence of TPs of pharmaceuticals and illicit drugs in municipal wastewater, in which most of the reported studies utilized low resolution tandem mass spectrometry (Evgenidou et al., 2015).

### 1.2.2 Suspect Screening

For targeted analysis of novel TPs, one substantial research challenge is the lack of commercial standards and corresponding analytical limitations to TP quantification methods and accuracy (Quifer-Rada et al., 2013). In addition, targeted analysis is biased toward pre-selected chemicals and cannot readily detect other high-risk but previously uncharacterized compounds. For example, Bradley et al. (2017) provided a comprehensive targeted analysis of >700 anthropogenic contaminants in 38 U.S. rivers and streams utilizing multiple methods, analytical instruments, collaboration, and numerous resources across several federal agencies (Bradley et al., 2017). This undertaking represents almost the technical limit of available conventional targeted analyses, yet even the >700 analytes is highly limited relative to the 30,000 - 70,000 compounds currently used commercially (Schwarzenbach et al., 2006), or the over 350,000 chemicals potentially present in aquatic systems (Wang et al., 2020). An alternative strategy for

characterizing environmental samples is to scan everything in them first and then prioritize and identify the compounds of most interest based on detected occurrence or other factors. Such idea has been practiced in new analytical assessment methods, including HRMS based suspect and non-target analyses, which provide more holistic and unbiased evaluations of chemical occurrence and risk relative to targeted analysis (Bletsou et al., 2015).

Suspect screening is a HRMS-based methodology that directed analytical characterization and capacity towards a pre-determined list of compounds potentially present in samples (the "suspects") based on databases or other external information (Bletsou et al., 2015). The minimum information required in these screening databases is name and molecular formula (representing an exact mass) of the prioritized suspects, which can be used to bias instrument detection or data analysis capacity towards identification of the user-generated list of suspects. Further information, such as retention time, isotope pattern, MS/MS spectra, and adduct formation, aids in subsequent identification confidence, but is not strictly necessary (Ccanccapa-Cartagena et al., 2019; García-Reyes et al., 2007; Kiefer et al., 2019). The major difference of suspect screening compared with targeted analysis is that reference standards are not required a priori, and in fact, the majority of the subsequent identification process proceeds without use of analytical standards. For application of suspect screening to TPs identification, the most important step is development of the screening databases, i.e. prediction of plausible TP structural and thus accurate mass (Bletsou et al., 2015). This can be achieved based on experimental data in literature or regulatory documents when such information is available. For example, Kiefer et al. (2019) built a database with >300 pesticides and >1000 pesticide TPs with information in the European pesticide registration literature, and then used this database to successfully screen for pesticide TPs occurrence in Swiss groundwater (Kiefer et al., 2019).

When experimental information is not available, suspect TPs databases can also be built by *in silico* prediction tools. One most commonly used platform is the Eawag/University of Minnesota Biocatalysis/Biodegradation Database Pathway Prediction System (Eawag/UM BBD/PPS; Gao et al., 2010). EAWAG BBD/PPS is a free software that predicts microbial catabolic reactions of chemical compounds based on functional groups and the biotransformation rules generated from EAWAG-BBD database or scientific literatures. The limitation of EAWAG BBD/PPS is that it is most amenable to predictions of microbial catabolic reactions, i.e. when the chemicals were the sole source of energy, carbon, nitrogen, or other essential element for microbial growth in these environments, rather than reflecting a potential for co-metabolism of contaminants that are present in trace amounts. Also, the false positive rates for EAWAG BBD/PPS predictions are typically high because of the many biotransformation pathways in the databases (Bletsou et al., 2015; Peng et al., 2014; Rösch et al., 2016). Despite these limitations, EAWAG BBD/PPS is often used to generate suspect TP screening databases or propose structures for identified TPs (Beretsou et al., 2016; Cai et al., 2021; X. Wang et al., 2020).

In reality, simple chemical intuition based upon plausible reaction pathways (i.e., expected and specific changes to mass/formula) often accounts for most identification of TPs via suspect screening. Many suspect screening databases are built upon general principles typical for many transformation reactions, where tentative TPs and associated molecular formulae can be proposed based upon the potential for common reactions such as hydroxylation, dihydroxylation, oxygen addition or loss, dehydration, dehydrogenation, etc. While changes to molecular formula and mass allow for initial detection, subsequent comparison of mass fragments (MS/MS data) often allows for confident identification of TPs, although structural uncertainty with respect to TPs often still exists with respect to specific reaction sites.

### 1.2.3 Non-Targeted Analysis

In non-targeted analysis, environmental samples are analyzed non-selectively without any *a priori* information about the underlying compounds present. After analysis, the detected compounds are filtered and prioritized based on end user needs, expert knowledge, or external information to select the most relevant components for further identification and characterization efforts (Bletsou et al., 2015; Hollender et al., 2017). Non-target analysis builds from the analytical observation of a specific molecular formula back towards structural identity based upon mass fragments, occurrence, or other information types. A typical workflow for non-targeted analysis of environmental samples, comprised of sampling, analysis, data pre-processing, feature prioritization, and compound identification, is summarized by Hollender et al., and presented in **Figure 1.2** (Hollender et al., 2017).

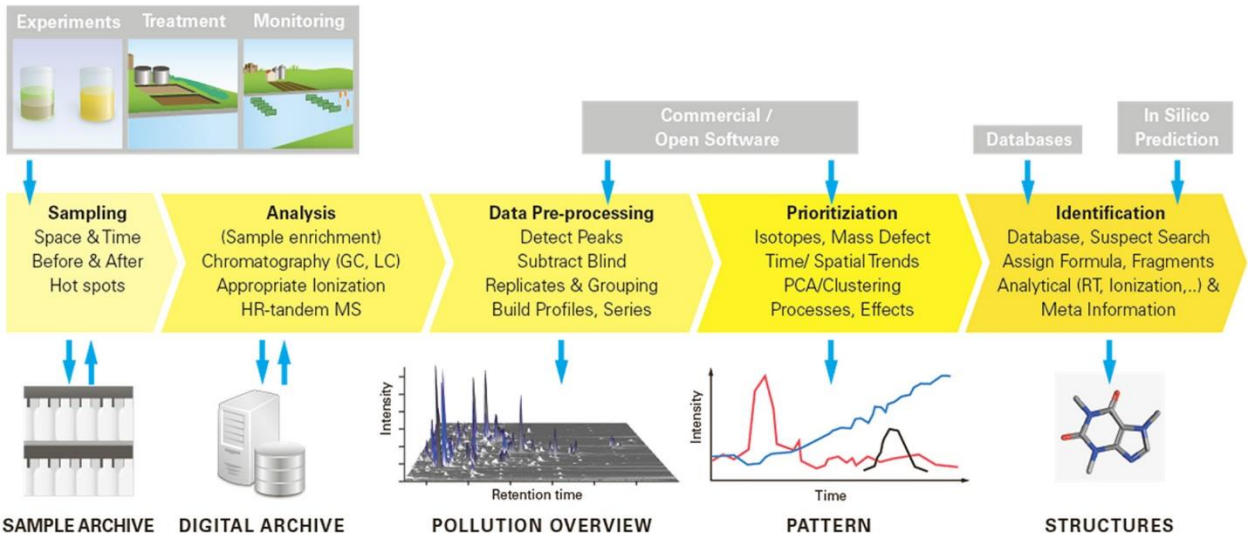


**Figure 1.2** Example non-targeted analysis workflow for environmental samples. Figure produced by Hollender et al. (2017).

Throughout most HRMS workflows, feature prioritization, which guides subsequent detection-specific efforts, is a critical step in non-targeted analysis. Approaches for this purpose can be characterized as data-driven or experiment-driven (Bletsou et al., 2015; Hollender et al.,

2017). For TP identifications, data-driven prioritization approaches included functional groups check (MS/MS neutral loss) (Zonja et al., 2015), homologous series search (mass difference or Kendrick mass defect) (Merel et al., 2017; Schollée et al., 2018; Tian et al., 2017b), and statistical approaches for temporal or spatial pattern screening (Gago-Ferrero et al., 2015; Ruff et al., 2015). Experiment-driven approaches for TP prioritization include reaction-based searches (Weizel et al., 2020), isotopically labeled incubations (Kolkman et al., 2015), or effect-directed analysis (Muschket et al., 2018). Data-driven approaches are typically faster but may produce more false positives, while the experiment-driven approaches produce more relevant features but are limited by sample throughput and experimental design.

Beyond which detected features to prioritize and allocate efforts toward, another substantial challenge for non-targeted analysis is structure elucidation from the available mass spectrometry data (Bletsou et al., 2015; Hollender et al., 2017). Several approaches have been developed to facilitate structural elucidation in non-targeted analysis, including searching external databases for spectral matches, MS/MS spectra based structure generation, and *in silico* fragmentation (Bletsou et al., 2015; Hollender et al., 2017). These approaches all enable spectral comparisons that can facilitate feature identification. However, most of these database driven approaches are best suited to "known unknowns", i.e. chemicals present in large compound databases (e.g. PubChem, ChemSpider, mzCloud, MassBank) where detailed comparative spectral information exists. In particular, environmental TPs often are not present in these databases and represent "true unknown" identifications that frequently lack appropriate spectral data in databases to enable confident identification. Therefore, the effective application of such computational methods on TP identifications is relatively limited (Tian et al., 2020). Especially for analytes such as steroid hormones, common *in silico* fragmentation software always have

poor performance due to the dynamic fragmentation chemistry (e.g. structural rearrangement during ionization) of the tetracyclic backbone (Guan et al., 2006). Additionally, compounds with common C-H-O (and sometimes N) atomic compositions are often subject to overwhelming numbers of matching chemical formulas and potential structures, including isomeric structures with substantially distinct MS/MS fragmentation patterns. Therefore, while tentative and likely structures can be derived, identification of novel TP structures often requires expert judgement on the ionization behaviors and MS/MS spectra, and confident structural confirmation relies on matching to authentic standards or NMR characterization (Bletsou et al., 2015; Prasse et al., 2011; Wick et al., 2011).

Structural identifications arising from HRMS analyses typically represent a range of potential confidence levels in the quality of the identification or structural assignment; such identification confidences are typically communicated explicitly as part of the data reporting. When the structures of the prioritized unknowns are unable to be independently confirmed, possible structures are typically proposed along with a criteria-driven identification confidence. For example, Schymanski et al. proposed a widely accepted confidence communication scale (**Figure 1.3**). In this Schymanski scale, "Level 1" indicates compounds confirmed with analytical reference standards; "Level 2" indicates highly probable structures arising from database or spectral library (Level 2a) or *in silico* (Level 2b) matches of MS/MS spectra; "Level 3" suggests tentative identifications based on full scan MS data matches; and "Level 4" suggests unequivocal molecular formula without proposed structures (Schymanski et al., 2014). Such confidence criteria better communicate relative uncertainties with respect to identifications; often initial reports might begin at Level 3 or 4 confidences, and with subsequent effort and

confirmation, rise higher in confidence to Level 1 or 2 identifications as prioritization workflows dedicate effort to more important or interesting contaminants or related TPs.

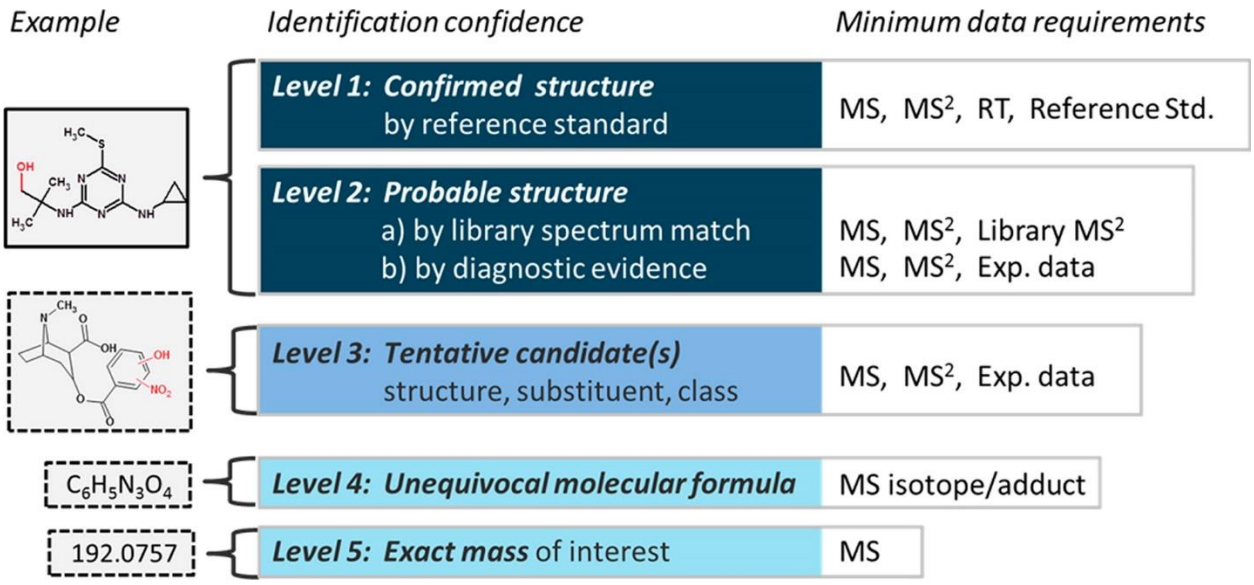


**Figure 1.3** Schymanski scale for communication of structural identification confidence in non-targeted analysis. Figure produced by Schymanski et al. (2014).

### 1.2.4 Effect-Directed Analysis

Effect-directed analysis (EDA) is an experimental approach to data-driven prioritization of chemical causation when unknown contaminants or pollutants in a complex mixture are driving some sort of biological response. Notably, EDA is especially amenable to analytical characterization with non-targeted HRMS: both techniques are data-driven methodologies that are intended to be relatively unbiased and open-ended conceptually. EDA is a screening technique utilizing effect based upon repeated testing across some type of biological endpoint, followed by iterative sequential fractionation and qualitative chemical analysis to identify the causative chemical(s) leading to a specific biological response (Brack, 2003; Brack et al., 2016). Steps in EDA usually include extraction, enrichment, stepwise fractionation to manipulate the

composition of the complex environmental mixture, followed by assessment of a specific biological response (Brack et al., 2016). Coupled with structural identification techniques such as high resolution tandem mass spectrometry (HRMS/MS) and nuclear magnetic resonance (NMR), EDA has been successfully applied to identify estrogenic (Weiss et al., 2009), antiandrogenic (Muschket et al., 2018; Thomas et al., 2009), and genotoxic compounds (Durant et al., 1998; Tian et al., 2017a) among many others. For instance, Thomas et al. identified petrogenic naphthenic acids as responsible for anti-androgenic activity in produced water from offshore oil production (Thomas et al., 2009). Muschket et al. identified 4-methyl-7-diethylaminocoumarin (Coumarin 47) as the major cause of anti-androgenicity in German river water (Muschket et al., 2018). Fang et al. revealed that fatty acids accounted for 30-50% of the human peroxisome proliferator-activated nuclear receptor gamma (PPARγ) agonism observed in indoor dust (Fang et al., 2015). Such techniques are especially amenable to efforts to diagnose the chemical causation of the unexplained lethal and sublethal impacts of urban stormwater runoff on aquatic organisms (Kayhanian et al., 2008; Mayer et al., 2011; McIntyre et al., 2014). Here, we focused on integrating EDA with HRMS detection to investigate the chemical basis of the lethal URMS toxicity events observed in U.S. Pacific Northwest coho salmon.

## 1.3 Specific Aims and Rationale

In this thesis, we utilized targeted analysis, suspect screening, non-targeted analysis, and effect-directed analysis techniques to characterize the environmental transformations of two classes of trace organic contaminants: steroid hormone pharmaceuticals and industrial antiozonants used in tire rubbers. The general aims of these research efforts included characterizing the fate and environmental occurrence of these compounds by determining TP identity using environmental mass spectrometry techniques.

*Aim 1 (Chapter 2): Targeted quantification of metastable photoproducts of trenbolone and altrenogest and evaluation of their relative sorption behaviors*

Trenbolone acetate (TBA) and altrenogest (ALT) are potent, endocrine active steroid hormones widely used in industrialized animal agriculture. TBA is used as a growth promoter in beef cattle production, ALT as an estrus synchronizer progestin in swine and breeding mares. Upon discharge, TBA metabolites (17α-trenbolone, 17β-trenbolone, trendione) and ALT can exhibit rapid photoreactions to form metastable 5- and 12-hydroxy photoproducts (for trenbolone) or cycloaddition and hydroxy photoproducts (for ALT). These photoproducts can revert back to the parent structures in dark, representing a coupled photohydration-thermal dehydration transformation mechanism in sunlight or under light/dark conditions (Qu et al., 2013). Given their rapid kinetics, these photoproducts dominated the environmental fate of trenbolone and ALT in sunlit systems, yet their quantification remains challenging due to the lack of analytical standards and the chemical metastability. Thus, their environmental fate has not been fully characterized. In Chapter 2, we developed a LC-MS/MS based targeted quantification method for metastable photoproducts of trenbolone and altrenogest and applied the method to a soil sorption study. We overcame the lack of commercial TP standards via in situ generation of the TPs and quantified these TPs based on reported NMR-based yields of the photohydration reactions.

*Aim 2 (Chapter 3 and 4): Identification of biotransformation products of novel progestins with suspect screening and non-targeted analysis.*

As described above, ALT is a potent synthetic progestin largely used in equine and swine farm agroecosystems. In sunlight, ALT reacts rapidly (~25s half-life) to form a bioactive 2 + 2 cycloaddition product (ALT-CAP) in the aquatic environment (Wammer et al., 2016). Therefore,

ALT and ALT-CAP represent the predominant chemical species of ALT discharged into aquatic environments, but their biotransformation fate outcomes in the aquatic environments are currently unknown.

In wastewater effluent systems, dienogest (DIE) and drospirenone (DRO) are two fourth-generation (most modern class, designed to avoid harmful side effects and promote efficacy) synthetic progestins widely used as oral contraceptives. Despite their increasing detection in wastewaters and surface waters, their fate during biological wastewater treatment is unclear. In Chapters 3 and 4, we combined suspect screening and non-targeted analysis approaches to identify potential biotransformation products of these four progestins in representative mixed culture laboratory-scale bioreactors. The environmental TPs of progestins (and other potent steroids) are especially of concern because simple environmental transformations often do not alter their tetracyclic backbone and C-21 progestins can sometimes be transformed into C-19 androgens or C-18 estrogens products analogous to the biochemical pathways expected for cholesterol metabolism. Therefore, these TPs are prone to exhibit retained or altered binding activities to hormone receptors. To accomplish this aim, we created customized TP lists for suspect screening based on reported biotransformation pathways of these or similar steroid hormones. We then used Agilent software packages (MassHunter Profinder (B.08.00) for feature extraction and alignment, Mass Profiler Professional (B.13.00) for feature prioritization) and XCMS Online for non-targeted TP identifications. Reaction-based (bioactive vs controls) feature prioritization was employed, and TP structural elucidation largely depended on manual interpretation of the ionization behaviors and diagnostic MS/MS fragments.

*Aim 3 (Chapter 5): Identification of the primary casual toxicant for coho salmon acute mortality with effect-directed analysis and subsequent environmental fate studies.*

As discussed above, stormwater exposure causes widespread unexplained acute mortality to adult coho salmon in urban and near-urban creeks of U.S. Pacific Northwest (Feist et al., 2017; Scholz et al., 2011). Previous studies have correlated the toxicant(s) to multilane roadway runoff and vehicle tire rubbers (Feist et al., 2017, 2011; Peter et al., 2018), but the causal toxicant(s) remained unknown. Our laboratory started a large collaborative research project, led by Dr. Zhenyu Tian (postdoc scientist of our group), to develop an EDA workflow to identify the salmon toxicant(s) from toxic aqueous leachates of tire tread wear particles (TWPs). After purification of the TWP leachate with reverse phase and normal phase large columns by Dr. Tian, Zhao and Tian developed the orthogonal HPLC fractionation steps that effectively separated the pure toxicant from ~600 chemicals in the purified TWP leachate. After much effort, and via many contributions from collaborators, the toxicant was identified as a quinone transformation product of 6PPD (*N*-(1,3-dimethylbutyl)-*N*′-phenyl-p-phenylenediamine), an antioxidant widely used in tire rubbers (mass fraction, 0.4-2%) (R.T. Vanderbilt Company, 2010). In tire rubbers, 6PPD scavenges ground-level atmospheric ozone, and potentially other oxidants like molecular oxygen to prevent oxidation of rubber elastomers (Huntink, 2003; Lattimer et al., 1983).

Beyond 6PPD-quinone, ozonation of 6PPD produces a suite of other TPs that are potentially discharged into the aquatic environments in large quantities. However, the identities and environmental levels of these TPs are currently unknown. In addition to 6PPD, other substituted paraphenylene diamines (substituted-PPDs, e.g., IPPD, 7PPD, DPPD, DTPD, DNP) are also used as antioxidants across a range of products (Huntink et al., 2004) and have been detected in multiple environmental matrices. Ozonation of these substituted-PPDs can potentially produce toxic PPD-quinones in the indoor and outdoor environment, yet quinone formation

behaviors of the substituted-PPDs as a class is unclear. In the second half of Chapter 5, we studied the ozonation TPs of 6PPD and other substituted-PPDs using heterogeneous gas-phase ozonation in a chamber reactor. We screened for PPD-quinones from the substituted-PPDs with structural confirmation through synthetic standards (From Dr. Kelly E. Kim at UWT). We then identified the ozonation TPs of 6PPD with UPLC-HRMS based non-targeted analysis, and proposed TP structures based on spectral interpretation and standard confirmation. Lastly, the identified 6PPD TPs were retrospectively quantified in archived stocks of TWP solvent extracts, TWP leachates, roadway runoffs, and creek stormwaters, to demonstrate their environmental relevance and transport behaviors.

## References


Ankley, G.T., Coady, K.K., Gross, M., Holbech, H., Levine, S.L., Maack, G., Williams, M., 2018. A critical review of the environmental occurrence and potential effects in aquatic vertebrates of the potent androgen receptor agonist 17β-trenbolone. Environ. Toxicol. Chem. 37, 2064–2078

Bauer, E.R.S., Daxenberger, A., Petri, T., Sauerwein, H., Meyer, H.H.D., 2000. Characterisation of the affinity of different anabolics and synthetic hormones to the human androgen receptor, human sex hormone binding globulin and to the bovine progestin receptor. APMIS 108, 838–846.

Beretsou, V.G., Psoma, A.K., Gago-Ferrero, P., Aalizadeh, R., Fenner, K., Thomaidis, N.S., 2016. Identification of biotransformation products of citalopram formed in activated sludge. Water Res. 103, 205–214.

Bhatti, H.N., Khera, R.A., 2012. Biological transformations of steroidal compounds: A review. Steroids 77, 1267–1290.

Bletsou, A.A., Jeon, J., Hollender, J., Archontaki, E., Thomaidis, N.S., 2015. Targeted and non-targeted liquid chromatography-mass spectrometric workflows for identification of transformation products of emerging pollutants in the aquatic environment. TrAC Trends Anal. Chem. 66, 32–44.

Boxall, A.B.A., Sinclair, C.J., Fenner, K., Kolpin, D., Maund, S.J., 2004. Peer reviewed: When synthetic chemicals degrade in the environment. Environ. Sci. Technol. 38, 368A-375A.

Brack, W., 2003. Effect-directed analysis: a promising tool for the identification of organic toxicants in complex mixtures? Anal. Bioanal. Chem. 377, 397–407.

Brack, W., Ait-Aissa, S., Burgess, R.M., Busch, W., Creusot, N., Di Paolo, C., Escher, B.I., Mark Hewitt, L., Hilscherova, K., Hollender, J., Hollert, H., Jonker, W., Kool, J., Lamoree, M., Muschket, M., Neumann, S., Rostkowski, P., Ruttkies, C., Schollee, J., Schymanski, E.L., Schulze, T., Seiler, T.-B., Tindall, A.J., De Aragão Umbuzeiro, G., Vrana, B., Krauss, M., 2016. Effect-directed analysis supporting monitoring of aquatic environments — An in-depth overview. Sci. Total Environ. 544, 1073–1118.

Bradley, P.M., Journey, C.A., Romanok, K.M., Barber, L.B., Buxton, H.T., Foreman, W.T., Furlong, E.T., Glassmeyer, S.T., Hladik, M.L., Iwanowicz, L.R., Jones, D.K., Kolpin, D.W., Kuivila, K.M., Loftin, K.A., Mills, M.A., Meyer, M.T., Orlando, J.L., Reilly, T.J., Smalling, K.L., Villeneuve, D.L., 2017. Expanded target-chemical analysis reveals extensive mixed-organic-contaminant exposure in U.S. streams. Environ. Sci. Technol. 51, 4792–4802.

Cai, W., Ye, P., Yang, B., Shi, Z., Xiong, Q., Gao, F., Liu, Y., Zhao, J., Ying, G., 2021. Biodegradation of typical azole fungicides in activated sludge under aerobic conditions. J. Environ. Sci. 103, 288–297.

Carpenter, C.M.G., Wong, L.Y.J., Johnson, C.A., Helbling, D.E., 2019. Fall creek monitoring station: highly resolved temporal sampling to prioritize the identification of nontarget micropollutants in a small stream. Environ. Sci. Technol. 53, 77–87

Ccanccapa-Cartagena, A., Pico, Y., Ortiz, X., Reiner, E.J., 2019. Suspect, non-target and target screening of emerging pollutants using data independent acquisition: Assessment of a Mediterranean River basin. Sci. Total Environ. 687, 355–368.

C. Pflug, N., Kupsco, A., P. Kolodziej, E., Schlenk, D., M. Teesch, L., B. Gloer, J., M. Cwiertny, D., 2017. Formation of bioactive transformation products during glucocorticoid chlorination. Environ. Sci. Water Res. Technol. 3, 450–461.

Cwiertny, D.M., Snyder, S.A., Schlenk, D., Kolodziej, E.P., 2014. Environmental designer drugs: When transformation may not eliminate risk. Environ. Sci. Technol. 48, 11737–11745

Durant, J.L., Lafleur, A.L., Plummer, E.F., Taghizadeh, K., Busby, W.F., Thilly, W.G., 1998. Human lymphoblast mutagens in urban airborne particles. Environ. Sci. Technol. 32, 1894–1906.

Escher, B.I., Fenner, K., 2011. Recent advances in environmental risk assessment of transformation products. Environ. Sci. Technol. 45, 3835–3847.

Evgenidou, E.N., Konstantinou, I.K., Lambropoulou, D.A., 2015. Occurrence and removal of transformation products of PPCPs and illicit drugs in wastewaters: A review. Sci. Total Environ. 505, 905–926.

Fang, M., Webster, T.F., Stapleton, H.M., 2015. Effect-directed analysis of human peroxisome proliferator-activated nuclear receptors (PPARγ1) Ligands in Indoor Dust. Environ. Sci. Technol. 49, 10065–10073.

Feist, B.E., Buhle, E.R., Baldwin, D.H., Spromberg, J.A., Damm, S.E., Davis, J.W., Scholz, N.L., 2017. Roads to ruin: conservation threats to a sentinel species across an urban gradient. Ecol. Appl. 27, 2382–2396.

Gago-Ferrero, P., Schymanski, E.L., Bletsou, A.A., Aalizadeh, R., Hollender, J., Thomaidis, N.S., 2015. Extended suspect and non-target strategies to characterize emerging polar organic contaminants in raw wastewater with LC-HRMS/MS. Environ. Sci. Technol. 49, 12333–12341.

Gao, J., Ellis, L.B.M., Wackett, L.P., 2010. The University of Minnesota Biocatalysis/Biodegradation Database: improving public access. Nucleic Acids Res. 38, D488–D491.

García-Reyes, J.F., Hernando, M.D., Molina-Díaz, A., Fernández-Alba, A.R., 2007. Comprehensive screening of target, non-target and unknown pesticides in food by LC-TOF-MS. TrAC Trends Anal. Chem. 26, 828–841.

Guan, F., Soma, L.R., Luo, Y., Uboh, C.E., Peterman, S., 2006. Collision-induced dissociation pathways of anabolic steroids by electrospray ionization tandem mass spectrometry. J. Am. Soc. Mass Spectrom. 17, 477–489.

Hollender, J., Schymanski, E.L., Singer, H.P., Ferguson, P.L., 2017. nontarget screening with high resolution mass spectrometry in the environment: Ready to go? Environ. Sci. Technol. 51, 11505–11512.

Howard, P.H., Muir, D.C.G., 2010. Identifying new persistent and bioaccumulative organics among chemicals in commerce. Environ. Sci. Technol. 44, 2277–2285.

Hu, J., Cheng, S., Aizawa, T., Terao, Y., Kunikane, S., 2003. Products of aqueous chlorination of 17β-estradiol and their estrogenic activities. Environ. Sci. Technol. 37, 5665–5670.

Hübner, U., von Gunten, U., Jekel, M., 2015. Evaluation of the persistence of transformation products from ozonation of trace organic compounds – A critical review. Water Res. 68, 150–170.

Huntink, N.M., 2003. Durability of rubber products: Development of new antidegradants for long-term protection.

Huntink, N.M., Datta, R.N., Noordermeer, J.W.M., 2004. Addressing durability of rubber compounds. Rubber Chem. Technol. 77, 476–511.
Kayhanian, M., Stransky, C., Bay, S., Lau, S.-L., Stenstrom, M.K., 2008. Toxicity of urban highway runoff with respect to storm duration. Sci. Total Environ. 389, 386–406.
Khanal, S.K., Xie, B., Thompson, M.L., Sung, S., Ong, S.-K., van Leeuwen, J. (Hans), 2006. Fate, transport, and biodegradation of natural estrogens in the environment and engineered systems. Environ. Sci. Technol. 40, 6537–6546.
Kidd, K.A., Blanchfield, P.J., Mills, K.H., Palace, V.P., Evans, R.E., Lazorchak, J.M., Flick, R.W., 2007. Collapse of a fish population after exposure to a synthetic estrogen. Proc. Natl. Acad. Sci. 104, 8897–8901.
Kidd, K.A., Paterson, M.J., Rennie, M.D., Podemski, C.L., Findlay, D.L., Blanchfield, P.J., Liber, K., 2014. Direct and indirect responses of a freshwater food web to a potent synthetic oestrogen. Philos. Trans. R. Soc. B Biol. Sci. 369, 20130578.
Kiefer, K., Müller, A., Singer, H., Hollender, J., 2019. New relevant pesticide transformation products in groundwater detected using target and suspect screening for agricultural and urban micropollutants with LC-HRMS. Water Res. 165, 114972.
Kolkman, A., Martijn, B.J., Vughs, D., Baken, K.A., van Wezel, A.P., 2015. Tracing nitrogenous disinfection byproducts after medium pressure uv water treatment by stable isotope labeling and high resolution mass spectrometry. Environ. Sci. Technol. 49, 4458–4465.
Lai, K.M., Scrimshaw, M.D., Lester, J.N., 2002. The effects of natural and synthetic steroid estrogens in relation to their environmental occurrence. Crit. Rev. Toxicol. 32, 113–132.
Lattimer, R.P., Hooser, E.R., Layer, R.W., Rhee, C.K., 1983. Mechanisms of ozonation of n-(1,3-dimethylbutyl)-n′-phenyl-p-phenylenediamine. Rubber Chem. Technol. 56, 431–439
Lee, L.S., Carmosini, N., Sassman, S.A., Dion, H.M., Sepúlveda, M.S., 2007. Agricultural contributions of antimicrobials and hormones on soil and water quality, Adv. Agron. 93, 1–68.
Ma, L., Yates, S.R., 2018. A review on structural elucidation of metabolites of environmental steroid hormones via liquid chromatography–mass spectrometry. TrAC Trends Anal. Chem. 109, 142–153.
Mayer, T., Rochfort, Q., Marsalek, J., Parrott, J., Servos, M., Baker, M., McInnis, R., Jurkovic, A., Scott, I., 2011. Environmental characterization of surface runoff from three highway sites in Southern Ontario, Canada: 2. Toxicology. Water Qual. Res. J. 46, 121–136.
McIntyre, J.K., Davis, J.W., Incardona, J.P., Stark, J.D., Anulacion, B.F., Scholz, N.L., 2014. Zebrafish and clean water technology: Assessing soil bioretention as a protective treatment for toxic urban runoff. Sci. Total Environ. 500–501, 173–180.
Merel, S., Lege, S., Yanez Heras, J.E., Zwiener, C., 2017. Assessment of n-oxide formation during wastewater ozonation. Environ. Sci. Technol. 51, 410–417.
Muschket, M., Di Paolo, C., Tindall, A.J., Touak, G., Phan, A., Krauss, M., Kirchner, K., Seiler, T.-B., Hollert, H., Brack, W., 2018. Identification of unknown antiandrogenic compounds in surface waters by effect-directed analysis (EDA) using a parallel fractionation approach. Environ. Sci. Technol. 52, 288–297.
Oberdörster, E., Cheek, A.O., 2001. Gender benders at the beach: Endocrine disruption in marine and estuarine organisms. Environ. Toxicol. Chem. 20, 23–36.
Peng, F.-Q., Ying, G.-G., Yang, B., Liu, S., Lai, H.-J., Liu, Y.-S., Chen, Z.-F., Zhou, G.-J., 2014. Biotransformation of progesterone and norgestrel by two freshwater microalgae

(Scenedesmus obliquus and Chlorella pyrenoidosa): Transformation kinetics and products identification. Chemosphere 95, 581–588.
Peter, K.T., Hou, F., Tian, Z., Wu, C., Goehring, M., Liu, F., Kolodziej, E.P., 2020. More than a first flush: urban creek storm hydrographs demonstrate broad contaminant pollutographs. Environ. Sci. Technol. 54, 6152–6165.
Peter, K.T., Tian, Z., Wu, C., Lin, P., White, S., Du, B., McIntyre, J.K., Scholz, N.L., Kolodziej, E.P., 2018. Using high-resolution mass spectrometry to identify organic contaminants linked to urban stormwater mortality syndrome in coho salmon. Environ. Sci. Technol. 52, 10317–10327.
Picó, Y., Barceló, D., 2015. Transformation products of emerging contaminants in the environment and high-resolution mass spectrometry: a new horizon. Anal. Bioanal. Chem. 407, 6257–6273.
Prasse, C., Wagner, M., Schulz, R., Ternes, T.A., 2011. Biotransformation of the Antiviral Drugs Acyclovir and Penciclovir in Activated Sludge Treatment. Environ. Sci. Technol. 45, 2761–2769.
Qu, S., Kolodziej, E.P., Long, S.A., Gloer, J.B., Patterson, E.V., Baltrusaitis, J., Jones, G.D., Benchetler, P.V., Cole, E.A., Kimbrough, K.C., Tarnoff, M.D., Cwiertny, D.M., 2013. Product-to-parent reversion of trenbolone: unrecognized risks for endocrine disruption. Science 342, 347–351.
Quifer-Rada, P., Martínez-Huélamo, M., Jáuregui, O., Chiva-Blanch, G., Estruch, R., Lamuela-Raventós, R.M., 2013. analytical condition setting a crucial step in the quantification of unstable polyphenols in acidic conditions: Analyzing prenylflavanoids in biological samples by liquid chromatography–electrospray ionization triple quadruple mass spectrometry. Anal. Chem. 85, 5547–5554.
Richardson, S.D., 2012. Environmental Mass Spectrometry: Emerging Contaminants and Current Issues. Anal. Chem. 84, 747–778.
Rösch, A., Anliker, S., Hollender, J., 2016. How Biotransformation Influences Toxicokinetics of Azole Fungicides in the Aquatic Invertebrate Gammarus pulex. Environ. Sci. Technol. 50, 7175–7188.
R.T. Vanderbilt Company, 2010. The Vanderbilt rubber handbook.
Ruff, M., Mueller, M.S., Loos, M., Singer, H.P., 2015. Quantitative target and systematic non-target analysis of polar organic micro-pollutants along the river Rhine using high-resolution mass-spectrometry – Identification of unknown sources and compounds. Water Res. 87, 145–154.
Runnalls, T.J., Margiotta-Casaluci, L., Kugathas, S., Sumpter, J.P., 2010. Pharmaceuticals in the aquatic environment: Steroids and anti-steroids as high priorities for research. hum. ecol. Risk Assess. Int. J. 16, 1318–1338.
Schollée, J.E., Bourgin, M., von Gunten, U., McArdell, C.S., Hollender, J., 2018. Non-target screening to trace ozonation transformation products in a wastewater treatment train including different post-treatments. Water Res. 142, 267–278.
Scholz, N.L., Myers, M.S., McCarthy, S.G., Labenia, J.S., McIntyre, J.K., Ylitalo, G.M., Rhodes, L.D., Laetz, C.A., Stehr, C.M., French, B.L., McMillan, B., Wilson, D., Reed, L., Lynch, K.D., Damm, S., Davis, J.W., Collier, T.K., 2011. Recurrent die-offs of adult coho salmon returning to spawn in puget sound lowland urban streams. PLOS ONE 6, e28013

Schwarzenbach, R.P., Escher, B.I., Fenner, K., Hofstetter, T.B., Johnson, C.A., Gunten, U. von, Wehrli, B., 2006. The challenge of micropollutants in aquatic systems. Science 313, 1072–1077.

Schymanski, E.L., Jeon, J., Gulde, R., Fenner, K., Ruff, M., Singer, H.P., Hollender, J., 2014. Identifying small molecules via high resolution mass spectrometry: communicating confidence. Environ. Sci. Technol. 48, 2097–2098.

Thomas, K.V., Langford, K., Petersen, K., Smith, A.J., Tollefsen, K.E., 2009. Effect-directed identification of naphthenic acids as important in vitro xeno-estrogens and anti-androgens in north sea offshore produced water discharges. Environ. Sci. Technol. 43, 8066–8071.

Tian, Z., Gold, A., Nakamura, J., Zhang, Z., Vila, J., Singleton, D.R., Collins, L.B., Aitken, M.D., 2017a. Nontarget analysis reveals a bacterial metabolite of pyrene implicated in the genotoxicity of contaminated soil after bioremediation. Environ. Sci. Technol. 51, 7091–7100.

Tian, Z., Peter, K.T., Gipe, A.D., Zhao, H., Hou, F., Wark, D.A., Khangaonkar, T., Kolodziej, E.P., James, C.A., 2020. Suspect and nontarget screening for contaminants of emerging concern in an urban estuary. Environ. Sci. Technol. 54, 889–901.

Tian, Z., Vila, J., Wang, H., Bodnar, W., Aitken, M.D., 2017b. Diversity and abundance of high-molecular-weight azaarenes in pah-contaminated environmental samples. Environ. Sci. Technol. 51, 14047–14054.

Wammer, K.H., Anderson, K.C., Erickson, P.R., Kliegman, S., Moffatt, M.E., Berg, S.M., Heitzman, J.A., Pflug, N.C., McNeill, K., Martinovic-Weigelt, D., Abagyan, R., Cwiertny, D.M., Kolodziej, E.P., 2016. Environmental photochemistry of altrenogest: photoisomerization to a bioactive product with increased environmental persistence via reversible photohydration. Environ. Sci. Technol. 50, 7480–7488.

Wang, X., Yu, N., Yang, J., Jin, L., Guo, H., Shi, W., Zhang, X., Yang, L., Yu, H., Wei, S., 2020. Suspect and non-target screening of pesticides and pharmaceuticals transformation products in wastewater using QTOF-MS. Environ. Int. 137, 105599.

Wang, Z., Walker, G.W., Muir, D.C.G., Nagatani-Yoshida, K., 2020. Toward a Global Understanding of chemical pollution: A first comprehensive analysis of national and regional chemical inventories. Environ. Sci. Technol. 54, 2575–2584.

Weiss, J.M., Hamers, T., Thomas, K.V., van der Linden, S., Leonards, P.E.G., Lamoree, M.H., 2009. Masking effect of anti-androgens on androgenic activity in European river sediment unveiled by effect-directed analysis. Anal. Bioanal. Chem. 394, 1385–1397.

Weizel, A., Schlüsener, M.P., Dierkes, G., Wick, A., Ternes, T.A., 2020. Analysis of the aerobic biodegradation of glucocorticoids: Elucidation of the kinetics and transformation reactions. Water Res. 174, 115561.

Wick, A., Wagner, M., Ternes, T.A., 2011. Elucidation of the transformation pathway of the opium alkaloid codeine in biological wastewater treatment. Environ. Sci. Technol. 45, 3374–3385.

Yang, Y.-Y., Pereyra, L.P., Young, R.B., Reardon, K.F., Borch, T., 2011. Testosterone-mineralizing culture enriched from swine manure: characterization of degradation pathways and microbial community composition. Environ. Sci. Technol. 45, 6879–6886.

Zgheib, S., Moilleron, R., Chebbo, G., 2012. Priority pollutants in urban stormwater: Part 1 – Case of separate storm sewers. Water Res., Special Issue on Stormwater in urban areas 46, 6683–6692.

Zhao, Y., Zhang, K., Fent, K., 2016. Corticosteroid fludrocortisone acetate targets multiple end points in zebrafish (Danio rerio) at low concentrations. Environ. Sci. Technol. 50, 10245–10254.

Zonja, B., Delgado, A., Pérez, S., Barceló, D., 2015. LC-HRMS suspect screening for detection-based prioritization of iodinated contrast media photodegradates in surface waters. Environ. Sci. Technol. 49, 3464–3472.

# Chapter 2

# A Quantification Method for Metastable Photoproducts of Trenbolone and Altrenogest Using Liquid Chromatography-Tandem Mass Spectrometry and Method Application in a Sorption Study

## 2.0 Publication and Contribution Statement

This chapter was summarized from the two collaborative publications below, mostly including sections for which HZ led the research effort. For Kenyon et al 2019, PTK developed and optimized the analytical method and wrote the original draft, while HZ optimized and validated the analytical method and led manuscript revision after the original draft. For Yang et al 2019, XY conducted and wrote the column transport study (not included in this thesis), while HZ conducted and wrote the static sorption study.

1. P. T. Kenyon,[*] H. Zhao,[*] X. Yang, C. Wu, D. M. Cwiertny and E. P. Kolodziej, Detection and quantification of metastable photoproducts of trenbolone and altrenogest using liquid chromatography-tandem mass spectrometry, J. Chromatogr. A, 2019, 1603, 150–159.
2. X. Yang,[*] H. Zhao,[*] D. M. Cwiertny and E. P. Kolodziej, Sorption and transport of trenbolone and altrenogest photoproducts in soil-water systems. Environ. Sci.: Processes Impacts, 2019, 21, 1650-1663.

[*] Equal contribution first authorship.

## 2.1 Introduction

Agricultural animal production can result in the discharge of various bioactive pharmaceuticals to soils, surface and ground waters near such facilities (Bartelt-Hunt et al., 2012; Blackwell et al., 2015; Webster et al., 2012). These synthetic pharmaceuticals, often highly potent, can pose ecological risks through mechanisms of endocrine disruption and teratogenicity (Ankley et al., 2018; Olmstead et al., 2012; Orlando et al., 2004). As one example, trienone steroids are a group of highly potent steroidal pharmaceuticals that include the androgenic trenbolone acetate (TBA), widely used as a growth promoter in beef cattle production (Ankley et al., 2018), and altrenogest (ALT), a progestin used as an estrus synchronizer in swine and breeding mares (Squires, 2008; Squires et al., 1983; van Leeuwen et al., 2011).

TBA is discharged to agro-ecosystems as phase I metabolites including 17α-trenbolone (17α-TBOH), 17β-trenbolone (17β-TBOH), and trendione (TBO) (Blackwell et al., 2014; Schiffer B et al., 2001). The TBA metabolites are subsequently detected in agroecosystems (Khan and Lee, 2012; Qu et al., 2012) and transported to surrounding environments principally via precipitation and irrigation runoff (Biswas et al., 2017), along with airborne particulate matter (Blackwell et al., 2015) or manure dispersal (Khan et al., 2008). In addition, TBA metabolites can disrupt endocrine function of aquatic organisms at low concentrations (Ankley et al., 2018). For example, 11 ng/L of 17α-TBOH reduced fecundity in fathead minnows (Jensen et al., 2006), and 9 ng/L of 17β-TBOH induced male-biased sex ratios in zebrafish (Morthorst et al., 2010). Synthetic progestins also are capable of disrupting endocrine function, although they have received less attention from the research community (Fent, 2015; Kumar et al., 2015; Orlando and Ellestad, 2014). In the United States, ALT usage is estimated at several thousand kg annually across ~3,600,000 horses and ~66,000,000 swine (Wammer et al., 2016). Notably, using *in vitro* assays, Wammer et al. (2016) demonstrated potent androgenic activity for both ALT and its primary photoproducts, a characteristic typically linked to endocrine disrupting potential (Wammer et al., 2016). Also, a recent (2018) exposure alert from U.S. FDA highlighted over 137 cases of incidental ALT exposure in humans resulting in abnormal menstrual cycles in females and decreased libido in males (U.S. FDA, 2018).

Recent research documents an increasing focus on transformation products (TPs) of toxic or bioactive contaminants formed in environmental (e.g., photolysis, biodegradation) or engineered (e.g., chlorination, advanced oxidation) systems (Cwiertny et al., 2014; von Gunten, 2018; Wang et al., 2018). However, most TP research focuses on structural elucidation and bioactivity assessment (Fu et al., 2018; Wong et al., 2019; Tian et al., 2017b); quantifying TP

occurrence and fate in aquatic environments remains difficult due to a lack of commercial standards and corresponding limitations to quantification methods. For TBA metabolites and ALT, detection of such bioactive TPs is critical to accurately characterize their fate and environmental risks. In the photic zone, trenbolone metabolites react rapidly (25-35 minute half-lives, $k_{obs}$ = 0.0254-0.0213 $min^{-1}$) via photohydration to form 5- and 12-hydroxy photoproducts (**Figure 2.1**) (Kolodziej et al., 2013; Qu et al., 2012). In the dark and over time scales of days, temperature and pH sensitive thermal dehydration can occur to revert these metastable photoproducts back to parent structures (Qu et al., 2013). Thus, up to 90% of 17α-TBOH, 65% of 17β-TBOH, and 30% of TBO parent mass can regenerate from photoproducts under some conditions (Qu et al., 2013). ALT is highly photosensitive, reacting very rapidly in sunlight (~25s half-life, $k_{obs}$ = 0.027 ± 0.002 $s^{-1}$) to form a 2+2 cycloaddition photoproduct (ALT-CAP). ALT-CAP further reacts (~40 s half-life, $k_{obs}$ ~ 0.02 $s^{-1}$) via photohydration to form ALT-CAP-OH, which can thermally dehydrate back to ALT-CAP (**Figure 2.1**) (Wammer et al., 2016). Therefore, in any sunlit systems, TBA metabolites and ALT are present in agricultural runoff not only as the parent compounds but also as hydroxylated and isomeric photoproducts. *In vivo* (for trenbolone photoproducts) and *in vitro* (for ALT photoproducts) bioassays have also indicated that both the trenbolone and ALT photoproducts have bioactivity distinct from that of the parent molecules and will themselves contribute to mixture endocrine disrupting potential (Kolodziej et al., 2013; Wammer et al., 2016). The complex reaction dynamics and retained bioactivity in these TPs illustrates the need for their quantitative analysis in agricultural receiving waters. However, to the best of our knowledge, analytical methods for these metastable trenbolone and ALT photoproducts have not been reported.

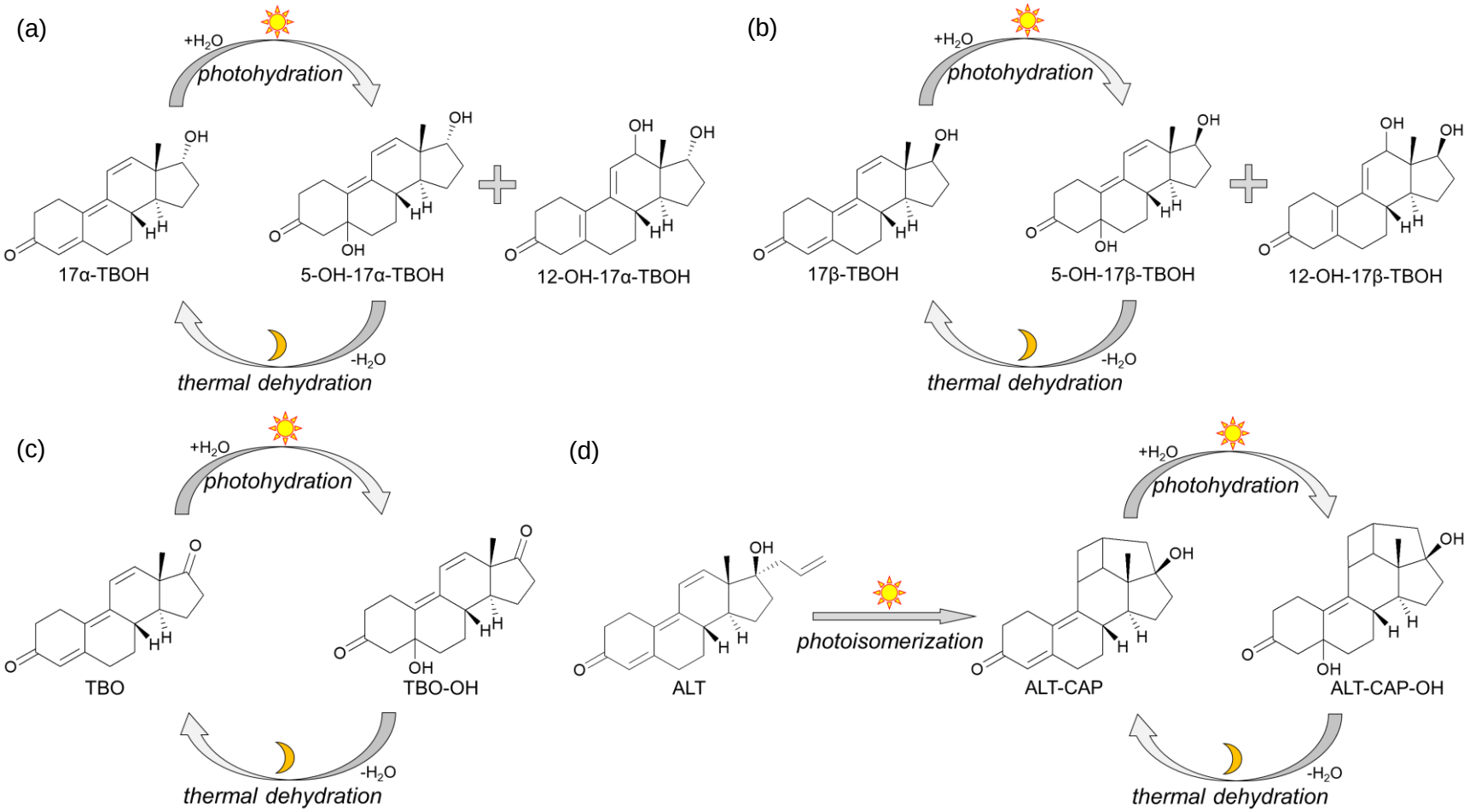


**Figure 2.1** Structures and photoreaction dynamics of the trenbolone metabolites (a: 17α-TBOH; b: 17β-TBOH; c: TBO;) and d: altrenogest; including related photoproducts. The sun and moon symbols indicate sunlit (via a photoreactor) and dark conditions, respectively. Arrows show photoreaction pathways including photoisomerization and coupled photohydration-thermal dehydration.

Before being discharged into the environment, agricultural runoff can be subject to different management practices (e.g., vegetated infiltration basins, riparian buffers) to improve water quality. Most of these processes rely upon surface or subsurface sequestration (i.e., hydrophobic partitioning) mechanisms to limit contaminant transport (Khan et al., 2009, 2008), for which the treatment efficiency is closely related to solute polarity (Goeppert et al., 2014). Vegetated filter strips and subsurface infiltration have been shown to be effective at attenuating TBA metabolite concentrations via partitioning to soil and organic matter (Jones et al., 2014a, 2014b). However, because the photohydration reactions increase compound polarity, the hydroxylated photoproducts would be expected to exhibit reduced sorption and enhanced transport potential in any of these soil-water treatment environments. Their potential for thermal dehydration also implies that highly potent parent steroids (i.e., TBA metabolites, ALT-CAP) can be regenerated during dark subsurface-treatment from more mobile photoproducts which act as metastable reservoirs of parent mass. Thus, shallow groundwater, vegetated filter strips, riparian buffers, and hyporheic zones may all exhibit reduced sequestration and treatment effectiveness for reactive trienone steroids whenever photoproducts are formed (**Figure 2.2**). Here in this study, we seek to better understand the possibility of such processes with batch sorption systems. Partitioning constants have not been reported for TBA metabolite photoproducts, for ALT, or ALT photoproducts in soil-water systems. In general, few data exist that characterize sorption and transport outcomes for reactive solutes or transformation products, especially those that lack pure standards to facilitate experimentation.

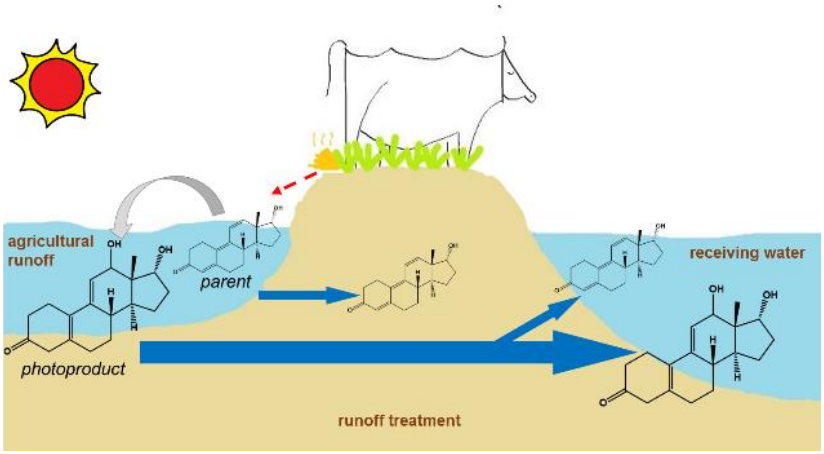


**Figure 2.2** Demonstration of the transport process for trenbolone and altrenogest photoproducts in soil. Trenbolone and altrenogest photoproducts move faster and regenerate parents during transport in dark soil. Traditional agricultural runoff management can exhibit lower than expected efficiencies for trienone steroids when photoproducts were considered.

Therefore, the first purpose of this study was to develop a liquid chromatography tandem mass spectrometry (LC-MS/MS) analytical method with sufficient sensitivity (e.g., for 0.1-1 ng $L^{-1}$ concentrations) (Durhan et al., 2006; Gall et al., 2011; Webster et al., 2012) and selectivity to characterize the fate and occurrence of the primary and secondary photoproducts of trenbolone metabolites and ALT. Quantifying such photoproducts, and unstable analytes more generally, is complicated by their sensitivity to solution conditions and the lack of any commercial standards for method development. Therefore, we generated photoproducts onsite with a solar simulator and quantified them based on reported yields of the photohydration reactions. Methodologies were optimized to promote photoproduct stability and the method was validated for linearity, limits of detection (LODs), recoveries, matrix effects, and inter- and intraday accuracy and precision. Finally, the stability of photoproducts during storage was assessed with a stability test (time-series analysis of stock water samples and SPE eluents).

The second objective of this study was to evaluate the sorption of TBA metabolites (17α-TBOH, 17β-TBOH and TBO), ALT, and their seven photoproducts (5/12-OH-17α/β-TBOH, TBO-OH, ALT-CAP and ALT-CAP-OH) onto a model soil with the quantification method developed. We generated photoproduct mixtures with a solar simulator first and then infiltrated these mixtures to batch soil-water systems. The sorption data were subsequently used to predict field scale transport potential and probable treatment efficacy for ALT, TBA metabolites, and their related photoproducts.

## 2.2 Materials and Methods

### 2.2.1 Reagents and Materials

17α-TBOH was purchased from BDG Synthesis (Wellington, New Zealand); 17β-TBOH from Shenzhen Shijingu Technology Co. Ltd (Shanghai, China); TBO from Steraloids (Newport, Rhode Island); and altrenogest from Fluka (Sigma Aldrich, St. Louis, MO). For deuterated standards, 17α-16,16,17-d3-TBOH (17α-d3-TBOH) and 17β-16,16,17-d3-TBOH (17β-d3-TBOH) were purchased from BDG Synthesis and altrenogest-$d_5$ (ALT-$d_5$) was purchased from ALSACHIM (Illkirch Graffenstaden, France). Resprep 6 mL C18 SPE cartridges were obtained from Restek (Bellefonte, Pennsylvania, USA). LC-MS grade methanol and LC-MS grade water were purchased from Fisher Scientific (Pittsburgh, Pennsylvania). The solar simulator was obtained from EYE Lighting (Solarlux 150R, Model # 93510, EYE Lighting, Mentor, OH) and employed four high pressure, 150 W xenon bulbs. It was rated to class ABB per manufacturer specification, simulating sunlight at sea level with low air pollution (rural setting). All glassware used in this study was silanized with 10% (v/v) dichlorodimethylsiloxane in toluene prior to use.

### 2.2.2 Sample Collection

For validation of the quantification method, representative agricultural receiving waters were collected from Samish River in Skagit County, WA (48.5315° N, 122,4442° W), located in a mixed-use agricultural area. For the stability test experiment (see section 2.1.6), water samples from a highly eutrophic lake, Wapato Lake, (Tacoma, WA, 47.1952° N, 122.4567° W) were used to represent an organic-rich high matrix water type. Water samples were stored on ice during transport, stored at 4 °C in lab, and processed within 24 hours of collection.

In lieu of acidic LC-MS grade water (pH = 5.5), a circumneutral (DOC <3 mg/L, pH = 7.0-7.2) river water collected from the South Fork of the Snoqualmie River (Ollalie State Park, WA, 47.4372° N, 121.6533° W) was used as a model water for method development. This choice limited the acid catalyzed dehydration of pH-sensitive photoproducts. pH adjustment of LC-MS grade water also was avoided because pH buffer ions could promote cationic adduct formation for the steroid analytes during mass spectrometry and decrease sensitivity (see section 2.3.1.3). The model water was filtered through 0.45 μm polyethersulfone (PES) membranes (Fisher Scientific, Pittsburgh, Pennsylvania) before use.

A silica sand-soil mixture (95:5, *w:w*, $f_{oc}$ = 0.06%) was used for batch sorption experiments as a representative porous media (**Figure 2.3**). Loamy sand (0-30 cm) was collected in Pierce County, WA, USA (122°16′57.688″ W, 47°7′46.027″ N), with physical-chemical properties shown in **Table S2.2**. Soil was air-dried, ground, and sieved to 1 mm prior to use. Commercial grade silica sand (<1 mm diameter) was washed and used as is. The model water collected from Snoqualmie River was used as the aqueous phase to limit photoproduct dehydration and to use environmentally relevant water compositions (e.g., natural organic matter). The soil, silica sand, model water, agricultural and lake water samples contained no detectable steroidal analytes.

### 2.2.3 Calibration Standards

Individual stock solutions (1000 mg/L) of trenbolone metabolites, ALT and the internal standards were prepared in methanol and stored at -20 ºC. Calibration standards for trenbolone metabolites and ALT were made in the range of 0.01-10 µg $L^{-1}$ by diluting the stock solutions with methanol. Standards for trenbolone or ALT photoproducts are not available commercially, and our many attempts at their independent synthesis were unsuccessful. Therefore, the hydroxy photoproducts (5,12-OH-17α,β-TBOH, TBO-OH, and ALT-CAP-OH) were generated via irradiation of parent compounds (6 h, >10 half-lives), and ALT-CAP was generated via complete thermal dehydration of ALT-CAP-OH (at 50 °C for 24 h, >10 half-lives). Stock solutions of parent compounds were diluted with sterilized (autoclaving, 121 ºC, 20 min) model water to 0.1-100 µg $L^{-1}$ (MeOH content <0.1%) in 20 mL glass vials (clear borosilicate glass with PTFE septa plastic screw cap). The vials were then irradiated with the solar simulator while partially immersed in a cold (0º C) water bath to minimize thermal dehydration of photoproducts.

To improve chromatography, all standards and extracts were diluted to 1:1 (v/v) methanol-water composition immediately prior to LC-MS/MS analysis. Internal standards (1 ng) were spiked into calibration standards with 17α-d3-TBOH as the internal standard for 17α-TBOH, TBO and corresponding photoproducts, 17β-d3-TBOH as the internal standard for 17β-TBOH and corresponding photoproducts, and ALT-$d_5$ as the internal standard for ALT and corresponding photoproducts. Photoproduct concentrations in the calibration standards were estimated based on the reported yields of the photoreactions (**Table 2.1**) (Baltrusaitis et al., 2016; Wammer et al., 2016). Standards were analyzed rapidly to minimize dehydration of photoproducts.

### 2.2.4 Solid Phase Extraction

C18 SPE cartridges were chosen for this study because of their prior use in analysis of trienone steroids (Durhan et al., 2006; Parker et al., 2012). Resprep C18 SPE cartridges (6 mL, 1g, RESTEK, Bellefonte, PA) were pre-conditioned with 12 mL methanol and 12 mL water. Water samples (1 L) were spiked with 1 ng internal standards and SPE-extracted under vacuum (~4 mL $min^{-1}$). After sample loading, cartridges were washed with 6 mL DI water, vacuum dried, and eluted with three 1.5 mL aliquots of methanol. The eluent was evaporated to 1 mL with $N_2$ gas, transferred to a 2 mL amber HPLC vial, and diluted with model water to 1:1 (v/v) methanol-water.

### 2.2.5 LC-MS/MS Detection

Instrumental analysis was performed with an Agilent (Santa Clara, California) 1290 Infinity binary pump liquid chromatography (LC) coupled with an Agilent 6430 triple quadrupole tandem mass spectrometer (MS/MS). To minimize thermal dehydration of photoproducts, analysis time and sample temperatures were minimized to the extent possible. Samples were injected from chilled autosampler tray (4$^{o}$ C) and separated using an Agilent Poroshell 120Å EC C18 column (3.0 × 50 mm, 2.7 μm) preceded by a C18 guard column (2.0 × 4mm) (Phenomenex, Torrance, California), both at 11$^{o}$ C. Mobile phases (0.2 mL/min) on the LC were A: LC-MS grade water (pH=5.5) and B: LC-MS grade methanol, with the following gradient used: 55% B initially, increased to 75% over 5 min, increased to 100% B over 3 min, isocratic at 100% B for 3 min, decreased to 55% over 1 min, isocratic at 55% B for 5 min, for a total runtime of 17 min. Agilent Jetstream ESI+ mode was used with 2.5 kV capillary voltage, 1.0 kV nozzle voltage, 350 $^{o}$C desolvation gas temp, 400 $^{o}$C sheath gas temp, 12.0 L $min^{-1}$ desolvation and sheath gas flows, 40 psi nebulizer pressure, and 400 V positive multiplier voltage (delta EMV). Analytes were identified and quantified with multiple reaction monitoring

(MRM) mode, and two transitions were monitored for each analyte. For all transitions, dwell time was 200 ms and collision cell voltage was 4 V. The quantification and identification transitions, fragmentor voltage, and collision energy for each analyte are shown (**Table 2.1**).

### 2.2.6 LC-MS/MS Method Validation

The developed method was validated for linearity, limits of detection and quantification, recovery, matrix effect, and inter- and intraday precision following strategies published in the literature (Dunphy et al., 2001; Quifer-Rada et al., 2013; Strahm et al., 2008) and guidelines for bioanalytical method validation from the U.S. Food and Drug Administration (U.S. FDA, 2018). Linearity was assessed based on correlation coefficients of the calibration curves. The instrument detection limits (IDLs) and quantification limits (IQLs) were estimated as the lowest concentration detected in standard injections (in pure methanol) with observed signal-to-noise ratios (S/N) of 3 and 10, respectively. The method detection limits (MDLs) and quantification limits (MQLs) were evaluated as the lowest concentrations of standards spiked into SPE extracts of agricultural water (1 L) that gave S/N of 3 and 10, respectively, divided by the SPE enrichment factor (1000). Recovery and matrix effects were evaluated at three concentrations (1, 5, 10 ng/L for parents; ~10, 50, 100 ng/L for photoproducts; N = 3 for each concentration; Photoproduct concentrations are approximated as parent concentrations before irradiation. Specific concentrations of each photoproduct were estimated from reported yields of the photo-reactions (**Table 2.1**). Absolute recovery was calculated as the peak area ratio of analytes spiked into 1 L water samples before and after SPE extraction. Relative recovery was estimated as the absolute recovery calibrated to the absolute recovery of the isotopic internal standard. Matrix effects were evaluated following the method of Matuszewki et al. (2003) as the peak area ratio of analytes spiked into water sample (1 L) SPE extracts to analytes in standard solutions (Matuszewski et al., 2003). Intraday precision was evaluated as the standard deviation of the

relative recovery results (at the above three concentrations, N = 3). The experiment was repeated after five and ten days (at three concentrations on each day, N = 3) and the interday precision was evaluated as the standard deviation of the relative recovery results across the three days.

Considering the complex interconversions between parent and metastable photoproducts, we generally recommend immediate processing and analysis of water samples. However, in recognition that this is not always possible, we evaluated analyte stability in both stored water samples and SPE extracts (Quifer-Rada et al., 2013) by making ~1 μg/L solutions of 17α-TBOH, 17β-TBOH, TBO and ALT photoproducts in both model water and Wapato Lake water (unsterilized) and processing them. The solutions were stored at 4 ºC and 40 mL aliquots were collected in triplicate, extracted, and analyzed after 0, 2, 5, 8, and 30 days. In addition, 600 mL (15 × 40 mL) samples of each photoproduct solution were SPE extracted on day 0 and eluted with 15 mL of methanol. The methanolic extracts were stored at -20 ºC, and 1 mL aliquots were analyzed in triplicate on day 0, 2, 5, 8, and 30 to evaluate extract stability. The photoproduct concentrations were quantified analytically with freshly prepared calibration standards.

### 2.2.7 Solvent-Water Partitioning Coefficients

To characterize solute hydrophobicity and polarity, octanol-water ($K_{ow}$) and hexane-water ($K_{hw}$) partitioning coefficients were measured using standard protocols (U.S. EPA, 1979). Briefly, octanol and hexane were extracted with 0.1 M NaOH and rinsed twice with ultra-pure water. The solvents were then passed through sodium sulfate (~0.5 g) (held on a layer of 0.2 μm glass fiber filter) to remove residual water. 1 mL of octanol or hexane was mixed with 3 mL of 10 mg/L aqueous solutions (in Milli Q water) of the target steroids, and the mixture was equilibrated on a shaker table (200 rmp, 24 hours). Upon equilibration, the samples were centrifuged (3000 rpm, 1 h), after which subsamples of the organic phase and aqueous phase were collected with glass pipettes. The samples were further diluted (organic phase with

methanol and aqueous phase with water) into linear ranges of the respective calibration curves for LC-MS/MS analysis. For $K_{ow}$ measurement of parent compounds, octanol was diluted 500X and water was analyzed directly. For $K_{hw}$ measurement of parent compounds, hexane and water were diluted 500X and 1000X, respectively. Octanol and water were diluted 500X and 20X in $K_{ow}$ measurement of photoproducts, and hexane and water were diluted 0.1X and 100X in $K_{hw}$ measurement of photoproducts, respectively. As an apolar solvent, hexane interacts with solutes largely through hydrophobic interactions, while octanol, as an amphiphilic solvent, interacts with solutes through both hydrophobic and H-bonding interactions (Schwarzenbach et al., 2003).

### 2.2.8 Batch Experiments

Photoproduct mixtures for batch experiments were generated from aqueous solutions of parent compounds under photoreaction conditions described above. Sorption isotherms were conducted at five concentrations, with parent compounds of 0.1, 0.5, 1, 5, 10 $\mu$g/L and photoproducts produced from 1, 5, 10, 50, 100 $\mu$g/L parents (specific photoproduct concentrations could be estimated from reported yields of the photoreactions in **Table 2.1**). Higher parent mass was used in photoproduct generation due to low yields of some photoproducts (e.g., 6.7% yield for 5-OH-17α-TBOH) and the higher analytical method detection limits for photoproducts relative to parent compounds (**Table 2.2**). A 2 g solid (sand-soil mixture) to 8 mL water ratio was selected as an environmentally representative composition (e.g. manure lagoons) (Liu et al., 2015) and to promote solute detection in both aqueous and solid phases. Studies were conducted in duplicate at each concentration. One no-soil control and one dark control (i.e., non-irradiated parent solutions) also were included at each concentration to monitor photoproduct stability during equilibration and to detect possible experimental artifacts (**Figure 2.3**).

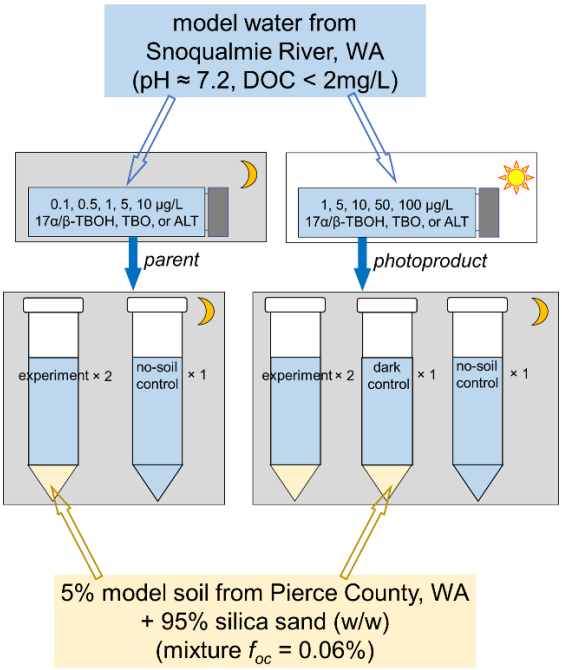


**Figure 2.3** Experimental setup for the batch sorption experiments. The sun and moon symbols indicate sunlit (via a photoreactor) and dark conditions, respectively.

Solid and aqueous phases were sterilized by autoclaving (121 ˚C, 20 min), and glassware by baking (450 ˚C, 4 h) prior to use. Batch systems were equilibrated on a rotary shaker (125 rpm) for 22 h at 4 ˚C in the dark. This temperature, lower than typical (i.e., 25 ˚C), was selected to promote photoproduct stability. Equilibration times were selected based on literature results (Khan et al., 2009) and preliminary studies designed to evaluate possible impacts of thermal dehydration on data quality (**Figures S2.4, S2.5**). However, the TBO-OH sorption was notably short of soil-water equilibrium at 22 h (**Figure S2.4c**), but we accepted this uncertainty because the error was within 25%. After equilibration, the systems were centrifuged (2500 rpm at 4 ˚C, 10 min), 500 µL of supernatant was withdrawn, 0.5 ng of 17β-$d_3$-TBOH was added as internal standard, and the solution was diluted to 1 mL with methanol. The remaining supernatant was discarded and the sand-soil mixture was spiked with 8 ng of 17β-$d_3$-TBOH and extracted with two 4 mL methanol aliquots under ultrasound (15 min). Extracts were centrifuged and 250 µL of

each supernatant was withdrawn, combined and diluted 1:1 (*v/v*) to 1 mL final volume with sterilized model water for liquid chromatography-tandem mass spectrometry analysis.

The resulting sorption data were fitted to linear isotherms, including only those solutes that were detected in both aqueous and solid phases. Due to some non-detects in the soil phases (**Table S2.4**), isotherms were not estimated for 5-OH- and 12-OH-17β-TBOH.

### 2.2.9 Batch Sorption Isotherms

Linear isotherms (i.e., Equation (2.1)) were used to fit the batch sorption data

$$(2.1)\quad C_s = K_d \times C_w$$

where $C_s$, $C_w$ were steroid concentrations of sorbed and aqueous phases, respectively. $K_d$ (L/kg) is the linear distribution coefficient. $K_d$ was then normalized to organic carbon content ($f_{oc}$) of the soil-sand mixture to produce $K_{oc}$ (Equation (2.2))

$$(2.2)\quad K_{oc} = \frac{K_d}{f_{oc}}.$$

## 2.3 Results and Discussion

### 2.3.1 LC-MS/MS Method Optimization

#### 2.3.1.1 Optimization of Liquid Chromatography

Working with unstable analytes in a quantitative analytical method typically requires some compromises and modifications to "typical" analytical practices (Tong et al., 2010). Here, due to the pH sensitivity of photoproducts, acidic or basic mobile phase additives are not recommended to enhance chromatography. Observationally, maintaining neutral conditions (pH 7) in all eluents and working solutions resulted in the most consistent method performance. Optimization of chromatography resulted in analyte elution between 4-9 min, although 12-OH-17α-TBOH and 17β-TBOH still co-eluted under these conditions in mixed standards and employed identical MS/MS transitions for detection (see Section 2.3.1.2 below) (**Table 2.1**,

**Figure S2.1**). Because 17α-TBOH and 17β-TBOH rarely co-occur at similar concentrations in environmental systems (17α-TBOH dominates TBA excretion profiles) (Bartelt-Hunt et al., 2012; Khan and Lee, 2012; Webster et al., 2012), we decided to leave these two peaks unresolved and optimize our chromatography for shorter run times (instead of greater separation) to maximize photoproduct stability during analysis. Should 17α-TBOH and 17β-TBOH photoproducts co-occur, longer runs could be used to improve separation to distinguish between 12-OH-17α-TBOH and 17β-TBOH.

During analysis of 17α-TBOH photoproducts, two minor peaks (at 6.49 min and 7.44 min) were observed in SPE extracts that were not present in direct injections of photoproduct standards (**Figure 2.4** and **S2.1**). The spectra of the 6.49 min peak closely resembled 5-OH-17α-TBOH (6.19 min) and 12-OH-17α-TBOH (6.70 min) spectra, while the 7.44 min peak had similar spectra to parent 17α-TBOH peak (7.16 min) (data not shown). In addition, the 6.49 min and 7.44 min peaks exhibited near identical retention time differences relative to 5-OH-17α-TBOH and 17α-TBOH (ΔRT: 0.29 ± 0.1 min), respectively. Therefore, these two peaks (6.49 min and 7.44 min) are tentatively identified as stereoisomeric analogs of 5-OH-17α-TBOH and 17α-TBOH, respectively. Similar analogs are not detected in SPE extracts of dark controls (i.e. 17α-TBOH), suggesting that photoproducts, and not parent compounds, can exhibit rearrangements to uncharacterized isomeric analogs during SPE. Extracts of 17α-TBOH photoproducts were reinjected after 24 hours, and we observed that 12-OH-17α-TBOH and 17α-TBOH remained stable, but 5-OH-17α-TBOH and its analogs decayed (data not shown) over this period. These observations are consistent with the lower stability of the 5-OH photoproducts (Baltrusaitis et al., 2016). Such observations indicate the analytical challenges inherent to the analysis of metastable TPs and complex product mixtures, and reinforce the value of rapid analysis.

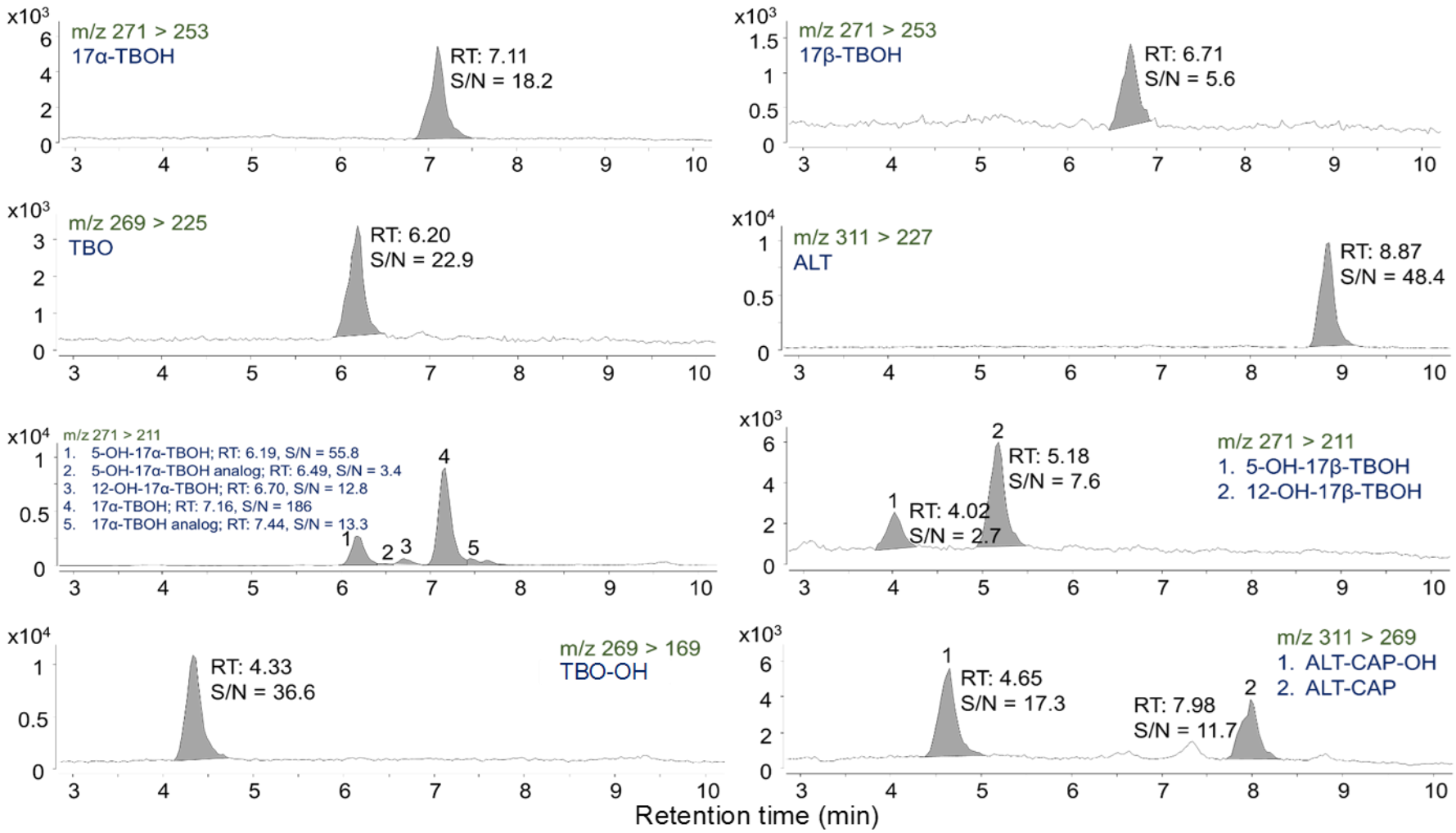


**Figure 2.4** Observed MRM chromatograms of 1 ng $L^{-1}$ 17α-TBOH, 17β-TBOH, TBO, ALT, or ~10 ng $L^{-1}$ photoproduct (as parent concentration before irradiation) in a representative agricultural receiving water, after solid phase extraction. Chromatograms were acquired with a Poroshell 120Å EC C18 column (3.0 × 50 mm, 2.7 μm) preceded by a C18 guard column (2.0 × 4mm), with mobile phases of pure water and pure methanol under a 12 min gradient elution program, and 100 μL injection volume.

**Table 2.1** Elution times, MRM transitions, fragmentor voltages, and collision energies for trenbolone metabolites, altrenogest, and related photoproducts, with values for confirmatory transitions (versus primary transitions for quantification) presented in parentheses.

| analyte | retention time (min) | MRM transitions (m/z) | fragmenter (V) | collision energy (eV) | photoproduct yield (%) |
|---|---|---|---|---|---|
| 17α-TBOH | 7.11 | 271>253 (271>211) | 135 (135) | 30 (30) | - |
| 5-OH-17α-TBOH | 6.19 | 271>211 (271>253) | 135 (135) | 30 (30) | 73.3 |
| 12-OH-17α-TBOH | 6.70 | 271>211 (271>253) | 135 (135) | 30 (30) | 6.7 |
| 5-OH-17α-TBOH analog | 6.49 | 271>211 (271>253) | 135 (135) | 30 (30) | - |
| 17α-TBOH analog | 7.44 | 271>211 (271>253) | 135 (135) | 30 (30) | - |
| 17α-d3-TBOH | 7.12 | 274>256 (274>214) | 135 (135) | 30 (30) | - |
| 17β-TBOH | 6.71 | 271>253 (271>211) | 135 (135) | 30 (30) | - |
| 5-OH-17β-TBOH | 4.02 | 271>211 (271>253) | 135 (135) | 30 (30) | 20 |
| 12-OH-17β-TBOH | 5.18 | 271>211 (271>253) | 135 (135) | 30 (30) | 60 |
| 17β-d3-TBOH | 6.73 | 274>256 (274>214) | 135 (135) | 30 (30) | - |
| TBO | 6.20 | 269>225 (269>169) | 135 (135) | 28 (28) | - |
| TBO-OH | 4.33 | 269>169 (269>225) | 135 (135) | 28 (28) | 80 |
| ALT | 8.87 | 311>227 (311>269) | 82 (82) | 24 (12) | - |
| ALT-CAP | 7.98 | 311>269 (311>227) | 82 (82) | 12 (24) | 100 |
| ALT-CAP-OH | 4.65 | 311>269 (311>227) | 82 (82) | 12 (24) | 80 |
| ALT-d5 | 8.89 | 316>227 (316>269) | 82 (82) | 24 (12) | - |

#### 2.3.1.2 Optimization of Mass Spectrometry

Precursor and product ions of the MRM transitions were identified by full and MS/MS scans, respectively. Fragmentor voltages, collision energies, and collision cell accelerator voltages of the MRM transitions were subsequently optimized to achieve maximum S/N and peak areas for each analyte (**Table 2.1**). Nebulizer pressure, capillary voltage, and sheath and desolvation gas flows and temperatures were then optimized to improve detector response for 17β-TBOH photoproducts, which were typically the least sensitive analytes. All target parent compounds and photoproducts showed higher responses in positive ionization mode (ESI+), consistent with previous LC-ESI-MS/MS method development for trenbolone and altrenogest (Lampinen-Salomonsson et al., 2006; Malone et al., 2009; Poucke et al., 2005). As expected, 17α-TBOH and 17β-TBOH had the same mass-to-charge ratio (m/z) of 271.2 Da for their $[M+H]^+$ ions. TBO was observed at 269.2 Da, and ALT and ALT-CAP (the isomeric photoproduct) at 311.2 Da. Notably, for all the hydrated photoproducts (i.e., 5,12-OH-17α-TBOH, 5,12-OH-17β-TBOH, TBO-OH, ALT-CAP-OH), the $[M+H-H_2O]^+$ ion was observed as the precursor ion for subsequent MRM fragmentation instead of the expected $[M+H]^+$ ion at +18 Da mass (**Table 2.1**, **Figure 2.5**). While typical in LC-MS/MS analysis of dienone and trienone steroids (Kolodziej et al., 2013), this observation was consequential for selective detection of photoproducts because it precludes the analytical resolution of parents and photoproducts by mass alone. Thus, chromatographic resolution plays a major role in unequivocal photoproduct detection.

#### 2.3.1.3 Cationic Adduct Formation

Under the analytical conditions tested, all of these trienone steroids were prone to the formation of cationic adducts during ionization (Wammer et al., 2016). Sodium adducts (i.e.,

$[M+Na]^+$ ions) of parent compounds had mass addition of +22 Da relative to their expected $[M+H]^+$ precursors. For photoproducts, addition occurred without neutral loss of a water molecule, resulting in +40 Da mass addition relative to their $[M+H-H_2O]^+$ precursors (**Figure 2.5**). Under full scan conditions, this +40 Da relative mass difference for sodium adducts is a characteristic spectral feature for trienone steroid photoproducts (and also other compounds prone to dehydration during ionization), and can be useful for identification if concentrations are high enough for full scan detection. For example, during MS/MS identification of ALT mixtures, identical precursor ions are observed for the isomeric primary photoproduct (ALT-CAP, with $[M+H]^+$ precursor ion) and secondary photohydration products (ALT-CAP-OH, with $[M+H-H_2O]^+$ precursor ion), but these compounds can be differentiated easily by the masses of their sodium adducts (**Figure 2.5**). Adduct characteristics can also help distinguish between 5- and 12-hydroxy photoproducts of 17α-TBOH and 17β-TBOH; with increasing collision energy, the 311.2 Da $[M+Na]^+$ ion for 12-OH-17β-TBOH fragmented more easily than that for 5-OH-17β-TBOH (**Figure S2.2**).

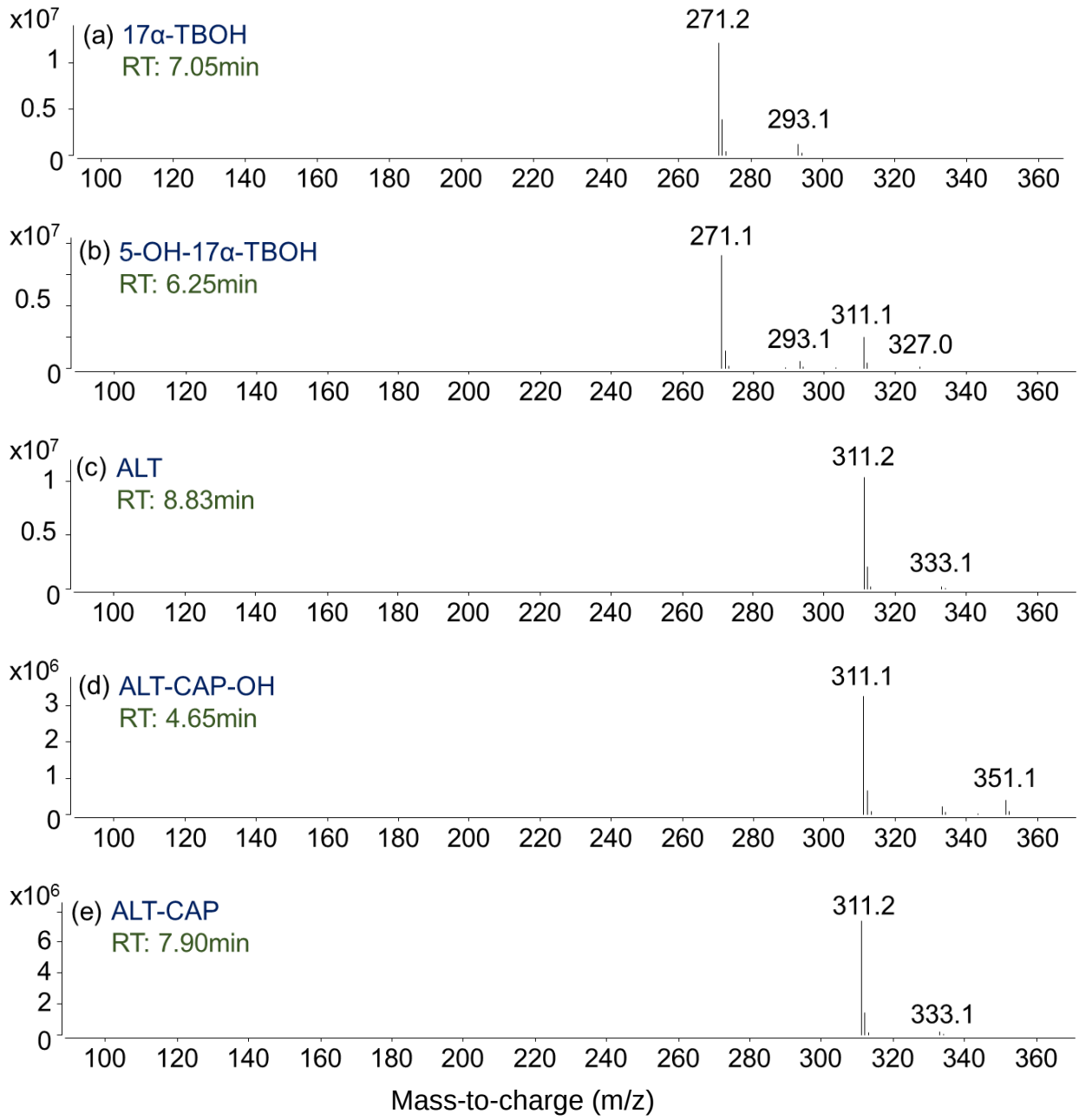


**Figure 2.5** Full-scan spectra for a) 17α-TBOH, b) 5-OH-17α-TBOH, c) ALT, d) ALT-CAP-OH, and e) ALT-CAP. Sodium adducts of parent compounds had mass addition of +22 Da relative to their $[M+H]^+$ precursors, whereas those of photoproducts had +40 Da mass addition relative to their $[M+H-H_2O]^+$ MRM precursors. Spectra were acquired with a Poroshell 120Å EC C18 column (3.0 × 50 mm, 2.7 µm) preceded by a C18 guard column (2.0 × 4mm), with mobile phases of pure water and pure methanol under a 12 min gradient elution program. Mass spectrometry parameters can be found in Section 2.3.1.2 and Table 2.1.

While potentially useful for identification, adduct formation is detrimental to method sensitivity because adducts compete with $[M+H]^+$ ions for analyte mass. For example, we have detected $[M+Na]^+$ responses >10 fold higher than responses for $[M+H]^+$ precursors. We suspect that this characteristic has, at times, adversely affected the detection of parent compound via LC/MS methods in environmental surveys. Thus, identification and mitigation of cation sources to limit adduct formation aids method sensitivity. Adduct formation was weakly related to matrix type (e.g. lake water vs. river water; data not shown), potentially because salts are not typically retained on SPE cartridges, but the matrix may be more consequential in feedlot and agricultural runoff samples. Qualitatively, low concentrations of NaCl (~1 mg/L) in standards that were injected directly typically suppressed analyte peak areas, while higher concentrations (~10 mg/L) tended to enhance peak area response (**Table S2.1**). As peak area responses showed no clear correlation with matrix ionic strength, we conclude that analytical system components such as glassware, LC eluents, ion sources, and transfer lines are more important sodium sources, consistent with previous observations (Birdsall et al., 2016; Ende and Spiteller, 1982; Keller et al., 2008). Therefore, adduct formation, a large source of day-to-day variability in performance, was controlled in the present method by glassware silanization, careful maintenance, dedicated mobile phase bottles, and purging LC lines.

### 2.3.2 LC-MS/MS Method Validation

#### 2.3.2.1 Selectivity, Linearity, Limits of Detection and Quantification

Blank samples, including methanol blanks (N = 5), field blanks (DI water, N = 5), model water, lake water, and the agricultural receiving water samples, were analyzed; no peaks were observed at each MRM transition within one minute of the retention times of analytes. Analytes (1 ng $L^{-1}$ for TBA metabolites and ALT, ~10 ng $L^{-1}$ for photoproducts) were then spiked into 1 L agricultural receiving water samples and SPE extracted; resulting chromatograms demonstrated good peak resolution and chromatographic selectivity (**Figure 2.4**). Seven-point calibration curves were run before and after each batch of samples. Calibration curves showed linear responses (correlation coefficients >0.99) for parent compounds in the range of 0.01-10 µg/L and for photoproducts in the range of ~0.1-100 µg/L (**Figure S2.3**). The IDLs for trenbolone metabolites and altrenogest, reported as mass on column, were 0.16 (TBO)-0.62 pg (17β-TBOH), and those for photoproducts were 0.42 (ALT-CAP-OH)-8.3 pg (TBO-OH). The MDLs for parent analytes (100 µL injection volumes) were 0.034 (ALT)-0.40 ng/L (17β-TBOH), whereas those for photoproducts were 0.16 (ALT-CAP)-2.1 ng/L (12-OH-17β-TBOH) (**Table 2.2**).

**Table 2.2** Method linearity ($R^2$), instrumental detection limits (IDLs), method detection (MDL) and quantification limits (MQL), matrix effects, recoveries, precision at low, middle, high spikes (1, 5, 10 ng $L^{-1}$ for parents; ~10, 50, 100 ng $L^{-1}$ for photoproducts), mass of photoproducts reverting to parent compounds during sample processing, for trenbolone metabolites, altrenogest, and photoproducts.

| analyte | $R^2$ | IDLs (pg) | MDLs (ng/L) | MQLs (ng/L) | matrix effect (%) | absolute recovery (%) | | | relative recovery (%) | | | intra-day precision (%) | | | inter-day precision (%) | | | process reversion |
|---|---|---|---|---|---|---|---|---|---|---|---|---|---|---|---|---|---|---|
| | | | | | | ~1[a] | ~5 | ~10 | ~1 | ~5 | ~10 | ~1 | ~5 | ~10 | ~1 | ~5 | ~10 | |
| 17α-TBOH | 0.999 | 0.22 | 0.04 | 0.13 | 17±1.1 | 75±2 | 67±1 | 72±3 | 112 | 106 | 115 | 17 | 1 | 2 | 15 | 7 | 5 | NA[b] |
| 5-OH-17α-TBOH | 0.999 | 2.8 | 0.22 | 0.73 | 11±1 | 69±5 | 62±5 | 72±8 | 75 | 91 | 103 | 9 | 15 | 12 | 15 | 17 | 14 | 11% |
| 12-OH-17α-TBOH | 0.998 | 4.7 | 0.68 | 2.2 | 18±0.2 | ND[c] | 29±3 | 40±3 | ND | 42 | 45 | ND | 9 | 5 | ND | 22 | 11 | 9% |
| 17β-TBOH | 0.999 | 0.62 | 0.40 | 1.3 | 15±2.2 | 58±5 | 80±1 | 88±7 | 106 | 100 | 107 | 2 | 1 | 7 | 24 | 11 | 9 | NA |
| 5-OH-17β-TBOH | 0.998 | 1.5 | 1.5 | 5.0 | 3.1±0.4 | 98±5 | 70±4 | 75±3 | 85 | 91 | 87 | 6 | 14 | 4 | 19 | 23 | 13 | 9% |
| 12-OH-17β-TBOH | 0.995 | 1.6 | 2.1 | 6.9 | 3.5±0.4 | 90±1 | 83±1 | 79±4 | 79 | 107 | 103 | 13 | 10 | 5 | 12 | 17 | 9 | 1% |
| TBO | 0.999 | 0.16 | 0.064 | 0.21 | 10±1.0 | 86±8 | 61±2 | 70±7 | 113 | 96 | 105 | 18 | 4 | 1 | 24 | 5 | 3 | NA |
| TBO-OH | 0.999 | 8.3 | 0.62 | 2.0 | 7.3±0.4 | 70±6 | 74±2 | 77±2 | 101 | 86 | 109 | 14 | 5 | 2 | 7 | 8 | 11 | 10% |
| ALT | 0.999 | 0.19 | 0.034 | 0.11 | 17±0.7 | 65±9 | 74±1 | 79±3 | 104 | 102 | 107 | 4 | 1 | 3 | 3 | 3 | 5 | NA |
| ALT-CAP | 0.999 | 0.51 | 0.16 | 0.53 | 19±2.1 | 122±7 | 91±7 | 100±4 | 100 | 125 | 117 | 5 | 16 | 8 | 21 | 13 | 15 | NA |
| ALT-CAP-OH | 0.999 | 0.42 | 0.62 | 2.0 | 5.4±0.8 | 82±6 | 60±4 | 69±2 | 109 | 90 | 101 | 6 | 6 | 1 | 15 | 6 | 7 | 0% |

[a] Photoproduct spiking concentrations were 10, 50, 100 ng $L^{-1}$ as the parent concentrations before irradiation, which corresponds to 7.3, 37, 73 ng $L^{-1}$ for 5-OH-17α-TBOH; 0.67, 3.3, 6.7 ng $L^{-1}$ for 12-OH-17α-TBOH; 2, 10, 20 ng $L^{-1}$ for 5-OH-17β-TBOH; 6, 30, 60 ng $L^{-1}$ for 12-OH-17β-TBOH; and 8, 40, 80 ng $L^{-1}$ for TBO-OH, ALT-CAP, and ALT-CAP-OH.

[b] NA = not applicable.

[c] Low-yield photoproducts were not detected.

Most analytical methods have focused on TBA metabolites, with limited assessment of ALT and no reported detection of photoproducts. The MDLs for TBA metabolites obtained here (0.04-0.40 ng/L) were similar to or lower than other reported methods (Khan and Lee, 2012: 0.7-64 ng/L; Webster et al., 2012: 0.5 ng/L; Snow et al., 2013: 3.2-4.5 ng/L) (Khan and Lee, 2012; Snow et al., 2013; Webster et al., 2012), and the MDL for ALT (0.034 ng/L) was similar to that reported in the only published study on ALT detection (Golovko et al., 2018: 0.02 ng/L) that we know of (Golovko et al., 2018). The MDLs and MQLs indicated this method is suitable for analyzing agricultural systems where these analytes may present at levels as low as sub ng/L (Ankley et al., 2018). Relative to parents, IDLs for photoproducts were higher due to their lower peak area response. For example, when comparing peak area for parents in dark controls with photoproducts in irradiated samples, the total peak areas of detected photoproducts were only 57 ± 7%, 53 ± 6%, 78 ± 8%, and 11 ± 3% of the corresponding parents for 17α-TBOH, 17β-TBOH, TBO and ALT-CAP controls, respectively.

#### 2.3.2.2 Matrix Effects, Recovery, and Precision

Under the current approach for matrix effect evaluation, a matrix factor <100% suggests matrix suppression of detector response, whereas a matrix factor >100% suggests enhancement. Using representative agricultural waters, strong matrix suppression was observed for all analytes, with observed matrix effect factors of 17% and 11-18% for 17α-TBOH and photoproducts, 15% and 3.1-3.5% for 17β-TBOH and photoproducts, 10% and 7.3% for TBO and photoproducts, and 17%, 19% and 5.4% for ALT, ALT-CAP and ALT-

CAP-OH, respectively (**Table 2.2**). Notably, the matrix suppression of 17β-TBOH photoproducts and ALT-CAP-OH was much stronger than suppression levels observed for the corresponding parent compounds, likely indicating a more matrix-sensitive ionization for these analytes. In contrast, matrix suppression of 17α-TBOH and TBO photoproducts were similar to the parents. Matrix suppression of steroidal analytes is common (Blackwell et al., 2011; Chang et al., 2008), and internal standard calibration or additional cleanup steps are often employed to mitigate the suppression (Snow et al., 2013). As deuterated standards were available for three (of four) parent steroids, the matrix effect factors for the isotopic standards were very similar to the corresponding target analytes (17α-TBOH-$d_3$: 16±1%, 17β-TBOH-$d_3$: 13±2%, ALT-$d_5$: 18±1%), suggesting the use of isotopic internal standard to correct for matrix effects was reliable, although the correction for 17β-TBOH photoproducts and ALT-CAP-OH may be somewhat less accurate than hoped. Therefore, we chose to avoid further cleanup steps to minimize sample processing time and maximize photoproduct stability, although we recognize additional cleanup (e.g., normal phase SPE, size exclusion cleanup) may be necessary in the heaviest matrix types.

Except for 12-OH-17α-TBOH, absolute recoveries were mostly within 100 ± 35%; specifically 62-75% for 17α-TBOH and its photoproducts, 58-98% for 17β-TBOH and its photoproducts, 61-86% for TBO and its photoproducts, and 65-122% for ALT and its photoproducts (**Table 2.2**). The absolute recovery of 12-OH-17α-TBOH was low, from not detected at 0.67 ng $L^{-1}$ to 40% at 6.7 ng $L^{-1}$. Considering the metastability of photoproducts, the low recovery for 12-OH-17α-TBOH likely derived from instability during sample

processing. Absolute recoveries of the internal standards well matched those of the analytes (17α-TBOH-$d_3$: 73±17%, 17β-TBOH-$d_3$: 81±18%, ALT-$d_5$: 69±5%), leading to relative recovery rates of 96-115% for parent compounds and 75-125% for photoproducts (except 12-OH-17α-TBOH; **Table 2.2**). Better accuracy for parent compounds derives from their isotope matched deuterated internal standards, while photoproducts are more affected by their instability during sample processing. The intraday variation was <20% for all analytes, specifically 1-18% for parent compounds and 1-16% for photoproducts, and the interday variation was <25% for all analytes and 3-24% for parent and 6-23% photoproducts (**Table 2.2**). Analytical precision for parents and photoproducts was similar, generally suggesting good repeatability of our method.

#### 2.3.2.3 Stability during Sample Processing

TBOH and ALT photohydration products are metastable because thermal dehydration is sensitive to time, temperature and pH (Qu et al., 2013). Because thermal dehydration occurring during sample processing limits analytical sensitivity and data accuracy, we optimized the direct detection of photoproducts via methodologies that relied upon rapid extraction and processing at low temperatures and near neutral pH. For trenbolone metabolites and altrenogest photoproducts, direct injection post-irradiation revealed that complete reaction to photoproducts (and ALT-CAP-OH) consistently occurred with no detectable parent remaining in irradiated samples. However, after SPE extraction of parallel samples, ~10% of the parent mass of 17α-TBOH, 17β-TBOH and TBO was often detected (indicating reversion from photoproducts), while ALT-CAP-OH remained stable during

sample processing (**Table 2.2**). Given the inherent instability of the photoproducts, we considered such losses undesirable but acceptable, and we were unable to clearly identify additional strategies or techniques to further enhance photoproduct stability during analysis.

#### 2.3.2.4 Storage Stability

Photoproduct instability, which varied depending on the specific analyte, also implies concerns for sample and extract storage steps. Stability tests indicated that ALT-CAP (the isomeric photoproduct of ALT) was generally stable in storage over time scales of up to one month (average mass recovery: 110±23% for water sample storage, 84±17% for eluent storage), but photohydration products were typically less stable in water samples (4 °C) or SPE eluents (-20 °C) (**Figure 2.6**). During both water and eluent storage, photoproduct mass loss occurred via thermal dehydration to parent structures (thus conserving the overall trienone steroid structure, but not speciation) and especially affected 5/12-OH-17α-TBOH and ALT-CAP-OH, which is consistent with the previously observed higher degree of regeneration for 17α-TBOH and ALT-CAP relative to 17β-TBOH and TBO (Qu et al., 2013). For example, when photoproduct-containing lake water was stored for 2, 5, 8, and 30 days, 92%, 48%, 36%, and 30% of the initial 17α-TBOH photoproduct mass was recovered as photoproducts while 12%, 13%, 28%, and 31% of the mass was recovered as 17α-TBOH parent. However, during storage of water samples, overall mass recoveries for photoproduct-parent pairs were <100% and decreased with increasing storage time (average mass recovery for all photoproduct-parent pairs on day 2, 5, 8, 30: 85±28%, 60±13%, 71±15%, 45±17%), indicating that other biological or abiotic transformation reactions were occurring in addition

to thermal dehydration. These results indicate that water samples for trenbolone and ALT photoproducts should be extracted as soon as possible to ensure accuracy.

However, the total mass of photoproducts and parent compounds was well conserved in SPE extracts over one month time scales (**Figure 2.6 c-d**), especially for 17α-TBOH and ALT. Average mass recoveries within lake water SPE extracts over 30 days were 101±10%, 64±24%, 86±12%, and 112±12% for 17α-TBOH, 17β-TBOH, TBO, ALT photoproducts, respectively. For model water SPE extracts, 83±14%, 128±11%, 74±20%, and 69±6% of the initial mass of 17α-TBOH, 17β-TBOH, TBO, ALT photoproducts were recovered. Therefore, while rapid initial sample extraction of water samples is recommended, the resulting SPE extracts are less sensitive to time and can be stored prior to instrumental detection.

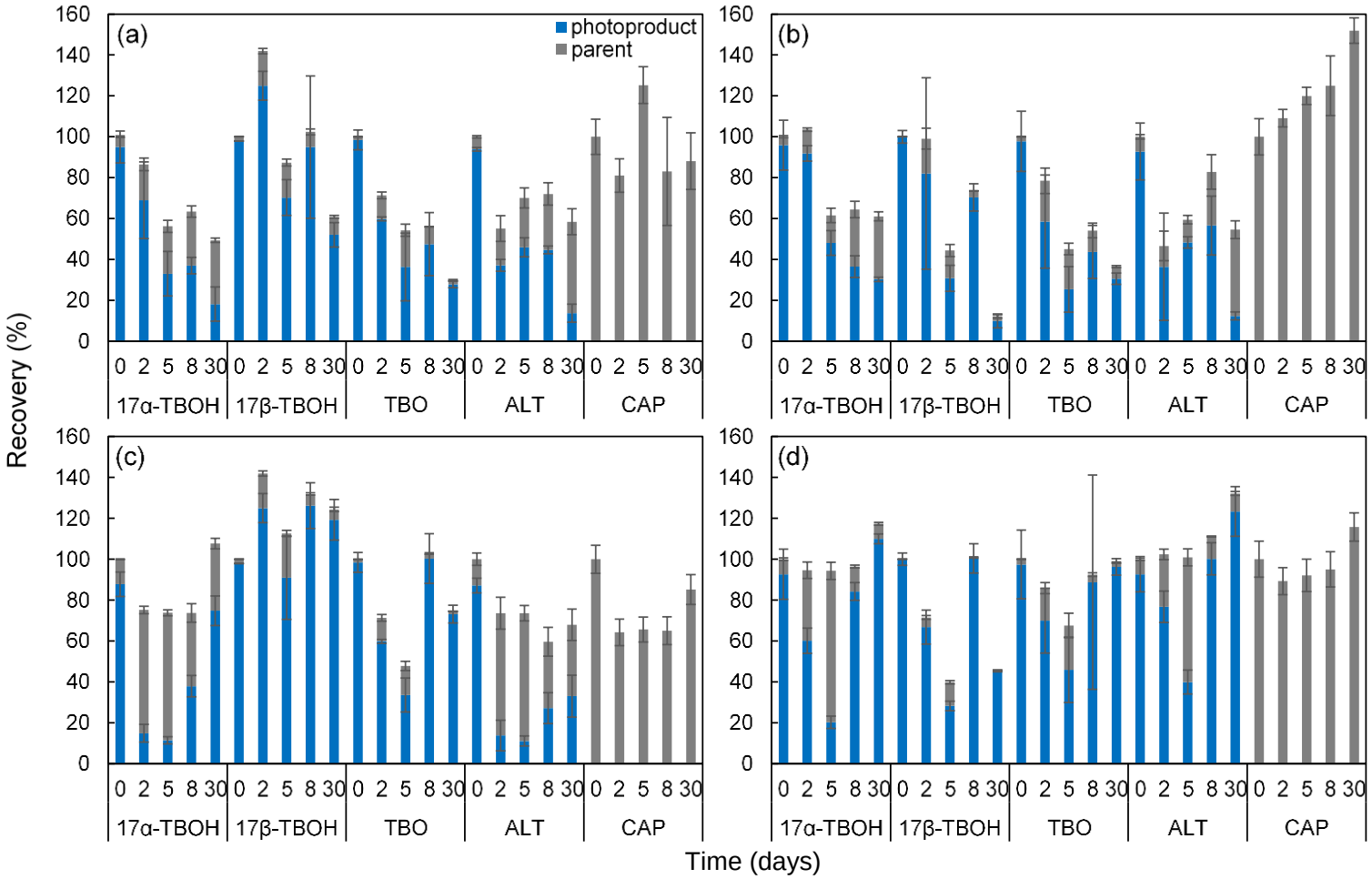


**Figure 2.6** Estimated mass recovery of photoproducts relative to initial concentration during storage studies of: (a) model water and (b) lake water stored at 4 °C; and (c) model water SPE extracts and (b) lake water SPE extracts stored at -20 °C. Storage studies were conducted in triplicate, and error bars represent standard deviation of triplicate analysis on each day.

Overall, when compared with parent analytes (TBA metabolites and ALT), photoproduct detection exhibited higher detection limits, stronger matrix effects, reduced accuracy, ~10% mass loss during sample processing, and similar analytical precision with this method. The reduced method performance for photoproducts largely resulted from their inherent instability and lower peak-area response on LC-MS/MS instrumentation. Rapid SPE extraction is necessary, but the data indicate that SPE extracts can be stored for up to a month for quantification of photoproduct-parent pairs with only a slight loss in accuracy. Despite the analytical challenges, the direct analysis of photoproducts was precise, sensitive enough for detection at environmentally relevant concentrations, and exhibited generally accurate quantification. The developed method was then applied to study the solvent partition and sorption behaviors of the target parent steroids and photoproducts.

### 2.3.3 Solvent Partition and Sorption

#### 2.3.3.1 Octanol-Water ($K_{ow}$) and Hexane-Water ($K_{hw}$) Partition Coefficients

Measured solvent-water partitioning coefficients (log$K_{ow}$ and log$K_{hw}$ values) for trenbolone, ALT and photoproducts were summarized in **Table 2.3** along with published data (Khan et al., 2009; Qu et al., 2014) and estimates by SPARC. Experimentally measured log$K_{ow}$ and log$K_{hw}$ values were only available for 17α-TBOH, 17β-TBOH, and TBO; the results in this study (log$K_{ow}$: 17α-TBOH: 2.70 ± 0.03, 17β-TBOH: 2.95 ± 0.02, TBO: 2.60 ± 0.02; log$K_{hw}$: 17α-TBOH: -0.29 ± 0.01, 17β-TBOH: -0.26 ± 0.02, TBO: 0.78 ± 0.04) were consistent with reported values ($\Delta\log K_{ow} < 0.13$, $\Delta\log K_{hw} < 0.27$) (Khan et al., 2009). Log$K_{ow}$ and log$K_{hw}$ values of ALT were 3.74 ± 0.05 and 1.31 ± 0.02, about one log unit higher than

values for TBA metabolites and consistent with ALT's larger molar volume (via ACD/Labs Percepta Platform: ALT 269.8 $cm^3$; TBOH 226 $cm^3$, TBO 225 $cm^3$).

Among photoproducts, ALT photoproducts exhibited the highest log$K_{ow}$ values (2.88-3.25), followed by 17α-TBOH (1.73-2.09), 17β-TBOH (1.64-1.83), and TBO (1.25) photoproducts. Notably, the log$K_{ow}$ of TBO and TBO-OH showed the largest disparity ($\Delta$log$K_{ow}$ of 1.35) among the observed parent-photoproduct pairs ($\Delta$log$K_{ow}$: 17α-TBOH pair, 0.61-0.97; 17β-TBOH pair, 1.12-1.31; ALT-CAP pair, 0.37). Unlike any other parent compound, TBO is only a hydrogen bond acceptor but not a donor; addition of a hydroxyl group during photoreaction allows TBO-OH to both donate and accept H-bonds and enhance hydrophilicity. Our observations also indicated that C-17 hydroxyl group stereochemistry impacts the H-bonding interactions and potentials for two-phase partitioning. Despite the inverse trend observed for parents (log$K_{ow}$: 17α-TBOH < 17β-TBOH), 17α-TBOH photoproducts unexpectedly exhibited higher measured log$K_{ow}$ values than 17β-TBOH photoproducts. Unfortunately, these observations could not be extended to the hexane-water system, as log$K_{hw}$ values for photoproducts were not available due to photoproduct non-detects in hexane even after pre-concentration.

Notably, while estimated (e.g. SPARC) and measured log$K_{ow}$ values of 5-OH photoproducts were similar, estimated log$K_{ow}$ for trenbolone, ALT, ALT-CAP, and 12-OH photoproducts were consistently higher than observed values by up to one log unit (**Table 2.3**). Thus, platforms like SPARC may struggle to accurately predict the polarity difference between parents and photoproducts or between structural isomers like 5-OH and 12-OH. In

addition, while the measured log$K_{ow}$ and log$K_{hw}$ values were different for 17α- and 17β-TBOH stereoisomers and the 5- and 12-OH photoproduct stereoisomers, SPARC could not differentiate solvent-water partitioning values for these stereoisomer pairs (**Table 2.3**). Such stereochemistry effects remain poorly resolved in most computational models (e.g. SPARC, PaDEL, KOWWIN), and relative predictions for stereoisomers should be used somewhat cautiously. Additional stereochemical resolution in such models may be merited to improve accuracy. Based on the above measured values, and consistent with our expectations of reduced partitioning and enhanced transport potential, the coupled photohydration - thermal dehydration reactions do shift hydrophobicity by log$K_{ow}$ 0.6-1.4 in magnitude when comparing the more polar photoproducts (measured log$K_{ow}$ of 1.25-3.25) to parents (log$K_{ow}$ of 2.60-3.74).

**Table 2.3** Estimated solvent-water partitioning coefficients and soil-water partitioning parameters for TBA metabolites, ALT, and related photoproducts.

| | log$K_{ow}$ | | | log$K_{hw}$ | | | linear isotherm | | | | |
|---|---|---|---|---|---|---|---|---|---|---|---|
| | result | *Khan et al.*[1] | SPARC | result | *Khan et al.*[1] | SPARC | mass balance (%) | $R^2$ | $K_d$ | log$K_{oc}$ | *Khan et al.*[1] log$K_{oc}$ |
| 17α-TBOH | 2.70 ± 0.03 | 2.72 ± 0.02 | 3.63 | -0.29 ± 0.01 | -0.114 ± 0.006 | 1.18 | 97 ± 10 | 0.90 | 1.72 ± 0.13 | 2.46 ± 0.03 | 2.77 ± 0.12 |
| 5-OH-17α-TBOH | 1.73 ± 0.02 | - | 1.63 | < -3.94[a] | - | -2.49 | 125 ± 9 | 0.99 | 0.50 ± 0.01 | 1.92 ± 0.01 | NA[b] |
| 12-OH-17α-TBOH | 2.09 ± 0.06 | - | 3.22 | < -3.55 | - | 0.91 | | 0.94 | 0.81 ± 0.07 | 2.13 ± 0.04 | NA |
| 17β-TBOH | 2.95 ± 0.02 | 3.08 ± 0.03, 3.09[2] | 3.63 | -0.26 ± 0.02 | -0.050 ± 0.010 | 1.18 | 87 ± 11 | 0.91 | 1.88 ± 0.20 | 2.50 ± 0.05 | 3.08 ± 0.10 |
| 5-OH-17β-TBOH | 1.64 ± 0.17 | - | 1.63 | < -3.75 | - | -2.49 | 89 ± 16 | NI[c] | NI | NI | NA |
| 12-OH-17β-TBOH | 1.83 ± 0.02 | - | 3.22 | < -5.50 | - | 0.91 | | NI | NI | NI | NA |
| TBO | 2.60 ± 0.02 | 2.63 ± 0.05 | 3.15 | 0.78 ± 0.04 | 1.045 ± 0.033 | 1.9 | 104 ± 8 | 0.96 | 3.48 ± 0.17 | 2.76 ± 0.02 | 3.38 ± 0.19 |
| TBO-OH | 1.25 ± 0.04 | - | 1.58 | -2.12 | - | -1.72 | 166 ± 42 | 0.92 | 1.02 ± 0.07 | 2.23 ± 0.03 | NA |
| ALT | 3.74 ± 0.05 | - | 4.67 | 1.31 ± 0.02 | - | 2.47 | 102 ± 9 | 0.99 | 3.14 ± 0.07 | 2.72 ± 0.01 | NA |
| ALT-CAP | 3.25 ± 0.02 | - | 4.25 | 0.23 ± 0.02 | - | 2.13 | 108 ± 7 | 0.94 | 2.25 ± 0.15 | 2.57 ± 0.03 | NA |
| ALT-CAP-OH | 2.88 ± 0.15 | - | 2.5 | < -3.73 | - | -1.53 | 91 ± 29 | 0.99 | 0.71 ± 0.02 | 2.07 ± 0.01 | NA |

[1] Khan, et al. *Environ. Sci. Technol.* **2009**, *43* (23), 8827−8833.

[2] Qu, et al. *J. Agric. Food Chem.* **2014**, *62* (51), 12277-12286.

[a] Photoproducts were not detected in hexane phase. The upper limit of $K_{hw}$ is estimated based on the instrument detection limits of photoproducts.

[b] NA = not analyzed, photoproducts were not evaluated in the previous study.

[c] NI = not included, isotherms for 17β-TBOH photoproducts were not generated due to low detection rates in soil samples.

#### 2.3.3.2 Batch Experiments

Near 100% mass recovery was observed in batch soil-water systems. Recoveries were 87 ± 11% to 104 ± 8% for parent steroids and 89 ± 16% to 166 ± 42% for photoproducts (**Table 2.3, S2.3, S2.4**). Photoproducts were not detected in dark controls and were typically stable in the no-soil controls (**Table S2.4**). However, despite silanization, recoveries for parents and photoproducts in no-soil controls were often lower (**Table S2.3, S2.4**) than expected. Solvent washes subsequently indicated that up to 50-65% of the input mass was sorbed onto the glassware in the absence of a competing soil matrix, and 0-30% when soil was present (**Table S2.5**). Partitioning to glassware may thus yield a slight positive bias in some partitioning estimates (overestimating partitioning potential). Such effects become evident, especially at lower input masses, via comparison to no-soil controls, and may be masked in those studies using high sorbate concentrations (μM-mM concentrations) (Khan et al., 2009; Qu et al., 2014).

Partitioning data for TBA metabolites, ALT, and photoproducts were well approximated ($R^2$ >0.90) by linear isotherms (**Figure 2.7**, **Table 2.3**). Consistent with previous observations (Khan et al., 2009; Lee et al., 2003; Ying and Kookana, 2005), isotherm linearity indicated that hydrophobic partitioning dominated solute interactions with soil-sand media. Among parent TBA metabolites, TBO showed the highest sorption capacity (log$K_{oc}$: 2.76 ± 0.02), followed by 17β-TBOH (log$K_{oc}$: 2.50 ± 0.05) and 17α-TBOH (log$K_{oc}$: 2.46 ± 0.03), consistent with prior studies (log$K_{oc}$: 3.38 for TBO, 3.08 for 17β-TBOH, 2.77 for 17α-TBOH) (Khan et al., 2009). The log$K_{oc}$ of ALT was 2.72 ± 0.01. The higher sorption

potential observed for TBO is likely related to its monopolar structure (less capable of H-bond donation versus the bipolar 17α,β-TBOH), and is consistent with its higher log$K_{hw}$ value but weakly correlated to its lower log$K_{ow}$ compared to 17α-TBOH and 17β-TBOH (**Table 2.3**). 17α-TBOH and 17β-TBOH showed similar capacities for sorption (Δlog$K_{oc}$: 0.04), which also scaled with their similar log$K_{hw}$ (Δlog$K_{hw}$: 0.03) values but did not scale with their log$K_{ow}$ values (Δlog$K_{ow}$: 0.25). We note the sorption potentials of TBA metabolites are better estimated by log$K_{hw}$ values rather than log$K_{ow}$, indicating the contribution of hydrophobic partitioning to partitioning. This observation contrasts with prior reports of log$K_{oc}$ for 17α-TBOH and 17β-TBOH (Khan et al., 2009), and may be a concentration dependent effect (~0.1-10 μg/L here versus ~4-500 μg/L elsewhere). 17β-TBOH exhibited higher sorption capacities than TBO in the Freundlich isotherms reported by Qu et al, ($K_f$: 0.98 for 17β-TBOH, 0.61 for TBO, 0.39 for 17α-TBOH), which may reflect the different soil types used or isotherm non-linearity effects (1/n of 0.63-0.85 in the Freundlich isotherms) (Qu et al., 2014).

Photoproducts, based on the $K_{oc}$ values, sorbed by a factor of 2-3 less than parent compounds. Observed log$K_{oc}$ values for photoproducts scaled with sorption capacities of parent steroids, with the more hydrophobic ALT photoproducts exhibiting the highest sorption capacities, followed by TBO and 17α-TBOH photoproducts (log$K_{oc}$: ALT-CAP (2.57 ± 0.03) > TBO-OH (2.23 ± 0.03) > 12-OH-17α-TBOH (2.13 ± 0.04) > ALT-CAP-OH (2.07 ± 0.01) > 5-OH-17α-TBOH (1.92 ± 0.01)). Notably, the observed log$K_{oc}$ disparities were quite similar between the parent-photoproduct pairs (Δlog$K_{oc}$: 17α-TBOH pair, 0.33-

0.54; TBO pair, 0.53; ALT-CAP pair, 0.50) despite the larger differences in $\Delta \log K_{ow}$. The lack of $\log K_{hw}$ values for photoproducts (discussed above) precluded further analysis.

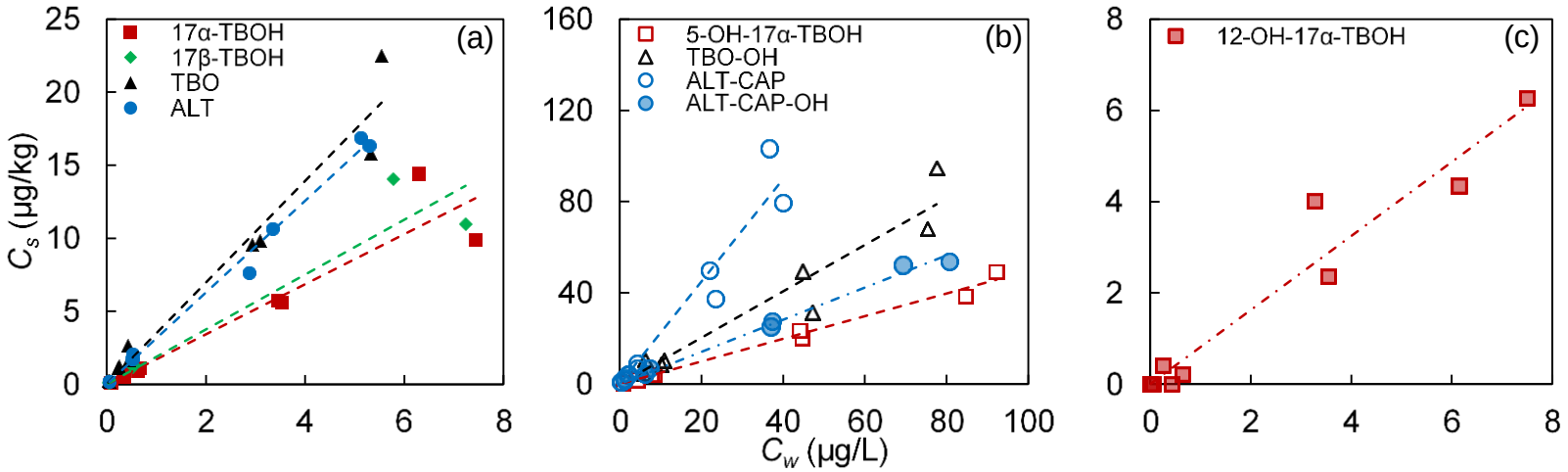


**Figure 2.7** Linear isotherms for: (a) TBA metabolites, ALT and (b,c) related photoproducts. 12-OH-17α-TBOH had a lower concentration range in (c) due to lower photoreaction yield. $C_w$ and $C_s$ are aqueous and solid phase concentrations of the solutes, respectively. Note the different X and Y axis scales across the figures.

Despite the subtle difference within parent compounds, these batch studies indicate that the sorption potential of parents and photoproducts, as quantified by log$K_{oc}$ values, generally scaled with their log$K_{ow}$ values ($p$ = 0.056; **Figure 2.8a**) except for TBO. Excluding TBO and TBO-OH, log$K_{oc}$ values were significantly correlated ($p$ <0.05) with log$K_{ow}$ values ($R^2$ of 0.75, **Figure 2.8b**). This relationship was used to predict the potential mobility of moderately hydrophobic steroids under different soil-water conditions and related implications for agricultural runoff treatment. These correlations, as suggested elsewhere (Schwarzenbach et al., 2003), again imply hydrophobic partitioning as the dominant steroid-soil interaction mechanism, although the outlier behavior of TBO may arise from potential contributions of H-bonding or other specific interactions contributing to partitioning.

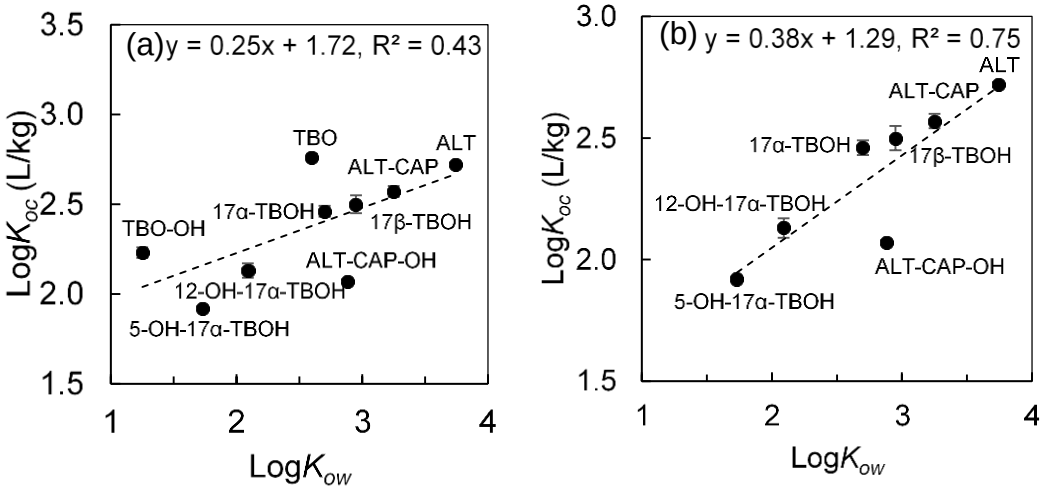


**Figure 2.8** Observed correlations between (a) log$K_{oc}$ and log$K_{ow}$ of TBA metabolites, ALT, and photoproducts and (b) repeat correlations but with outlier values for TBO and TBO-OH removed. Error bars represent standard deviations.

## 2.4 Environmental Implications

Bioactive TPs such as the trienone photoproducts are potentially important contributors to the environmental burden and ecological risk of potent steroidal agrochemicals; therefore, an analytical method to detect and quantify these compounds in agroecosystems is needed. In the

present study, we first developed a multi-residue LC-MS/MS method coupled with SPE extraction and optimized it for the detection and quantification of the photoproducts of TBA metabolites and ALT along with the corresponding parent compounds at environmentally relevant concentrations. This method relied upon rapid sample processing and optimized processing conditions to minimize product-to-parent reversion and enable photoproduct quantification (intra-day RSD <20%). This method can detect TBA metabolites, ALT, and photoproducts with method detection limits of sub ng $L^{-1}$ for TBA metabolites and ALT and low ng $L^{-1}$ for their photoproducts. At ~1-10 ng $L^{-1}$ concentrations and employing isotope dilution techniques, overall method recoveries were 96-115% for parent compounds and 75-125% for photoproducts (except 12-OH-17α-TBOH). Optimal method performance relies upon the use of a dedicated instrument to minimize inter-day variability, rapid sample processing and careful eluent storage, and minimization of cationic constituents in eluents and the detection system to reduce adduct formation.

The developed method was then applied to study the batch sorption of the trienone steroids (17α-TBOH, 17β-TBOH, TBO, ALT) and their photoproducts in soil-water systems, where we observed reduced sorption of photoproducts in soil-sand mixtures relative to parents ($\log K_{oc}$ difference of parent and photoproduct: 0.33-0.65). Building from the linear correlation between $\log K_{oc}$ and $\log K_{ow}$ ($\log K_{oc} = 0.38 \log K_{ow} + 1.29$), we estimated the expected dissolved fraction of trienone steroids ($\log K_{ow}$ = 1-4) in several soil-water systems representative of agroecosystems (**Figure 2.9**). In most surface waters (i.e., receiving river, agricultural runoff, marshes), photoproduct formation would be expected to have little effect on the transport potential of trenione steroids due to the low availability of suspended particles for partitioning. However, for transport in agricultural systems with higher solids loadings (i.e., manure lagoon), or subsurface systems (i.e., hyporheic zones, shallow tile drain systems) (Ward et al., 2015) and treatment (i.e.,

infiltration basins), a unit reduction of log$K_{ow}$ (parent median log$K_{ow}$: 2.83; photoproduct median log$K_{ow}$: 1.83) can result in 5-10% increases in water-dissolved fractions and impacts to transport. Based on such data, we anticipate that treatment efficiencies of agricultural runoff management measures (e.g., 30-60% 17α-TBOH removal by subsurface infiltration, 70-90% by vegetative filter strips) (Jones et al., 2014b) for trienone steroids would be overestimated if phototransformation was not considered. Moreover, parent steroids (TBA metabolites and ALT-CAP) can regenerate from photoproducts during soil-water transport, which extends the persistence of these steroids in soil-water systems.

Our previous work has demonstrated the impact of product-to-parent reversion on fate consideration of trenbolone parents, indicating that reversion cycling affects transport in systems like hyporheic zones and increases persistence and alters bioactivity of trienone steroids in surface waters (Ward et al., 2015). Here, we demonstrate that the photohydration-dehydration cycling also increases the transport potential of trienone steroids in soil-water systems. We anticipate these coupled sorption-phototransformation processes are important fate outcomes whenever ALT and TBA metabolites leach from animal manures and occur in sunlit surface waters (e.g., agricultural runoff, irrigation canals, vernal pools). In particular, the extreme photoreactivity of ALT, with 25-40 second half-lives to ALT-CAP and ALT-CAP-OH, respectively, suggests that photoreaction and photoproducts should dominate fate outcomes for this lightly studied potent steroid pharmaceutical, although such outcomes have not been carefully considered in directed studies (Wammer et al., 2016). Future studies on environmental fate of dienone and trienone steroids should consider photoproducts, including consideration of their physicochemical properties, reactivity and transport potential, to better understand the occurrence and ecological risks of these potent pharmaceuticals.

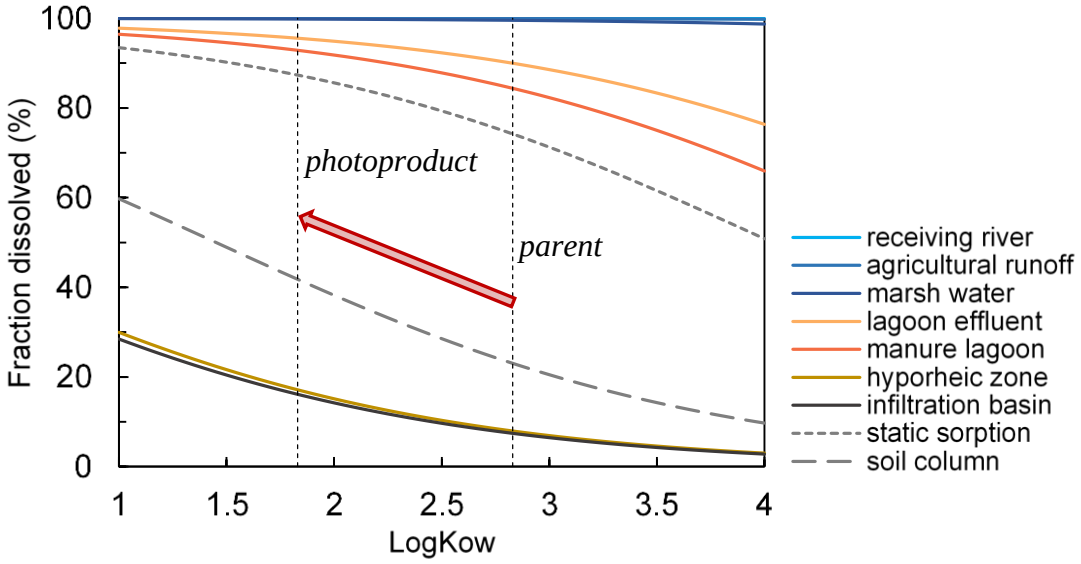


**Figure 2.9** Predicted fraction of trienone steroids dissolved in water (i.e. mobile) as a function of log$K_{ow}$ under conditions representative of model agro-ecosystems. Dashed black lines mark the median log$K_{ow}$ values of the parent trienone steroids (2.83) versus values for photoproducts (1.83). The batch sorption and soil column systems represent experimental conditions described in this study. For model agricultural systems, manure lagoon and lagoon effluent represent conditions described for swine production (TSS of 2000 mg · $L^{-1}$ for manure lagoon and 1200 mg · $L^{-1}$ for lagoon effluent, with organic carbon content ($f_{oc}$) of 40%) (Huang et al., 2006; Liu et al., 2015). Agricultural runoff, hyporheic zone, river, and marsh water represent potential transport pathways on manure-fertilized lands. The agricultural runoff and receiving water are modeled as a representative manured fields (TSS of 300 mg · $L^{-1}$ for agricultural runoff and 100 mg · $L^{-1}$ for receiving water, with $f_{oc}$ of 1.3%) (Jordan et al., 2003), and the hyporheic zone and marsh water conditions reflect typical reported values (hyporheic zone: porosity of 0.2, bulk density of 2.5 kg·$L^{-1}$, and $f_{oc}$ of 0.5%; marsh water: TSS of 100 mg solids · $L^{-1}$, $f_{oc}$ of 20%) (Jones et al., 2014b). For treatment systems, subsurface infiltration conditions are modeled as those reported for a grazing rangeland (porosity: 0.47, bulk density: 1.5 kg·$L^{-1}$, $f_{oc}$: 1.7%) (Rene P. Schwarzenbach et al., 2019).

## References


Ankley, G.T., Coady, K.K., Gross, M., Holbech, H., Levine, S.L., Maack, G., Williams, M., 2018. A critical review of the environmental occurrence and potential effects in aquatic vertebrates of the potent androgen receptor agonist 17β-trenbolone. Environ. Toxicol. Chem. 37, 2064–2078.

Baltrusaitis, J., Patterson, E.V., O'Connor, M., Qu, S., Kolodziej, E.P., Cwiertny, D.M., 2016. Reversible photohydration of trenbolone acetate metabolites: mechanistic understanding of product-to-parent reversion through complementary experimental and theoretical approaches. Environ. Sci. Technol. 50, 6753–6761.

Bartelt-Hunt, S.L., Snow, D.D., Kranz, W.L., Mader, T.L., Shapiro, C.A., Donk, S.J. van, Shelton, D.P., Tarkalson, D.D., Zhang, T.C., 2012. Effect of growth promotants on the occurrence of endogenous and synthetic steroid hormones on feedlot soils and in runoff from beef cattle feeding operations. Environ. Sci. Technol. 46, 1352–1360.

Birdsall, R.E., Gilar, M., Shion, H., Yu, Y.Q., Chen, W., 2016. Reduction of metal adducts in oligonucleotide mass spectra in ion-pair reversed-phase chromatography/mass spectrometry analysis. Rapid Commun. Mass Spectrom. 30, 1667–1679.

Biswas, S., Kranz, W.L., Shapiro, C.A., Snow, D.D., Bartelt-Hunt, S.L., Mamo, M., Tarkalson, D.D., Zhang, T.C., Shelton, D.P., van Donk, S.J., Mader, T.L., 2017. Effect of rainfall timing and tillage on the transport of steroid hormones in runoff from manure amended row crop fields. J. Hazard. Mater. 324, 436–447.

Blackwell, B.R., Brown, T.R., Broadway, P.R., Buser, M.D., Brooks, J.C., Johnson, B.J., Cobb, G.P., Smith, P.N., 2014. Characterization of trenbolone acetate and estradiol metabolite excretion profiles in implanted steers. Environ. Toxicol. Chem. 33, 2850–2858.

Blackwell, B.R., Cai, Q., Smith, P.N., Cobb, G.P., 2011. Liquid chromatography–tandem mass spectrometry analysis of 17α-trenbolone, 17β-trenbolone and trendione in airborne particulate matter. Talanta 85, 1317–1323.

Blackwell, B.R., Wooten, K.J., Buser, M.D., Johnson, B.J., Cobb, G.P., Smith, P.N., 2015. Occurrence and characterization of steroid growth promoters associated with particulate matter originating from beef cattle feedyards. Environ. Sci. Technol. 49, 8796–8803.

Chang, H., Wu, S., Hu, J., Asami, M., Kunikane, S., 2008. Trace analysis of androgens and progestogens in environmental waters by ultra-performance liquid chromatography–electrospray tandem mass spectrometry. J. Chromatogr. A 1195, 44–51.

Cwiertny, D.M., Snyder, S.A., Schlenk, D., Kolodziej, E.P., 2014. Environmental designer drugs: when transformation may not eliminate risk. Environ. Sci. Technol. 48, 11737–11745.

Dunphy, J.C., Pessler, D.G., Morrall, S.W., Evans, K.A., Robaugh, D.A., Fujimoto, G., Negahban, A., 2001. Derivatization LC/MS for the simultaneous determination of fatty alcohol and alcohol ethoxylate surfactants in water and wastewater samples. Environ. Sci. Technol. 35, 1223–1230.

Durhan, E. J., Lambright, C. S., Makynen, E. A., Lazorchak, J., Hartig, P. C., Wilson, V. S., Gray, L. E., Ankley, G. T., 2006. Identification of metabolites of trenbolone acetate in androgenic runoff from a beef feedlot. Environ. Health Perspect. 114, 65–68.

Ende, M., Spiteller, G., 1982. Contaminants in mass spectrometry. Mass Spectrom. Rev. 1, 29–62.

Fent, K., 2015. Progestins as endocrine disrupters in aquatic ecosystems: Concentrations, effects and risk assessment. Environ. Int. 84, 115–130.

Food and Drug Administration, 2018. Guidance for industry: bioanalytical method validation.

FDA Animal Drug Safety Communication: FDA highlights potential health risks to people exposed to altrenogest products for horses or pigs. https://www.fda.gov/AnimalVeterinary/NewsEvents/CVMUpdates/ucm612395.htm (accessed 4.13.19).
Fu, Q., Dudley, S., Sun, C., Schlenk, D., Gan, J., 2018. Stable isotope labeling-assisted metabolite probing for emerging contaminants in plants. Anal. Chem. 90, 11040–11047.
Gall, H.E., Sassman, S.A., Lee, L.S., Jafvert, C.T., 2011. Hormone discharges from a midwest tile-drained agroecosystem receiving animal wastes. Environ. Sci. Technol. 45, 8755–8764.
Goeppert, N., Dror, I., Berkowitz, B., 2014. Detection, fate and transport of estrogen family hormones in soil. Chemosphere 95, 336–345.
Golovko, O., Šauer, P., Fedorova, G., Kroupová, H.K., Grabic, R., 2018. Determination of progestogens in surface and waste water using SPE extraction and LC-APCI/APPI-HRPS. Sci. Total Environ. 621, 1066–1073.
Huang, G.F., Wu, Q.T., Wong, J.W.C., Nagar, B.B., 2006. Transformation of organic matter during co-composting of pig manure with sawdust. Bioresour. Technol. 97, 1834–1842.
Jensen, K.M., Makynen, E.A., Kahl, M.D., Ankley, G.T., 2006. Effects of the feedlot contaminant 17α-trenbolone on reproductive endocrinology of the fathead minnow. Environ. Sci. Technol. 40, 3112–3117.
Jones, G.D., Benchetler, P.V., Tate, K.W., Kolodziej, E.P., 2014a. Trenbolone acetate metabolite transport in rangelands and irrigated pasture: observations and conceptual approaches for agro-ecosystems. Environ. Sci. Technol. 48, 12569–12576.
Jones, G.D., Benchetler, P.V., Tate, K.W., Kolodziej, E.P., 2014b. Surface and subsurface attenuation of trenbolone acetate metabolites and manure-derived constituents in irrigation runoff on agro-ecosystems. Environ. Sci. Process. Impacts 16, 2507–2516.
Jordan, T.E., Whigham, D.F., Hofmockel, K.H., Pittek, M.A., 2003. Nutrient and sediment removal by a restored wetland receiving agricultural runoff. J. Environ. Qual. 32, 1534–1547.
Karickhoff, S.W., Brown, D.S., 1979. Determination of octanol/water distribution coefficients, water solubilities, and sediment/water partition coefficients for hydrophobic organic pollutants, EPA-600/4-79-032.
Keller, B.O., Sui, J., Young, A.B., Whittal, R.M., 2008. Interferences and contaminants encountered in modern mass spectrometry. Anal. Chim. Acta, Mass Spectrometry 627, 71–81.
Khan, B., Lee, L.S., 2012. Estrogens and synthetic androgens in manure slurry from trenbolone acetate/estradiol implanted cattle and in waste-receiving lagoons used for irrigation. Chemosphere 89, 1443–1449.
Khan, B., Lee, L.S., Sassman, S.A., 2008. Degradation of synthetic androgens 17α- and 17β-trenbolone and trendione in agricultural soils. Environ. Sci. Technol. 42, 3570–3574.
Khan, B., Qiao, X., Lee, L.S., 2009. Stereoselective sorption by agricultural soils and liquid-liquid partitioning of trenbolone (17alpha and 17beta) and trendione. Environ. Sci. Technol. 43, 8827–8833.
Wong, K.L., Webb, D.T., Nagorzanski, M.R., Kolpin, D.W., Hladik, M.L., Cwiertny, D.M., LeFevre, G.H., 2019. Chlorinated byproducts of neonicotinoids and their metabolites: an unrecognized human exposure potential? Environ. Sci. Technol. Lett. 6, 98–105.
Kolodziej, E.P., Qu, S., Forsgren, K.L., Long, S.A., Gloer, J.B., Jones, G.D., Schlenk, D., Baltrusaitis, J., Cwiertny, D.M., 2013. Identification and environmental implications of

photo-transformation products of trenbolone acetate metabolites. Environ. Sci. Technol. 47, 5031–5041.
Kumar, V., Johnson, A.C., Trubiroha, A., Tumová, J., Ihara, M., Grabic, R., Kloas, W., Tanaka, H., Kroupová, H.K., 2015. The challenge presented by progestins in ecotoxicological research: a critical review. Environ. Sci. Technol. 49, 2625–2638.
Lampinen-Salomonsson, M., Beckman, E., Bondesson, U., Hedeland, M., 2006. Detection of altrenogest and its metabolites in post administration horse urine using liquid chromatography tandem mass spectrometry—increased sensitivity by chemical derivatisation of the glucuronic acid conjugate. J. Chromatogr. B 833, 245–256.
Lee, L.S., Strock, T.J., Sarmah, A.K., Rao, P.S.C., 2003. Sorption and dissipation of testosterone, estrogens, and their primary transformation products in soils and sediment. Environ. Sci. Technol. 37, 4098–4105.
Liu, S.-S., Ying, G.-G., Liu, Y.-S., Yang, Y.-Y., He, L.-Y., Chen, J., Liu, W.-R., Zhao, J.-L., 2015. Occurrence and removal of progestagens in two representative swine farms: Effectiveness of lagoon and digester treatment. Water Res. 77, 146–154.
Malone, E.M., Elliott, C.T., Kennedy, D.G., Regan, L., 2009. Development of a rapid method for the analysis of synthetic growth promoters in bovine muscle using liquid chromatography tandem mass spectrometry. Anal. Chim. Acta, Papers presented at EuroResidue VI 637, 112–120.
Matuszewski, B.K., Constanzer, M.L., Chavez-Eng, C.M., 2003. Strategies for the assessment of matrix effect in quantitative bioanalytical methods based on HPLC−MS/MS. Anal. Chem. 75, 3019–3030.
Morthorst, J.E., Holbech, H., Bjerregaard, P., 2010. Trenbolone causes irreversible masculinization of zebrafish at environmentally relevant concentrations. Aquat. Toxicol. 98, 336–343.
Olmstead, A.W., Kosian, P.A., Johnson, R., Blackshear, P.E., Haselman, J., Blanksma, C., Korte, J.J., Holcombe, G.W., Burgess, E., Lindberg-Livingston, A., Bennett, B.A., Woodis, K.K., Degitz, S.J., 2012. Trenbolone causes mortality and altered sexual differentiation in Xenopus tropicalis during larval development. Environ. Toxicol. Chem. 31, 2391–2398.
Orlando, E.F., Kolok, A.S., Binzcik, G.A., Gates, J.L., Horton, M.K., Lambright, C.S., Gray, L.E., Soto, A.M., Guillette, L.J., 2004. Endocrine-disrupting effects of cattle feedlot effluent on an aquatic sentinel species, the fathead minnow. Environ. Health Perspect. 112, 353–358.
Orlando, E.F., Ellestad, L.E., 2014. Sources, concentrations, and exposure effects of environmental gestagens on fish and other aquatic wildlife, with an emphasis on reproduction. Gen. Comp. Endocrinol. 203, 241–249.
Parker, J.A., Webster, J.P., Kover, S.C., Kolodziej, E.P., 2012. Analysis of trenbolone acetate metabolites and melengestrol in environmental matrices using gas chromatography–tandem mass spectrometry. Talanta 99, 238–246.
Poucke, C.V., Velde, M.V.D., Peteghem, C.V., 2005. Combination of liquid chromatography/tandem mass spectrometry and gas chromatography/mass spectrometry for the detection of 21 anabolic steroid residues in bovine urine. J. Mass Spectrom. 40, 731–738.
Qu, S., Kolodziej, E.P., Cwiertny, D.M., 2014. Sorption and mineral-promoted transformation of synthetic hormone growth promoters in soil systems. J. Agric. Food Chem. 62, 12277–12286.

Qu, S., Kolodziej, E.P., Cwiertny, D.M., 2012. Phototransformation rates and mechanisms for synthetic hormone growth promoters used in animal agriculture. Environ. Sci. Technol. 46, 13202–13211.
Qu, S., Kolodziej, E.P., Long, S.A., Gloer, J.B., Patterson, E.V., Baltrusaitis, J., Jones, G.D., Benchetler, P.V., Cole, E.A., Kimbrough, K.C., Tarnoff, M.D., Cwiertny, D.M., 2013. Product-to-parent reversion of trenbolone: unrecognized risks for endocrine disruption. Science 342, 347–351.
Quifer-Rada, P., Martínez-Huélamo, M., Jáuregui, O., Chiva-Blanch, G., Estruch, R., Lamuela-Raventós, R.M., 2013. Analytical condition setting a crucial step in the quantification of unstable polyphenols in acidic conditions: Analyzing prenylflavanoids in biological samples by liquid chromatography–electrospray ionization triple quadruple mass spectrometry. Anal. Chem. 85, 5547–5554.
Schwarzenbach, R.P., Gschwend, P.M., Imboden, D.M., 2003. Environmental Organic Chemistry, 2nd Edition. John Wiley & Sons, Inc.
Schiffer, B., Daxenberger, A., Meyer, K., Meyer, H.H., 2001. The fate of trenbolone acetate and melengestrol acetate after application as growth promoters in cattle: environmental studies. Environ. Health Perspect. 109, 1145–1151.
Snow, D.D., Damon-Powell, T., Onanong, S., Cassada, D.A., 2013. Sensitive and simplified analysis of natural and synthetic steroids in water and solids using on-line solid-phase extraction and microwave-assisted solvent extraction coupled to liquid chromatography tandem mass spectrometry atmospheric pressure photoionization. Anal. Bioanal. Chem. 405, 1759–1771.
Squires, E.L., 2008. Hormonal manipulation of the mare: a review. J. Equine Vet. Sci. 28, 627–634.
Squires, E.L., Heesemann, C.P., Webel, S.K., Shideler, R.K., Voss, J.L., 1983. Relationship of altrenogest to ovarian activity, hormone concentrations and fertility of mares. J. Anim. Sci. 56, 901–910.
Strahm, E., Kohler, I., Rudaz, S., Martel, S., Carrupt, P.-A., Veuthey, J.-L., Saugy, M., Saudan, C., 2008. Isolation and quantification by high-performance liquid chromatography–ion-trap mass spectrometry of androgen sulfoconjugates in human urine. J. Chromatogr. A, 1196–1197, 153–160.
Tian, Z., Gold, A., Nakamura, J., Zhang, Z., Vila, J., Singleton, D.R., Collins, L.B., Aitken, M.D., 2017. Nontarget analysis reveals a bacterial metabolite of pyrene implicated in the genotoxicity of contaminated soil after bioremediation. Environ. Sci. Technol. 51, 7091–7100.
Tong, W., Chowdhury, S.K., Su, A.-D., Alton, K.B., 2010. Quantitation of parent drug and its unstable metabolites by in situ coulometric oxidation and liquid chromatography−tandem mass spectrometry. Anal. Chem. 82, 10251–10257.
van Leeuwen, J.J.J., Williams, S.I., Martens, M.R.T.M., Jourquin, J., Driancourt, M.A., Kemp, B., Soede, N.M., 2011. The effect of different postweaning altrenogest treatments of primiparous sows on follicular development, pregnancy rates, and litter sizes. J. Anim. Sci. 89, 397–403.
von Gunten, U., 2018. Oxidation processes in water treatment: are we on track? Environ. Sci. Technol. 52, 5062–5075.
Wammer, K.H., Anderson, K.C., Erickson, P.R., Kliegman, S., Moffatt, M.E., Berg, S.M., Heitzman, J.A., Pflug, N.C., McNeill, K., Martinovic-Weigelt, D., Abagyan, R., Cwiertny, D.M., Kolodziej, E.P., 2016. Environmental photochemistry of altrenogest:

photoisomerization to a bioactive product with increased environmental persistence via reversible photohydration. Environ. Sci. Technol. 50, 7480–7488.
Wang, W.-L., Wu, Q.-Y., Huang, N., Xu, Z.-B., Lee, M.-Y., Hu, H.-Y., 2018. Potential risks from UV/H2O2 oxidation and UV photocatalysis: A review of toxic, assimilable, and sensory-unpleasant transformation products. Water Res. 141, 109–125.
Ward, A.S., Cwiertny, D.M., Kolodziej, E.P., Brehm, C.C., 2015. Coupled reversion and stream-hyporheic exchange processes increase environmental persistence of trenbolone metabolites. Nat. Commun. 6, 7067.
Webster, J.P., Kover, S.C., Bryson, R.J., Harter, T., Mansell, D.S., Sedlak, D.L., Kolodziej, E.P., 2012. Occurrence of trenbolone acetate metabolites in simulated confined animal feeding operation (CAFO) runoff. Environ. Sci. Technol. 46, 3803–3810.
Ying, G.-G., Kookana, R.S., 2005. Sorption and degradation of estrogen-like-endocrine disrupting chemicals in soil. Environ. Toxicol. Chem. 24, 2640–2645.

## Supplementary Materials

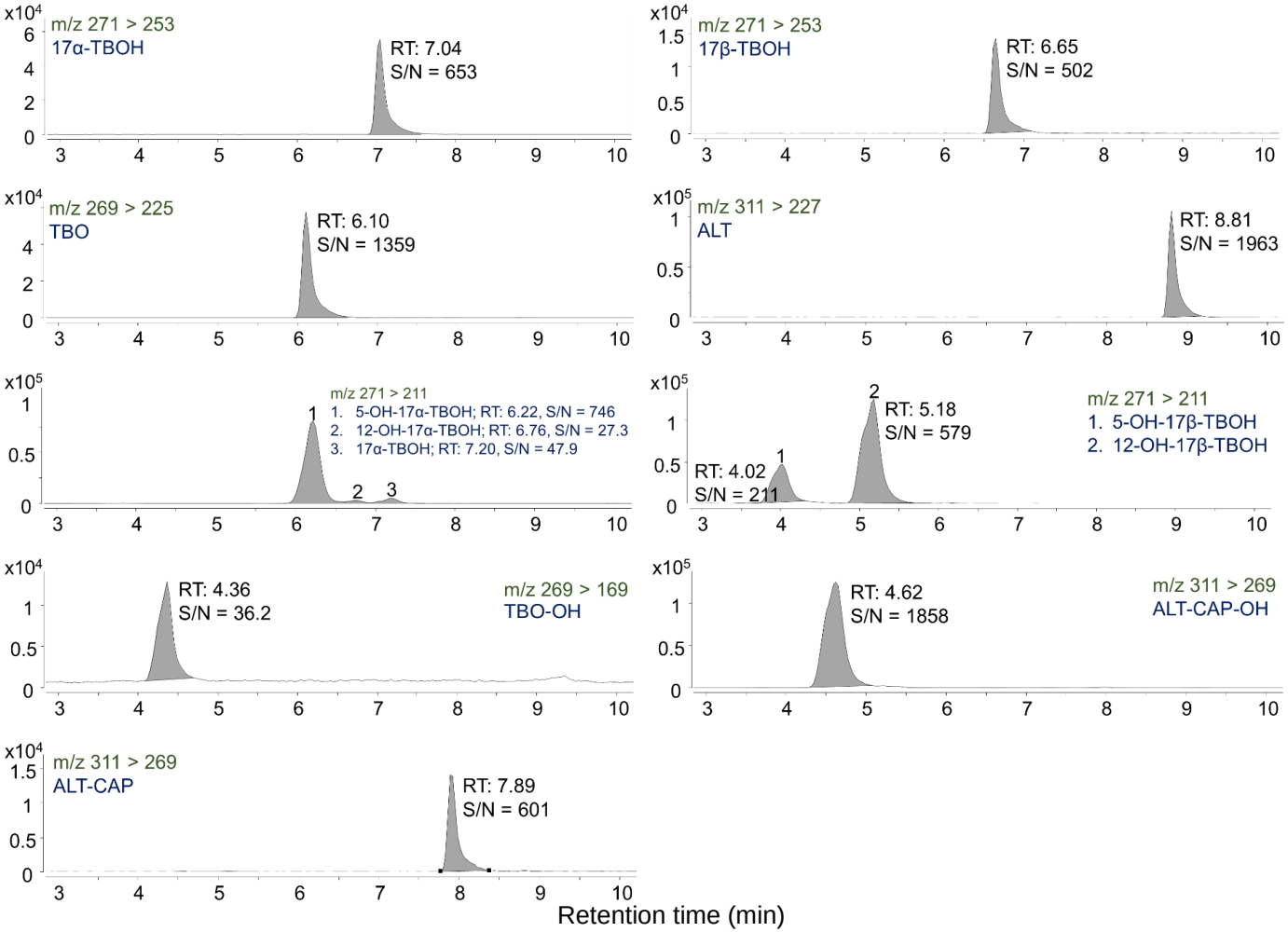


**Figure S2.1** Chromatograms of 1 µg $L^{-1}$ 17α-TBOH, 17β-TBOH, TBO, ALT, or 10 µg $L^{-1}$ photoproduct (as parent concentration before irradiation) standards, without solid phase extraction. Chromatograms were acquired with a Poroshell 120Å EC C18 column (3.0 × 50 mm, 2.7 µm) preceded by a C18 guard column (2.0 × 4mm), with mobile phases of pure water and pure methanol under a 12 min gradient elution program, and 100 µL injection volume.

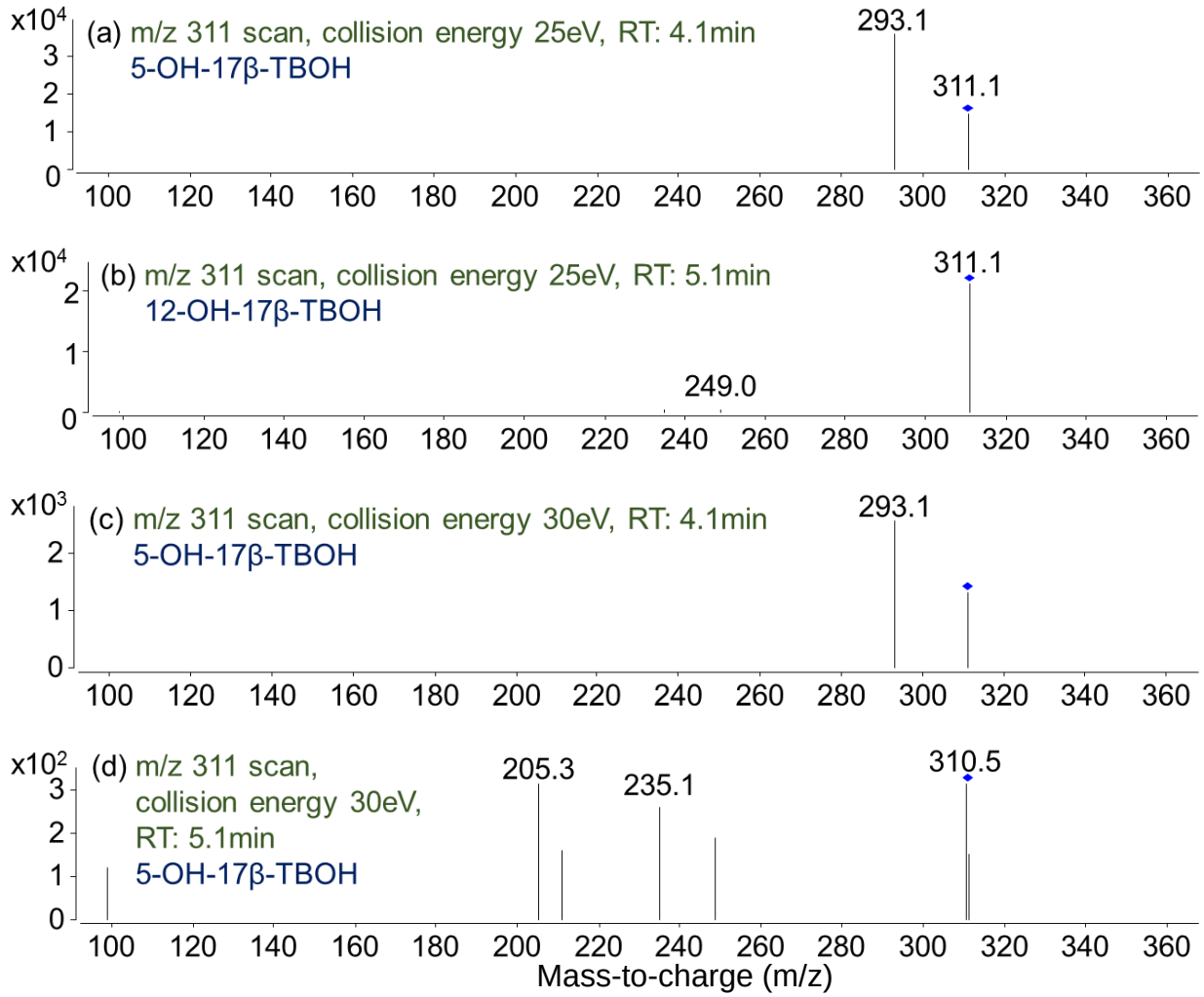


**Figure S2.2** MS/MS spectra for m/z 311 (sodium adduct of 17β-TBOH photoproducts) under 25 eV collision energy at (a) 4.1 min (5-OH-17β-TBOH), (b) 5.1 min (12-OH-17β-TBOH); and under 30 eV collision energy at (c) 4.1 min (5-OH-17β-TBOH), (d) 5.1 min (12-OH-17β-TBOH). Sodium adducts of 12-OH-17β-TBOH were less stable than that of 5-OH-17β-TBOH in ion collision. Spectra were acquired with a Poroshell 120Å EC C18 column (3.0 × 50 mm, 2.7 μm) preceded by a C18 guard column (2.0 × 4mm), with mobile phases of pure water and pure methanol under a 12 min gradient elution program. Mass spectrometry parameters can be found in Section 2.3.1.2 of the main text and Table 2.1.

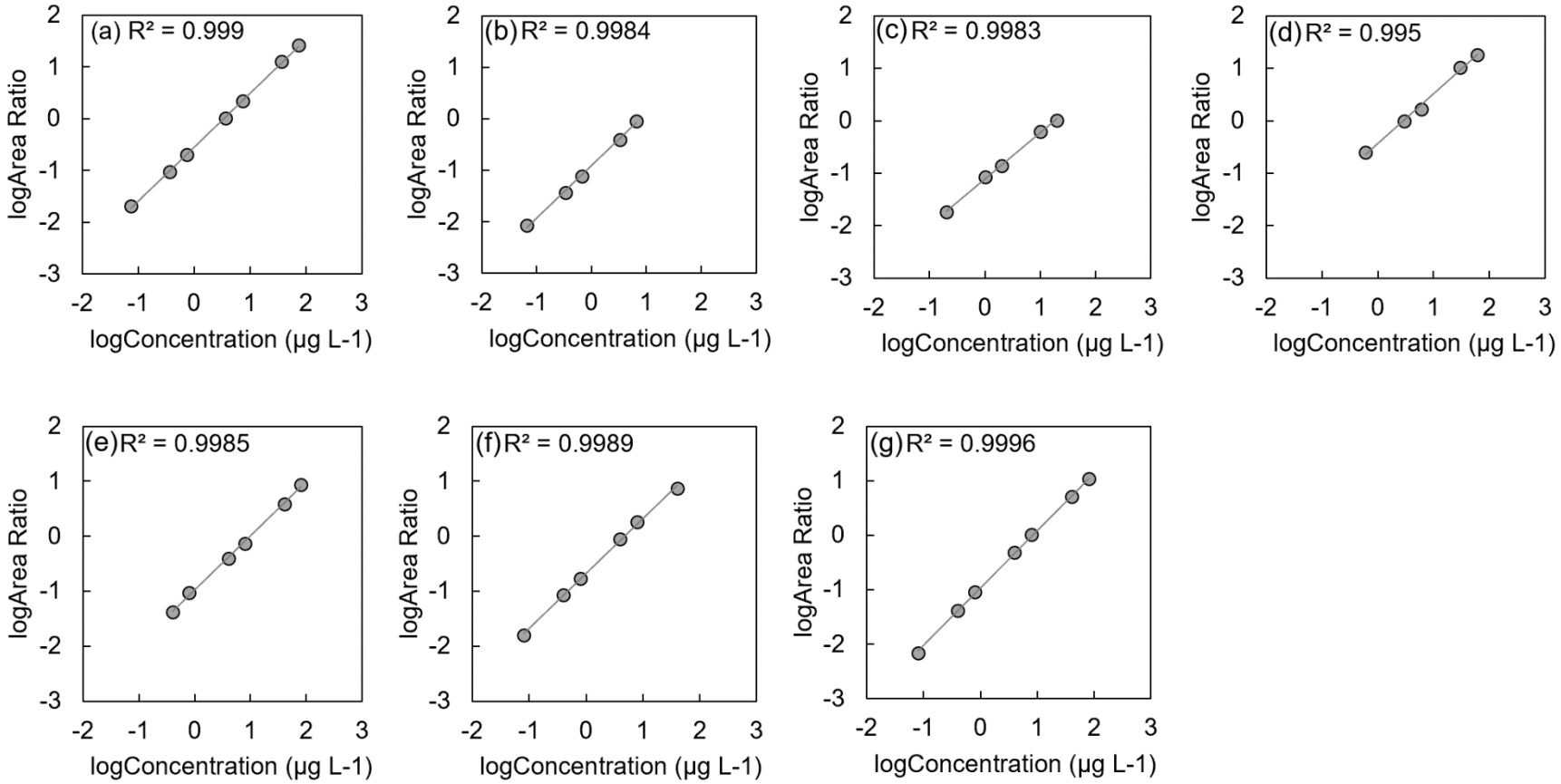


**Figure S2.3** Calibration curves of (a) 5-OH-17α-TBOH, (b) 12-OH-17α-TBOH, (c) 5-OH-17β-TBOH, (d) 12-OH-17β-TBOH, (e) 5-OH-TBO, (f) ALT-CAP, (g) ALT-CAP-OH at 0.1-100 µg $L^{-1}$ as parent concentrations before irradiation, corresponding to 0.073-73 ug $L^{-1}$ for 5-OH-17α-TBOH, 0.0067-6.7 µg $L^{-1}$ for 12-OH-17α-TBOH, 0.02-20 µg $L^{-1}$ for 5-OH-17β-TBOH, 0.06-60 µg $L^{-1}$ for 12-OH-17β-TBOH, and 0.08-80 µg $L^{-1}$ for 5-OH-TBO, ALT-CAP, and ALT-CAP-OH. When observed, calibration curves with fewer than seven data points represent no detection of the analytes at low concentrations. Area ratio refers to ratio of the LC-MS/MS peak areas of the analytes over that of the isotopic internal standard.

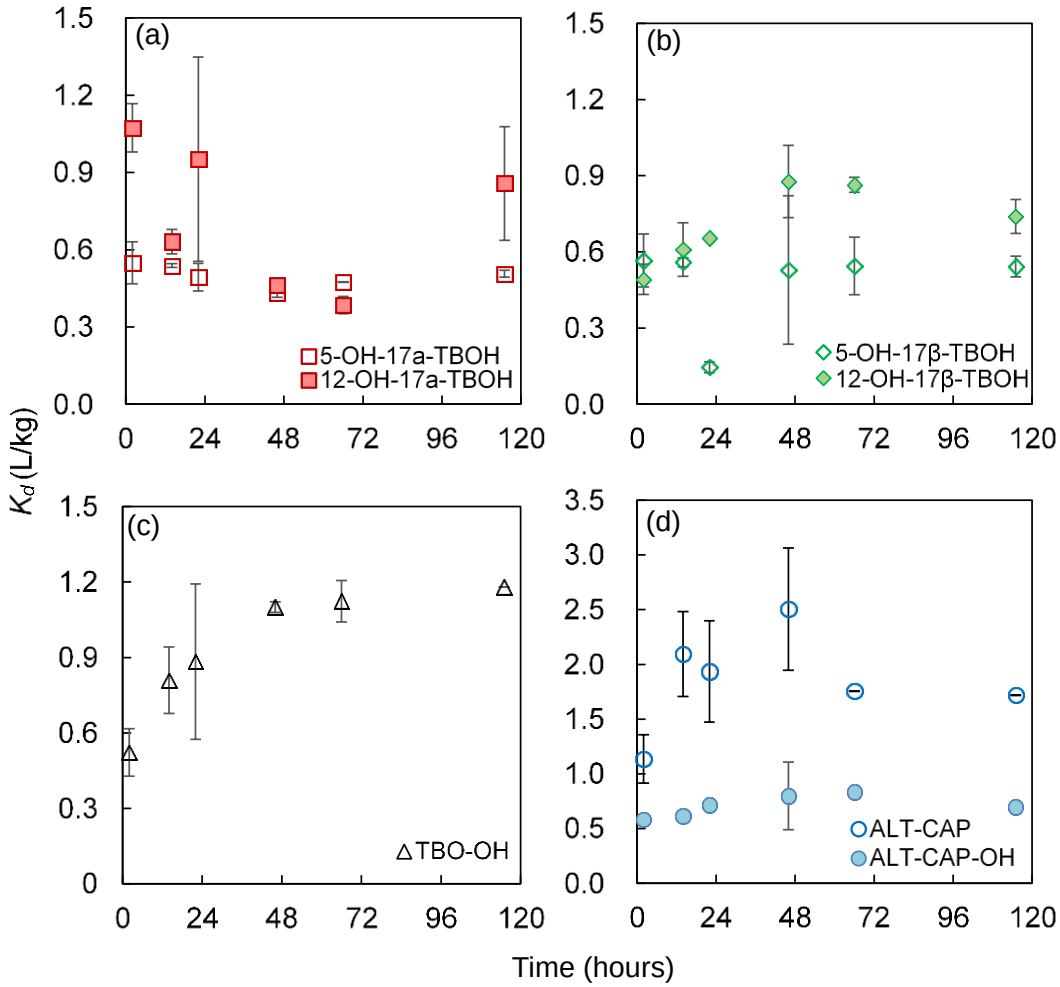


**Figure S2.4** The partitioning coefficients in single concentration (~50 µg/L as parents before irradiation) time series study for (a) 17α-TBOH, (b) 17β-TBOH, (c) TBO and (d) ALT photoproducts. Sorption was tested in duplicates at each time spot. The sorption system generally reaches equilibrium at 22 hours. Error bars represent standard deviations.

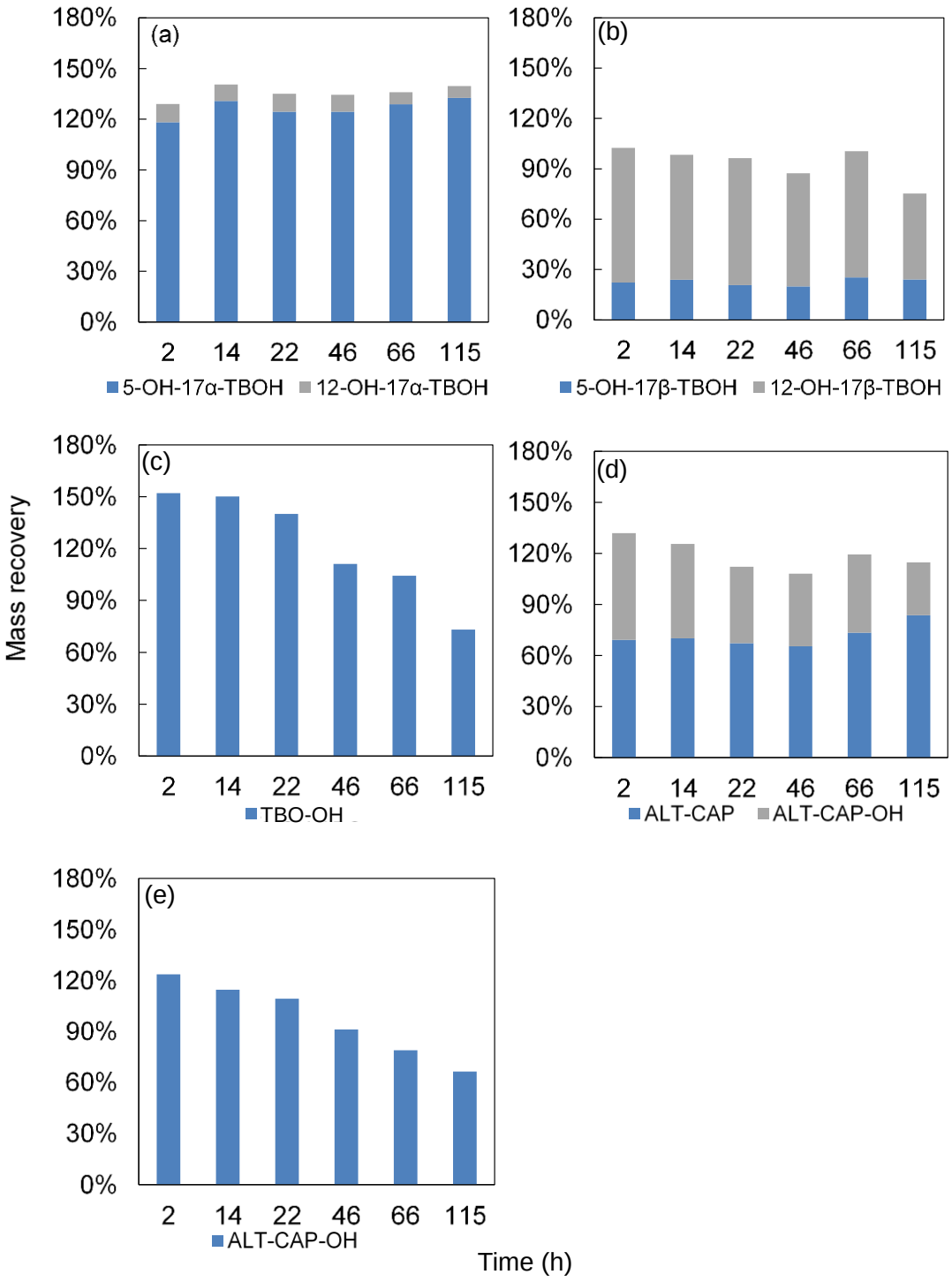


**Figure S2.5** The mass recoveries in single concentration (~50 µg/L as parents before irradiation) time series study for (a) 17α-TBOH, (b) 17β-TBOH, (c) TBO (d) ALT and (e) ALT-CAP photoproducts. Product-to-parent reversion was observed for ALT-CAP-OH. Mass recoveries were calculated as the mass ratio of photoproducts detected over the photoproducts spiked.

**Table S2.1** Peak areas percentage of 17α-TBOH, 17β-TBOH, TBO, ALT and the photoproducts in 0.001 g/L and 0.01 g/L sodium chloride solutions, compared with the peak areas in model water. These solutions were analyzed directly, without SPE concentration.

| compounds | NaCl concentration (g/L) | |
|---|---|---|
| | 0.001 | 0.01 |
| 17α-TBOH | 32% | 348% |
| 5-OH-17α-TBOH | 65% | 57% |
| 12-OH-17α-TBOH | 70% | 112% |
| 17α-TBOH-d3 | 68% | 109% |
| 17β-TBOH | 125% | 464% |
| 5-OH-17β-TBOH | 57% | 48% |
| 12-OH-17β-TBOH | 69% | 104% |
| 17β-TBOH-d3 | 76% | 128% |
| TBO | 101% | 227% |
| 5-OH-TBO | 36% | 33% |
| 17α-TBOH-d3 | 43% | 61% |
| ALT | 58% | 347% |
| ALT-CAP | 73% | 318% |
| ALT-CAP-OH | 85% | 48% |
| ALT-d5 | 83% | 101% |

**Table S2.2** Physical-chemical properties of model soil used in batch and column studies.

| parameter | | value | parameters | | value |
|---|---|---|---|---|---|
| pH | | 6.36 | metal | K | 827 |
| organic carbon (%) | | 1.13 | content | Mg | 7120 |
| CEC (meq/100 g) | | 11.5 | (μg/g) | Mn | 393 |
| total nitrogen (%) | | 0.086 | | Mo | 31.1 |
| metal | Al | 11400 | | Na | 113 |
| content | As | ND[a] | | Ni | 46.1 |
| (μg/g) | B | 35.3 | | P | 962 |
| | Ba | 49.2 | | Pb | 48.4 |
| | Ca | 2870 | | S | 215 |
| | Cd | ND | | Se | 43.6 |
| | Cr | 23.3 | | Zn | 60.4 |
| | Cu | 17.4 | | Si | 353 |
| | Fe | 21400 | | Ag | ND |

[a] ND = Not detected.

**Table S2.3** Isotherm data for TBA metabolites and ALT. Batch sorption was tested in duplicate experiments, plus a water control with no load of soil to test on the aqueous phase stability of TBA metabolites and ALT during equilibration period. $C_{in}$ (µg/L), $C_w$ (µg/L) and $C_s$ (µg/kg) are input concentrations and concentrations in the aqueous and sorbed phases, respectively.

| $C_{in}$ | | 17α-TBOH | | | 17β-TBOH | | | TBO | | | ALT | | |
|---|---|---|---|---|---|---|---|---|---|---|---|---|---|
| | | $C_w$ | $C_s$ | mass recovery (%) | $C_w$ | $C_s$ | mass recovery (%) | $C_w$ | $C_s$ | mass recovery (%) | $C_w$ | $C_s$ | mass recovery (%) |
| 0.1 | 1 | 0.059 | 0.10 | 84 | 0.056 | 0.14 | 91 | 0.033 | 0.28 | 103 | 0.055 | 0.22 | 109 |
| | 2 | 0.096 | 0.10 | 121 | 0.033 | 0.13 | 65 | 0.048 | 0.22 | 104 | 0.050 | 0.21 | 103 |
| | no-soil control | 0.059 | n.a.[a] | 59 | 0.078 | n.a. | 78 | 0.031 | n.a. | 31 | 0.060 | n.a. | 60 |
| 0.5 | 1 | 0.34 | 0.54 | 94 | -[b] | - | - | 0.22 | 1.1 | 99 | - | - | - |
| | 2 | 0.33 | 0.72 | 102 | - | - | - | 0.25 | 1.2 | 112 | - | - | - |
| | no-soil control | 0.25 | n.a. | 51 | - | - | - | 0.22 | n.a. | 43 | - | - | - |
| 1 | 1 | 0.63 | 0.94 | 86 | 0.54 | 1.3 | 87 | 0.44 | 1.7 | 87 | 0.53 | 2.1 | 105 |
| | 2 | 0.66 | 1.1 | 93 | 0.52 | 1.2 | 83 | 0.43 | 2.7 | 109 | 0.51 | 1.8 | 95 |
| | no-soil control | 0.81 | n.a. | 81 | 0.85 | n.a. | 85 | 0.54 | n.a. | 54 | 1.0 | n.a. | 104 |
| 5 | 1 | 3.4 | 5.8 | 98 | - | - | - | 2.9 | 9.6 | 107 | 3.3 | 11 | 120 |
| | 2 | 3.5 | 5.6 | 98 | - | - | - | 3.1 | 9.9 | 111 | 2.9 | 7.7 | 96 |
| | no-soil control | 2.2 | n.a. | 45 | - | - | - | 3.3 | n.a. | 65 | 3.6 | n.a. | 73 |
| 10 | 1 | 6.3 | 14 | 99 | 7.2 | 11 | 100 | 5.3 | 16 | 93 | 5.1 | 17 | 94 |
| | 2 | 7.4 | 9.9 | 99 | 5.8 | 14 | 93 | 5.5 | 23 | 112 | 5.3 | 16 | 94 |
| | no-soil control | 7.5 | n.a. | 75 | 10 | n.a. | 102 | 3.5 | n.a. | 35 | 8.0 | n.a. | 80 |

[a] n.a.: not applicable. The control only contained aqueous phase.

[b] The sorption of 17β-TBOH was not tested under 0.5 µg/L and 5 µg/L, and the sorption of ALT was not tested under 0.5 µg/L, due to inconsistent experiment design for different batches of experiment.

**Table S2.4** Isotherm data for photoproducts of TBA metabolites and ALT in static soil-water systems. Batch sorption was tested in duplicate which included a no-soil control and a dark control. $C_{in}$(μg/L), $C_w$ (μg/L) and $C_s$ (μg/kg) are input concentrations and concentrations in the aqueous and sorbed phases, respectively.

| $C_{in}$ | | 17α-TBOH photoproducts | | | | | | | 17β-TBOH photoproducts | | | | | | |
|---|---|---|---|---|---|---|---|---|---|---|---|---|---|---|---|
| | | 5-OH-17α-TBOH | | 12-OH-17α-TBOH | | 17α-TBOH | | mass | 5-OH-17β-TBOH | | 12-OH-17β-TBOH | | 17β-TBOH | | mass |
| | | $C_w$ | $C_s$ | $C_w$ | $C_s$ | $C_w$ | $C_s$ | recovery (%) | $C_w$ | $C_s$ | $C_w$ | $C_s$ | $C_w$ | $C_s$ | recovery (%) |
| 1 | 1 | 0.80 | 0.39 | ND[a] | ND | 0.065 | 0.11 | 119 | ND | ND | ND | ND | ND | ND | 0 |
| | 2 | 0.82 | 0.46 | ND | ND | 0.074 | 0.12 | 117 | ND | ND | ND | ND | ND | ND | 0 |
| | no-soil control | 0.61 | n.a.[b] | ND | n.a. | 0.11 | n.a. | 76 | ND | n.a. | ND | n.a. | ND | n.a. | 0 |
| | dark control | ND | ND | ND | ND | 0.83 | 0.89 | 105 | ND | ND | ND | ND | 0.59 | 1.5 | 96 |
| 5 | 1 | 3.9 | 2.4 | ND | ND | 0.39 | 0.44 | 113 | 0.49 | 1.6 | 3.0 | 4.0 | 0.042 | ND | 122 |
| | 2 | 4.3 | 1.9 | ND | ND | 0.37 | 0.42 | 119 | 0.57 | ND | 2.4 | ND | 0 | ND | 74 |
| | no-soil control | 3.0 | n.a. | ND | n.a. | 0.47 | n.a. | 75 | 0.89 | n.a. | 2.1 | n.a. | 0.12 | n.a. | 74 |
| | dark control | ND | ND | ND | ND | 4.3 | 3.8 | 104 | ND | ND | ND | ND | 2.3 | 9.5 | 93 |
| 10 | 1 | 8.5 | 4.1 | 0.25 | 0.41 | 0.72 | 0.85 | 123 | 1.8 | ND | 6.0 | ND | 0.047 | ND | 99 |
| | 2 | 7.7 | 4.1 | 0.64 | 0.23 | 0.72 | 0.83 | 118 | 2.1 | ND | 5.6 | ND | 0.055 | 0.077 | 96 |
| | no-soil control | 5.9 | n.a. | 0.17 | n.a. | 1.5 | n.a. | 76 | 0.99 | n.a. | 3.3 | n.a. | 0.37 | n.a. | 54 |
| | dark control | ND | ND | ND | ND | 8.5 | 8.1 | 105 | ND | ND | ND | ND | 6.5 | 15 | 102 |
| 50 | 1 | 45 | 20 | 3.5 | 2.4 | 4.9 | 5.7 | 135 | 6.0 | 6.1 | 21 | 13 | 0.35 | 0.56 | 78 |
| | 2 | 44 | 23 | 3.3 | 4.0 | 3.6 | 5.4 | 135 | 7.6 | 6.3 | 13 | 21 | 0.39 | 0.81 | 70 |
| | no-soil control | 38 | n.a. | 2.8 | n.a. | 7.6 | n.a. | 101 | 4.8 | n.a. | 16 | n.a. | 1.5 | n.a. | 52 |
| | dark control | ND | ND | ND | ND | 43 | 39 | 105 | ND | ND | ND | ND | 32 | 69 | 98 |
| 100 | 1 | 85 | 39 | 6.1 | 4.4 | 8.8 | 10 | 127 | 13 | 13 | 50 | 36 | 0.61 | 1.8 | 94 |
| | 2 | 92 | 49 | 7.5 | 6.3 | 9.3 | 12 | 142 | 11 | 5.4 | 44 | 14 | 0.77 | 1.8 | 75 |
| | no-soil control | 86 | n.a. | 5.4 | n.a. | 21 | n.a. | 114 | 3.5 | n.a. | 11 | n.a. | 4.5 | n.a. | 18 |
| | dark control | ND | ND | ND | ND | 81 | 79 | 101 | ND | ND | ND | ND | 72 | 130 | 106 |

| $C_{in}$ | | TBO photoproducts | | | | | ALT-CAP | | | | | | | ALT-CAP-OH | | | | | | |
|---|---|---|---|---|---|---|---|---|---|---|---|---|---|---|---|---|---|---|---|---|
| | | TBO-OH | | TBO | | mass recovery | ALT-CAP | | ALT-CAP-OH | | ALT | | mass recovery | ALT-CAP | | ALT-CAP-OH | | ALT | | mass recovery |
| | | $C_w$ | $C_s$ | $C_w$ | $C_s$ | (%) | $C_w$ | $C_s$ | $C_w$ | $C_s$ | $C_w$ | $C_s$ | (%) | $C_w$ | $C_s$ | $C_w$ | $C_s$ | $C_w$ | $C_s$ | (%) |
| 1 | 1 | 2.0 | ND | ND | ND | 252 | 0.34 | 0.89 | 0.39 | ND | 0.019 | 0.076 | 99 | 0.089 | ND | ND | ND | ND | ND | 0 |
| | 2 | ND[a] | ND | ND | ND | 0 | 0.30 | 1.1 | 0.32 | ND | 0.015 | 0.056 | 93 | 0.097 | ND | ND | ND | ND | ND | 0 |
| | no-soil control | 1.1 | n.a.[b] | ND | n.a. | 143 | 0.47 | n.a. | 0.47 | n.a. | 0.039 | n.a. | 98 | 0.14 | n.a. | 0.33 | n.a. | ND | n.a. | 42 |
| | dark control | ND | ND | 0.32 | 2.9 | 104 | ND | ND | ND | ND | 0.25 | 1.0 | 51 | ND | ND | ND | ND | 0.25 | 1.0 | 51 |
| 5 | 1 | 6.2 | 11 | 0.071 | 0.54 | 220 | 2.1 | 4.2 | 2.2 | 1.2 | 0.11 | 0.29 | 117 | 0.46 | 0.56 | 1.2 | 1.8 | ND | ND | 40 |
| | 2 | 5.8 | 4.9 | 0.058 | 0.42 | 177 | 1.9 | 4.0 | 1.9 | 1.1 | 0.090 | 0.27 | 105 | 0.49 | 0.43 | 1.1 | 2.4 | ND | ND | 43 |
| | no-soil control | 4.5 | n.a. | 0.16 | n.a. | 113 | 2.5 | n.a. | 2.2 | n.a. | 0.20 | n.a. | 100 | 0.27 | n.a. | 4.1 | n.a. | ND | n.a. | 101 |
| | dark control | ND | ND | 3.0 | 12 | 119 | ND | ND | ND | ND | 1.5 | 7.2 | 66 | ND | ND | ND | ND | 1.5 | 7.2 | 66 |
| 10 | 1 | 10 | 8.6 | 0.14 | 1.2 | 153 | 4.4 | 6.7 | 4.1 | 2.2 | 0.23 | 0.55 | 110 | 0.99 | 1.9 | 7.3 | 7.0 | ND | ND | 113 |
| | 2 | 11 | 10 | 0.20 | 0.80 | 168 | 4.3 | 8.8 | 3.5 | 2.3 | 0.19 | 0.62 | 110 | 0.90 | 1.8 | 6.2 | 4.3 | ND | ND | 91 |
| | no-soil control | 8.8 | n.a. | 0.36 | n.a. | 109 | 5.4 | n.a. | 4.5 | n.a. | 0.46 | n.a. | 104 | 0.42 | n.a. | 8.1 | n.a. | ND | n.a. | 101 |
| | dark control | ND | ND | 8.0 | 20 | 131 | ND | ND | ND | ND | 3.5 | 9.6 | 59 | ND | ND | ND | ND | 3.5 | 9.6 | 59 |
| 50 | 1 | 45 | 49 | 0.98 | 5.8 | 143 | 22 | 50 | 19 | 13 | 1.1 | 4.0 | 117 | 4.0 | 7.7 | 37 | 25 | ND | ND | 108 |
| | 2 | 47 | 31 | 1.4 | 3.4 | 137 | 23 | 38 | 20 | 13 | 1.3 | 3.0 | 116 | 4.4 | 8.9 | 37 | 28 | ND | ND | 110 |
| | no-soil control | 42 | n.a. | 2.0 | n.a. | 105 | 21 | n.a. | 23 | n.a. | 1.9 | n.a. | 91 | DATA MISSING | | | | | | |
| | dark control | ND | ND | 28 | 110 | 111 | ND | ND | ND | ND | 14 | 55 | 55 | ND | ND | ND | ND | 14 | 55 | 55 |
| 100 | 1 | 78 | 95 | 2.5 | 11 | 127 | 37 | 100 | 33 | 29 | 1.8 | 8.5 | 106 | 5.4 | 8.7 | 81 | 54 | ND | ND | 118 |
| | 2 | 75 | 68 | 2.2 | 12 | 115 | 40 | 80 | 37 | 24 | 2.3 | 6.6 | 107 | 13 | 38 | 69 | 52 | ND | ND | 103 |
| | no-soil control | 73 | n.a. | 4.1 | n.a. | 92 | 35 | n.a. | 44 | n.a. | 3.5 | n.a. | 82 | 4.8 | n.a. | 81 | n.a. | ND | n.a. | 101 |
| | dark control | ND | ND | 61 | 160 | 100 | ND | ND | ND | ND | 38 | 150 | 76 | ND | ND | ND | ND | 38 | 150 | 76 |

[a] ND: not detected;

[b] n.a.: not applicable. The no-soil control only contained aqueous phase.

**Table S2.5** Observed mass distribution across water, soil, glass tubes, and tube caps when 0.1, 1, 10 μg/L of 17α-TBOH was spiked into glass tubes with water only or with soil and water.

| | spiked levels (μg/L) | 17α-TBOH mass (%) | | | |
|---|---|---|---|---|---|
| | | water | soil | tube | cap |
| water only | 0.1 | 49 | - | 56 | 0 |
| | 1 | 19 | - | 78 | 0 |
| | 10 | 28 | - | 59 | 0 |
| soil-water system | 0.1 | 66 | 16 | 0 | 0 |
| | 1 | 58 | 18 | 8 | 0 |
| | 10 | 52 | 14 | 30 | 0 |

# Chapter 3

# Biotransformation of Altrenogest and its Primary Photo-Transformation Product

## 3.1 Introduction

Synthetic progestins are commonly used as human and agricultural pharmaceuticals and thus occur widely in wastewater influent, effluent and receiving surface water (Chang et al., 2008; Golovko et al., 2018; Weizel et al., 2018). Upon discharge, progestins can induce diverse adverse effects in aquatic organisms at the low to sub-nanogram per liter range (Kumar et al., 2015). For example, 21 day exposure to 0.8 ng/L of levonorgestrel or 1.0 ng/L of norethisterone reduces fecundity in adult fathead minnows (*Pimephales promelas*; Paulos et al., 2010; Zeilinger et al., 2009). 14 day exposure to 1 ng/L cyproterone acetate decreased plasma testosterone levels in mummichog (*Fundulus heteroclitus*; Sharpe et al., 2004). Because of the potential impacts on reproduction, progestins were considered as the most important environmental pharmaceutical contaminant class after estrogens (Fent, 2015; Kumar et al., 2015). However, their environmental fate is poorly described relative to estrogens and androgens (Fent, 2015). In particular, characterizing the risk of these contaminants should include their transformation products (TPs) because TPs of steroids often retain the steroid skeleton and exhibit retained, enhanced, or even altered endocrine disrupting potentials (Cwiertny et al., 2014; Jenkins et al., 2004; Liu et al., 2013).

One such example is altrenogest (ALT, 17-α-allyl-17-β-hydroxyestra-4,9,11-trien-3-one), a potent synthetic progestin used in equine and swine industries to maintain pregnancy, synchronize estrus for breeding, or postpone estrus after weaning (Squires et al., 1983; van Leeuwen et al., 2011; Willmann et al., 2011). The annual usage of ALT in the United States was

estimated at several thousand kg and usage in the United Kingdom was reported as 380 kg (year 2000 data), which was 15 times higher than usage of ethinyl estradiol for human contraceptive purposes (Wammer et al., 2016). In EU regulatory assessments of ALT, exposure models predicted ALT concentrations to be <20 ng/L in a static farm pond scenario and 0.6−9 ng/L in impacted receiving waters (European Medical Agency Environmental Impact Assessment, 2013). These values fall within concentration ranges where other similar synthetic progestins impair fecundity in exposed fish (Kumar et al., 2015; Orlando and Ellestad, 2014).

In sunlit waters, ALT structures showed unexpected environmental persistence through rapid formation (half-life ~25 s) of a bioactive 2 + 2 cycloaddition product (ALT-CAP). ALT-CAP then reacted via photohydration (half-life ~30 min) to form hydroxylated secondary photoproducts (ALT-CAP-OH), which could revert back to ALT-CAP via thermal dehydration in the dark (Wammer et al., 2016). Therefore, ALT and ALT-CAP represent the major chemical species of ALT discharged into aquatic environments. Considering ALT as a potent veterinary progestin with large usage, the release of ALT and ALT-CAP pose significant risks to agricultural receiving waters.

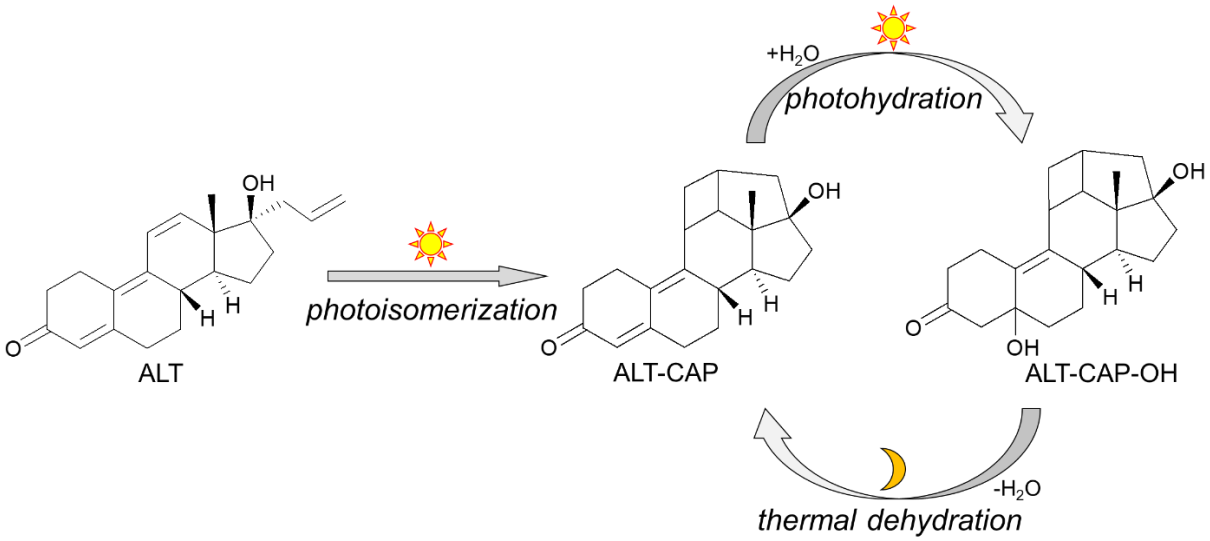


**Figure 3.1** ALT phototransformation dynamics in sunlit aquatic environments.

Biotransformation of ALT and ALT-CAP via microbial communities represents an important fate pathway for these compounds, yet this information remains unavailable in current literature. To address this need, we investigated the biotransformation of ALT and ALT-CAP in agricultural receiving waters following OECD Guideline 309 (OECD, 2004). Due to recent chemical legislation in Europe, standardized OECD 309 protocols have become increasingly important for persistence assessment of pharmaceuticals (Seller et al., 2020). In OECD 309, biotransformation potential can be assessed in two experimental setups: pelagic test (testing biotransformation in natural water only) and suspension test (testing biotransformation in water amended with 0.01-1 g/L sediment; OECD, 2004). Most OECD 309 studies to date are carried out as pelagic tests. However, the suspension test employs higher cell densities, which are closer to environmental conditions and often promote biotransformation. In addition, a recent study demonstrated that the suspension test setup produced more consistent results for biotransformation rates compared with the pelagic tests (Seller et al., 2020).

In this study, we employed suspension tests with mixed microbial inocula to characterize the biotransformation of ALT and ALT-CAP in representative agricultural receiving waters. We first evaluated the biotransformation kinetics of ALT and ALT-CAP at 1 µg/L by quantifying their concentrations in the pelagic test reactors across 30 days with liquid chromatography-triple quad mass spectrometry (LC-MS/MS). The biotransformation products were then identified with suspect screening and non-target analysis using LC coupled to high-resolution mass spectrometry (LC-HRMS). Generated product formulae and structures were proposed based on accurate mass, isotope patterns, retention time (RT), MS/MS spectra, as well as published biotransformation pathways in similar systems.

## 3.2 Materials and Methods

### 3.2.1 Reagents and Materials

ALT, reagent grade KH2PO4, K2HPO4, Na2HPO4, NH4Cl, CaCl2, MgSO4·7H2O, FeCl3·4H2O, ammonium fluoride (99.9%) and concentrated HCl were all purchased from Sigma Aldrich (St. Louis, MO, USA). ALT-$d_5$, used as the internal standard for both ALT and ALT-CAP, was purchased from ALSACHIM (Illkirch Graffenstaden, France). ALT-CAP was generated following the method described in Chapter 2 section 2.2. Briefly, aqueous stock solutions of ALT (1-10 mg/L; prepared by diluting 10 µL of 1-10 g/L methanolic stock into 10 mL water; methanol content, 0.01%) were irradiated for 4 hours in a solar simulator (EYE Lighting, Mentor, OH, USA) equipped with four high pressure, 150 W xenon bulbs, to transform ALT to ALT-CAP-OH. ALT-CAP was then generated via complete thermal dehydration of ALT-CAP-OH by incubating at 50 °C under dark conditions for 24 h. The yield of ALT-CAP in this process was assumed to be ~100% based on previous studies (Kenyon et al., 2019; Wammer et al., 2016). Restek C18 solid phase extraction (SPE) cartridges (1000 mg, 6cc) were obtained from Restek Corporation (Bellefonte, PA, USA). Optima® LC/MS grade methanol, water, and formic acid were purchased from Fisher Scientific (Pittsburgh, Pennsylvania, USA).

### 3.2.2 Inocula Collection

Surface water and sediment inocula were collected (August 2020) from Newaukum Creek, an agriculturally-impacted creek in Pierce County, WA (47.2283, -121.97057). Surface water (total suspended solids (TSS), 11 mg/L; volatile suspended solids (VSS), 6 mg/L) was collected with a pre-washed dipper from the middle of the creek (depth 50 cm). Surface sediment was obtained by agitating the top 3 cm of sediment at the sediment-water interface and collecting the resulting high-turbidity water (TSS, 910 mg/L; VSS, 190 mg/L). Inocula was transported to the laboratory on ice and allowed to acclimate to room temperature prior to immediate use.

### 3.2.3 Microcosm Design

The microcosm suspension was constructed according to OECD 309 by amending the collected mixed community inocula samples types with mineral salts to maintain pH and supply nutrients (OECD, 2004). Specifically, the collected surface water was amended with stock solutions of phosphorus buffer (final concentrations: 85 mg/L KH2PO4, 220 mg/L K2HPO4, 330 mg/L Na2HPO4·H2O, 5 mg/L $NH_4Cl$) and mineral media (final concentrations: 28 mg/L CaCl2, 23 mg/L MgSO4·7H2O, and 0.2 mg/L FeCl3·4H2O). The sediment suspension was not amended with phosphorus buffer and mineral media. Microcosm suspensions used 120 mL amber glass vials with 80 mL of the mineral amended surface water and 20 mL of the sediment suspension. For kinetics assessment, 100 µL of 1 mg/L ALT and ALT-CAP aqueous solutions were spiked into the microcosm to achieve analyte concentrations of 1 µg/L. While 1 µg/L incubation is still well above environmentally realistic concentrations of steroid hormones, it represents the lowest range of incubation levels used in literature for such experiments, and as low as we could get given our analytical technology. The microcosms were loosely covered with aluminum foil and shaken (100 rpm) in dark at 20 °C. After 0, 1, 3, 5, 7, 14, 21, 30 days, whole microcosms were harvested in triplicate (n = 24 in total). Harvested microcosms were thoroughly mixed and 5 mL mixture was withdrawn from each replicate and combined for cell viability measurement (discussed below). One sterile control was included for each sampling day (n = 8 in total), which was prepared in the same procedure as the bioactive microcosms followed by autoclaving at 121 °C for 20 minutes. ALT and ALT-CAP were stable during autoclaving; microcosms spiked with ALT and ALT-CAP before or after autoclaving showed no difference in detected concentrations (data not shown). The cell viability in the sterile control was measured on each sampling day by mixing and withdrawing 5 mL of the microcosm mixture. For the remaining bioactive and sterile microcosms (95 mL), 50 µL of 100 µg/L ALT-$d_5$ was spiked, and

the microcosms were extracted onto Restek C18 SPE cartridges (preconditioned with 12 mL methanol and 12 mL LC/MS-grade water). After extraction, the SPE cartridges were rinsed with 6 mL LC/MS-grade water, vacuum dried, and eluted with two 2.5 mL aliquots of methanol. The eluent was concentrated to 1 mL under nitrogen for mass spectrometry analysis. The absolute recoveries of these systems, evaluated as the peak area ratios of ALT and ALT-CAP in SPE extracts of the spiked bioreactor (n = 3) over those in methanolic standards, were 57% ± 1% for ALT and 51% ± 1% for ALT-CAP. After internal standard calibration, the relative recoveries were 105% ± 1% for ALT and 94% ± 1% for ALT-CAP.

For TPs identification, ALT and ALT-CAP were studied in separate microcosms at higher initial concentrations (100 µg/L; prepared by spiking 1 mL of 10 mg/L aqueous solutions into the 100 mL microcosms). One bioactive microcosm was harvested for each analyte on day 0, 3, 7, 14, 30. Single sterile and unspiked controls (microcosms prepared in the same way without ALT or ALT-CAP spiking) were included for each analyte on each sampling day (total sterile controls: n = 5 for ALT and n = 5 for ALT-CAP; total unspiked controls: n = 5 shared by ALT and ALT-CAP). Cell viability was measured for the bioreactors and sterile controls of 100 µg/L ALT incubations on each day by mixing and withdrawing 5 mL of suspensions. Due to cost, cell viability was not measured for 100 µg/L ALT-CAP incubations, but was assumed to be similar to that observed for ALT. The microcosms were extracted with SPE without ALT-$d_5$ spiking, and ALT and ALT-CAP were quantified by LC-MS/MS with a 7-point calibration curve (0.05-100 µg/L) after 1000-fold extract dilution to overcome matrix effects and detector saturation.

### 3.2.4 Cell Viability Assessment

Cell viability in microcosms were assessed by measuring adenosine triphosphate (ATP) concentrations with a luminescence assay (Promega Water-Glo, Madison, WI, USA). The

microcosm subsample (1 µg/L incubation: 15 mL for bioreactors combining 5 mL from each triplicate, 5 mL for sterile control; 100 µg/L ALT incubation: 5 mL for bioreactor and 5 mL for sterile control) was passed through a 0.2 µm syringe filter to retain the biomass. Cell lysis reagent (5 mL) was then passed through the syringe filter to leach the cellular content, then 100 µL of the lysate was mixed with luminance reagent (100 µL) in a 1.5 mL microfuge tube. The microfuge tube was swirled and mixed (1 min), and 100 µL of the mixture was transferred immediately onto a 96-well plate and the luminance was measured on a Synergy LX multi-mode plate reader (BioTek Instruments, Winooski, VT, USA). The ATP concentrations were calibrated by an ATP standard solution (1 ng/mL, single point calibration) following manufacturer protocols.

### 3.2.5 Analytical Mass Spectrometry

ALT and ALT-CAP concentrations were quantitatively analyzed with an Agilent (Santa Clara, California) 1290 Infinity binary pump liquid chromatography (LC) coupled with an Agilent 6430 triple quadrupole tandem mass spectrometer (MS/MS). Details of the LC-MS/MS methods were described in Chapter 2. For TPs structural characterization, SPE extracts of the bioreactors and controls in the 100 µg/L incubations were analyzed in triplicate injections on an Agilent 1290 Infinity UPLC coupled to an Agilent 6530 quadrupole time-of-flight HRMS (qTOF-HRMS) under both ESI+ and ESI-. Full scan HRMS data were first acquired and processed in a non-target approach with Agilent software packages (MassHunter Profinder (B.08.00) for feature extraction and alignment, Mass Profiler Professional (B.13.00) for feature prioritization). Features (exact mass-retention time pairs) in the bioreactors that were present in all triplicate injections (3/3), with peak area both >5000 and 5-fold greater than the sterile controls, non-spike controls, and solvent blanks, were retained in a preferred list for characterization. MS/MS data were then acquired for these features with data-dependent

acquisition under three collision energies (10, 20, 40 eV). Details for the instrumental methods and data analysis parameters match those described previously (Du et al., 2017; Peter et al., 2018; Tian et al., 2020) and are summarized in Supplementary Materials (SM).

Potential TPs were identified from the preferred lists based on relevant formula, retention time (RT), and diagnostic MS/MS neutral losses and fragments. Structures were then proposed based on RT shifts, ionization behavior, MS/MS fragmentation pattern, and biotransformation pathways for similar compounds reported in literature. Identification confidence was assigned according to Schymanski et al. with modifications.(Schymanski et al., 2014) The highest confidence (level 1) communicates that observed RT and MS/MS fragments match analytical standards. Level 2 confidence communicates that MS/MS fragmentation patterns match standard-confirmed TPs (level 2a) or diagnostic information indicates no other possible structure (level 2b). Level 3 describes tentative candidates matching plausible biotransformation reactions, but reaction sites can (level 3a) or cannot (level 3b) be assigned to molecular sub-structures. Level 4 stands for unequivocal TP molecular formula when MS/MS spectra are not available.

## 3.3 Results and Discussion

### 3.3.1 Biotransformation Kinetics

For both 1 µg/L and 100 µg/L incubations, ALT and ALT-CAP remained stable (1 µg/L incubation: ALT, 1.1 ± 0.03 µg/L, ALT-CAP, 0.92 ± 0.02 µg/L; 100 µg/L incubation: ALT, 130 ± 9 µg/L, ALT-CAP, 130 ± 7 µg/L) in the sterile controls over 30 days (**Figure 3.2**). Therefore, abiotic attenuation and sorption mechanisms had negligible contributions to observed losses in bioreactors. This was consistent with the low ATP concentrations in the sterile controls that demonstrated maintenance of sterility throughout the experiment (**Figure 3.2**). For the 1 µg/L bioactive microcosms, ALT and ALT-CAP degraded steadily over time (**Figure 3.2 a**). First order kinetic fits indicated half-lives of 3.5 days ($k$ = 0.20 day$^{-1}$, $r^2$ = 0.997) and 1.6 days ($k$ =

0.44 day$^{-1}$, $r^2$ = 0.998) for ALT and ALT-CAP, respectively. The stable decrease of ALT and ALT-CAP is explained by the prolonged bioactivity in the reactors. The ATP concentrations increased ~1.5-fold over the first three days, indicating at least partial adaptation of the microbial consortium. ATP concentrations then decreased by ~1.8-fold from day 3 - 5, and generally remained at this level with some fluctuation over days 5 - 30 (**Figure 3.2b**).

For the 100 µg/L incubation, an initial lag-phase of 3 days was observed (**Figure 3.2c**). In this phase, measured ALT concentrations decreased only 3% and ALT-CAP concentrations increased 6%, likely effects of analytical variance. Thereafter, a rapid dissipation phase happened for both ALT and ALT-CAP, following first order kinetics with half-lives of 15 days ($k$ = 0.046 day$^{-1}$, $r^2$ = 0.923) and 9.3 days ($k$ = 0.075 day$^{-1}$, $r^2$ = 0.997), respectively. The lag-phase followed by a fast dissipation is consistent with adaption of the microbial consortium to use ALT or ALT-CAP as the carbon source for growth (Madigan et al., 2017). Notably, such lag-phase was not observed in the 1 µg/L incubation, indicating reduced adaptation of the microbial community at the lower spiking concentrations. This phenomenon (appearance of lag-phase only at high spike concentrations) was also observed in the biotransformation of pregabalin and gabapentin in surface water (Henning et al., 2021). While the relative trends were consistent (ALT degrading slower than ALT-CAP), the differences in kinetic rates also suggest some variability and disparities between the resulting microbial consortia responsible for biotransformation, although microbial community composition and function were not evaluated explicitly as part of this study.

Consistent with the concentration trends, the ATP concentrations in the 100 µg/L ALT incubation increased rapidly (~3.5-fold) over the first 3 days compared with the 1 µg/L incubation (~1.5 times increase). Following the sharp increase, the ATP concentrations then decreased over days 3 - 7 (~3-fold decrease from day 3 to day 7) and additionally over days 7 -

14 (~2.5-fold decrease from day 7 to day 14), and then remained stable over days 14 - 30 in the 100 µg/L ALT incubation (**Figure 3.2 d**). Notably, ALT and ALT-CAP transformed ~5-fold slower at 100 µg/L relative to 1 µg/L, indicating limitations of available biomass or microbial activity for transformation at 100 µg/L. In fact, 100 µg/L ALT biotransformation is better fitted with second order kinetics ($r^2$ = 0.993), indicating that the biotransformation was controlled not only by ALT concentrations but also by the microbial biomass and activity aspects in the batch system (Schwarzenbach et al., 2004). Such substrate inhibited kinetics has been observed elsewhere, although it is less common than substrate enhanced kinetics (e.g. Michaelis-Menten kinetics) (Svendsen et al., 2020). Under both concentrations, ALT-CAP transformed faster than ALT by ~2-fold. These results suggested that rapid phototransformation of ALT to ALT-CAP can be expected to facilitate more efficient subsequent microbial transformation in the aquatic environment.

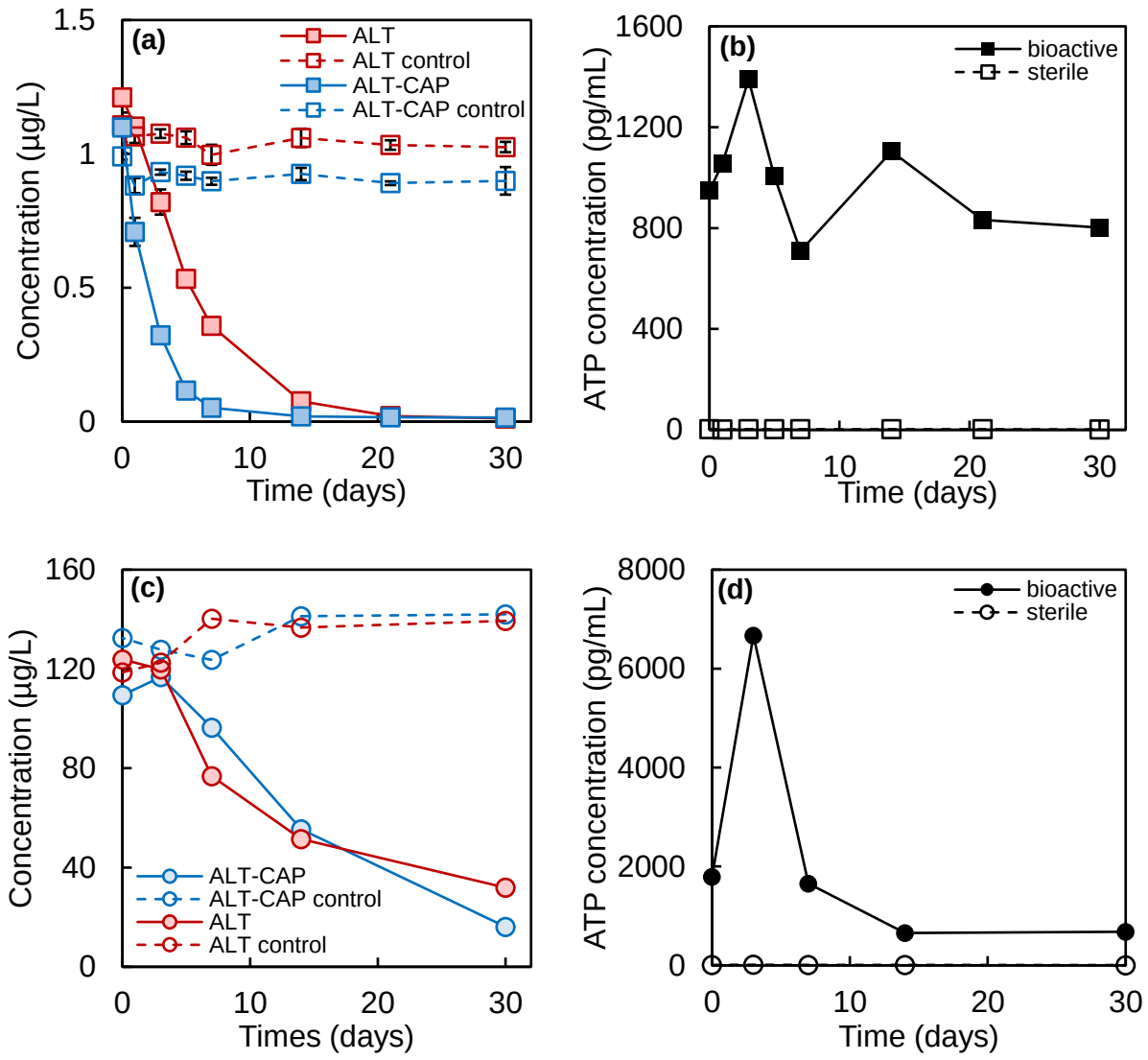


**Figure 3.2** Biotransformation of ALT and ALT-CAP by mixed microbial communities inoculated from an agriculturally-impacted receiving water and sediment. (a) Decay curves and (b) cell viability (measured as ATP concentration) of 1 µg/L ALT (red square) and ALT-CAP (blue square) in bioactive microcosms (filled symbol) and sterile controls (hollow symbol). (c) Decay curves and (d) cell viability (measured as ATP concentration) of 100 µg/L ALT (red circle) and ALT-CAP (blue circle) in bioactive microcosms (filled symbol) and sterile controls (hollow symbol). Error bars represent standard deviation of three replicates.

### 3.3.2 Biotransformation Products

Identification of TPs focused on the 100 µg/L incubation where higher concentrations facilitated characterization efforts. Following the blank and replicate screening criteria listed in the Material and Methods section, 42 ESI+ features and 38 ESI- features were initially

prioritized in the ALT incubations and 33 ESI+ features and 25 ESI- features were prioritized for ALT-CAP. Based on relevant formula, RT, and MS/MS neutral losses and fragments, fifteen probable TPs were subsequently identified for ALT. Relatively confident structures (level 2b) were possible for 3 of these; possible biotransformation pathways (level 3) were proposed for other 12 TPs (**Table S3.2**). Fourteen probable TPs were identified for ALT-CAP. Of these, a relatively confident structure (level 2b) was possible for 1 TP, however, confident structures were not possible for other ALT-CAP TPs (level 3 and level 4) due to the complex biotransformation and MS/MS fragmentation possibilities of the atypical 5-ring steroid structure of ALT-CAP (**Table S3.3**).

*ALT and ALT-CAP*. ALT ($C_{21}H_{26}O_2$) was detected under both ESI+ (*m/z* 311.2006) and ESI- (*m/z* 309.1850) at RT 10.1 min, with ~30 times higher peak area response in ESI+ (**Figure 3.4**). Diagnostic fragments for ALT in ESI+ include *m/z* 293.1870 ($C_{21}H_{25}O^+$), 269.1516 ($C_{18}H_{21}O_2^+$), and 251.1454 ($C_{18}H_{19}O^+$), representing losses of $H_2O$ and the C17 allyl chain. Additional fragments include those characteristic for the 4,9,11-triene-3-keto steroids, including *m/z* 227.1413 ($C_{16}H_{19}O^+$), 212.1243 ($C_{15}H_{16}O^+$), and 199.1086 ($C_{14}H_{15}O^+$). Previous studies showed that 4,9,11-triene steroids with C13-methyl group (e.g. trenbolone) produced fragments at *m/z* 227, while those with C13-ethyl group (e.g. dihydrogestrinone) produced *m/z* 241 (Pozo et al., 2008; Thevis et al., 2005; Thevis and Schänzer, 2007). Therefore, the *m/z* 227 ion for ALT was proposed to contain C1-C15 and C18 (**Figure 3.3**). The *m/z* 212 fragment resulted from a neutral loss of 15 Da ($CH_3$) from *m/z* 227 and was proposed to contain C1-C14 and C18. The *m/z* 199 fragment was -28 Da ($C_2H_4$) of *m/z* 227 and was proposed to contain C1-C14 (A, B, C rings) (**Figure 3.3**). Under ESI-, ALT showed diagnostic fragments at *m/z* 225.1262 ($C_{16}H_{17}O^-$), 211.1105 ($C_{15}H_{15}O^-$), and 197.0943 ($C_{14}H_{13}O^-$), corresponding to the *m/z* 227, 212, 199 under ESI+ (Lampinen-Salomonsson et al., 2006) (**Figure 3.3**). The mass shifts of the *m/z* 227 (ESI+),

199 (ESI+), 211 (ESI-), and 197 (ESI-) fragments in the TPs were the key information to propose biotransformation reaction sites (on the A/B/C rings or on the D ring) in this study.

ALT-CAP was detected under ESI+ (*m/z* 311.2009) and ESI- (*m/z* 309.1830) at RT 9.0 min, with ~200 times higher response in ESI+ (**Figure 3.4**). The ESI+ MS/MS spectra of ALT-CAP resembled those of ALT, with characteristic fragments at *m/z* 293.1901, 269.1511, 251.1392, 227.1448, and 199.1100. However, ALT-CAP fragmented differently under ESI- relative to ALT and was dominated by *m/z* 253.1201 ($C_{17}H_{17}O_2$-), 223.1096 ($C_{16}H_{15}O$-), and 199.1102 ($C_{14}H_{15}O$-). The *m/z* 253 was likely composed of C1-C17 (A, B, C, D rings) of ALT-CAP and the *m/z* 199 likely contained C1-C14 (A, B, C rings). However, because ALT-CAP was only discovered recently, its MS/MS fragmentation has not been well studied in literature and such structural assignments are currently speculative.

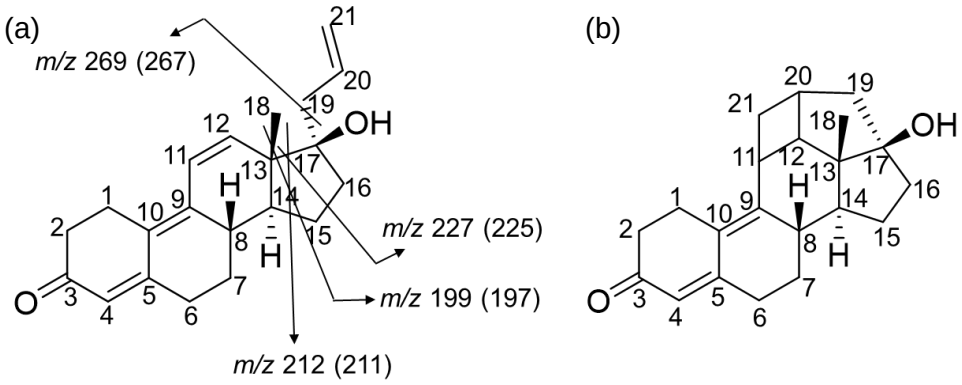


**Figure 3.3** Structures of (a) ALT and (b) ALT-CAP with carbon numbering. The cleavage sites of ALT in MS/MS fragmentation were marked in (a). The *m/z* outside and inside the parenthesis were for ESI+ and ESI- fragments, respectively.

*TP 326s.* TP 326s were observed as one of the most abundant TPs for ALT and ALT-CAP based on LC-HRMS peak areas (**Figure 3.4**, **3.5**). Based on the *m/z* of 327.1960 (ESI+) and 325.1775 (ESI-), a molecular formula of $C_{21}H_{26}O_3$ could be proposed, indicating hydroxylation TPs. Three TP 326s isomers (a, 6.78 min; b, 7.0 min; c, 7.6 min) were observed for ALT (**Table S3.2**). For TP 326a and b, characteristic ESI+ fragments included *m/z* 225.1279 ($C_{16}H_{17}O^+$) and

ESI- fragments included *m/z* 209.0941 ($C_{15}H_{13}O^-$) and 195.0791 ($C_{14}H_{11}O^-$), corresponding to the *m/z* 227 (ESI+), and *m/z* 211 and 197 (ESI-) fragments of ALT minus 2H. This indicates that the hydroxylation of TP 326a and b of ALT probably happened on ring A, B, or C (level 3a identification). In contrast, TP 326c showed ESI+ fragments of *m/z* 227.1420, 199.1129 and ESI- fragments of *m/z* 211.1102 and 197.0938, identical to ALT. Such fragmentation patterns indicated that the hydroxylation likely happened on D ring for ALT TP 326c. The observed fragment at *m/z* 285.1472, corresponding to loss of unchanged allyl chain, ruled out hydroxylation on C19-C21 for ALT TP 326c (**Table S3.2**). Therefore, the TP 326c was likely C15 or C16 hydroxylated ALT (level 3a identification).

For ALT-CAP, two TP 326s isomers were observed (a, 6.0 min; b, 7.5 min; **Table S3.3**). ALT-CAP TP 326a showed an ESI+ fragment of *m/z* 225.1250, which corresponded to *m/z* 227 of ALT-CAP minus 2H and indicated probable hydroxylation sites on A, B, or C rings (level 3a identification; **Table S3.3**). For ALT-CAP TP 326b, the fragmentation pattern was very different from that of ALT-CAP: Except for the *m/z* 309.1828 and 285.1493 fragments (initial losses of $H_2O$ and the allyl chain), the ESI+ MS/MS spectra of ALT-CAP TP 326b demonstrated extensive fragmentation at <240 Da without diagnostic fragments. A previous study on mono-hydroxylated progesterone (*m/z* 97 and 109 as the diagnostic fragments for progesterone) showed that C or D ring hydroxylation did not alter fragmentation patterns, but hydroxylation on some A or B ring carbons drastically affected fragmentation pathways and produced non-specific MS/MS spectra (Kang et al., 2004). Following similar logic, we tentatively proposed ALT-CAP TP 326b to be A or B ring hydroxylated (level 3a identification).

*TP 308s.* TP 308s were observed as another group of ALT and ALT-CAP TPs with large peak areas (**Figure 3.4**, **3.5**). Two isobaric TP 308s were observed each for ALT (a, 7.3 min; b, 10.4 min; **Table S3.2**) and ALT-CAP (a, 7.8 min; b, 9.2 min; **Table S3.3**). Except for ALT TP

308a, all the isomers were observed under both ESI+ and ESI-. The *m/z* of 309.1873 (ESI+) and 307.1685 (ESI-) suggested a molecular formula of $C_{21}H_{24}O_2$, indicating dehydrogenation TPs. ALT TP 308a showed ESI+ fragments at *m/z* 291.1682 ($C_{21}H_{23}O^+$; $H_2O$ loss) and 251.1432 ($C_{18}H_{19}O^+$; $C_3H_4$ loss), suggesting relationship to ALT; smaller diagnostic fragments were not available and precluded detailed structural diagnosis for ALT TP 308a (level 3b identification). ALT TP 308b showed diagnostic ESI+ fragments at *m/z* 291.1719 ($C_{21}H_{23}O^+$; $H_2O$ loss), 267.1369 ($C_{18}H_{19}O_2^+$; allyl chain loss), 223.1110 ($C_{16}H_{15}O^+$), 208.0881 ($C_{15}H_{12}O^+$) (**Table S3.2**). The *m/z* 223 and 208 fragments potentially corresponded to the *m/z* 227 and 212 of ALT minus 4H. Such mass shifts indicated that the dehydrogenation of ALT TP 308b likely happened on ring A, B, or C instead of ring D; possibilities include 1,2-dehydrogenation and 6,7-dehydrogenation.

ALT-CAP TP 308a showed more extensive fragmentation under ESI+ with multiple characteristic fragments, including *m/z* 291.1723 ($C_{21}H_{23}O^+$; $H_2O$ loss), 267.1345 ($C_{18}H_{19}O_2^+$; allyl chain loss), 225.1258 ($C_{16}H_{17}O^+$), 209.0931 ($C_{15}H_{13}O^+$), and 197.0943 ($C_{14}H_{13}O^+$). The *m/z* 225, 209 and 197 (all corresponding to ALT-CAP fragments minus 2H) suggested that the dehydrogenation happened on ring A, B, or C. This is confirmed by ESI- fragments of ALT-CAP TP 308a that included *m/z* 249.0883 ($C_{17}H_{13}O_2^-$; likely corresponding to ALT-CAP *m/z* 253 minus 4H), 221.0926 ($C_{16}H_{13}O^-$; ALT-CAP *m/z* 223 minus 2H), and 195.0782 ($C_{14}H_{11}O^-$; ALT-CAP *m/z* 199 minus 4H; **Table S3.3**). Notably, 1,2-dehydro steroids often exhibit RTs ~1 min earlier than the parent compounds on C18 chromatography (e.g., testosterone 9.02 min vs 1,2-dehydrotestosterone 7.82 min, (Yang et al., 2010); 1,2-hydrospirorenone 8.83 min vs spirorenone 8.12 min; Chapter 4 of this thesis). Here, the ALT-CAP TP 308a (RT 7.8 min) showed up at ~1.2 min earlier than ALT-CAP (RT 9.0 min). Based on the RT evidence, we proposed ALT-CAP TP 308a to be a 1,2-dehydrogenation product (level 2b identification), although it is impossible to

conclusively confirm the structure without the analytical standard or nuclear magnetic resonance (NMR) analysis.

MS/MS spectra of ALT-CAP TP 308b were interesting; its ESI+ MS/MS spectra matched those for ALT TP 308b (diagnostic fragments at *m/z* 267.1368 ($C_{18}H_{19}O_2^+$), 223.1126 ($C_{16}H_{15}O^+$), 208.0883 ($C_{15}H_{12}O^+$)), while its ESI- MS/MS spectra were identical with those for ALT-CAP TP 308a (*m/z* 249.0900 ($C_{17}H_{13}O_2^-$), 221.0947 ($C_{16}H_{13}O^-$), 210.1015 ($C_{15}H_{14}O^-$), and 195.0783 ($C_{14}H_{11}O^-$); **Table S3.2**, **S3.3**). Such similarity in MS/MS spectra indicated that ALT TP 308b, ALT-CAP TP 308a, and ALT-CAP TP 308b were likely related, such as complementary 1,2- and 6,7-dehydrogenations. Therefore, dehydrogenations of ALT-CAP TP 308b and ALT TP 308b were proposed to happen on A or B rings, probably on C6 and C7 (level 3a identifications).

*TP 310s.* Isomers of ALT and ALT-CAP was also observed at relatively large peak area (**Figure 3.4**, **3.5**). The ALT isomer (TP 310) showed identical ESI+ MS/MS spectra with ALT (e.g., fragments at *m/z* 293.1870 ($C_{21}H_{25}O^+$), 269.1527 ($C_{18}H_{21}O_2^+$), 227.1410 ($C_{16}H_{19}O^+$)), indicating that it was a stereoisomer (level 2b identification). The $[M-H]^-$ ion of the ALT-CAP isomer (TP 310) did not show much fragmentation even under 40 eV (**Table S3.2**, **S3.3**). Based on similar RT changes between the ALT and ALT-CAP TP310-parent pairs (RT of TP 310 0.2-0.7 min later than parents), we propose the TP 310 of ALT-CAP to also be a stereoisomer (level 3a identification).

*ALT TP 328 and TP 284*. TP 328 of ALT was observed at 5.76 min under ESI-. Based on $[M-H]^-$ of 327.1570, a molecular formula of $C_{20}H_{24}O_4$ could be proposed. The ESI- MS/MS spectra showed identical dominant fragments with ALT (*m/z* 211.1112 ($C_{15}H_{15}O^-$) and 197.0914 ($C_{14}H_{13}O^-$)), indicating unchanged A, B, and C rings for TP 328. In addition, a diagnostic neutral loss of $CO_2$ was observed (from $[M-H]^-$ 327.1570 to *m/z* 283.1670 fragment), indicating a

carbonic acid group (**Table S3.2**). Therefore, an allyl chain oxidative dealkylation product was most likely (level 2b identification). Such oxidative dealkylation through carbonic acid is commonly observed as a microbial transformation pathway (Chiang et al., 2020).

Another dealkylation product of ALT, TP 284, was also observed under ESI-. $[M-H]^-$ of 283.1676 indicated a molecular formula of $C_{19}H_{24}O_2$. Similar with TP 328, TP 284 also showed identical dominant fragments with ALT under ESI- (*m/z* 211.1104 and 197.0954), indicating unchanged A, B, and C rings. For loss of $C_2H_2$ on the D-ring, the most likely reaction site was the C20-C21 alkene group (level 2b identification). This was supported by the lack of the diagnostic $C_3H_6$ neutral loss of ALT in the ESI- MS/MS spectra of TP 284. Notably, the proposed TP 284 structure is actually an anabolic steroid called metribolone (i.e., 17α-methyltrenbolone), although we could not purchase this controlled substance to confirm. Considering its potentially potent bioactivity, the structure and molar yield of TP 284 merits further characterization.

Other TPs observed for ALT and ALT-CAP likely formed through combinations of the above-mentioned transformation pathways. For example, TP 324s ($C_{21}H_{24}O_3$) may reflect dehydrogenation-hydroxylation; TP 342s ($C_{21}H_{26}O_4$) indicate hydroxylation at two sites; TP 306s ($C_{21}H_{22}O_2$) indicate dehydrogenation at two sites; and TP 340s ($C_{21}H_{24}O_4$), TP 344 ($C_{21}H_{28}O_4$), and TP 360s ($C_{21}H_{28}O_5$) reflect multiple oxidative steps. A sulfate conjugated TP (TP 390; $C_{21}H_{26}SO_5$) was also observed for ALT-CAP. However, structural characterizations for these TPs from MS/MS data are difficult because of the disparate fragmentation patterns compared with ALT and ALT-CAP. These various probable structures and their identifications mostly remain at level 3b confidence absent mass accumulation and confirmation with commercial standards (which are not available to the best of our knowledge), synthetic analytical standards, or NMR analysis.

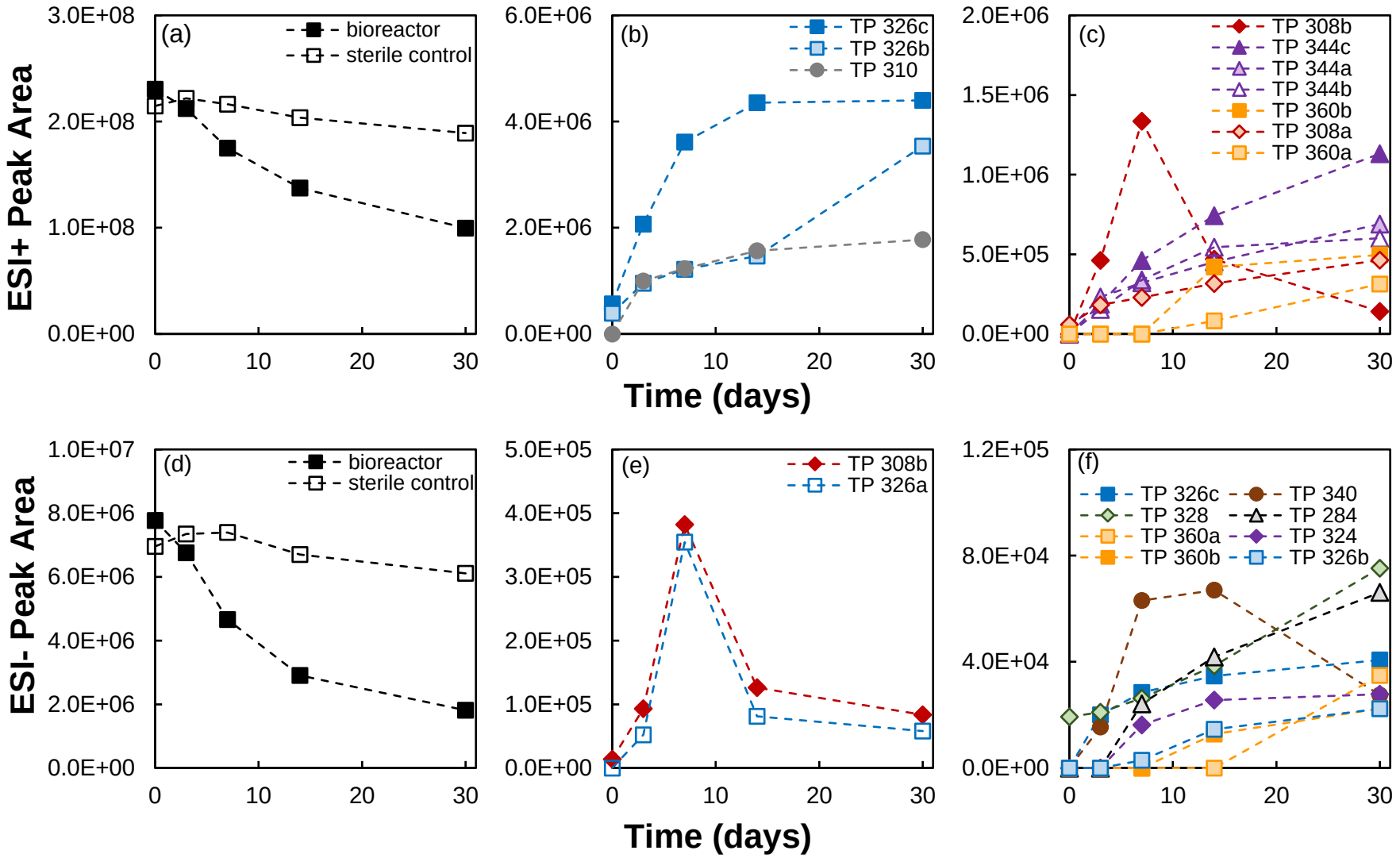


**Figure 3.4** Observed LC-qTOF-HRMS peak areas of ALT and biotransformation TPs in 100 µg/L incubations with mixed microbial communities. ESI+ peak areas of (a) ALT, (b) major ALT TPs (peak areas >2 times higher than minor TPs), and (c) minor TPs. ESI- peak areas of (d) ALT, (e) major TPs (peak areas >2 times higher than minor TPs), and (f) minor TPs.

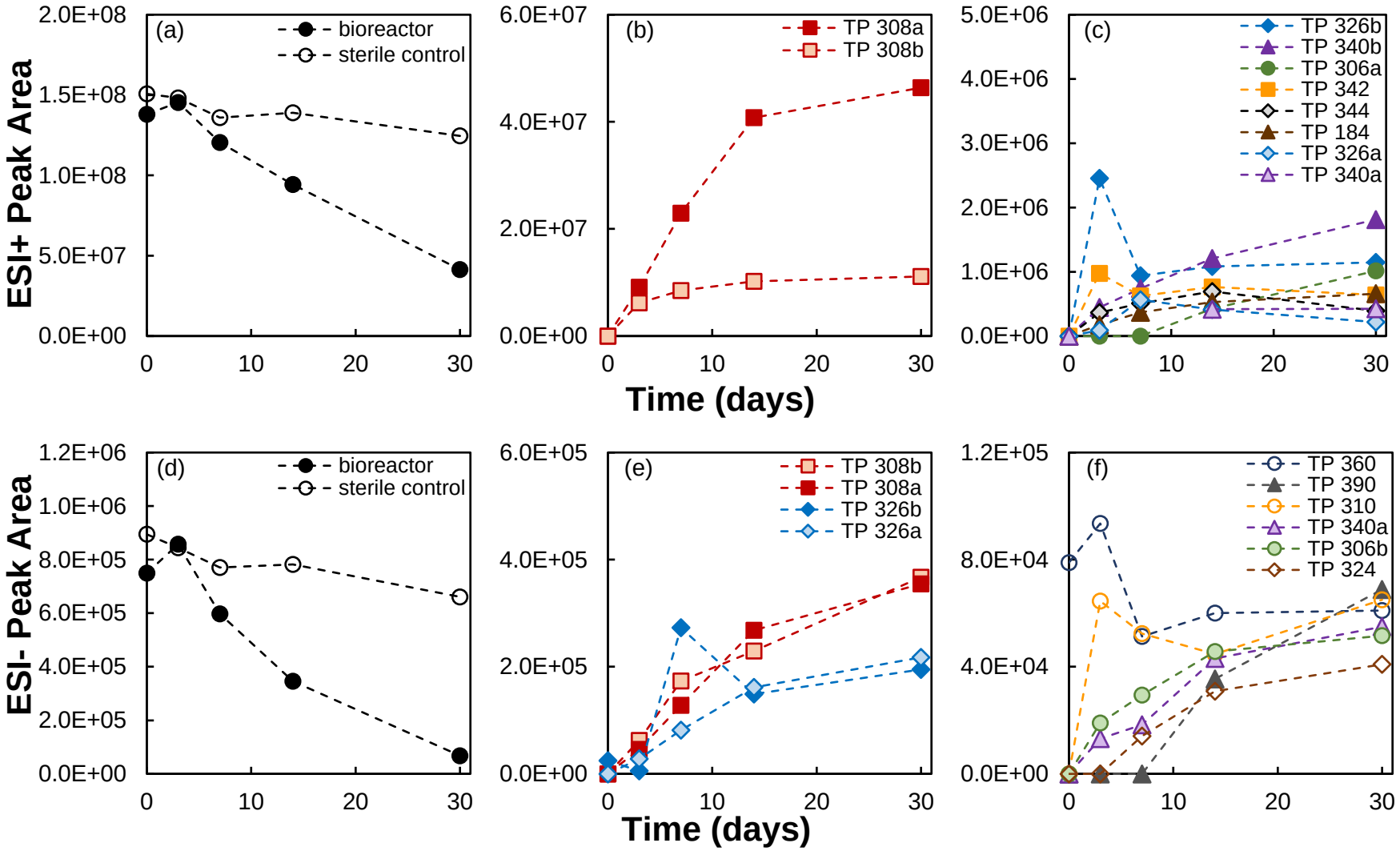


**Figure 3.5** Observed LC-qTOF-HRMS peak areas of ALT-CAP and biotransformation TPs in 100 µg/L incubations with mixed microbial communities. ESI+ peak areas of (a) ALT-CAP, (b) major ALT-CAP TPs (peak areas >3 times higher than minor TPs), and (c) minor TPs. ESI- peak areas of (d) ALT-CAP, (e) major TPs (peak areas >3 times higher than minor TPs), and (f) minor TPs.

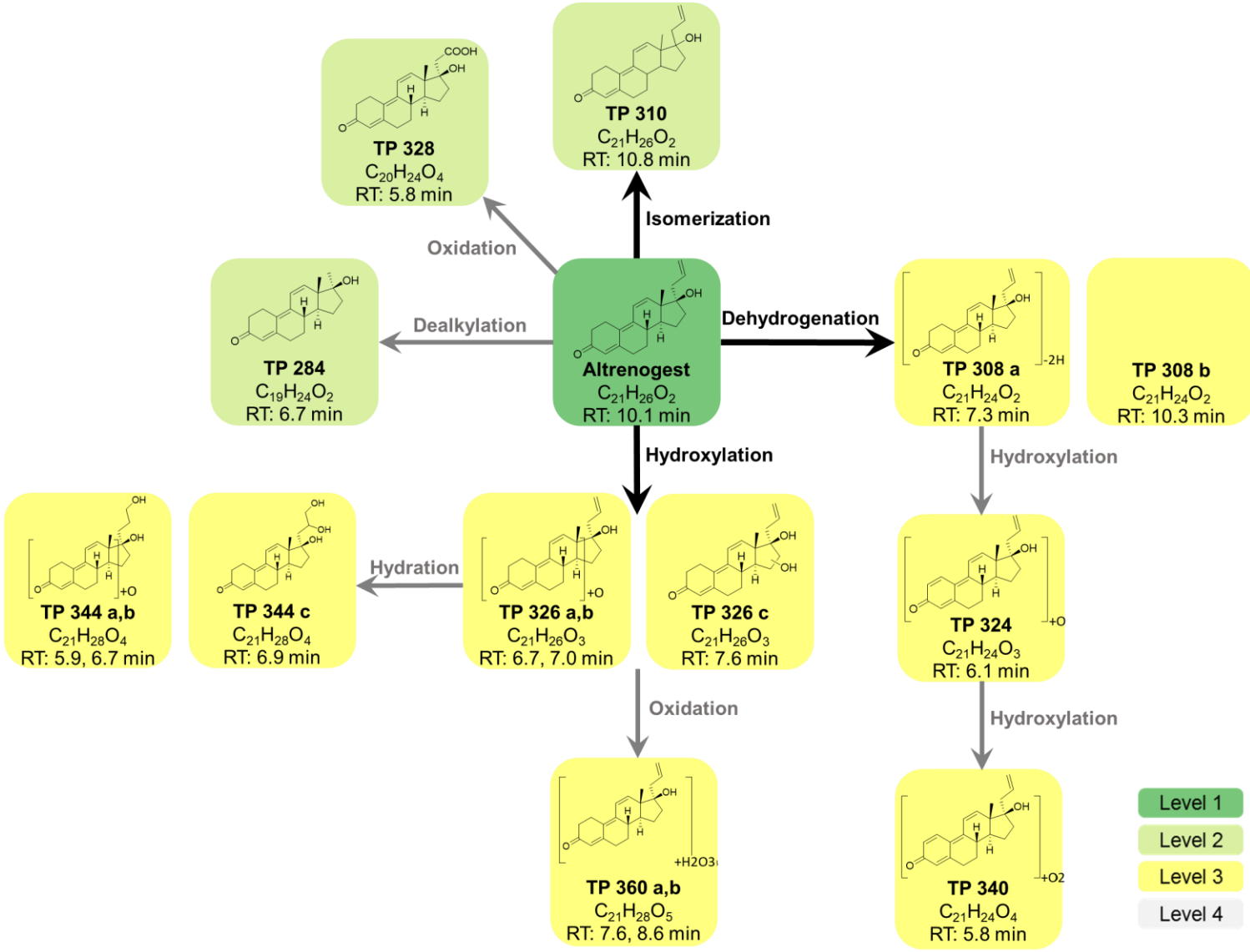


**Figure 3.6** Proposed biotransformation pathways of ALT. Blank arrows highlight major pathways. TP structures identified with confidence level 1, 2, 3 and 4 were communicated in dark green, light green, yellow, and gray shades, respectively.

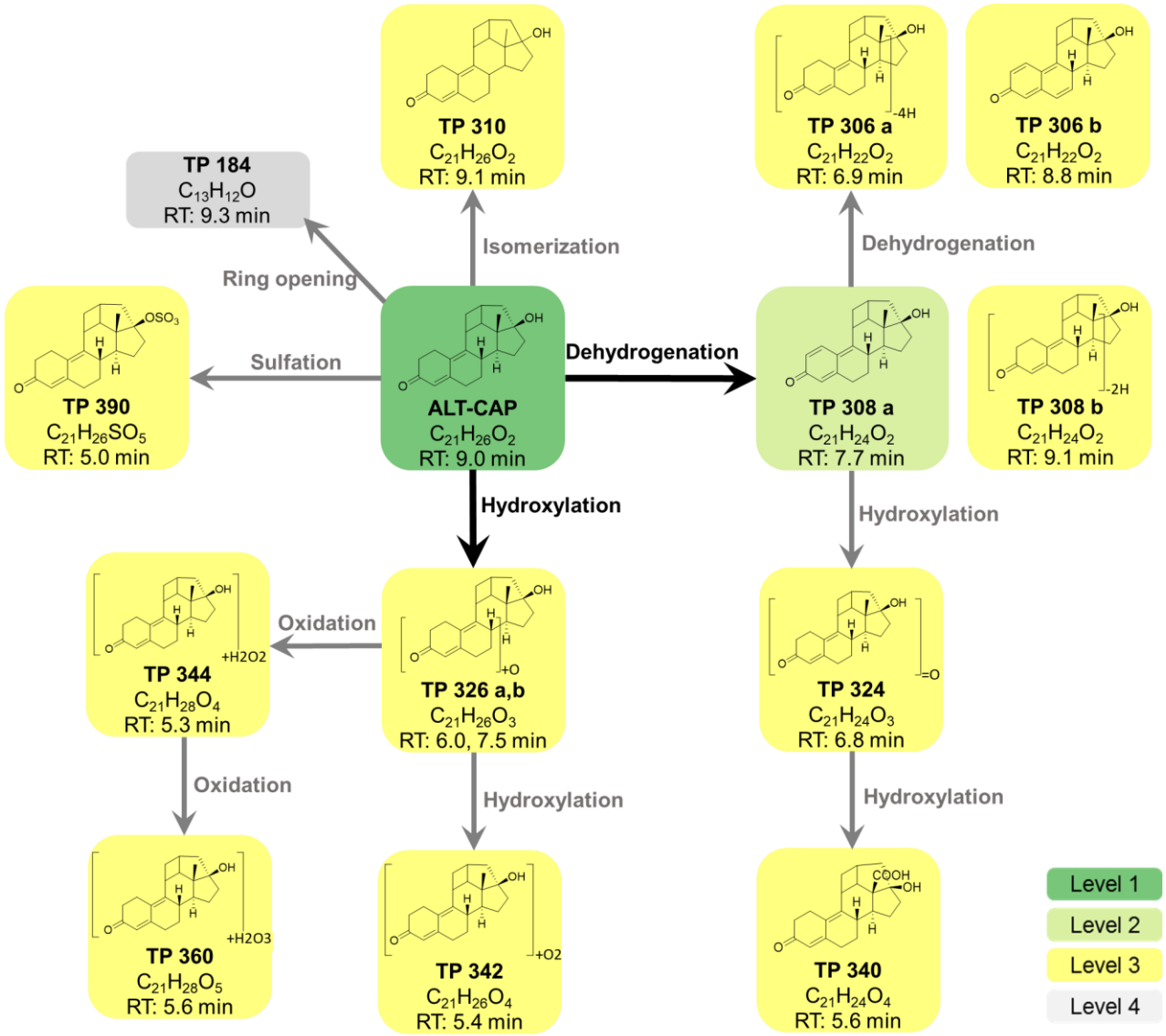


**Figure 3.7** Proposed biotransformation pathways of ALT-CAP. Blank arrows highlight major pathways. TP structures identified with confidence level 1, 2, 3 and 4 were communicated in dark green, light green, yellow, and gray shades, respectively.

### 3.3.3 Biotransformation Pathways

Based on the above likely and probable TPs, biotransformation pathways of ALT (**Figure 3.6**) and ALT-CAP (**Figure 3.7**) were proposed. In general, ALT and ALT-CAP showed similar transformations, including pathways typical for similar steroids (Cole et al., 2015; Ma and Yates, 2018; Weizel et al., 2020). One main group identified for ALT and ALT-CAP were the hydroxylation TPs (**Figure 3.4**, **3.5**). Based on their MS/MS spectra, the observed hydroxylation reactions were not regio-selective and could occur on all of A, B, C rings and D rings, consistent with reactions previously reported for other steroids (Cole et al., 2015; Weizel et al., 2021, 2020). Hydroxylation TPs are common intermediates in the biotransformation of steroids that are further oxidized into carboxylate TPs and subsequent ring cleavages to ketones and carboxylic acids. Such hypotheses match the time profiles of the observed TPs. For example, ALT TP 326a and ALT-CAP TP 326 b increased in peak areas over day 0 - 7, followed by a rapid peak area decrease from days 7 - 30. Correspondingly, ALT TP 284 and TP 360s, for which the MS/MS spectra were consistent with $CO_2$ neutral losses, appeared on day 7 and day 14, respectively.

Dehydrogenation was another main transformation pathway observed for ALT and ALT-CAP. Based on the MS/MS spectra evidence, dehydrogenation sites were probable for A and B rings of ALT and ALT-CAP, especially 1,2-dehydrogenation and 6,7-dehydrogenation. Notably, microbially mediated 1,2-dehydrogenation is frequently observed across multiple classes of steroids including androgens such as testosterone and the similar trienone steroid trenbolone (Cole et al., 2015; Yang et al., 2010), glucocorticoids (Weizel et al., 2020), and progestins (Liu et al., 2013; Weizel et al., 2021). Here, ALT TP 308a represented a stable TP with increasing peak area throughout the incubation, while ALT TP 308b formed rapidly to day 7 and substantially decreased thereafter (**Figure 3.4**). These time profiles were consistent with dehydrogenation as

an primary biotransformation reaction, followed by further hydroxylation of dehydrogenation TPs (e.g., TP 324s and TP 340s; Figures 3.6, 3.7).

Isomerization, likely epimerization, also generated relatively high peak area TPs (Figures 3.4, 3.5). Epimerization is commonly observed in steroid biotransformation. For example, 17α-estradiol and 17β-estradiol interchanged in dairy lagoon water, anaerobic sediment, and aerobic alluvial sediment (Mashtare et al., 2013; Zhang et al., 2016; Zheng et al., 2012), and interconversions between 17α-trenbolone and 17β-trenbolone were observed in soil, aerobic creek water, and aerobic alluvial sediment (Cole et al., 2015; Khan and Lee, 2012; Zhang et al., 2016). The observed stereoisomers of ALT and ALT-CAP are probable candidates for retained bioactivities in TPs.

Notably, although ALT and ALT-CAP showed similarities across transformation pathways, the absolute abundance of ALT-CAP TPs was often an order of magnitude higher than that of ALT TPs despite similar peak area response of ALT and ALT-CAP under ESI+ and ~10-fold higher peak area response of ALT than ALT-CAP under ESI- (**Figure 3.4**, **3.5**). Considering ESI+ peak areas, the sum peak area of the observed ALT-CAP TPs scaled with 200%, 129%, and 66% of the decreased ALT-CAP peak areas ($\Sigma PeakArea_{TP\_day\ t}$ / ($PeakArea_{ALT\_day0-}$ - $PeakArea_{ALT\_day\ t}$)) on days 7, 14, and 30, respectively. In contrast, ALT TPs explained only 18%, 12%, and 11% of the decreased ALT peak areas on the same days. This indicated that biotransformation of ALT-CAP tended to produce larger, and more stable TPs with higher potential for retained steroid structures. In contrast, biotransformation of ALT seemed to produce less abundant and less stable TPs, assuming similar shifts in TP peak area response across the two parent steroids. Therefore, although ALT-CAP demonstrated ~2-fold faster removal kinetics than ALT, it was transformed into more stable steroid TPs at larger abundances. Therefore, the exposure risks of ALT are prone to underestimation if the formation and subsequent

biotransformation products of ALT-CAP are not considered as part of the environmental fate of these compounds. Additional screening and analysis of these possibilities in agro-ecosystems is merited to better understand the environmental risks of these potent steroidal pharmaceuticals.

## References


Chang, H., Wu, S., Hu, J., Asami, M., Kunikane, S., 2008. Trace analysis of androgens and progestogens in environmental waters by ultra-performance liquid chromatography–electrospray tandem mass spectrometry. J. Chromatogr. A 1195, 44–51.

Chiang, Y.-R., Wei, S.T.-S., Wang, P.-H., Wu, P.-H., Yu, C.-P., 2020. Microbial degradation of steroid sex hormones: Implications for environmental and ecological studies. Microb. Biotechnol. 13, 926–949.

Cole, E.A., McBride, S.A., Kimbrough, K.C., Lee, J., Marchand, E.A., Cwiertny, D.M., Kolodziej, E.P., 2015. Rates and product identification for trenbolone acetate metabolite biotransformation under aerobic conditions. Environ. Toxicol. Chem. 34, 1472–1484.

Cwiertny, D.M., Snyder, S.A., Schlenk, D., Kolodziej, E.P., 2014. environmental designer drugs: When transformation may not eliminate risk. Environ. Sci. Technol. 48, 11737–11745.

Du, B., Lofton, J.M., Peter, K.T., Gipe, A.D., James, C.A., McIntyre, J.K., Scholz, N.L., Baker, J.E., Kolodziej, E.P., 2017. Development of suspect and non-target screening methods for detection of organic contaminants in highway runoff and fish tissue with high-resolution time-of-flight mass spectrometry. Environ. Sci. Process. Impacts 19, 1185–1196.

European Medical Agency Environmental Impact Assessment, 2013. Overall summary of the scientific evaluation of Suifertil 4 mg/ml Oral Solution for Pigs.

Fent, K., 2015. Progestins as endocrine disrupters in aquatic ecosystems: Concentrations, effects and risk assessment. Environ. Int. 84, 115–130.

Golovko, O., Šauer, P., Fedorova, G., Kroupová, H.K., Grabic, R., 2018. Determination of progestogens in surface and waste water using SPE extraction and LC-APCI/APPI-HRPS. Sci. Total Environ. 621, 1066–1073.

Henning, N., Wick, A., Ternes, T.A., 2021. Biotransformation of pregabalin in surface water matrices and the occurrence of transformation products in the aquatic environment - comparison to the structurally related gabapentin. Water Res. 117488.

Jenkins, R.L., Wilson, E.M., Angus, R.A., Howell, W.M., Kirk, M., Moore, R., Nance, M., Brown, A., 2004. Production of androgens by microbial transformation of progesterone in vitro: A model for androgen production in rivers receiving paper mill effluent. Environ. Health Perspect. 112, 1508–1511.

Kang, M.-J., Lisurek, M., Bernhardt, R., Hartmann, R.W., 2004. Use of high-performance liquid chromatography/electrospray ionization collision-induced dissociation mass spectrometry for structural identification of monohydroxylated progesterones. Rapid Commun. Mass Spectrom. RCM 18, 2795–2800.

Kenyon, P.T., Zhao, H., Yang, X., Wu, C., Cwiertny, D.M., Kolodziej, E.P., 2019. Detection and quantification of metastable photoproducts of trenbolone and altrenogest using liquid chromatography–tandem mass spectrometry. J. Chromatogr. A 1603, 150–159.

Khan, B., Lee, L.S., 2012. Estrogens and synthetic androgens in manure slurry from trenbolone acetate/estradiol implanted cattle and in waste-receiving lagoons used for irrigation. Chemosphere 89, 1443–1449.

Kumar, V., Johnson, A.C., Trubiroha, A., Tumová, J., Ihara, M., Grabic, R., Kloas, W., Tanaka, H., Kroupová, H.K., 2015. The challenge presented by progestins in ecotoxicological research: A critical review. Environ. Sci. Technol. 49, 2625–2638.

Lampinen-Salomonsson, M., Beckman, E., Bondesson, U., Hedeland, M., 2006. Detection of altrenogest and its metabolites in post administration horse urine using liquid chromatography tandem mass spectrometry—increased sensitivity by chemical derivatisation of the glucuronic acid conjugate. J. Chromatogr. B 833, 245–256.

Liu, S., Ying, G.-G., Liu, Y.-S., Peng, F.-Q., He, L.-Y., 2013. Degradation of norgestrel by bacteria from activated sludge: Comparison to progesterone. Environ. Sci. Technol. 47, 10266–10276.
Ma, L., Yates, S.R., 2018. A review on structural elucidation of metabolites of environmental steroid hormones via liquid chromatography–mass spectrometry. TrAC Trends Anal. Chem. 109, 142–153.
Madigan, M., Bender, K., Buckley, D., Stahl, D., Sattley, W., 2017. Brock Biology of Microorganisms, 15th Edition. Boston: Pearson Education.
Mashtare, M.L., Lee, L.S., Nies, L.F., Turco, R.F., 2013. Transformation of 17α-estradiol, 17β-estradiol, and estrone in sediments under nitrate- and sulfate-reducing conditions. Environ. Sci. Technol. 47, 7178–7185.
OECD, 2004. Test No. 309: Aerobic Mineralisation in Surface Water - Simulation Biodegradation Test.
Orlando, E.F., Ellestad, L.E., 2014. Sources, concentrations, and exposure effects of environmental gestagens on fish and other aquatic wildlife, with an emphasis on reproduction. Gen. Comp. Endocrinol., 203, 241–249.
Paulos, P., Runnalls, T.J., Nallani, G., La Point, T., Scott, A.P., Sumpter, J.P., Huggett, D.B., 2010. Reproductive responses in fathead minnow and Japanese medaka following exposure to a synthetic progestin, Norethindrone. Aquat. Toxicol. 99, 256–262.
Peter, K.T., Tian, Z., Wu, C., Lin, P., White, S., Du, B., McIntyre, J.K., Scholz, N.L., Kolodziej, E.P., 2018. Using high-resolution mass spectrometry to identify organic contaminants linked to urban stormwater mortality syndrome in coho salmon. Environ. Sci. Technol. 52, 10317–10327.
Pozo, O.J., Eenoo, P.V., Deventer, K., Delbeke, F.T., 2008. Detection and characterization of anabolic steroids in doping analysis by LC-MS. TrAC Trends Anal. Chem. 27, 657–671.
Schwarzenbach, R. P., Gschwend, P.M., Imboden, D.M., 2003. Environmental Organic Chemistry, 2nd Edition. John Wiley & Sons, Inc.
Schymanski, E.L., Jeon, J., Gulde, R., Fenner, K., Ruff, M., Singer, H.P., Hollender, J., 2014. Identifying small molecules via high resolution mass spectrometry: Communicating confidence. Environ. Sci. Technol. 48, 2097–2098.
Seller, C., Honti, M., Singer, H., Fenner, K., 2020. Biotransformation of chemicals in water–sediment suspensions: Influencing factors and implications for persistence assessment. Environ. Sci. Technol. Lett. 7, 854–860.
Sharpe, R.L., MacLatchy, D.L., Courtenay, S.C., Van Der Kraak, G.J., 2004. Effects of a model androgen (methyl testosterone) and a model anti-androgen (cyproterone acetate) on reproductive endocrine endpoints in a short-term adult mummichog (Fundulus heteroclitus) bioassay. Aquat. Toxicol. 67, 203–215.
Squires, E.L., Heesemann, C.P., Webel, S.K., Shideler, R.K., Voss, J.L., 1983. Relationship of altrenogest to ovarian activity, hormone concentrations and fertility of mares. J. Anim. Sci. 56, 901–910.
Svendsen, S.B., El-taliawy, H., Carvalho, P.N., Bester, K., 2020. Concentration dependent degradation of pharmaceuticals in WWTP effluent by biofilm reactors. Water Res. 186, 116389.
Thevis, M., Bommerich, U., Opfermann, G., Schänzer, W., 2005. Characterization of chemically modified steroids for doping control purposes by electrospray ionization tandem mass spectrometry. J. Mass Spectrom. 40, 494–502.
Thevis, M., Schänzer, W., 2007. Mass spectrometry in sports drug testing: Structure characterization and analytical assays. Mass Spectrom. Rev. 26, 79–107.

Tian, Z., Peter, K.T., Gipe, A.D., Zhao, H., Hou, F., Wark, D.A., Khangaonkar, T., Kolodziej, E.P., James, C.A., 2020. Suspect and nontarget screening for contaminants of emerging concern in an urban estuary. Environ. Sci. Technol. 54, 889–901.

van Leeuwen, J.J.J., Williams, S.I., Martens, M.R.T.M., Jourquin, J., Driancourt, M.A., Kemp, B., Soede, N.M., 2011. The effect of different postweaning altrenogest treatments of primiparous sows on follicular development, pregnancy rates, and litter sizes. J. Anim. Sci. 89, 397–403.

Wammer, K.H., Anderson, K.C., Erickson, P.R., Kliegman, S., Moffatt, M.E., Berg, S.M., Heitzman, J.A., Pflug, N.C., McNeill, K., Martinovic-Weigelt, D., Abagyan, R., Cwiertny, D.M., Kolodziej, E.P., 2016. Environmental photochemistry of altrenogest: Photoisomerization to a bioactive product with increased environmental persistence via reversible photohydration. Environ. Sci. Technol. 50, 7480–7488.

Weizel, A., Schlüsener, M.P., Dierkes, G., Ternes, T.A., 2018. Occurrence of glucocorticoids, mineralocorticoids, and progestogens in various treated wastewater, rivers, and streams. Environ. Sci. Technol. 52, 5296–5307.

Weizel, A., Schlüsener, M.P., Dierkes, G., Wick, A., Ternes, T.A., 2021. Fate and behavior of progestogens in activated sludge treatment: Kinetics and transformation products. Water Res. 188, 116515.

Weizel, A., Schlüsener, M.P., Dierkes, G., Wick, A., Ternes, T.A., 2020. Analysis of the aerobic biodegradation of glucocorticoids: Elucidation of the kinetics and transformation reactions. Water Res. 174, 115561.

Willmann, C., Schuler, G., Hoffmann, B., Parvizi, N., Aurich, C., 2011. Effects of age and altrenogest treatment on conceptus development and secretion of LH, progesterone and eCG in early-pregnant mares. Theriogenology 75, 421–428.

Yang, Y.-Y., Borch, T., Young, R.B., Goodridge, L.D., Davis, J.G., 2010. Degradation kinetics of testosterone by manure-borne bacteria: Influence of temperature, pH, glucose amendments, and dissolved oxygen. J. Environ. Qual. 39, 1153–1160.

Zeilinger, J., Steger-Hartmann, T., Maser, E., Goller, S., Vonk, R., Länge, R., 2009. Effects of synthetic gestagens on fish reproduction. Environ. Toxicol. Chem. 28, 2663–2670.

Zhang, Y., Snow, D.D., Bartelt-Hunt, S.L., 2016. Stereoselective degradation of estradiol and trenbolone isomers in alluvial sediment. Environ. Sci. Technol. 50, 13256–13264.

Zheng, W., Li, X., Yates, S.R., Bradford, S.A., 2012. Anaerobic transformation kinetics and mechanism of steroid estrogenic hormones in dairy lagoon water. Environ. Sci. Technol. 46, 5471–5478.

## Supplementary Materials

### High-Resolution Mass Spectrometry Instrumental Method

For the UPLC-qTOF-HRMS analysis, LC separation was achieved on an Agilent ZORBAX Eclipse Plus C18 column (2.1 × 100 mm, 1.8 μm) preceded with an Agilent ZORBAX Eclipse Plus C18 guard column (2.1 × 5 mm, 1.8 μm). For ESI+, the mobile phases (0.4 mL/min) were 5 mM ammonium acetate and 0.1% acetic acid in each of water (A) and methanol (B), with a gradient of 5% B at 0-1 min, 50% B at 4 min, 100% B at 17-20 min, 5% B at 20.1 min, stop time 22.5 min, and post-time 2 min. For ESI-, the mobile phases were 1 mM ammonium fluoride in water (A) and pure methanol (B), and the same gradient was used as ESI+. Full scan HRMS data were acquired at the m/z range of 100-1700. MS/MS data was acquired at the m/z range of 50-500 (no features in the preferred list have m/z > 500) under three collision energy (10, 20, and 40 eV), by data-dependent acquisition with the preferred lists generated with the full scan data through replicate filtration and blank (controls) subtraction.

For quality assurance and quality control (QA/QC), a checktune including mass calibration was performed before each analytical run, and mass accuracy was corrected via continuous infusion of purine and HP-921 calibrants during the run. Solvent blanks and instrumental internal standard (ISTD) controls were analyzed every 12 samples. The retention time (RT), mass accuracy, and abundance of ISTD controls were used for performance evaluation of each analytical run. The RT deviation and mass error of the ISTDs were <0.15 min and <5 ppm, respectively. Response (peak area) variations of ISTDs were <15% within each analytical batch.

**Table S3.1** Key parameters of the feature extraction and alignment method in MassHunter Profinder.

| Category | Item | Setting |
|---|---|---|
| Molecular Feature Extraction (MFE) – Extraction Parameters | Noise peak height | ≥ 300 counts |
| | Ion Species | ESI+: +H, +Na, +$NH_4$ |
| | | ESI-: -H, +HCOO, +CH3COO |
| | Isotope model | Common organic molecules |
| Compound Binning and Alignment | RT window | 0.4 min |
| | Mass window | 30 ppm |
| MFE – Post-Processing Filters | Absolute height | ≥ 5000 counts |
| | Score (MFE) | ≥ 70 |
| | Satisfy MFE conditions in | ≥ 2 files |
| Find by Ion – Matching Tolerances and Scoring | Scoring | Mass score (100), isotope abundance score (60), isotope spacing score (50), retention time score (50) |
| | Do not match if score | < 30 |
| Find by Ion – EIC Peak Integration and Filtering | Integration | Agile 2 |
| | Peak height | ≥ 3000 counts |
| Find by Ion – Post-Processing Filters | Absolute height | ≥ 1000 counts |
| | Score (Tgt) | ≥ 50 |
| | Satisfy Find by Ion conditions in | ≥ 2 files |

**Table S3.2** Identification details for ALT TPs.

| Name | Formula | Isomer | Polarity | m/z | RT (min) | Characteristic fragments | | | | Confidence level | Proposed structure |
|---|---|---|---|---|---|---|---|---|---|---|---|
| | | | | | | Fragment m/z | Formula | Δm/z | Structural insights | | |
| ALT | $C_{21}H_{26}O_2$ | - | ESI+ | 311.2006 | 10.08 | 293.187 | $C_{21}H_{25}O^+$ | 18 | H2O loss | 1 | 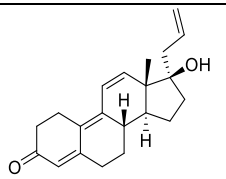 |
| | | | | | | 269.1516 | $C_{18}H_{21}O_2^+$ | 42 | C3H6 loss, C17-allyl chain | | |
| | | | | | | 251.1454 | $C_{18}H_{19}O^+$ | 60 | H2O loss | | |
| | | | | | | 227.1413 | $C_{16}H_{19}O^+$ | 84 | C1-C15 and C18, common fragments for all C13-methyl triene steroids | | |
| | | | | | | 199.1086 | $C_{14}H_{15}O^+$ | 112 | C1-C14, common fragments for all triene steroids | | |
| | | | ESI- | 309.1850 | 10.08 | 267.1359 | $C_{18}H_{19}O_2^-$ | 42 | C3H6 loss, C17-allyl chain | | |
| | | | | | | 225.1262 | $C_{16}H_{17}O^-$ | 84 | maybe correspond to m/z 227 under ESI+ | | |
| | | | | | | 211.1105 | $C_{15}H_{15}O^-$ | 98 | m/z 225-14 | | |
| | | | | | | 197.0943 | $C_{14}H_{13}O^-$ | 112 | maybe correspond to m/z 199 under ESI+, C1-C14 | | |
| TP 284 | $C_{19}H_{24}O_2$ | - | ESI- | 283.1676 | 6.72 | 211.1104 | $C_{15}H_{15}O^-$ | 72 | same as ALT, indicating unchanged A/B/C rings | 2b | 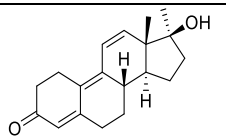 |
| | | | | | | 197.0954 | $C_{14}H_{13}O^-$ | 86 | | | |
| | | | | | | 161.0942 | $C_{11}H_{13}O^-$ | 122 | | | |
| TP 308 | $C_{21}H_{24}O_2$ | a | ESI+ | 309.1873 | 7.27 | 291.1682 | $C_{21}H_{23}O^+$ | 18 | | 3b | 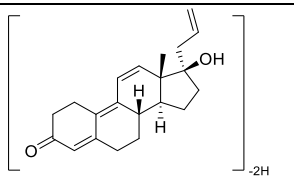 |
| | | | | | | 251.1432 | $C_{18}H_{19}O^+$ | 58 | | | |
| | | b | ESI+ | 309.1873 | 10.41 | 291.1719 | $C_{21}H_{23}O^+$ | 18 | | 3a | 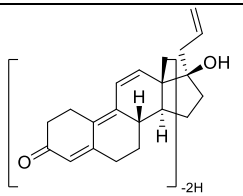 |
| | | | | | | 267.1369 | $C_{18}H_{19}O_2^+$ | 42 | | | |
| | | | | | | 249.1288 | $C_{18}H_{17}O^+$ | 60 | | | |
| | | | | | | 223.1110 | $C_{16}H_{15}O^+$ | 86 | | | |
| | | | | | | 208.0881 | $C_{15}H_{12}O^+$ | 101 | | | |
| | | | ESI- | 307.1685 | 10.25 | 266.1279 | $C_{18}H_{18}O_2^-$ | 41 | | | |
| | | | | | | 251.1052 | $C_{17}H_{15}O_2^-$ | 56 | | | |
| TP 310 | $C_{21}H_{26}O_2$ | - | ESI+ | 311.2018 | 10.82 | 293.187 | $C_{21}H_{25}O^+$ | 18 | same MS/MS spectra with ALT, maybe stereoisomer | 2b | 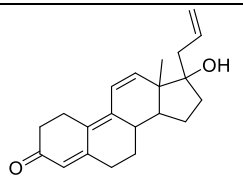 |
| | | | | | | 269.1527 | $C_{18}H_{21}O_2^+$ | 42 | | | |
| | | | | | | 252.1535 | $C_{18}H_{20}O^+$ | 59 | | | |
| | | | | | | 227.141 | $C_{16}H_{19}O^+$ | 84 | | | |
| TP 324 | $C_{21}H_{24}O_3$ | - | ESI- | 323.1618 | 6.14 | 267.0993 | $C_{17}H_{15}O_3^-$ | 56 | m/z 251 of TP 308 + O | 3b | 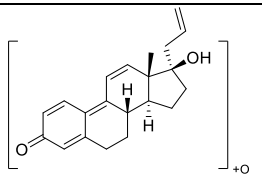 |
| | | | | | | 239.1041 | $C_{16}H_{15}O_2^-$ | 84 | | | |
| | | | | | | 211.0754 | $C_{14}H_{11}O_2^-$ | 112 | | | |
| | | | | | | 173.0593 | $C_{11}H_9O_2^-$ | 150 | | | |
| | | | | | | 145.0629 | $C_{10}H_9O^-$ | 178 | | | |

| | | | | | | | | | | |
|---|---|---|---|---|---|---|---|---|---|---|
| TP 326 | $C_{21}H_{26}O_3$ | a | ESI- | 325.1775 | 6.68 | 307.1687 | $C_{21}H_{23}O_2$- | 18 | | 3a |
| | | | | | | 283.1666 | $C_{19}H_{23}O_2$- | 42 | | |
| | | | | | | 209.0941 | $C_{15}H_{13}O$- | 116 | m/z 211 of ALT - 2H | |
| | | | | | | 195.0791 | $C_{14}H_{11}O$- | 130 | m/z 197 of ALT - 2H, indicating hydroxylation on A/B/C ring | |
| | | b | ESI+ | 327.195 | 6.97 | 309.1856 | $C_{21}H_{25}O_2$+ | 18 | | 3a |
| | | | | | | 285.1492 | $C_{18}H_{21}O_3$+ | 42 | | |
| | | | | | | 243.1371 | $C_{16}H_{19}O_2$+ | 84 | | |
| | | | | | | 225.1279 | $C_{16}H_{17}O$+ | 102 | m/z 227 of ALT - 2H, indicating hydroxylation on C1-C15 or C18 | |
| | | | ESI- | 325.1775 | 6.99 | 307.1668 | $C_{21}H_{23}O_2$- | 18 | | |
| | | | | | | 269.1162 | $C_{17}H_{17}O_3$- | 56 | | |
| | | | | | | 209.0945 | $C_{15}H_{13}O$- | 116 | m/z 211 of ALT - 2H | |
| | | | | | | 195.0765 | $C_{14}H_{11}O$- | 130 | m/z 197 of ALT - 2H, indicating hydroxylation on A/B/C ring | |
| | | c | ESI+ | 327.196 | 7.61 | 309.1825 | $C_{21}H_{25}O_2$+ | 18 | | 3a |
| | | | | | | 285.172 | $C_{18}H_{21}O_3$+ | 42 | | |
| | | | | | | 269.1548 | $C_{18}H_{21}O_2$+ | 58 | | |
| | | | | | | 251.143 | $C_{18}H_{19}O$+ | 76 | | |
| | | | | | | 227.1409 | $C_{16}H_{19}O$+ | 100 | same as ALT, indicating hydroxylation on D ring | |
| | | | | | | 199.1133 | $C_{14}H_{15}O$+ | 128 | same as ALT, indicating hydroxylation on D ring | |
| | | | ESI- | 325.1775 | 7.51 | 307.1673 | $C_{21}H_{23}O_2$- | 18 | | |
| | | | | | | 269.1146 | $C_{17}H_{17}O_3$- | 56 | | |
| | | | | | | 211.1102 | $C_{15}H_{15}O$- | 114 | same as ALT, indicating hydroxylation on D ring | |
| | | | | | | 197.0938 | $C_{14}H_{13}O$- | 128 | same as ALT, indicating hydroxylation on D ring | |
| TP 328 | $C_{20}H_{24}O_4$ | - | ESI- | 327.157 | 5.76 | 283.167 | $C_{19}H_{23}O_2$- | 44 | COO loss for carbonic acid | 2b |
| | | | | | | 243.0999 | $C_{15}H_{15}O_3$- | 84 | | |
| | | | | | | 211.1112 | $C_{15}H_{15}O$- | 116 | same as ALT, indicating unchanged A/B/C rings | |
| | | | | | | 197.0914 | $C_{14}H_{13}O$- | 130 | same as ALT, indicating unchanged A/B/C rings | |
| | | | | | | 147.0436 | $C_9H_7O_2$- | 180 | | |
| | | | | | | 95.0473 | $C_6H_7O$- | 232 | | |
| TP 340 | $C_{21}H_{24}O_4$ | - | ESI- | 339.1577 | 5.82 | 321.1456 | $C_{21}H_{21}O_3$- | 18 | | 3b |
| | | | | | | 297.1122 | $C_{18}H_{17}O_4$- | 42 | | |
| | | | | | | 243.1001 | $C_{15}H_{13}O_3$- | 96 | | |
| | | | | | | 225.0891 | $C_{15}H_{13}O_2$- | 114 | | |
| | | | | | | 147.0429 | $C_9H_7O_2$- | 192 | | |
| | | | | | | 95.0489 | $C_6H_7O$- | 244 | | |
| TP 344 | $C_{21}H_{28}O_4$ | a | ESI+ | 345.2036 | 5.91 | 327.1957 | $C_{21}H_{27}O_3$+ | 18 | H2O loss | 3a |
| | | | | | | 309.1826 | $C_{21}H_{25}O_2$+ | 36 | H2O loss from m/z 327 | |
| | | | | | | 285.1469 | $C_{18}H_{21}O_3$+ | 60 | C3H6 (C17-allyl chain) loss from m/z 327 | |
| | | | | | | 267.1393 | $C_{18}H_{19}O_2$+ | 78 | H2O loss from m/z 285 | |
| | | | | | | 249.1489 | $C_{18}H_{17}O$+ | 96 | H2O loss from m/z 249 | |

| | | | | | | | | | | |
|---|---|---|---|---|---|---|---|---|---|---|
| | | | | | 225.1271 | $C_{16}H_{17}O^+$ | 120 | m/z 227 of ALT - 2H, indicating one hydroxylation on C1-C15 or C18 | | 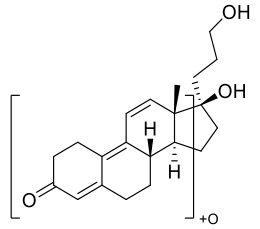 |
| | | b | ESI+ | 345.2036 | 6.73 | 327.1922 | $C_{21}H_{27}O_3^+$ | 18 | | 3a |
| | | | | | | 309.1811 | $C_{21}H_{25}O_2^+$ | 36 | | |
| | | | | | | 253.1582 | $C_{18}H_{21}O^+$ | 92 | | |
| | | | | | | 225.1293 | $C_{16}H_{17}O^+$ | 120 | m/z 227 of ALT - 2H, indicating one hydroxylation on C1-C15 or C18 | 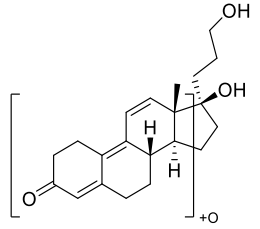 |
| | | c | ESI+ | 345.2067 | 6.85 | 327.1967 | $C_{21}H_{27}O_3^+$ | 18 | | 3a |
| | | | | | | 309.1834 | $C_{21}H_{25}O_2^+$ | 36 | | |
| | | | | | | 291.1677 | $C_{21}H_{23}O^+$ | 54 | losses of three water molecules | |
| | | | | | | 253.1558 | $C_{18}H_{21}O^+$ | 92 | | |
| | | | | | | 227.1422 | $C_{16}H_{19}O^+$ | 118 | same as ALT, indicating hydrogenation and hydroxylation on D ring | 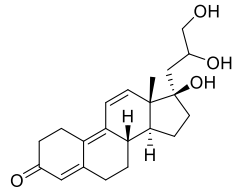 |
| TP 360 | $C_{21}H_{28}O_5$ | a | ESI+ | 361.2004 | 7.6 | N/A | | | different RT under ESI+ and ESI- due to ion species difference | 3b |
| | | | ESI- | 359.1812 | 5.57 | 355.1558 | $C_{21}H_{23}O_5^-$ | 4 | | |
| | | | | | | 315.1933 | $C_{20}H_{27}O_3^-$ | 44 | COO loss for carbonic acid | |
| | | b | ESI+ | 361.203 | 8.62 | 343.1879 | $C_{21}H_{27}O_4^+$ | 18 | | 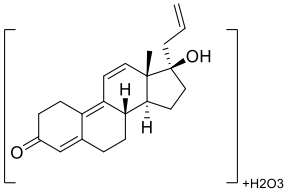 |
| | | | | | | 325.1737 | $C_{21}H_{25}O_3^+$ | 36 | | |
| | | | | | | 315.1986 | $C_{20}H_{27}O_3^+$ | 46 | CO loss from m/z 343 | |
| | | | | | | 297.1886 | $C_{20}H_{25}O_2^+$ | 64 | CO loss from m/z 325 | |
| | | | | | | 255.1394 | $C_{17}H_{19}O_2^+$ | 106 | | |
| | | | ESI- | 359.1857 | 6.1 | N/A | | | | |

**Table S3.3** Identification details for ALT-CAP TPs.

| Name | Formula | Isomer | Polarity | m/z | RT | Characteristic fragments | | | | Confidence level | Proposed structure |
|---|---|---|---|---|---|---|---|---|---|---|---|
| | | | | | | Fragment m/z | Formula | Δm/z | Structural insights | | |
| ALT-CAP | $C_{21}H_{26}O_2$ | - | ESI+ | 311.2009 | 8.98 | 293.1901 | $C_{21}H_{25}O+$ | 18 | same fragments as ALT | 1 | 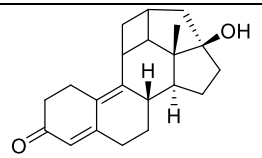 |
| | | | | | | 269.1511 | $C_{18}H_{21}O_2+$ | 42 | | | |
| | | | | | | 251.1392 | $C_{18}H_{19}O+$ | 60 | | | |
| | | | | | | 227.1448 | $C_{16}H_{19}O+$ | 84 | | | |
| | | | | | | 199.11 | $C_{14}H_{15}O+$ | 112 | | | |
| | | | ESI- | 309.183 | 8.91 | 291.1718 | $C_{21}H_{23}O-$ | 18 | different spectra from ALT. Major fragment is m/z 199, while those for ALT are m/z 197 and 211 | | |
| | | | | | | 253.1201 | $C_{17}H_{17}O_2-$ | 56 | | | |
| | | | | | | 223.1096 | $C_{16}H_{15}O-$ | 86 | | | |
| | | | | | | 199.1102 | $C_{14}H_{15}O-$ | 110 | | | |
| TP 184 | $C_{13}H_{12}O$ | - | ESI+ | 185.0972 | 9.31 | 157.0656 | $C_{11}H_9O+$ | 28 | | 4 | N/A |
| | | | | | | 144.0564 | $C_{10}H_8O+$ | 41 | | | |
| | | | | | | 129.0708 | $C_{10}H_9+$ | 56 | | | |
| TP 306 | $C_{21}H_{22}O_2$ | a | ESI+ | 307.1735 | 6.94 | 265.1561 | $C_{19}H_{21}O+$ | 42 | | 3b | 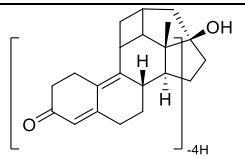 |
| | | | | | | 223.1086 | $C_{16}H_{15}O+$ | 84 | | | |
| | | | | | | 209.0955 | $C_{15}H_{13}O+$ | 98 | | | |
| | | b | ESI- | 305.1519 | 8.76 | 247.0732 | $C_{17}H_{11}O_2-$ | 58 | | 3a | 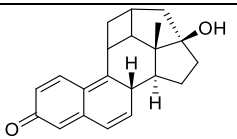 |
| | | | | | | 192.0559 | $C_{14}H_8O-$ | 113 | stable C14 ion, indicating conjugated A/B/C ring | | |
| TP 308 | $C_{21}H_{24}O_2$ | a | ESI+ | 309.1864 | 7.72 | 291.1723 | $C_{21}H_{23}O+$ | 18 | | 2b | 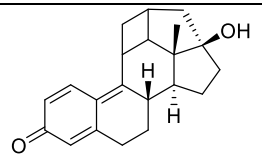 |
| | | | | | | 267.1345 | $C_{18}H_{19}O_2+$ | 42 | | | |
| | | | | | | 249.1302 | $C_{18}H_{17}O+$ | 60 | | | |
| | | | | | | 225.1258 | $C_{16}H_{17}O+$ | 84 | m/z 227 of ALT-CAP -2H | | |
| | | | | | | 209.0931 | $C_{15}H_{13}O+$ | 100 | | | |
| | | | | | | 197.0943 | $C_{14}H_{13}O+$ | 112 | m/z 199 of ALT-CAP -2H, indicating dehydrogenation on A/B/C/ ring | | |
| | | | ESI- | 307.1676 | 7.85 | 249.0883 | $C_{17}H_{13}O_2-$ | 58 | | | |
| | | | | | | 221.0936 | $C_{16}H_{13}O-$ | 86 | | | |
| | | | | | | 210.1005 | $C_{15}H_{14}O-$ | 97 | | | |
| | | | | | | 195.0782 | $C_{14}H_{11}O-$ | 112 | | | |
| | | | | | | 183.0767 | $C_{13}H_{11}O-$ | 124 | | | |
| | | b | ESI+ | 309.1842 | 9.31 | 267.1368 | $C_{18}H_{19}O_2+$ | 42 | similar spectra with TP 308b of ALT | 3a | |
| | | | | | | 247.1091 | $C_{18}H_{15}O+$ | 61 | | | |
| | | | | | | 223.1126 | $C_{16}H_{15}O+$ | 86 | | | |
| | | | | | | 208.0883 | $C_{15}H_{12}O+$ | 101 | | | |
| | | | ESI- | 307.1676 | 9.1 | 249.09 | $C_{17}H_{13}O_2-$ | 58 | similar spectra with TP 308a | | |
| | | | | | | 221.0947 | $C_{16}H_{13}O-$ | 86 | | | |

| | | | | | | | | | | | |
|---|---|---|---|---|---|---|---|---|---|---|---|
| | | | | | | 210.1015 | $C_{15}H_{14}O$- | 97 | | | 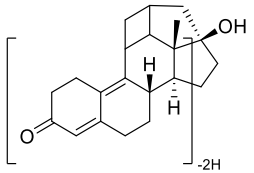 |
| | | | | | | 195.0783 | $C_{14}H_{11}O$- | 112 | | | |
| | | | | | | 183.0785 | $C_{13}H_{11}O$- | 124 | | | |
| TP 310 | $C_{21}H_{26}O_2$ | - | ESI- | 309.1794 | 9.06 | 291.1754 | $C_{21}H_{23}O$- | 18 | isomer of ALT-CAP | 3a | 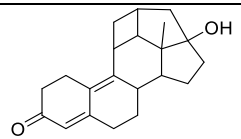 |
| | | | | | | 267.1372 | $C_{18}H_{19}O_2$- | 42 | | | |
| TP 324 | $C_{21}H_{24}O_3$ | - | ESI- | 323.1622 | 6.8 | 307.1673 | $C_{21}H_{23}O_2$- | 16 | | 3b | 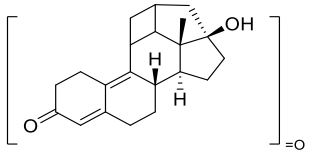 |
| | | | | | | 289.1207 | $C_{20}H_{17}O_2$- | 34 | | | |
| | | | | | | 249.0882 | $C_{17}H_{13}O_2$- | 74 | | | |
| | | | | | | 186.0634 | $C_{12}H_{10}O_2$- | 137 | | | |
| | | | | | | 160.0513 | $C_{10}H_8O_2$- | 163 | | | |
| | | | | | | 131.0494 | $C_9H_7O$- | 192 | m/z 160 - CHO, indicating ketone group | | |
| TP 326 | $C_{21}H_{26}O_3$ | a | ESI+ | 327.1975 | 6.00 | 309.187 | $C_{21}H_{25}O_2$+ | 18 | | 3a | 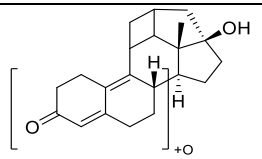 |
| | | | | | | 225.125 | $C_{16}H_{17}O$+ | 102 | | | |
| | | | ESI- | 325.1780 | 6.13 | 307.1666 | $C_{21}H_{23}O_2$- | 18 | similar spectra with TP 308 | | |
| | | | | | | 249.0894 | $C_{17}H_{13}O_2$- | 76 | | | |
| | | | | | | 210.1014 | $C_{15}H_{14}O$- | 115 | | | |
| | | b | ESI+ | 327.1975 | 7.55 | 309.1863 | $C_{21}H_{25}O_2$+ | 18 | all fragments were <200 Da indicating hydrolation on A/B ring to change the fragmentation dynamics | 3a | 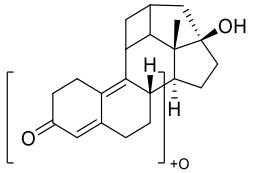 |
| | | | | | | 147.0772 | $C_{10}H_{11}O$+ | 180 | | | |
| | | | | | | 119.0852 | $C_9H_{11}$+ | 208 | | | |
| | | | | | | 107.0839 | $C_8H_{11}$+ | 220 | | | |
| | | | | | | 91.0558 | $C_7H_7$+ | 236 | | | |
| | | | ESI- | 325.178 | 7.41 | 307.1663 | $C_{21}H_{23}O_2$- | 18 | | | |
| | | | | | | 161.0944 | $C_{11}H_{13}O$- | 164 | | | |
| TP 340 | $C_{21}H_{24}O_4$ | - | ESI+ | 341.1819 | 5.66 | N/A | | | | 3a | 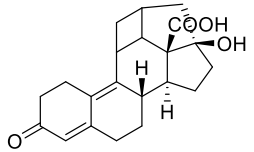 |
| | | | ESI- | 339.1569 | 5.55 | 323.1598 | $C_{21}H_{23}O_3$- | 16 | | | |
| | | | | | | 305.1519 | $C_{21}H_{21}O_2$- | 34 | | | |
| | | | | | | 147.0433 | $C_9H_7O_2$- | 192 | | | |
| | | | | | | 123.0427 | $C_7H_7O_2$- | 216 | | | |
| TP 342 | $C_{21}H_{26}O_4$ | - | ESI+ | 343.1894 | 5.35 | 325.1786 | $C_{21}H_{25}O_3$+ | 18 | all fragments were <200 Da indicating hydroxylation on A/B ring to change the fragmentation dynamics | 3b | 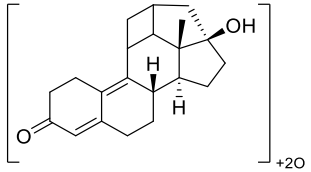 |
| | | | | | | 307.1687 | $C_{21}H_{23}O_2$+ | 36 | | | |
| | | | | | | 195.0832 | $C_{14}H_{11}O$+ | 148 | | | |
| | | | | | | 163.0764 | $C_{10}H_{11}O_2$+ | 180 | | | |
| | | | | | | 133.0645 | $C_9H_9O$+ | 210 | | | |
| | | | | | | 119.0832 | $C_9H_{11}$+ | 224 | | | |
| | | | | | | 91.0534 | $C_7H_7$+ | 252 | | | |
| TP344 | $C_{21}H_{28}O_4$ | - | ESI+ | 345.2017 | 5.33 | 327.1917 | $C_{21}H_{27}O_3$+ | 18 | | 3b | |

| | | | | | | | | | | |
|---|---|---|---|---|---|---|---|---|---|---|
| | | | | | | 309.1863 | $C_{21}H_{25}O_2$+ | 36 | | 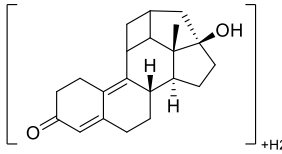 |
| TP 360 | $C_{21}H_{28}O_5$ | - | ESI- | 359.1811 | 5.56 | 341.1709 | $C_{21}H_{25}O_4$- | 18 | 3b | 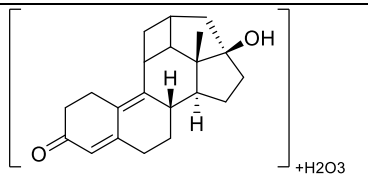 |
| | | | | | | 323.1617 | $C_{21}H_{23}O_3$- | 36 | | |
| | | | | | | 107.0497 | $C_7H_7O$- | 252 | | |
| TP 390 | $C_{21}H_{26}SO_5$ | - | ESI- | 389.1413 | 4.96 | 248.9567 | $C_{11}H_5SO_5$- | 140 | 3a | 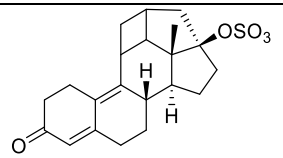 |
| | | | | | | 204.9686 | $C_{10}H_5SO_3$- | 184 | | |
| | | | | | | 154.9709 | $C_6H_3SO_3$- | 234 | | |
| | | | | | | 112.983 | $C_4HO_4$- | 276 | | |
| | | | | | | 79.9562 | $SO_3$- | 309 | | |

# Chapter 4

# Biotransformation of Current-Use Progestins Dienogest and Drospirenone in Laboratory-Scale Activated Sludge Systems Forms High-Yield Products with Altered Endocrine Activity

## 4.0 Publication Statement

This chapter is in revision for publication in *Environmental Science &Technology*.

## 4.1 Introduction

Transformation products (TPs) can contribute substantially to the environmental hazard of organic micropollutants (Cui et al., 2021; Mahler et al., 2021; Zind et al., 2021). Accordingly, identifying stable and/or toxic TPs in risk assessments of micropollutants, including pesticides, industrial chemicals, and pharmaceuticals, is a priority (Escher and Fenner, 2011). Among bioactive environmental contaminants, steroid hormones used as pharmaceuticals are of especially high priority because of their high potency, widespread use, and their potential to affect endocrine function (e.g., reproductive dysfunction) after exposure (Cwiertny et al., 2014; Kidd et al., 2007; Runnalls et al., 2010). Because simple environmental transformations often do not alter their tetracyclic backbone, TPs of steroids are especially prone to exhibit retained or altered binding activities to hormone receptors (Bhatti and Khera, 2012; Cwiertny et al., 2014; Ma and Yates, 2018). For example, testosterone biotransformation generated boldenone (i.e., 1-dehydrotestosterone) as the major TP, an anabolic steroid 56% more androgenic than testosterone (Bauer et al., 2000; Yang et al., 2011). Progesterone “degradation” by freshwater microalgae formed androstenedione, a weak endogenous androgen (Peng et al., 2014). Therefore,

it is crucial to understand such transformation processes to facilitate accurate assessment of environmental hazard.

Dienogest (DIE) and drospirenone (DRO) are two fourth (newest) generation synthetic progestins used as oral contraceptives (Louw-du Toit et al., 2016; Regidor and Schindler, 2017; Zucchi et al., 2014). They were developed as "pure" progestogens with high specific progesterone receptor (PR) activity and reduced androgenic activity, which prevents side effects (e.g. weight gain, acne, breast cancer and cardiovascular disease risks) typical for early generation synthetic progestins (Kumar et al., 2015; Louw-du Toit et al., 2016; Regidor and Schindler, 2017). DIE was the most prescribed synthetic progestin in Germany (~760 kg in 2018) (Weizel et al., 2021). DRO was the most prescribed synthetic progestin in the Czech Republic (250 kg in 2014) and Switzerland (~100 kg in 2010) (Fent, 2015; Golovko et al., 2018) and was among the top 100 most prescribed medications in the US (~8,000,000 annual prescriptions) (ClinCalc DrugStats Database). Consistent with usage, DIE was the most frequently detected synthetic progestin in wastewater and surface water in Germany (effluent, 1.3-4.4 ng/L; surface water, <0.05-2.3 ng/L) (Weizel et al., 2018) and the Czech Republic (influent, 1.9-11 ng/L; effluent, <0.05-1.0 ng/L; surface water, <0.09 ng/L) (Golovko et al., 2018). DRO was detected in wastewater in the Czech Republic (influent, 0.64 ng/L; effluent, 0.29 ng/L) (Golovko et al., 2018), in China (influent, 0.69 ng/L; effluent, 0.39 ng/L) (Yu et al., 2019), and in surface water (0.26-4.30 ng/L) from Hungary (Avar et al., 2016). Chronic exposure (160 days) of 2 ng/L DRO lowered *fshβ* mRNA levels (follicle-stimulating hormone encoding gene) in pituitary of common carp and increased macrovacuoles in hepatocytes (Šauer et al., 2020). DRO exposure at slightly higher concentration (55 ng/L) alters gene transcription involved in hormone homeostasis and circadian rhythm in zebrafish embryos and adults (Zhao et

al., 2015; Zucchi et al., 2014). Little ecotoxicological data exists for DIE, with minor transcriptional alterations indicated at ~10 µg/L in zebrafish embryos (Schmid et al., 2020).

Wastewater treatment plant (WWTP) effluents are primary sources of progestins to aquatic environments. Despite the prevalence of DIE and DRO, their fate during biological wastewater treatment is unclear. Weizel et al. recently reported that DIE was the second most recalcitrant (4.55 hr half-life) synthetic progestin in lab-scale sludge incubation experiments, while DRO was rapidly degraded over time scales of a few minutes (Weizel et al., 2021). In addition, DIE formed estrogen-like TPs with aromatized A rings during biotransformation (Weizel et al., 2021). However, the yields and structures of these estrogenic DIE TPs were not confirmed and DRO TPs were not investigated (Weizel et al., 2021). Particularly for DRO, its rapid kinetics may indicate facile modifications to more stable TPs with retained steroidal pharmacophores because biological treatment often fails to mineralize steroids (Liu et al., 2013; Weizel et al., 2020).

To address the above knowledge gaps, we evaluated the biotransformation kinetics and products of DIE and DRO using activated sludge batch incubations under aerobic conditions. TPs were identified using liquid chromatography-high resolution mass spectrometry (LC-HRMS) and TP structures proposed through spectral interpretation and sometimes confirmed with commercial or synthesized standards. Structural diagnosis with MS/MS spectra are intrinsically difficult for steroids due to lack of distinguishing heteroatoms in the molecules and the dynamic fragmentation chemistry of the tetracyclic backbone (Guan et al., 2006). Many studies utilizing LC-MS/MS fail to propose confident structures for steroid TPs because reference standards are not commercially available and mass limitations preclude structural characterization by NMR (Cole et al., 2015; Liu et al., 2020; Weizel et al., 2020). Here, we used

published ionization behaviors and comparative fragmentation patterns to propose some reasonably confident structures (Level 1 or Level 2 as Schymanski criteria) (Schymanski et al., 2014) for half of the observed TPs. Bioactivity of the TPs was then assessed based on available literature to improve environmental hazard identification of these new generation progestins.

## 4.2 Materials and Methods

Analytical standards of DIE and DRO were purchased from Sigma Aldrich (St. Louis, MO, USA). For TPs, Δ9,11-dehydro-17α-cyanomethyl estradiol (TP 309) was purchased from TLC Pharmaceutical Standards (Newmarket, ON, Canada). DRO acid sodium salt (TP 384) was purchased from Toronto Research Chemicals (North York, ON, Canada). Spirorenone (TP 364) was self-synthesized. Sources of other materials and synthesis details for spirorenone are summarized in the Supporting Information. Wastewater-adapted microbial consortia were obtained as inocula by sampling the mixed liquor (total suspended solids, 1.39 g/L; volatile suspended solids, 1.36 g/L) from the aeration tank of the West Point Treatment Plant in King County, WA, USA (~700,000 population; 400,000,000 L/day average dry weather flow; 4 hr hydraulic retention time in aeration basin). The samples were stored at 4°C and used within 24 hr of sampling. Before experiments, sludge was equilibrated to room temperature for 0.5 hr.

Biotransformation batch experiments, conducted in triplicate, were adopted from Helbling et al. (2010) and Gulde et al. (2016) (Gulde et al., 2016; Helbling et al., 2010). To measure kinetics, 50 mL sludge was placed into 120 mL amber jars and spiked with 50 µL of 1 mg/L DIE and DRO mixed stock (in methanol, 0.1% v/v final methanol concentration) to achieve 1 µg/L test concentrations. Sterile controls (sludge autoclaved twice for 30 min at 121 °C; spiked identically) were included to isolate potential abiotic transformation and sorption effects. Unspiked controls were included in duplicate to check for background steroid levels and

cross-contamination; no analytes were detected. Bioreactors were loosely covered with aluminum foil to allow oxygen diffusion and shaken (60 rpm) for 72 hours in a 37 °C incubator (higher than optimal WWTP operation temperature (28-35 °C) but within maximum acceptable ranges (<40 °C)) (C. P. Leslie Grady et al., 1999). After 0, 2, 4, 7, 10, 28, 52, and 72 hours, bioreactors were thoroughly mixed, 1 mL was withdrawn and spiked with 0.5 ng of DIE-d8 and DRO-$^{13}C_3$, then twice extracted immediately with ethyl acetate (3 mL, 1 min vortex mixing) and centrifuged (2500 rpm, 10 min). The supernatants were combined, solvent-exchanged into 1 mL methanol, and analyzed quantitatively with liquid chromatography coupled with a triple quadrupole tandem mass spectrometry (LC-MS/MS). The absolute recoveries of the methods, evaluated as the peak area ratios of DIE and DRO in spiked sterile sludges over those in standards, were 90% ± 3% for DIE and 83% ± 2% for DRO. After internal standard calibration, the relative recoveries were 93% ± 6% for DIE and 90% ± 4% for DRO. Analytical details and other quality assurance and quality control data are included in the Supporting Information and **Table S4.1**.

For TPs identification, DIE and DRO were studied in separate bioreactors at higher concentrations (1 mg/L, using 70 mL inocula spiked with 70 µL of 1 g/L DIE or DRO stock solutions in methanol) and enrichment factors (10-fold enrichment vs 1-fold for kinetics) to facilitate detection of low-yield TPs. A single sterile control, un-spiked control, and un-spiked sterile controls were included to facilitate blank feature subtraction during HRMS data analysis. Based on initial results from kinetics experiments and common hydraulic retention times of WWTP aeration basins, TPs of DIE and DRO were identified at 0, 4, 10, and 29 hours. Bioreactors were thoroughly mixed at each time point. 5 mL reaction mixture was withdrawn in duplicate, and each aliquot was immediately extracted with 5 mL ethyl acetate twice.

Supernatants (5 mL × 4) from the two aliquots were combined and solvent-exchanged into 1 mL methanol for instrumental analysis.

TP identification used an Agilent 1290 Infinity UPLC coupled to an Agilent 6530 quadrupole time-of-flight HRMS (qTOF-HRMS) under both ESI+ and ESI- ionization. Full scan data were first acquired and processed in a non-target approach with Agilent software packages (MassHunter Profinder (B.08.00) for feature extraction and alignment, Mass Profiler Professional (B.13.00) for feature prioritization) and XCMS Online, to enable better coverage of any potential TPs. Features present in all bioreactor sample replicates (3/3) with peak area both >5000 and 3-fold greater than all controls were retained in a preferred list. MS/MS data were then acquired for the list with data-dependent acquisition under three collision energies (10, 20, 40 eV). Instrumental methods and data analysis parameters were described previously (Du et al., 2017; Peter et al., 2018; Tian et al., 2020) and are summarized in Supporting Information and **Table S4.2, S4.3**.

TPs were identified from the preferred lists based on relevant formula, retention time (RT), and diagnostic MS/MS neutral losses and fragments. Structures were then proposed based on RT shifts, ionization behavior, MS/MS fragmentation pattern, and reported transformation pathways of DIE and DRO, for which ionization behaviors and diagnostic MS/MS fragments of different steroid structures reported in literature were especially valuable. Structures for key TPs were confirmed with commercial (for TP 309 and TP 384) or synthesized (for TP 364) standards. Identification confidence was assigned according to Schymanski et al., with modifications (Schymanski et al., 2014). The highest confidence (level 1) communicates that RT and MS/MS fragments match standards. Level 2 confidence communicates that MS/MS fragmentation patterns match standard-confirmed TPs (level 2a) or diagnostic information indicates no other

possible structure (level 2b). Level 3 describes tentative candidates matching plausible biotransformation reactions, but reaction sites can (level 3a) or cannot (level 3b) be assigned to molecular sub-structures. Level 4 stands for unequivocal TP molecular formula when MS/MS spectra are not available.

DIE, DRO, and level 1 TPs were quantified in 1 mg/L bioreactors by 5-point external standard calibration curves (0.5-50 µg/L; $R^2 > 0.995$) on LC-qTOF-HRMS. The extracts were diluted 1000-fold with methanol to reduce matrix effects and detector saturation. Additionally, the level 1 TPs were quantified in the 1 µg/L kinetics bioreactors using LC-MS/MS to validate that identified TPs were environmentally relevant at lower concentrations.

## 4.3 Results and Discussion

### 4.3.1 Biotransformation Kinetics

DIE and DRO were stable (90 ± 4% and 87 ± 4% of initial concentrations) in the sterile controls over 72 hr (**Figure 4.1**), indicating that microbial activity is necessary to the observed losses in bioreactors. This, however, does not preclude abiotic reactions in the biotransformation pathways. For example, aerobic degradation of androgens through the 9,10-seco pathway involve an abiotic ring cleavage step (Chiang et al., 2020; Horinouchi et al., 2018); aerobic degradation of estrogens through the 4,5-seco pathway can produce pyridinestrone acid through abiotic recyclization with ammonium (Chiang et al., 2020; Wu et al., 2019). The ~10% mass deficits in the sterile controls likely reflect irreversible sorption to solids. Biotransformation data are typically fit to first order kinetic models (Chang et al., 2011; Weizel et al., 2020; Yang et al., 2010). In this study, although aerobic biotransformation could be fit to first order kinetics ($r^2$ of 0.979 for DIE and 0.920 for DRO), the data exhibited biases over time (**Figure S4.1**) as biotransformation slowed with time. For comparison, the second order kinetic model exhibited

better fit ($r^2$ of 0.998 for DIE and 0.983 for DRO, **Table 4.1**, **Figure S4.1**). This indicates that the biotransformation may be affected by microbial activity or mass-transfer limitations in such batch systems, in addition to possible concentration dependences (Schwarzenbach et al., 2003; Svendsen et al., 2020).

The rate constant ($k$) and half-life ($t_{1/2}$) of DIE were 0.023 $hr^{-1}$ and 30 hr under first order kinetics, while second order kinetic parameters were 0.066 L $\mu g^{-1}$ $hr^{-1}$ and 16 hr (**Table 4.1**). The slow removal of DIE (compared with DRO) agreed with Weizel et al. that identified DIE as the second most recalcitrant progestin ($t_{1/2}$ of 4.55 ± 0.11 h) among the nine progestins studied; the half-lives observed here is ~5 times higher than Weizel et al., which may be explained by the different temperature (this study, 37 °C; Weizel et al., 26 °C), incubation concentrations (this study, 1 µg/L; Weizel et al., 0.2 µg/L), and aeration methods (this study, diffusion; Weizel et al., aeration by synthetic air) used in the two studies (Weizel et al., 2021). Slow transformation of DIE is consistent with observations in WWTP effluent where DIE was the most frequently detected among 18 progestins (Weizel et al., 2021, 2018). DRO was degraded rapidly over the first 7 hours with $t_{1/2}$ <0.5 h (50% ± 3% spiked mass recovered at $t_0$ ), then concentration loss plateaued (0.12 ± 0.03 µg/L) over 7-72 hours. This was consistent with the <0.02 h half-life previously reported for DRO (Weizel et al., 2021). Although rapid transformation suggests reduced probability of detection, DRO was detected in WWTP effluents from Czech Republic, Hungary and China (Avar et al., 2016; Golovko et al., 2018; Yu et al., 2019). This aligns with high DRO use in these regions as one of the most consumed synthetic progestins (Golovko et al., 2018), and may also indicate that some fraction of DRO exhibited limited bioavailability for transformation within WWTPs.

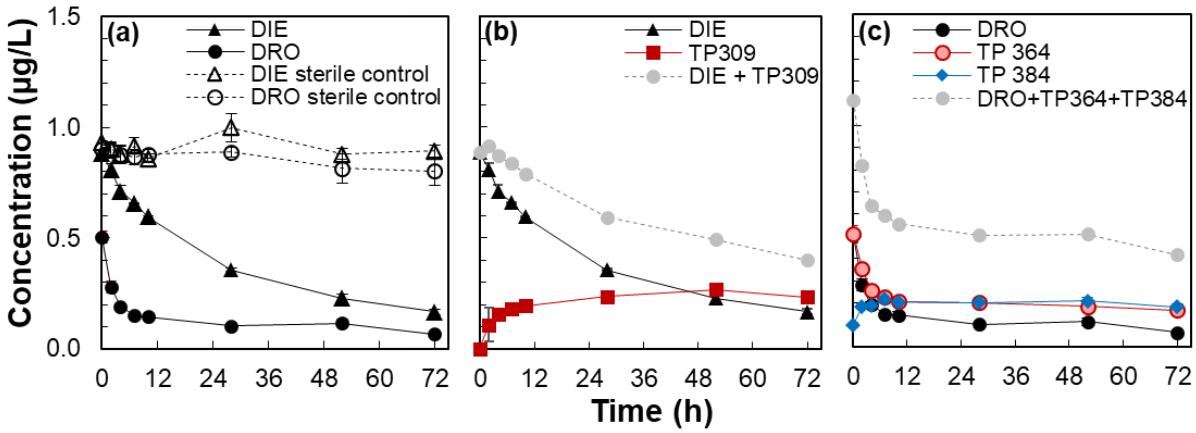


**Figure 4.1** Biotransformation of DIE and DRO (1 µg/L) in batch systems inoculated with mixed liquor from aeration basins (TSS: 1.39 g/L; VSS: 1.36 g/L). (a) DIE and DRO concentrations in bioactive and sterile microcosms, represented by filled and hollow symbols, respectively; (b) DIE and major TP concentrations in bioactive microcosms; (c) DRO and major TP concentrations in bioactive microcosms. Error bars represent standard deviation of three replicates.

**Table 4.1** Structures and kinetic parameters of DIE and DRO in 1 µg/L batch sludge systems. Kinetic rates are derived from time periods where ongoing mass loss was observed.

| Compound | Dienogest (DIE) | | Drospirenone (DRO) | |
|---|---|---|---|---|
| Structure | 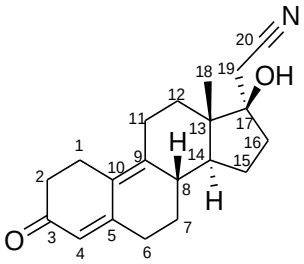 | | 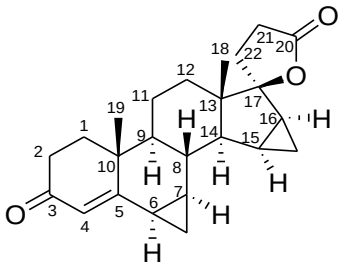 | |
| Formula | $C_{20}H_{25}NO_2$ | | $C_{24}H_{30}O_3$ | |
| Molar weight (Da) | 311.19 | | 366.22 | |
| Kinetics | first order | second order | first order[a] | second order[a] |
| $t_{1/2}$ (hr) | 30 ± 1.1 | 16 ± 0.4 | < 0.5 | < 0.5 |
| $k$ | 0.023 ± 0.0008 $h^{-1}$ | 0.066 ± 0.002 L $\mu g^{-1}$ $h^{-1}$ | 0.17 ± 0.02 $h^{-1}$ | 0.67 ± 0.04 L $\mu g^{-1}$ $h^{-1}$ |
| $r^2$ | 0.979 | 0.998 | 0.920 | 0.983 |

[a] The rate constant for DRO was modelled for 0-7 hours because the reaction plateaued over 7-72 hours.

### 4.3.2 Product Identification

To identify TPs, 1 mg/L batch systems (nominal concentrations) of DIE and DRO were incubated separately for 29 hours. In general, three steps were used to identify TPs with acquired spectral data: (1) identification of the molecular mass (via MS full scan); (2) identification of potential transformation reactions (via mass difference, spectral and RT comparisons); and (3) identification of the reaction site (via ionization behavior, MS/MS spectra, RT comparisons and external information).

When identifying molecular masses, we have learned that results generated from HRMS data workflows need to be treated with caution because in-source neutral losses are frequently ignored. When such analytical artifacts occur, focusing on $[M+Na]^+$ and other adducts, and analysis under different ionization modes, can sometimes aid accurate identification. For example, TP 327s ($C_{20}H_{25}NO_3$) of DIE, representing hydroxyl addition products, were detected under both ESI+ and ESI- (RT (a) 4.86 min and (b) 5.78 min, **Figure 4.2a-b**, **Table S4.6**). Initially, this TP resembled a dehydrogenation TP under ESI+ with a precursor ion of *m/z* 310.1814. However, we observed a $[M+Na]^+$ ion at *m/z* 350.1739, which instead indicated $[M-H_2O+H]^+$ for *m/z* 310.1814 and suggested identification of hydroxylation products (**Figure 4.2d**) (Kenyon et al., 2019). This was further confirmed by $[M-H]^-$ *m/z* 326.1773 detection at the same RTs under ESI- (**Table S4.6**). By MS/MS spectral comparison with the standard of a structurally similar steroid (TP 309), we propose a C1/2 hydroxylation (**Table S4.6**). We note that 39.9925 Da is a diagnostic mass difference between $[M-H_2O+H]^+$ and $[M+Na]^+$ that was often ignored by commercial feature extraction software. Recognition of this particular mass may enable identifications for structures prone to in-source water loss.

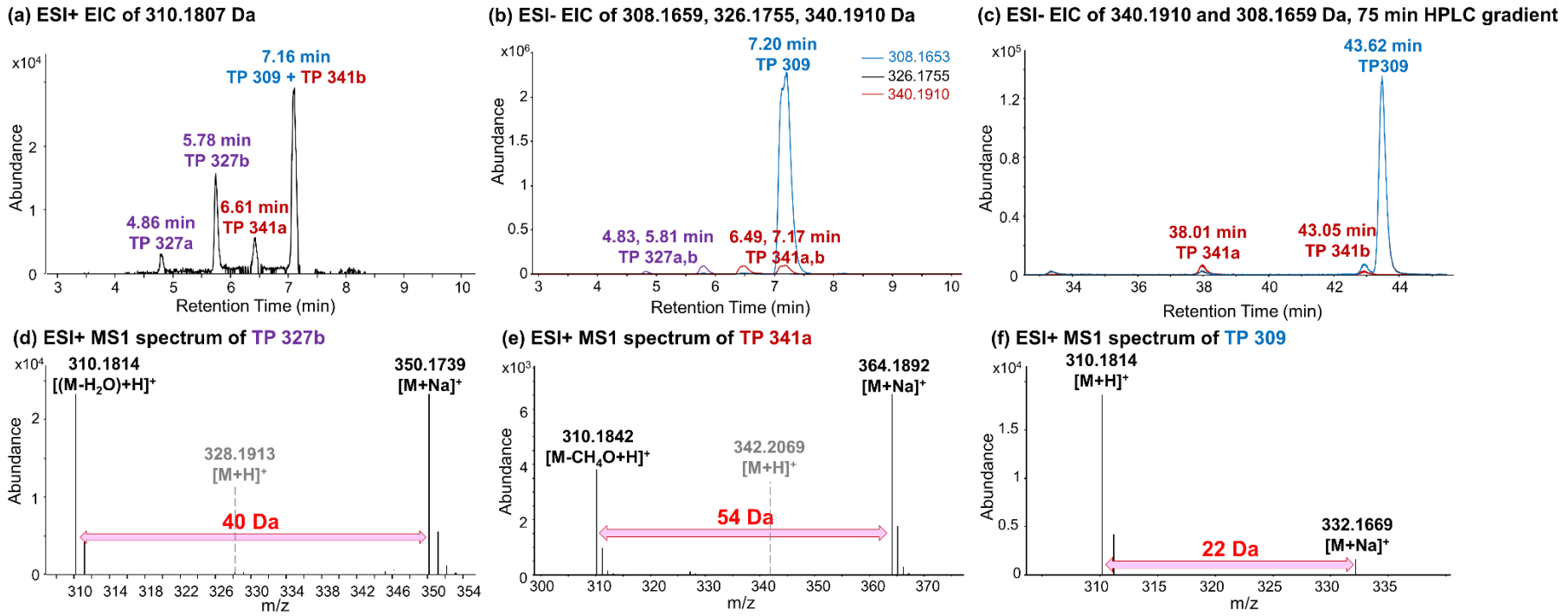


**Figure 4.2** Identifying molecular masses of DIE TP 309, TP 327s, and TP 341s. (a) ESI+ chromatogram of *m/z* 310.1807. The 4.86 min and 5.78 min peaks represent the responses of $[(M\text{-}H_2O)+H]^+$ ions of TP 327s. The 6.61 min peak represents the $[(M\text{-}CH_4O)+H]^+$ ion of TP 341a, while the 7.16 min peak represents the $[M+H]^+$ ion of TP 309 plus the $[(M\text{-}CH_4O)+H]^+$ ion of TP 341b. Purple, red, and blue colors represent TP 327s, TP 341s and TP 309, respectively. (b) ESI- chromatogram of *m/z* 308.1653, 326.1755, and 340.1910. (c) ESI- chromatograms of *m/z* 308.1659 and 340.1910 under a 75 min HPLC gradient, demonstrating the resolution of TP 341b and TP 309. (d) ESI+ spectrum of TP 327b. The $[M+Na]^+$ at 350.1739 suggested a 328 Da molecular mass, corresponding to hydroxylation. $[M+H]^+$ was missing due to in-source water loss. (e) ESI+ MS1 spectrum of TP 341a at 6.61 min. The $[M+Na]^+$ at 364.1892 indicated a 341 Da molecular mass, corresponding to a methoxylation TP. $[M+H]^+$ was missing because TP 341s experienced in-source $CH_4O$ loss. (f) ESI+ MS1 spectrum of TP 309 at 7.16 min. The $[M+Na]^+$ at 332.1669 indicated a 309 Da molecular mass, corresponding to a dehydrogenation TP.

Occasionally, in-source neutral loss may inhibit identification when TPs are poorly resolved chromatographically. In these cases, ESI- comparison enabled their differentiation. For example, DIE TP 341a ($C_{21}H_{27}NO_3$, RT 6.47 min) appeared at *m/z* 310.1842 ($[M\text{-}CH_4O+H]^+$) under ESI+ (**Figure 4.2a**). $[M+Na]^+$ at *m/z* 364.1892 and $[M-H]^-$ at *m/z* 340.1910 observations suggested a 341 Da parent mass, which indicated methoxy addition, presumably as a methylation product of the C1/2 hydroxylated TP 327 (**Figure 4.2e**). However, unlike TP 341a, TP 341b was only detected at 7.17 min under ESI- ($[M-H]^-$ 340.1910; **Figure 4.2b**). We suspected that TP 341b was also ionized as $[M\text{-}CH_4O+H]^+$ (hypothetical *m/z* 310.1807) under ESI+, but it co-eluted with TP 309 (RT 7.16 min, $[M+H]^+$ 310.1814, **Figure 4.2f**), the major TP of DIE, and thus cannot be resolved under initial chromatography. A subsequent 75 min HPLC gradient was then used to resolve TP 341b and TP 309 at 43.05 min and 43.62 min (**Figure 4.2c**), respectively. With this separation, TP 341s were observed to partially ionize to $[M\text{-}CH_4O\text{-}H]^-$ under ESI- (**Figure 4.2c; Table S4.6**). Therefore, the responses attributed to $[M+H]^+$ and $[M-H]^-$ of TP 309 can potentially include contributions from $[M\text{-}CH_4O+H]^+$ and $[M\text{-}CH_4O\text{-}H]^-$ ions of TP 341b, respectively. While here we estimated such contributions to be <10%, we note this is potentially a source of systemic error in analyte quantification in both non-targeted full-scan and targeted MRM analysis because many steroidal (and other compounds) parent-TP pairs are poorly resolved chromatographically especially using fast separation gradients, and they also tend to share common adducts and MS/MS transitions (Kenyon et al., 2019). We anticipate there exists a subset of overestimated environmental occurrence data in the literature due to contributions from co-eluting TPs with common diagnostic transitions, although such effects are hard to identify a priori.

When characterizing TPs, translating mass spectra to tentative structures is typically the most difficult and uncertain task. Unlike pharmaceuticals with heteroatoms and non-repetitive

structural units, steroids typically undergo complex fragmentation and re-arrangement during ionization so subtle structural differences sometimes translate to highly disparate MS/MS spectra (Guan et al., 2006; Thevis and Schänzer, 2007, 2005). Therefore, it is frequently difficult to rationalize the structures of steroid MS/MS fragments, precluding structure identification using direct spectral interpretation. However, such spectral sensitivity could sometimes be exploited to identify the transformation reaction sites in conjunction with the abundant information on steroid fragmentation patterns present in literature. For example, TP 364 ($C_{24}H_{28}O_3$) of DRO was ESI+ detected (RT 8.12 min, $[M+H]^+$ 365.2121), with diagnostic fragments of *m/z* 121.0649 ($[C_8H_9O]^+$), 147.0798 ($[C_{10}H_{11}O]^+$), and 161.0958 ($[C_{11}H_{13}O]^+$), much different from that of the DRO parent (single diagnostic fragment at m/z 97.0646 ($[C_6H_9O]^+$), **Table S4.7**). Because DRO was a 3-keto-4-ene steroid, we speculated that any dehydrogenation TPs should demonstrate a diene structure. Therefore, we compared the MS/MS spectrum of TP 364 to the characteristic fragments of diene steroids summarized in literature, and observed that only 3-keto-1,4-diene steroids showed similar spectral patterns (**Figure 4.3a-b**) (Schänzer et al., 2006; Thevis and Schänzer, 2005). In addition, the RT difference between DRO (8.83 min) and TP 364 (8.12 min) was consistent with that between methyltestosterone (9.11 min) and its 1,2-dehydrogenation metabolite (8.53 min) using similar C18 chromatography (Zeng et al., 2013). Because TP 364 was a major TP of DRO by peak area, we subsequently synthesized the 1,2-dehydrogenation product of DRO (Bittler et al., 1982), otherwise known as “spirorenone” (standard confirmed with nuclear magnetic resonance (NMR) analysis; see SI); RT and MS/MS spectra matched the synthetic standard (**Table S4.7**).

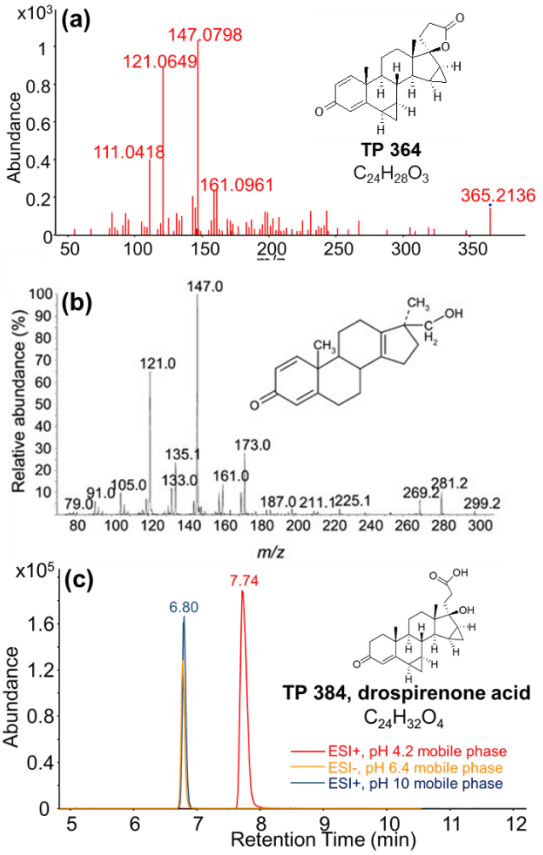


**Figure 4.3** Structural identification of DRO TP 364 and TP 384. (a) MS/MS spectrum of DRO TP 364. (b) Example MS/MS spectrum of 3-keto-1,4-diene steroids exemplified by a metandienone metabolite.(Schänzer et al., 2006) TP 364 showed common diagnostic fragments of 3-keto-1,4-diene steroids, including *m/z* 121, 147, and 161. (c) Retention time shift of DRO TP 384 under different mobile phase pHs.

Beyond MS/MS spectra, ionization behaviors, RT difference and other external information provide additional structural insights. Unlike DRO which exhibited ~100 times lower response in ESI- than ESI+, DRO TP 384 showed similar ESI+ and ESI- responses, suggesting the formation of an ESI- ionizable group in TP 384 (**Figure 4.3c**). In addition, RTs of TP 384 varied under different mobile phase pHs, indicating a dissociable proton. For example, TP 384 eluted at 7.74 min under pH 4.2 (5mM $NH_4Ac$ + 0.1% HAc, regular ESI+ mobile phase) and at 6.80 min under pH 6.4 (1 mM $NH_4F$, regular ESI- mobile phase) and pH 10 (0.1% $NH_3 \cdot H_2O$) (**Figure 4.3c**). Thus, TP 384 acted neutral at the acidic conditions and ionized as pH increased. The ESI+ MS/MS spectrum of TP 384 resembled that of DRO with *m/z* 97.0639 as

the dominant fragment, indicating retained steroid A-ring structure. Finally, a neutral loss of $CO_2$ (*m/z* 383.2204 to 339.2335) was observed in ESI- MS/MS spectrum of TP 384 (**Table S4.7**). The above evidence suggested the presence of a carboxylic acid. Via an authentic standard of "drospirenone acid", we confirmed TP 384 to be the lactone ring hydrolysis product of DRO group (SPARC predicted pKa for DRO acid: 4.26).

Overall, the above strategies were able to identify probable structures for ~50% of the TPs of DIE and DRO without standards (Cole et al., 2015; Liu et al., 2013; Weizel et al., 2020). In total, 22 likely TPs were identified for DIE; relatively confident structures (level 1 and 2) were possible for 11 TPs with one (TP 309) standard-confirmed. 13 likely TPs were identified for DRO; confident structures (levels 1-2) were proposed for 7 TPs with two (TP 384 and TP 364) confirmed by authentic standards. Identification details are summarized in **Table S4.4-S4.7**.

### 4.3.3 Transformation Pathways

In the 1 mg/L batch systems, 71% of the initial DIE mass and 49% of the DRO mass were removed after 29 hrs (**Figure 4.4a, d**). Notably, DRO decay at 1 mg/L was much slower ($t_{1/2}$ ~29 hour) than that in 1 µg/L batch systems ($t_{1/2}$ <0.5 h). Substrate inhibited kinetics has been observed elsewhere, although it is less common than substrate enhanced kinetics (e.g. Michaelis-Menten kinetics) (Svendsen et al., 2020). To prioritize transformation pathways, we quantified the yields of DIE TP 309, DRO TP 384 and TP 364 with authentic standards. Because DIE and DRO were only partially biotransformed at 29 hrs, TP yields were estimated as mole product formed ($C_{TP\_t}$) per mole parent consumed ($C_{parent\_t}$ - $C_{parent\_t0}$). TPs lacking standards were tentatively prioritized if their peak areas were >1% of the peak area decrease of the parents based on the vulnerable assumption of similar peak area response between parent and TPs. Among the 22 TPs of DIE, the aromatic dehydrogenation TP (TP 309) was quantitatively the most important with maximum molar yield of 55% at 29 hr (**Figure 4.4a**). Aromatic

isomerization (TP 311), 1/2-hydroxylation (TP 327b), 1/2-methoxylation (TP 341a and TP341b), and 3-keto hydrogenation (TP 313) products exhibited larger peak areas (**Figure 4.4b-c**, **Table S4.4**). Similar to DIE, 1,2-dehydrogenation (TP 364) was the most relevant transformation pathway for DRO with molar yields peaking at 40% at 10 hr prior to subsequent decay (**Figure 4.4e**). Lactone ring hydrolysis (TP 384) was an additional important transformation pathway for DRO with maximum yield of 21% (**Figure 4.4d**). Other relevant pathways, similar to DIE observations, included 3-keto and 4,5-hydrogenation (TP 368, TP 370s) and hydroxylation (TP 382b-d, TP 380) (**Figure 4.4e-f**, **Table S4.5**).

Observed yields of TP 309, TP 364, and TP 384 were also validated at 1 µg/L for 72 hrs batch incubation systems through quantification on LC-MS/MS. The molar yields of TP 309 were ~50% over the first 10 hrs and subsequently decreased to ~28% over 72 hours (**Figure 4.1b**). TP 364 explained stoichiometric DRO loss initially (100% molar yield at $t_0$), while its yields decreased subsequently to ~20% at 72 hr via biotransformation. TP 384 concentrations plateaued over the incubation period and explained ~20% the mass loss of DRO (**Figure 4.1c**). The TP profiles before ~10 hr resembled yield data observed at higher concentrations; TP dissipation over longer incubation time indicated formation of secondary products or mineralization.

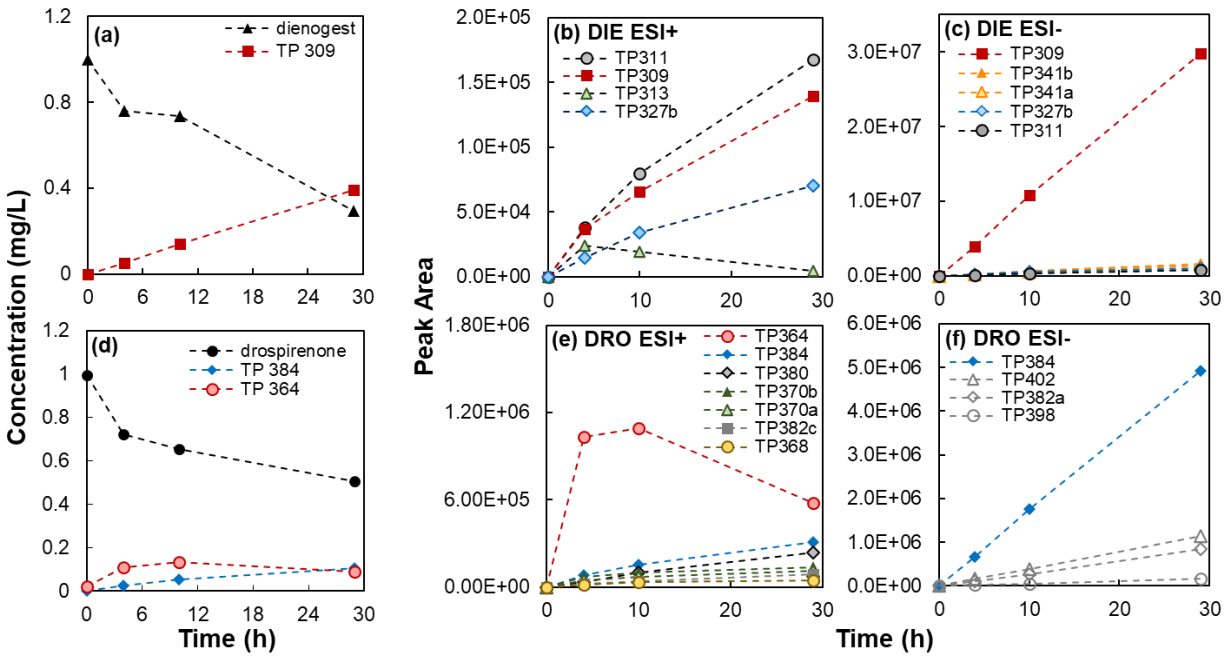


**Figure 4.4** Time trends of DIE, DRO, and the main TPs at 1 mg/L. (a) Concentrations of DIE and TP 309 quantified by authentic standards; (b) ESI+ and (c) ESI- peak areas of DIE TPs whose peak areas were >1% of DIE peak area decreases ; (d) Concentrations of DRO and TP 384 quantified by authentic standards; (e) ESI+ and (f) ESI- peak areas of DRO TPs whose peak areas were >1% of DRO peak area decreases.

*1,2-Dehydrogenation.* To generalize the implications of DIE and DRO transformation pathways, we first note aromatic TP 309 formation for DIE. TP 309 was reported as the major TP of DIE in sludge by Weizel et al. (2020) with ESI+ peak area reaching ~8% of the DIE parent (Weizel et al., 2021). Here, through standard quantification, we observed TP 309 yields as high as 55%. As a phenolic compound, TP 309 exhibited 10-100 times higher intensities under ESI- relative to ESI+ (**Figure 4.4b-c**). Therefore, not surprisingly for these structures, ESI+ peak area comparisons can lead to underestimation of reaction yields. Indeed, TP 309 was detected with 100% frequency in German WWTP effluents and estimated concentrations (1.2-16 ng/L, based upon identical peak area responses as DIE standard) were ~4 times higher than the DIE parent (Weizel et al., 2021). Such data support high biotransformation yields observed here and demonstrate clear environmental relevance of TP 309. We also observed a sulfate conjugate (TP

389) of TP 309 with low yield (<1%), which is consistent with observations for phenolic estrogens during activated sludge treatment (Khunjar et al., 2011; Weizel et al., 2021). Another aromatic TP (TP 311) was observed, which may reflect hydrogenation of the C9(11) double bond of TP 309.

Aromatization is a common metabolic process with important biological implications (Kuhl and Wiegratz, 2007). Endogenously, aromatization of C19-methyl steroids (e.g. testosterone and androstenedione) is initiated through oxidative elimination of the C19-methyl group to form an A-ring double-bond, while steroids lacking C19-methyl groups were aromatized via A-ring hydroxylation followed by dehydration (Kuhl and Wiegratz, 2007). Microbially, aromatization of C19-methyl progestins may require special C19-methyl oxidative enzymes, while aromatization of steroids lacking the C19-methyl group can proceed through 1,2-dehydrogenation (Weizel et al., 2021). Here, we propose TP 309 formation via 1,2-dehydrogenation of DIE, either through direct catalysis by microbial 1,2-dehydrogenase or by rapid C1 or C2 hydroxylation followed by dehydration (Chiang et al., 2020). The 1,2-dehydrogenated DIE forms a transient quinonic ring and could isomerize into the TP 309 phenol structure by enolization of the 3-keto group (**Figure S4.5**), which is thermodynamically favorable (ΔE of -46 kJ/mol) based on single point energies (see calculation details in SI). The transient quinonic ring structure was also proposed in the anaerobic methylation of estradiol to androgen (Wang et al., 2020). Pflug et al. observed TP 309 as a minor phototransformation product of DIE and proposed formation through an initial C9 and C10 di-hydroxy intermediate, followed by a thermal dehydration of the 9-hydroxy group to form the C9(11) olefin and dehydration of the 10-hydroxy to yield an aromatic A-ring (Pflug et al., 2017). Such observations suggest multiple formation pathways of TP 309 in the environment.

Although it is often underappreciated as an important fate pathway for steroids, 1,2-dehydrogenation was also the dominant biotransformation pathway for DRO in activated sludge. However, aromatization was not subsequently observed, likely because the C19-methyl group hinders this pathway. Presumptive 1,2-dehydrogenation TPs were consistently observed for other C19-methyl progestins (i.e. medroxyprogesterone acetate, chlormadinone acetate) (Weizel et al., 2021) and also reported for other classes of steroids; including testosterone transformation by manure-derived bacteria (Yang et al., 2011), trenbolone in agricultural runoff (Cole et al., 2015), and hydrocortisone in activated sludge (Weizel et al., 2020). Here, the 1,2-dehydrogenation product (TP 364) of DRO was an unstable TP that peaked at 10 hours of incubation (**Figure 4.4d**), subsequently forming a secondary hydroxylation product (TP 380) that explained ~27% of the dissipation of TP 364, based on ESI+ peak area.

*Hydrolysis*. Lactone ring hydrolysis was the other major transformation pathway for DRO. The hydrolysis product (TP 384) was a stable TP with a maximum yield of 21% (standard-quantified). The fast hydrolysis of DRO is consistent with that for norethisterone acetate, another 17β-ester progestin, and is in contrast to the behaviors of 17α-ester progestins (medroxyprogesterone acetate, chlormadinone acetate, cyproterone acetate) whose direct hydrolysis is sterically hindered (Weizel et al., 2021, 2020).

*Hydroxylation*. Hydroxylation was observed consistently for DIE and DRO although the product peak areas were smaller than for major TPs mentioned above. Weizel et al. stated that hydroxylation was not regioselective for progestin biotransformations (Weizel et al., 2021). Through structural characterization, hydroxylation of DIE mainly occurred at C1/2, while that for DRO happened on C1/2 and other A/B ring positions. These hydroxylation TPs further reacted to form methoxylation products (DIE TP 341s) and secondary hydroxylation products (DRO TP 398), and are likely intermediates to further oxidative TPs (i.e. DIE TP 357, TP 373;

DRO TP 416). Neutral losses of $CO_2$ were evident in the MS/MS spectra of these high-level oxidative TPs (**Table S4.6-7**), suggesting oxidation to carboxylate acids that may further proceed to carbon skeleton cleavage and mineralization (Chen et al., 2017; Ma and Yates, 2018; Wang et al., 2014).

*Hydrogenation*. Hydrogenation of the 3-keto and C4(5) double bond was also observed. DIE was prone to 3-keto hydrogenation (TP 313) and 3-keto and C4(5) double-hydrogenation (TP 315) was observed at small abundances, although no evidence for single hydrogenation of the C4(5) double bond was observed (**Table S4.4**). In contrast, hydrogenation of DRO was dominated by 3-keto and C4(5) double-hydrogenation (TP 370s, accounting for ~17% of DRO peak area decrease) (**Figure 4.4e**). Schubert et al. reported that 5α-hydrogenation, common for other 3-keto-4-ene steroids without a 9-double bond, was prevented in microbial hydrogenation of DIE, while 5β-hydrogenation only happened concurrently with 3-keto hydrogenation (Schubert et al., 1983). Therefore, the 9,11-double bond likely precluded 4,5-hydrogenation reactions for DIE.

Based on above identified and probable TPs, biotransformation pathways of DIE (**Figure 4.5**) and DRO (**Figure 4.6**) were proposed.

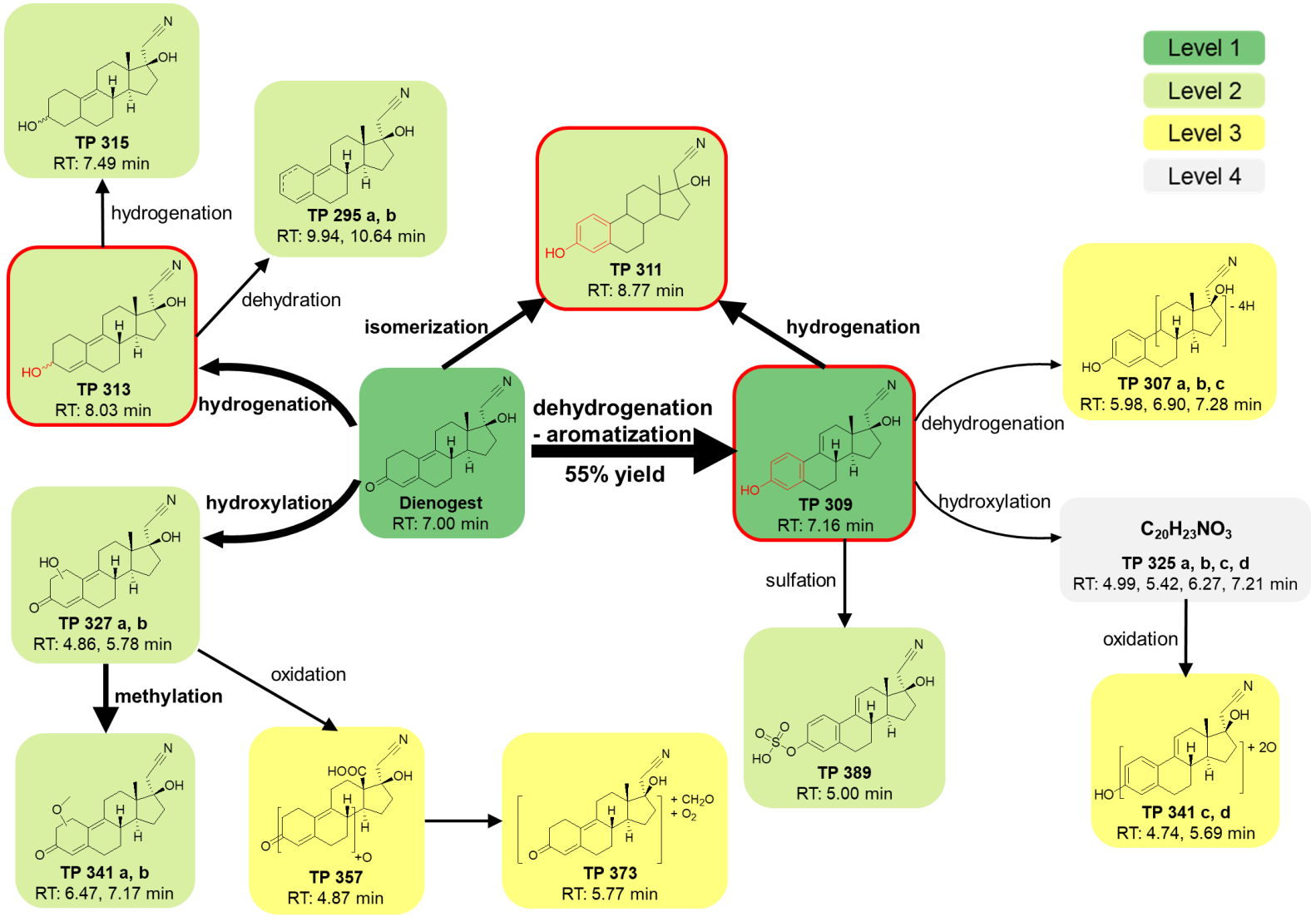


**Figure 4.5** Proposed biotransformation pathways of DIE. Larger arrows and pathway name in bold highlight major pathways. Red boxes highlight structures with known bioactivities in literature, and related functional group changes were highlighted in red. TP structures identified with confidence level 1, 2, 3 and 4 were communicated in dark green, light green, yellow, and gray shades, respectively.

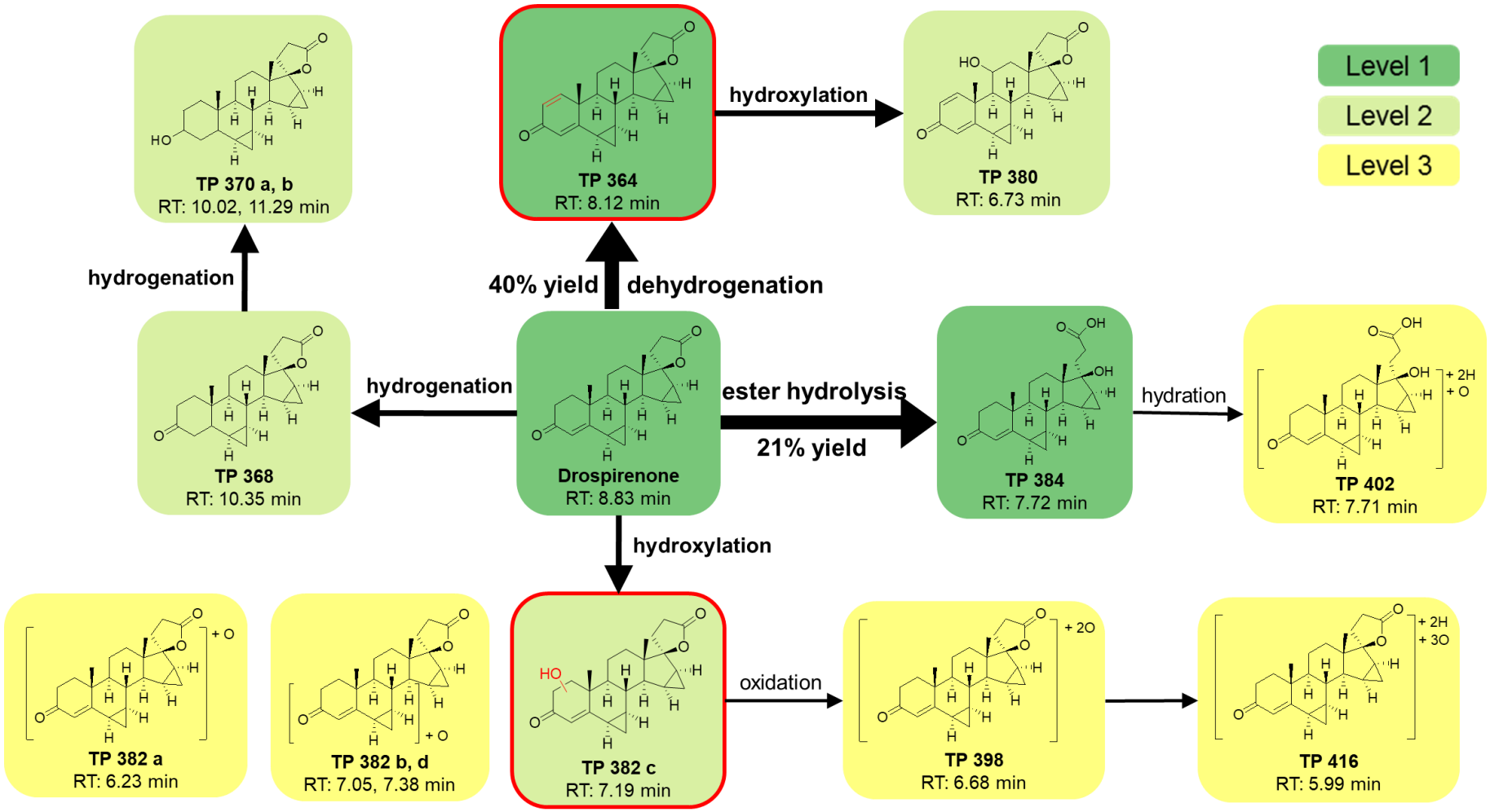


**Figure 4.6** Proposed biotransformation pathways of DRO. Larger arrows and pathway name in bold highlight major pathways. Red boxes highlight structures with known bioactivities in literature, and related functional group changes were highlighted in red. TP structures identified with confidence levels 1, 2 and 3 were communicated using dark green, light green, and yellow shades, respectively.

## 4.4 Environmental Implications

The biotransformation half-lives of DIE and DRO were 16-30 hr and <0.5 hr in our lab system (1 µg/L incubation at 37 °C). We expect the conversion rates to be faster in full-scale WWTPs, considering the adapted microbial microbial communities (Grady et al., 1999), lower DIE and DRO levels (Weizel et al., 2018), and more efficient aeration methods typically employed (Grady et al., 1999). The observed biotransformation products, including moderately stable TPs, generally retained steroidal structures that suggested a potential for retained or distinct bioactivity compared with DIE and DRO parents. Although TPs bioactivities were not evaluated explicitly here, this information was sometimes available from literature. For example, aromatic TP 309 and TP 311 of DIE were previously identified as DIE metabolites in microbes, mammals, and humans, as well as minor photoproducts (Hobe et al., 1983b, 1983a, 1982; Pflug et al., 2017; Schubert et al., 1983). A-ring aromatization implies biotransformation of the progestogenic DIE into estrogenic TPs (**Figure 4.5**). Notably, both TP 309 and TP 311 exhibit estrogen receptor binding activities ~30% of 17β-estradiol (Kaufmann et al., 1999; Oettel et al., 1993), similar to those observed for estrone. Our data suggest that TP 309, with a molar yield of up to 55% and stability over 30 hours, may dominate fate outcomes of DIE during wastewater treatment. More broadly, we speculate A ring aromatization represents a key fate outcome for progestins lacking C19-methyl groups during wastewater treatment (Weizel et al., 2021); therefore, these progestins could ultimately contribute to unexplained estrogenic activity in WWTP-impacted receiving waters and associated ecological impacts (Adeel et al., 2017; Conley et al., 2017).

Beyond its estrogenicity, TP 309 is reported to have anti-gestagenic activity (~4-fold more potent than DIE), anti-gonadotropic activity (~2-fold more potent than DIE), and

pregnancy inhibition effects (unique from DIE, and 75% of that observed for the abortion agent mifepristone) (Oettel et al., 1993). The related TP 311 exhibits anti-gestagenic activity ~6-fold more potent than DIE (Oettel et al., 1993). Another relatively abundant TP of DIE, TP 313, was reported to have slight gestagenic activity (200-fold lower than DIE; **Figure 4.5**) (Oettel et al., 1993). Therefore, unlike 1,2-dehydrogenation pathways, 3-keto hydrogenation might be expected to strongly reduce the endocrine disruption potential of DIE.

Most notably, the 1,2-dehydrogenation TP of DRO (TP 364) was itself a potent anti-mineralocorticoid drug spirorenone (~8-fold more potent than spironolactone) that was developed in the 1980s (Laurent et al., 1983). Despite its potency and promise, spirorenone was never marketed because it unexpectedly lowered testosterone levels in men during clinical trials, which was later found to arise from metabolic hydrogenation of spirorenone to 1,2-dihydrospirorenone, i.e. drospirenone (Krause and Kühne, 1982; Nickisch et al., 1985)! Therefore, spirorenone development was discontinued, while DRO was investigated, developed, and eventually introduced as a synthetic progestin pharmaceutical. Interconversion between these two structures is obviously biologically relevant and relevant to WWTP fate. Compared with DRO, spirorenone showed ~40% of the PR binding activity and similar anti-mineralocorticoid activity (Nickisch et al., 1985). The yield of spirorenone could reach 40% under typical hydraulic retention times (e.g. 4-8 hours) of WWTP aeration basins. Therefore, spirorenone formation is a key fate pathway for DRO discharge into surface waters, and metabolic conversion back to DRO in exposed aquatic organisms and humans is plausible. For other TPs of DRO, the lactone hydrolysis TP (TP 384) is a known human metabolite (so called "drospirenone acid") which is pharmacologically inactive (Kuhl, 2005; U.S. Food & Drug Administration, 2020). Hydroxylated DRO (1-OH-, 11-OH-, and 12-OH-DRO) exhibit reduced

progestagenic (1%-14%) and anti-mineralocorticoid (0%-6%) activities compared with DRO (**Figure 4.6**) (Nickisch et al., 1985). We note here that the endocrinological activities discussed above were tested in vitro or in vivo in mammals and may not necessarily be extrapolated to aquatic organisms. Studies have shown that the ligand-binding domain of fish nuclear PR is highly conserved among species (Ellestad et al., 2014), and many human progestins do not act or act weakly as fish PR agonists (e.g. agonism $EC_{50}$ of DRO in human PR, 5.72 ± 1.38 nM; in zebrafish PR, 14.1 ± 4.49 nM; in fathead minnow PR, 465.7 ± 191.7 nM) (Bain et al., 2015; Ellestad et al., 2014; Garoche et al., 2020). Nevertheless, other receptor binding activities were observed for human progestins in aquatic organisms, such as androgen receptor agonism (Ellestad et al., 2014) and PR antagonism (Garoche et al., 2020), and various adverse effects have been reported in aquatic organisms exposed to human progestins such as decreased fecundity, altered hormone levels, and changes in steroidogenic genes expression (Kumar et al., 2015). Therefore, the discharge of these progestogenic chemicals and bioactive TPs is still of risk to aquatic organisms, and their endocrinological effects to exposed mammals are of concern.

These results again demonstrated the unique bioactivity profiles expected for complex mixtures of steroid pharmaceutical TPs and parent contaminants and continue to highlight the need to consider TPs within environmental fate assessments (Cwiertny et al., 2014; Escher and Fenner, 2011). Although we did not detect DIE, DRO, or the related TPs in a small survey of three Seattle region WWTP effluents, their environmental occurrence merits further investigation, especially in regions such as the EU where these contraceptives are popular. Additionally, comparative exposure risks of observed bioactive and stable TPs to aquatic organisms also merit further evaluation.

## Reference


Adeel, M., Song, X., Wang, Y., Francis, D., Yang, Y., 2017. Environmental impact of estrogens on human, animal and plant life: A critical review. Environ. Int. 99, 107–119.

Avar, P., Maasz, G., Takács, P., Lovas, S., Zrinyi, Z., Svigruha, R., Takátsy, A., Tóth, L.G., Pirger, Z., 2016. HPLC-MS/MS analysis of steroid hormones in environmental water samples. Drug Test. Anal. 8, 123–127.

Bain, P.A., Kumar, A., Ogino, Y., Iguchi, T., 2015. Nortestosterone-derived synthetic progestogens do not activate the progestogen receptor of Murray–Darling rainbowfish (Melanotaenia Fluviatilis) but are potent agonists of androgen receptors alpha and beta. Aquat. Toxicol. 163, 97–101.

Bauer, E.R.S., Daxenberger, A., Petri, T., Sauerwein, H., Meyer, H.H.D., 2000. Characterisation of the affinity of different anabolics and synthetic hormones to the human androgen receptor, human sex hormone binding globulin and to the bovine progestin receptor. APMIS 108, 838–846.

Bhatti, H.N., Khera, R.A., 2012. Biological transformations of steroidal compounds: A review. Steroids 77, 1267–1290.

Bittler, D., Hofmeister, H., Laurent, H., Nickisch, K., Nickolson, R., Petzoldt, K., Wiechert, R., 1982. Synthesis of spirorenone—a novel highly active aldosterone antagonist. Angew. Chem. Int. Ed. Engl. 21, 696–697.

Grady, C. P. L., Daigger, G.T., Lim, H.C., 1999. Biological wastewater treatment, 2nd ed. New York: Marcel Dekker.

Chang, H., Wan, Y., Wu, S., Fan, Z., Hu, J., 2011. Occurrence of androgens and progestogens in wastewater treatment plants and receiving river waters: Comparison to estrogens. Water Res. 45, 732–740.

Chen, Y.-L., Yu, C.-P., Lee, T.-H., Goh, K.-S., Chu, K.-H., Wang, P.-H., Ismail, W., Shih, C.-J., Chiang, Y.-R., 2017. Biochemical mechanisms and catabolic enzymes involved in bacterial estrogen degradation pathways. Cell Chem. Biol. 24, 712-724.e7.

Chiang, Y.-R., Wei, S.T.-S., Wang, P.-H., Wu, P.-H., Yu, C.-P., 2020. Microbial degradation of steroid sex hormones: Implications for environmental and ecological studies. Microb. Biotechnol. 13, 926–949.

Cole, E.A., McBride, S.A., Kimbrough, K.C., Lee, J., Marchand, E.A., Cwiertny, D.M., Kolodziej, E.P., 2015. Rates and product identification for trenbolone acetate metabolite biotransformation under aerobic conditions. Environ. Toxicol. Chem. 34, 1472–1484.

Conley, J.M., Evans, N., Cardon, M.C., Rosenblum, L., Iwanowicz, L.R., Hartig, P.C., Schenck, K.M., Bradley, P.M., Wilson, V.S., 2017. Occurrence and in vitro bioactivity of estrogen, androgen, and glucocorticoid compounds in a nationwide screen of United States stream waters. Environ. Sci. Technol. 51, 4781–4791.

Cui, H., Chang, H., Zheng, H., Wan, Y., 2021. Determination and occurrence of sulfonamide transformation products in surface waters. Sci. Total Environ. 779, 146562.

Cwiertny, D.M., Snyder, S.A., Schlenk, D., Kolodziej, E.P., 2014. Environmental designer drugs: When transformation may not eliminate risk. Environ. Sci. Technol. 48, 11737–11745.

ClinCalc DrugStats Database, Drospirenone; Ethinyl Estradiol - Drug Usage Statistics, https://clincalc.com/DrugStats/Drugs/DrospirenoneEthinylEstradiol (accessed Aug 30, 2020).

Du, B., Lofton, J.M., Peter, K.T., Gipe, A.D., James, C.A., McIntyre, J.K., Scholz, N.L., Baker, J.E., Kolodziej, E.P., 2017. Development of suspect and non-target screening methods for detection of organic contaminants in highway runoff and fish tissue with high-resolution time-of-flight mass spectrometry. Environ. Sci. Process. Impacts 19, 1185–1196.

Ellestad, L.E., Cardon, M., Chambers, I.G., Farmer, J.L., Hartig, P., Stevens, K., Villeneuve, D.L., Wilson, V., Orlando, E.F., 2014. Environmental gestagens activate fathead minnow (pimephales promelas) nuclear progesterone and androgen receptors in vitro. Environ. Sci. Technol. 48, 8179–8187.

Escher, B.I., Fenner, K., 2011. Recent advances in environmental risk assessment of transformation products. Environ. Sci. Technol. 45, 3835–3847.

Fent, K., 2015. Progestins as endocrine disrupters in aquatic ecosystems: Concentrations, effects and risk assessment. Environ. Int. 84, 115–130.

Garoche, C., Aït-Aïssa, S., Boulahtouf, A., Creusot, N., Hinfray, N., Bourguet, W., Balaguer, P., Brion, F., 2020. Human and zebrafish nuclear progesterone receptors are differently activated by manifold progestins. Environ. Sci. Technol. 54, 9510–9518.

Golovko, O., Šauer, P., Fedorova, G., Kroupová, H.K., Grabic, R., 2018. Determination of progestogens in surface and waste water using SPE extraction and LC-APCI/APPI-HRPS. Sci. Total Environ. 621, 1066–1073.

Guan, F., Soma, L.R., Luo, Y., Uboh, C.E., Peterman, S., 2006. Collision-induced dissociation pathways of anabolic steroids by electrospray ionization tandem mass spectrometry. J. Am. Soc. Mass Spectrom. 17, 477–489.

Gulde, R., Meier, U., Schymanski, E.L., Kohler, H.-P.E., Helbling, D.E., Derrer, S., Rentsch, D., Fenner, K., 2016. Systematic exploration of biotransformation reactions of amine-containing micropollutants in activated sludge. Environ. Sci. Technol. 50, 2908–2920.

Helbling, D.E., Hollender, J., Kohler, H.-P.E., Singer, H., Fenner, K., 2010. High-throughput identification of microbial transformation products of organic micropollutants. Environ. Sci. Technol. 44, 6621–6627.

Hobe, G., Hillesheim, H.G., Schumann, W., Ritter, P., Claussen, C., Chemnitius, K.H., Erdmann, A., Wagner, H., Wehrberger, K., Wesemann, R., Carol, W., Klinger, G., Komor, A., Goncharov, N.P., 1983a. Studies on pharmacokinetics of STS 557 in animal species and man. Exp. Clin. Endocrinol. 81, 158–167.

Hobe, G., Schön, R., Frankenberg, G., Schade, W., Schubert, K., 1983b. Urinary metabolites of the new progestagen STS 557 (17 alpha-cyanomethyl-17-hydroxy-4,9-estradien-3-one) in the dog and rat. Steroids 41, 23–33.

Hobe, G., Schön, R., Hörhold, C., Hübner, M., Schade, W., Schubert, K., 1982. Microbial transformation of 17 alpha-cyanomethyl-17-hydroxy-4,9-estradien-3-one (STS 557) and 17 alpha-cyanomethyl-19-nortestosterone by Mycobacterium smegmatis. Steroids 39, 399–409.

Horinouchi, M., Koshino, H., Malon, M., Hirota, H., Hayashi, T., 2018. Steroid degradation in Comamonas testosteroni TA441: Identification of metabolites and the genes involved in the reactions necessary before D-ring cleavage. Appl. Environ. Microbiol. 84, e01324-18.

Kaufmann, G., Dautzenberg, H., Henkel, H., Müller, G., Schäfer, T., Undeutsch, B., Oettel, M., 1999. Nitrile hydratase from Rhodococcus erythropolis: Metabolization of steroidal compounds with a nitrile group. Steroids 64, 535–540.

Kenyon, P.T., Zhao, H., Yang, X., Wu, C., Cwiertny, D.M., Kolodziej, E.P., 2019. Detection and quantification of metastable photoproducts of trenbolone and altrenogest using liquid chromatography–tandem mass spectrometry. J. Chromatogr. A 1603, 150–159.
Khunjar, W.O., Mackintosh, S.A., Skotnicka-Pitak, J., Baik, S., Aga, D.S., Love, N.G., 2011. Elucidating the relative roles of ammonia oxidizing and heterotrophic bacteria during the biotransformation of 17α-ethinylestradiol and trimethoprim. Environ. Sci. Technol. 45, 3605–3612.
Kidd, K.A., Blanchfield, P.J., Mills, K.H., Palace, V.P., Evans, R.E., Lazorchak, J.M., Flick, R.W., 2007. Collapse of a fish population after exposure to a synthetic estrogen. Proc. Natl. Acad. Sci. 104, 8897–8901.
Krause, W., Kühne, G., 1982. Isolation and identification of spirorenone metabolites from the monkey (Macaca fascicularis). Steroids 40, 81–90.
Kuhl, H., 2005. Pharmacology of estrogens and progestogens: Influence of different routes of administration. Climacteric 8, 3–63.
Kuhl, H., Wiegratz, I., 2007. Can 19-nortestosterone derivatives be aromatized in the liver of adult humans? Are there clinical implications? Climacteric J. Int. Menopause Soc. 10, 344–353.
Kumar, V., Johnson, A.C., Trubiroha, A., Tumová, J., Ihara, M., Grabic, R., Kloas, W., Tanaka, H., Kroupová, H.K., 2015. The challenge presented by progestins in ecotoxicological research: a critical review. Environ. Sci. Technol. 49, 2625–2638.
Laurent, H., Bittler, D., Hofmeister, H., Nickisch, K., Nickolson, R., Petzoldt, K., Wiechert, R., 1983. Synthesis and Activities of Anti-aldosterones. *J. Steroid Biochem.* 19, 771-776.
Liu, S., Ying, G.-G., Liu, Y.-S., Peng, F.-Q., He, L.-Y., 2013. Degradation of norgestrel by bacteria from activated sludge: Comparison to progesterone. Environ. Sci. Technol. 47, 10266–10276.
Liu, S.-S., Chen, J., Zhang, J.-N., Liu, Y.-S., Hu, L.-X., Chen, X.-W., Liu, S., Xu, X.-R., Ying, G.-G., 2020. Microbial transformation of progesterone and dydrogesterone by bacteria from swine wastewater: Degradation kinetics and products identification. Sci. Total Environ. 701, 134930.
Louw-du Toit, R., Perkins, M.S., Snoep, J.L., Storbeck, K.-H., Africander, D., 2016. Fourth-generation progestins inhibit 3β-hydroxysteroid dehydrogenase type 2 and modulate the biosynthesis of endogenous steroids. PLoS ONE 11.
Ma, L., Yates, S.R., 2018. A review on structural elucidation of metabolites of environmental steroid hormones via liquid chromatography–mass spectrometry. TrAC Trends Anal. Chem. 109, 142–153.
Mahler, B.J., Nowell, L.H., Sandstrom, M.W., Bradley, P.M., Romanok, K.M., Konrad, C.P., Van Metre, P.C., 2021. Inclusion of pesticide transformation products is key to estimating pesticide exposures and effects in small U.S. streams. Environ. Sci. Technol. 55, 4740–4752.
Nickisch, K., Bittler, D., Casals-Stenzel, J., Laurent, H., Nickolson, R., Nishino, Y., Petzoldt, K., Wiechert, R., 1985. Aldosterone antagonists. 1. Synthesis and activities of 6 beta,7 beta:15 beta,16 beta-dimethylene steroidal spirolactones. J. Med. Chem. 28, 546–550.
Oettel, M., Kaufmann, G., Kurischko, A., 1993. The endocrinologic profile of metabolites of the progestin dienogest. Pharm. 48, 541–545.
Peng, F.-Q., Ying, G.-G., Yang, B., Liu, S., Lai, H.-J., Liu, Y.-S., Chen, Z.-F., Zhou, G.-J., 2014. Biotransformation of progesterone and norgestrel by two freshwater microalgae

(Scenedesmus obliquus and Chlorella pyrenoidosa): Transformation kinetics and products identification. Chemosphere 95, 581–588.
Peter, K.T., Tian, Z., Wu, C., Lin, P., White, S., Du, B., McIntyre, J.K., Scholz, N.L., Kolodziej, E.P., 2018. Using high-resolution mass spectrometry to identify organic contaminants linked to urban stormwater mortality syndrome in coho salmon. Environ. Sci. Technol. 52, 10317–10327.
Pflug, N.C., Hankard, M.K., Berg, S.M., O'Connor, M., Gloer, J.B., Kolodziej, E.P., Cwiertny, D.M., Wammer, K.H., 2017. Environmental photochemistry of dienogest: Phototransformation to estrogenic products and increased environmental persistence via reversible photohydration. Environ. Sci. Process. Impacts 19, 1414–1426.
Regidor, P.-A., Schindler, A.E., 2017. Antiandrogenic and antimineralocorticoid health benefits of COC containing newer progestogens: Dienogest and drospirenone. Oncotarget 8, 83334–83342.
Schwarzenbach, R. P., Gschwend, P. M., Imboden, D. M., 2003. Environmental Organic Chemistry, 2nd Edition; John Wiley & Sons, Inc, page 468-482.
Runnalls, T.J., Margiotta-Casaluci, L., Kugathas, S., Sumpter, J.P., 2010. Pharmaceuticals in the aquatic environment: Steroids and anti-steroids as high priorities for research. Hum. Ecol. Risk Assess. Int. J. 16, 1318–1338.
Šauer, P., Tumová, J., Steinbach, C., Golovko, O., Komen, H., Maillot-Maréchal, E., Máchová, J., Grabic, R., Aït-Aïssa, S., Kocour Kroupová, H., 2020. Chronic simultaneous exposure of common carp (Cyprinus carpio) from embryonic to juvenile stage to drospirenone and gestodene at low ng/L level caused intersex. Ecotoxicol. Environ. Saf. 188, 109912.
Schänzer, W., Geyer, H., Fusshöller, G., Halatcheva, N., Kohler, M., Parr, M.-K., Guddat, S., Thomas, A., Thevis, M., 2006. Mass spectrometric identification and characterization of a new long-term metabolite of metandienone in human urine. Rapid Commun. Mass Spectrom. RCM 20, 2252–2258.
Schmid, S., Willi, R.A., Salgueiro-González, N., Fent, K., 2020. Effects of new generation progestins, including as mixtures and in combination with other classes of steroid hormones, on zebrafish early life stages. Sci. Total Environ. 709, 136262.
Schubert, K., Hobe, G., Kaufmann, G., Schumann, G., Wehrberger, K., Hörhold, C., 1983. Studies on biotransformation of STS 557. Exp. Clin. Endocrinol. 81, 168–174.
Schymanski, E.L., Jeon, J., Gulde, R., Fenner, K., Ruff, M., Singer, H.P., Hollender, J., 2014. Identifying small molecules via high resolution mass spectrometry: Communicating confidence. Environ. Sci. Technol. 48, 2097–2098.
Svendsen, S.B., El-taliawy, H., Carvalho, P.N., Bester, K., 2020. Concentration dependent degradation of pharmaceuticals in WWTP effluent by biofilm reactors. Water Res. 186, 116389.
Thevis, M., Schänzer, W., 2007. Mass spectrometry in sports drug testing: Structure characterization and analytical assays. Mass Spectrom. Rev. 26, 79–107.
Thevis, M., Schänzer, W., 2005. Mass spectrometric analysis of androstan-17beta-ol-3-one and androstadiene-17beta-ol-3-one isomers. J. Am. Soc. Mass Spectrom. 16, 1660–1669.
Tian, Z., Peter, K.T., Gipe, A.D., Zhao, H., Hou, F., Wark, D.A., Khangaonkar, T., Kolodziej, E.P., James, C.A., 2020. Suspect and nontarget screening for contaminants of emerging concern in an urban estuary. Environ. Sci. Technol. 54, 889–901.
U.S. Food & Drug administration, 2020. Yasmin Label.

Wang, P.-H., Chen, Y.-L., Wei, S.T.-S., Wu, K., Lee, T.-H., Wu, T.-Y., Chiang, Y.-R., 2020. Retroconversion of estrogens into androgens by bacteria via a cobalamin-mediated methylation. Proc. Natl. Acad. Sci. 117, 1395–1403.

Wang, P.-H., Yu, C.-P., Lee, T.-H., Lin, C.-W., Ismail, W., Wey, S.-P., Kuo, A.-T., Chiang, Y.-R., 2014. Anoxic androgen degradation by the denitrifying bacterium sterolibacterium denitrificans via the 2,3-seco Pathway. Appl. Environ. Microbiol. 80, 3442–3452.

Weizel, A., Schlüsener, M.P., Dierkes, G., Ternes, T.A., 2018. Occurrence of glucocorticoids, mineralocorticoids, and progestogens in various treated wastewater, rivers, and streams. Environ. Sci. Technol. 52, 5296–5307.

Weizel, A., Schlüsener, M.P., Dierkes, G., Wick, A., Ternes, T.A., 2021. Fate and behavior of progestogens in activated sludge treatment: Kinetics and transformation products. Water Res. 188, 116515.

Weizel, A., Schlüsener, M.P., Dierkes, G., Wick, A., Ternes, T.A., 2020. Analysis of the aerobic biodegradation of glucocorticoids: Elucidation of the kinetics and transformation reactions. Water Res. 174, 115561.

Wu, K., Lee, T.-H., Chen, Y.-L., Wang, Y.-S., Wang, P.-H., Yu, C.-P., Chu, K.-H., Chiang, Y.-R., 2019. Metabolites involved in aerobic degradation of the a and b rings of estrogen. Appl. Environ. Microbiol. 85, e02223-18.

Yang, Y.-Y., Borch, T., Young, R.B., Goodridge, L.D., Davis, J.G., 2010. Degradation kinetics of testosterone by manure-borne bacteria: Influence of temperature, pH, glucose amendments, and dissolved oxygen. J. Environ. Qual. 39, 1153–1160.

Yang, Y.-Y., Pereyra, L.P., Young, R.B., Reardon, K.F., Borch, T., 2011. Testosterone-mineralizing culture enriched from swine manure: Characterization of degradation pathways and microbial community composition. Environ. Sci. Technol. 45, 6879–6886.

Yu, Q., Geng, J., Zong, X., Zhang, Y., Xu, K., Hu, H., Deng, Y., Zhao, F., Ren, H., 2019. Occurrence and removal of progestagens in municipal wastewater treatment plants from different regions in China. Sci. Total Environ. 668, 1191–1199.

Zeng, Z., Liu, R., Zhang, J., Yu, J., He, L., Shen, X., 2013. Determination of seven free anabolic steroid residues in eggs by high-performance liquid chromatography–tandem mass spectrometry. J. Chromatogr. Sci. 51, 229–236.

Zhao, Y., Castiglioni, S., Fent, K., 2015. Environmental progestins progesterone and drospirenone alter the circadian rhythm network in zebrafish (Danio rerio). Environ. Sci. Technol. 49, 10155–10164.

Zind, H., Mondamert, L., Remaury, Q.B., Cleon, A., Leitner, N.K.V., Labanowski, J., 2021. Occurrence of carbamazepine, diclofenac, and their related metabolites and transformation products in a French aquatic environment and preliminary risk assessment. Water Res. 196, 117052.

Zucchi, S., Mirbahai, L., Castiglioni, S., Fent, K., 2014. Transcriptional and physiological responses induced by binary mixtures of drospirenone and progesterone in Zebrafish (Danio rerio). Environ. Sci. Technol. 48, 3523–3531.

## Supplementary Materials

### Chemicals

Analytical standards of dienogest (DIE) and drospirenone (DRO) were purchased from Sigma Aldrich (St. Louis, MO, USA). Internal standards and reference standards for TPs confirmation, including DIE-$d_8$, DRO-$^{13}C_3$, 6β-hydroxy DIE, (17α)-17-hydroxy-3-oxo-19-norpregna-5(10),9(11)-diene-21-nitrile, and DRO acid sodium salt, were purchased from Toronto Research Chemicals (North York, ON, Canada). DIE-$d_6$, 11β-hydroxy DIE, 17α-cyanomethyl-19-nortestosterone, Δ9,11-dehydro-17α-cyanomethyl estradiol, and 17α-cyanomethylestra-1,3,5(10)-triene-3,17β-diol, were purchased from TLC Pharmaceutical Standards (Newmarket, ON, Canada). 2,3-Dichloro-5,6-dicyano-p-benzoquinone and dioxane for spirorenone (TP 364) synthesis were purchased from Sigma Aldrich. Acetic acid (99.7%), formic acid (99.7%), and ammonium acetate (HPLC grade, 97.8%) were purchased from VWR Scientific (Radnor, PA, USA). Ammonium fluoride (99.9%) was purchased from Sigma Aldrich (St. Louis, MO, USA). HPLC-grade solvents, including n-hexane, dichloromethane, ethyl acetate, and methanol, were purchased from Fisher Scientific (Pittsburgh, PA, U.S.A.). Deionized (DI) water was produced by a Nanopure system (Thermo Barnstead Nanopure Diamond UV, Dubuque, IA, USA).

### Spirorenone (TP 364) Synthesis

A flame-dried round bottom flask was prepared with a magnetic stir bar, drospirenone (36.6 mg, 0.10 mmol, 1.0 equiv), and 1,4-dioxane (5 mL). 2,3-Dichloro-5,6-dicyano-1,4-benzoquinone (49.9 mg, 0.22 mmol, 2.2 equiv) was added to this solution (**Figure S4.3**). The resulting mixture was heated to reflux (115 °C), and reaction progress was monitored by thin layer chromatography. After 6 hours, heating was stopped and the reaction mixture was concentrated under reduced pressure. The crude residue was purified by silica gel column chromatography to isolate spirorenone (TP 364) as a pale yellow amorphous solid (12.9 mg, 35% yield). Characterization data: $R_f$ = 0.15 (2:1 ethyl acetate/hexanes); $^1$H NMR ($CDCl_3$, 500 MHz) δ 6.86 (d, *J* = 10.1 Hz, 1H), 6.33 (d, *J* = 1.9 Hz, 1H), 6.18 (dd, *J* = 10.1, 1.9 Hz, 1H), 2.67–2.60 (m, 1H), 2.55–2.48 (m, 1H), 2.40 (ddd, *J* = 13.1, 9.1, 5.5 Hz, 1H), 2.10 (ddd, *J* = 13.1, 9.4, 8.1 Hz, 1H), 1.96–1.89 (m, 2H), 1.81–1.75 (m, 2H), 1.62–1.55 (m, 3H), 1.51–1.47 (m, 1H), 1.44–1.39 (m, 1H), 1.39–1.31 (m, 3H), 1.27–1.19 (m, 2H), 1.14 (s, 3H), 1.03 (s, 3H), 0.55 (td, *J* = 8.0, 6.3 Hz, 1H); $^{13}$C NMR ($CDCl_3$, 126 MHz) δ 185.0, 176.6, 168.0, 154.9, 127.2, 125.9, 96.1, 51.5, 51.0, 43.1, 42.1, 37.2, 34.5, 30.8, 29.4, 24.5, 23.0, 21.0, 20.6, 20.0, 19.9, 18.0, 16.9, 10.1; IR (neat film) 3019, 2926, 2861, 1769, 1655, 1615, 1588, 1290, 1198, 1015, 914, 817, 733 $cm^{-1}$. HRMS (ESI+) *m/z* calculated for $C_{24}H_{29}O_3$ $[M+H]^+$ predicted 365.2117 Da, 365.2121 Da was observed.

### Spectral Data for Synthetic Spirorenone (TP 364)

*General Information*. All $^1$H and $^{13}$C nuclear magnetic resonance (NMR) spectra were recorded on a Bruker Advance DRX series spectrometer equipped with a triple resonance BBO probe (500 and 126 MHz, respectively) and are reported in terms of chemical shift relative to residual $CHCl_3$ (δ 7.26 and δ 77.16 ppm, respectively). Data for $^1$H NMR spectra are reported as follows: chemical shift (δ ppm) (multiplicity, coupling constant (Hz), integration). Abbreviations are used as follows: s = singlet, d = doublet, t = triplet, q = quartet, m = complex multiplet. Infrared (IR) spectra were recorded using thin film samples on a PerkinElmer Spectrum 100

spectrometer equipped with a diamond/ZnSe UATR and are reported in frequency absorption ($cm^{-1}$).

*Interpretation of NMR Data for Synthetic Spirorenone*. Signals at 6.86, 6.33, and 6.18 ppm in the $^{1}H$ NMR spectrum indicate the presence of three vinylic protons $H_d$, $H_a$, and $H_b$, respectively, which correspond to the $^{13}C$ NMR signals at 154.9, 125.9, and 127.2 ppm, respectively, as indicated by HSQC analysis (**Figure S4.4a-c**). Signals at 185.0 and 176.6 ppm in the $^{13}C$ NMR spectrum confirm the presence of two carbonyls, corresponding to the A-ring cyclohexadienone carbonyl and the E-ring γ-lactone carbonyl, respectively (**Figure S4.4c**). The HSQC spectrum confirms the presence of seven aliphatic methine (CH) protons, six pairs of methylene ($CH_2$) protons, and two sets of methyl ($CH_3$) protons (**Figure S4.4e**). HMBC correlations between the methyl $H_e$ singlet at 1.14 ppm and the alkenyl $^{13}C$ signals at 168.0 and 154.9 ppm indicate the presence of two C=C bonds in the six-membered A-ring (**Figure S4.4f**), confirming the site of dehydrogenation in the synthesis of spirorenone from drospirenone.

**LC-MS/MS Quantification**

Quantification of DIE, DRO, and the major standard-confirmed TPs (DIE TP 309, DRO TP 364 and TP 384) in the 1 µg/L kinetics bioreactors was performed with an Agilent (Santa Clara, CA, USA) 1290 Infinity ultrahigh-performance liquid chromatography (UPLC) system coupled with an Agilent 6430 triple quadrupole tandem mass spectrometer (MS/MS). Samples (5 µL injection volume) were separated with an Agilent Poroshell 120Å EC C18 column (2.1 × 100 mm, 2.7 µm) preceded with an Agilent Poroshell 120Å EC C18 guard column (2.0 × 5 mm, 2.7 µm) at 40 °C. LC-MS grade water (A) and methanol (B) with 0.1% formic acid were used as the mobile phases (0.4 mL/min) with the following gradient: 0 min, 5% B; 5 min, 35% B; 20 min, 68.75% B; 20.5 min, 100% B, 25 min, 100% B, 25.5 min, 5% B, 30.5 min, 5% B. Agilent Jetstream electrospray ionization in positive mode (ESI+) was used with 2.5 kV capillary voltage, 1.0 kV nozzle voltage, 350 °C desolvation gas temp, 400 °C sheath gas temp, 12.0 L $min^{-1}$ desolvation and sheath gas flows, 40 psi nebulizer pressure, and 400 V positive multiplier voltage (delta EMV). Analytes were quantified in the dynamic multiple reaction monitoring (MRM) mode and three transitions were monitored for each analyte (**Table S4.1**).

DIE, DRO, and the TPs were quantified with 7-point calibration curves (0.05-5 µg/L; $R^2$ >0.995). DIE-$d_8$ was used as the internal standard for DIE and TP309, and DRO-$^{13}C_3$ was used as the internal standard for DRO, TP 364, and TP 384. Method detection limits (MDLs) were estimated as the lowest concentrations of target analytes in spiked sludge samples with observed signal-to-noise ratios of 3, and were 30 ng/L for DIE, 40 ng/L for TP 309, 8 ng/L for DRO, 8 ng/L for TP 364, and 15 ng/L for TP 384. Recovery rates were evaluated for DIE and DRO at three concentrations (0.1, 0.5, 1 µg/L in sludge) in triplicate. Absolute recoveries were calculated as the peak area ratios of analytes in spiked sludge samples over those in standards, and were 90% ± 3% for DIE and 83% ± 2% for DRO. Relative recoveries were estimated as the absolute recoveries calibrated to the absolute recoveries of the isotopic standards, and were 93% ± 6% for DIE and 90% ± 4% for DRO.

**High-Resolution Mass Spectrometry Instrumental Method**

For the UPLC-qTOF-HRMS analysis, LC separation was achieved on an Agilent ZORBAX Eclipse Plus C18 column (2.1 × 100 mm, 1.8 µm) preceded with an Agilent ZORBAX Eclipse Plus C18 guard column (2.1 × 5 mm, 1.8 µm). For ESI+, the mobile phases (0.4 mL/min) were 5 mM ammonium acetate and 0.1% acetic acid in each of water (A) and methanol (B), with

a gradient of 5% B at 0-1 min, 50% B at 4 min, 100% B at 17-20 min, 5% B at 20.1 min, stop time 22.5 min, and post-time 2 min. For ESI-, the mobile phases were 1 mM ammonium fluoride in water (A) and pure methanol (B), and the same gradient was used as ESI+. Full scan HRMS data were acquired at the m/z range of 100-1700. MS/MS data was acquired at the m/z range of 50-500 (no features in the preferred list have m/z > 500) under three collision energy (10, 20, and 40 eV), by data-dependent acquisition with the preferred lists generated with the full scan data through replicate filtration and blank (controls) subtraction.

For quality assurance and quality control (QA/QC), a checktune including mass calibration was performed before each analytical run, and mass accuracy was corrected via continuous infusion of purine and HP-921 calibrants during the run. Solvent blanks and instrumental internal standard (ISTD) controls were analyzed every 12 samples. The retention time (RT), mass accuracy, and abundance of ISTD controls were used for performance evaluation of each analytical run. The RT deviation and mass error of the ISTDs were <0.15 min and <5 ppm, respectively. Response (peak area) variations of ISTDs were <15% within each analytical batch. Additional instrumental parameters and QA/QC procedures are described in Du et al.(Du et al., 2017)

**Single Point Energy Calculation**

The structures of 1,2-dehydrogenated DIE and TP 309 were optimized by Gaussian 16 program suite using Becke's non-local three parameter exchange and correlation function with the Lee-Yang-Parr function (B3LYP) in combination with the 6-31G(d) basis set. To obtain highly accurate single point energies ($E_{sp}$), the optimized structures were recalculated by using B3LYP with 6-311+G(2d,2p) basis set.

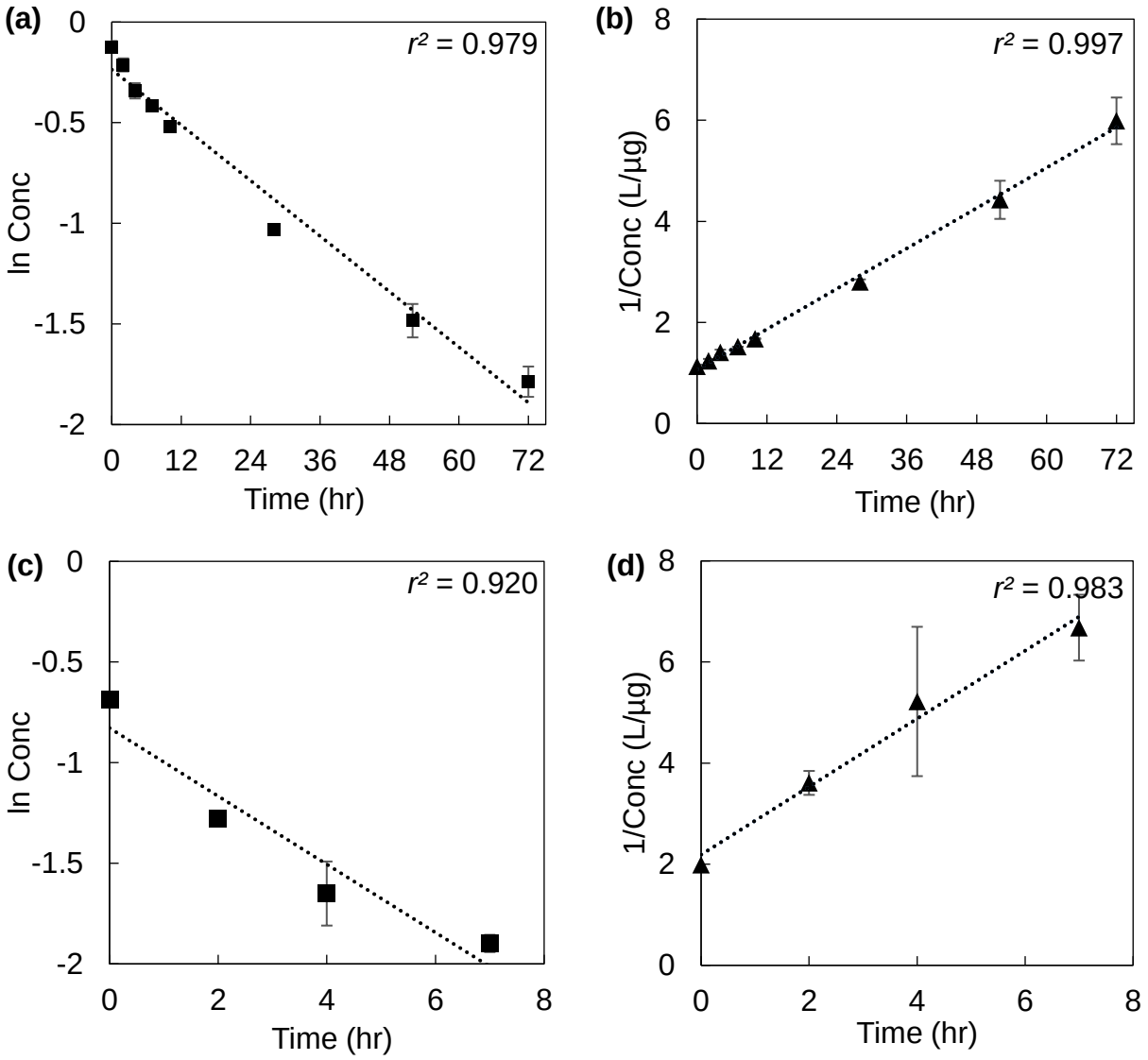


**Figure S4.1** Kinetics modelling for biotransformation of 1 µg/L DIE and DRO in batch systems inoculated with mixed liquor from aeration basins (TSS: 1.39 g/L; VSS: 1.36 g/L). (a) First (ln concentration vs time) and (b) second (concentration$^{-1}$ vs time) order kinetics for DIE. (c) First and (d) second order kinetics for DRO. The kinetics for DRO were modelled for 0-7 hours because the reaction plateaued over 7-72 hours timescales. Error bars represent standard deviation of three replicates.

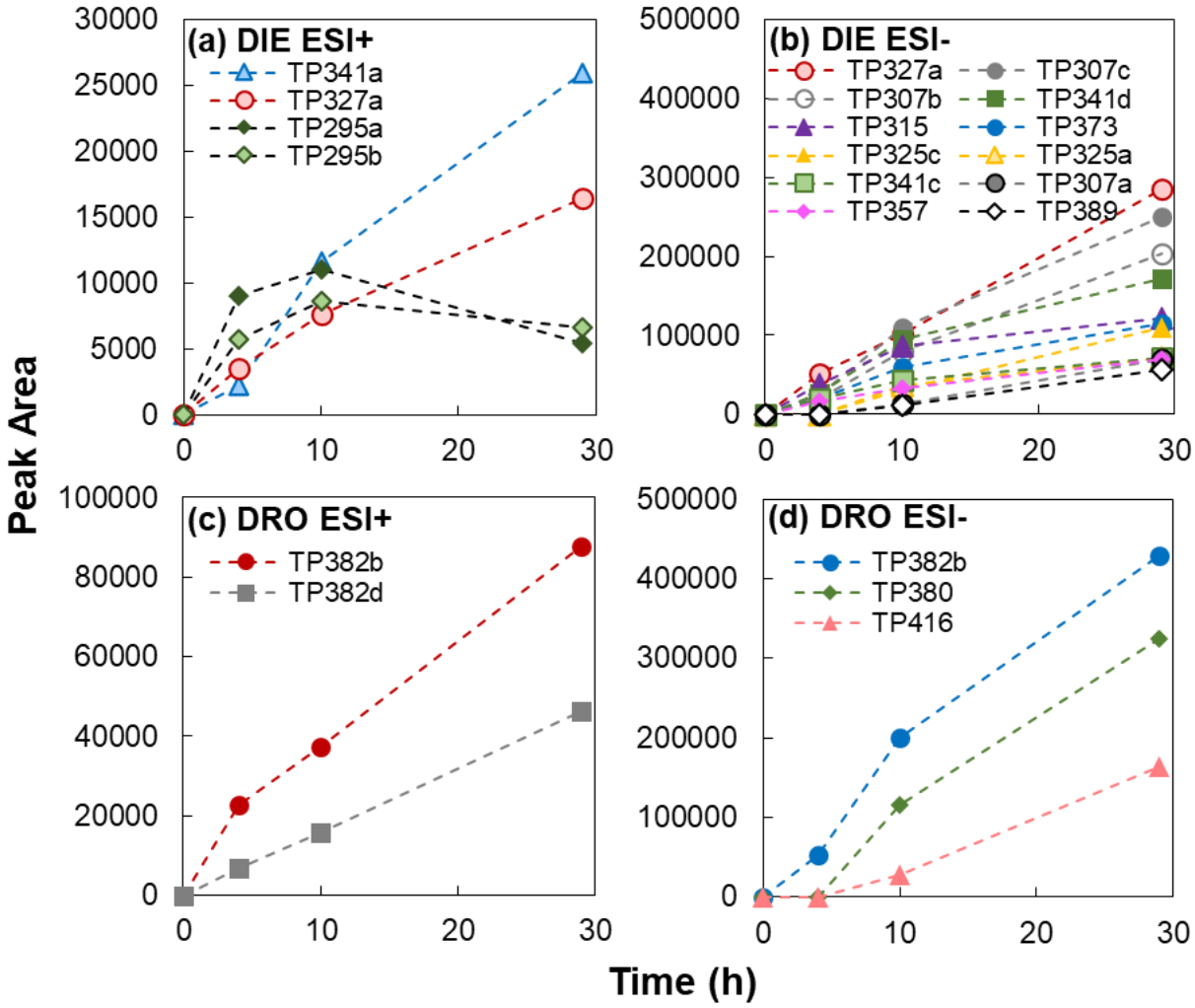


**Figure S4.2** Time trends of minor DIE and DRO TPs whose peak areas were <1% of parent peak area decreases. (a) ESI+ and (b) ESI- peak areas of minor DIE TPs; (c) ESI+ and (d) ESI- peak areas of minor DRO TPs.

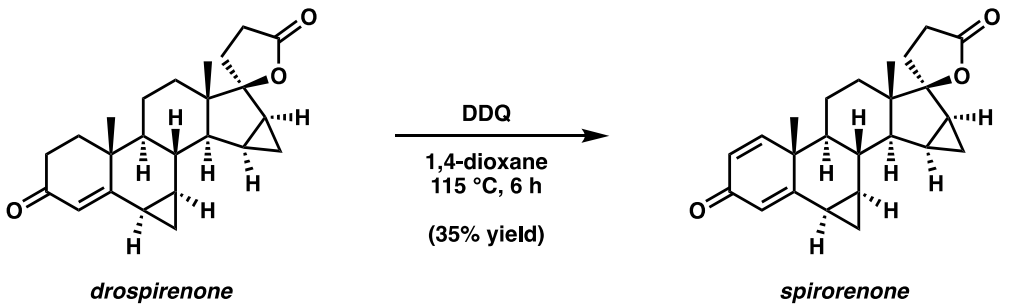


**Figure S4.3** Synthetic pathway for spirorenone (TP 364) from DRO.

(a)

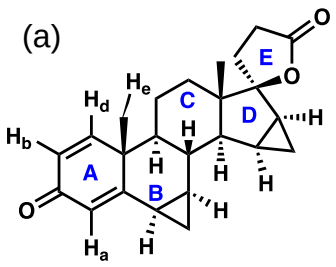


***spirorenone***

(b)

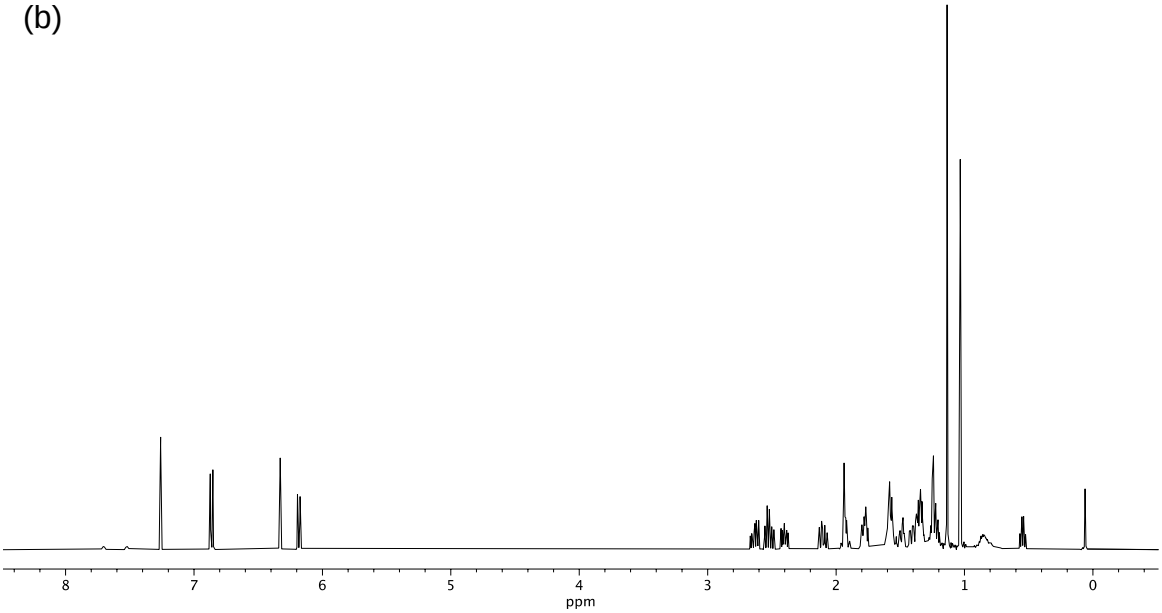


(c)

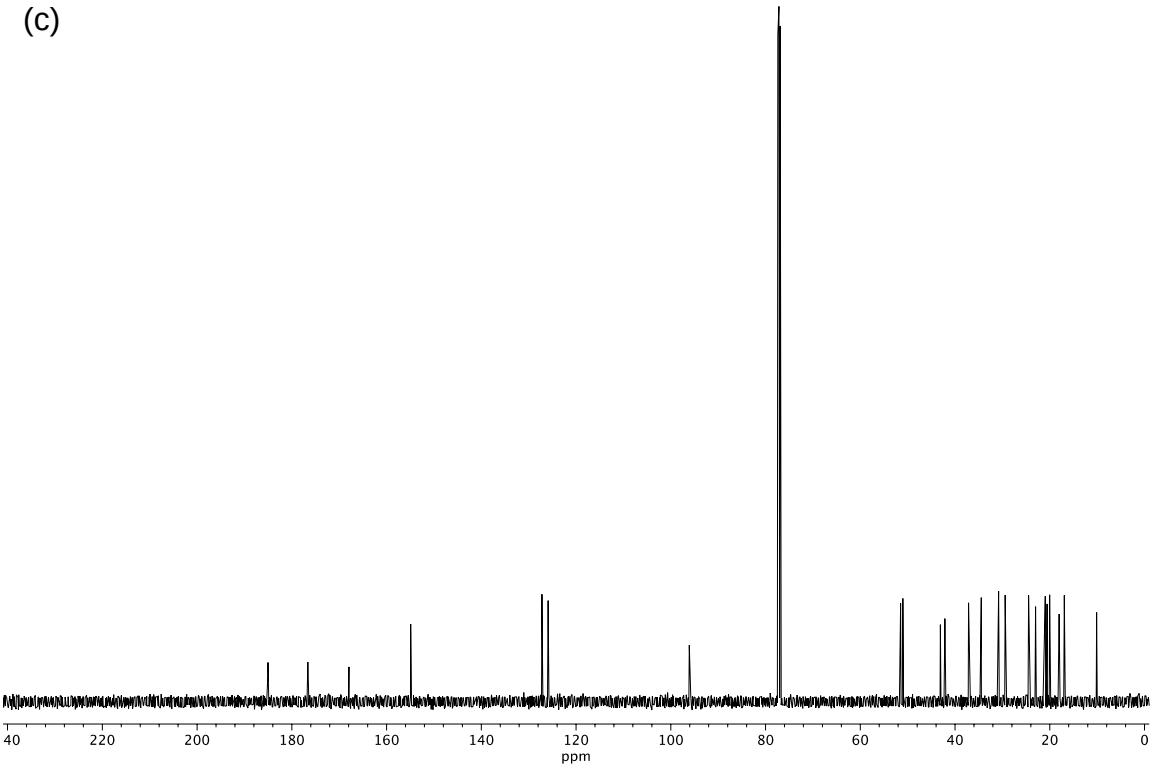

(d)

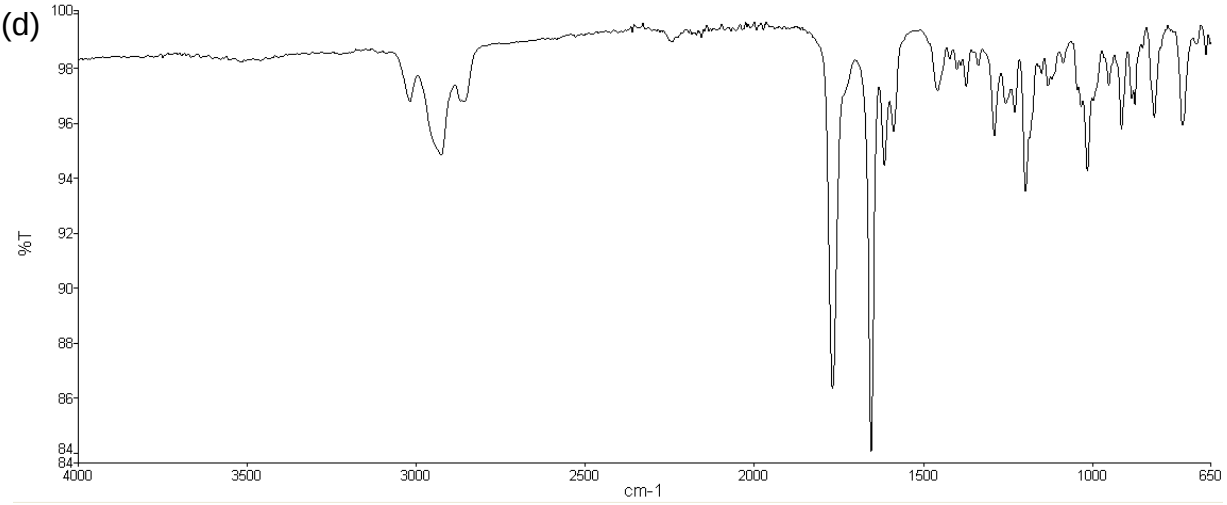


(e)

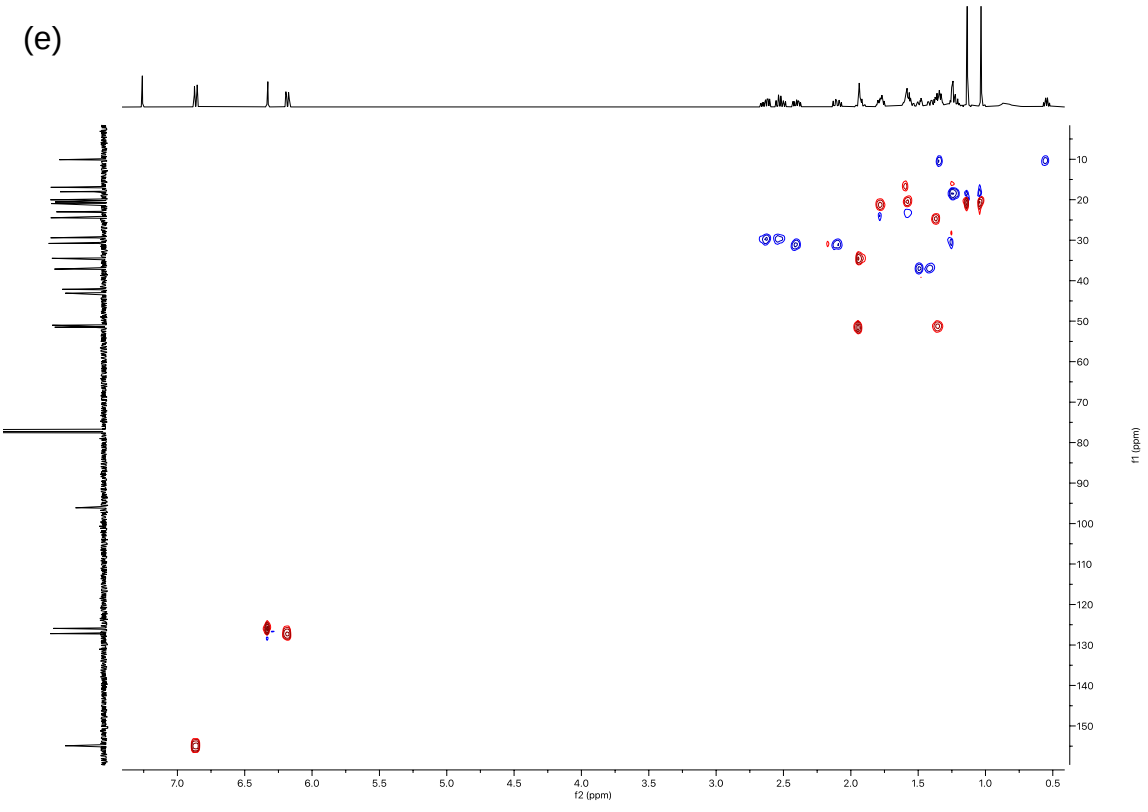

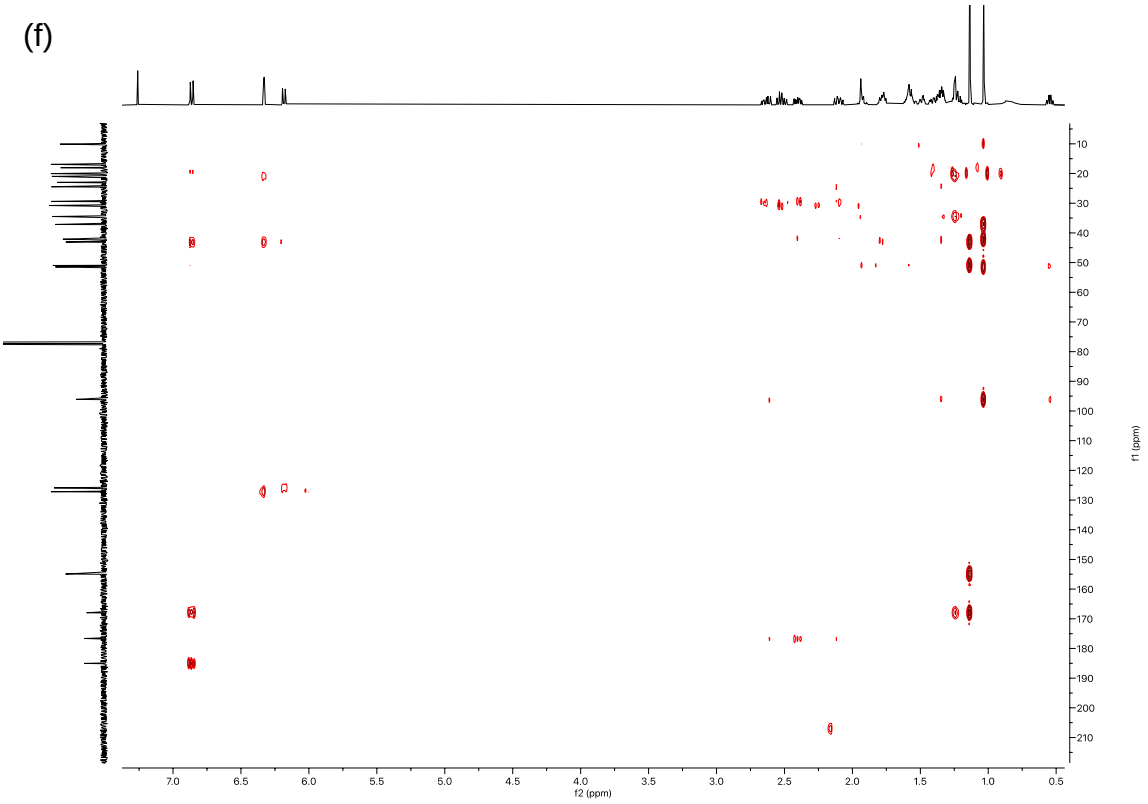


**Figure S4.4** NMR and infrared spectra of synthetic spirorenone (TP 364). (a) Structure of spirorenone (TP 364); (b) $^{1}H$ NMR (500 MHz, $CDCl_3$); (c) $^{13}C$ NMR (126 MHz, $CDCl_3$); (d) Infrared spectrum (thin film); (e) HSQC (500, 126 MHz, $CDCl_3$); (f) HMBC (500, 126 MHz, $CDCl_3$).

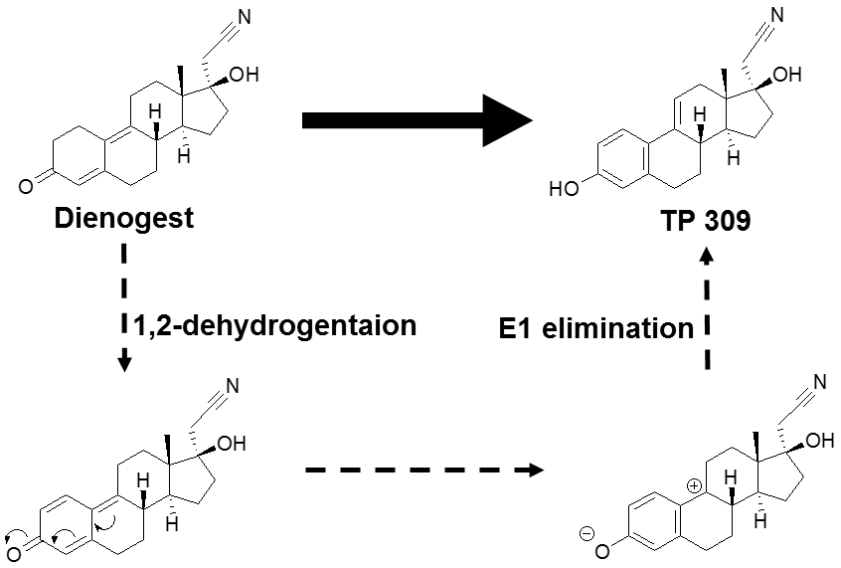


**Figure S4.5** Proposed formation mechanism of TP 309 through 1,2-dehydrogenation of DIE.

**Table S4.1** MRM parameters for targeted analysis of DIE, DRO, and the major TPs.

| Target analyte | Retention time (min) | Precursor ion (m/z) | Quantifier ion (m/z) | Qualifier ion (m/z) | Fragmentor voltage (V) | Quantifier collision energy (eV) | Qualifier collision energy (eV) |
|---|---|---|---|---|---|---|---|
| DIE | 13.1 | 312.3 | 135.2 | 91.2/161.2 | 120 | 30 | 60/30 |
| DIE-$d_8$ | 13.0 | 320.3 | 139.2 | 93.1/167.2 | 120 | 30 | 60/30 |
| DRO | 17.3 | 367.3 | 97.2 | 105.2/131.2 | 120 | 30 | 50/40 |
| DRO-$^{13}C_3$ | 17.3 | 370.3 | 97.1 | 105.1/131.1 | 120 | 30 | 50/40 |
| TP 309 | 14.0 | 310.3 | 159.1 | 133.1/144.1 | 80 | 30 | 30/50 |
| TP 364 | 16.1 | 365.4 | 121.1 | 147.1/91.1 | 80 | 35 | 20/70 |
| TP 384 | 15.7 | 385.4 | 97.1 | 131./105.1 | 100 | 20 | 40/40 |

**Table S4.2** Key parameters of the feature extraction and alignment method in MassHunter Profinder.

| Category | Item | Setting |
|---|---|---|
| Molecular Feature Extraction (MFE) – Extraction Parameters | Noise peak height | ≥ 300 counts |
| | Ion Species | ESI+: +H, +Na, +$NH_4$<br>ESI-: -H, +HCOO, +CH3COO |
| | Isotope model | Common organic molecules |
| Compound Binning and Alignment | RT window | 0.4 min |
| | Mass window | 30 ppm |
| MFE – Post-Processing Filters | Absolute height | ≥ 5000 counts |
| | Score (MFE) | ≥ 70 |
| | Satisfy MFE conditions in | ≥ 2 files |
| Find by Ion – Matching Tolerances and Scoring | Scoring | Mass score (100), isotope abundance score (60), isotope spacing score (50), retention time score (50) |
| | Do not match if score | < 30 |
| Find by Ion – EIC Peak Integration and Filtering | Integration | Agile 2 |
| | Peak height | ≥ 3000 counts |
| Find by Ion – Post-Processing Filters | Absolute height | ≥ 1000 counts |
| | Score (Tgt) | ≥ 50 |
| | Satisfy Find by Ion conditions in | ≥ 2 files |

**Table S4.3** Key parameters of the feature extraction and alignment method in XCMS Online.

| Category | Item | Setting |
|---|---|---|
| Feature detection | Mass tolerance | 15 ppm |
| | Peak width | 5-30 seconds |
| | S/N threshold | 6 |
| | Prefilter intensity | 100 |
| Retention time correction | Method | obiwarp |
| | profStep | 0.2 |
| Alignment | Mass tolerance | 0.015 Da |
| | Satisfy conditions in | > 66% files |
| Statistics | Statistical test | Unpaired parametric t-test |
| | P-value threshold | 0.05 |
| Identification | Adducts | ESI+: +H, +Na, $+NH_4$ |
| | | ESI-: -H, +Cl, +F |

**Table S4.4** Characterization details of transformation products (TPs) of DIE observed in 1 mg/L activated sludge bioreactors.

| Name | Proposed pathway | Formula | Theoretical mass | Confidence level | RT (min) | Peak area time trend | Maximum yield (%) | Proposed structure |
|---|---|---|---|---|---|---|---|---|
| Dienogest | - | $C_{20}H_{25}NO_2$ | 311.1885 | 1 | 7.00 | ↘ | - | 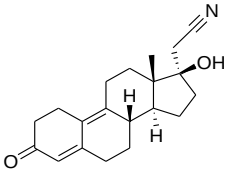 |
| TP 309 | dehydrogenation - aromatization | $C_{20}H_{23}NO_2$ | 309.1729 | 1 | 7.16 | ↗ | 55[a] | 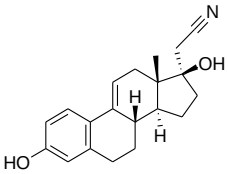 |
| TP 327 a, b | hydroxylation | $C_{20}H_{25}NO_3$ | 327.1834 | 2a | 4.86, 5.78 | ↗ | 2.9[b] | 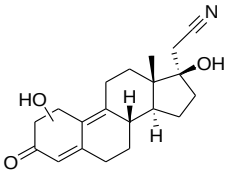 |
| TP 341 a, b | hydroxylation - methylation | $C_{21}H_{27}NO_3$ | 341.1991 | 2a | 6.47, 7.17 | ↗ | 3.8[b] | 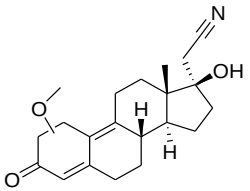 |
| TP 295 a, b | carbonyl group hydrogenation - dehydration | $C_{20}H_{25}NO$ | 295.1936 | 2b | 9.94, 10.64 | ↗ ↘ | 0.7[b] | 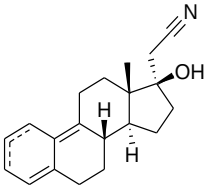 |

| | | | | | | | | |
|---|---|---|---|---|---|---|---|---|
| TP 311 | isomerization | $C_{20}H_{25}NO_2$ | 311.1885 | 2b | 8.77 | ↗ | 3.2[b] | 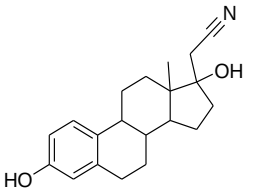 |
| TP 313 | carbonyl group hydrogenation | $C_{20}H_{27}NO_2$ | 313.2042 | 2b | 8.03 | ↗ ↘ | 2.0[b] | 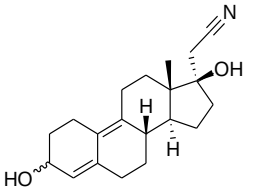 |
| TP 315 | 2X hydrogenation | $C_{20}H_{29}NO_2$ | 315.2198 | 2b | 7.49 | ↗ | 0.5[b] | 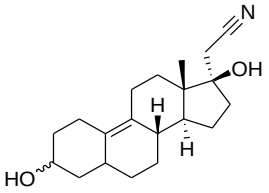 |
| TP 389 | dehydrogenation - sulfation | $C_{20}H_{23}NSO_5$ | 389.1297 | 2b | 5.00 | ↗ | 0.1[b] | 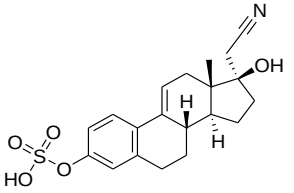 |
| TP 307 a, b, c | aromatization - 2X dehydrogenation | $C_{20}H_{21}NO_2$ | 307.1572 | 3a | 5.98, 6.90, 7.28 | ↗ | 0.6[b] | 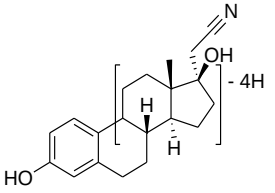 |

| | | | | | | | | |
|---|---|---|---|---|---|---|---|---|
| TP 357 | oxidation | $C_{20}H_{23}NO_5$ | 357.1576 | 3a | 4.87 | ↗ | 0.2[b] | 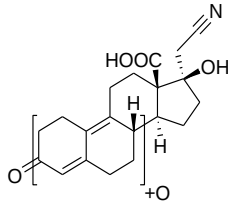 |
| TP 341 c, d | dehydrogenation - oxidation | $C_{20}H_{23}NO_4$ | 341.1627 | 3b | 4.74, 5.69 | ↗ | 0.6[b] | 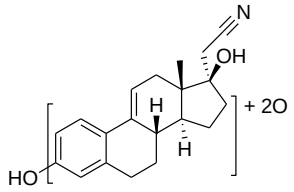 |
| TP 373 | oxidation - methylation | $C_{21}H_{27}NO_5$ | 373.1889 | 3b | 5.77 | ↗ | 0.3[b] | 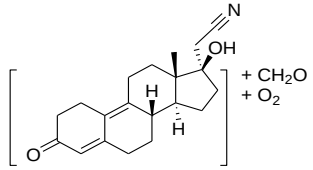 |
| TP 325 a, b, c, d | dehydrogenation - oxidation | $C_{20}H_{23}NO_3$ | 325.1678 | 4 | 4.99, 5.42, 6.27, 7.21 | ↗ | 0.3[b] | - |

[a] Yields quantified with authentic standards as mole product formed ($C_{TP\_t}$) per mole parent consumed ($C_{parent\_t}$ - $C_{parent\_t0}$).

[b] Yields estimated as LC-qTOF-MS peak areas of TPs over peak area decreases of DIE.

**Table S4.5** Characterization details of transformation products (TPs) of DRO observed in 1 mg/L activated sludge bioreactors.

| Name | Proposed pathway | Formula | Theoretical mass | Confidence level | RT (min) | Peak area time trend | Maximum yield (%) | Proposed structure |
|---|---|---|---|---|---|---|---|---|
| DRO | - | $C_{24}H_{30}O_3$ | 366.2195 | 1 | 8.83 | ↘ | - | 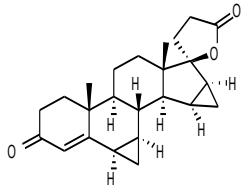 |
| TP 384 | hydration | $C_{24}H_{32}O_4$ | 384.2301 | 1 | 7.72 or 6.75[d] | ↗ | 21[a] | 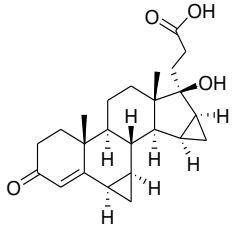 |
| TP 364 | dehydrogenation | $C_{24}H_{28}O_3$ | 364.2038 | 1 | 8.12 | ↗ ↘ | 40[a] | 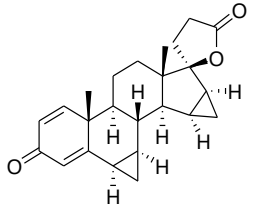 |
| TP 382 c | hydroxylation | $C_{24}H_{30}O_4$ | 382.2144 | 2a | 7.19 | ↗ | 3.3[b] | 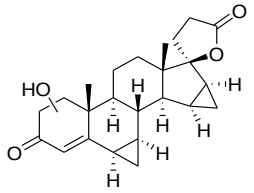 |

| | | | | | | | | |
|---|---|---|---|---|---|---|---|---|
| TP 368 | hydrogenation | $C_{24}H_{32}O_3$ | 368.2351 | 2b | 10.35 | ↗ | 1.8[b] | 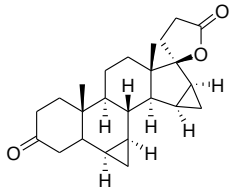 |
| TP 370 a, b | 2X hydrogenation | $C_{24}H_{34}O_3$ | 370.2508 | 2b | 10.02, 11.29 | ↗ | 11[b] | 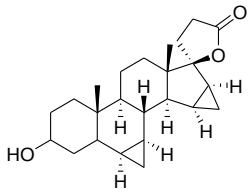 |
| TP 380 | dehydrogenation - hydroxylation | $C_{24}H_{28}O_4$ | 380.1988 | 2b | 6.73 | ↗ | 7.1[b] | 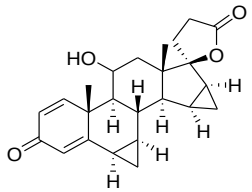 |
| TP 382 b | hydroxylation | $C_{24}H_{30}O_4$ | 382.2144 | 3a | 7.05 | ↗ | 3.3[b] | 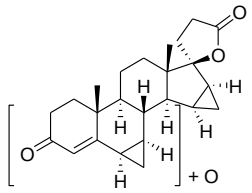 |
| TP 382 d | hydroxylation | $C_{24}H_{30}O_4$ | 382.2144 | 3a | 7.38 | ↗ | 1.4[b] | 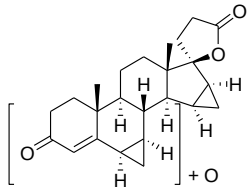 |

| | | | | | | | | |
|---|---|---|---|---|---|---|---|---|
| TP 382 a | hydroxylation | $C_{24}H_{30}O_4$ | 382.2144 | 3b | 6.23 | ↗ | 440[c] | 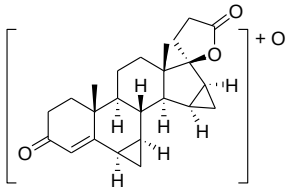 |
| TP 398 | 2X hydroxylation | $C_{24}H_{30}O_5$ | 398.2093 | 3b | 6.68 | ↗ | 88[c] | 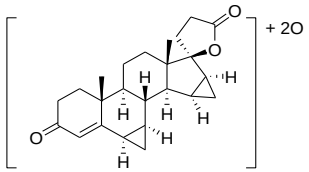 |
| TP 402 | 2X hydration | $C_{24}H_{34}O_5$ | 402.2406 | 3b | 7.71 or 5.65[d] | ↗ | 620[c] | 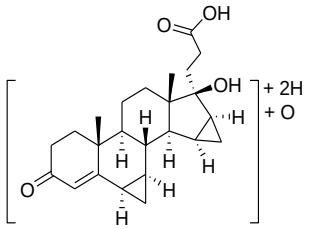 |
| TP 416 | oxidation | $C_{24}H_{32}O_6$ | 416.2199 | 3b | 5.99 | ↗ | 63[c] | 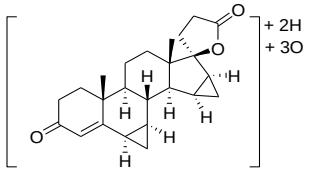 |

[a] Yields quantified with authentic standards as mole product formed ($C_{TP\_t}$) per mole parent consumed ($C_{parent\_t}$ - $C_{parent\_t0}$).

[b] Yields estimated as LC-qTOF-MS peak areas of TPs over peak area decreases of DRO.

[c] Yields estimated based on ESI- peak area. Due to the low ESI- response of DRO, these yields were likely highly overestimated.

[d] Different RTs under ESI+ and ESI- due to ion species difference.

**Table S4.6** Chromatographic and spectral details of DIE, related standards, and TPs.

| **Name:** DIE | **Formula:** $C_{20}H_{25}NO_2$ | **Precursor:** $[M+H]^+$, $[M+Na]^+$, $[M-H]^-$, $[M+F]^-$ | **RT:** 7.00 min | **SPARC log$K_{ow}$:** 3.44 |
|---|---|---|---|---|
| **Structure:** 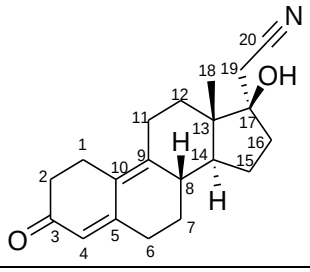 | **Comments:**<br>• Parent compound.<br>• ESI+ diagnostic fragments: 161.0964 ($[C_{11}H_{13}O]^+$), 147.0815 ($[C_{10}H_{11}O]^+$), 135.0804 ($[C_9H_{11}O]^+$), 117.0693 ($[C_9H_9]^+$), 105.0698 ($[C_8H_9]^+$), 91.0540 ($[C_7H_7]^+$), 79.0546 ($[C_6H_7]^+$).<br>• ESI- diagnostic fragment: 173.0971 ($[C_{12}H_{13}O]^-$)<br>• Diagnostic neutral loss: 41.0265 ($C_2H_3N$, evident under lower collision energy). | | | |

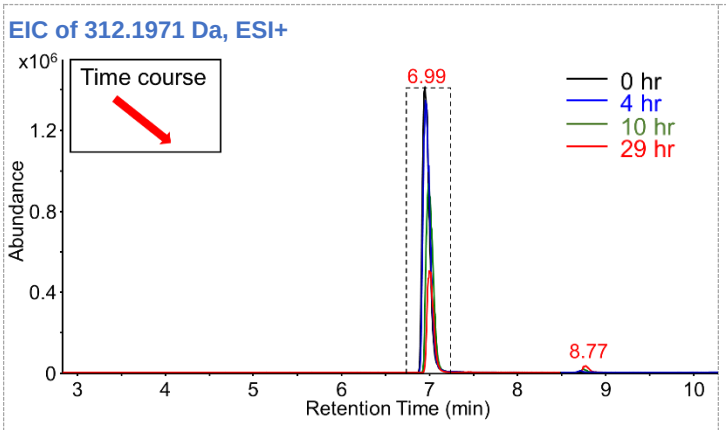


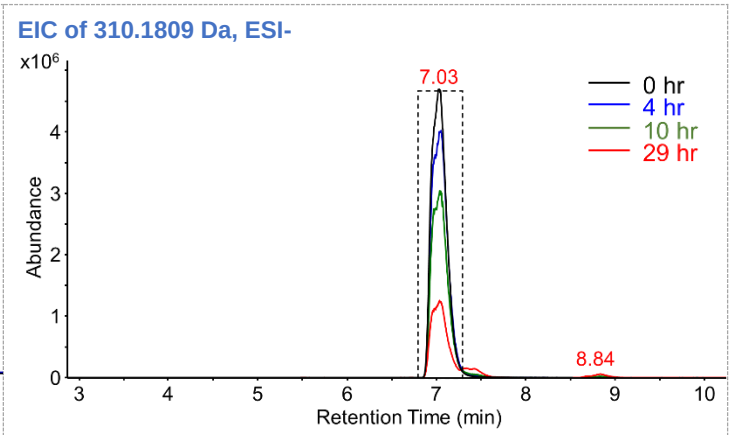


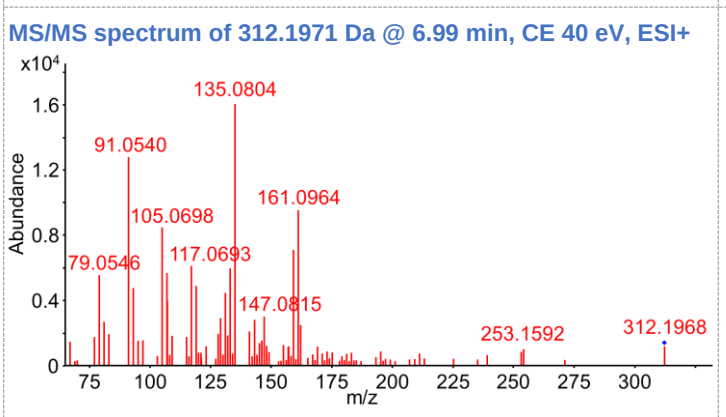


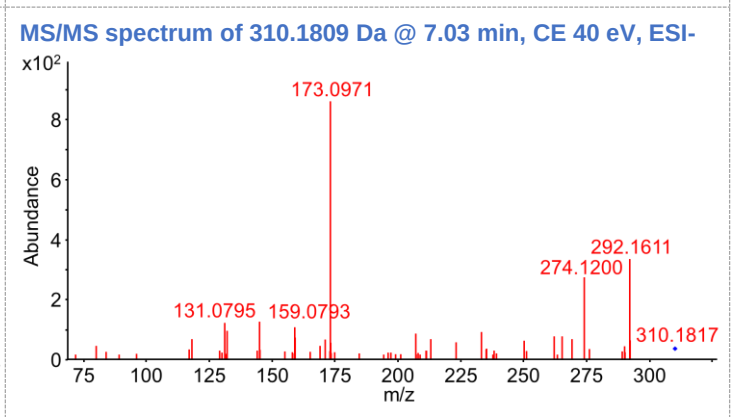


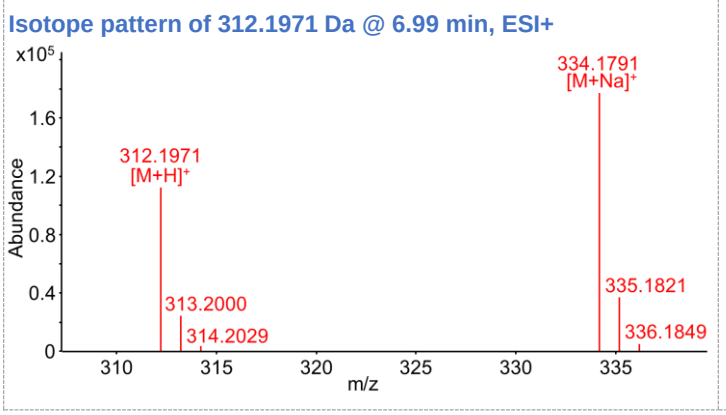


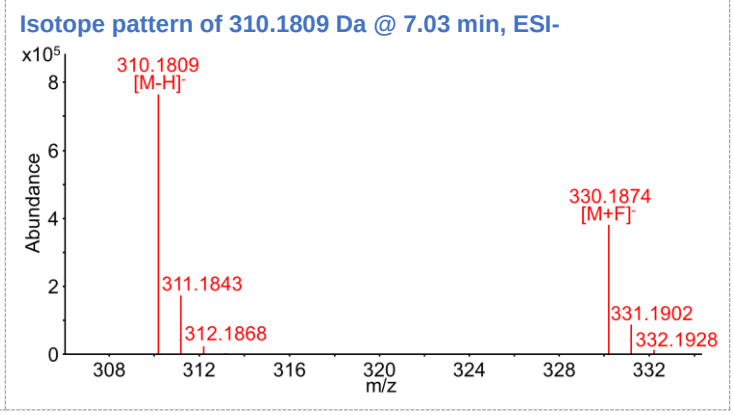

| **Name:** 17α-cyanomethylestra-1, 3,5(10)-triene-3,17β-diol | **Formula:** $C_{20}H_{25}NO_2$ | **Precursor:** $[M+H]^+$ (low), $[M+NH_4]^+$, $[M+Na]^+$, $[M-H]^-$ | **RT:** 7.31 min | **SPARC log$K_{ow}$:** 4.01 | **SPARC pKa:** 10.53 |
|---|---|---|---|---|---|
| **Structure:** 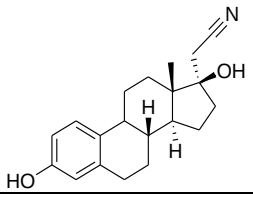 | **Comments:**<br>• DIE metabolite standard.<br>• MS/MS spectrum matches with TP 311. RT does not match. | | | | |

**EIC of 312.1964 Da, ESI+**

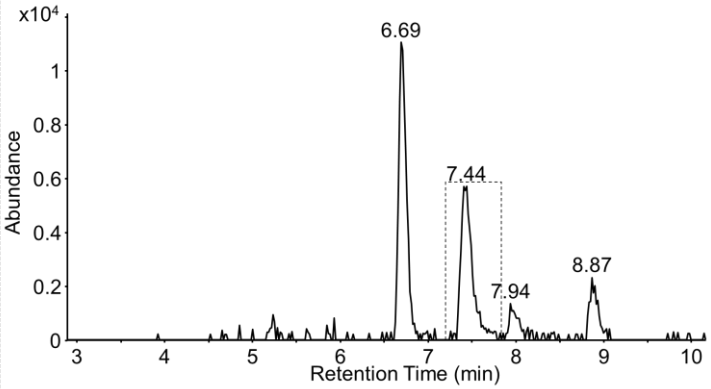


**EIC of 310.1840 Da, ESI-**

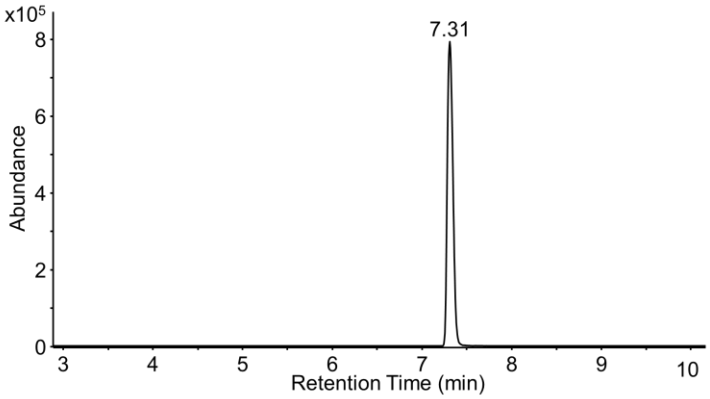


**MS/MS spectrum of 312.1964 Da @ 7.44 min, CE 20 eV, ESI+**

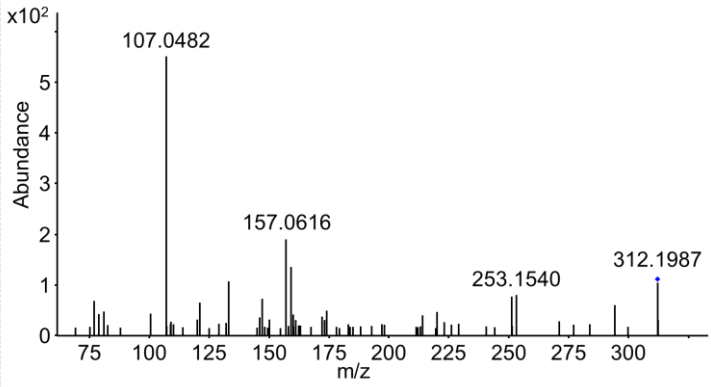


**MS/MS spectrum of 310.1840 Da @ 7.31 min, CE 40 eV, ESI-**

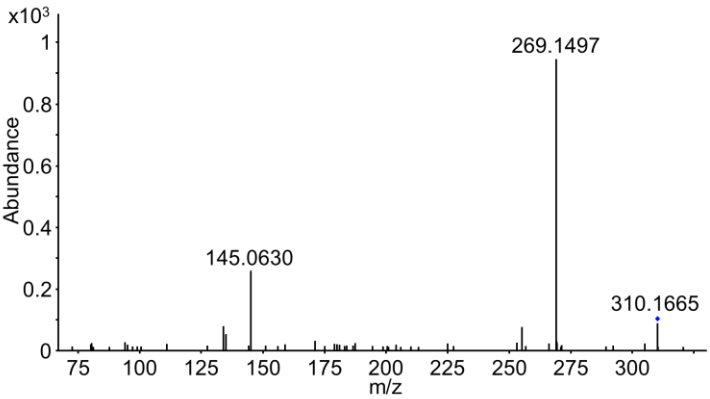


**Isotope pattern of 312.1964 Da @ 7.44 min, ESI+**

**Isotope pattern of 310.1840 Da @ 7.31 min, ESI-**

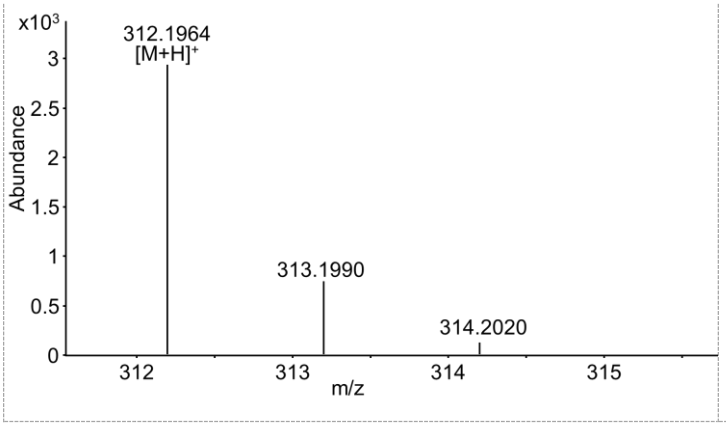
x10^3
312.1964
[M+H]+
313.1990
314.2020
Abundance
m/z
312
313
314
315

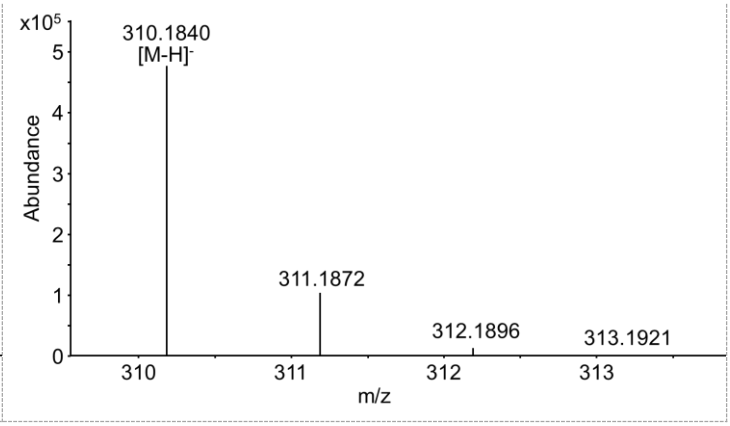
x10^5
310.1840
[M-H]-
311.1872
312.1896
313.1921
Abundance
m/z
310
311
312
313

| **Name:** 9-hydrogenation-dienogest | **Formula:** $C_{20}H_{27}NO_2$ | **Precursor:** $[M+H]^+$, $[M-H]^-$ | **RT:** 7.18 min | **SPARC log$K_{ow}$:** 3.15 |
|---|---|---|---|---|
| **Structure:** 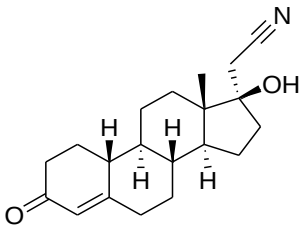 | **Comments:**<br>• DIE metabolite standard.<br>• Does not match TP 313. | | | |



**EIC of 314.2118 Da, ESI+**

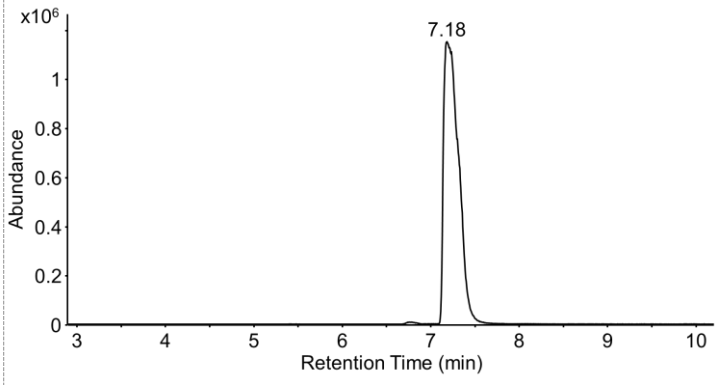


**EIC of 312.1986 Da, ESI-**

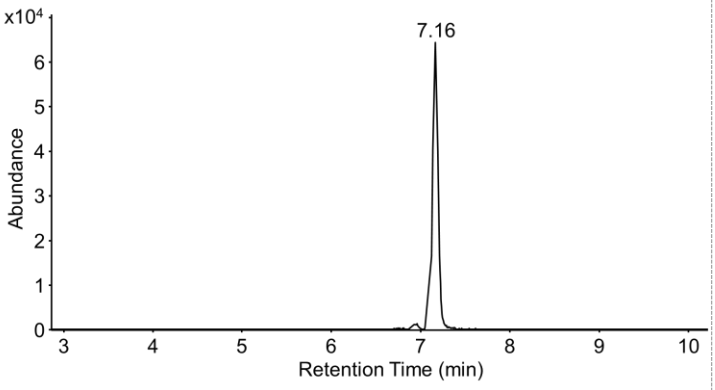


**MS/MS spectrum of 314.2118 Da @ 7.18 min, CE 20 eV, ESI+**

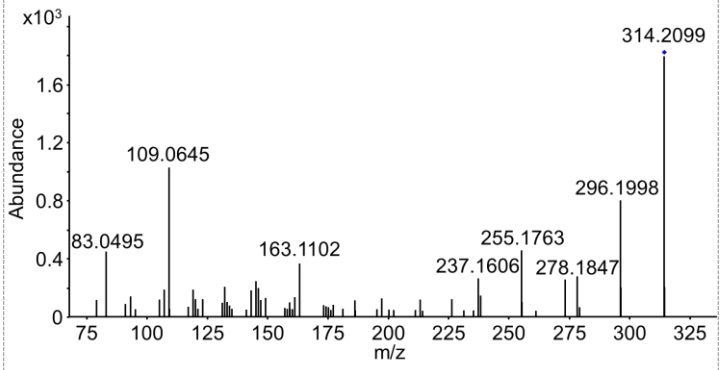


**MS/MS spectrum of 312.1986 Da @ 7.16 min, CE 40 eV, ESI-**

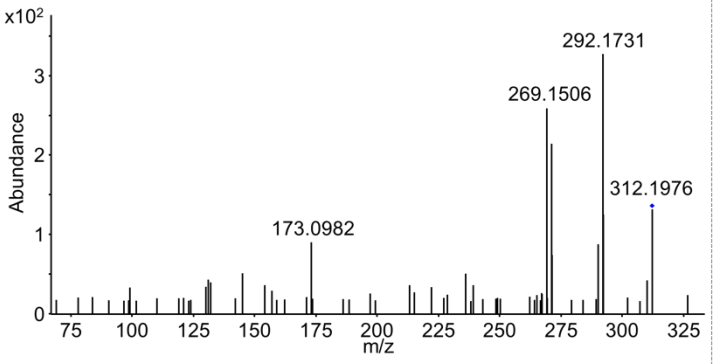


**Isotope pattern of 314.2118 Da @ 7.18 min, ESI+**

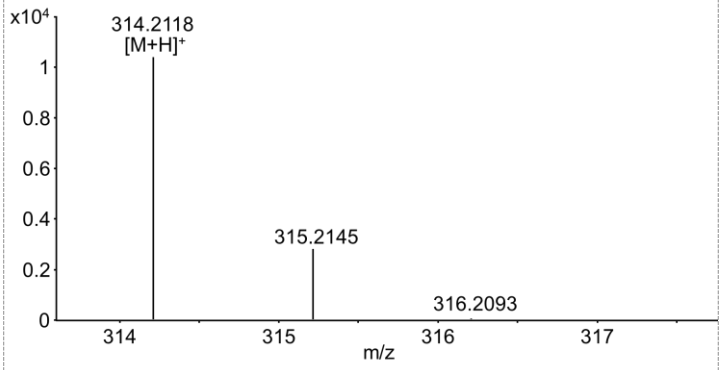


**Isotope pattern of 312.1986 Da @ 7.16 min, ESI-**

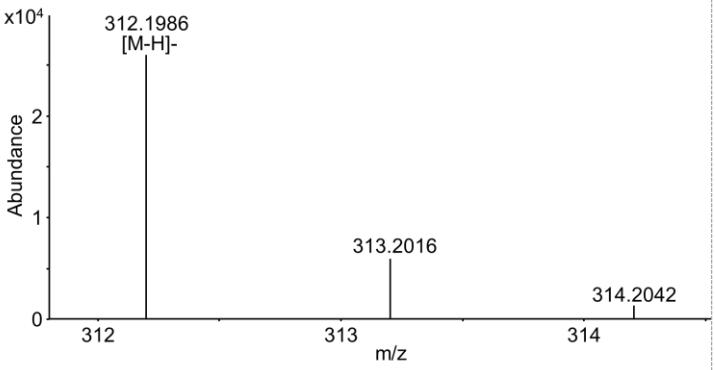

| **Name:** 11-OH-dienogest | **Formula:** $C_{20}H_{25}NO_3$ | **Precursor:** $[M+H]^+$, $[M-H]^-$ | **RT:** 5.45 min | **SPARC log$K_{ow}$:** 1.58 |
|---|---|---|---|---|
| **Structure:** 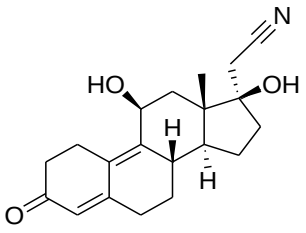 | **Comments:**<br>• DIE metabolite standard.<br>• Does not match TP 327. | | | |



**EIC of 328.1913 Da, ESI+**

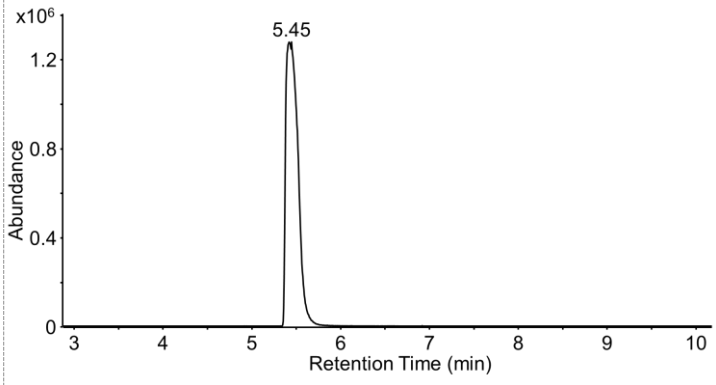


**EIC of 326.1782 Da, ESI-**

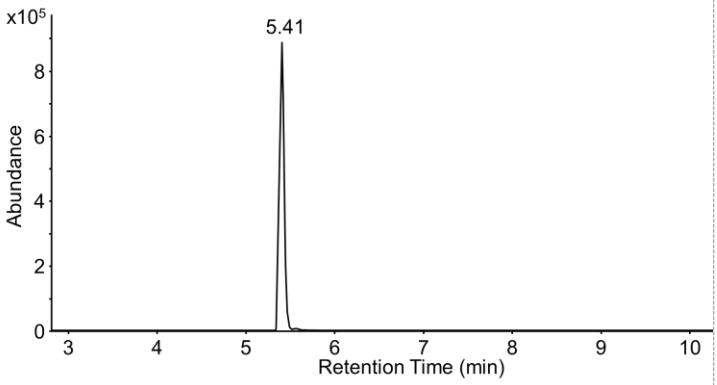


**MS/MS spectrum of 328.1913 Da @ 5.45 min, CE 30 eV, ESI+**

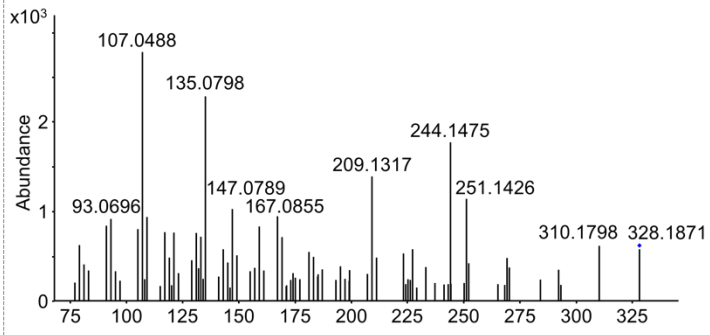


**MS/MS spectrum of 326.1782 Da @ 5.41 min, CE 40 eV, ESI-**

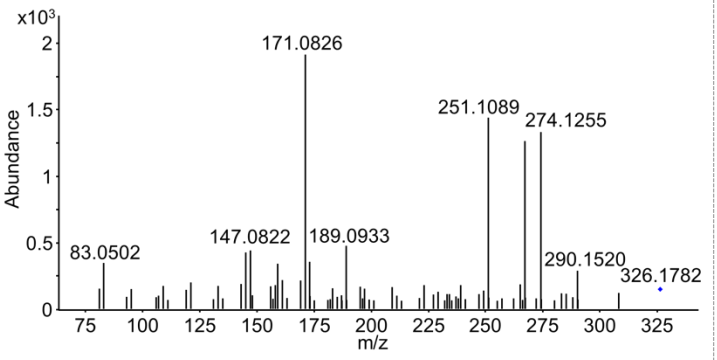


**Isotope pattern of 328.1913 Da @ 5.45 min, ESI+**

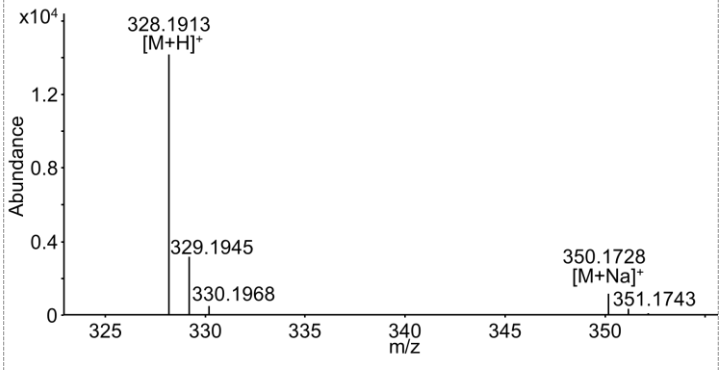


**Isotope pattern of 326.1782 Da @ 5.41 min, ESI-**

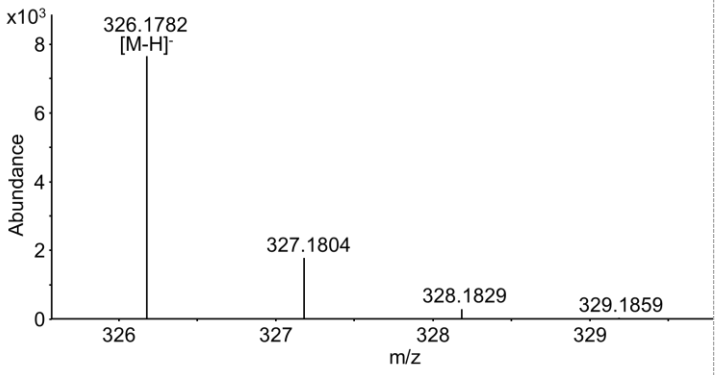

| **Name:** 6-OH-dienogest | **Formula:** $C_{20}H_{25}NO_3$ | **Precursor:** $[M+H]^+$, $[M-H]^-$ | **RT:** 5.41 min | **SPARC log$K_{ow}$:** 1.58 |
|---|---|---|---|---|
| **Structure:** 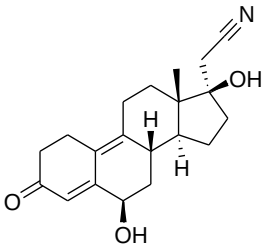 | **Comments:**<br>• DIE metabolite standard.<br>• Does not match TP 327. | | | |

**EIC of 328.1917 Da, ESI+**

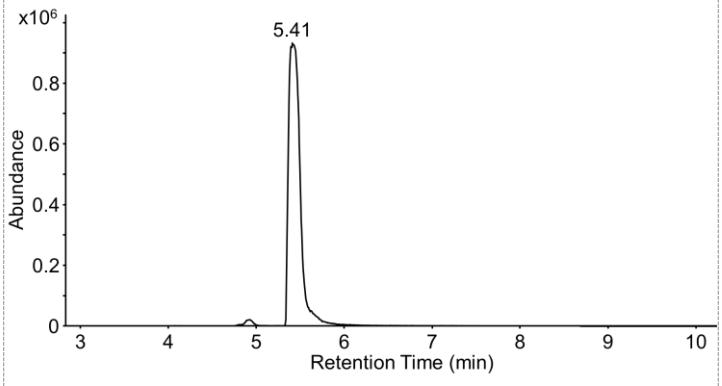


**EIC of 326.1768 Da, ESI-**

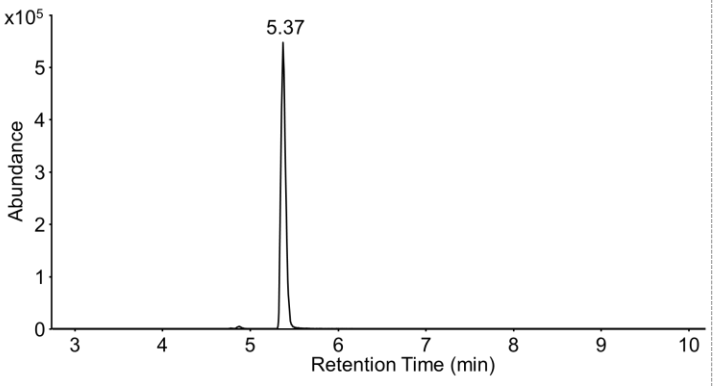


**MS/MS spectrum of 328.1917 Da @ 5.41 min, CE 30 eV, ESI+**

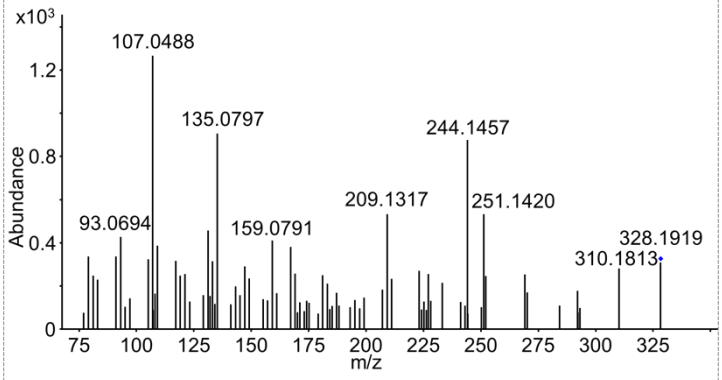


**MS/MS spectrum of 326.1768 Da @ 5.37 min, CE 40 eV, ESI-**

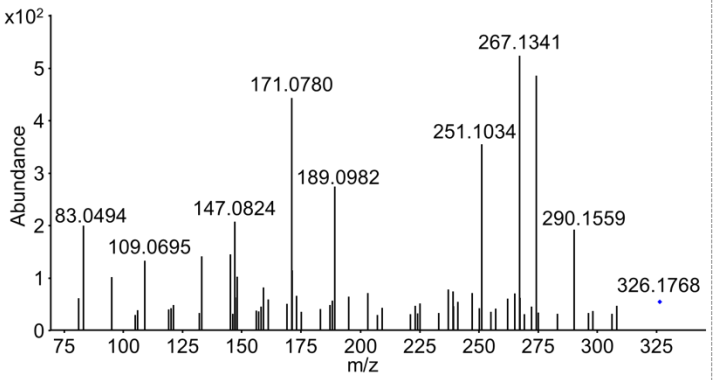


**Isotope pattern of 328.1917 Da @ 5.41 min, ESI+**

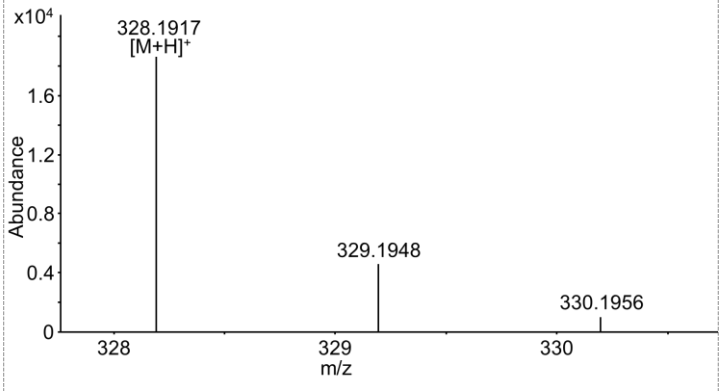


**Isotope pattern of 326.1768 Da @ 5.37 min, ESI-**

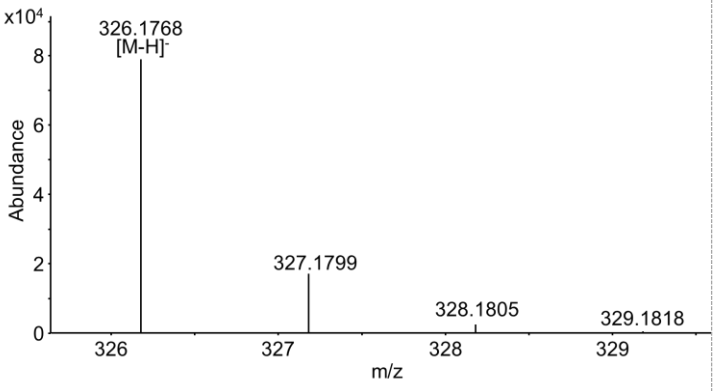

| Name: | Confidence level: | Formula: | Precursor: | RT shift: | Atomic Modification: | SPARC $\log K_{ow}$: | SPARC pKa: |
|---|---|---|---|---|---|---|---|
| TP 309 | 1 | $C_{20}H_{23}NO_2$ | $[M+H]^+$, $[M-H]^-$ | +0.2 min | -2H | 4.03 | 9.99 |

**Structure:**

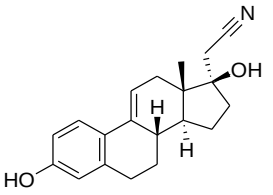


**Comments:**

- Major TP of DIE (yield: 55% at 29 h).
- 100X higher response in ESI- than ESI+.
- Diagnostic fragment ions of aromatic A-ring under ESI+ (m/z 133, 157, 159) (Bourcier et al., 2010).
- Reported as DIE metabolite *in vitro* in rat liver microsome, *in vivo* in dog, rat, and rabbit, and in microbial cultures (Hobe et al., 1983b, 1983a, 1982; Schubert et al., 1983).

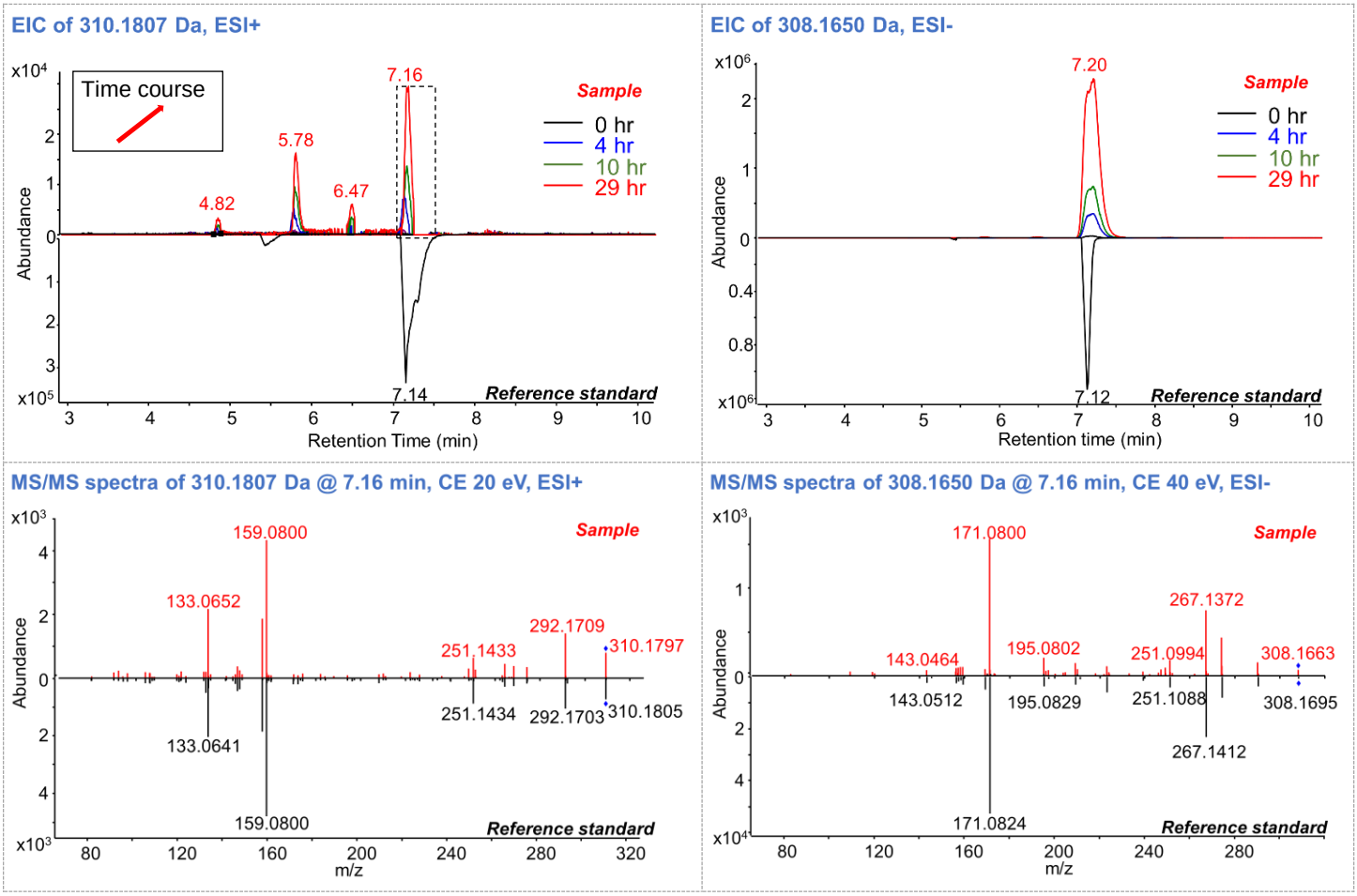

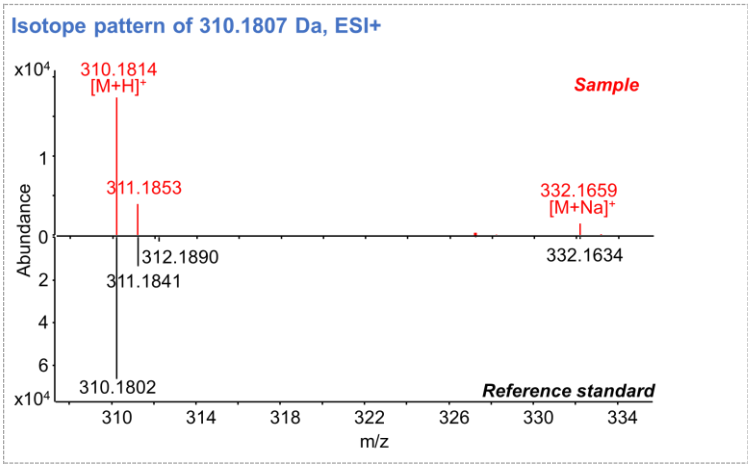
Isotope pattern of 310.1807 Da, ESI+
x10⁴
310.1814
[M+H]⁺
Sample
311.1853
332.1659
[M+Na]⁺
Abundance
312.1890
311.1841
332.1634
310.1802
Reference standard
m/z

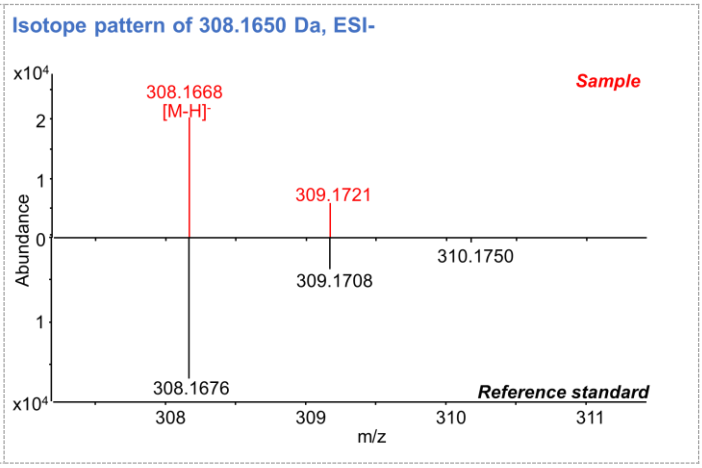
Isotope pattern of 308.1650 Da, ESI-
x10⁴
308.1668
[M-H]⁻
Sample
309.1721
Abundance
310.1750
309.1708
308.1676
Reference standard
m/z

| **Name:** TP 295a | **Confidence level:** 2b | **Formula:** $C_{20}H_{25}NO$ | **Precursor:** $[M+H]^+$ | **RT shift:** +2.9 min | **Atomic Modification:** -O | **SPARC log$K_{ow}$:** 2,4,9(10)-triene: 4.48<br>1,4,9(10)-triene: 4.51 |
|---|---|---|---|---|---|---|
| **Structure:** 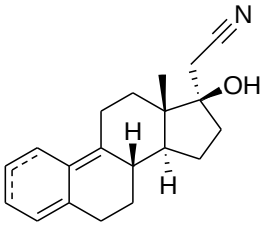 | **Comments:**<br>• m/z of characteristic MS/MS fragments equal to those of DIE minus O (91.0543, $[C_7H_7]^+$, = 107-16; 119.0851, $[C_{11}H_{13}]^+$, = 135-16; 145.1014, $[C_{11}H_{13}]^+$, = 161-16).<br>• $[M+H]^+$ as the dominant precursor.<br>• Backward RT shift consistent with log$K_{ow}$ prediction.<br>• Therefore, the TP was tentatively proposed as carbonyl deoxygenation product. | | | | | |

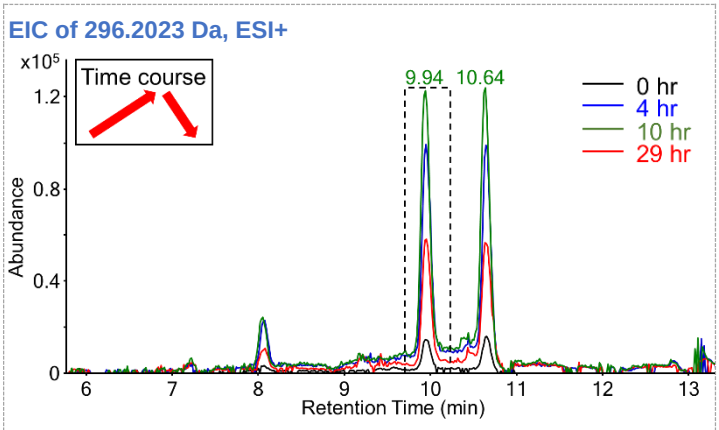


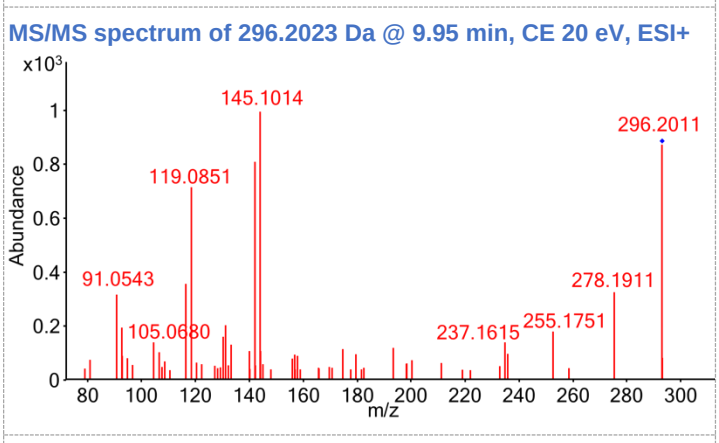


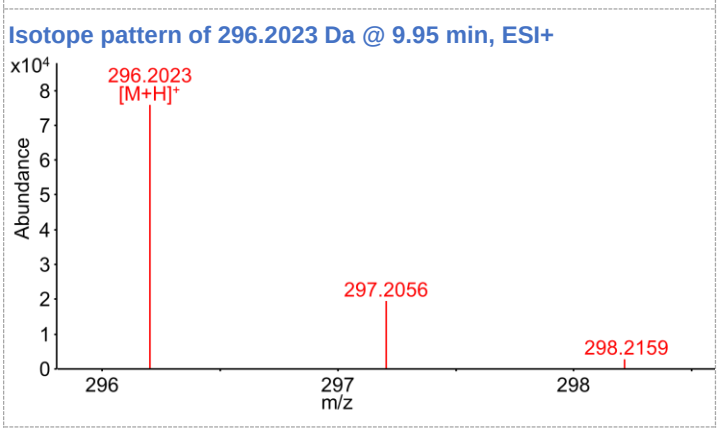

| Name: TP 295b | Confidence level: 2b | Formula: $C_{20}H_{25}NO$ | Precursor: $[M+H]^+$ | RT shift: +3.6 min | Atomic Modification: -O | SPARC log$K_{ow}$: 2,4,9(10)-triene: 4.48<br>1,4,9(10)-triene: 4.51 |
|---|---|---|---|---|---|---|
| **Structure:** 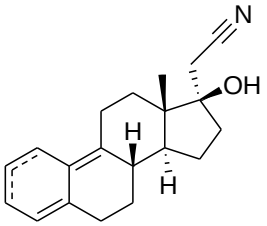 | **Comments:**<br>• Same MS/MS spectrum, different RT with TP 295a | | | | | |



**EIC of 296.2023 Da, ESI+**

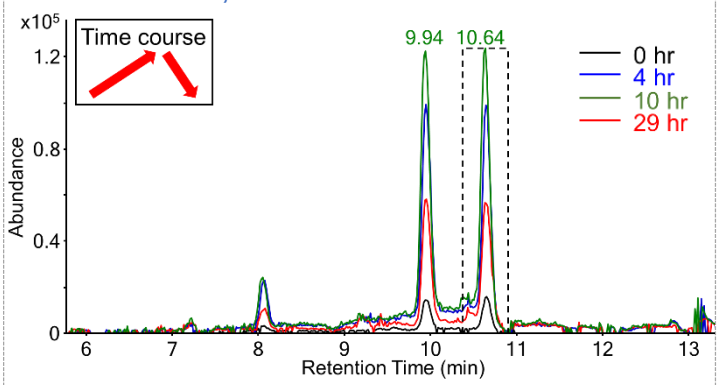


**MS/MS spectrum of 296.2023 Da @ 10.64 min, CE 20 eV, ESI+**

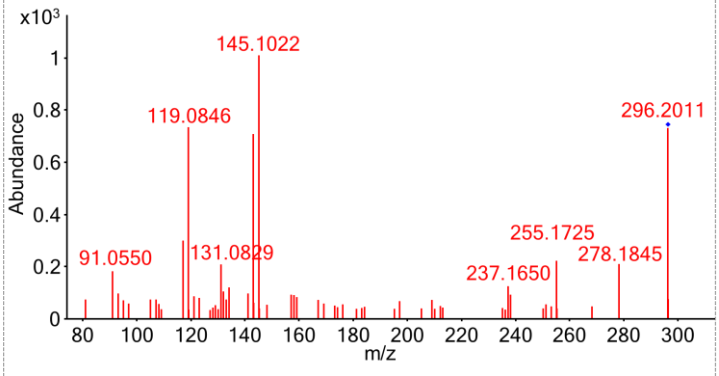


**Isotope pattern of 296.2023 Da @ 10.64 min, ESI+**

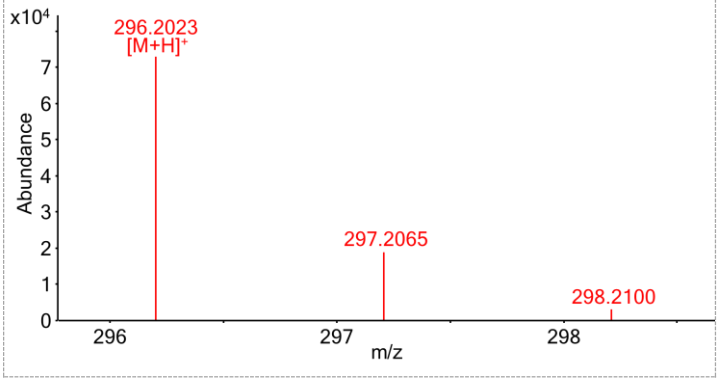

| **Name:** TP 307a | **Confidence level:** 3a | **Formula:** $C_{20}H_{21}NO_2$ | **Precursor:** $[M-H]^-$ | **RT shift:** -1.0 min | **Atomic Modification:** -4H |
|---|---|---|---|---|---|
| **Structure:** 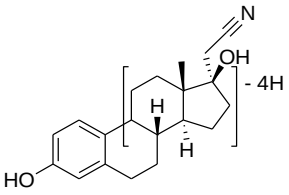 | **Comments:**<br>• No response in ESI+, indicating aromatic A-ring structure.<br>• m/z of characteristic MS/MS fragments equal to those of TP 309 (195.0817, $[C_{14}H_{11}O_2]^-$; 209.0965, $[C_{15}H_{13}O]^-$), or those of TP 309 minus 2H (221.0978, $[C_{16}H_{13}O]^-$, = 223-2; 237.1270, $[C_{17}H_{17}O]^-$, = 239-2; 249.0893, $[C_{17}H_{13}O_2]^-$, = 251-2; 265.1280, $[C_{18}H_{17}O_2]^-$, = 267-2).<br>• Unlike TP 309, fragments with m/z > 195 have much higher response than fragments with m/z < 195, indicating stable conjugated A, B, C rings.<br>• Therefore, the two dehydrogenation sites are tentatively assigned to C-ring and D-ring. | | | | |

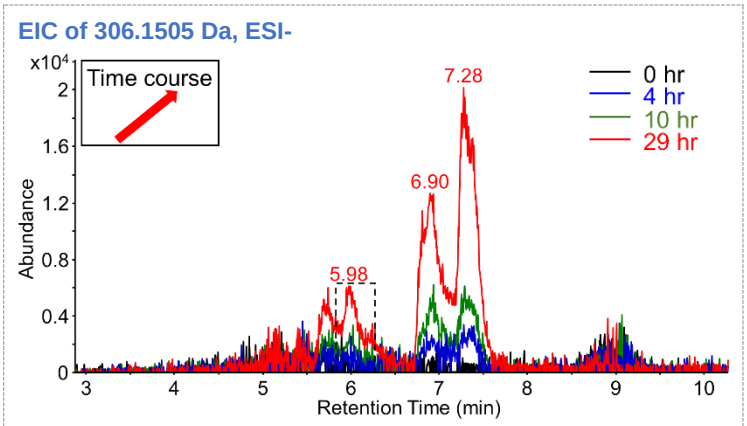


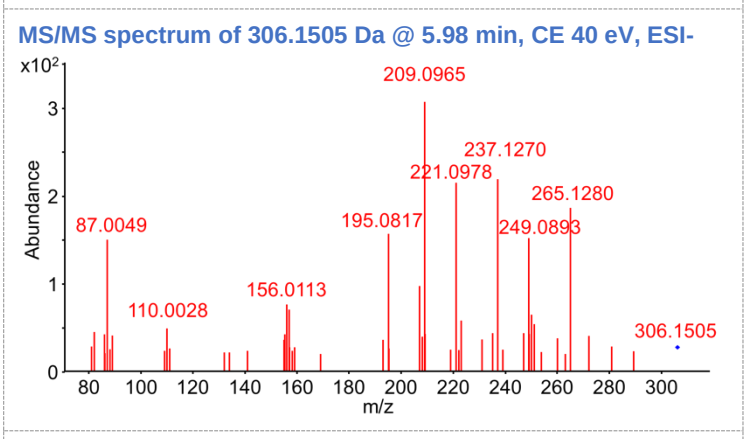


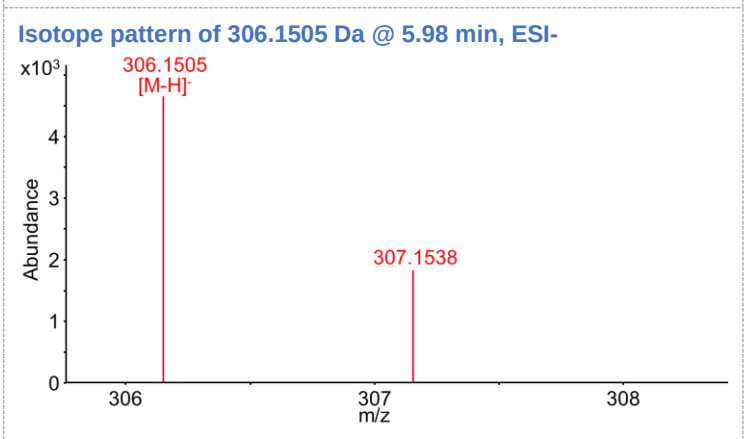

| **Name:** TP 307b | **Confidence level:** 3a | **Formula:** $C_{20}H_{21}NO_2$ | **Precursor:** $[M-H]^-$ | **RT shift:** -0.1 min | **Atomic Modification:** -4H |
|---|---|---|---|---|---|
| **Structure:** 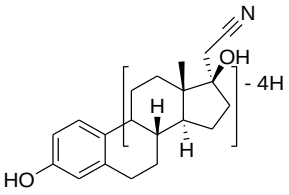 | **Comments:**<br>• 2X dehydrogenation TP.<br>• No response in ESI+, indicating aromatic A-ring structure.<br>• Stable 265.1233 ($[C_{18}H_{17}O_2]^-$) fragment, indicating stable conjugated A, B, C, D rings.<br>• Therefore, the two dehydrogenation sites are tentatively assigned to C-ring and D-ring. | | | | |

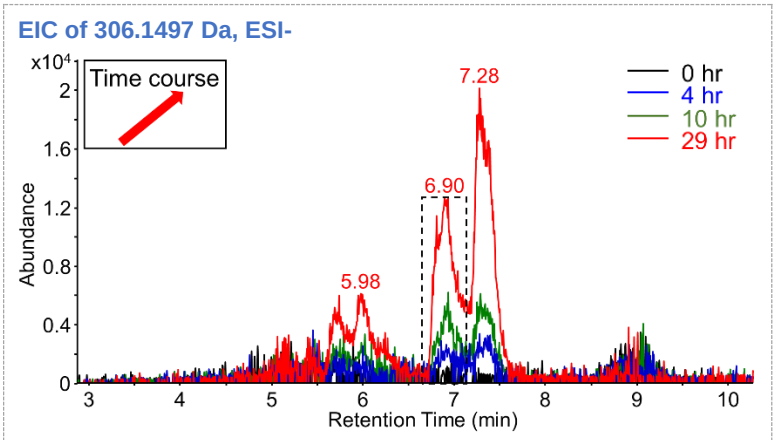


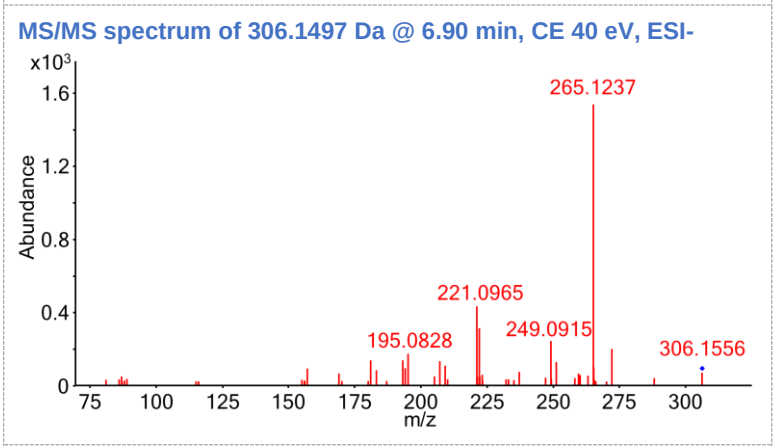


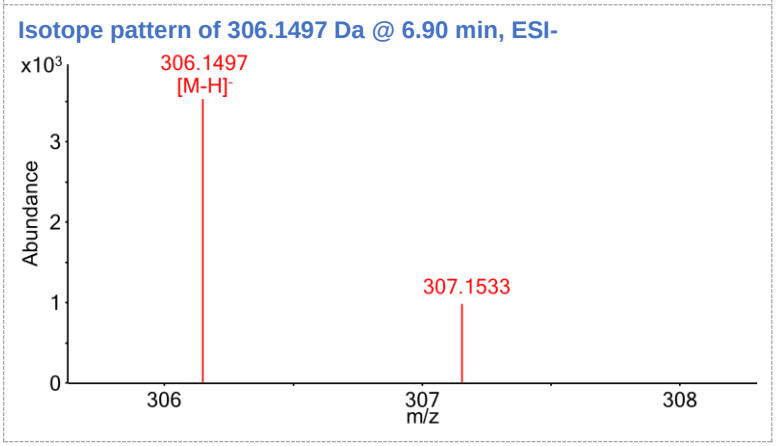

| **Name:** TP 307c | **Confidence level:** 3a | **Formula:** $C_{20}H_{21}NO_2$ | **Precursor:** $[M-H]^-$ | **RT shift:** +0.3 min | **Atomic Modification:** -4H |
|---|---|---|---|---|---|
| **Structure:** 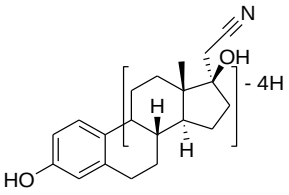 | **Comments:**<br>• Same MS/MS spectrum, different RT with TP 307a. | | | | |



**EIC of 306.1491 Da, ESI-**

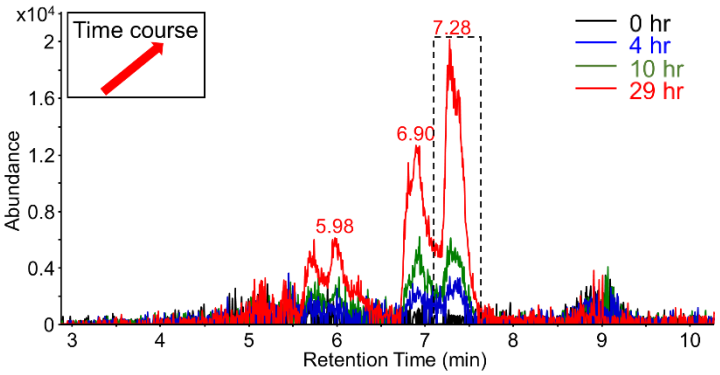


**MS/MS spectrum of 306.1491 Da @ 7.28 min, CE 40 eV, ESI-**

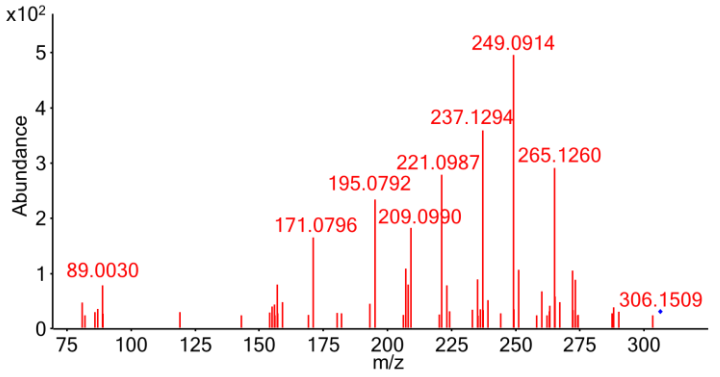


**Isotope pattern of 306.1491 Da @ 7.28 min, ESI-**

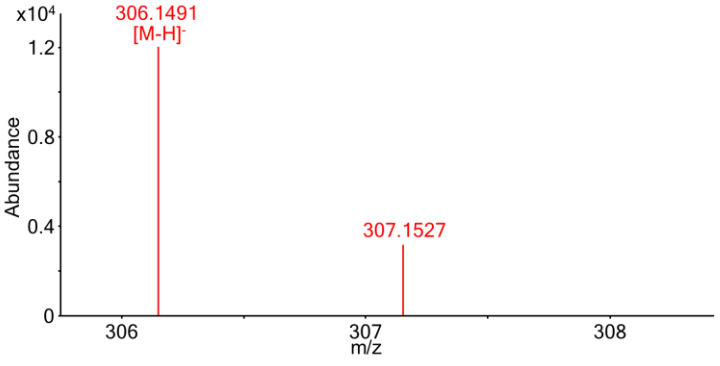

| **Name:** TP 311 | **Confidence level:** 2b | **Formula:** $C_{20}H_{25}NO_2$ | **Precursor:** $[M+H]^+$ (low), $[M+NH_4]^+$, $[M+Na]^+$, $[M-H]^-$ | **RT shift:** +1.7 min | **Atomic Modification:** none | **SPARC $logK_{ow}$:** 4.01 | **SPARC pKa:** 10.53 |
|---|---|---|---|---|---|---|---|

**Structure:**

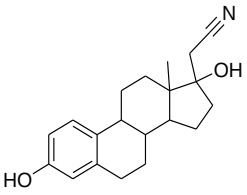


**Comments:**

- Isomerization TP, MS/MS spectra similar with aromatic estrogens such as 17α-ethynylestradiol (EE2) and estrone, with characteristic fragments of 107, 133, 157, 159 under ESI+, and 145 under ESI- (Bourcier et al., 2010; *mzCloud* database; Zheng et al., 2019).
- $[M+NH_4]^+$ and $[M+Na]^+$ as dominant ESI+ precursors, consistent with that for EE2 (*mzCloud* database).
- Backward RT shift consistent with $logK_{ow}$ and literature (Hobe et al., 1989).
- Standard of 17α-cyanomethylestra-1,3,5(10)-triene-3,17β-diol showed identical MS/MS spectra but different RT, indicating configuration difference.
- A-ring aromatized isomerization TP reported as DIE metabolites in microbial transformation and in rabbit (Hobe et al., 1989, 1982; Schubert et al., 1983).

**EIC of 312.1958 Da, ESI+**

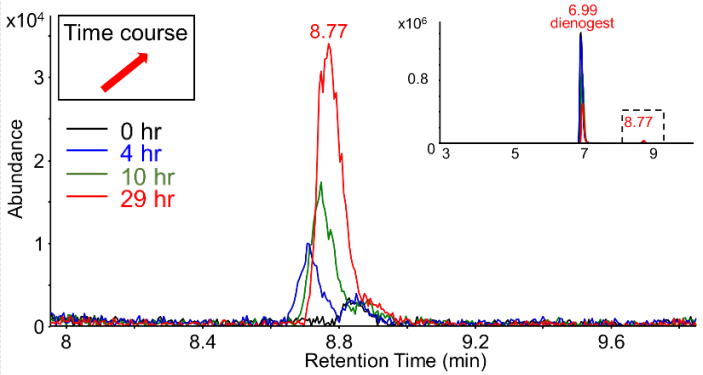


**EIC of 310.1813 Da, ESI-**

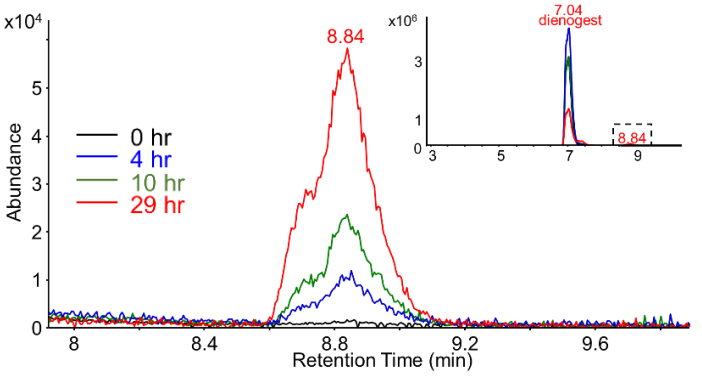


**MS/MS spectrum of 312.1958 Da @ 8.77 min, CE 20 eV, ESI+**

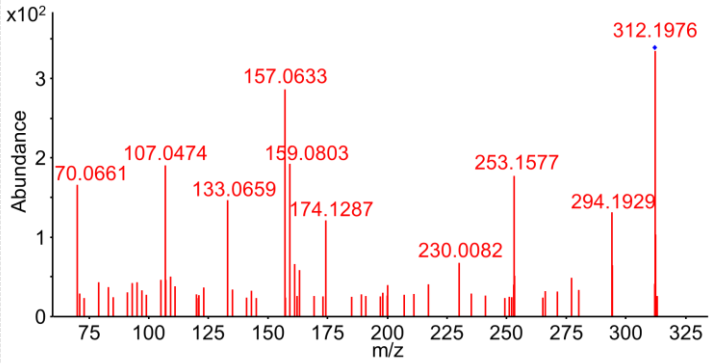


**MS/MS spectrum of 310.1813 Da @ 8.84 min, CE 40 eV, ESI-**

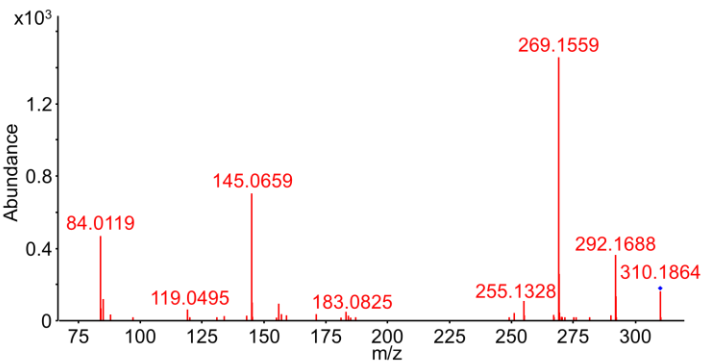


**Isotope pattern of 312.1958 Da @ 8.77 min, ESI+**

**Isotope pattern of 310.1813 Da @ 8.84 min, ESI-**

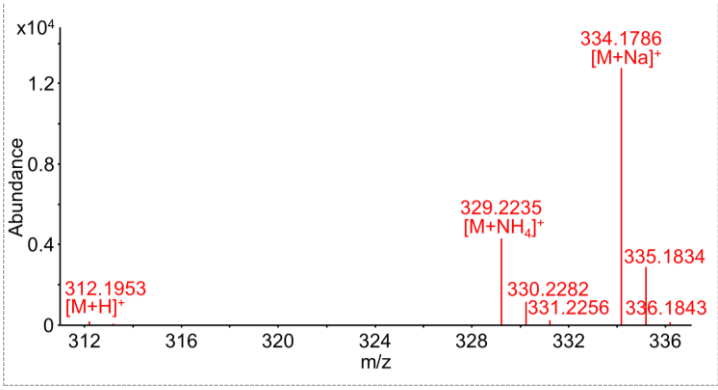
x10^4
1.2
0.8
0.4
0
Abundance
312.1953
[M+H]+
329.2235
[M+NH4]+
330.2282
331.2256
334.1786
[M+Na]+
335.1834
336.1843
312
316
320
324
328
332
336
m/z

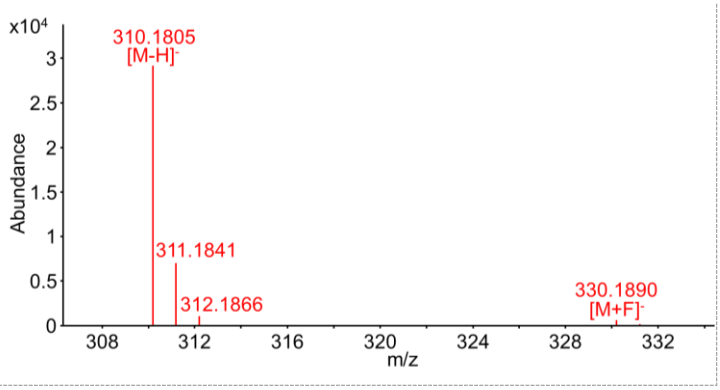
x10^4
3
2.5
2
1.5
1
0.5
0
Abundance
310.1805
[M-H]-
311.1841
312.1866
330.1890
[M+F]-
308
312
316
320
324
328
332
m/z

| Name: TP 313 | Confidence level: 2b | Formula: $C_{20}H_{27}NO_2$ | Precursor: $[M-H_2O+H]^+$, $[M+Na]^+$ | RT shift: +1.0 min | Atomic Modification: +2H | SPARC $logK_{ow}$: 3.21 |
|---|---|---|---|---|---|---|

**Structure:**

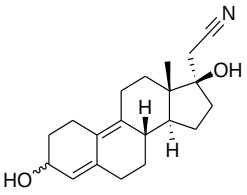


**Comments:**

- Hydrogenation TP.
- The hydrogenation site is not C9(10) based on the standard (see DIE section).
- m/z of characteristic MS/MS fragments equal to those of dienogest -O (91.0529, $[C_7H_7]^+$, = 107-16; 119.0864, $[C_9H_{11}]^+$, = 135-16; 145.1019, $[C_{11}H_{13}]^+$, = 161-16).
- $[M-H_2O+H]^+$ as the dominant precursor, low ESI- response, consistent with other steroids with OH group in C3 (Pozo et al., 2008).
- Backward RT shift consistent with literature (Hobe et al., 1989).
- Carbonyl hydrogenation TP reported as DIE metabolites in microbial transformation and in rabbit (Hobe et al., 1998, 1989; Schubert et al., 1983).
- Therefore, the TP was proposed as carbonyl hydrogenation product.

**EIC of 296.2009 Da, ESI+**

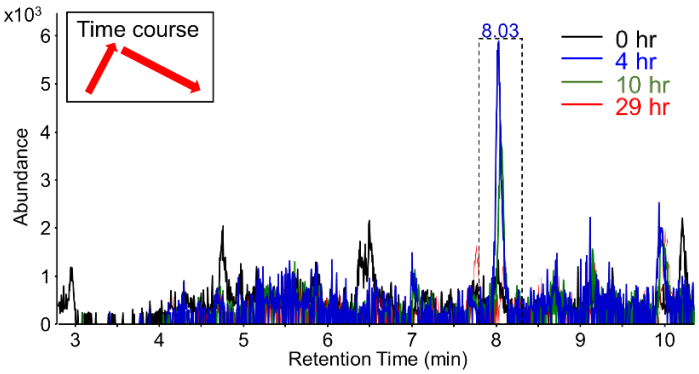


**MS/MS spectrum of 296.2009 Da @ 8.03 min, CE 20 eV, ESI+**

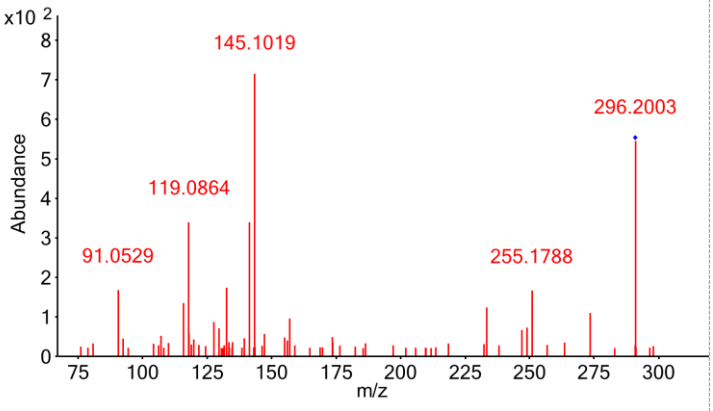


**Isotope pattern of 296.2009 Da @ 8.03 min, ESI+**

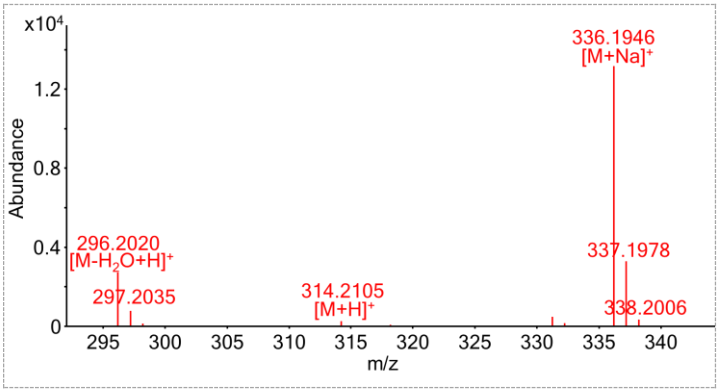
x10^4
1.2
0.8
0.4
0
Abundance
336.1946
[M+Na]+
296.2020
[M-H2O+H]+
297.2035
314.2105
[M+H]+
337.1978
338.2006
295
300
305
310
315
320
325
330
335
340
m/z

| Name: TP 315 | Confidence level: 2b | Formula: $C_{20}H_{29}NO_2$ | Precursor: $[M+F]^-$ | RT shift: +0.4 min | Atomic Modification: +4H | SPARC $logK_{ow}$: 3.07 |
|---|---|---|---|---|---|---|
| **Structure:** 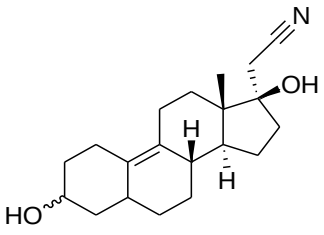  | **Comments:**<br>• No $[M+H]^+$ or $[M-H]^-$, only $[M+F]^-$ is observed.<br>• Ionization behavior consistent with previous reports for 3-OH sterol, where ESI ionization was ineffective and mobile phase anion facilitated ESI- ionization (Liebisch et al., 2006; Rannulu and Cole, 2012).<br>• 9-en-3,17-diol TP reported as DIE metabolites in microbial transformation (Schubert et al., 1983) and in rabbit (Hobe et al., 1998, 1989).<br>• Backward RT shift inconsistent with $logK_{ow}$ prediction but consistent with literature (Hobe et al., 1989).<br>• Therefore, hydrogenation is proposed to happen on C3 carbonyl and C4 double bond. | | | | | |

**EIC of 334.2170 Da, ESI-**

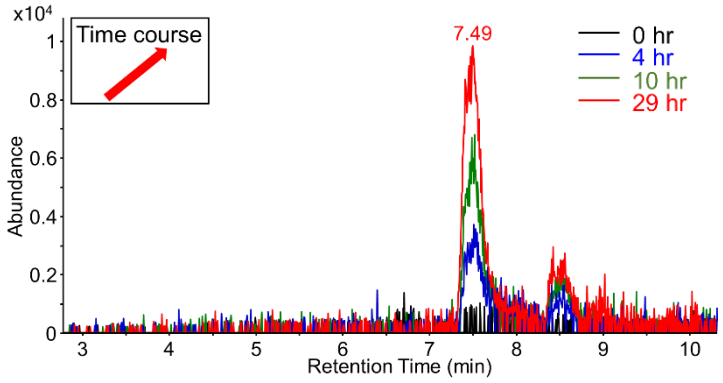


**MS/MS spectrum of 334.2170 Da @ 7.49 min, CE 20 eV, ESI-**

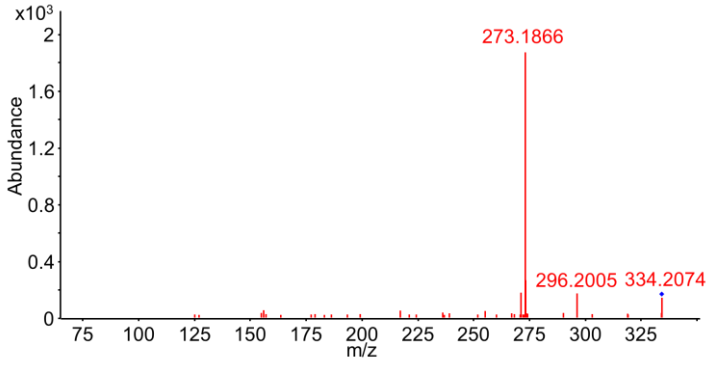


**Isotope pattern of 334.2170 Da @ 7.49 min, ESI-**

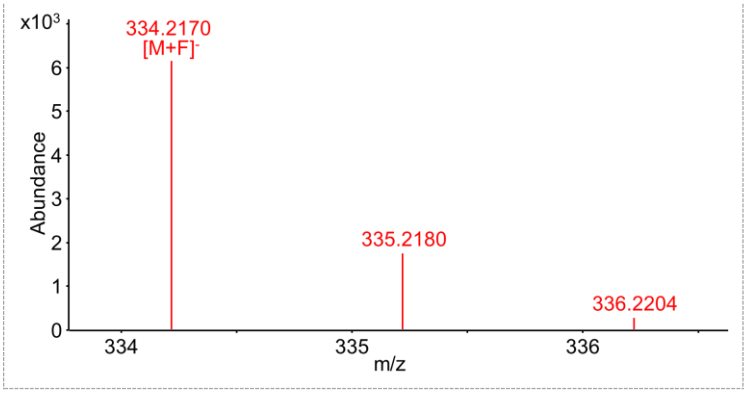
x10^3
334.2170
[M+F]-
335.2180
336.2204
Abundance
m/z
334
335
336
0
1
2
3
4
5
6

| Name: | Confidence level: | Formula: | Precursor: | RT shift: | Atomic Modification: |
|---|---|---|---|---|---|
| TP 325a-d | 4 | $C_{20}H_{23}NO_3$ | $[M-H]^-$, $[M+F]^-$ | -2.0, -1.6, -0.7, +0.2 min | -2H+O |

**Comments:**

- MS/MS spectrum not available due to low response.
- $C_{20}H_{23}NO_3$ was observed as DIE metabolite in rabbit, which was proposed to be hydroxylated-TP 309 (Hobe et al., 1989).
- RT differences between TP 309 and TP 325s generally match those between DIE and TP 327s (hydroxylated-dienogest).

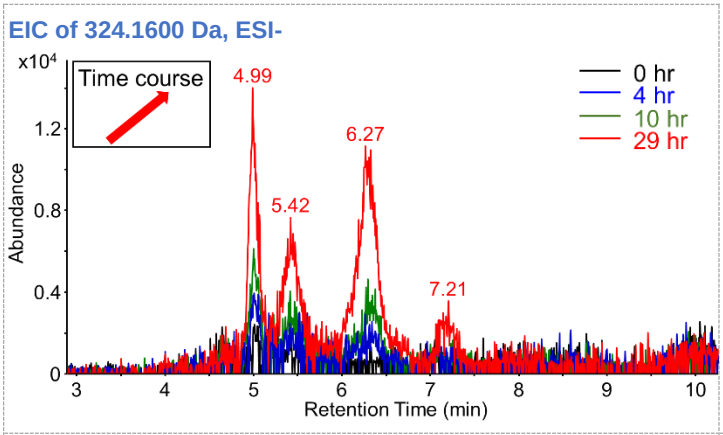


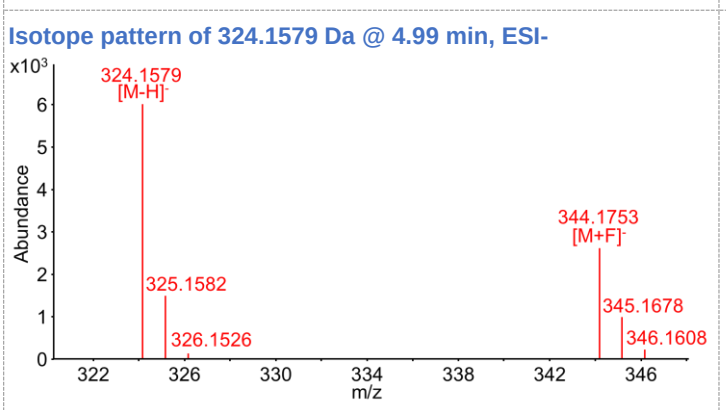


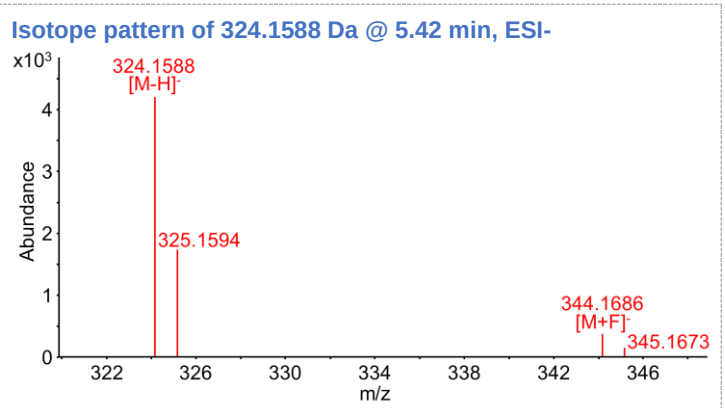


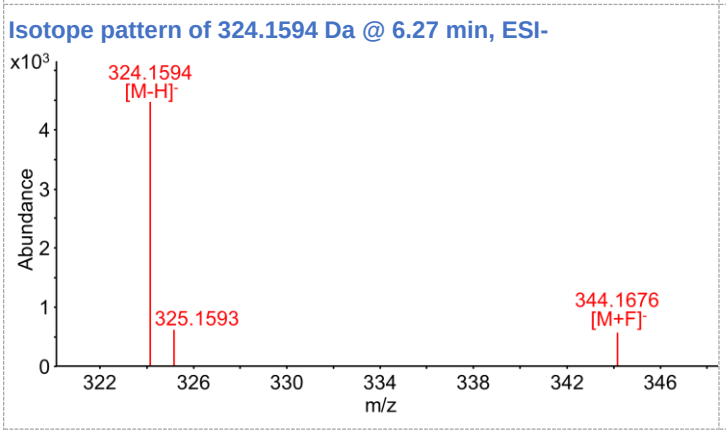


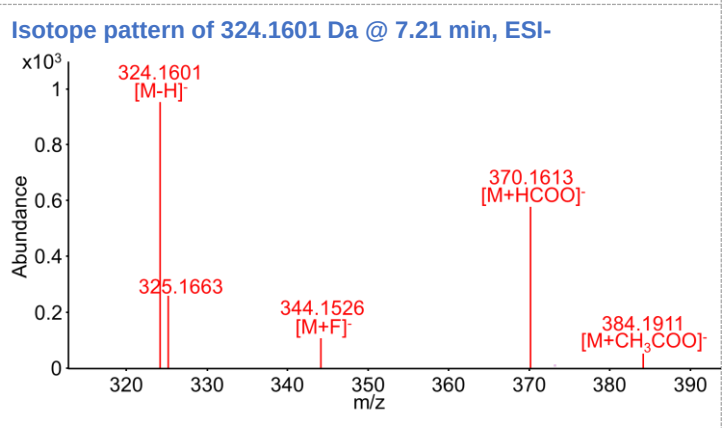

| Name: TP 327a | Confidence level: 2a | Formula: $C_{20}H_{25}NO_3$ | Precursor: $[M-H_2O+H]^+$, $[M+Na]^+$, $[M-H]^-$ | RT shift: -2.1 min | Atomic Modification: +O | SPARC log$K_{ow}$: 1-OH: 1.58; 2-OH: 2.36 |
|---|---|---|---|---|---|---|

**Structure:**

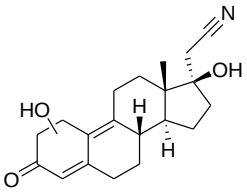


**Comments:**

- RT and MS/MS spectra different from those of 6-OH-DIE and 11-OH-DIE (see DIE section).
- MS/MS spectra resemble A-ring aromatized TP 309.
- C1 and C2 hydroxylation products have been reported as DIE metabolite (Schubert et al., 1983).
- Therefore, hydroxylation site is assigned to C1 or C2 for TP 327s.

**EIC of 310.1820 Da, ESI+**

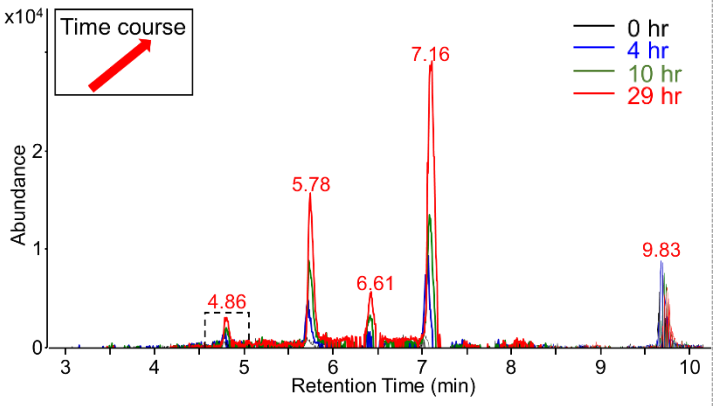


**EIC of 326.1757 Da, ESI-**

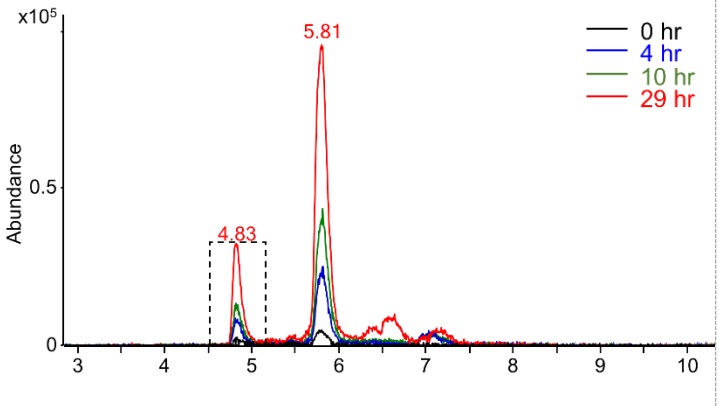


**MS/MS spectrum of 310.1820 Da @ 4.86 min, CE 20 eV, ESI+**

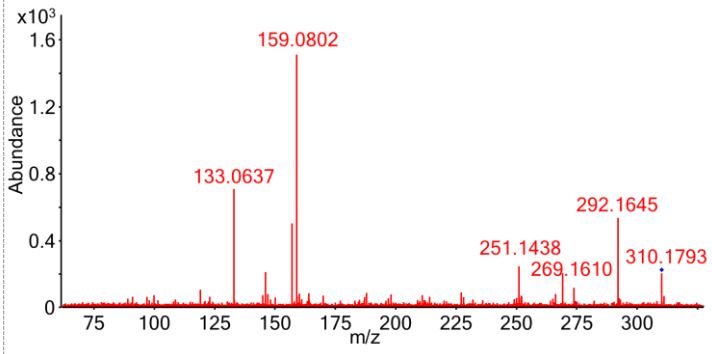


**MS/MS spectrum of 326.1757 Da @ 4.82 min, CE 40 eV, ESI-**

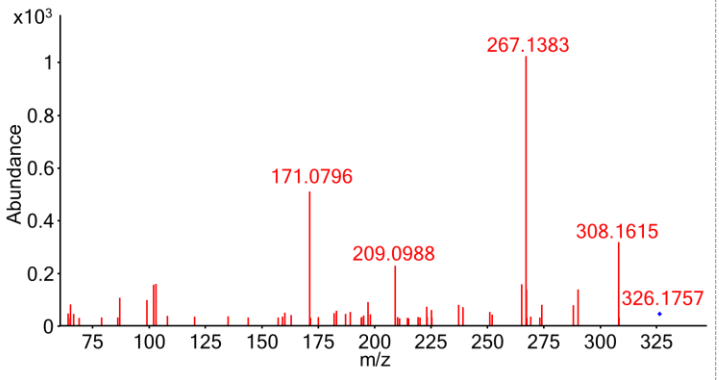


**Isotope pattern of 310.1820 Da @ 4.86 min, ESI+**

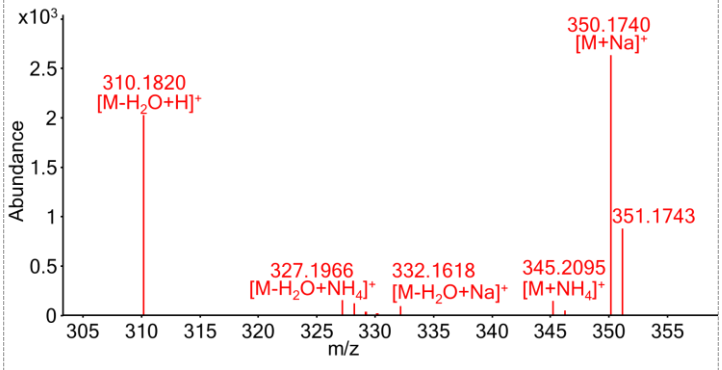


**Isotope pattern of 326.1757 Da @ 4.82 min, ESI-**

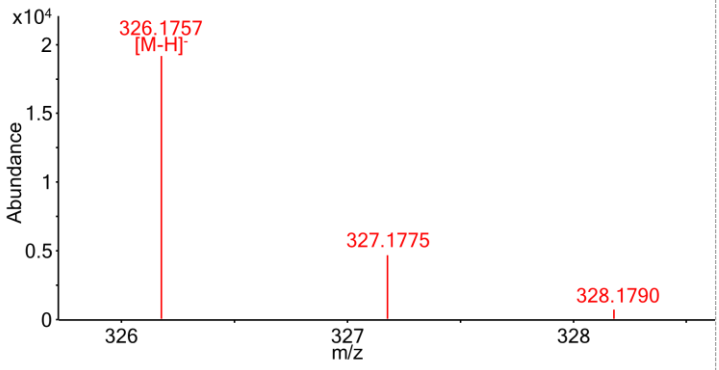

| Name: TP 327b | Confidence level: 2a | Formula: $C_{20}H_{25}NO_3$ | Precursor: $[M\text{-}H_2O+H]^+$, $[M+Na]^+$, $[M\text{-}H]^-$ | RT shift: -1.2 min | Atomic Modification: +O | SPARC $logK_{ow}$: 1-OH: 1.58; 2-OH: 2.36 |
|---|---|---|---|---|---|---|
| **Structure:** 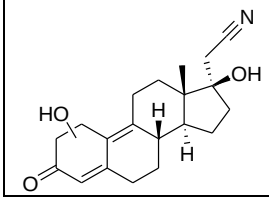 | **Comments:** • Same MS/MS spectra and different RT with TP 327a. | | | | | |

| Name: TP 341a | Confidence level: 2a | Formula: $C_{21}H_{27}NO_3$ | Precursor: $[M\text{-}CH_4O+H]^+$, $[M+Na]^+$, $[M-H]^-$ | RT shift: -0.53 min | Atomic Modification: $+CH_2O$ | SPARC log$K_{ow}$: 1-$CH_3O$: 2.72<br>2-$CH_3O$: 2.85 |
|---|---|---|---|---|---|---|

**Structure:**

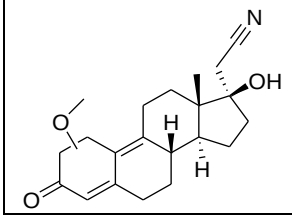


**Comments:**

- Appeared as $[C_{20}H_{24}NO_2]^+$ under ESI+, but based on ESI- detection, adduct identification, and 75 min HPLC gradient separation (no separation of $C_{20}H_{23}NO_2$ and $C_{21}H_{27}NO_3$), the product was identified as methoxy conjugation TP (see main manuscript for detail).
- MS/MS spectra resemble TP 309.
- Therefore, methoxy conjugation site was proposed as C1 or C2.

**EIC of 310.1802 Da, ESI+**

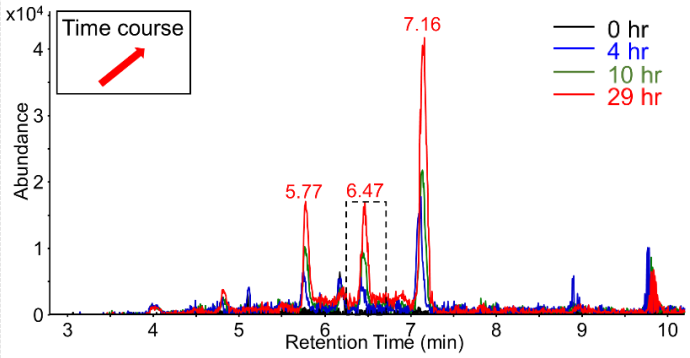


**EIC of 340.1918 Da, ESI-**

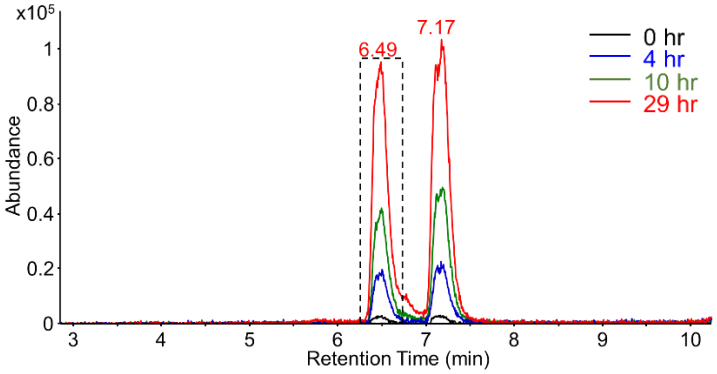


**MS/MS spectrum of 310.1802 Da @ 6.47 min, CE 20 eV, ESI+**

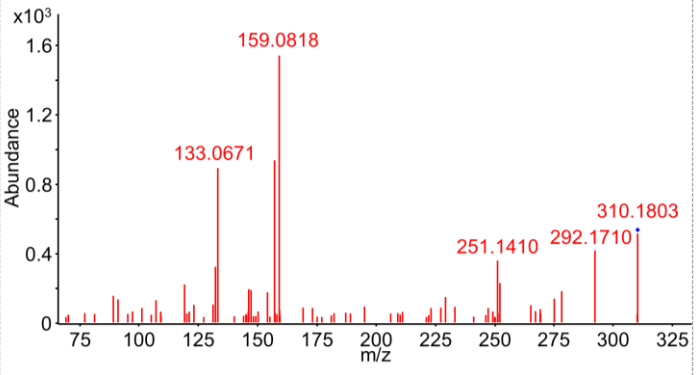


**MS/MS spectrum of 340.1918 Da @ 6.49 min, CE 40 eV, ESI-**

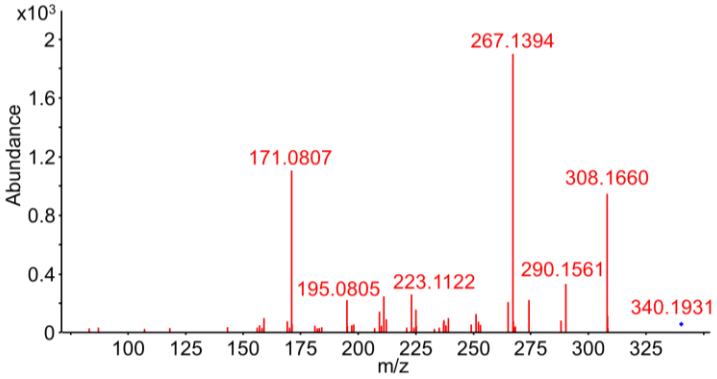


**Isotope pattern of 310.1802 Da @ 6.47 min, ESI+**

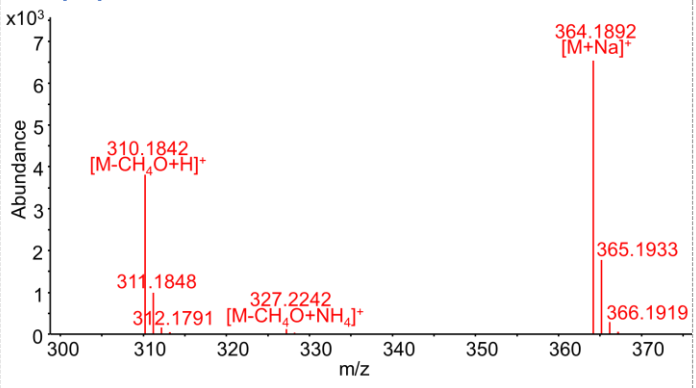


**Isotope pattern of 340.1918 Da @ 6.49 min, ESI-**

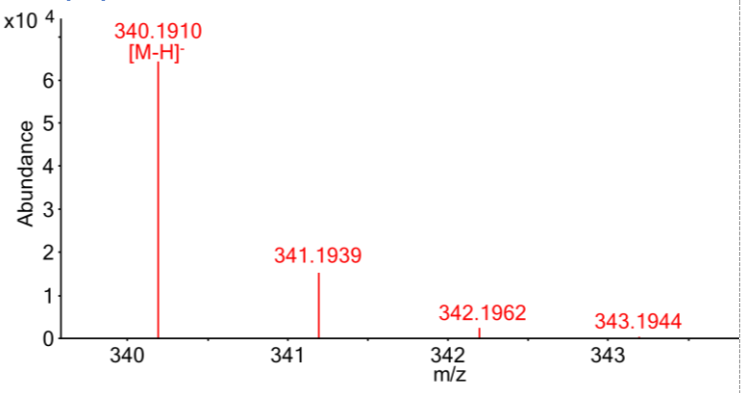

| Name: TP 341b | Confidence level: 2a | Formula: $C_{21}H_{27}NO_3$ | Precursor: $[M-H]^-$ | RT shift: +0.17 min | Atomic Modification: $+CH_2O$ | SPARC log$K_{ow}$: 1-$CH_3O$: 2.72<br>2-$CH_3O$: 2.85 |
|---|---|---|---|---|---|---|

**Structure:**

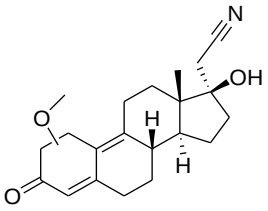


**Comments:**

- Precursor (340.1910, $[C_{21}H_{26}NO_3]^-$) underwent in-source neutral loss of $CH_4O$ to form 308.1659 ($[C_{20}H_{22}NO_2]^-$). Under 24.5 min HPLC gradient, the 308.1659 feature co-eluted with TP 309. Under 75 min HPLC gradient, the two features were separated, confirming that TP 341b were not adduct of TP 309.
- ESI+ MS/MS spectrum not available due to co-elution with TP 309.
- ESI- MS/MS spectrum resembles TP 309.
- Therefore, methoxy conjugation site is assigned to C1 or C2.

**EIC of 340.1910 Da, ESI-**

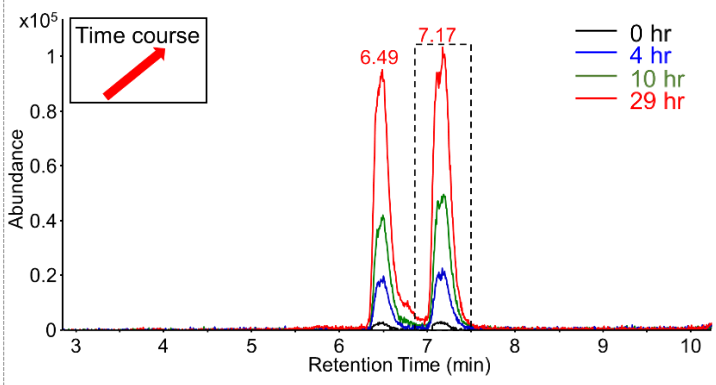


**EIC of 340.1910 and 308.1659 Da, 75 min HPLC gradient, ESI-**

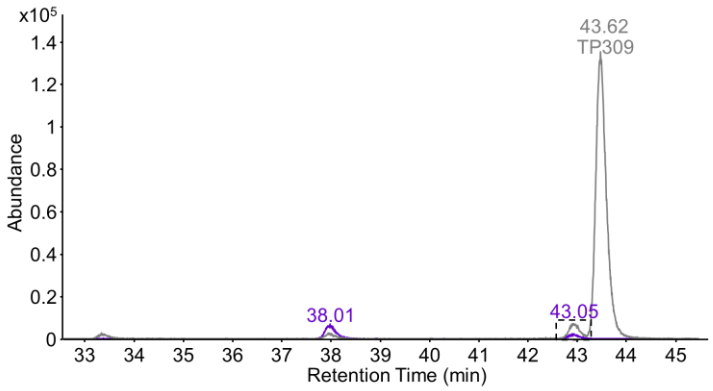


**MS/MS spectrum of 340.1910 Da @ 7.17 min, CE 40 eV, ESI-**

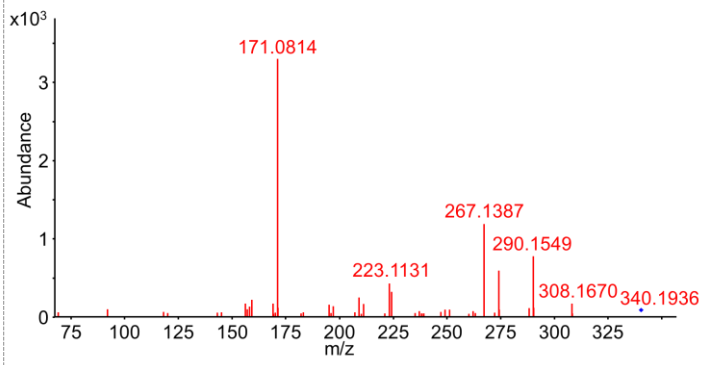


**Isotope pattern of 340.1910 Da @ 7.17 min, ESI-**
**(308.1650 ($[M-CH_4O-H]^-$) also observed, but was from co-eluting TP309)**

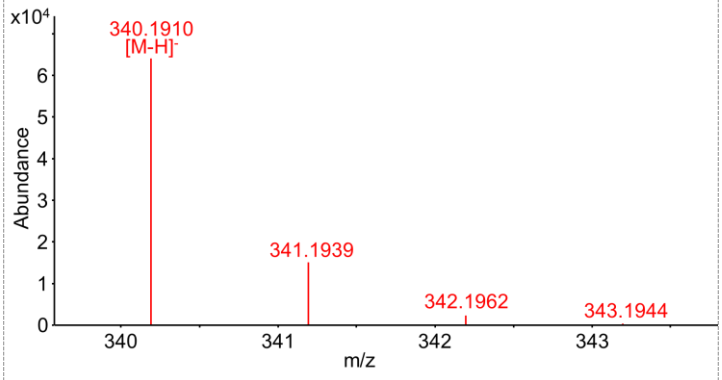


**Isotope pattern of 340.1910 Da, 75 min HPLC gradient, ESI-**

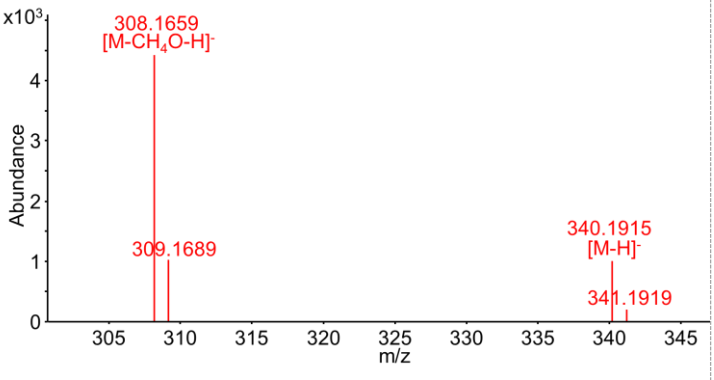

| **Name:** TP 341c | **Confidence level:** 3b | **Formula:** $C_{20}H_{23}NO_4$ | **Precursor:** $[M-H]^-$ | **RT shift:** -2.3 min | **Atomic Modification:** -2H+2O |
|---|---|---|---|---|---|
| **Structure:** 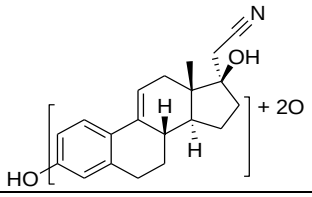 | **Comments:** • Low ESI+ response. • May be 2X hydroxylation product of TP 309. • 147.0441 ($[C_9H_7O_2]^-$) fragment indicates one of the hydroxylation sites may be in A/B ring. | | | | |



**EIC of 340.1542 Da, ESI-**

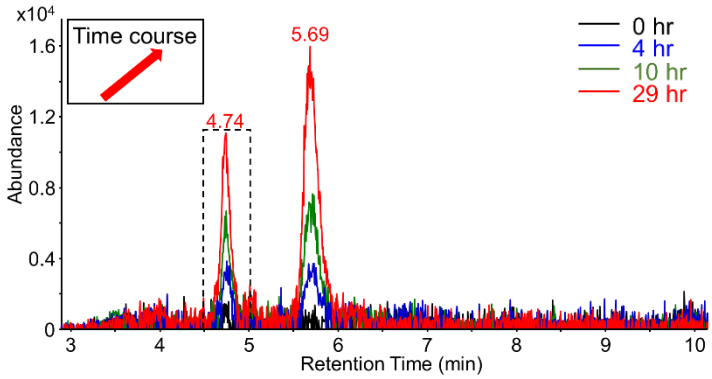


**MS/MS spectrum of 340.1542 Da @ 4.74 min, CE 20 eV, ESI-**

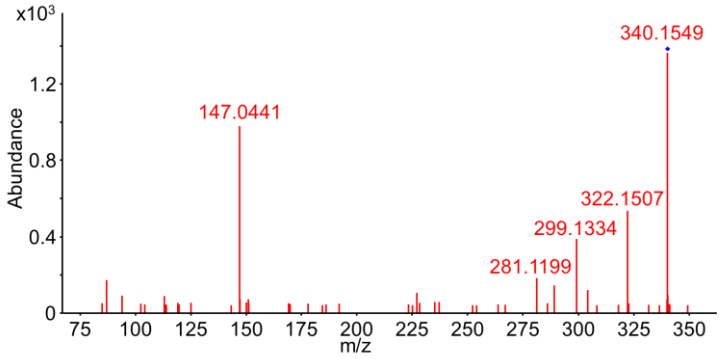


**Isotope pattern of 340.1542 Da @ 4.74 min, ESI-**

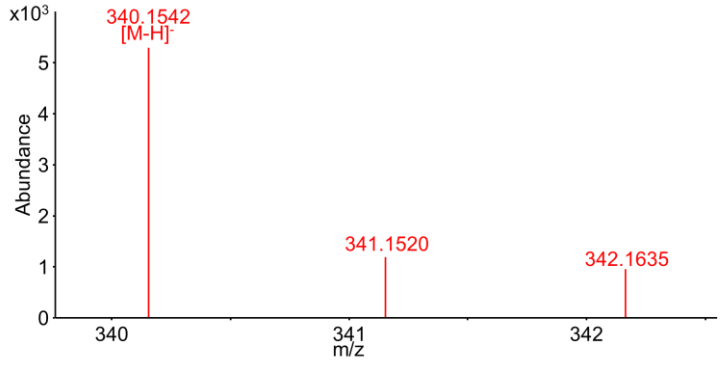

| **Name:** TP 341d | **Confidence level:** 3b | **Formula:** $C_{20}H_{23}NO_4$ | **Precursor:** $[M-H]^-$ | **RT shift:** -1.3 min | **Atomic Modification:** -2H+2O |
|---|---|---|---|---|---|
| **Structure:** 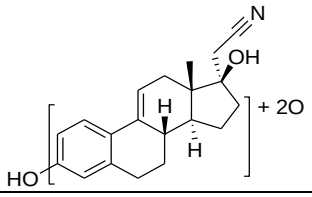 | | **Comments:** • Low ESI+ response. • May be 2X hydroxylation product of TP 309. | | | |



**EIC of 340.1547 Da, ESI-**

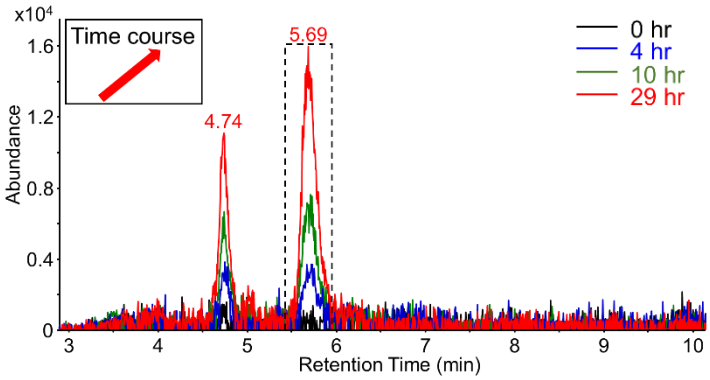


**MS/MS spectrum of 340.1547 Da @ 5.69 min, CE 20 eV, ESI-**

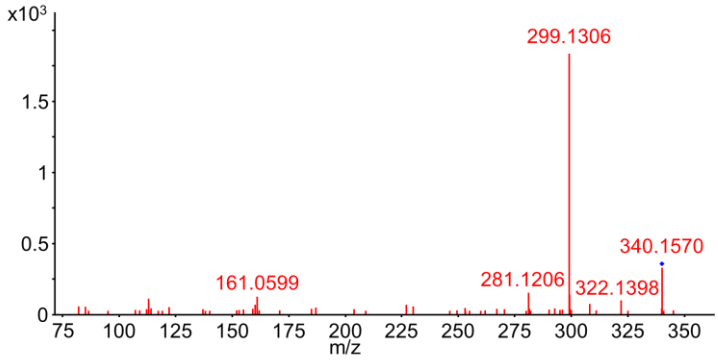


**Isotope pattern of 340.1547 Da @ 5.69 min, ESI-**

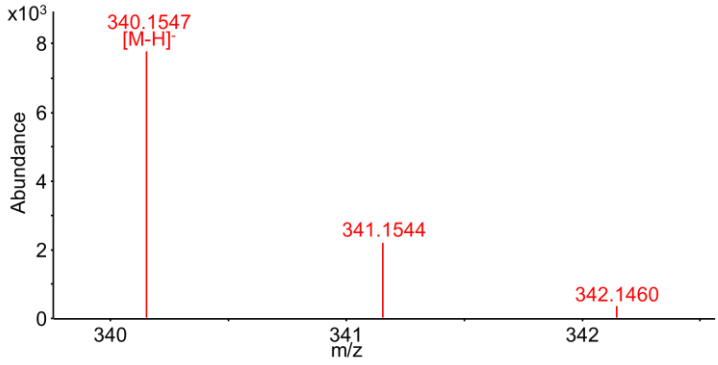

| **Name:** TP 357 | **Confidence level:** 3a | **Formula:** $C_{20}H_{23}NO_5$ | **Precursor:** $[M-H]^-$ | **RT shift:** -2.1 min | **Atomic Modification:** -2H+3O |
|---|---|---|---|---|---|
| **Structure:** 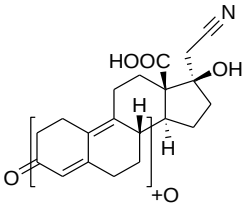 | **Comments:**<br>• Low ESI+ response.<br>• Neutral loss of $CO_2$ in the MS/MS spectrum (315.1238 ($[C_{18}H_{19}O_5]^-$) to 271.1332 ($[C_{17}H_{19}O_3]^-$)) indicates carboxyl group.<br>• 161.0591 ($[C_{10}H_9O_2]^-$) indicates oxygen addition at A/B ring. | | | | |

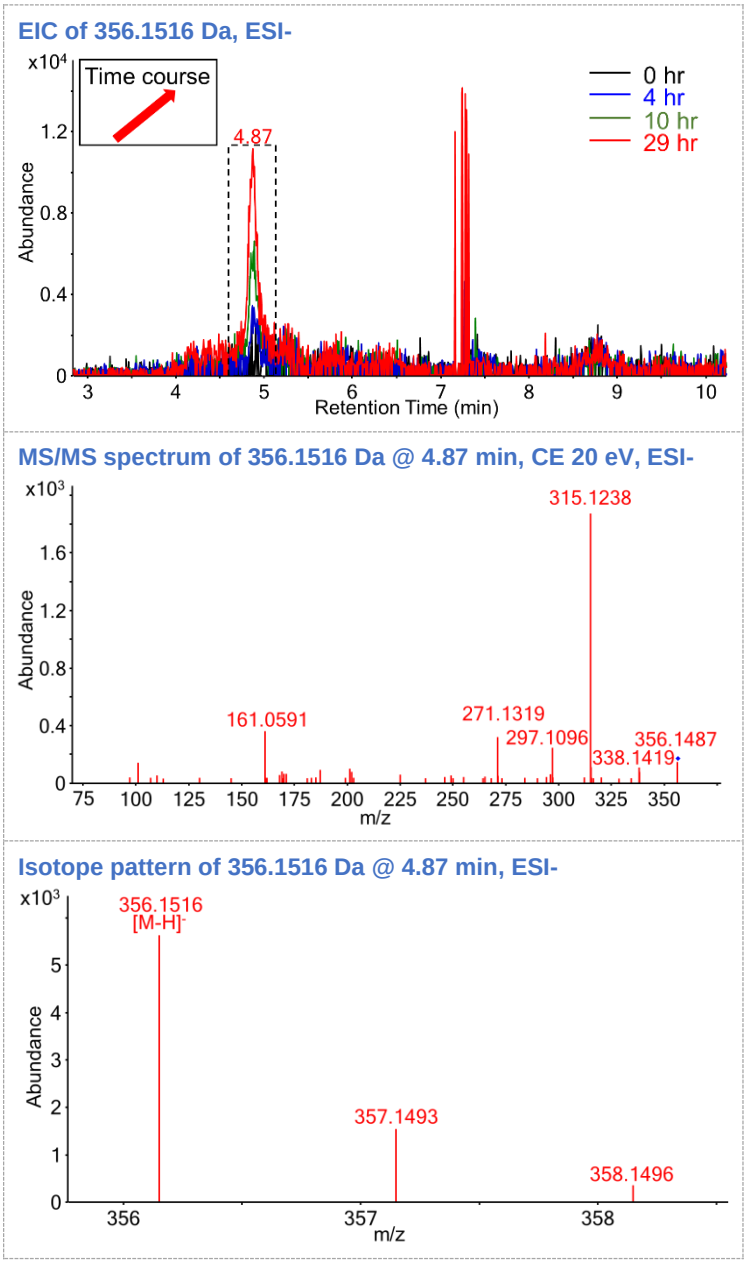

| **Name:** TP 373 | **Confidence level:** 3b | **Formula:** $C_{21}H_{27}NO_5$ | **Precursor:** $[M-H]^-$, $[M+F]^-$ | **RT shift:** -1.2 min | **Atomic Modification:** $+CH_2O_3$ |
|---|---|---|---|---|---|
| **Structure:** 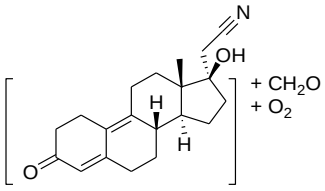  | | **Comments:**<br>• Low ESI+ response.<br>• Neutral loss of $CH_4O$ in the MS/MS spectrum (372.1879 ($[C_{21}H_{26}NO_5]^-$) to 340.1548 ($[C_{20}H_{22}NO_4]^-$)) indicates hydroxylation-methylation. | | | |

**EIC of 372.1802 Da, ESI-**

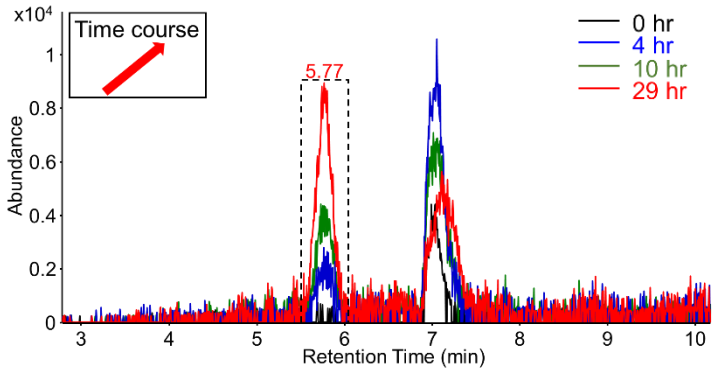


**MS/MS spectrum of 372.1802 Da @ 5.77 min, CE 20 eV, ESI-**

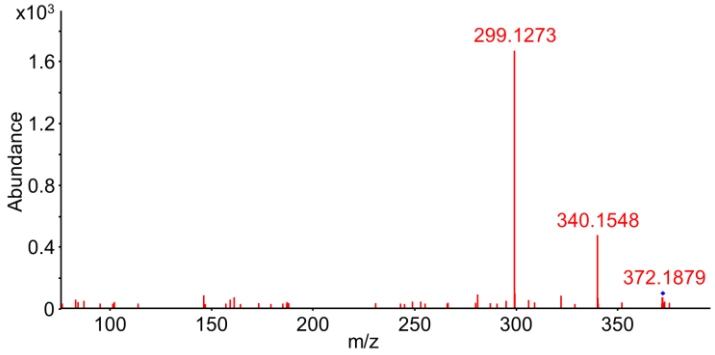


**Isotope pattern of 372.1802 Da @ 5.77 min, ESI-**

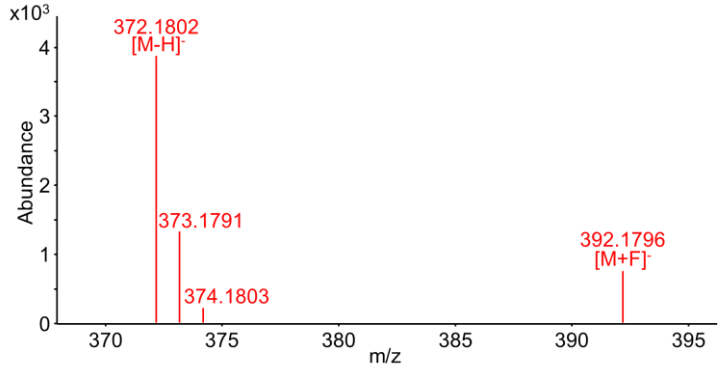

| Name: | Confidence level: | Formula: | Precursor: | RT shift: | Atomic Modification: | SPARC $logK_{ow}$: |
|---|---|---|---|---|---|---|
| TP 389 | 2b | $C_{20}H_{23}NSO_5$ | $[M-H]^-$ | -2.0 min | -2H+S+3O | -0.19 |

**Structure:**

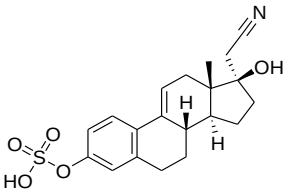


**Comments:**

- Low ESI+ response.
- Neutral loss of $SO_3$ in the MS/MS spectrum (388.1253 ($[C_{20}H_{22}NO_5S]^-$) to 308.1658 ($[C_{20}H_{22}NO_2]^-$)) indicates sulfate conjugation of $C_{20}H_{23}NO_2$ (TP 309).
- Forward RT shift consistent with $logK_{ow}$ prediction.

**EIC of 388.1218 Da, ESI-**

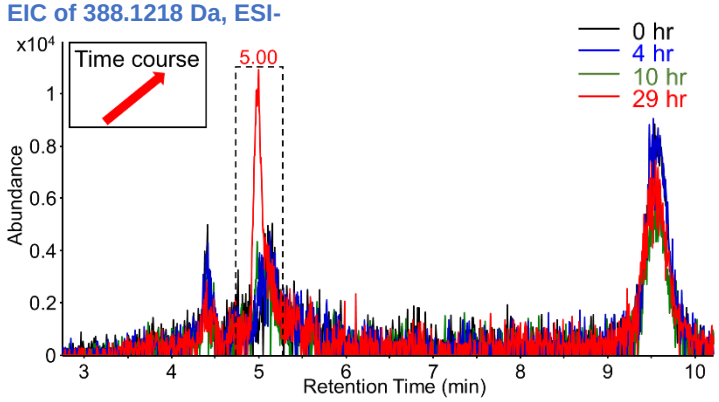


**MS/MS spectrum of 388.1218 Da @ 5.00 min, CE 40 eV, ESI-**

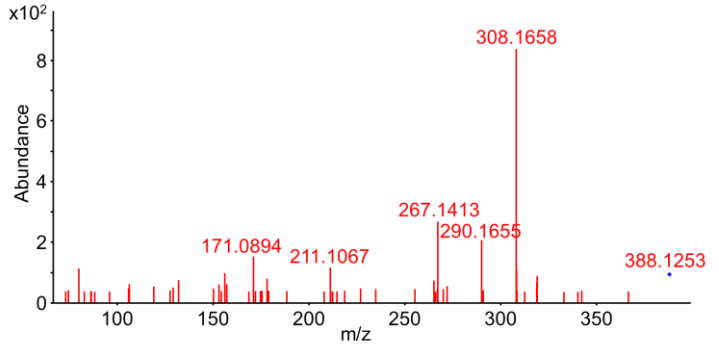


**Isotope pattern of 388.1218 Da @ 5.00 min, ESI-**

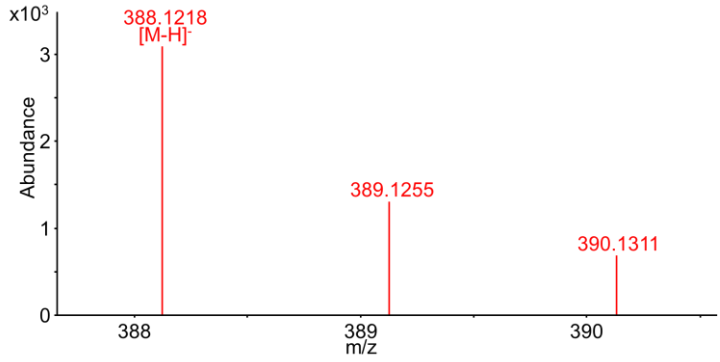

**Table S4.7** Chromatographic and spectral details of DRO, related standards, and TPs.

| **Name:** DRO | **Formula:** $C_{24}H_{30}O_3$ | **Precursor:** $[M+H]^+$, $[M+Na]^+$, $[M-H]^-$, $[M+F]^-$ | **RT:** 8.83 min | **SPARC log$K_{ow}$:** 3.61 |
|---|---|---|---|---|
| **Structure:** 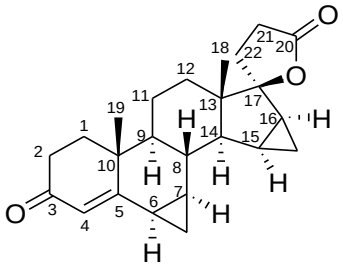 | **Comments:**<br>• Only one ESI+ diagnostic fragment: 97.0646 ($[C_6H_9O]^+$).<br>• m/z 97, 109, 123 are reported as diagnostic fragments for 3-keto-4-ene steroids with 19-methyl residue (e.g. testosterone) in ESI-CID fragmentation. Fragment structures, confirmed with multiple isotope-labeled standards, are: 97 ($[C_6H_9O]^+$), C1-4, C10, C19; 109 ($[C_7H_9O]^+$), C1-7; 123 ($[C_8H_{11}O]^+$), C1-6, C10, C19 (Thevis et al., 2012, 2005; Williams et al., 1999). For drospirenone, C6, C7 were occupied by the methylene group, inhibiting the formation of 109 and 123.<br>• 100X lower response in ESI-. Neither $[M-H]^-$ nor $[M+F]^-$ generated high-quality MS/MS spectrum. | | | |

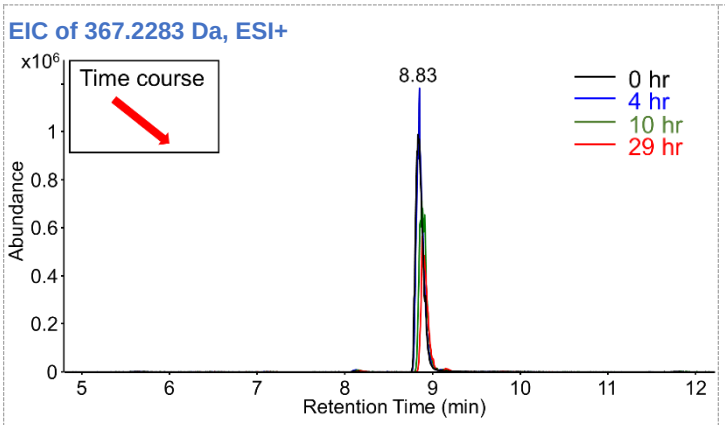


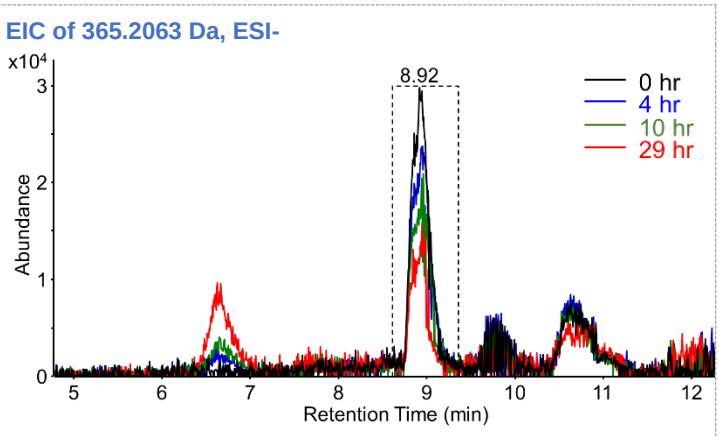


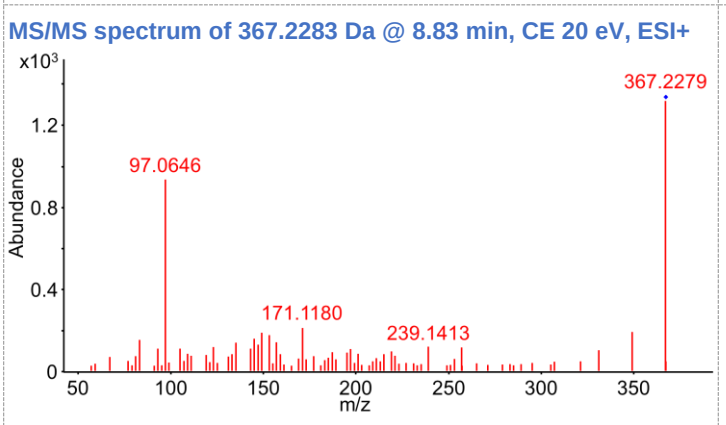



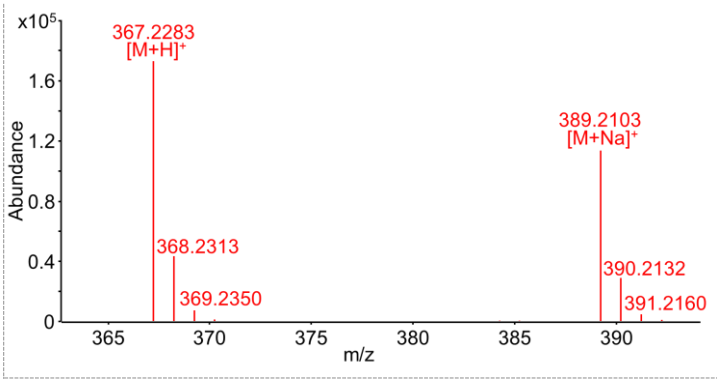
x10^5
Abundance
1.6
1.2
0.8
0.4
0
367.2283
[M+H]+
368.2313
369.2350
389.2103
[M+Na]+
390.2132
391.2160
365
370
375
380
385
390
m/z

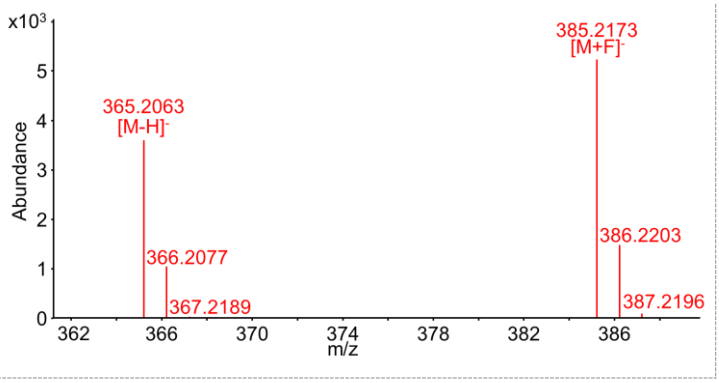
x10^3
Abundance
5
4
3
2
1
0
365.2063
[M-H]-
366.2077
367.2189
385.2173
[M+F]-
386.2203
387.2196
362
366
370
374
378
382
386
m/z

| **Name:** TP 384 | **Confidence level:** 1 | **Formula:** $C_{24}H_{32}O_4$ | **Precursor:** $[M+H]^+$, $[M+Na]^+$, $[M-H]^-$ | **RT shift:** ESI+: -1.1 min ESI-: -2.0 min | **Atomic Modification:** +2H+O | **SPARC $logK_{ow}$:** pH 4: 3.0 pH 6.5: 0.9 | **SPARC pKa:** 4.26 |
|---|---|---|---|---|---|---|---|
| **Structure:** 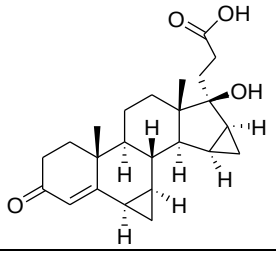 | **Comments:** • Major TP of DRO (yield: 21% at 29 h). • Different RT under ESI+ (mobile phase pH 4.2, molecule in neutral form) and ESI- (mobile phase pH 6.4, molecule as anion) due to mobile phase pH. • ESI+ MS/MS spectrum similar with DRO with 97.0639 as the single diagnostic fragment, indicating unchanged steroid carbon skeleton. • ESI- MS/MS spectrum showed neutral loss of $CO_2$ (383.2204 ($[C_{24}H_{31}O_4]^-$) to 339.2335 ($[C_{23}H_{31}O_2]^-$)), consistent with the ester group. | | | | | | |

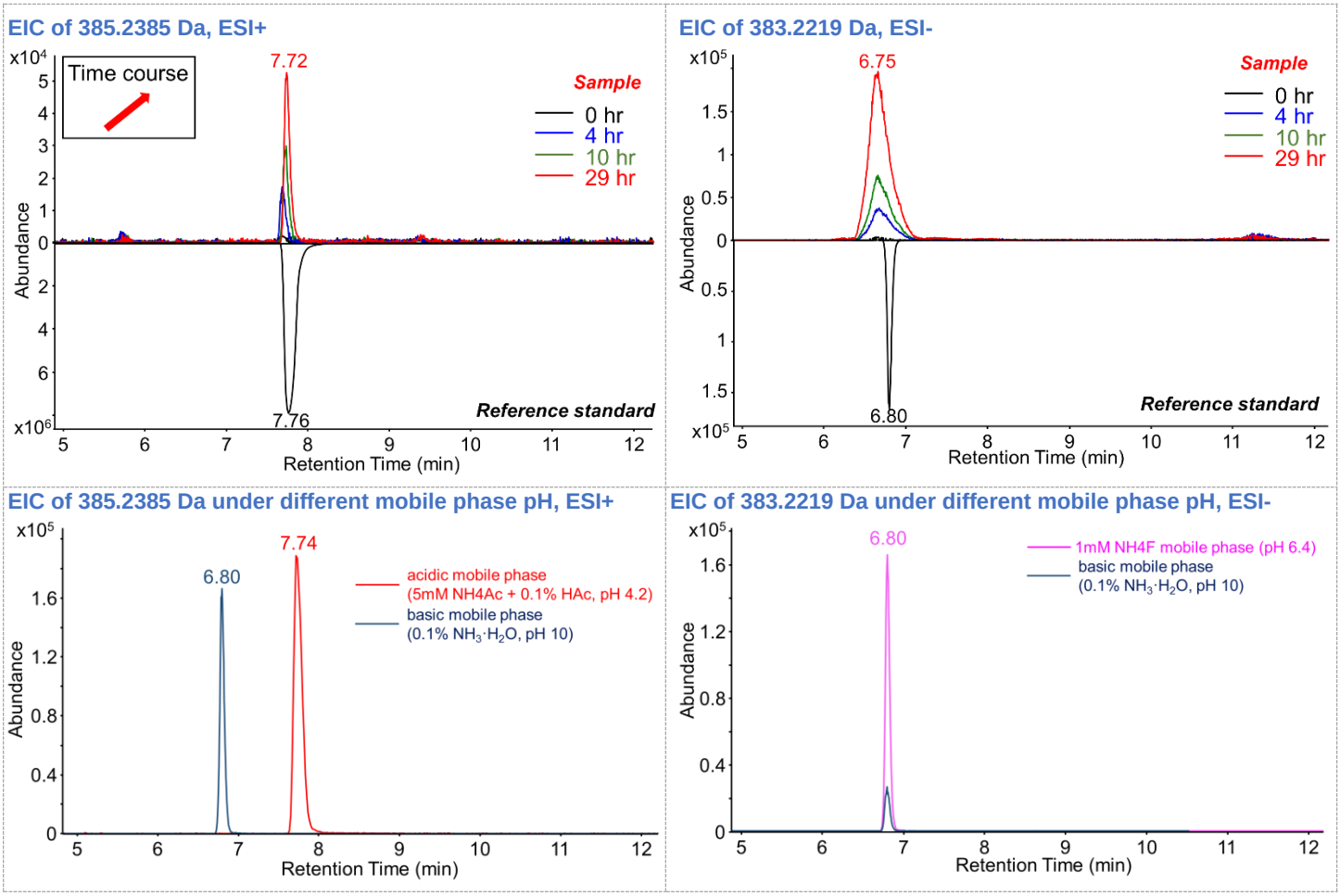

MS/MS spectrum of 385.2385 Da @ 7.93 min, CE 20 eV, ESI+

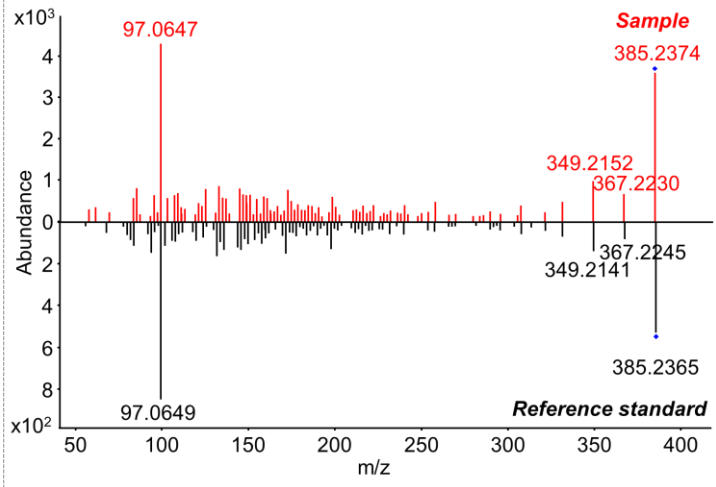


MS/MS spectrum of 383.2219 Da @ 5.75 min, CE 40 eV, ESI-

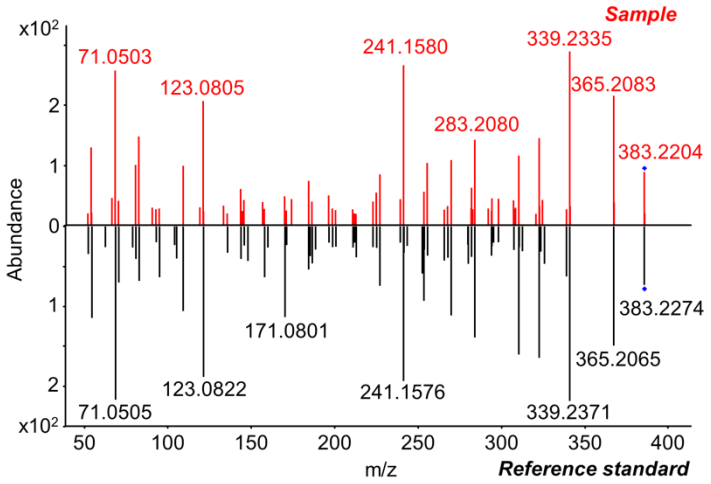


Isotope pattern of 385.2385 Da @ 7.93 min, ESI+

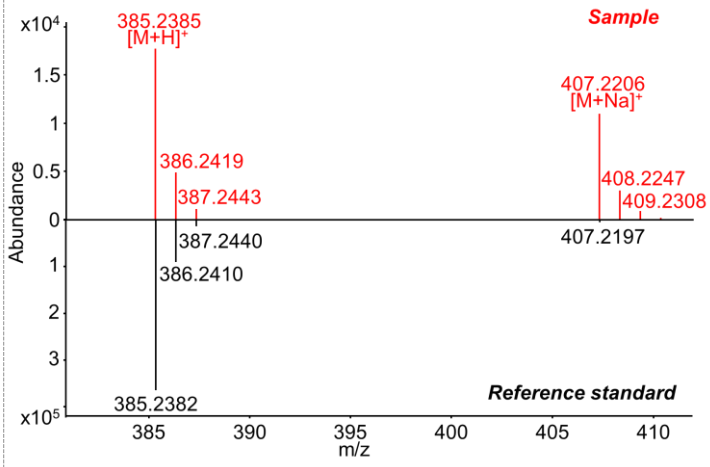


Isotope pattern of 383.2219 Da @ 5.75 min, ESI-

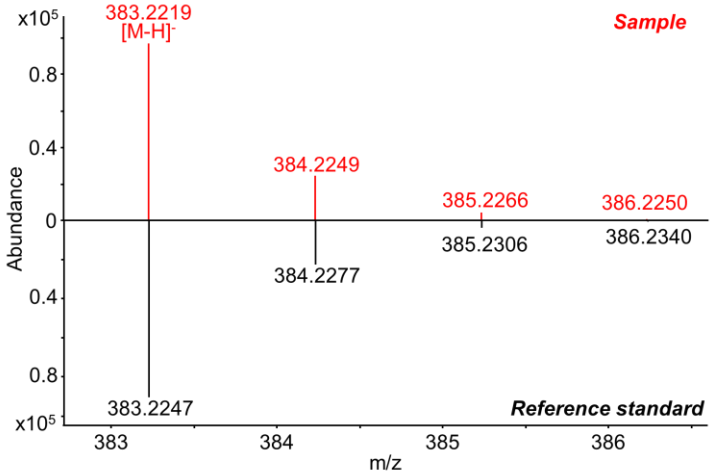

| Name: TP 364 | Confidence level: 1 | Formula: $C_{24}H_{28}O_3$ | Precursor: $[M+H]^+$, $[M+Na]^+$ | RT shift: -0.7 min | Atomic Modification: -2H | SPARC $logK_{ow}$: 3.81 |
|---|---|---|---|---|---|---|

**Structure:**

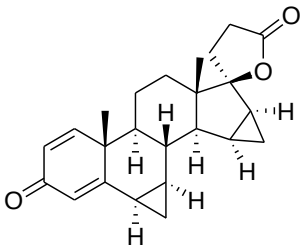

**Comments:**

- Low ESI- response.
- Diagnostic fragments m/z 121.0649 ($[C_8H_9O]^+$), 147.0798 ($[C_{10}H_{11}O]^+$), 161.0958 ($[C_{11}H_{13}O]^+$) consistent with 3-keto-1,4-diene steroids (Schänzer et al., 2006; Thevis and Schänzer, 2005).
- Forward RT shift consistent with RT difference between methyltestosterone (9.11 min) and methandienone (8.53 min, methyltestosterone – 2H at C1(2)) on C18 column (Zeng et al., 2013).
- Structure confirmed with a synthesized standard.

**EIC of 365.2121 Da, ESI+**

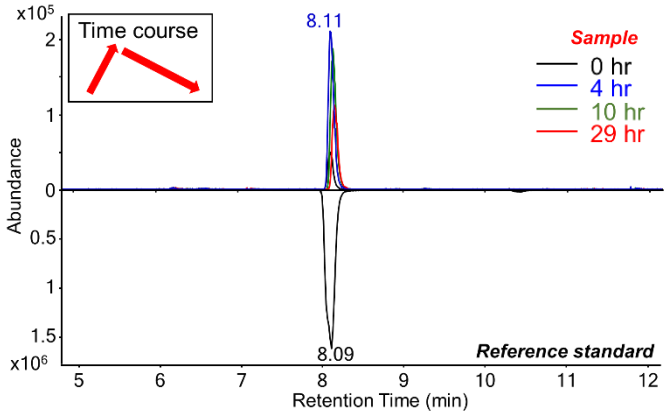


**MS/MS spectrum of 365.2121 Da @ 8.11 min, CE 20 eV, ESI+**

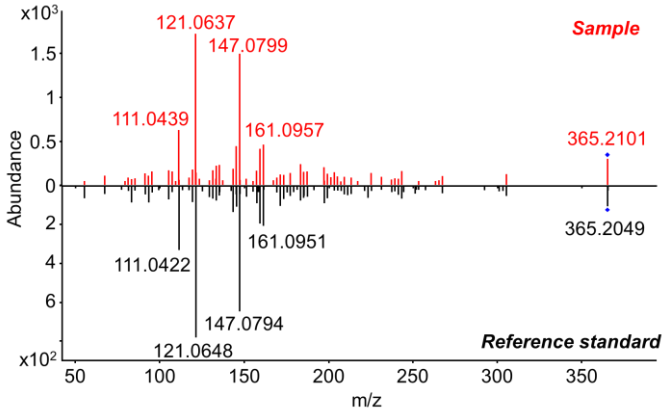


**Isotope pattern of 365.2121 Da @ 8.11 min, ESI+**

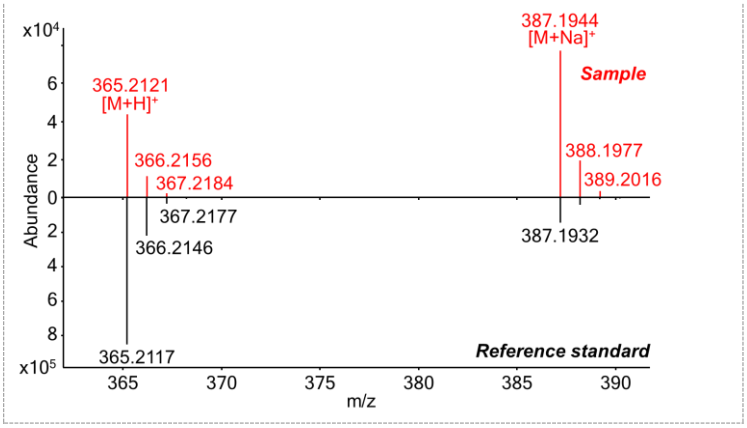
x10^4
6
4
2
0
2
4
6
8
x10^5
Abundance
365.2121
[M+H]+
366.2156
367.2184
367.2177
366.2146
365.2117
387.1944
[M+Na]+
Sample
388.1977
389.2016
387.1932
Reference standard
365
370
375
380
385
390
m/z

| Name: TP 368 | Confidence level: 2b | Formula: $C_{24}H_{32}O_3$ | Precursor: $[M+H]^+$, $[M+NH_4]^+$, $[M+Na]^+$ | RT shift: +1.5 min | Atomic Modification: +2H | SPARC $logK_{ow}$: 3.47 |
|---|---|---|---|---|---|---|

**Structure:**

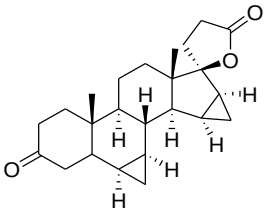

**Comments:**

- MS/MS spectrum consistent with saturated 3-keto steroids with product ions of low specificity (Thevis and Schänzer, 2007).
- $[M+H]^+$ and $[M+NH_4]^+$ generated different MS/MS spectra, indicating $H^+$ and $NH_4^+$ attached to different sites on the molecule, and the 3-keto group was likely still present.
- If hydrogenation happened to the 3-keto group, the 3-OH-4-ene would generate $[M-H_2O+H]^+$ precursor, which was not observed (Pozo et al., 2008).
- RT shift inconsistent with $logK_{ow}$ prediction, but consistent with RT difference between dihydrotestosterone (10.46 min, testosterone + 2H at C4(5)) and testosterone (8.57 min) on C18 column (Liu et al., 2011).
- Therefore, the hydrogenation site was proposed at C4(5).

**EIC of 369.2493 Da, ESI+**

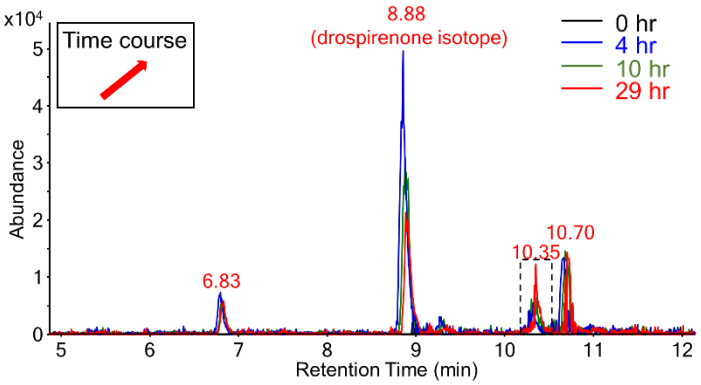


**MS/MS spectrum of 369.2493 Da @ 10.35 min, CE 20 eV, ESI+**

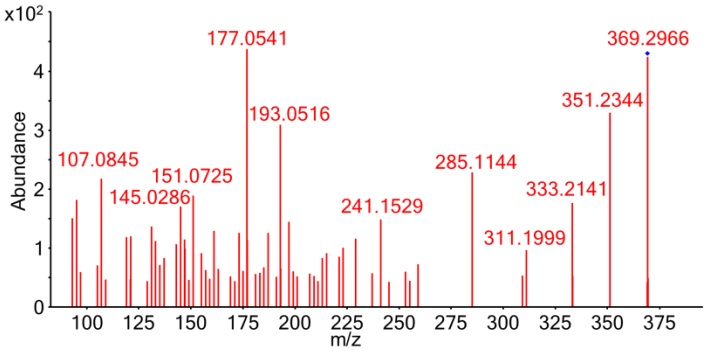


**MS/MS spectrum of 386.2723 Da @ 10.35 min, CE 20 eV, ESI+**

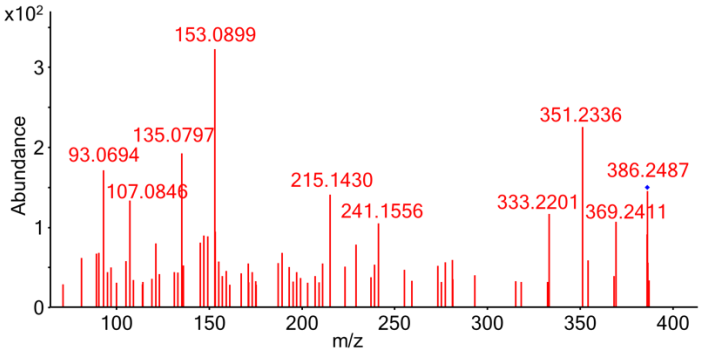


**Isotope pattern of 369.2493 Da @ 10.35 min, ESI+**

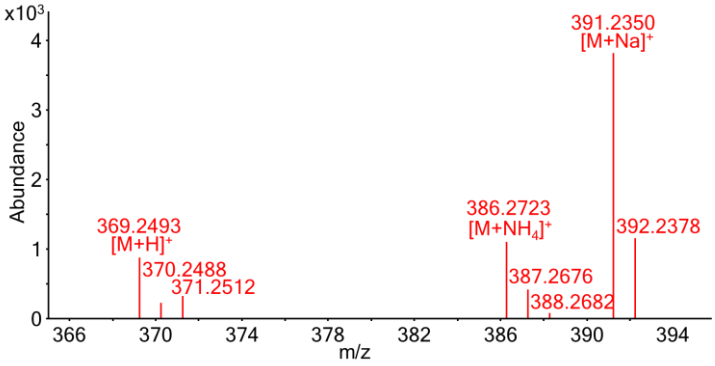
x10^3
4
3
2
1
0
Abundance
391.2350
[M+Na]+
386.2723
[M+NH4]+
392.2378
369.2493
[M+H]+
370.2488
371.2512
387.2676
388.2682
366
370
374
378
382
386
390
394
m/z

| **Name:** TP 370a | **Confidence level:** 2b | **Formula:** $C_{24}H_{34}O_3$ | **Precursor:** $[M+H]^+$, $[M+NH_4]^+$, $[M+Na]^+$ | **RT shift:** +1.2 min | **Atomic Modification:** +4H | **SPARC $logK_{ow}$:** 4.08 |
|---|---|---|---|---|---|---|

**Structure:**

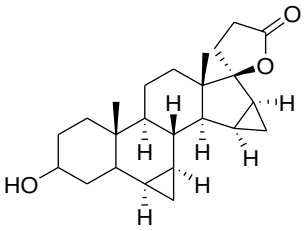

**Comments:**

- Low ESI- response. Mostly ionized as $[M+Na]^+$, consistent with that for 3-OH saturated steroids (Pozo et al., 2008).
- ESI+ MS/MS spectrum was composed by product ions without oxygen atom ($[C_xH_y]^+$), similar with those of 3-OH saturated steroids such as androsterone (mzcloud database). Typical fragments of steroidal core, including 91.0544 ($[C_7H_7]^+$), 105.0666 ($[C_8H_9]^+$) (Pozo et al., 2008), were present.
- Hydrogenation of C3-carbonyl group and C4(5)-double bond was observed in biotransformation of other 3-keto-4-ene steroids (Hobe et al., 1998).
- Backward RT shift consistent with $logK_{ow}$ prediction.
- Therefore, the hydrogenations were proposed to happen at C3-carbonyl group and C4(5)-double bond.

**EIC of 371.2599 Da, ESI+**

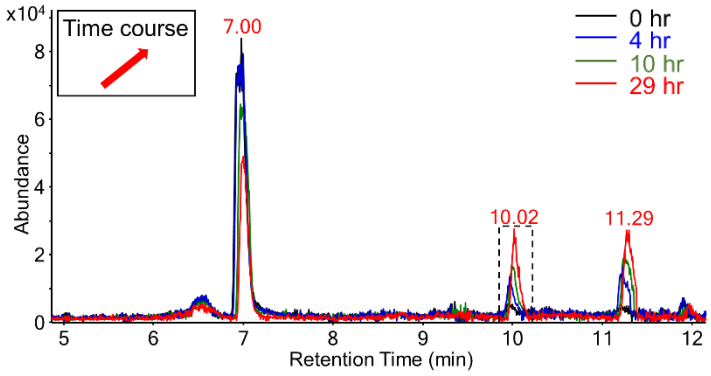


**MS/MS spectrum of 371.2599 Da @ 10.02 min, CE 40 eV, ESI+**

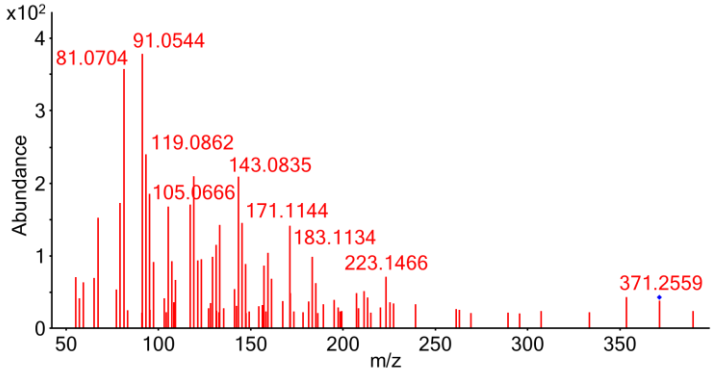


**Isotope pattern of 371.2599 Da @ 10.02 min, ESI+**

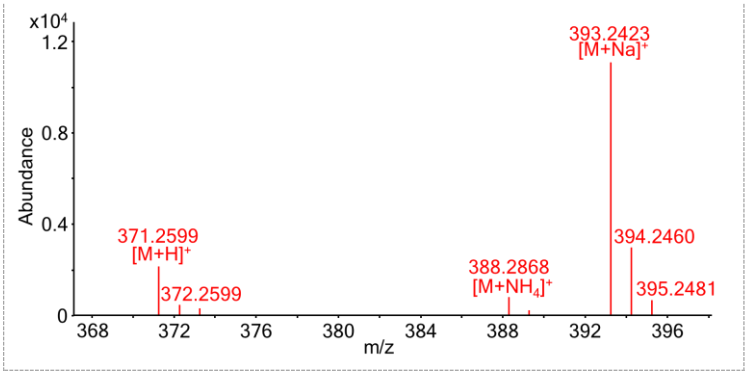
x10^4
1.2
0.8
0.4
0
Abundance
393.2423
[M+Na]+
371.2599
[M+H]+
372.2599
388.2868
[M+NH4]+
394.2460
395.2481
368
372
376
380
384
388
392
396
m/z

| **Name:** TP 370b | **Confidence level:** 2b | **Formula:** $C_{24}H_{34}O_3$ | **Precursor:** $[M+H]^+$, $[M+NH_4]^+$, $[M+Na]^+$ | **RT shift:** +2.5 min | **Atomic Modification:** +4H | **SPARC log$K_{ow}$:** 4.08 |
|---|---|---|---|---|---|---|
| **Structure:** 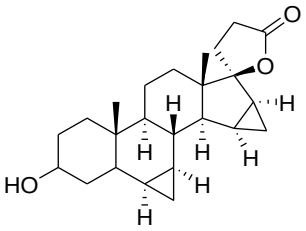 | **Comments:** • Similar MS/MS spectra and different RT with TP 370a. | | | | | |

| Name: TP 380 | Confidence level: 2b | Formula: $C_{24}H_{28}O_4$ | Precursor: $[M+H]^+$, $[M+Na]^+$, $[M-H]^-$, $[M+F]^-$ | RT shift: -2.1 min | Atomic Modification: -2H+O | SPARC $logK_{ow}$: 2.52 |
|---|---|---|---|---|---|---|

**Structure:**

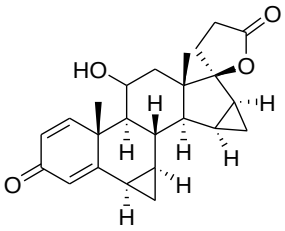


**Comments:**

- Preferably ionized as $[M+F]^-$ in ESI-. MS/MS spectrum not available for $[M-H]^-$.
- $[M+H]^+$ MS/MS spectrum similar with 1,4-diene-11-OH glucocorticoids (e.g. dexamethasone, betamethasone, prednisolone; mzcloud database), with diagnostic fragments of 121.0630 ($[C_8H_9O]^+$), 147.0798 ($[C_{10}H_{11}O]^+$), 159.0793 ($[C_{11}H_{11}O]^+$), 171.0787 ($[C_{12}H_{11}O]^+$), and 185.0949 ($[C_{13}H_{13}O]^+$).
- Forward RT shift was consistent with $logK_{ow}$ prediction.
- C11 hydroxylation was observed in fungal biotransformation of DRO (Baydoun et al., 2017; Quintana et al., 2013).
- Therefore, the TP was proposed as 1(2)-dehydrogenation and 11-hydroxylation product.

**EIC of 381.2069 Da, ESI+**

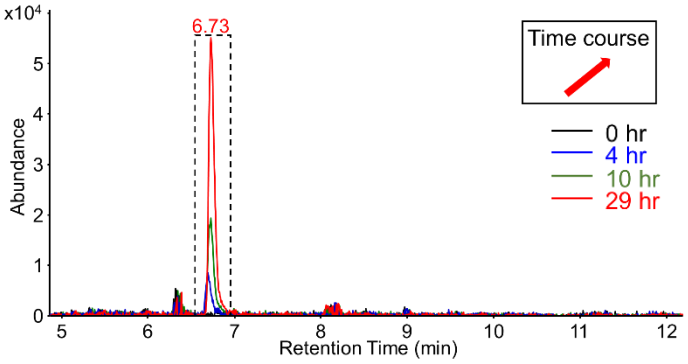


**EIC of 379.1908 Da, ESI-**

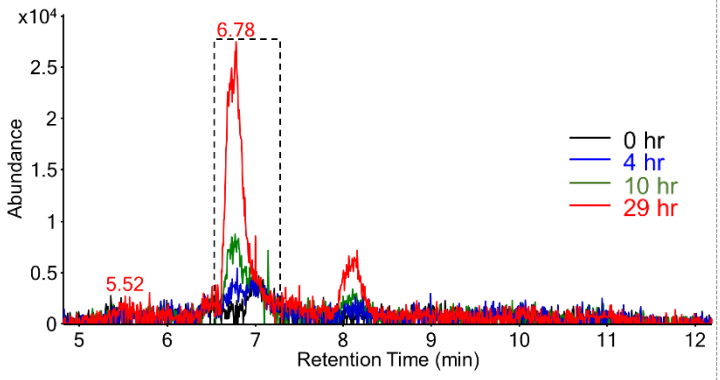


**MS/MS spectrum of 381.2069 Da @ 6.73 min, CE 20 eV, ESI+**

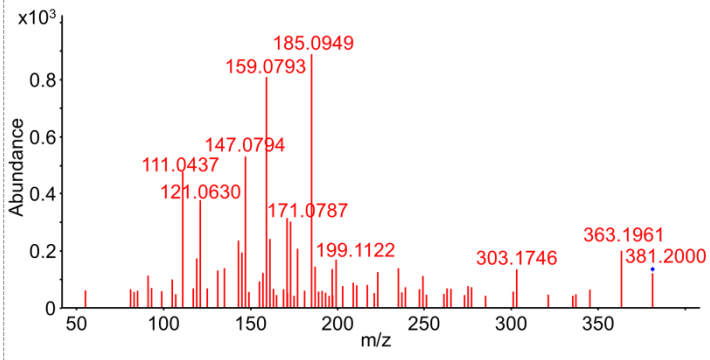


**Isotope pattern of 381.2069 Da @ 6.73 min, ESI+**

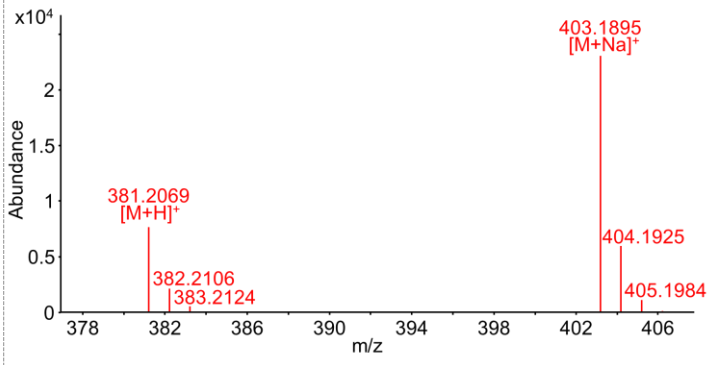


**Isotope pattern of 379.1908 Da @ 6.78 min, ESI-**

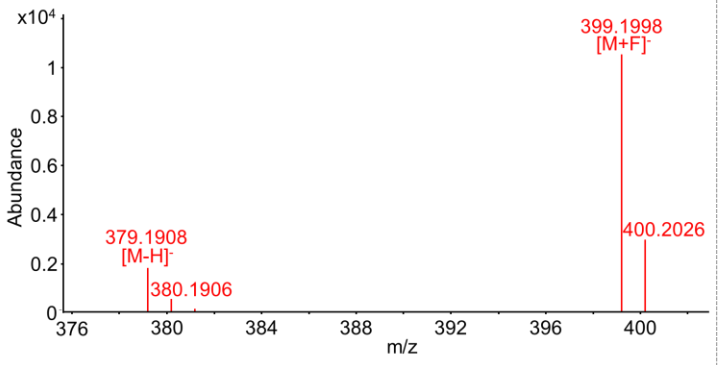

| **Name:** TP 382a | **Confidence level:** 3b | **Formula:** $C_{24}H_{30}O_4$ | **Precursor:** $[M-H]^-$ | **RT shift:** -2.6 min | **Atomic Modification:** +O |
|---|---|---|---|---|---|
| **Structure:** 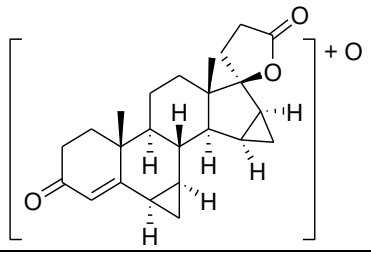 | | **Comments:**<br>• Low ESI+ response. | | | |



**EIC of 381.2059 Da, ESI-**

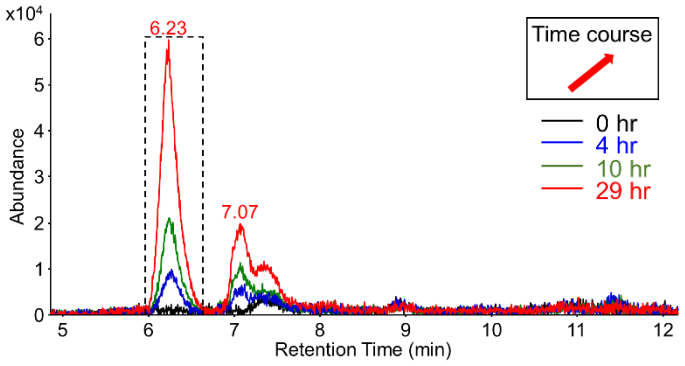


**MS/MS spectrum of 381.2059 Da @ 6.23 min, CE 40 eV, ESI-**

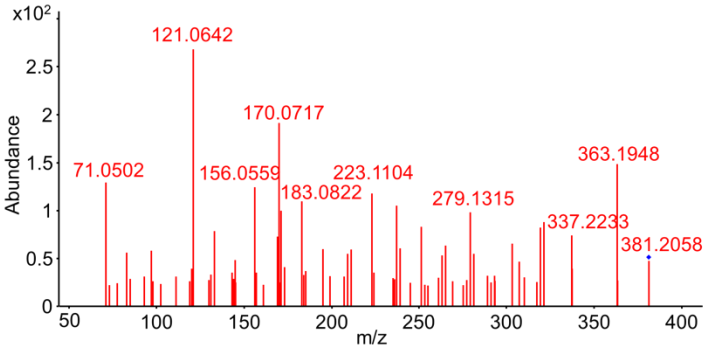


**Isotope pattern of 381.2059 Da @ 6.23 min, ESI-**

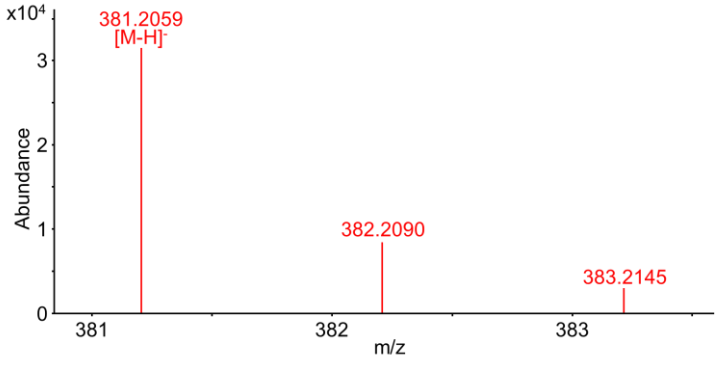

| Name: | Confidence level: | Formula: | Precursor: | RT shift: | Atomic Modification: |
|---|---|---|---|---|---|
| TP 382b | 3a | $C_{24}H_{30}O_4$ | $[M+H]^+$, $[M+Na]^+$, $[M-H]^-$, $[M+F]^-$ | -1.8 min | +O |

**Structure:**

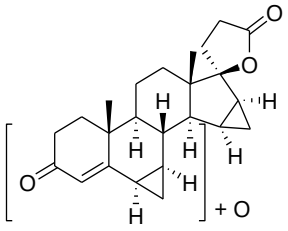


**Comments:**

- $[M+F]^-$ more abundant than $[M-H]^-$ under ESI-.
- ESI+ MS/MS spectrum demonstrated extensive fragmentations and did not show evident diagnostic fragments. A previous study on fragmentation of monohydroxylated progesterones showed that hydroxylation at C6 and C19 converted the progesterone MSMS spectrum (97 and 109 as diagnostic fragments) to one with extensive fragmentations. Spectra of C,D-ring hydroxylated progesterones were similar with that of progesterone (Kang et al., 2004).
- Therefore, the hydroxylation site was proposed at A/B ring.

**EIC of 383.2226 Da, ESI+**

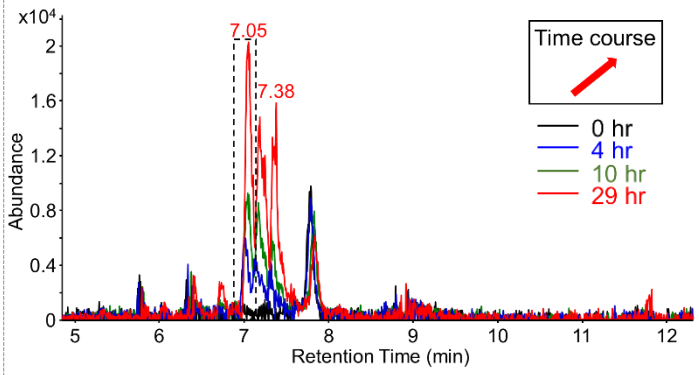


**EIC of 381.2074 Da, ESI-**

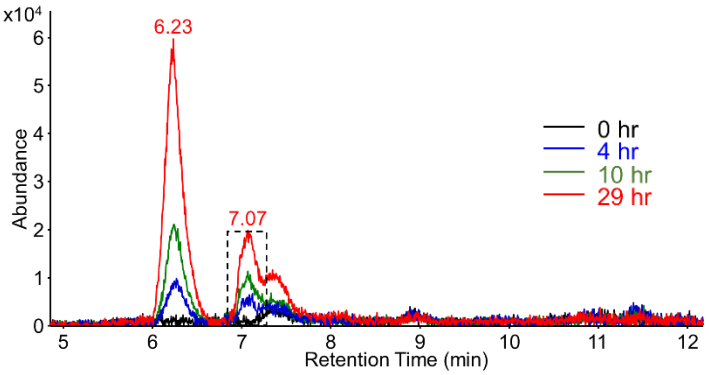


**MS/MS spectrum of 383.2226 Da @ 7.05 min, CE 40 eV, ESI+**

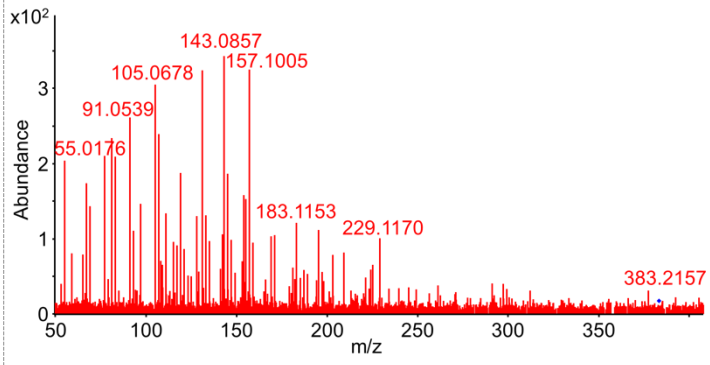


**MS/MS spectrum of 381.2074 Da @ 7.07 min, CE 40 eV, ESI-**

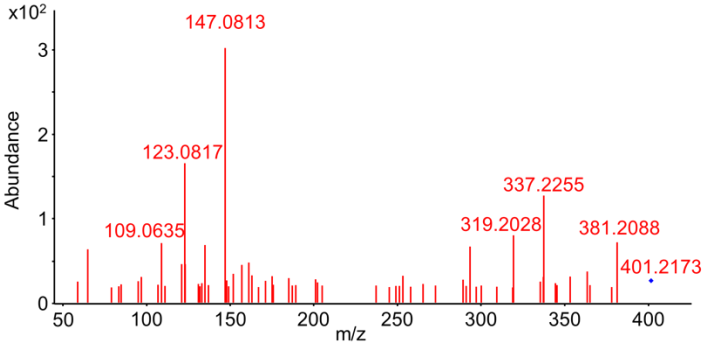


**Isotope pattern of 383.2226 Da @ 7.05 min, ESI+**

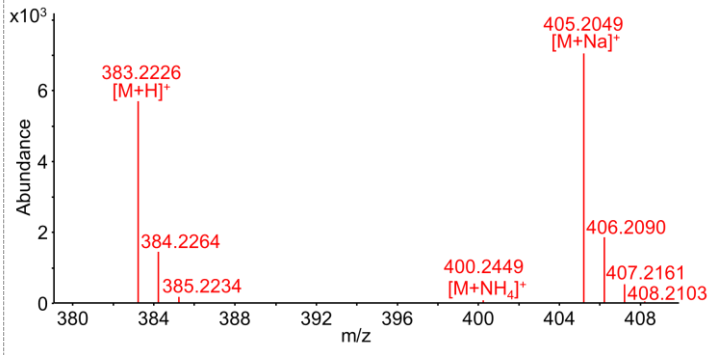


**Isotope pattern of 381.2074 Da @ 7.07 min, ESI-**

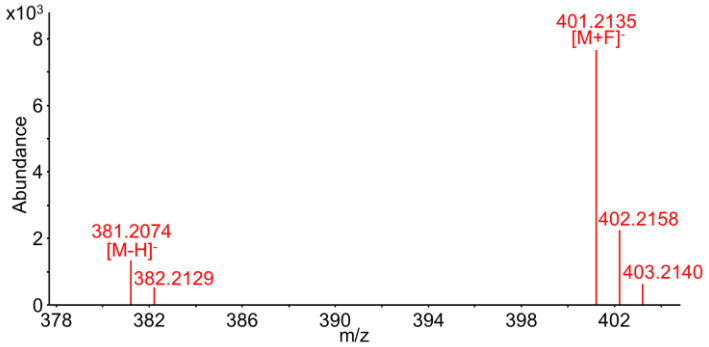

| Name: | Confidence level: | Formula: | Precursor: | RT shift: | Atomic Modification: | SPARC log$K_{ow}$: |
|---|---|---|---|---|---|---|
| TP 382c | 2a | $C_{24}H_{30}O_4$ | $[M+H]^+$, $[M+Na]^+$ | -1.6 min | +O | 1-OH: 2.33;<br>2-OH: 2.80 |

**Structure:**

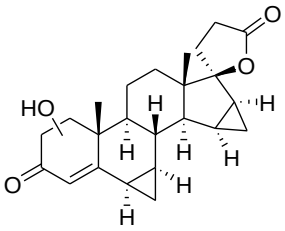


**Comments:**

- Hydroxylation TP.
- Low ESI- response.
- MSMS spectrum resembled that for TP 364 and showed diagnostic fragments for 3-keto-1,4-diene steroids (121, 147, 161) (Schänzer et al., 2006; Thevis and Schänzer, 2005).
- Forward RT shift consistent with log$K_{ow}$ prediction.
- 2-OH-DRO was reported as DRO metabolite in fungal biotransformation (Quintana et al., 2013).
- Therefore, the hydroxylation site was proposed at C1 or C2.

**EIC of 383.2225 Da, ESI+**

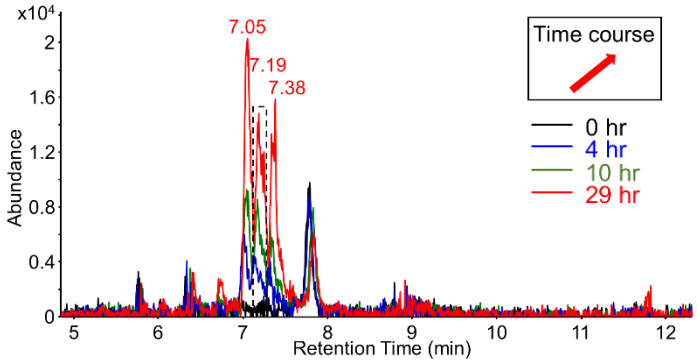


**MS/MS spectrum of 383.2225 Da @ 7.19 min, CE 20 eV, ESI+**

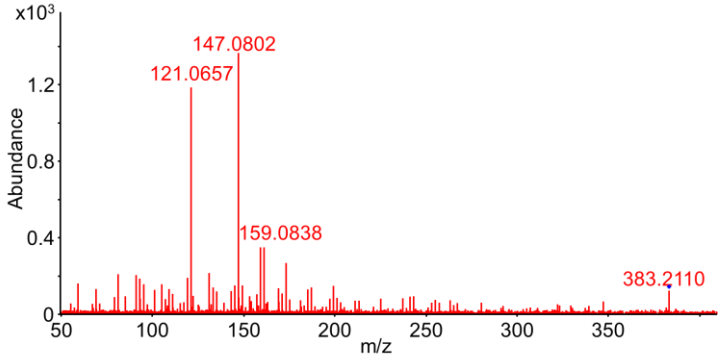


**Isotope pattern of 383.2225 Da @ 7.19 min, ESI+**

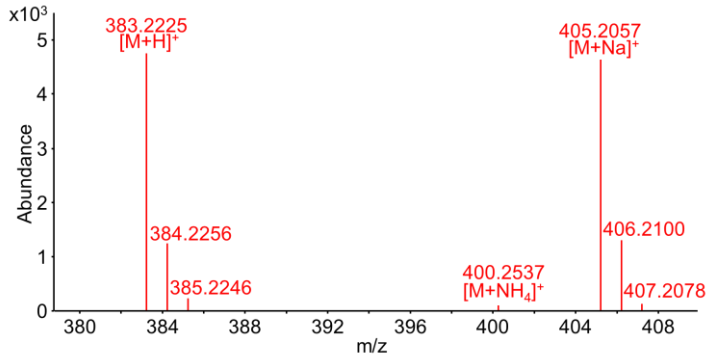

| Name: | Confidence level: | Formula: | Precursor: | RT shift: | Atomic Modification: |
|---|---|---|---|---|---|
| TP 382d | 3a | $C_{24}H_{30}O_4$ | $[M+H]^+$, $[M+Na]^+$ | -1.5 min | +O |

**Structure:**

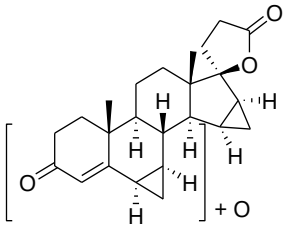


**Comments:**

- Low ESI- response. MS/MS spectrum only available for ESI+.
- ESI+ MS/MS spectrum demonstrated extensive fragmentations and did not show evident diagnostic fragments, similar with that of TP 382b.
- The hydroxylation site was proposed at A/B ring following the same logic for TP 382b.

**EIC of 383.2228 Da, ESI+**

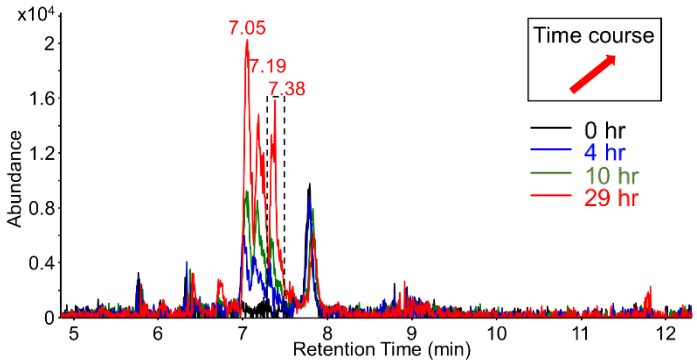


**MS/MS spectrum of 383.2228 Da @ 7.38 min, CE 40 eV, ESI+**

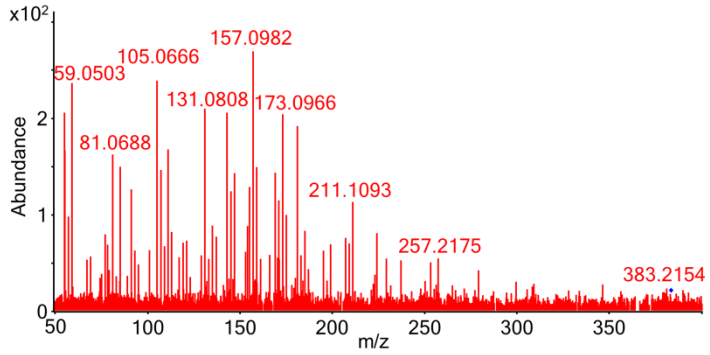


**Isotope pattern of 383.2228 Da @ 7.38 min, ESI+**

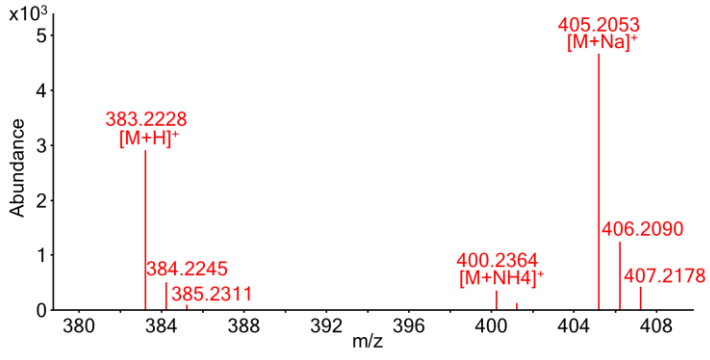

| **Name:** TP 398 | **Confidence level:** 3b | **Formula:** $C_{24}H_{30}O_5$ | **Precursor:** $[M+H]^+$, $[M+Na]^+$, $[M-H]^-$, $[M+F]^-$ | **RT shift:** -2.2 min | **Atomic Modification:** +2O |
|---|---|---|---|---|---|
| **Structure:** 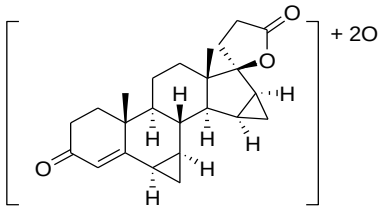 | | **Comments:**<br>• 2X oxidation TP.<br>• Low ESI+ response.<br>• Neutral loss of $CO_2$ (379.1914 ($[C_{24}H_{27}O_4]^-$) to 335.2015 ($[C_{23}H_{27}O_2]^-$)) in MS/MS of $[M-H]^-$. | | | |

**EIC of 399.2104 Da, ESI+**

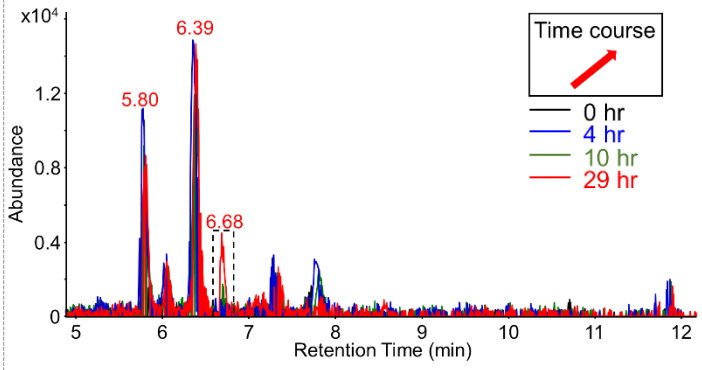


**EIC of 397.2025 Da, ESI-**

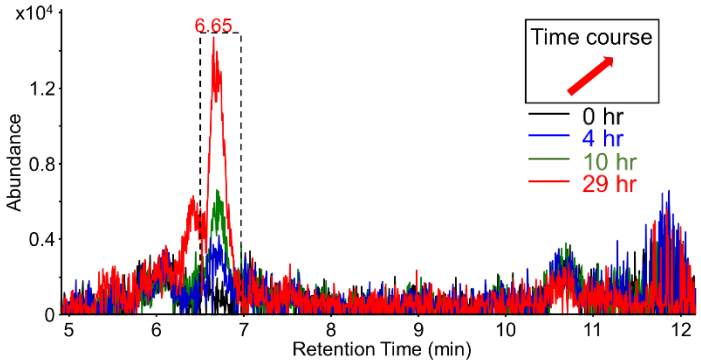


**MS/MS spectrum of 397.2025 Da @ 6.65 min, CE 20 eV, ESI-**

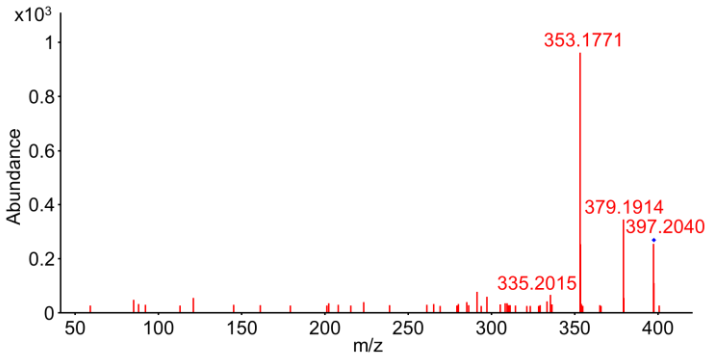


**Isotope pattern of 399.2104 Da @ 6.68 min, ESI+**

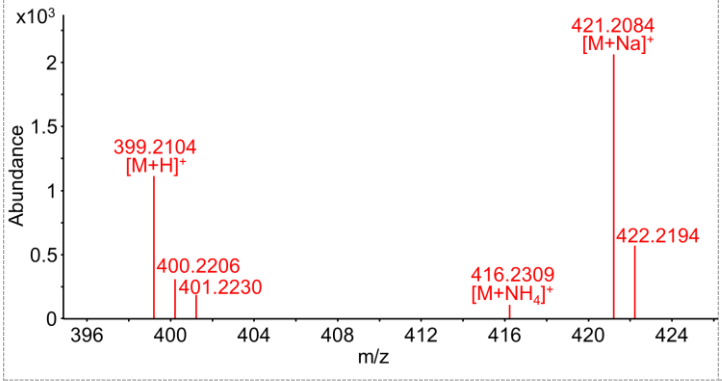


**Isotope pattern of 397.2025 Da @ 6.65 min, ESI-**

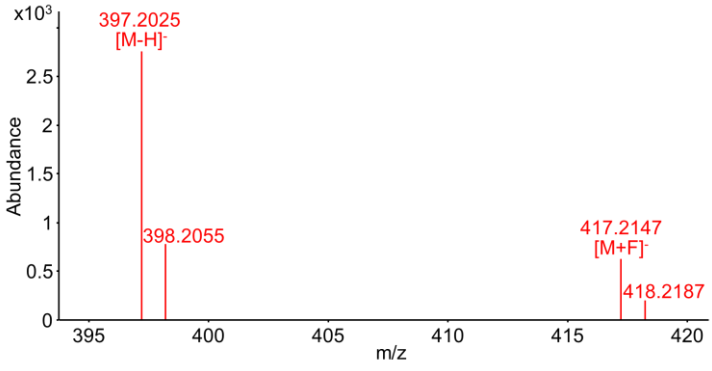

| **Name:** TP 402 | **Confidence level:** 3b | **Formula:** $C_{24}H_{34}O_5$ | **Precursor:** $[M+H]^+$, $[M+NH_4]^+$, $[M+Na]^+$, $[M-H]^-$ | **RT shift:** ESI+: -1.1 min ESI-: -3.2 min | **Atomic Modification:** +4H+2O |
|---|---|---|---|---|---|

**Structure:**

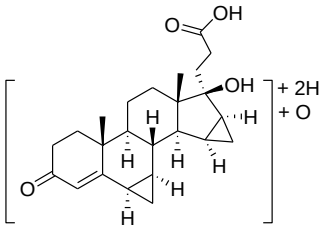


**Comments:**

- 2X hydration TP.
- Different RT under ESI+ and ESI- due to pH, similar with TP 384 (ester hydrolysis product).
- $[M+H]^+$ and $[M+NH_4]^+$ generated unique MS/MS fragments, similar with TP 368 (carbonyl hydrogenation product).
- $[M+H]^+$ MS/MS spectrum showed continuous loss of 4 $H_2O$ (403.2410 - 385.2313 - 367.2229 - 349.2166 - 331.2015).
- $[M+NH_4]^+$ MS/MS spectrum showed fragments of 93.0680 ($[C_7H_9]^-$), 135.0848 ($[C_9H_{11}O]^-$), and 153.0915 ($[C_9H_{13}O_2]^-$), similar with TP 368.
- ESI- MS/MS spectrum showed fragments of 123.0817 ($[C_8H_{11}O]^-$) and 147.0799 ($[C_{10}H_{11}O]^-$), similar with TP 382b (hydroxylation product).
- Therefore, the first hydration site was assigned to E ring ester group. The second hydration may be hydrogenation + hydroxylation.

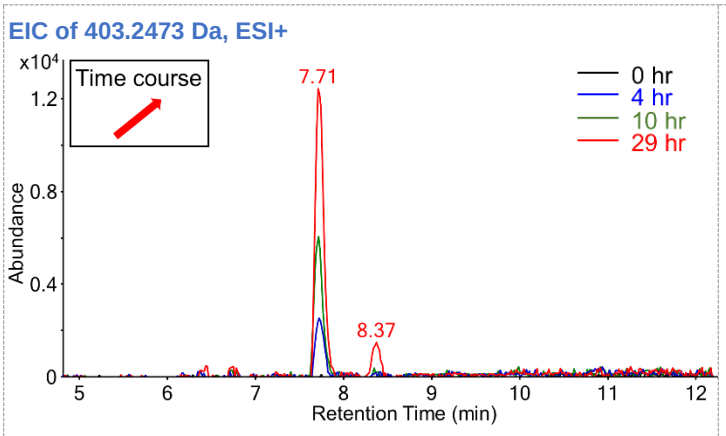


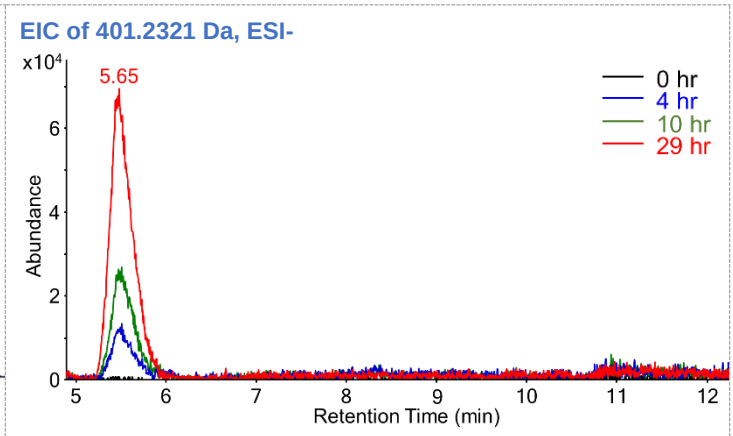


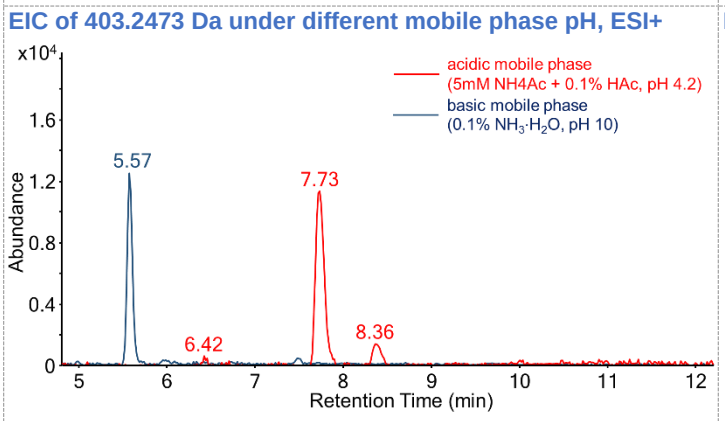


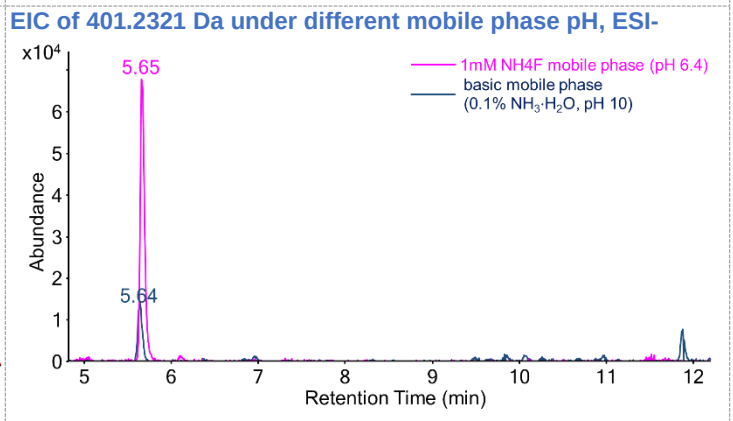

MS/MS spectrum of 403.2473 Da @ 7.52 min, CE 20 eV, ESI+

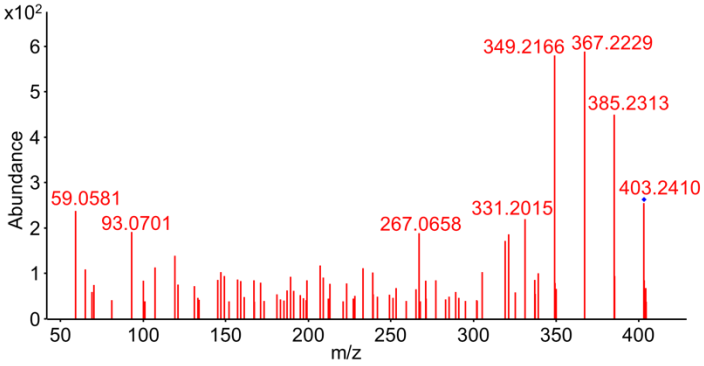


MS/MS spectrum of 401.2321 Da @ 6.48 min, CE 40 eV, ESI-

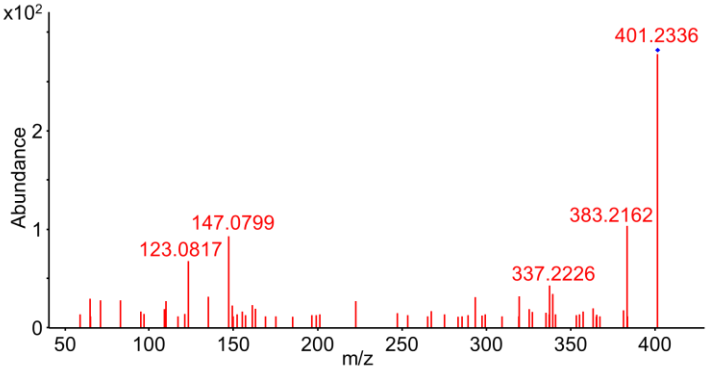


MS/MS spectrum of 420.2735 Da @ 7.52 min, CE 20 eV, ESI+

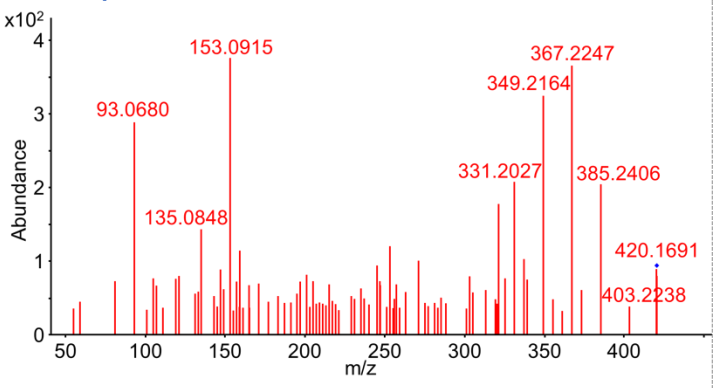


Isotope pattern of 403.2473 Da @ 7.52 min, ESI+

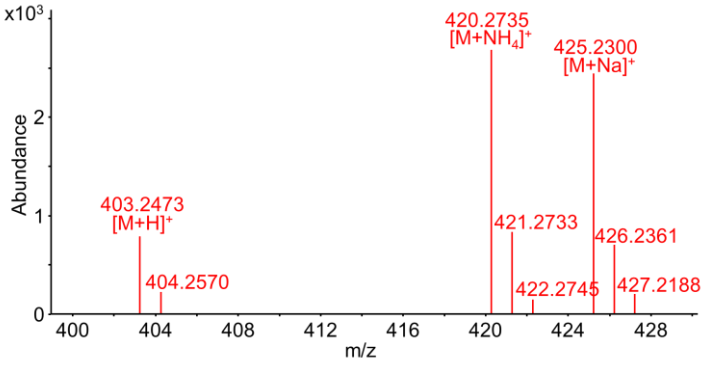


Isotope pattern of 401.2321 Da @ 6.48 min, ESI-

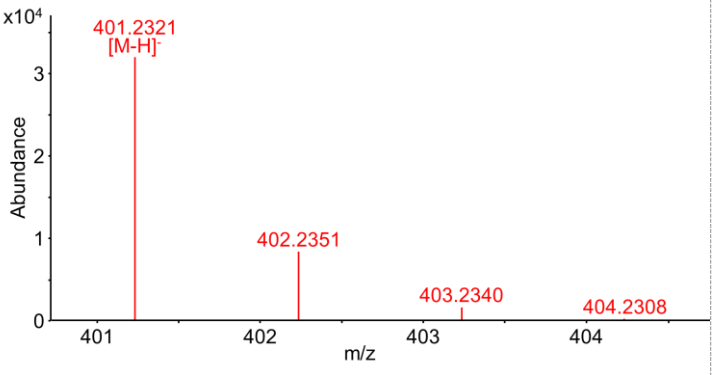

| Name: | Confidence level: | Formula: | Precursor: | RT shift: | Atomic Modification: |
|---|---|---|---|---|---|
| TP 416 | 3b | $C_{24}H_{32}O_6$ | $[M-H]^-$ | -2.8 min | +2H+3O |

**Structure:**

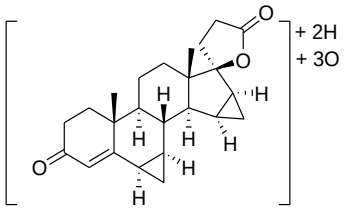


**Comments:**

- Low ESI+ response.
- ESI- MS/MS spectrum showed neutral loss of $CO_2$ (415.2093 ($[C_{24}H_{31}O_6]^-$) to 371.2214 ($[C_{23}H_{31}O_4]^-$)), indicating ester group.

**EIC of 415.2105 Da, ESI-**

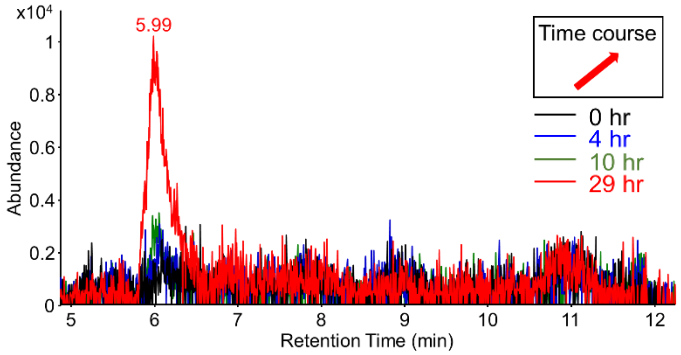


**MS/MS spectrum of 415.2105 Da @ 5.99 min, CE 40 eV, ESI-**

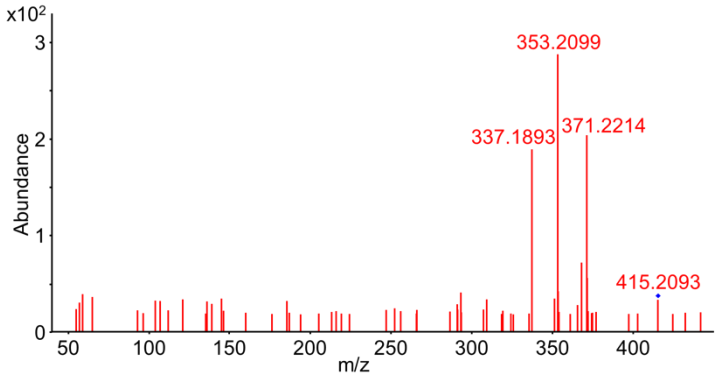


**Isotope pattern of 415.2105 Da @ 5.99 min, ESI-**

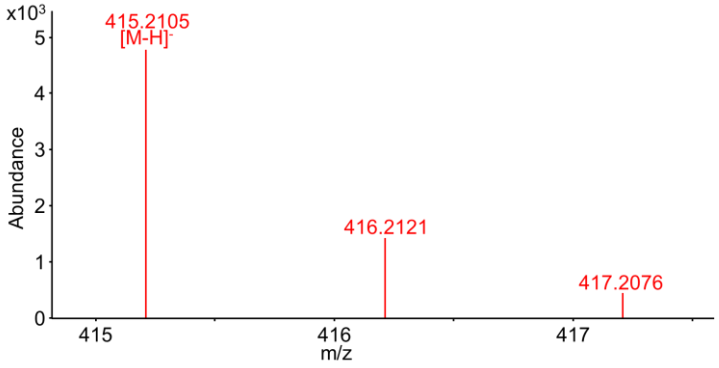

## Reference


Baydoun, E., Atia-tul-Wahab, Iqbal, S., Smith, C., Choudhary, M.I., 2017. Biotransformation of drospirenone, a contraceptive drug, with Cunninghamella elegans. Steroids 126, 30–34.

Bourcier, S., Poisson, C., Souissi, Y., Kinani, S., Bouchonnet, S., Sablier, M., 2010. Elucidation of the decomposition pathways of protonated and deprotonated estrone ions: Application to the identification of photolysis products. Rapid Commun. Mass Spectrom. RCM 24, 2999–3010.

Du, B., Lofton, J.M., Peter, K.T., Gipe, A.D., James, C.A., McIntyre, J.K., Scholz, N.L., Baker, J.E., Kolodziej, E.P., 2017. Development of suspect and non-target screening methods for detection of organic contaminants in highway runoff and fish tissue with high-resolution time-of-flight mass spectrometry. Environ. Sci. Process. Impacts 19, 1185–1196.

Hobe, G., Hillesheim, H.G., Schumann, W., Ritter, P., Claussen, C., Chemnitius, K.H., Erdmann, A., Wagner, H., Wehrberger, K., Wesemann, R., Carol, W., Klinger, G., Komor, A., Goncharov, N.P., 1983a. Studies on pharmacokinetics of STS 557 in animal species and man. Exp. Clin. Endocrinol. 81, 158–167.

Hobe, G., Schön, R., Frankenberg, G., Schade, W., Schubert, K., 1983b. Urinary metabolites of the new progestagen STS 557 (17 alpha-cyanomethyl-17-hydroxy-4,9-estradien-3-one) in the dog and rat. Steroids 41, 23–33.

Hobe, G., Schön, R., Hajek, M., Undisz, K., Härtl, A., 1998. Studies on the hydrogenation of the progestagen dienogest in vivo and in vitro in the female rabbit. Steroids 63, 393–400.

Hobe, G., Schön, R., Hörhold, C., Hübner, M., Schade, W., Schubert, K., 1982. Microbial transformation of 17 alpha-cyanomethyl-17-hydroxy-4,9-estradien-3-one (STS 557) and 17 alpha-cyanomethyl-19-nortestosterone by Mycobacterium smegmatis. Steroids 39, 399–409.

Hobe, G., Schön, R., Wehrberger, K., Schade, W., Ritter, P., Hillesheim, H.G., 1989. Studies on the biotransformation of the progestagen dienogest in the rabbit. Exp. Clin. Endocrinol. 94, 203–210.

Kang, M.-J., Lisurek, M., Bernhardt, R., Hartmann, R.W., 2004. Use of high-performance liquid chromatography/electrospray ionization collision-induced dissociation mass spectrometry for structural identification of monohydroxylated progesterones. Rapid Commun. Mass Spectrom. RCM 18, 2795–2800.

Liebisch, G., Binder, M., Schifferer, R., Langmann, T., Schulz, B., Schmitz, G., 2006. High throughput quantification of cholesterol and cholesteryl ester by electrospray ionization tandem mass spectrometry (ESI-MS/MS). Biochim. Biophys. Acta 1761, 121–128.

Liu, S., Ying, G.-G., Zhao, J.-L., Chen, F., Yang, B., Zhou, L.-J., Lai, H., 2011. Trace analysis of 28 steroids in surface water, wastewater and sludge samples by rapid resolution liquid chromatography–electrospray ionization tandem mass spectrometry. J. Chromatogr. A 1218, 1367–1378.

Pozo, O. J., Deventer, K., Eenoo, P.V., Delbeke, F.T., 2008. Efficient approach for the comprehensive detection of unknown anabolic steroids and metabolites in human urine by liquid chromatography−electrospray-tandem mass spectrometry. Anal. Chem. 80, 1709-1720.

Pozo, O.J., Eenoo, P.V., Deventer, K., Delbeke, F.T., 2008. Detection and characterization of anabolic steroids in doping analysis by LC-MS. TrAC Trends Anal. Chem. 27, 657–671.
Quintana, P.G., Romero, S.M., Vaamonde, G., Baldessari, A., 2013. New metabolites of drospirenone obtained in Mucorales fungi culture. J. Mol. Catal. B Enzym. 97, 110–117.
Rannulu, N.S., Cole, R.B., 2012. Novel fragmentation pathways of anionic adducts of steroids formed by electrospray anion attachment involving regioselective attachment, regiospecific decompositions, charge-induced pathways, and ion-dipole complex intermediates. J. Am. Soc. Mass Spectrom. 23, 1558–1568.
Schänzer, W., Geyer, H., Fusshöller, G., Halatcheva, N., Kohler, M., Parr, M.-K., Guddat, S., Thomas, A., Thevis, M., 2006. Mass spectrometric identification and characterization of a new long-term metabolite of metandienone in human urine. Rapid Commun. Mass Spectrom. RCM 20, 2252–2258.
Schubert, K., Hobe, G., Kaufmann, G., Schumann, G., Wehrberger, K., Hörhold, C., 1983. Studies on biotransformation of STS 557. Exp. Clin. Endocrinol. 81, 168–174.
Thevis, M., Beuck, S., Höppner, S., Thomas, A., Held, J., Schäfer, M., Oomens, J., Schänzer, W., 2012. Structure elucidation of the diagnostic product ion at m/z 97 derived from androst-4-en-3-one-based steroids by ESI-CID and IRMPD spectroscopy. J. Am. Soc. Mass Spectrom. 23, 537–546.
Thevis, M., Bommerich, U., Opfermann, G., Schänzer, W., 2005. Characterization of chemically modified steroids for doping control purposes by electrospray ionization tandem mass spectrometry. J. Mass Spectrom. 40, 494–502.
Thevis, M., Schänzer, W., 2007. Mass spectrometry in sports drug testing: Structure characterization and analytical assays. Mass Spectrom. Rev. 26, 79–107.
Thevis, M., Schänzer, W., 2005. Mass spectrometric analysis of androstan-17beta-ol-3-one and androstadiene-17beta-ol-3-one isomers. J. Am. Soc. Mass Spectrom. 16, 1660–1669.
Williams, T.M., Kind, A.J., Houghton, E., Hill, D.W., 1999. Electrospray collision-induced dissociation of testosterone and testosterone hydroxy analogs. J. Mass Spectrom. 34, 206–216.
Zeng, Z., Liu, R., Zhang, J., Yu, J., He, L., Shen, X., 2013. Determination of seven free anabolic steroid residues in eggs by high-performance liquid chromatography–tandem mass spectrometry. J. Chromatogr. Sci. 51, 229–236.
Zheng, Y., Zhao, H., Zhu, L., Cai, Z., 2019. Comprehensive identification of steroid hormones in human urine based on liquid chromatography-high resolution mass spectrometry. Anal. Chim. Acta 1089, 100–107.

# Chapter 5

# Identification and Environmental Fate of Tire Rubber-Derived Chemicals Acutely Toxic to Coho Salmon

## 5.0 Publication and Contribution Statement

Section 5.3.1 of this chapter discussed the contribution of HZ to a collaborative research led by Dr. Zhenyu Tian (Tian et al, *Science* 2021). HZ developed the prep-scale HPLC fractionation steps in the effect-directed analysis scheme to identify the salmon toxicants from aqueous leachates of tire tread wear particles. The writing of section 5.3.1 was adapted from Tian et al 2021 (written by ZT, HZ, KTP, EPK) with modifications. Section 5.3.2-5.3.4 (ozonation of substituted-PPDs) of this chapter was led and written by HZ.

Related publications:

(1) Tian, Z., Zhao, H., Peter, K.T., Gonzalez, M., Wetzel, J., Wu, C., Hu, X., Prat, J., Mudrock, E., Hettinger, R., Cortina, A.E., Biswas, R.G., Kock, F.V.C., Soong, R., Jenne, A., Du, B., Hou, F., He, H., Lundeen, R., Gilbreath, A., Sutton, R., Scholz, N.L., Davis, J.W., Dodd, M.C., Simpson, A., McIntyre, J.K., Kolodziej, E.P., 2021. A ubiquitous tire rubber–derived chemical induces acute mortality in coho salmon. Science 371, 185–189.

## 5.1 Introduction

In U.S. Pacific Northwest, stormwater exposure annually causes unexplained acute mortality when adult coho salmon (*Oncorhynchus kisutch*) migrate to urban creeks to reproduce (Feist et al., 2017; Scholz et al., 2011). This phenomenon, known as urban runoff mortality syndrome (URMS), threatened salmonid species conservation across ~40% of Puget Sound land area. In the most urbanized watersheds with extensive impervious surfaces, 40-90% of returning salmon die before spawning (Feist et al., 2017; Scholz et al., 2011). Under such mortality rates, local coho populations will go extinct within 10-50 years (Spromberg and Scholz, 2011).

Previous assessments have discounted the physical condition of spawners, disease, and conventional water quality parameters (e.g., temperature and dissolved oxygen) as the causal

factors of coho mortality. Evidences suggested that the culprit was toxic chemicals in urban stormwater (Scholz et al., 2011), but coho exposure to common stormwater contaiminants (e.g., mixtures of common metals and polycyclic aromatic hydrocarbons) was not able to reproduce the URMS symptoms (Spromberg et al., 2016). In the meanwhile, landscape modeling linked coho mortality rates with impervious surface area and traffic intensity of the watersheds (Feist et al., 2017, 2011), and coho exposure to high-traffic arterial roadway runoff reproduced the mortality symptoms (Spromberg et al., 2016). High-resolution mass spectrometry (HRMS) analyses revealed similar chemical compositions between URMS-associated waters, roadway runoff, and tire tread wear particle (TWP) leachates (Peter et al., 2018). Further, TWP leachate exposure to coho salmon reproduced the URMS symptoms, confirming that the culprits were tire-derived (McIntyre et al., 2021). However, the causal toxicant(s) remained unidentified.

Led by Dr. Zhenyu Tian (postdoc scientist of our group), our group started a collaborative research project to identify the causal toxicant(s) of URMS from TWP leachate. To achieve this goal, we developed an effect-directed analysis (EDA) workflow by consecutive fractionation of TWP leachate with multiple reverse phase and normal phase liquid chromatography columns. The fraction toxicities were tested by juvenile coho salmon exposure experiments with 24-hour mortality as the phenotypic anchor. Toxic fractions were analyzed with ultrahigh performance liquid chromatography coupled to HRMS (UPLC-HRMS) for chemical profiling and toxicant identification. The first aim of this chapter was to discuss the development of the prep-scale HPLC fractionation steps in this EDA workflow – the key steps for the toxicant separation and the major contribution of HZ to this project.

After much effort, and via many contributions from collaborators, the coho toxicant was identified to be a highly toxic quinone transformation product (TP) of 6PPD (*N*-(1,3-

dimethylbutyl)-*N*′-phenyl-p-phenylenediamine), a globally ubiquitous tire rubber antioxidant (Tian et al., 2021). 6PPD is substantially used in tire rubbers (mass fraction 0.4-2%) (R.T. Vanderbilt Company, 2010) and it reacts with ground-level atmospheric ozone to prevent oxidation of rubber elastomers (Huntink, 2003; Lattimer et al., 1983). Accordingly, 6PPD is transformed into a suite of currently uncharacterized ozonation transformation products (TPs) in the environment during the product life (Lattimer et al., 1983). Considering their ubiquity and substantial mass discharge potential, it is important to identify such ozonation TPs of 6PPD and understand their occurrence and environmental fate.

In addition to 6PPD, other substituted paraphenylene diamines [substituted-PPDs; e.g., IPPD (*N*-Isopropyl-*N*′-phenyl-*p*-phenylenediamine), 7PPD (*N*-(1,4-dimethylpentyl)-*N'*-phenyl-*p*-phenylendiamine), DPPD (*N,N*′-Diphenyl-*p*-phenylenediamine), DTPD (*N,N'*-ditolyl-*p*-phenylene diamine), DNP (*N,N*′-Di-2-naphthyl-*p*-phenylenediamine); **Table 5.1**] are also used as antioxidants (Huntink et al., 2004) and have been detected in multiple environmental matrices including house dust (Huang et al., 2021; Wu et al., 2020), wastewater, and landfill leachates (Zhang et al., 2021). Considering their structural similarity to 6PPD, ozonation of these substituted-PPDs may also form quinone structure products that are likely toxic to aquatic organisms. It is important to characterize the PPD-quinone formation potentials of the multiple substituted-PPDs.

The second aim of this chapter was to study the ozonation TPs of the substituted-PPDs. Using heterogeneous gas-phase ozonation in a chamber reactor, we studied the formation potentials of PPD-quinones from the multiple substituted-PPDs with the structures and reaction yields confirmed by synthetic standards. We then identified the structures of 6PPD ozonation TPs in detail with an UPLC-HRMS/MS based workflow, with TP structures proposed through

spectral interpretation and standard confirmation (when available). Lastly, the identified 6PPD TPs were screened and semi-quantified in solvent extracts of ozonated TWPs and in archived solid phase extraction (SPE) extracts of TWP leachate, roadway runoff, and creek stormwater samples, to investigate their occurrence multiple environmental matrices.

## 5.2 Materials and Methods

### 5.2.1 Chemicals and Reagents

6PPD was purchased at industrial grade (95%) from Usolf Chemicals (Shandong, China) and at analytical grade (98%) from Ambeed (Arlington Heights, IL, USA). IPPD, 7PPD, DPPD, DTPD, and DNP were purchased at industrial grade (95%) from Richest Group Ltd (Shanghai, China). The PPD solids were stored in airtight bags (for industrial grade PPDs) or an airtight bottle (for analytical grade 6PPD) at 4 °C prior to use. For TP standards, 6PPD-quinone (>98.8%) was purchased from HPC Standards Inc. (Atlanta, GA, USA); 4-nitrodiphenylamine (4-NDPA; 99%), 4-aminodiphenylamine (4-ADPA; 98%), and 1,3-dimethylbutylamine (1,3-DMBA; 98%) were purchased from Sigma-Aldrich (St. Louis, MO, USA); 4-nitrosodiphenylamine (4s DPA) was purchased from ChemService Inc (West Chester, PA, USA); 4-hydroxydiphenylamine (4-HDPA) was purchased from Fisher Scientific (Pittsburgh, PA, USA). Acetone (OPTIMA® grade), methanol (MeOH, OPTIMA® grade), hexane (HPLC grade), dichloromethane (DCM, HPLC grade), absolute ethanol (EtOH, 99.5%, 200 proof), ethyl acetate (OPTIMA® grade), formic acid (LC-MS grade), ammonium fluoride (99.9%, trace metal grade), sodium hydroxide (NaOH, 10 N solution, 30% w/w), hydrogen chloride (HCl, 34-37% solution in water, trace metal grade), anhydrous sodium sulfate ($Na_2SO_4$, 99.7%), and sand (Ottawa, 20-30 mesh) were purchased from Fisher Scientific (Pittsburgh, PA, USA). Cation exchange (CEX) resin (Amberlite® IR120) and hydrophobic copolymer (reverse phase) resin

(Amberlite® XAD-2 and Supelite™ DAX-8) were purchased from Sigma Aldrich (St. Louis, MO, USA). Silica gel (0.03-0.20 mm, 60 Å) was purchased from Acros Organics (Fairlawn, NJ, USA). Deionized (DI) water was produced by a Nanopure water purification system (Thermo Barnstead Nanopure Diamond UV, Dubuque, IA, USA).

### 5.2.2 TWP Leachate Fractionation

*XAD-2 Extraction of TWP Leachate.* CEX resin (80 mL, pre-cleaned and conditioned by 0.1 M NaOH, 0.1 M HCl, DI water) and XAD-2 resin (40 mL, pre-cleaned by MeOH, ethyl acetate, acetone, and hexane) were loaded into two sequential glass chromatography columns (300 mm × 20 mm ID, fused mesh base), each topped with ~5 cm sand and a stainless-steel mesh. 45 L of 1000 mg/L TWP leachate (see details on leachate generation in Supplementary Materials, **Figure S5.1**, **Table S5.1**) was loaded directly onto the CEX column with CEX effluent sent to the XAD-2 column. The TWP leachate was loaded onto each column by up-flow (60 mL/min, driven by a peristaltic pump) to maximize mass transfer during subsequent elution. Organic compounds were eluted from XAD-2 consecutively with 200 mL ethanol (EtOH) and 200 mL ethyl acetate by gravity (~10 mL/min). The EtOH eluent was concentrated to 15 mL with rotary evaporation (Büchi R-210, Flavil, Switzerland; 65°C, 360 mBar); the ethyl acetate eluent was concentrated to ~5 mL, then solvent exchanged to 15 mL ethanol with rotary evaporation (45 °C, 500 mBar). One third of each eluent (5 mL in ethanol), and the first 15 L of effluent leachate passed through the column, were exposed to juvenile coho salmon for toxicity test.

*Silica Gel Fractionation.* A 5 mL aliquot of the CEX-XAD-2 EtOH extract was concentrated to ~1 mL using a rotary evaporator (65 °C, 360 mbar) and diluted with 2 mL hexane. Then, 5 g of 10% deactivated silica gel was wet-packed (in hexane) into a thin

chromatography column (250 mm × 10 mm ID; glass wool plug at the bottom) with ~1 cm of anhydrous Na2SO4 added on top. The packing solvent was drained and 10 mL of hexane was passed through by gravity flow (~10 mL/min) to condition the column. The extract was then loaded on top of the column with minimum disturbance. The column was eluted (~10 mL/min) consecutively with 15 mL each of hexane, hexane:DCM 2:1 (v/v), hexane:DCM 1:2 (v/v), and DCM. Each fraction was concentrated using the rotary evaporator, and solvent exchanged to ~5 mL EtOH for fish exposure.

*Parallel HPLC Fractionation.* The silica gel hexane:DCM 2:1 (v/v) fraction (15 mL) was solvent exchanged to ~0.5 mL EtOH under nitrogen, mixed with 0.5 mL DI water, and filtered through a 0.2 μm PTFE syringe filter (Pall, Port Washington, NY, USA). The filtered extract was further fractionated by a high-performance liquid chromatography (HPLC) system (Agilent 1290 Infinity, Santa Clara, CA, USA) equipped with a UV/Vis diode array detector (Agilent 1260) and a fraction collector (Agilent 1260). Three semi-preparative scale reverse phase HPLC columns with different stationary phase functionalities were used for the parallel fractionation: Aquasil C18 (250 × 4.6 mm, 5 μm, Thermo Fisher), Curosil PFP (pentafluorophenyl, 250 × 4.6 mm, 5 μm, Phenomenex), and Microsorb phenyl (250 × 4.6 mm, 5 μm, Varian) (**Figure 5.1**). Because MeOH and acetonitrile are more toxic to coho salmon, DI water (A) and EtOH (B) were used as mobile phases without additives, with a gradient elution program: 0-1 min, 50 % B; 1-13.5 min, 50-100% B; 13.5-16 min, 100% B; 16-17 min, 100-50% B; stop time 20 min. The column was maintained at 45 °C, with flow rate 1 mL/min and injection volume 200 μL (5 injections per 1 mL sample). The UV/Vis (210 nm, 280 nm, 306 nm) response did not show any peaks before 5 min (instrument dead volume ~3 mL); accordingly, we collected one-minute fractions from 5 - 15 min, yielding ten fractions (F1 to F10) for each column. 5% of the volume

of each HPLC fraction was kept and diluted two-fold for instrumental analysis, the remaining volume was used for fish exposure.

*Sequential HPLC Fractionation.* For sequential fractionation through the C18, PFP, and phenyl HPLC columns (identical to above), a centrifuge evaporator (Thermo SpeedVac Savant SC210A) was employed to concentrate the toxic fractions from each column: C18-F6 (~5 mL) was concentrated (0.3 torr, room temperature) to ~0.5 mL in $H_2O$, and 0.5 mL EtOH was added to dissolve the solid. After fractionation on PFP, PFP-F6 was concentrated (same conditions) and further injected onto the phenyl column for separation. Finally, phenyl-F4 was evaporated to dryness (overnight) in a pre-weighed test tube. A pink-magenta solid precipitate was observed, and the dry mass was recorded.

### 5.2.3 Ozonation of Substituted-PPDs

*Gas Phase Ozonation*. Stock solutions of industrial grade substituted-PPDs (2 g/L for 6PPD, 5 g/L for other substituted-PPDs, nominal concentrations, different concentrations due to experimental batch variance) were prepared in acetone, then 20 µL of the stocks (6PPD: 40 µg mass, ~150 nmol; others: 100 µg mass, ~280-440 nmol) were evenly applied onto pre-cleaned glass slides (~9.5 $cm^2$ surface area) with a glass syringe and dried (~30 min) under ambient air. The surface concentrations were ~4.2 µg/$cm^2$ for 6PPD and ~10.5 µg/$cm^2$ for other substituted-PPDs. Six slides, each coated with one of the substituted-PPDs, were ozonated in a batch in a PTFE chamber reactor, and three batches of the slides were ozonated separately for 1, 3, and 7 days. The 1, 3, and 7-day trials were conducted in series to ensure consistent substituted-PPDs masses, and thus ozone demands, in the reactor. Fresh stock solutions were prepared from the solid standards at the beginning of each ozonation period due to the reported instability of 6PPD in water (European Union, 2006) and MeOH (personal communication by Eurofins Scientific). Ozone was

produced (1 L/min) by a photochemical ozone generator (Model 97-0066-01, UVP, Upland, CA, USA), with 206-225 ppbv output concentrations measured at the beginning of each ozonation period using an ozone detector (Model IN2000-LC benchtop configuration, IN USA, Needham, MA, USA). Ozone entered the chamber from a bottom front port and flowed out from a top rear port (**Figure S5.2**). After reaction, the slides were thoroughly rinsed with ~9 mL MeOH and these eluents were brought to 10 mL in volumetric flasks for analysis. One blank control (glass slide spiked with 20 µL acetone and dried) was included for each ozonation period (n = 3 in total), subject to the same ozonation and elution procedure. One spiked control was made for each substituted-PPD by applying the corresponding stock solution onto the slide, drying, and eluting (after ~30 min) without ozonation. The recovery of all the substituted-PPDs from the spike controls was 101% ± 7%.

*Instrumental Analysis.* The eluents were stored at 4 °C and analyzed as one batch within 48 hours after ozonation experiments were completed (storage time: 1-day trial, ~12 days; 3-day trial, ~9 days; 7-day trial, ~2 days). Undiluted eluents were analyzed in triplicate injections to identify TPs, and 1000-fold diluted eluents (reduced matrix effects and detector saturation) were then analyzed to quantify residual substituted-PPDs with 7-point external standard calibration curves (0.5-100 µg/L; $R^2 > 0.995$). Due to the longer storage time for the 1-day and 3-day trials and potential storage loss, we report here the residual substituted-PPD concentrations as semi-quantitative, although separate observations of 6PPD held at -20 °C indicated 6PPD stability over 3 months in similar methanolic extracts (see *6PPD TP identification* section below). Instrumental analysis employed an Agilent 1290 Infinity ultra-performance liquid chromatography (UPLC) coupled to an Agilent 6530 quadrupole time-of-flight HRMS (qTOF-HRMS). Full scan analysis was first performed for all samples, and MS/MS spectra were then

acquired for prioritized features (exact mass-retention time pairs) with data-dependent acquisition under three collision energies (10, 20, 40 eV). Analysis used only positive electrospray ionization (ESI+) because ESI+ is preferred relative to ESI- for amines (Kassler et al., 2014; Lu et al., 2017). Detailed instrumental methods and data analysis parameters are reported previously (Du et al., 2017; Peter et al., 2018; Tian et al., 2020) and are summarized in the Supporting Information. For instrumental quality assurance and quality control (QA/QC), a checktune including mass calibration was performed before each analytical run, and mass accuracy was corrected via continuous infusion of purine and HP-921 calibrants during the run. Solvent blanks and instrumental internal standard (ISTD) controls were analyzed every 12 samples. The retention time (RT), mass accuracy, and abundance of ISTD controls were used for performance evaluation of each analytical run. The RT deviation and mass error of the ISTDs were <0.15 min and <5 ppm, respectively. Response (peak area) variations of ISTDs were <15% within each analytical batch.

*PPD-quinones Confirmation.* After three months of extract storage (-20 °C), 6PPD-quinone, 7PPD-quinone, IPPD-quinone, DPPD-quinone, and DTPD-quinone in the reaction mixture were confirmed with synthetic standards (see synthesis detail in Supplementary Materials) through RT, accurate mass, and MS/MS spectra matches. The concentrations of PPD-quinones were then quantified in 10-fold diluted eluent extracts with 7-point external standard calibration curves (1-200 μg/L; $R^2 > 0.995$). PPD-quinone formation during the extract storage is likely negligible because 6PPD demonstrated stability over the 3-month storage (see *6PPD TP identification* section below).

*6PPD TP Identification.* To identify 6PPD ozonation TPs beyond 6PPD-quinone, full-scan data of the reaction mixtures were processed in a non-target approach with Agilent software

packages (MassHunter Profinder (B.08.00) for feature extraction and alignment, Mass Profiler Professional (B.13.00) for feature prioritization; **Table S5.2**). Features were prioritized if they were detected in triplicate injections (n = 3/3) for one of the ozonation periods, had peak area 3-fold greater than the spike and blank controls, and >1% the initial peak area of 6PPD. MS/MS data were then acquired for all prioritized features under three collision energies (10, 20, 40 eV). 6PPD TPs were identified from the prioritized features based on relevant formula (assigned in Agilent MassHunter ID Browser based on accurate mass and isotope pattern), retention time (RT), diagnostic MS/MS neutral losses and fragments, and previous reports on 6PPD ozonation and hydrolysis pathways (European Union, 2006; Lattimer et al., 1983). TP structures were confirmed with commercial standards when available. Based on the scale proposed by Schymanski et al. to communicate identification confidence (Schymanski et al., 2014), level 1 identification was assigned to TPs with precursor mass, isotope pattern, RT and MS/MS fragments matching commercial standards. Level 2a identification stood for spectra matches to databases but was not observed in this study. Level 2b confidence reflected TPs for which MS/MS information and expert knowledge of ozonation chemistry indicated no other possible structure. Level 3 described tentative structural candidates with MS/MS fragments matching plausible ozonation reactions, and level 4 describes relevant molecular formula assignment without diagnostic MS/MS spectra.

After identification of the level 1 TPs (-20 °C storage for ~3 months), their concentrations were quantified in 10-fold diluted 6PPD ozoantion mixtures with 7-point external standard calibration curves (1-200 μg/L; $R^2 > 0.995$) via LC-qTOF-HRMS. Despite potential instability of 6PPD in MeOH (personal communication by Eurofins Scientific), the residual 6PPD mass quantified within these 10-fold diluted mixtures after ~3 month storage at -20 °C were quite similar

to the original quantification data (109 ± 4% relative recovery). Therefore, TP formation from 6PPD during the 3-month storage period was considered negligible. Abundance comparisons of other TPs reflected relative peak areas observed in undiluted reaction mixtures that were analyzed within 48 hours after concluding the ozonation experiments.

*Semi-Quantification of 6PPD TPs in Environmental Samples.* The compounds 6PPD, five 6PPD level 1 ozonation TPs, TP 282 (6PPD ozonation TP with the second highest peak area), TP 274 (6PPD ozonation TP previously observed in stormwaters with high peak area; Peter et al., 2018), and 4-OH DPA (6PPD hydrolysis TP; European Union, 2006) were semi-quantified in diluted methanolic extracts of TWP and archived methanolic extracts of TWP leachate, roadway runoff, and creek stormwater derived from SPE. The TWP samples (n = 3) were equal weight mixtures of rubber tread particles from nine used and new tires (**Table S5.1**; Tian et al., 2021). TWPs (160 mg) extracts were prepared by Ximin Hu (PhD student of our group), by extracting with 32 mL MeOH under sonication (30 min), filtering with 0.7 µm glass fiber filter paper and 0.2 µm PTFE syringe filter, and diluting 10-fold with MeOH before analysis. For comparison, the TPs were also quantified in TWPs (n = 3) exposed to either 6 h of ozone or air (see details in the publication in preparation led by Ximin Hu). The TWP leachates (250 mg TWP/L; diluted from 1000 mg/L TWP leachate; n = 3 leachates, one replicate per leachate) were prepared previously (6/2/2019, 7/2/2019, 7/16/19) as positive controls for the coho salmon exposures (see details in Supplementary Materials and Tian et al., 2021) by recirculating (0.5 L/min) DI water through columns packed with TWP and glass beads. Roadway runoff (n = 3 storms, triplicate extracts for each event) were grab samples collected for a previous study (led by Dr. Zhenyu Tian, manuscript in preparation) in 6/16/2017, 3/13/2019, and 4/8/2019 from a multilane highway in Seattle, WA, USA (47°38'38.4"N, 122°18'13.7"W). Roadway-impacted creek stormwater (n = 6 storms, one

replicate each) were time-weighted composite samples collected across the hydrograph peak of six storm events (10/9/2020, 10/23/2020, 11/3/2020, 11/13/2020, 3/4/2021, 3/18/2021) from Miller Creek in Burien, WA, USA (47°27'04.0"N, 122°20'47.8"W) via ISCO sampler (150 mL/15 min; model 6712, Teledyne ISCO, Lincoln, NE, USA), collected for a study led by Dr. Zhenyu Tian (manuscript in preparation). All aqueous samples (1 L for TWP leachate and roadway runoff, 200 mL for creek stormwater) were previously solid-phase extracted into 1 mL MeOH extracts (Oasis HLB cartridges; Waters, Milford, MA, USA) with extracts stored at -20 °C before analysis.

To mitigate matrix effects and detector saturation, extracts were typically diluted with methanol prior to analysis: TWP leachate extracts 2-10 fold, roadway runoff extracts 20-50 fold, creek stormwater extracts 10-50 fold, TWP methanolic extracts 10 fold. Preliminary trials indicated that such dilution stabilized detected peak areas (after correcting for dilution ratios) of prioritized TPs and analytes such as 6PPD-quinone. Diluted extracts were analyzed (duplicate injection for extracts without triplicates) by full-scan HRMS. 6PPD, level 1 ozonation TPs, and 4-OH DPA were quantified with 7-point calibration curves (0.5-100 µg/L, $R^2 > 0.995$). TP 282 and TP 274 were tentatively semi-quantified by creating an average calibration curves of 4-ADPA, 1,3-DMBA, 4s DPA, and 4-HDPA because of their tight slope variation (9% variation; **Figure S5.3**) across this TP family and the related amine structures of these TPs (Henning et al., 2021; Weizel et al., 2021). To quantitatively evaluate method recovery, 6PPD and the level 1 TPs were spiked in triplicate into 160 mg TWP (50 µg/g for TPs, 5000 µg/g for 6PPD), 1L TWP leachate (20 µg/L for 1,3-DMBA and 4-HDPA, 0.5 µg/L for other analytes), 1L roadway runoff (20 µg/L for 1,3-DMBA, 5 µg/L for other analytes), or 200 mL creek stormwater samples (5 µg/L for 1,3-DMBA, 0.5 µg/L for other analytes) at levels close to their detected concentrations (**Table S5.3**). The samples were processed identically through the original SPE (for TWP leachate, roadway runoff,

and creek stormwater), solvent extraction (for TWP), and subsequent dilution schemes. Unspiked samples were included in triplicate for each matrix and triplicate lab blanks were included. The spike recoveries were defined as the detected levels in spiked samples (corrected for detection in unspiked samples) over the nominal spike levels. Across the target analytes, the recoveries ranged 70%-107% in TWP extraction, 46%-76% in TWP leachate, 27%-62% in roadway runoff, and 43%-106% in creek stormwater (**Table S5.3**)**.** We considered the recoveries acceptable due to the multiple analytes included, the complex and variable matrix types, and the semi-quantified aspect of this study (for example, no isotopic standards were used); subsequent concentration data were not normalized to observed recoveries. Archived field and process blanks (n = 3 for TWP leachate, n = 1 for roadway runoff, n = 8 for creek stormwater, n = 3 for TWP methanolic extract) were analyzed and average blank levels were subtracted from detected analyte concentrations in environmental samples. Limits of detection (LODs)/limits of quantifications (LOQs) were defined as the average plus 3/10-fold standard deviation of blank levels, or analyte concentrations with 3/10 signal to noise ratios, whichever was higher (**Table S5.3**). The LODs ranged 0.29-6.0 µg/g in TWP methanolic extracts, 2.4-30 ng/L in TWP leachate, 12-690 ng/L in roadway runoff, and 21-750 in creek stormwater. The LOQs were 0.97-20 µg/g in TWP methanolic extracts, 8.0-100 ng/L in TWP leachate, 38-2300 ng/L in roadway runoff, and 68-2500 in creek stormwater (**Table S5.3**). Concentrations between LODs and LOQs were reported as "detected".

## 5.3 Results and Discussion

### 5.3.1 Fractionation of the TWP Leachate and Identification of 6PPD-quinone

Mixture complexity (measured here as number of UPLC-HRMS ESI+ chemical features in SPE-extracted fish exposure water) was a significant barrier to identify the causal toxicant from TWP leachate. For example, 250 mg/L TWP leachate (diluted from 1000 mg/L TWP

leachate for positive controls in fish exposure) typically contained >2000 ESI+ features. To reduce the number of candidate toxicants, we employed EDA to produce chemically simpler fractions with retained fish toxicity. The TWP leachate fractionation scheme was demonstrated in **Figure 5.2**. In contrast to traditional EDA, which often employed in vitro bioassay as the biological endpoint, the phenotypic anchor in this study was a in vivo species-specific mortality event. Therefore, larger sample loads (45 L 1000 mg/L TWP leachate) and fish-safe solvents (water and EtOH) were employed in our fractionation scheme. Throughout the fractionation, observed toxicity remained confined to one fraction, indicating the causal toxicant to be a single compound or a small, structurally related family of compounds. No mortality occurred in negative controls, including solvent- and process-matched method blanks subjected to identical separations (0 of 80 fish, 16 exposures) or exposure water blanks (0 of 45 fish, 9 exposures).

Cation exchange chromatography was first utilized to remove the charged chemicals. Cation exchange reduced 39% of the features in the TWP leachate extracts, attributable to the many TWP-derived compounds with amine functionalities that are positively charged. The eluent from the cation exchange column remained lethal to coho, indicating that the toxicant was not strongly ionic. After loading the cation exchange eluent onto a reverse-phase column (XAD-2 resin), toxicity eluted with EtOH from the XAD-2 resin with ~1355 features; aqueous effluent and ethyl acetate eluents were not lethal. We further reduced the mixture complexity leveraging the orthogonality of normal phase chromatography to XAD-2 resin. The XAD-2 EtOH fraction was solvent-exchanged into hexane and loaded onto a silica gel column. Gradient elution of the silica gel column with 3:0, 2:1, 1:2, and 0:3 (v/v) of hexane:dichloromethane (Hex:DCM) yielded toxicity (after solvent-exchange into EtOH for fish exposure) only in the 2:1 Hex:DCM eluent with ~660 features.

The higher resolution of high-performance liquid chromatography (HPLC) was then leveraged to further reduce the mixture complexity. Using a semi-preparative C18 column, the 2:1 Hex:DCM silica gel fraction (solvent exchanged into EtOH/$H_2O$ 50:50 (v/v) before injection) was separated into ten 1-min HPLC fractions (C18-F1 to F10). Only the C18-F6 (10-11 min) was lethal to coho; it contained ~225 ESI+ features and ~26 ESI- features. Having removed ~90% of the features in the original TWP leachate, Dr. Zhenyu Tian began to prioritize the remaining chemical features based on their abundance (ESI+/- peak area). However, over ~ 6 months and many rounds of identification and subsequent exposure to juvenile coho, none of the identified chemical exposures reproduced URMS symptoms or induced mortality. This indicated that the mixture complexity is still too high to prioritize the culprit toxicant, and further fractionation is needed.

To sharpen our search, I developed multi-dimensional semi-preparative HPLC using two additional structurally distinct column phases (pentafluorophenyl (PFP) and phenyl; same column dimensions, mobile phase, and gradient as for C18-HPLC). Parallel fractionations (Muschket et al., 2018) of the 2:1 Hex:DCM silica gel fraction generated toxic fractions of PFP-F6 (10-11 min; ~204 ESI+, 60 ESI- features) and phenyl-F4 (8-9 min; ~237 ESI+, 75 ESI- features); all other fractions were non-toxic. Notably, across the three toxic fractions (C18-F6, PFP-F6, phenyl-F4), only 4 ESI+ and 3 ESI- HRMS features co-occurred (**Figure 5.1**). One unknown compound (*m/z* 299.1752, $C_{18}H_{22}N_2O_2$, RT 11.0 min on analytical UPLC) dominated the detected peak area of these 4 features (10-fold higher intensity in both ESI+ and ESI-). To further resolve candidate toxicants for synthetic efforts, the three-dimensional HPLC workflow was converted from parallel to serial through sequential C18, PFP, and phenyl columns (C18-F6 to PFP-F6 to phenyl-F4; with solvent removal by centrifugal evaporation). The purified final

fraction was chemically simple (4 ESI+, 3 ESI- features), highly lethal (100% mortality in 4 hour; N=15 coho, 3 exposures), and was again dominated by the $C_{18}H_{22}N_2O_2$. Drying this fraction yielded a pink-magenta precipitate (**Figure 5.2**).

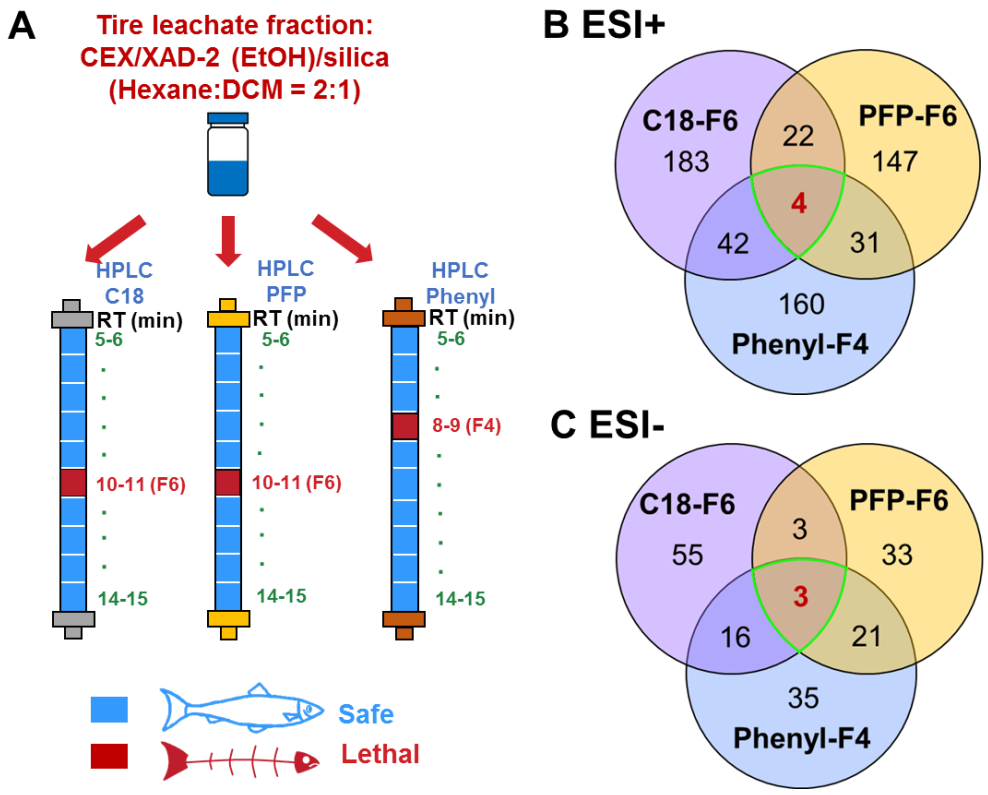


**Figure 5.1** Parallel HPLC fractionation of the TWP leachate. (A) Schematic of the parallel HPLC fractionation. The toxic 2:1 hexane/DCM (v/v) silica gel eluent was fractionated with each of semi-preparative C18, PFP, and Phenyl columns separately, and their toxic fractions were identified through fish exposures. Blue colors represent fractions that were safe for juvenile coho salmon; red colors represent lethal fractions. TWP, tire tread wear particles; CEX, cation exchange; EtOH, ethanol; DCM, dichloromethane; RT, retention time. (B) Venn diagram of chemical feature numbers (after isotope grouping and blank subtraction) detected by UPLC-HRMS under ESI+ in the toxic fractions, i.e. C18 F6, PFP F6, and Phenyl F4. The chemical features were detected in SPE-extracted fish exposure water samples. (C) Venn diagram of UPLC-HRMS chemical feature numbers detected under ESI-.

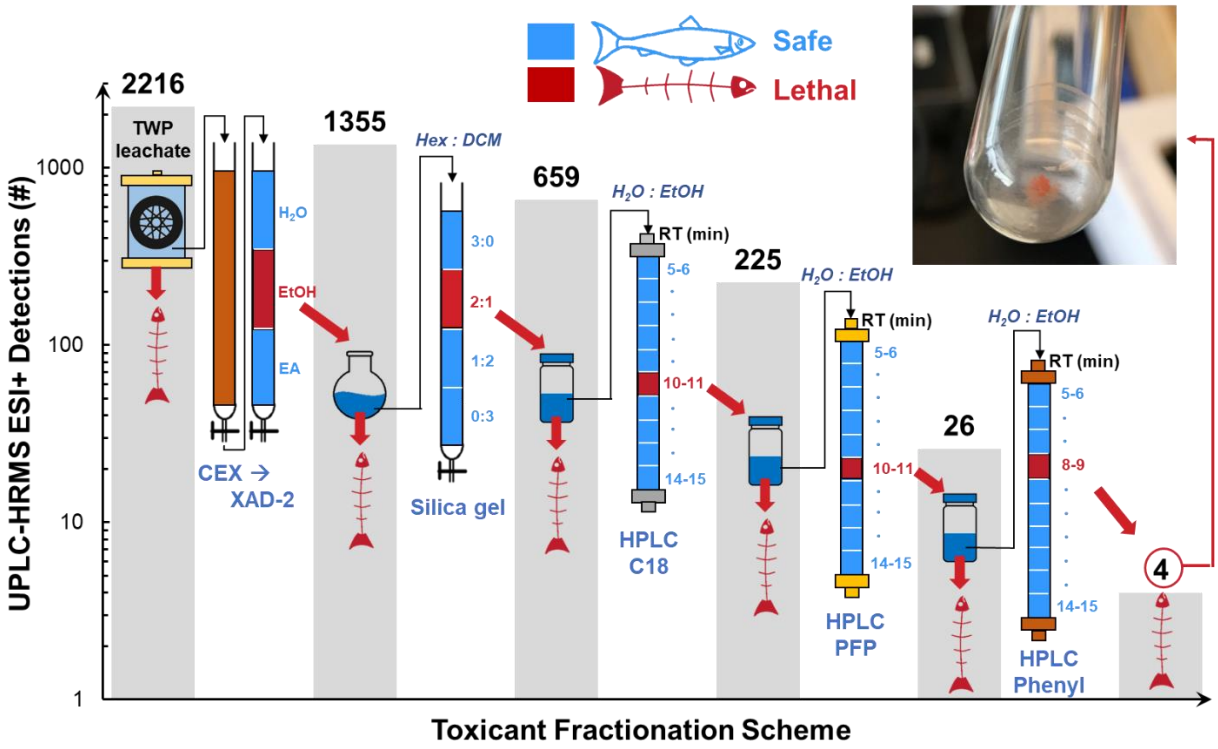


**Figure 5.2** Tire rubber leachate fractionation scheme. As a metric of mixture complexity and separation efficiency, the numbers above gray bars represent unique chemical features detected in solid-phase extracted fish exposure water (1 L) and subsequent fractions by UPLC-HRMS. Green colors represent non-lethal fractions; red colors represent lethal fractions. All fractionation steps and exposures were replicated at least twice; positive and negative controls were included throughout fractionations. The inset photo depicts purified product (~700 µg from 30 L of TWP leachate) in the final lethal fraction. TWP, tire tread wear particles; CEX, cation exchange; EA, ethyl acetate; EtOH, ethanol; H2O, water; Hex, hexane; DCM, dichloromethane; RT, retention time.

After confirming the molecular formula of the toxicant, Dr. Tian extensively searched published characterizations of crumb rubber (U.S. EPA, 2019) with related formulas (i.e., $C_{18}H_{0-x}N_{2-4}O_{0-y}$), and noticed that several characteristics of the $C_{18}H_{24}N_2$ anti-ozonant "6PPD" (N-(1,3-dimethylbutyl)-N'-phenyl-p-phenylenediamine) matched necessary attributes. Through gas-phase ozonation experiments, we confirmed the $C_{18}H_{22}N_2O_2$ to be an ozonation TP of 6PPD. 2D NMR analysis further confirmed this $C_{18}H_{22}N_2O_2$ to be "6PPD-quinone" (2-anilino-5-[(4-methylpentan-2-yl)amino]cyclohexa-2,5-diene-1,4-dione). Subsequent exposures of ozone-

synthesized and tire leachate-derived 6PPD-quinone (~20 µg/L nominal concentrations) both induced rapid (<5 h, with initial symptoms evident within 90 minutes) mortality (N=15 fish, 3 exposures) in coho which matched the 2-6 hour mortality observed for TWP leachate positive controls. Controlled dosing experiments (10 concentrations, N=160 fish in two independent exposures) estimated $LC_{50}$ (0.79±0.16 µg/L) with pure 6PPD-quinone closely matched the $LC_{50}$ (0.82±0.27 µg/L) derived from mixture exposure of bulk roadway runoff and TWP leachate. The above evidence suggested that the mixture toxicity of roadway runoff and TWP leachate was primarily contributed by 6PPD-quinone. Retrospective analysis of archived roadway runoff and stormwater receiving water samples also revealed ubiquitous presence of 6PPD-quinone in U.S. West Coast road at levels near or above the $LC_{50}$. Therefore, we concluded that 6PPD-quinone was the primary causal toxicant for decades of stormwater-linked coho salmon acute mortality observations. For more details, see Tian et al. (2021).

### 5.3.2 PPD-quinones Formation in Ozonation of Substituted-PPDs

To identify other potential sources of the PPD-quinone compounds, we studied the PPD-quinone formations during ozonation of other substituted-PPDs in comparison to 6PPD. We acquired industrial grade IPPD, 7PPD, DPPD, DTPD, and DNP, purchased commercial standards of 6PPD-quinone and DPPD-quinone, and synthesized analytical standards of IPPD-quinone, 7PPD-quinone, and DTPD-quinone through collaboration with Dr. Kelly Kim at the University of Washington-Tacoma (see synthesis details in the Supplementary Materials; **Table 5.1**). None of the PPD-quinones were detected in the blank solvent controls in the ozonation experiments. 6PPD-quinone, 7PPD-quinone, and IPPD-quinone were detected in the corresponding spiked controls (i.e. industrial 6PPD, 7PPD, and IPPD stocks applied onto the glass slide without ozonation, respectively), while DPPD-quinone, DTPD-quinone, and the

DNP-quinone feature (feature with $C_{26}H_{18}N_2O_2$ formula but not confirmed to be DNP-quinone with an authentic standard) were not detected. Levels of 6PPD-quinone, 7PPD-quinone, and IPPD-quinone were <1.5% in the spiked control relative to the 1-day ozonation mixture. The PPD-quinones masses in the spiked controls likely reflected oxidation during the PPDs solids transport and storage despite air-tight bags were used.

The substituted-PPDs can be divided into two structural groups, *N*-alkyl-*N'*-aryl-PPDs (6PPD, 7PPD, IPPD) and *N*,*N'*-diaryl PPDs (DPPD, DTPD, DNP), and they showed distinct behaviors during the ozonation. For the *N*-alkyl-*N'*-aryl-PPDs, 90% of the initial 6PPD and 7PPD mass and 70% of the initial IPPD mass were removed after 1 day of ozonation. The removal of *N*-alkyl-*N'*-aryl-PPDs was insensitive to longer exposure times: 83%-88% of 6PPD, 90%-92% of 7PPD, and 65%-70% of IPPD were transformed in 3-day and 7-day ozonations (**Figure 5.3a**), while ~10% masses of 6PPD and 7PPD and ~30% mass of IPPD remained recalcitrant. The recalcitrance to complete ozonation was consistent with past observations for 6PPD where formation of protective films on rubber surfaces occurred via oxidative polymerization or radical interactions (Cataldo et al., 2015; Huang et al., 2001; Huntink, 2003; Lattimer et al., 1983). We speculate that such protective films may have formed at the PPDs solid-air interfaces during the ozonation and limited further oxidation of the substituted-PPDs. This observation implied implicit surface area and particle size dependencies of substituted-PPDs ozonation. Further research to characterize the influence of such dependencies on the rates and extent of substituted-PPDs ozonation is merited.

In contrast to *N*-alkyl-*N'*-aryl-PPDs, the *N*,*N'*-diaryl PPDs showed much less removal during ozonation. DPPD showed no apparent removal (within the variance of the analytical method), and DTPD and DNP showed 8% and 17% removal after 1 day of ozonation,

respectively; further removal was not seen under longer exposure time (**Figure 5.3c**). The lower removal of *N*,*N'*-diaryl PPDs is consistent with previous studies showing slower reaction rates of *N*,*N'*-diaryl PPDs than *N*-alkyl-*N'*-aryl-PPDs toward ozone (Braden and Gent, 1962; Huntink, 2003). This difference could be explained by the electron withdrawing effects of the additional aromatic rings in the *N*,*N'*-diaryl PPDs, leading to lower electron density on the nitrogens and thus lower reactivity (Huntink, 2003). Alternatively, the aromatic ring could also strongly stabilize the nitrogen cation radical intermediates formed during ozone decomposition (Tian et al., 2021), leading to chain reactions of ozone decomposition. To reveal the detailed mechanisms, further research to characterize the stoichiometry of ozone reaction with substituted-PPDs is merited.

Formation of PPD-quinones was observed for all substituted-PPDs. Five of the PPD-quinones (6PPD-quinone, IPPD-quinone, 7PPD-quinone, DPPD-quinone, DTPD-quinone) were confirmed with commercial or synthetic standards, and a "$C_{26}H_{18}N_2O_2$ at 10.6 min feature" observed in DNP ozonation mixture was likely DNP-quinone based on RT and MS/MS evidence (**Figure 5.4**). Notably, the PPD-quinones for *N*-alkyl-*N'*-aryl-PPDs showed RTs 2.7-4.1 min later than the corresponding substituted-PPDs, while the PPD-quinones for *N*,*N'*-diaryl-PPDs showed RTs 1.7-3.5 min earlier than the corresponding parent compounds (**Table 5.1**). Previously, we observed that the amino groups on 6PPD-quinone showed much lower p$K_a$ values (estimated p$K_a$ < 0) in comparison to 6PPD (p$K_a$ 6.73), likely caused by the strong electron withdrawing effects of the neighboring quinone oxygens (Tian et al., 2021). *N*,*N'*-diaryl-PPDs likely also had lower p$K_a$ values than *N*-alkyl-*N'*-aryl-PPDs because of the electron withdrawing effects of the additional aromatic rings. Therefore, the PPD-quinones and the *N*,*N'*-diaryl-PPDs were likely present in their neutral form under the HPLC mobile phases conditions (0.1% formic

acid, pH 4.2), while the *N*-alkyl-*N'*-aryl-PPDs were ionized. The MS/MS spectra of 6PPD-quinone ($[M+H]^+$ 299.1758, $[C_{18}H_{23}N_2O_2]^+$), IPPD-quinone ($[M+H]^+$ 257.1287, $[C_{15}H_{17}N_2O_2]^+$), and 7PPD-quinone ($[M+H]^+$ 313.1914, $[C_{19}H_{25}N_2O_2]^+$) showed diagnostic fragments at *m/z* 215.0810 ($[C_{12}H_{11}N_2O_2]^+$) and 187.0858 ($[C_{11}H_{11}N_2O]^+$) (**Figure 5.4**), representing losses of the alkyl chains and further losses of a CO, characteristic of the quinone structural feature (Zhang et al., 2009). Similar fragmentation pathway was observed for DTPD-quinone ($[M+H]^+$ 319.1446, $[C_{20}H_{19}N_2O_2]^+$), with diagnostic fragments at *m/z* 212.0715 ($[C_{13}H_{10}NO_2]^+$) and 184.0750 ($[C_{12}H_{10}NO]^+$), representing consecutive losses of a toluidine group and a CO. For DPPD-quinone ($[M+H]^+$ 291.1135, $[C_{18}H_{15}N_2O_2]^+$) and the DNP-quinone feature ($[M+H]^+$ 391.1444, $[C_{26}H_{19}N_2O_2]^+$), the CO losses occurred first, corresponding to the fragments at m/z 263.1139 $[C_{17}H_{15}N_2O]^+$) and 363.1475 $[C_{25}H_{19}N_2O]^+$), respectively. Further losses of the aromatic groups produced the fragments at *m/z* 185.0718 ($[C_{11}H_9N_2O]^+$, benzene group loss) for DPPD and at *m/z* 235.1863 ($[C_{15}H_{11}N_2O]^+$, naphthyl group loss) for DNP.

Based on quantification with authentic standards, the formation of 6PPD-quinone, IPPD-quinone, 7PPD-quinone, and DTPD-quinone stabilized after 1 day of ozone exposure (**Figure 5.3b,d**), consistent with the ceased removal of the parent substituted-PPDs. Under these conditions, the molar yields of the PPD-quinones (mole PPD-quinone formed per mole 6PPD consumed) averaged approximately at 8.8% ± 0.4% for 6PPD-quinone, 14.7% ± 0.7% for IPPD-quinone, 9.8% ± 1.0% for 7PPD-quinone, and 2.7% ± 0.7% for DTPD-quinone (**Table 5.1**). The molar yields were consistent throughout the reaction, suggesting that the PPD-quinones are stable and terminal TPs for the substituted-PPDs under the timescales and $O_3$ concentrations in this study. For DPPD-quinone, its levels decreased in 3-day and 7-day ozonation compared with 1-day exposure (**Figure 5.3d**), likely indicating that DPPD-quinone can be further oxidized

under longer exposure time. The molar yields of DPPD-quinone were not estimated due to the apparent increased levels of DPPD, likely caused by analytical errors because the *N*,*N'*-diaryl-PPDs were not removed much in general.

Overall, our results demonstrated PPD-quinones formation in ozonation of all the substituted-PPDs. These PPD-quinones had high environmental risks considering their structural similarity to 6PPD-quinone and the severe toxicity to coho salmon posed by 6PPD-quinone at environmentally realistic concentrations ($LC_{50}$ <1 µg/L). Regrettable substitution of 6PPD in tire rubbers with these structural analogues will likely lead to similar ecological risks. Nontoxic, environmentally benign replacement antioxidants outside the PPDs groups are likely needed to protect coho salmon and other aquatic organisms.

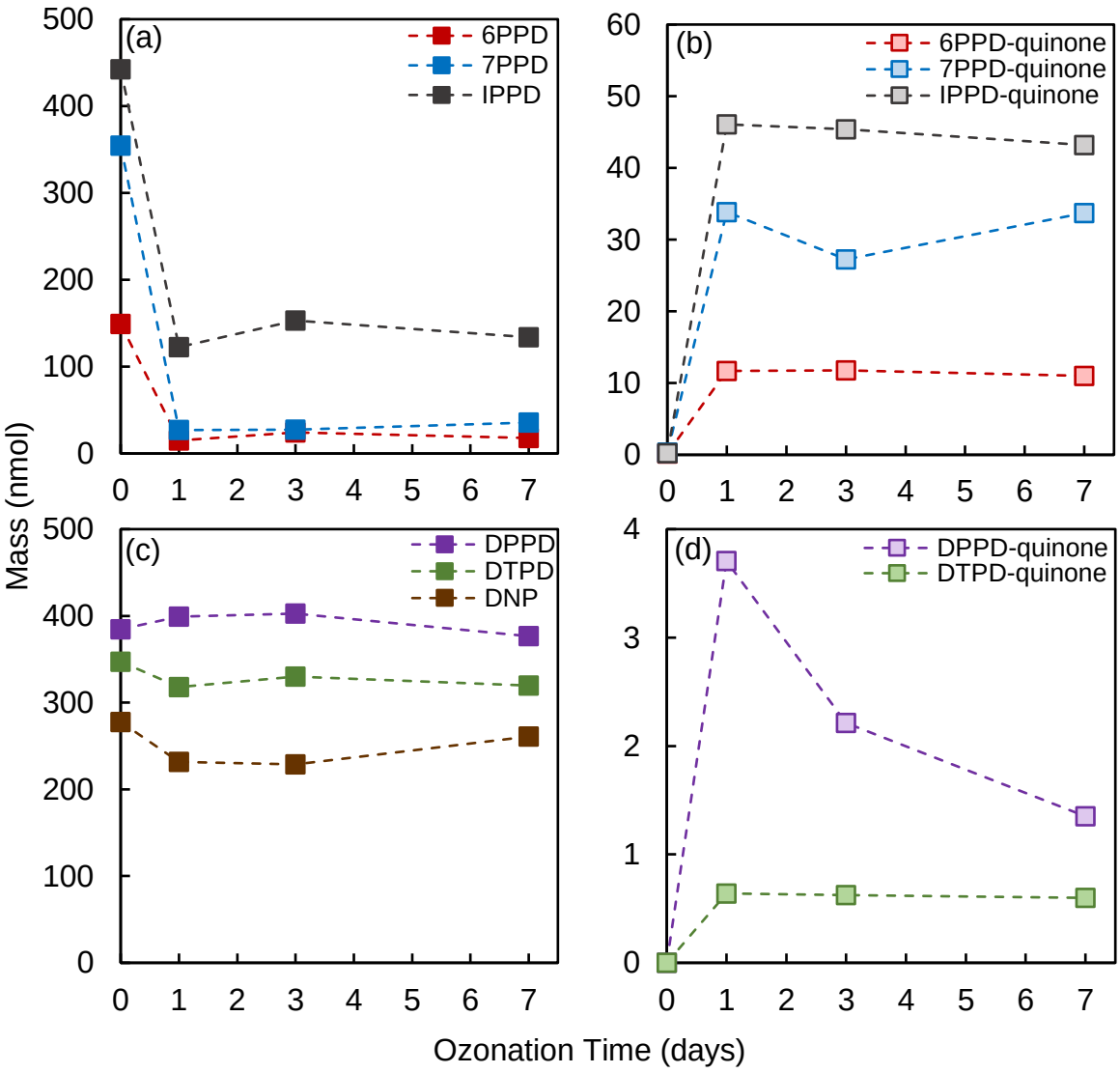


**Figure 5.3** Time trends of (a) *N*-alkyl-*N'*-aryl-PPDs (6PPD, 7PPD, and IPPD), (b) 6PPD-quinone, 7PPD-quinone, IPPD-quinone, (c) *N*,*N'*-diaryl PPDs (DPPD, DTPD, DNP), (d) DPPD-quinone, and DTPD-quinone in gas phase ozonation (~215 ppbv). Mass was quantified by authentic standards.

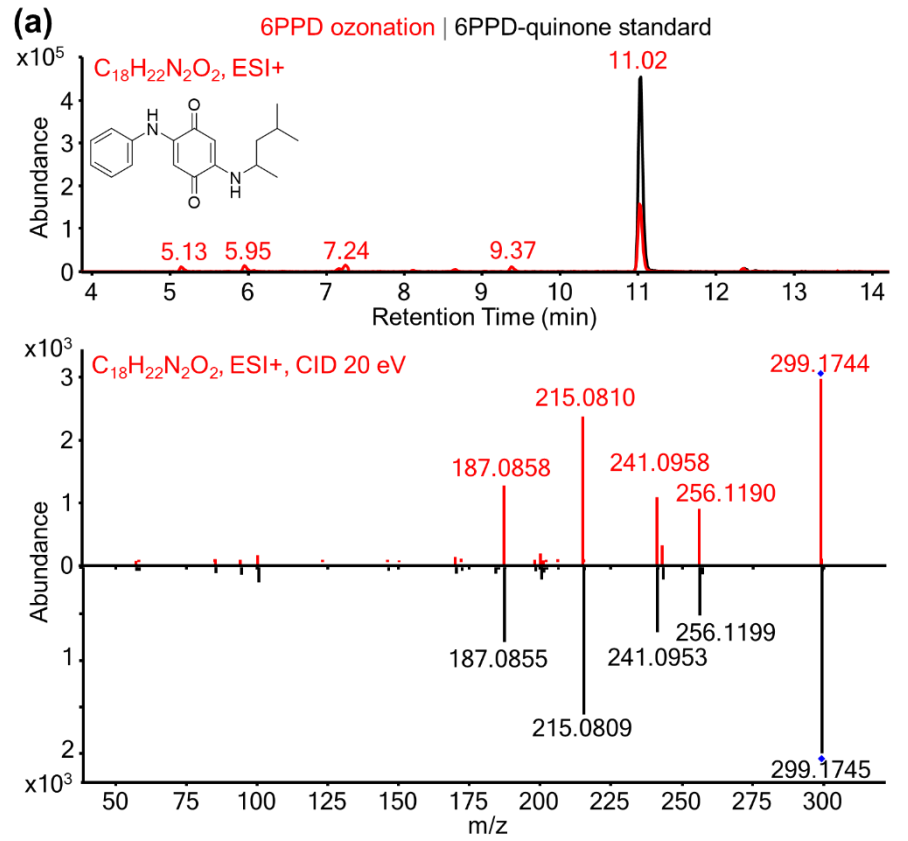
(a)
6PPD ozonation | 6PPD-quinone standard
C18H22N2O2, ESI+
11.02
5.13
5.95
7.24
9.37
Abundance
Retention Time (min)
C18H22N2O2, ESI+, CID 20 eV
299.1744
215.0810
187.0858
241.0958
256.1190
187.0855
241.0953
256.1199
215.0809
299.1745
m/z

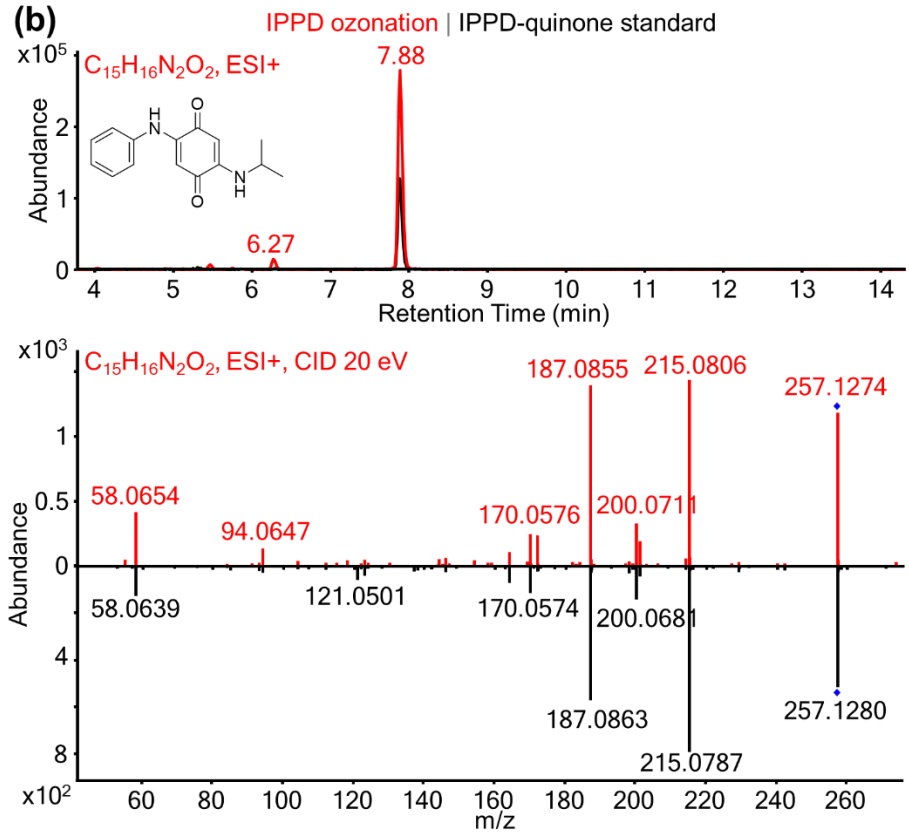
(b)
IPPD ozonation | IPPD-quinone standard
C15H16N2O2, ESI+
7.88
6.27
Abundance
Retention Time (min)
C15H16N2O2, ESI+, CID 20 eV
187.0855
215.0806
257.1274
58.0654
94.0647
170.0576
200.0711
58.0639
121.0501
170.0574
200.0681
187.0863
257.1280
215.0787
m/z

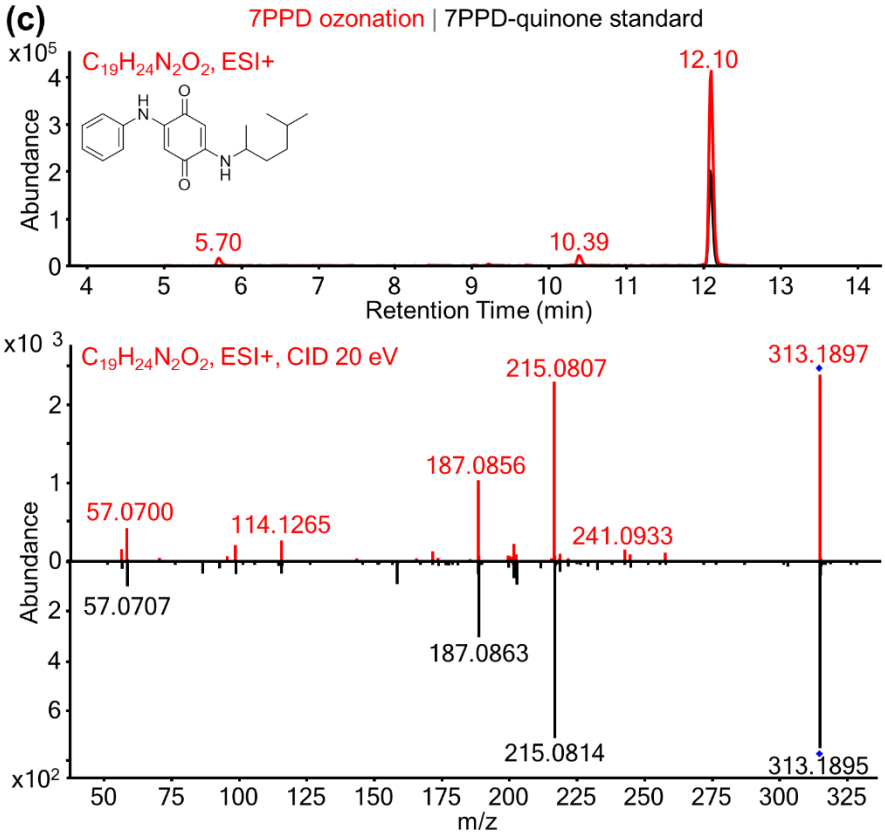
(c)
7PPD ozonation | 7PPD-quinone standard
C19H24N2O2, ESI+
12.10
5.70
10.39
Abundance
Retention Time (min)
C19H24N2O2, ESI+, CID 20 eV
215.0807
313.1897
187.0856
57.0700
114.1265
241.0933
57.0707
187.0863
215.0814
313.1895
m/z

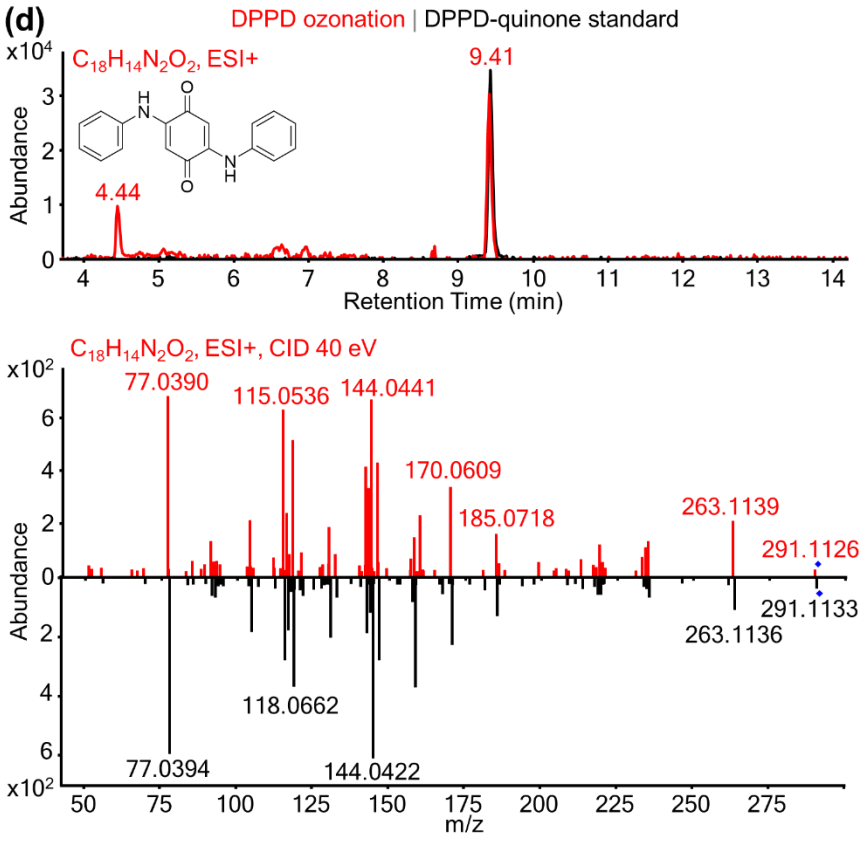
(d)
DPPD ozonation | DPPD-quinone standard
C18H14N2O2, ESI+
9.41
4.44
Abundance
Retention Time (min)
C18H14N2O2, ESI+, CID 40 eV
77.0390
115.0536
144.0441
170.0609
185.0718
263.1139
291.1126
291.1133
263.1136
118.0662
77.0394
144.0422
m/z

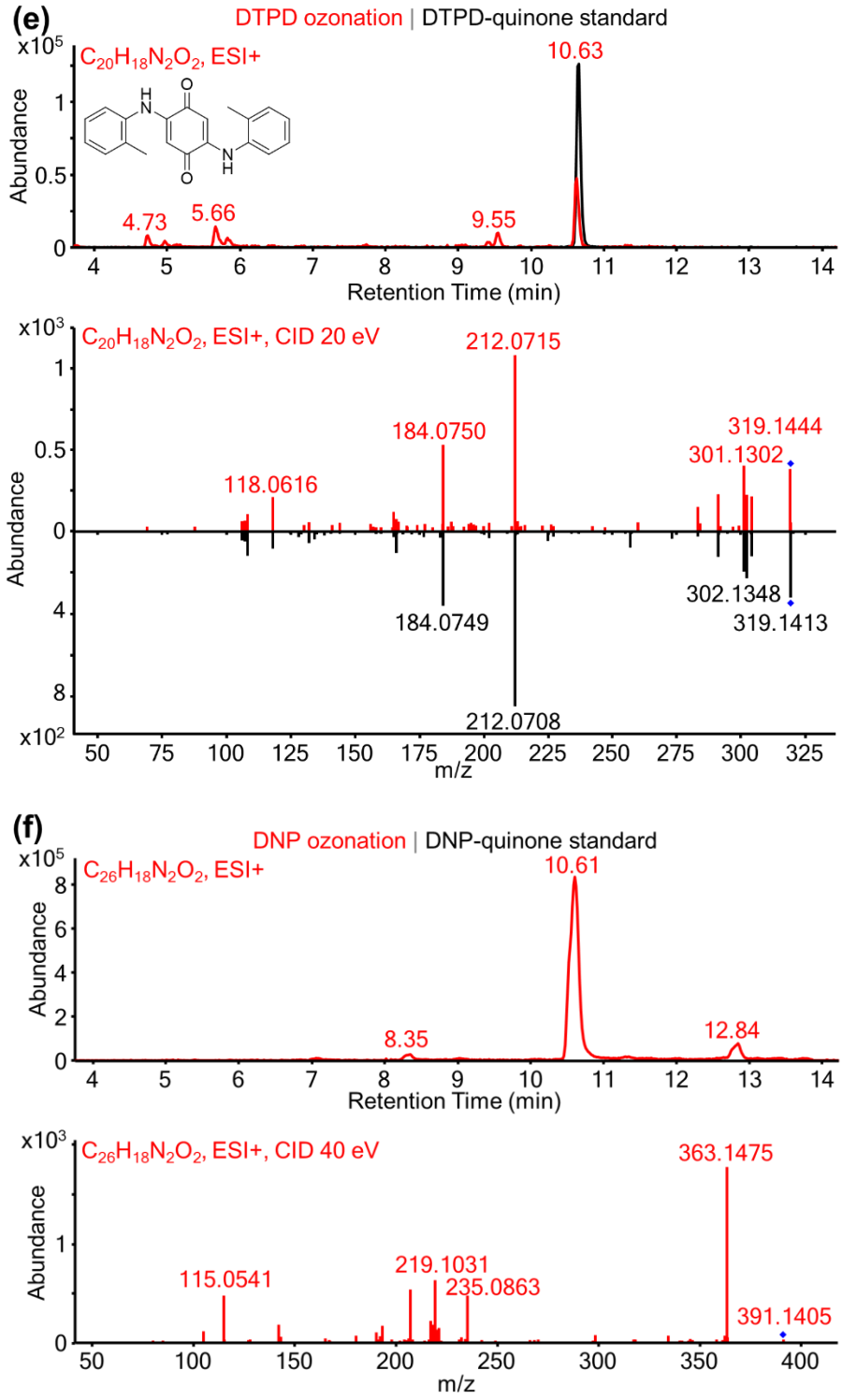


**Figure 5.4** Retention times and MS/MS spectra match of (a) 6PPD-quinone, (b) IPPD-quinone, (c) 7PPD-quinone, (d) DPPD-quinone, and (e) DTPD-quinone in the ozonation reaction mixtures (red color) with the analytical standards (black color). (f) Chromatogram and MS/MS spectrum of the $C_{26}H_{18}N_2O_2$ feature (corresponding to DNP-quinone) in the ozonated DNP mixture.

**Table 5.1** Structure, formula, precursor ion, and retention time (RT; min) of the substituted-PPDs and PPD-quinones and stoichiometric yields of the PPD-quinones in the ozonation reactions (average values from three ozonation periods).

| | Name | Formula | Precursor *m/z* | RT | Structure | PPD-quinone | Formula | Precursor *m/z* | RT | Yield (%) | Structure |
|---|---|---|---|---|---|---|---|---|---|---|---|
| *N*-alkyl-*N'*-aryl-PPDs | 6PPD | $C_{18}H_{24}N_2$ | $[M+H]^+$ 269.2012 | 6.9 | 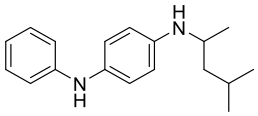 | 6PPD-quinone[a] | $C_{18}H_{22}N_2O_2$ | $[M+H]^+$ 299.1758 | 11.0 | 8.8 ± 0.4 | 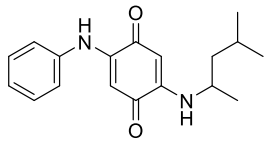 |
| | IPPD | $C_{15}H_{18}N_2$ | $[M+H]^+$ 227.1544 | 5.2 | 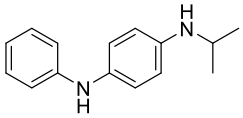 | IPPD-quinone[a] | $C_{15}H_{16}N_2O_2$ | $[M+H]^+$ 257.1287 | 7.9 | 14.7 ± 0.7 | 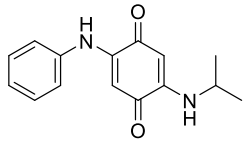 |
| | 7PPD | $C_{19}H_{26}N_2$ | $[M+H]^+$ 283.2168 | 8.1 | 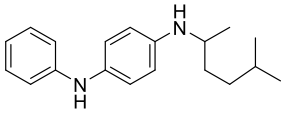 | 7PPD-quinone[a] | $C_{19}H_{24}N_2O_2$ | $[M+H]^+$ 313.1914 | 12.1 | 9.8 ± 1.0 | 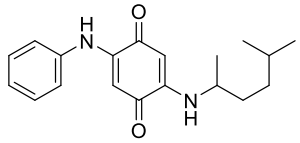 |
| *N*,*N'*-diaryl PPDs | DPPD | $C_{18}H_{16}N_2$ | $[M+H]^+$ 261.1388; $[M]^+$ 260.1310 | 11.1 | 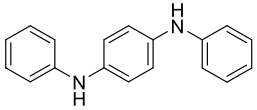 | DPPD-quinone[a] | $C_{18}H_{14}N_2O_2$ | $[M+H]^+$ 291.1135 | 9.4 | N/A[c] | 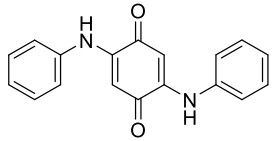 |
| | DTPD | $C_{20}H_{20}N_2$ | $[M+H]^+$ 289.1700; | 13.0 | 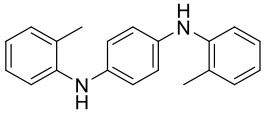 | DTPD-quinone[a] | $C_{20}H_{18}N_2O_2$ | $[M+H]^+$ 319.1446 | 10.6 | 2.7 ± 0.7 | 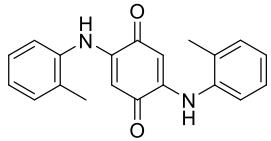 |
| | DNP | $C_{26}H_{20}N_2$ | $[M]^+$ 360.1622; $[M+H]^+$ 361.1700 | 14.1 | 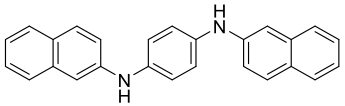 | DNP-quinone[b] | $C_{26}H_{18}N_2O_2$ | $[M+H]^+$ 391.1444 | 10.6 | N/A[c] | N/A[c] |

[a] Structure confirmed with synthetic standards;

[b] Observed *m/z* with $C_{26}H_{18}N_2O_2$ formula, matching that for DNP-quinone.

[c] N/A, not available. Yield of DPPD-quinone is not available due to the apparent increased DPPD levels after 1-day and 3-day ozonations, likely caused by to analytical variance. Structure and yield of DNP-quinone is not available due to lack of the synthetic standard.

### 5.3.3 Identification of 6PPD Ozonation TPs

To identify the ozonation TPs of 6PPD beyond 6PPD-quinone, 29 HRMS features were prioritized based on the criteria outlined in Section 5.2.3. Twenty-one potential TPs were identified from them, with five subsequently confirmed with reference standards (level 1) and eleven with likely (level 2b) or probable (level 3) structures proposed based on MS/MS spectra and literature information (**Table 5.2**) (Lattimer et al., 1983). Notably, seven of the TPs were detected in the 6PPD spiked control (i.e. the industrial 6PPD stock applied onto the glass slide without ozonation), including 6PPD-quinone, 4s DPA, TP 546a, TP 546b, 1,3-DMBA, TP 312, and TP 280b (**Table S5.4**). Peak areas of 1,3-DMBA, TP 312 and TP 280b in the spiked control reached ~20% of those observed in the 1-day ozonation mixture, while other TPs were <1.5% in the spiked control relative to the 1-day ozonation mixture (**Table S5.4**). These TPs reflect either impurities in the industrial grade 6PPD or oxidation TPs formed during 6PPD solid storage. Among all the TPs, 6PPD-quinone (TP 298c, level 1) showed the highest ESI+ peak area (**Table S5.4**). TP 282 ($C_{18}H_{22}N_2O$, level 3) was observed with the second largest ESI+ peak area, but molar yields were not estimated due to lack of analytical standards. TP 184 (*N*-phenyl-*p*-phenylenediamine, level 1) and TP 198 (4-nitrosodiphenylamine, level 1) were observed with the third and the fourth largest ESI+ peak areas; their molar yields were 6.2% ± 0.2% and 2.0% ± 0.5% across the three ozonation periods, respectively. All other TPs were detected at <10% of the initial 6PPD intensity (**Figure 5.5**).

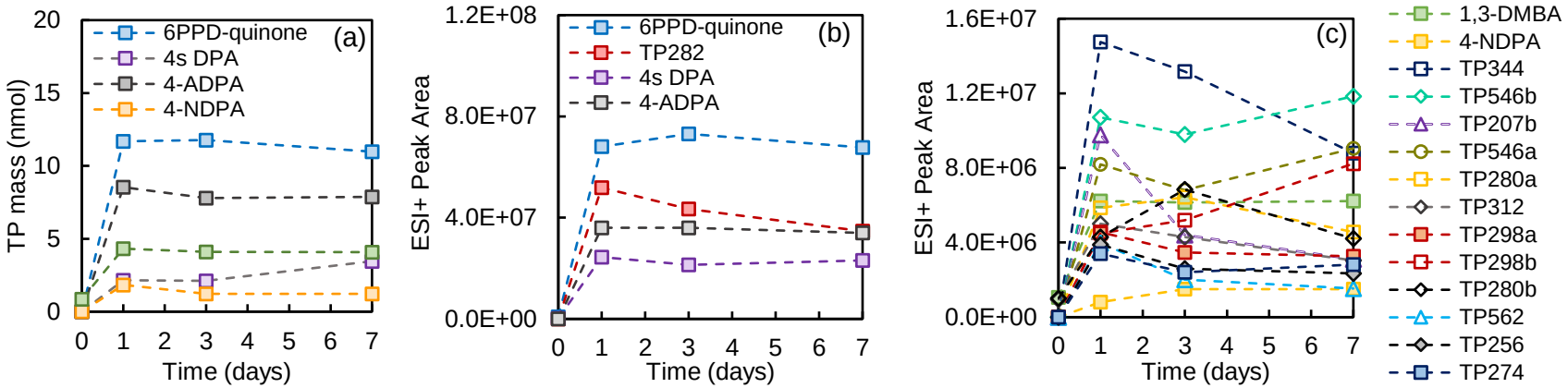


**Figure 5.5** Time trends of detected 6PPD TPs in gas phase ozonation (~215 ppbv). (a) Amount of level 1 TPs quantified by authentic standards; (b) ESI+ peak areas of 6PPD TPs with peak areas >10% of initial 6PPD peak area; (c) ESI+ peak areas of other 6PPD TPs with peak areas <10% of initial 6PPD peak area.

*6PPD-quinone, TP 282, TP 298a, TP 298b.* 6PPD-quinone (TP 298c, RT 11.07 min) was observed as the largest TP based on ESI+ peak area. Based on the *m/z* of 299.1754, a molecular ion of $C_{18}H_{23}N_2O_2^+$ could be proposed. The chemical structure was identified in our previous study through nuclear magnetic resonance (NMR) analysis (Tian et al., 2021), and was further confirmed here with a commercial standard (**Table S5.7**). Characteristic fragments of *m/z* 241.0958 ($C_{14}H_{13}N_2O_2^+$) and 215.0810 ($C_{12}H_{11}N_2O_2^+$) represented respective losses of $C_4H_{10}$ and $C_6H_{12}$ from the *N*-1,3-dimethylbutyl chain, and *m/z* 187.0858 ($C_{11}H_{11}N_2O^+$) represented CO loss from *m/z* 215.0810, characteristic of the quinone structural feature (Zhang et al., 2009). We previously proposed 6PPD-quinone formation through initial $O_3$ addition at one of the *ortho*- positions of the phenylenediamine ring relative to the amine groups of 6PPD, consistent with the *ortho*-/*para*-directing resonance character of electron-donating substituents such as amino and hydroxy groups in oxidation reactions involving activated aromatic compounds (Mvula and Sonntag, 2003; Tekle-Röttering et al., 2016; Tentscher et al., 2018; Tian et al., 2021). The primary ozone adduct could then decay by heterolytic O-O scission, yielding an *ortho*- hydroxy intermediate product and singlet oxygen, followed by attack by a second $O_3$ molecule at the position *ortho*- to the other amine group on the phenylenediamine ring to yield an ozone adduct that could then decay by heterolytic O-O scission into 6PPD-quinone and hydrogen peroxide (Tian et al., 2021).

Two isomers of 6PPD-quinone were observed at 5.34 min (TP 298a) and 7.25 min (TP 298b); their earlier retention times indicate more polar characteristics compared to 6PPDQ. TP 298a showed diagnostic fragments of *m/z* 215.0808 ($C_{12}H_{11}N_2O_2^+$) and 122.0227 ($C_6H_4NO_2^+$) under 10 eV collision energy (not shown in **Table S5.7** because only the 40 eV MS/MS spectrum was shown), representing losses of unaltered 1,3-dimethylbutyl and aniline substructures. Fragments of *m/z* 122.0227 ($C_6H_4NO_2^+$), 94.0294 ($C_5H_4NO^+$), and 66.0344 ($C_4H_4N^+$), representing

consecutive losses of CO, were evident under 40 eV collision energy for TP 298a, which are characteristic MS/MS spectral features of *ortho*-quinone compounds (**Table S5.7**; Khan et al., 2021; McCoull et al., 1999; Tian et al., 2017). Based on the MS/MS information, we propose an *ortho*-quinone structure for TP 298a. The ESI+ peak areas of TP 298a decreased ~25% from day 1 to day 3, then remained stable to day 7 (**Figure 5.5c**). In contrast to TP 298a, TP 298b showed consecutive neutral losses of OH groups in the MS/MS spectra (fragments of *m/z* 282.1690 and 265.1701), the characteristic hydroxyl radical neutral losses of the nitrone structures (Miao et al., 2003; Wu et al., 2003). The ESI+ peak areas of TP 298b increased over the 3-day and 7-day ozonation periods (**Figure 5.5c**). Interestingly, we observed TP 282 (*m/z* 283.1801, molecular ion of $C_{18}H_{23}N_2O^+$) with decreased peak area in 3-day and 7-day ozonation periods (**Figure 5.5b**). The MS/MS spectra of TP 282 also showed the neutral loss of a OH group (*m/z* 266.1761 fragment), indicating that TP 282 may demonstrate a nitrone structure while TP 298b may be a dinitrone. 6PPD-dinitrone was previously proposed as an ozonation product of 6PPD (Lattimer et al., 1983), with a formation pathway through $O_3$ addition to the *N*-alkyl amine to yield a nitroxide radical intermediate, which could then (a) react directly with a second molecule of $O_3$ to yield a dinitrone, or (b) first deprotonate to yield a mononitrone product and then react with a second molecule of $O_3$ to yield the dinitrone. However, the structure proposal cannot be confirmed without analytical standards.

*4-ADPA (TP 184).* TP 184 was the third most abundant TP based on ESI+ peak area. Based on *m/z* of 185.1072, a molecular ion of $C_{12}H_{13}N_2^+$ could be proposed. The MS/MS spectra showed characteristic fragments at 167.0722 ($C_{12}H_9N^+$), 108.0673 ($C_6H_8N_2^+$), and 93.0577 ($C_6H_7N^+$), representing losses of an amine ($NH_4$) group and a benzene ring (**Table S5.7**). Such fragmentation patterns matched 4-aminodiphenylamine (4-ADPA), which was confirmed with an authentic

standard. Upon quantification, 4-ADPA exhibited a molar yield of 6.2% ± 0.2% across the three ozonation periods (**Figure 5.5a**).

*4s DPA (TP 198) and 4-NDPA (TP 214).* TP 198 was the fourth most abundant TP based on ESI+ peak area. A molecular ion of $C_{12}H_{11}N_2O^+$ fit the observed *m/z* of 199.0860 and a *m/z* 168.0785 ($C_{12}H_{10}N^+$) fragment demonstrated the neutral loss of a NOH group, consistent with the nitroso structure proposed previously for the "$C_{12}H_{10}N_2O$" 6PPD ozonation product (Lattimer et al., 1983). TP 198 was confirmed with the authentic standard of 4-nitrosodiphenylamine (4s DPA; **Table S5.7**); a potential formation pathway could be $O_3$ addition on the electron rich aryl-alkyl amine and formation via an amide oxide intermediate (Lattimer et al., 1983). Further oxidation of TP 198 could then lead to TP 214 (*m/z* 215.0815, molecular ion of $C_{12}H_{11}N_2O_2^+$), which was confirmed to be 4-nitrodiphenylamine (4-NDPA) by authentic standard. Characteristic fragments of 4-NDPA included *m/z* 198.0780 ($C_{12}H_{10}N_2O^+$) and 168.0811 ($C_{12}H_{10}N^+$), representing OH and NO losses, respectively. Notably, the ESI+ peak area response of 4-NDPA standard was ~10 times lower than 4s DPA standard (**Figure S5.3**). Although 4-NDPA was not observed with high peak area, its molar yield averaged 1.1% ± 0.2% across the three ozonation periods (quantified by authentic standards), which was ~50% that of 4s DPA (molar yield of 4s DPA, 2.0% ± 0.5%; **Figure 5.5a,c**).

*TP 274.* TP 274 is an environmentally interesting TP. It was not abundant (by peak area) after pure-phase 6PPD ozonation (**Figure 5.5c**), yet it exhibited high molar yields in the ozonated TWP and occurred at high levels in the environmental samples screened in this study (see **Figure 5.7** and discussion below). It was also previously identified by Peter et al. (as its adduct form at *m/z* 333.2212) as a relatively abundant chemical feature correlated with coho salmon mortality events (Peter et al., 2018). Observed at *m/z* 275.1753, TP 274 has a molecular formula of

$C_{16}H_{22}N_2O_2$. Characteristic fragments at *m/z* 182.1162 ($C_{10}H_{16}NO_2^+$; loss of the aniline group) and 98.0233 ($C_4H_4NO_2^+$; loss of the 1,3-dimethylbutyl chain from *m/z* 182.1162) were consistent with a ring cleavage product resulting from ozonolysis and elimination of two carbons from the diphenylene aromatic ring. In addition, CO loss between *m/z* 98.0233 and 70.0280 was observed (**Table S5.7**). Based on plausible structures and reaction mechanisms, we proposed an α,β-unsaturated dicarbonyl diamide structure for TP 274. Similar compounds were observed in aqueous ozonation of phenols and furans (Mvula and Sonntag, 2003; Ramseier and Gunten, 2009; Zoumpouli et al., 2021), and were potentially formed through ozone addition to the aromatic rings which leads to ozonide structures and further ring cleavage. The α,β-unsaturated dicarbonyl compounds identified elsewhere could damage proteins by reacting with lysine and cysteine groups (Prasse et al., 2018; Zoumpouli et al., 2021). Therefore, the bioactivity of TP 274 merits further investigation.

*TP 546, TP 562.* Consistent with oxidative coupling, dimerization products of 6PPD were observed, such as TP 546a and TP 546b (*m/z* 547.3441, molecular ion of $C_{36}H_{43}N_4O^+$, RT 10.57 min (a) and 10.95 min (b)) and TP 562 (*m/z* 563.3379, molecular ion of $C_{36}H_{43}N_4O_2^+$). Dimerization was previously reported in ozonation of 6PPD and a formation pathway through nitrogen radicals was proposed (Lattimer et al., 1983). This pathway is unique to the aryl-substituted *p*-phenylenediamines, as the aromatic substituent sufficiently stabilizes the nitrogen radical intermediate to allow oxidative coupling reactions to proceed (presumably concentration dependent). Here, the observed TP 546 and TP 562 likely reflect oxidation products of 6PPD-dimer. For TP 562, a MS/MS fragment of *m/z* 535.3415 ($C_{35}H_{43}N_4O^+$) showed a CO neutral loss. No further suggestive structural information was available from the MS/MS spectra; more conclusive structures would require analysis of authentic standards. The MS/MS spectra of TP

546a and TP 546b only showed neutral losses of the alkyl chains; further structural characterization lacked definition.

*1,3-DMBA (TP 101).* Cleavage of 6PPD into small molecules also occurred. For example, TP 101 was observed at *m/z* 102.1282 (molecular ion of $C_6H_{16}N^+$); analysis of an authentic standard confirmed TP 101 as 1,3-dimethylbutylamine (1,3-DMBA). 1,3-DMBA was previously reported as a hydrolysis product of 6PPD (European Union, 2006); its molar yield from pure phase 6PPD ozonation was 3.2% ± 0.1% (**Table 5.2**). These data suggest that ozonation is another formation pathway for 1,3-DMBA because another sister hydrolysis product of 6PPD, 4-HDPA (European Union, 2006), was not observed, indicating that concurrent water vapor-mediated transformation reactions were not occurring during ozonation. Other small molecule TPs observed include isomeric TP 207a,b (*m/z* 208.1329, molecular ion $C_{12}H_{18}NO_2^+$), but structures could not be proposed based on the MS/MS spectra.

Based on above identified and probable TPs, candidate ozonation pathways and TP structures for 6PPD are summarized in **Figure 5.6**.

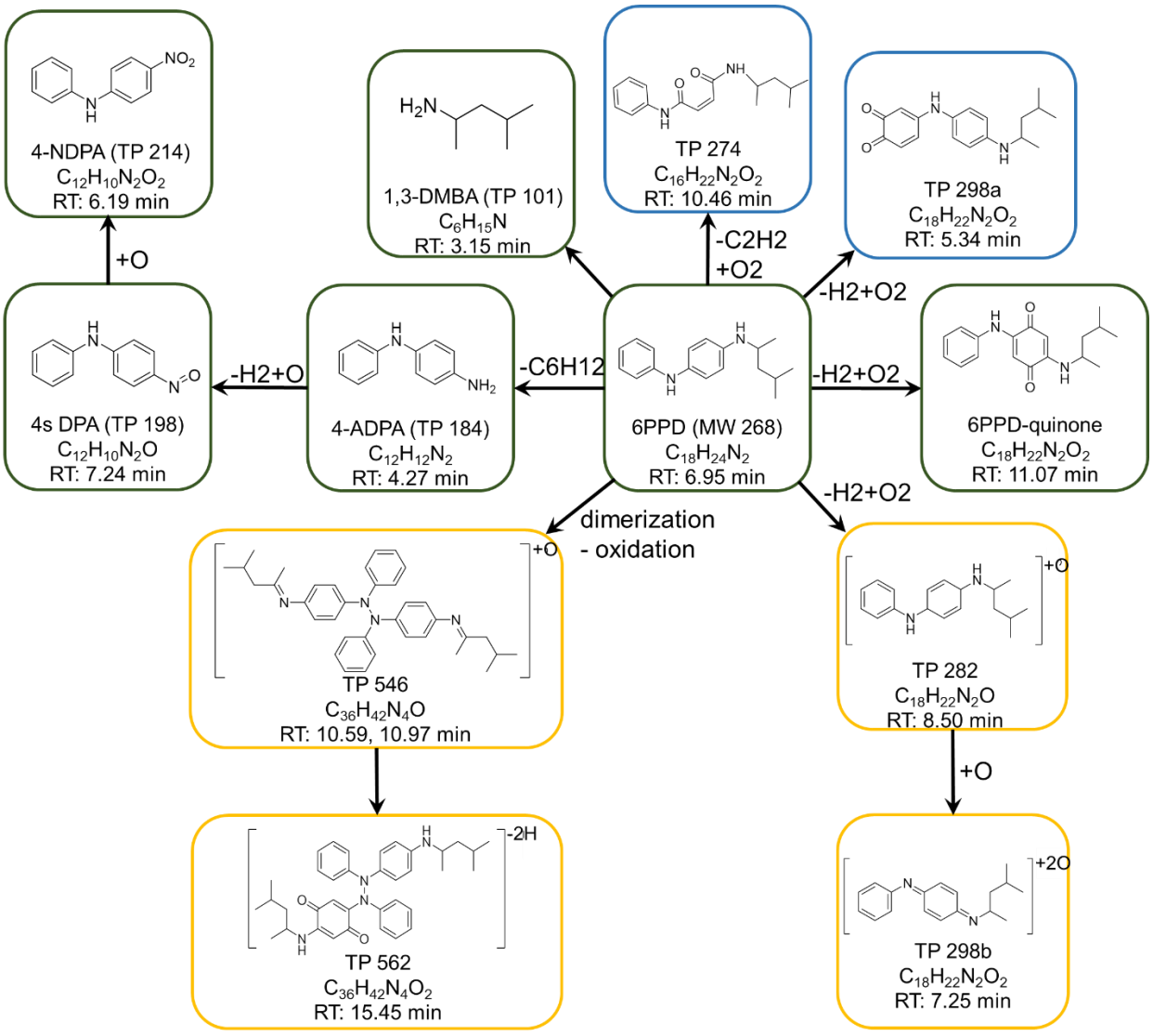


**Figure 5.6** Proposed ozonation pathways of 6PPD along with chemical formulas, retention times (RT), and tentative structures for detected TPs. TP structures identified with confidence levels 1, 2, and 3 are communicated with green, blue, and yellow boxes, respectively.

**Table 5.2** Ozonation products of 6PPD in thin film gas-phase reaction. Stoichiometric yields were reported for level 1 TPs based on quantification with authentic standards as mole of product formed ($M_{TP\_t}$) per mole 6PPD consumed ($M_{6PPD\_t}$ - $M_{6PPD\_t0}$).

| Name | Atomic change | Formula | Retention Time (min) | Molar yield in pure 6PPD ozonation (%) | Molar yield in TWP ozonation (%) | Confidence level | Proposed structure |
|---|---|---|---|---|---|---|---|
| 6PPD | parent | $C_{18}H_{24}N_2$ | 6.9 | n/a | n/a | 1 | 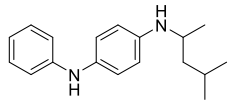 |
| 6PPD-quinone (TP 298c) | $-H_2+O_2$ | $C_{18}H_{22}N_2O_2$ | 11.1 | 8.8 ± 0.4 | 2.3 ± 0.1 | 1 | 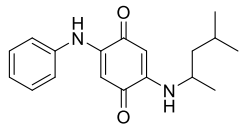 |
| 4-ADPA (TP 184) | $-C_6H_{12}$ | $C_{12}H_{12}N_2$ | 4.3 | 6.2 ± 0.2 | 2.9 ± 0.2 | 1 | 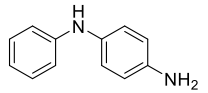 |
| 4s DPA (TP 198) | $-C_6H_{14}+O$ | $C_{12}H_{10}N_2O$ | 7.2 | 2.0 ± 0.5 | 3.4 ± 0.2 | 1 | 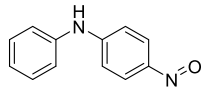 |
| 1,3-DMBA (TP 101) | $-C_{12}H_9N$ | $C_6H_{15}N$ | 3.2 | 3.2 ± 0.1 | 4.8 ± 0.3 | 1 | 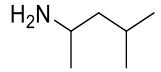 |
| 4-NDPA (TP 214) | $-C_6H_{14}+O_2$ | $C_{12}H_{10}N_2O_2$ | 8.9 | 1.1 ± 0.2 | 2.7 ± 0.2 | 1 | 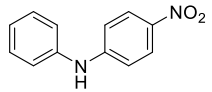 |
| 4-HDPA | $-C_6H_{13}N+O$ | $C_{12}H_{11}NO$ | 6.2 | 0 | 0.9 ± 0.1 | 1 | 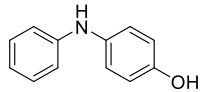 |
| TP 298a | $-H_2+O_2$ | $C_{18}H_{22}N_2O_2$ | 5.4 | n/a | n/a | 2b | 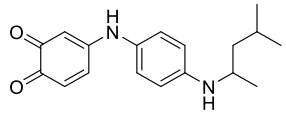 |

| | | | | | | | |
|---|---|---|---|---|---|---|---|
| TP 274 | -$C_2H_2$+$O_2$ | $C_{16}H_{22}N_2O_2$ | 10.4 | n/a | n/a | 2b | 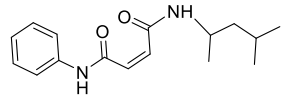 |
| TP 207a | -$C_6H_7N$+$O_2$ | $C_{12}H_{17}NO_2$ | 5.1 | n/a | n/a | 3 | 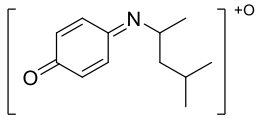 |
| TP 207b | -$C_6H_7N$+$O_2$ | $C_{12}H_{17}NO_2$ | 7.0 | n/a | n/a | 3 | 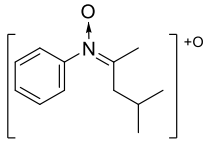 |
| TP 256 | -$C_2H_4$+O | $C_{16}H_{20}N_2O$ | 9.5 | n/a | n/a | 3 | 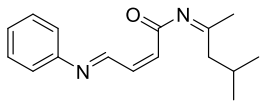 |
| TP 282 | -$H_2$+O | $C_{18}H_{22}N_2O$ | 8.5 | n/a | n/a | 3 | 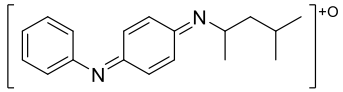 |
| TP 296 | -$H_4$+$O_2$ | $C_{18}H_{20}N_2O_2$ | 10.4 | n/a | n/a | 3 | 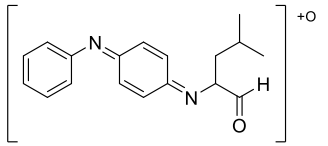 |
| TP 298b | -$H_2$+$O_2$ | $C_{18}H_{22}N_2O_2$ | 7.3 | n/a | n/a | 3 | 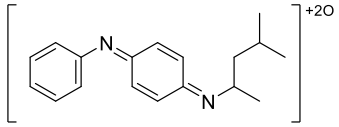 |
| TP 546a,b | 6PPD×2–$H_6$+O | $C_{36}H_{42}N_4O$ | 10.6, 11.0 | n/a | n/a | 3 | 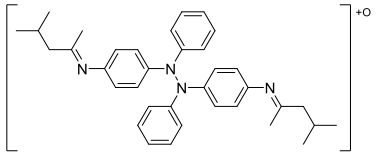 |

| | | | | | | | |
|---|---|---|---|---|---|---|---|
| TP 562 | 6PPD×2–$H_6$+$O_2$ | $C_{36}H_{42}N_4O_2$ | 15.4 | n/a | n/a | 3 | 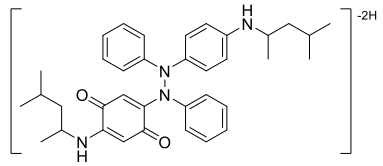 |
| TP 280a,b | -$H_4$+O | $C_{18}H_{20}N_2O$ | 5.8, 10.4 | n/a | n/a | 4 | - |
| TP 312 | +$CO_2$ | $C_{19}H_{24}N_2O_2$ | 5.6 | n/a | n/a | 4 | - |
| TP 344 | +$C_2H_4O_3$ | $C_{20}H_{28}N_2O_3$ | 14.2 | n/a | n/a | 4 | - |

### 5.3.4 Environmental Occurrence of 6PPD TPs

To investigate the discharge of 6PPD ozonation TPs into aquatic systems, we screened the identified TPs in ozone-exposed TWP prepared in 2021 (n = 3), as well as archived sample extracts of TWP leachate (n = 3) (Tian et al., 2021), roadway runoff (n = 3) (Tian et al., 2021), and creek stormwater (n = 6) collected between 2017 and 2021, and previously reported in Tian et al. We semi-quantified the 5 level 1 ozonation TPs and 4-HDPA, the major 6PPD hydrolysis product (OECD, 2004), with external calibration curves. Excepting the TWP extracts (<2 months storage time), 6PPD was detected but not quantified because we are not confident of 6PPD stability during extract storage. TP 282 and TP 274 were tentatively semi-quantified using the average of calibration curves for 4-ADPA, 1.3-DMBA, 4s DPA, and 4-HDPA (see Materials and Method sections for details).

*Solvent extracts of TWP*. 6PPD dominated the detected chemical mass in pre-ozonation TWP (1300 ± 20 µg/g TWP) (**Table 5.3**). This 6PPD concentration is lower than the expected mass ratio (0.4%-2%) of 6PPD in new rubber (R.T. Vanderbilt Company, 2010), which likely reflects the presence of both new and used tires in this TWP mixture and non-exhaustive extraction. 6PPD was previously detected in tire and road wear particles (TRWPs) at 1000 ± 630 µg/g TRWP (Unice et al., 2015). Assuming equal mass of tread polymer and mineral in TRWP (Unice et al., 2013), the 6PPD levels in our TWPs were quite similar to those reported for the TRWP tread polymer (~2000 ± 1260 µg/g TWP). All the TPs reported here were detected in the pre-ozonation TWP except 4-NDPA (ΣTPs, 110 µg/g TWP). 1,3-DMBA was the most abundant TP at 52 µg/g TWP, followed by 4-HDPA (19 µg/g TWP), 6PPD-quinone (15 µg/g TWP), TP 274 (14 µg/g TWP), and 4-ADPA (7.7 µg/g TWP). 4-HDPA (42 ± 33 µg/g TWP) and 4-ADPA (17 ± 25 µg/g TWP) were previously reported in TRWPs; their equivalent levels in tread

polymer (4-HDPA, 84 ± 66 µg/g TWP; 4-ADPA, 34 ± 50 µg/g TWP) were ~4.4 times higher than those in our TWP (Unice et al., 2015). Differences in tire formulations extracted or extraction methods (Soxhlet versus sonication) may explain these differences.

After 6 hr of lab ozone exposure (360 ± 12 ppbv), 59% of the detected 6PPD in TWP reacted and the ΣTPs concentrations increased ~3 fold (**Table 5.3, Figure 5.7a**). 6PPD loss (10%) and ΣTPs formation (14%) were substantially lower in the corresponding air control (TWP exposed to 6 hr of ambient air flow at identical conditions), confirming the critical role of ozone in TP formation at these time scales (**Table 5.3, Figure 5.7a**). The molar yields of the TPs ranged from 0.9% to 7.4% (calculated as mole TP formed per mole 6PPD removed) in the TWP ozonation, indicating that no single TP pathway dominated reaction outcomes. Compared with pure phase 6PPD ozonation, the yields of 6PPD-quinone and 4-ADPA in TWP ozonation were lower and the yields for other TPs were higher (**Table 5.2**). While the molar yield of TP 274 was low (~1%) in 6PPD ozonation, its molar yield in TWP ozonation was substantially higher (7.4%), indicating that TP 274 should be considered as a major, and environmentally relevant TP of 6PPD. We again note that the above concentrations of TP 274 were estimated using an average calibration curve derived from other TPs due to lack of an analytical standard. Therefore, these estimates should be considered with appropriate caution. TP 282 (5.1%; calculated with an average calibration curve derived from other TPs) and 1,3-DMBA (4.8%) exhibited the second and the third highest yields in TWP ozonation. 6PPD-quinone, 4s DPA, 4-NDPA, 4-ADPA, 4-HDPA were formed at similar yields of 2.3% to 3.4%. Notably, 4-HDPA also showed increased levels in TWP after the 6-h ozonation, although with a lower molar yield (0.9%). 4-HDPA was not observed as a TP in the pure phase 6PPD ozonation but has been reported as a 6PPD hydrolysis TP (Unice et al., 2015). The increased levels of 4-HDPA in the

ozonated TWP, as well as the different yields of other TPs (e.g., TP 274) in TWP compared with pure-phase 6PPD, indicated that ozonation mechanisms or rates can differ in pure compound versus TWP matrix.

*TWP leachate*. 6PPD was detected in all (n=3) of the archived TWP leachate SPE-extracts. However, given its potential instability, we did not quantify 6PPD in these extracts considering the multi-year storage time for some of the extracts (European Union, 2006). We note here that even for new samples, highly variable or no-detect concentrations of 6PPD might be reasonable for aqueous environments, given the rapid photolysis (t1/2, 1 h) and hydrolysis (t1/2 as low as 2-3 hours) rates for 6PPD and its sensitivity to dissolved oxygen, trace heavy metals, and pH (European Union, 2006). All the TPs were detected in TWP leachate except for 4-NDPA and 4-ADPA (**Table 5.3**). The ΣTPs (11000 ± 2700 ng/L) in TWP leachate was dominated by 4-HDPA (7600 ± 1800 ng/L), 1,3-DMBA (1800 ± 450 ng/L) and TP 274 (1400 ± 360 ng/L), followed by 6PPD-quinone (250 ± 62 ng/L), 4s DPA (37 ± 9 ng/L), and TP 282 (23 ± 7 ng/L) (**Figure 5.7b**). 4-HDPA and 1,3-DMBA are each hydrolysis products of 6PPD (European Union, 2006); their high levels likely reflect the importance of hydrolysis for residual 6PPD in TWP leachates. The importance of TP 274 was interesting; compared with 1,3-DMBA, which appears to be both an ozonation and hydrolysis TP, the TP 274/1,3-DMBA ratio in TWP leachate (0.78) was even higher than that in TWP (0.27) (**Figure 5.7c**). The high abundance of TP 274 in TWP leachate indicated its high potential for environmental occurrence. Aside from a possibly increased yield of TP 274 in TWP versus pure 6PPD, this may reflect variations in TP 274 partitioning behavior compared to other TPs, though the high TP 274/1,3-DMBA ratio in TWP leachate cannot be explained by the predicted logKow (SPARC logKow: TP 274, 2.86; 1,3-DMBA, -1.43; **Table S5.5**). In previous TRWP column leaching tests, Unice et al. and

Klockner et al reported 4-ADPA, 4-HDPA, 4-NDPA, and 6PPD-quinone to be absent in aqueous leachate of TRWP (Klöckner et al., 2021; Unice et al., 2015). However, both studies used ionic solutions (0.001 M CaCl2 in Unice et al; 0.2 M phosphate buffer in Klockner et al) for aqueous leaching (this study: DI water) and did not employ sample enrichment (this study: 1000-fold pre-concentration via SPE and subsequent 10-fold dilution of extracts) (Klöckner et al., 2021; Unice et al., 2015), which may result in lower leaching potentials of positively charged chemicals, higher LODs, or higher ion suppression in mass spectrometry. In addition, Klockner et al used syringe filter (0.45 µm cellulose acetate) to separate TWP from aqueous solutions, which may lead to sorption of 6PPD-quinone on the filter plastics based on our recent observations. Each of the above factor could lead to different observations.

*Roadway runoff*. 6PPD was qualitatively detected in 2/3 of the archived roadway runoff samples. All of the TPs reported here except 4-NDPA were detected in all of the roadway runoff extracts. Similar to the TWP leachate, the ΣTPs (40000 ± 15000 ng/L) was dominated by TP 274 (16000 ± 5900 ng/L, semi-quantitatively) and 1,3-DMBA (13000 ± 5800) ng/L. However, 4-HDPA, the most abundant TP in TWP leachate, showed much lower concentrations in roadway runoff (680 ± 460 ng/L). The low levels of 4-HDPA suggest environmental instability, supported by a photodegradation half-life of 1.3 hrs (European Union, 2006). Interestingly, 4s DPA, 4-ADPA, and TP 282 were much more abundant in roadway runoff relative to the TWP leachate samples **(Figure 5.7c**). When using 6PPD-quinone as a marker of TWP-sourced compounds (Klöckner et al., 2021), the respective 6PPD-quinone/4s DPA, 6PPD-quinone/4-ADPA, and 6PPD-quinone/TP282 ratios were 6.8, ~35 (<LOD 4-ADPA levels estimated as LOD/√2), and 11 in TWP leachate, but were substantially reduced to 0.23, 0.39, and 0.25 in roadway runoff. These

results indicated lower environmental mobility or stability of 6PPD-quinone compared with 4s DPA, 4-ADPA, and TP 282.

*Urban Creeks*. 6PPD was qualitatively detected in 2/6 of the urban receiving waters. Except for 4-NDPA, all the TPs were detected in at least one creek sample (**Table 5.3**), but only 1,3-DMBA (2200 ± 630 ng/L; 6/6 detection), TP 274 (1800 ± 890 ng/L; 6/6 detection), and TP 282 (1200 ± 510 ng/L; 6/6 detection) showed levels above LOQs. 6PPD-quinone, 4-ADPA, 4s DPA, and 4-HDPA were occasionally detected in the creek stormwaters at levels near LOQs (**Table 5.3**). The dominance of 1,3-DMBA, TP 274, and TP 282 is consistent with the TP profiles in roadway runoff (**Figure 5.7c**); the 6PPD-quinone/1,3-DMBA, 6PPD-quinone/TP274, and 6PPD-quinone/TP282 ratios varied <3-fold between roadway runoff and creek stormwater, indicating roadway runoff as the major source of these contaminants into receiving surface waters during rainfall events. Using a more sensitive isotope dilution analytical method based upon triple quadrupole tandem mass spectrometry, 6PPD-quinone was quantified in the same samples at 18-100 ng/L (manuscript in preparation led by Dr. Zhenyu Tian). These concentrations were substantially lower than those recently reported in Canadian creek stormwaters (0.21-2.85 µg/L) (Johannessen et al., 2021b, 2021a). However, the Canadian study used crude 6PPD ozonation mixture as the calibration standard for 6PPD-quinone, which, based on the molar yield in our pure 6PPD ozonation experiments, overestimated the 6PPD-quinone concentrations by ~10-fold.

We previously identified TP 274 in the "coho mortality signature" reported in Peter et al (2018) (as its adduct form at m/z 333.2212) as a chemical feature correlated with coho salmon mortality events (Peter et al., 2018). In addition, a $C_{16}H_{22}N_2O_2$ chemical, with the same formula as TP 274, was reported in the 2019 EPA crumb rubber report as being present in tire recycling

plants and indoor and outdoor playing field crumb rubbers (US EPA, 2019). $C_{16}H_{22}N_2O_2$ and $C_{18}H_{22}N_2O$ (same formula as TP 282) chemical features were recently identified in tire composite and road dust samples (Klöckner et al., 2021). To the best of our knowledge, no other quantitative information on these 6PPD related chemicals exist in the literature; further characterization of these apparently common environmental contaminants is merited.

Overall, these data are consistent with the release of numerous 6PPD-derived TPs into the aqueous environment through leaching of TWPs by rainfall. 1,3-DMBA, TP 274, and TP 282 were the most environmentally abundant TPs, yet 6PPD-quinone is of large concern from the toxicity perspective (<1 µg/L LC50 for coho salmon; Tian et al., 2021). Notably, these 6PPD TPs are seemingly abundant in roadway runoff and associated runoff-impacted receiving waters relative to other reports of tire-rubber or roadway derived contaminants (Masoner et al., 2019). For example, 1,3-diphenylguanidine, a widely used tire vulcanization accelerator, was detected in stormwater samples from the same watersheds at 5.4-540 ng/L (Hou et al., 2019) and in European surface waters at <LOD-170 ng/L (Montes et al., 2019). Methyl-1H-benzotriazole, used as a corrosion inhibitor, was detected at up to 5600 ng/L in U.S. stormwater runoff (Fairbairn et al., 2018). Hexa(methoxymethyl)melamine (HMMM), used in part for tire manufacture (Elmer, 1982), was detected at up to 1740 ng/L in Canadian storm receiving waters (Johannessen et al., 2021c), at 5000 ng/L (including 12 TPs) in European surface water (Alhelou et al., 2019), and <LOD-280 ng/L in Australian surface waters (Rauert et al., 2020). While our concentration estimates reported here are largely semi-quantitative and not based upon isotope dilution methodologies, these data clearly indicate the relative abundance of 6PPD ozonation TPs, including 6PPD-quinone and others, as a novel class of environmental contaminants in roadway runoff and roadway-impacted receiving waters.

**Table 5.3** Limit of detections (LODs), limit of quantifications (LOQs), detection frequencies (DF), and semi-quantification of 6PPD and related ozonation and hydrolysis TPs in TWP leachate (250 mg TWP/L; n = 3), roadway runoff (n =3), creek stormwater (n = 6), and solvent-extracted TWP before and after ozonation (n = 3). Concentration estimates are derived from archived samples, and thus do not reflect recovery optimization or internal standard signal normalization to account for potential matrix effects. Italic font noted TPs without analytical standards (TP 282 and TP 274) tentatively semi-quantified by an average calibration curve derived from other TPs.

| | TWP leachate (ng/L) | | | Roadway runoff (ng/L) | | | Creek stormwater (ng/L) | | | TWP methanolic extract (µg/g TWP) | | | |
|---|---|---|---|---|---|---|---|---|---|---|---|---|---|
| Compound | LOD /LOQ | DF | concentration[b] | LOD /LOQ | DF | concentration[b] | LOD /LOQ | DF | concentration[b] | LOD /LOQ | non-ozonated | ozonated | air control |
| 6PPD | 8.4/28 | 3/3 | detected[c] | 52/170 | 2/3 | detected[c] | 36/120 | 2/6 | <LOD | 0.84/2.8 | 1300 ± 20 | 550 ± 37 | 1200 ± 33 |
| 6PPD-quinone | 8.6/29 | 3/3 | 250 ± 62 | 83/280 | 3/3 | 860 ± 380 | 120/410 | 3/6 | detected | 2.3/7.6 | 15 ± 0.5 | 36 ± 2 | 17 ± 1 |
| 4s DPA | 13/43 | 3/3 | 37 ± 9 | 110/380 | 3/3 | 3700 ± 900 | 73/240 | 1/6 | <LOD | 0.29/0.97 | detected | 20 ± 2 | 7.2 ± 1.0 |
| 1,3-DMBA | 30/100 | 3/3 | 1800 ± 450 | 150/500 | 3/3 | 13000 ± 5800 | 750/2500 | 6/6 | 2200 ± 630 | 6/20 | 52 ± 4 | 66 ± 3 | 40 ± 2 |
| 4-NDPA | 30/100 | 0/3 | <LOD | 150/500 | 0/3 | <LOD | 150/500 | 0/6 | <LOD | 1.3/4.4 | <LOD | 17 ± 1 | <LOD |
| 4-ADPA | 10/40 | 0/3 | <LOD | 97/320 | 3/3 | 2200 ± 330 | 160/540 | 3/6 | detected | 1.6/5.4 | 7.7 ± 0.4 | 23 ± 0.2 | 9.6 ± 0.3 |
| 4-HDPA | 5.9/20 | 3/3 | 7600 ± 1800 | 36/120 | 3/3 | 680 ± 460 | 21/68 | 2/6 | <LOD | 0.72/2.4 | 19 ± 1 | 24 ± 2 | 24 ± 0.4 |
| *TP282*[a] | *2.4/8* | *3/3* | *23 ± 7* | *12/38* | *3/3* | *3500 ± 1700* | *70/230* | *6/6* | *1200 ± 510* | *0.48/1.6* | *detected* | *43 ± 7* | *11 ± 1* |
| *TP274*[a] | *26/87* | *3/3* | *1400 ± 360* | *690/2300* | *3/3* | *16000 ± 5900* | *280/920* | *6/6* | *1800 ± 890* | *1.7/5.5* | *14 ± 1* | *74 ± 4* | *15 ±1* |
| ΣTPs[d] | - | - | 11000 ± 2700 | - | - | 40000 ± 15000 | - | - | 5900 ± 2000 | - | 110 ± 7 | 300 ± 21 | 120 ± 7 |

[a] TPs lacking analytical standards and estimated by average peak area responses of 4-ADPA, 1.3-DMBA, 4s DPA, and 4-HDPA .

[b] Average concentrations were only reported for analytes detected in >50% of samples. Values between the LOD and the LOQ were replaced by LOQ/√2 in the average calculation.

[c] 6PPD levels were not quantified due to its instability during long-term sample storage.

[d] Values between the LOD and the LOQ were replaced by LOQ/√2, values <LOD were replaced by 0.

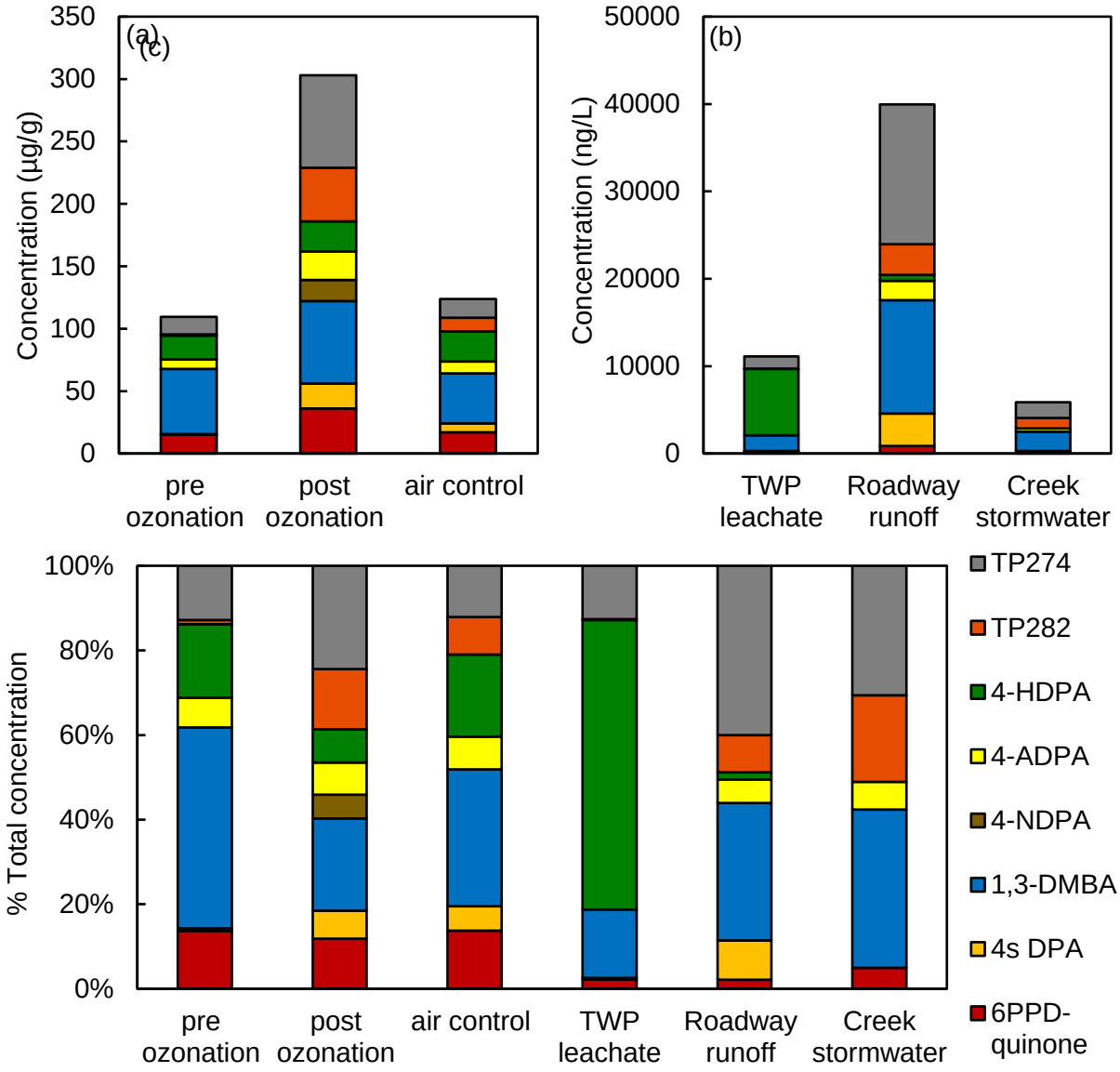


**Figure 5.7** Semi-quantification of level 1 TPs, TP 282, and TP 274 concentrations in (a) TWP before and after ozonation (n = 3), and (b) TWP leachate (250 mg TWP/L; n = 3), roadway runoff (n =3), and creek stormwater (n = 6). (c) Relative contributions of individual TPs to total semi-quantified TP concentrations in different matrixes. TP 282 and TP 274 levels were estimated by an average calibration curve derived from other level 1 TPs. Values between the LODs and the LOQs were estimated as LOQ/√2, and values below the LODs were estimated as 0.

## Reference


Alhelou, R., Seiwert, B., Reemtsma, T., 2019. Hexamethoxymethylmelamine – A precursor of persistent and mobile contaminants in municipal wastewater and the water cycle. Water Res. 165, 114973.

Braden, M., Gent, A.N., 1962. The attack of ozone on stretched rubber vulcanizates. III. Action of antiozonants. J. Appl. Polym. Sci. 6, 449–455.

Cataldo, F., Faucette, B., Huang, S., Ebenezer, W., 2015. On the early reaction stages of ozone with N,N′-substituted p-phenylenediamines (6PPD, 77PD) and N,N′,N″-substituted-1,3,5-triazine "Durazone®": An electron spin resonance (ESR) and electronic absorption spectroscopy study. Polym. Degrad. Stab. 111, 223–231.

Du, B., Lofton, J.M., Peter, K.T., Gipe, A.D., James, C.A., McIntyre, J.K., Scholz, N.L., Baker, J.E., Kolodziej, E.P., 2017. Development of suspect and non-target screening methods for detection of organic contaminants in highway runoff and fish tissue with high-resolution time-of-flight mass spectrometry. Environ. Sci. Process. Impacts 19, 1185–1196.

Elmer, O.C., 1982. Tire cord adhesives. US4338263A.

European Union, 2006. OSPAR background document on 4-(dimethylbutylamino)diphenylamine (6PPD).

Fairbairn, D.J., Elliott, S.M., Kiesling, R.L., Schoenfuss, H.L., Ferrey, M.L., Westerhoff, B.M., 2018. Contaminants of emerging concern in urban stormwater: Spatiotemporal patterns and removal by iron-enhanced sand filters (IESFs). Water Res. 145, 332–345.

Feist, B.E., Buhle, E.R., Arnold, P., Davis, J.W., Scholz, N.L., 2011. landscape ecotoxicology of Coho salmon spawner mortality in urban streams. PLOS ONE 6, e23424.

Feist, B.E., Buhle, E.R., Baldwin, D.H., Spromberg, J.A., Damm, S.E., Davis, J.W., Scholz, N.L., 2017. Roads to ruin: Conservation threats to a sentinel species across an urban gradient. Ecol. Appl. 27, 2382–2396.

Henning, N., Wick, A., Ternes, T.A., 2021. Biotransformation of pregabalin in surface water matrices and the occurrence of transformation products in the aquatic environment - comparison to the structurally related gabapentin. Water Res. 117488.

Hou, F., Tian, Z., Peter, K.T., Wu, C., Gipe, A.D., Zhao, H., Alegria, E.A., Liu, F., Kolodziej, E.P., 2019. Quantification of organic contaminants in urban stormwater by isotope dilution and liquid chromatography-tandem mass spectrometry. Anal. Bioanal. Chem. 411, 7791–7806.

Huang, D., LaCount, B.J., Castro, J.M., Ignatz-Hoover, F., 2001. Development of a service-simulating, accelerated aging test method for exterior tire rubber compounds I. Cyclic aging. Polym. Degrad. Stab. 74, 353–362.

Huang, W., Shi, Y., Huang, J., Deng, C., Tang, S., Liu, X., Chen, D., 2021. Occurrence of substituted p-phenylenediamine antioxidants in dusts. Environ. Sci. Technol. Lett. 8, 381–385.

Huntink, N.M., 2003. Durability of rubber products: Development of new antidegradants for long-term protection. PhD thesis, University of Twente.

Huntink, N.M., Datta, R.N., Noordermeer, J.W.M., 2004. addressing durability of rubber compounds. Rubber Chem. Technol. 77, 476–511.

Johannessen, C., Helm, P., Lashuk, B., Yargeau, V., Metcalfe, C.D., 2021a. The tire wear compounds 6PPD-quinone and 1,3-diphenylguanidine in an urban watershed. Arch. Environ. Contam. Toxicol. Aug 4: 1-9.

Johannessen, C., Helm, P., Metcalfe, C.D., 2021b. Detection of selected tire wear compounds in urban receiving waters. Environ. Pollut. 287, 117659.
Johannessen, C., Helm, P., Metcalfe, C.D., 2021c. Runoff of the tire-wear compound, hexamethoxymethyl-melamine into urban watersheds. Arch. Environ. Contam. Toxicol. Jan 30: 1-9.
Kassler, A., Pittenauer, E., Doerr, N., Allmaier, G., 2014. Ultrahigh-performance liquid chromatography/electrospray ionization linear ion trap Orbitrap mass spectrometry of antioxidants (amines and phenols) applied in lubricant engineering. Rapid Commun. Mass Spectrom. 28, 63–76.
Khan, W., Wang, Y.-H., Nanayakkara, N.P.D., Herath, H.M.T.B., Catchings, Z., Khan, S., Fasinu, P.S., ElSohly, M.A., McChesney, J.D., Khan, I.A., Chaurasiya, N.D., Tekwani, B.L., Walker, L.A., 2021. Quantitative determination of primaquine-5,6-ortho-quinone and carboxyprimaquine-5,6-ortho-quinone in human erythrocytes by UHPLC-MS/MS. J. Chromatogr. B 1163, 122510.
Klöckner, P., Seiwert, B., Wagner, S., Reemtsma, T., 2021. Organic markers of tire and road wear particles in sediments and soils: Transformation products of major antiozonants as promising candidates. Environ. Sci. Technol. 55, 11723-11732.
Lattimer, R.P., Hooser, E.R., Layer, R.W., Rhee, C.K., 1983. Mechanisms of ozonation of n-(1,3-dimethylbutyl)-n′-phenyl-p-phenylenediamine. Rubber Chem. Technol. 56, 431–439.
Lu, Z., Smyth, S.A., Peart, T.E., De Silva, A.O., 2017. Occurrence and fate of substituted diphenylamine antioxidants and benzotriazole UV stabilizers in various Canadian wastewater treatment processes. Water Res. 124, 158–166.
Masoner, J.R., Kolpin, D.W., Cozzarelli, I.M., Barber, L.B., Burden, D.S., Foreman, W.T., Forshay, K.J., Furlong, E.T., Groves, J.F., Hladik, M.L., Hopton, M.E., Jaeschke, J.B., Keefe, S.H., Krabbenhoft, D.P., Lowrance, R., Romanok, K.M., Rus, D.L., Selbig, W.R., Williams, B.H., Bradley, P.M., 2019. Urban stormwater: An overlooked pathway of extensive mixed contaminants to surface and groundwaters in the United States. Environ. Sci. Technol. 53, 10070–10081.
McCoull, K.D., Rindgen, D., Blair, I.A., Penning, T.M., 1999. Synthesis and characterization of polycyclic aromatic hydrocarbon *o*-quinone depurinating N7-guanine adducts. Chem. Res. Toxicol. 12, 237–246.
McIntyre, J.K., Prat, J., Cameron, J., Wetzel, J., Mudrock, E., Peter, K.T., Tian, Z., Mackenzie, C., Lundin, J., Stark, J.D., King, K., Davis, J.W., Kolodziej, E.P., Scholz, N.L., 2021. Treading water: Tire wear particle leachate recreates an urban runoff mortality syndrome in coho but not chum salmon. Environ. Sci. Technol.
Miao, X.-S., March, R.E., Metcalfe, C.D., 2003. A tandem mass spectrometric study of the N-oxides, quinoline N-oxide, carbadox, and olaquindox, carried out at high mass accuracy using electrospray ionization. Int. J. Mass Spectrom., Special Issue: In honour of John H. Beynon 230, 123–133.
Montes, R., Rodil, R., Cela, R., Quintana, J.B., 2019. Determination of persistent and mobile organic contaminants (pmocs) in water by mixed-mode liquid chromatography–tandem mass spectrometry. Anal. Chem. 91, 5176–5183.
Muschket, M., Di Paolo, C., Tindall, A.J., Touak, G., Phan, A., Krauss, M., Kirchner, K., Seiler, T.-B., Hollert, H., Brack, W., 2018. Identification of unknown antiandrogenic compounds

in surface waters by effect-directed analysis (eda) using a parallel fractionation approach. Environ. Sci. Technol. 52, 288–297.
Mvula, E., Sonntag, C. von, 2003. Ozonolysis of phenols in aqueous solution. Org. Biomol. Chem. 1, 1749–1756.
OECD, 2004. Test No. 309: Aerobic mineralisation in surface water - simulation biodegradation test.
Peter, K.T., Tian, Z., Wu, C., Lin, P., White, S., Du, B., McIntyre, J.K., Scholz, N.L., Kolodziej, E.P., 2018. Using high-resolution mass spectrometry to identify organic contaminants linked to urban stormwater mortality syndrome in coho salmon. Environ. Sci. Technol. 52, 10317–10327.
Prasse, C., Ford, B., Nomura, D.K., Sedlak, D.L., 2018. Unexpected transformation of dissolved phenols to toxic dicarbonyls by hydroxyl radicals and UV light. Proc. Natl. Acad. Sci. 115, 2311–2316.
Ramseier, M.K., Gunten, U. von, 2009. Mechanisms of phenol ozonation—kinetics of formation of primary and secondary reaction products. Ozone Sci. Eng. 31, 201–215.
Rauert, C., Kaserzon, S.L., Veal, C., Yeh, R.Y., Mueller, J.F., Thomas, K.V., 2020. The first environmental assessment of hexa(methoxymethyl)melamine and co-occurring cyclic amines in Australian waterways. Sci. Total Environ. 743, 140834.
R.T. Vanderbilt Company, 2010. The Vanderbilt rubber handbook.
Scholz, N.L., Myers, M.S., McCarthy, S.G., Labenia, J.S., McIntyre, J.K., Ylitalo, G.M., Rhodes, L.D., Laetz, C.A., Stehr, C.M., French, B.L., McMillan, B., Wilson, D., Reed, L., Lynch, K.D., Damm, S., Davis, J.W., Collier, T.K., 2011. Recurrent die-offs of adult coho salmon returning to spawn in puget sound lowland urban streams. PLOS ONE 6, e28013.
Schymanski, E.L., Jeon, J., Gulde, R., Fenner, K., Ruff, M., Singer, H.P., Hollender, J., 2014. Identifying small molecules via high resolution mass spectrometry: Communicating confidence. Environ. Sci. Technol. 48, 2097–2098.
Spromberg, J.A., Baldwin, D.H., Damm, S.E., McIntyre, J.K., Huff, M., Sloan, C.A., Anulacion, B.F., Davis, J.W., Scholz, N.L., 2016. Coho salmon spawner mortality in western US urban watersheds: Bioinfiltration prevents lethal storm water impacts. J. Appl. Ecol. 53, 398–407.
Spromberg, J.A., Scholz, N.L., 2011. Estimating the future decline of wild coho salmon populations resulting from early spawner die-offs in urbanizing watersheds of the Pacific Northwest, USA. Integr. Environ. Assess. Manag. 7, 648–656.
Tekle-Röttering, A., von Sonntag, C., Reisz, E., Eyser, C.V., Lutze, H.V., Türk, J., Naumov, S., Schmidt, W., Schmidt, T.C., 2016. Ozonation of anilines: Kinetics, stoichiometry, product identification and elucidation of pathways. Water Res. 98, 147–159.
Tentscher, P.R., Bourgin, M., von Gunten, U., 2018. Ozonation of para-substituted phenolic compounds yields p-benzoquinones, other cyclic α,β-unsaturated ketones, and substituted catechols. Environ. Sci. Technol. 52, 4763–4773.
Tian, Z., Gold, A., Nakamura, J., Zhang, Z., Vila, J., Singleton, D.R., Collins, L.B., Aitken, M.D., 2017. Nontarget analysis reveals a bacterial metabolite of pyrene implicated in the genotoxicity of contaminated soil after bioremediation. Environ. Sci. Technol. 51, 7091–7100.

Tian, Z., Peter, K.T., Gipe, A.D., Zhao, H., Hou, F., Wark, D.A., Khangaonkar, T., Kolodziej, E.P., James, C.A., 2020. Suspect and nontarget screening for contaminants of emerging concern in an urban estuary. Environ. Sci. Technol. 54, 889–901.

Tian, Z., Zhao, H., Peter, K.T., Gonzalez, M., Wetzel, J., Wu, C., Hu, X., Prat, J., Mudrock, E., Hettinger, R., Cortina, A.E., Biswas, R.G., Kock, F.V.C., Soong, R., Jenne, A., Du, B., Hou, F., He, H., Lundeen, R., Gilbreath, A., Sutton, R., Scholz, N.L., Davis, J.W., Dodd, M.C., Simpson, A., McIntyre, J.K., Kolodziej, E.P., 2021. A ubiquitous tire rubber–derived chemical induces acute mortality in coho salmon. Science 371, 185–189.

Unice, K.M., Bare, J.L., Kreider, M.L., Panko, J.M., 2015. Experimental methodology for assessing the environmental fate of organic chemicals in polymer matrices using column leaching studies and OECD 308 water/sediment systems: Application to tire and road wear particles. Sci. Total Environ. 533, 476–487.

Unice, K.M., Kreider, M.L., Panko, J.M., 2013. Comparison of tire and road wear particle concentrations in sediment for watersheds in France, Japan, and the United States by quantitative pyrolysis GC/MS analysis. Environ. Sci. Technol. 47, 8138–8147.

U.S. EPA, 2019. Synthetic Turf Field Recycled Tire Crumb Rubber Research Under the Federal Research Action Plan Final Report: Part 1 - Tire Crumb Characterization Volume 1 334.

Weizel, A., Schlüsener, M.P., Dierkes, G., Wick, A., Ternes, T.A., 2021. Fate and behavior of progestogens in activated sludge treatment: Kinetics and transformation products. Water Res. 188, 116515.

Wu, Y., Farrell, J.T., Lynn, K., Euler, D., Kwei, G., Hwang, T.-L., Qin, X.-Z., 2003. The importance of chromatographic separation in LC/MS/MS quantitation of drugs in biological fluids: Detection, characterization, and synthesis of a previously unknown low-level nitrone metabolite of a substance p antagonist. Anal. Chem. 75, 426–434.

Wu, Y., Venier, M., Hites, R.A., 2020. Broad exposure of the north American environment to phenolic and amino antioxidants and to ultraviolet filters. Environ. Sci. Technol. 54, 9345–9355.

Zhang, J.-J., Liu, H., Xiao, Y., Zhang, X.-E., Zhou, N.-Y., 2009. Identification and Characterization of catabolic para-nitrophenol 4-monooxygenase and para-benzoquinone reductase from pseudomonas sp. strain WBC-3. J. Bacteriol. 191, 2703–2710.

Zhang, Z.-F., Zhang, Xue, Zhang, Xianming, Sverko, E., Smyth, S.A., Li, Y.-F., 2021. Diphenylamine antioxidants in wastewater influent, effluent, biosolids and landfill leachate: Contribution to environmental releases. Water Res. 189, 116602.

Zoumpouli, G.A., Zhang, Z., Wenk, J., Prasse, C., 2021. Aqueous ozonation of furans: Kinetics and transformation mechanisms leading to the formation of α,β-unsaturated dicarbonyl compounds. Water Res. 203, 117487.

## Supplementary Materials

### Additional Methods for Coho Salmon Toxicant Identification (led by Dr. Zhenyu Tian)

Tire tread wear particles leaching

Tire tread wear particles (TWP) were made by physical abrasion of the tread of nine tires (brand, vehicle type, and use history in **Table S5.1**) using an angle grinder with a steel carbide disk (Parkes MCM90; Miller Tire, Wauseon, OH, U.S.A.) and mixed in equal weights (**Figure S5.1 A**). To produce TWP leachate (**Figure S5.1 B, C, D**), TWP was dispersed with 1100 g glass beads (3mm OD, pre-cleaned with methanol) in 1 L stainless steel columns, and system water or DI water was recirculated from a stainless steel reservoir through the columns via upward flow at 0.5 L/min for 24 h with a peristaltic pump (Masterflex L/S Tygon® tubing, 3/8" ID). TWP leachate was generated at ambient laboratory conditions. TWP leachate stock was always generated at 1000 mg TWP/L water (maximum 35 g TWP load per leaching column; total volume generated based on experimental requirements). TWP leachate stock was stored in 4 L amber glass jars at 4 °C until fractionation or exposure (storage confirmed to have no impact on lethality over several months), which generally happened within a week of leachate generation.

Coho salmon and exposure experiments

Coho salmon from Soos Creek or Diru Creek stock were reared at the Puyallup Research and Extension Center of Washington State University on 12:12 h light:dark cycle in a custom recirculating water system and fed commercial food (Bio-vita, Bio-Oregon, Oregon, WA, USA). Fish system water was dechlorinated municipal water treated by reverse osmosis to Type 3 (>4 MΩ-cm, <0.25 µS/cm) in a Rios 200 purification system (Millipore Sigma) and then reconstituted with buffered Instant Ocean salts (Blacksburg, VA, USA) to approximately pH 7.5 and 1300 µS/cm conductivity at 10-13 °C. Individual coho salmon used in experiments were age 0+ or 1+ yr (1.3-28.0 g); experimental results reflect replication across year classes and sources of fish. Experiments were conducted in accordance with Experimental Protocol #04860-002, as approved by Washington State University's Institutional Animal Care and Use Committee (IACUC).

For each set of fish exposures, TWP leachate fractions or stock 1000 mg/L TWP leachate were first diluted in 37 L glass aquaria with system water to achieve 30 L total volume (initial experiments) or 16 L total volume, depending on the size of the fish. Aquaria were held in a recirculating water bath used to control temperature, and placements for different exposure conditions were randomized. Temperature (10-12 °C), conductivity (1250-1300 µS/cm), pH (7.6-7.8), and dissolved oxygen levels provided by aeration (airstones, >98% saturation) were verified in aquaria before transferring fish to exposure waters. For all screening exposures, five juvenile coho salmon were transferred into each exposure tank (**Figure S5.2**), and the mortality rate was recorded after 24 hours. A positive control (250 or 500 mg/L TWP leachate) occurred during each exposure round (initial exposures: 7.5 L of 1000 mg/L TWP leachate diluted to 30 L with system water; subsequent exposures: 4 L of 1000 mg/L TWP leachate diluted to 16 L with system water). A negative control was also included in every set of exposures, including fractionation method controls (when available, details in Data S1), solvent controls, or one exposure tank containing only system water. Subsequent fractionations utilized 1000 mg/L TWP leachate to counter possible recovery losses, with final exposure tank dilutions equivalent to 250-1000 mg/L TWP concentrations. Separations and exposures were replicated at least twice for all "critical" fractionation steps that successfully manipulated extract lethality and composition. Controlled

dose fish exposures were conducted following screening exposures for 6PPD and 6PPD-quinone isolated from ozonated 6PPD. For these exposures, 8 fish were used per concentration in 30 L of test solution, with a 10-concentrations dilutions series per chemical. A solvent control and a positive control (250 mg/L TWP leachate) were additionally included. These exposures were repeated twice.

Fish exposure water sample processing

After TWP leachate fractions or method blanks were diluted in the exposure tanks, 0.5-1 L water samples were collected from each tank prior to fish exposure. Water samples were extracted (within 12 h) by established methods with modifications (Hou et al., 2019). Briefly, solid phase extraction (SPE) cartridges (200 mg, 6 mL Oasis HLB, Waters, MA) were preconditioned (5 mL methanol, 25 mL DI water; 5-10 mL/min), and then water samples (1 L) were loaded onto SPE cartridges at 5-10 mL/min. Cartridges were then rinsed with 10 mL DI water, vacuum-dried (15 min), and eluted with methanol (4 × 2.5 mL). Eluates were concentrated to 1 mL under nitrogen and spiked with a set of isotopically-labelled internal standards (ISTDs) for instrument analysis (Hou et al., 2019). Lab blanks (1 L DI × 3) were extracted in parallel and used for quality control and blank subtraction (described below). Complementary exposure water sampling (e.g., controlled exposures) employed direct analysis via collection of 2 mL of exposure tank water with a disposable glass pipette into a prelabeled amber glass HPLC vial.

High resolution mass spectrometry (HRMS) analysis

Sample analysis primarily used an Agilent 1290 Infinity ultrahigh performance liquid chromatography (UPLC) coupled to an Agilent 6530 Quadrupole Time-of-Flight high resolution mass spectrometry (QTOF HRMS; Santa Clara, CA, USA) with electrospray ionization in both positive and negative modes (ESI+/-). Full scan HRMS data was acquired at the range of 100-1700 *m/z* in 2 GHz Extended Dynamic Range mode. For structure elucidation, MS/MS data was acquired by data-dependent acquisition (*m/z* 50-1700, collision-induced dissociation at 10, 20, and 40 eV) using lists of preferred precursors prioritized during initial MS-only screening. UPLC separation used a reversed-phase C18 analytical column (Agilent ZORBAX Eclipse Plus 2.1×100 mm, 1.8 µm) with a C18 guard column (2.1×5 mm, 1.8 µm) at 45 ºC with 5 µL injection volume. For ESI+, the mobile phase (0.4 mL/min) consisted of 0.1% formic acid in each of water (A) and methanol (B) using a gradient of: 5% B at 0-1 min, 50% B at 4 min, 100% B at 17-20 min, 5% B at 20.1 min; stop time 22.5 min; post-time 2 min. For ESI-, the mobile phase consisted of 1 mM ammonium fluoride in water (A) and pure methanol (B), using the same gradient as ESI+. All fractionation samples were analyzed in triplicate.

HRMS (UPLC-QTOF) data analysis methods

Primary analytical characterization used Agilent MassHunter Profinder (B.10.00) for non-target feature extraction and alignment across samples, with features prioritized in Mass Profiler Professional (B.13.00) by replicate filters and blank subtraction. Features with peak area >5000, occurring in all replicates, and present at peak area 5-fold greater than solvent, lab, and field blanks (for stormwater analysis) or negative controls (for TWP leachate fraction analysis) were retained. Formula assignment, suspect screening and feature identification were performed in MassHunter ID Browser (B.07.00) and MassHunter Qualitative Analysis (B.08.00).

Initial 6PPD ozonation for 6PPD-quinone generation

6PPD ozonation studies first used an ozone chamber following a published method (Lattimer et al., 1983). Industrial grade 6PPD was ground by ceramic mortar and pestle, then 0.5 g of powder was dispersed as a thin layer on each of three glass plates and sealed in a reaction chamber. Ozone was produced by a photochemical $O_3$ generator (UVP, IN USA, Norwood, MA, USA) and pumped into the chamber at ~500 ppbv, flow rate 1 L/min. One plate was taken out on each of days 1, 3, and 7, and ozonated solids were dissolved in 50 mL EtOH (10 mg/mL). An aliquot of each solution (10 μL) was diluted 1000X with MeOH for instrumental analysis. Remaining volumes were stored at 4 °C for further purification.

6PPD ozonation was then optimized using a flow through packed column setup to achieve higher ozone consumption rates by 6PPD solids and higher yields of 6PPD-quinone. 1 g of ground industrial grade 6PPD was packed into glass chromatography columns (50 cm × 1.2 cm ID), and ~6.9% (v/v) ozone was generated from pure oxygen by a corona-discharge $O_3$ generator (AC2025, IN USA, Norwood, MA, USA) and passed through the column (up flow) at 500 mL/min. The color of 6PPD solids darkened from purple to black during 20 min ozonation, and the ozonated solids mixture was dissolved in 100 mL ethanol (10 mg/mL) for purification and analysis (stored at 4 °C).

6PPD-quinone purification from ozonation mixture

The amino groups on 6PPD protonate under acidic conditions but the amino groups on 6PPD-quinone do not, due to the much lower p$K_a$ values (estimated p$K_a$ < 0) of 6PPD-quinone in comparison to 6PPD (p$K_a$ 6.73). This difference can be explained by the strong electron withdrawing effects of the neighboring quinone oxygens. Because the ozonation mixture contained a large amount of unreacted 6PPD, we exploited this charge state difference between 6PPD and 6PPD-quinone in acidic conditions to remove unreacted 6PPD mass and purify 6PPD-quinone. 3 mL of 6PPD column-ozonation mixture was diluted into 300 mL DI water and acidified by 0.3 mL 10% (v/v) HCl. The acidified solution was passed through 20 mL CEX resin in a chromatography column (250 mm × 10 mm ID; glass wool plug at the bottom) at a slow flowrate (~10 mL/min) to retain the unreacted 6PPD. The effluent was split into three 100 mL volumes; each 100 mL was loaded (5-10 mL/min) onto a C18 SPE cartridge (Resprep C18, 1g, 6 mL; preconditioned with 10 mL MeOH and 10 mL DI water; Restek, Bellefonte, PA, USA). SPE cartridges were rinsed with 5 mL DI water and dried for 3 min under vacuum. To further remove 6PPD, 4 mL MeOH:DI 7:3 (v/v) acidified with 0.1% formic acid was passed through the cartridge and discarded. The cartridge was then eluted with pure MeOH (2.5 mL + 5 mL). Eluents from three cartridges were combined and concentrated to 1 mL under nitrogen (35 ºC). After filtration (0.2 μm PTFE), the concentrate was fractionated with semi-preparative C18 HPLC. Mobile phases [$H_2O$ (A) and MeOH (B)] were acidified with 0.1% formic acid; all other LC parameters were identical to the above-detailed parallel fractionation method. C18-F6 (retention time, RT, 10-11 min) was collected as the purified 6PPD-quinone, dried with the centrifuge evaporator (0.3 torr, room temperature), and 6PPD-quinone dry mass weighed.

**Synthesis of PPD-quinone Standards (led by Dr. Kelly E. Kim)**

Unless noted in the specific procedure, reactions were performed in flame-dried glassware under ambient atmosphere. Dichloromethane was dried and deoxygenated by passage through columns of activated aluminum before use (Pangborn et al., 1996). Pyridine was purchased from MilliporeSigma in a SureSeal bottle and used as received. Commercial reagents were used as received.

All $^{1}H$ and $^{13}C$ nuclear magnetic resonance (NMR) spectra were recorded on a Bruker Avance DRX series spectrometer equipped with a triple resonance BBO probe (500 and 126 MHz, respectively) or a Bruker Avance series spectrometer equipped with a PABBI-ATMA 1H {X-BB} multinuclear probe (300 MHz) and are reported in terms of chemical shift relative to residual $CHCl_3$ (δ 7.26 and δ 77.16 ppm, respectively). Data for $^{1}H$ NMR spectra are reported as follows: chemical shift (δ ppm) (multiplicity, coupling constant (Hz), integration). Abbreviations are used as follows: s = singlet, d = doublet, t = triplet, q = quartet, m = complex multiplet. Infrared (IR) spectra were recorded using thin film samples on a PerkinElmer Spectrum 100 spectrometer equipped with a diamond/ZnSe UATR and are reported in frequency absorption ($cm^{-1}$).

Synthesis of 7PPD-quinone

Synthesis methods of the PPD-quinone derivatives were adapted from the method reported by Agua et al (Agua et al., 2021), as described below.

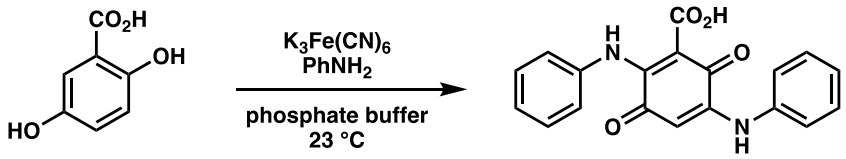


***1***

A round-bottom flask was charged with 2,5-dihydroxybenzoic acid (200 mg, 1.30 mmol, 1.00 equiv) and 7.2 pH phosphate buffer (20 mL). Potassium hexacyanoferrate(III) (854.5 mg, 2.60 mmol, 2.00 equiv) was added to the mixture as a single portion, turning the solution dark brown. Aniline (0.33 mL, 3.90 mmol, 3.00 equiv) was then added dropwise, and the resulting mixture was stirred at 23 °C. After 21 hours, the reaction was extracted with methylene chloride (3 × 25 mL), and the combined organic layers were washed with 0.5 M hydrochloric acid (3 × 25 mL) and brine (2 × 25 mL) and dried over sodium sulfate. Filtration and concentration under reduced pressured afforded quinone **1** as a brown solid (104.9 mg, 24% yield) which matched reported characterization data (Agua et al., 2021), and was used with no further purification.

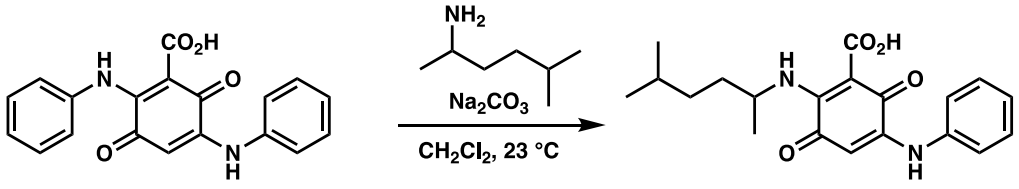


***1*** ***3***

To a solution of quinone **1** (83.6 mg, 0.250 mmol, 1.00 equiv) in methylene chloride (12 mL) was added sodium carbonate (53.0 mg, 0.500 mmol, 2.00 equiv) and 5-methylhexan-2-amine (0.038 mL, 0.250 mmol, 1.00 equiv). The resulting deep red solution was stirred at 23 °C for 27 hours. The reaction mixture was then diluted with methylene chloride (10 mL) and washed with 0.5 M hydrochloric acid (3 × 10 mL) and brine (10 mL). The combined organic layers were dried

over sodium sulfate, filtered, and concentrated to provide quinone **3** as a red amorphous solid (89.0 mg, 99% yield) that was used with no further purification. $^1$H NMR (300 MHz, $CDCl_3$) δ 14.17 (s, 1H), 12.32 (s, 1H), 8.11 (s, 1H), 7.47–7.38 (m, 2H), 7.30–7.20 (m, 3H), 6.03 (s, 1H), 5.03 (dq, *J* = 8.5, 6.5 Hz, 1H), 1.71–1.44 (m, 3H), 1.33 (d, *J* = 6.4 Hz, 3H), 1.28–1.17 (m, 2H), 0.88 (d, *J* = 6.6 Hz, 6H). IR (neat film) 3237 (br), 2956, 2930, 2869, 1736, 1683, 1615, 1575, 1515, 1445, 1390, 1347, 1248, 754, 693 cm$^{-1}$.

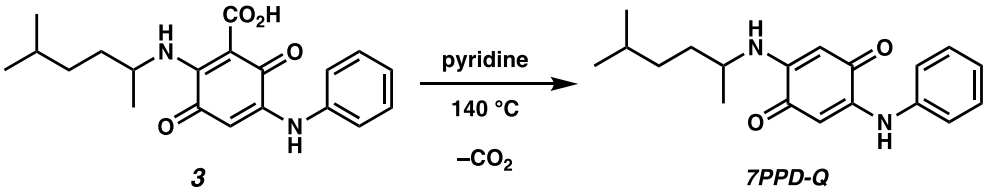


*3* *7PPD-Q*

A solution of quinone **3** (66.8 mg, 0.190 mmol, 1.00 equiv) in pyridine (8 mL) was heated to reflux at 140 °C. After 5 hours, the reaction was removed from heat and concentrated under reduced pressure. The resulting brown residue was diluted with methylene chloride (10 mL) and washed with 0.1 M hydrochloric acid (3 × 10 mL) and brine (10 mL). The combined organic layers were dried over sodium sulfate, filtered, and concentrated to afford crude **7PPD-quinone** as a dark magenta solid. Recrystallization from hexanes furnished pure **7PPD-quinone** as a dark pink solid (36.9 mg, 63% yield): $^1$H NMR (500 MHz, $CDCl_3$) δ 8.22 (s, 1H), 7.44–7.35 (m, 2H), 7.27–7.17 (m, 3H), 6.42 (d, *J* = 8.6 Hz, 1H), 5.97 (s, 1H), 5.41 (s, 1H), 3.44 (dq, *J* = 8.8, 6.5 Hz, 1H), 1.64–1.48 (m, 4H), 1.24 (d, *J* = 6.5 Hz, 3H), 1.23–1.15 (m, 1H), 0.89 (dd, *J* = 6.6, 1.2 Hz, 6H); $^{13}$C NMR ($CDCl_3$, 126 MHz) δ 180.2, 178.5, 149.7, 147.7, 137.4, 129.7, 126.1, 122.9, 95.7, 93.0, 49.0, 35.2, 34.2, 28.1, 22.7, 19.9; IR (neat film) 3263, 3231, 2952, 2868, 1638, 1557, 1485, 1442, 1356, 1288, 1225, 729, 692 cm$^{-1}$; HRMS (ESI+) *m/z* calcd for $C_{19}H_{25}N_2O_2$ $[M+H]^+$ 313.1916, found 313.1914.

Synthesis of IPPD-quinone

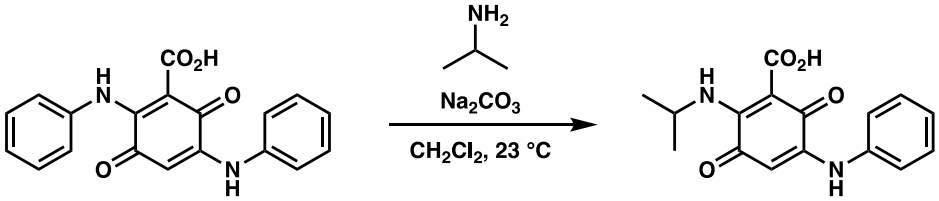


*1* *4*

To a solution of quinone **1** (21.1 mg, 0.0615 mmol, 1.00 equiv) in methylene chloride (3 mL) was added sodium carbonate (13.0 mg, 0.123 mmol, 2.00 equiv) and isopropylamine (5.3 µL, 0.0615 mmol, 1.00 equiv). The resulting deep red solution was stirred at 23 °C for 18 hours. The reaction mixture was then diluted with methylene chloride (5 mL) and washed with 0.5 M hydrochloric acid (3 × 5 mL) and brine (5 mL). The combined organic layers were dried over sodium sulfate, filtered, and concentrated to provide quinone **4** as a dark pink amorphous solid (18.4 mg, 99% yield) that was used with no further purification. $^1$H NMR (500 MHz, $CDCl_3$) δ 14.15 (s, 1H), 12.32 (s, 1H), 8.11 (s, 1H), 7.47–7.41 (m, 2H), 7.31–7.21 (m, 3H), 6.04 (s, 1H), 5.15 (m, *J* = 8.2, 6.4 Hz, 1H), 1.37 (d, *J* = 6.4 Hz, 6H).

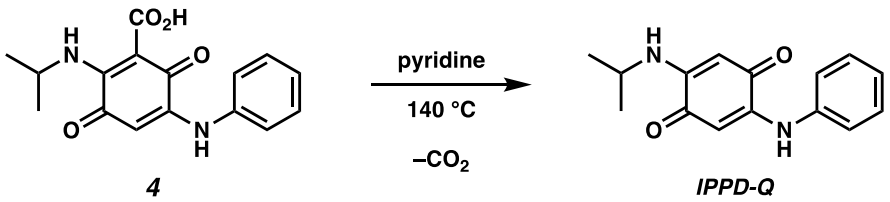


*4* *IPPD-Q*

A solution of quinone **3** (66.8 mg, 0.190 mmol, 1.00 equiv) in pyridine (8 mL) was heated to reflux at 140 °C. After 5 hours, the reaction was removed from heat and concentrated under reduced pressure. The resulting brown residue was diluted with methylene chloride (10 mL) and washed with 0.1 M hydrochloric acid (3 × 10 mL) and brine (10 mL). The combined organic layers were dried over sodium sulfate, filtered, and concentrated to afford crude **IPPD-quinone** as a dark magenta solid. Recrystallization from hexanes furnished pure **IPPD-quinone** as a dark pink solid (36.9 mg, 63% yield): $^{1}$H NMR (500 MHz, $CDCl_3$) δ 8.23 (s, 1H), 7.47–7.38 (m, 2H), 7.29–7.25 (m, 2H), 7.23 (td, *J* = 7.4, 1.3 Hz, 1H), 6.42 (d, *J* = 7.7 Hz, 1H), 5.99 (s, 1H), 5.44 (s, 1H), 3.65 (m, *J* = 8.3, 6.5 Hz, 1H), 1.31 (d, *J* = 6.4 Hz, 6H); $^{13}$C NMR ($CDCl_3$, 126 MHz) δ 180.2, 178.6, 149.4, 147.6, 137.4, 129.7, 126.0, 122.8, 95.8, 93.3, 44.4, 21.9; IR (neat film) 3261, 3233, 2925, 1637, 1557, 1500, 1487, 1445, 1358, 1291, 730 cm$^{-1}$; HRMS (ESI+) *m/z* calcd for $C_{15}H_{17}N_2O_2$ $[M+H]^+$ 257.1290, found 257.1287.

Synthesis of DTPD-quinone

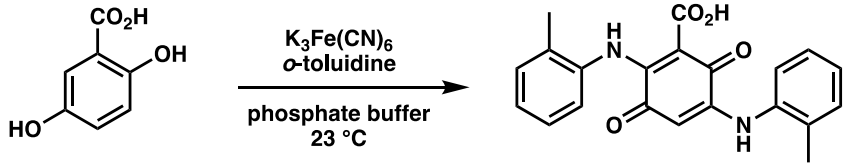


*5*

A round-bottom flask was charged with 2,5-dihydroxybenzoic acid (200 mg, 1.30 mmol, 1.00 equiv) and 7.2 pH phosphate buffer (20 mL). Potassium hexacyanoferrate(III) (854.5 mg, 2.60 mmol, 2.00 equiv) was added to the mixture as a single portion, turning the solution dark brown. *o*-Toluidine (0.41 mL, 3.90 mmol, 3.00 equiv) was then added dropwise, and the resulting mixture was stirred at 23 °C. After 18 hours, the reaction was extracted with methylene chloride (3 × 25 mL), and the combined organic layers were washed with 0.5 M hydrochloric acid (3 × 25 mL) and brine (2 × 25 mL) and dried over sodium sulfate. Filtration and concentration under reduced pressured afforded quinone **1** as a brown solid (170.4 mg, 36% yield) that was used with no further purification. $^{1}$H NMR (300 MHz, $CDCl_3$) δ 13.95 (s, 1H), 13.28 (s, 1H), 7.93 (s, 1H), 7.40–7.18 (m, 7H), 7.09 (dd, *J* = 7.2, 1.6 Hz, 1H), 5.63 (s, 1H), 2.34 (s, 3H), 2.31 (s, 3H); $^{13}$C NMR ($CDCl_3$, 126 MHz) δ 180.3, 177.1, 170.6, 156.1, 146.9, 137.8, 134.6, 133.3, 132.5, 131.7, 131.0, 128.1, 127.8, 127.3, 126.9, 124.8, 124.7, 99.2, 97.0, 18.1, 17.8.

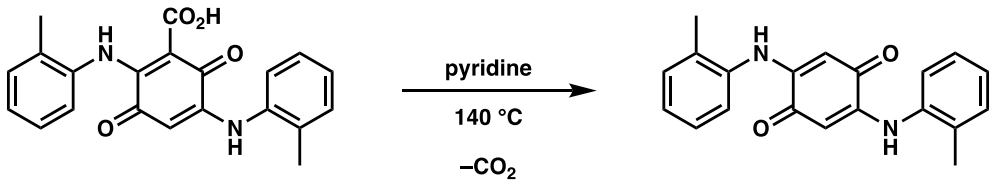


*5* *DTPD-Q*

A solution of quinone **5** (35.0 mg, 0.0966 mmol, 1.00 equiv) in pyridine (5.5 mL) was heated

to reflux at 140 °C. After 5 hours, the reaction was removed from heat and concentrated under reduced pressure. The resulting brown residue was diluted with methylene chloride (10 mL) and washed with 0.1 M hydrochloric acid (3 x 10 mL) and brine (10 mL). The combined organic layers were dried over sodium sulfate, filtered, and concentrated to afford crude **DTPD-quinone** as a dark magenta solid. Recrystallization from hexanes furnished pure **DTPD-quinone** as a pale brown solid: $^{1}$H NMR (500 MHz, $CDCl_3$) δ 7.90 (s, 2H), 7.31–7.27 (m, 6H), 7.23–7.18 (m, 2H), 5.66 (s, 2H), 2.29 (s, 6H); IR (neat film) 3231, 1635, 1555, 1503, 1472, 1460, 1280, 732 $cm^{-1}$; HRMS (ESI+) *m/z* calcd for $C_{20}H_{19}N_2O_2$ $[M+H]^+$ 319.1447, found 319.1446.

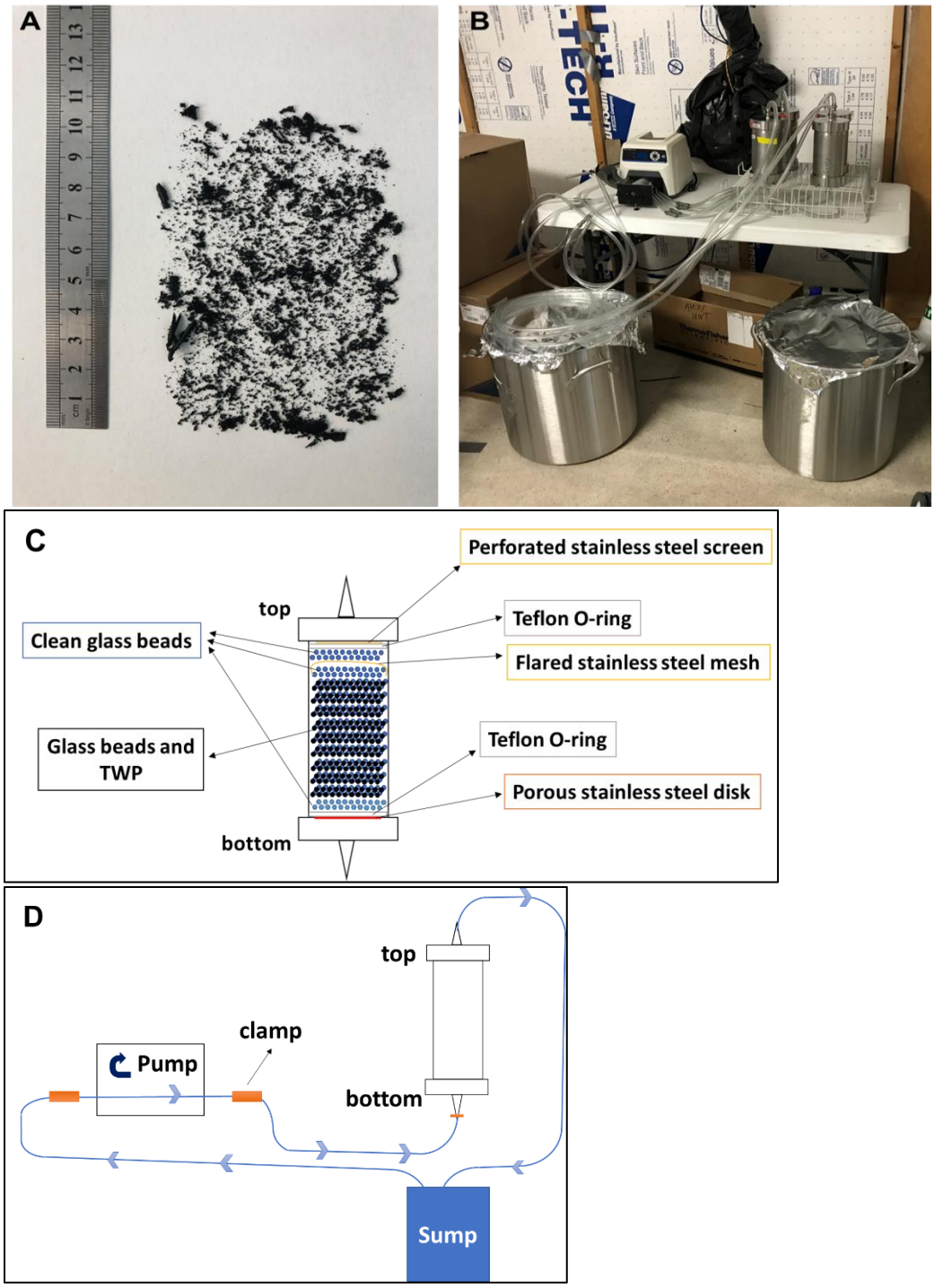


**Figure S5.1** Tire tread wear particles (TWP) and TWP leaching system. (A) Representative photo of TWP made from nine different types of tires. TWP (average surface area 0.2 ± 0.3 $mm^2$, range 0.002- 23.9 $mm^2$) typically included a mixture of fine particles, thin strips, and flakes. The heterogeneity in TWP size and composition was a function of the specific tire being abraded; tire composition and use strongly affected generated TWP particle characteristics. (B) Photo of TWP leaching system including the pump, columns, sumps, and tubing. (C) Cross section of the TWP leaching column. (D) Schematic of flow through the tire leaching system.

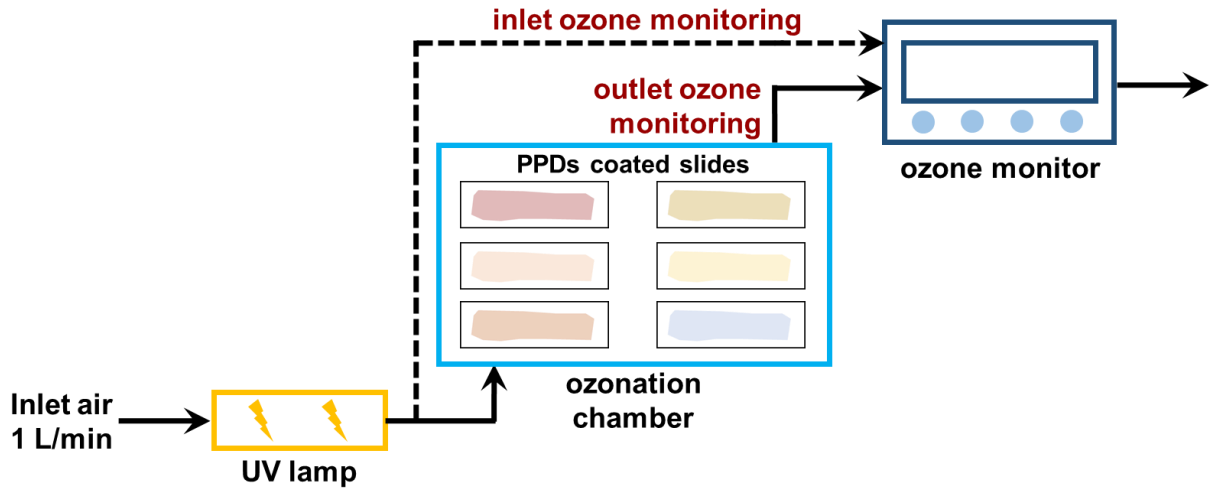


**Figure S5.2** Schematic diagram of the ozonation system. Filled black arrows demonstrated the gas flow during ozonation. Dashed black arrow demonstrated the gas flow for monitoring the inlet ozone levels at the beginning of each ozonation period.

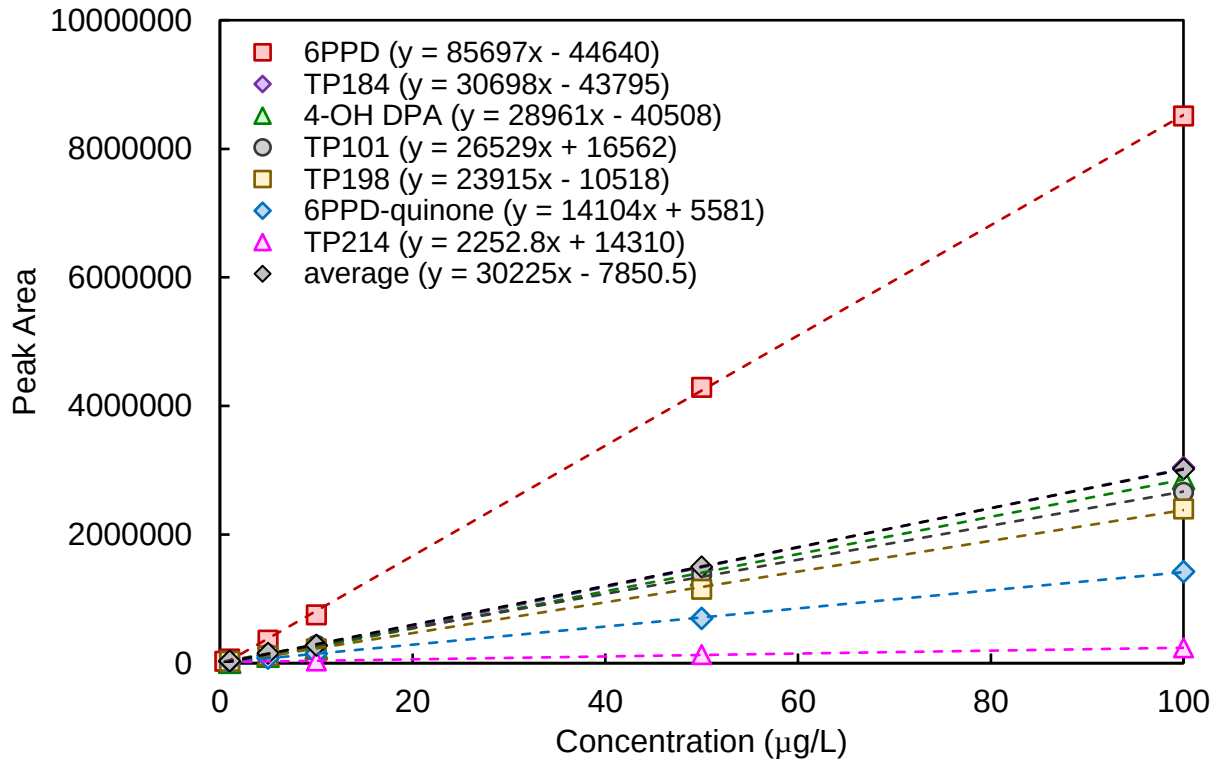


**Figure S5.3** Calibration curves of 0.1-100 µg/L 6PPD, 5 level 1 TPs, and 4-OH DPA.

**Table S5.1** Manufacturers and use histories of the nine tires used to produce tire tread wear particles for TWP leachate stock generation.

| Tire ID | Manufacturer | Season | New/Used | Vehicle Type | Tire code |
|---|---|---|---|---|---|
| 1 | A | All-season | Used | Car | 205/55R16 91H |
| 2 | B | All-season | Used | Car | 195/70R14 91H |
| 3 | C | All-season | Used | Car | P185/65R15 86T |
| 4 | D | Winter | Used | Car | 175/65R14 82S |
| 5 | E | All-season | Used | Car | P185/85R15 86S |
| 6 | E | All-season | Used | Light Truck | LT235/85R16 120R |
| 7 | F | All-season | New | Car | P205/60R15 90T |
| 8 | G | All-season | New | Car | P205/60R16 92H |
| 9 | H | All-season | Used | Car | P225/60R17 98T |

**Table S5.2** Key parameters of the feature extraction and alignment method in MassHunter Profinder.

| Category | Item | Setting |
|---|---|---|
| Molecular Feature Extraction (MFE) – Extraction Parameters | Noise peak height | ≥ 300 counts |
| | Ion Species | ESI+: +H, +Na, +$NH_4$<br>ESI-: -H, +HCOO, +CH3COO |
| | Isotope model | Common organic molecules |
| Compound Binning and Alignment | RT window | 0.4 min |
| | Mass window | 30 ppm |
| MFE – Post-Processing Filters | Absolute height | ≥ 5000 counts |
| | Score (MFE) | ≥ 70 |
| | Satisfy MFE conditions in | ≥ 2 files |
| Find by Ion – Matching Tolerances and Scoring | Scoring | Mass score (100), isotope abundance score (60), isotope spacing score (50), retention time score (50) |
| | Do not match if score | < 30 |
| Find by Ion – EIC Peak Integration and Filtering | Integration | Agile 2 |
| | Peak height | ≥ 3000 counts |
| Find by Ion – Post-Processing Filters | Absolute height | ≥ 1000 counts |
| | Score (Tgt) | ≥ 50 |
| | Satisfy Find by Ion conditions in | ≥ 2 files |

**Table S5.3** Limits of detection (LODs; ng/L), limits of quantification (LOQs; ng/L), spike concentrations (spike conc), and recoveries (Rec; %) of the quantified analytes in TWP leachate, roadway runoff, creek stormwater, and TWP methanolic extracts.

| Compound | Creek stormwater | | | | TWP leachate | | | | Roadway runoff | | | | TWP methanolic extracts | | | |
|---|---|---|---|---|---|---|---|---|---|---|---|---|---|---|---|---|
| | LOD | LOQ | Spike conc. (µg/L) | Rec | LOD | LOQ | Spike conc. (µg/L) | Rec | LOD | LOQ | Spike conc. (µg/L) | Rec | LOD | LOQ | Spike conc. (µg/g) | Rec |
| 6PPD | 36 | 120 | 0.5 | 100 ± 5 | 8.4 | 28 | 0.5 | 46 ± 2 | 52 | 170 | 5 | 46 ± 4 | 0.84 | 2.8 | 5000 | 70 ± 1 |
| 6PPD-quinone | 120 | 410 | 0.5 | 56 ± 2 | 8.6 | 29 | 0.5 | 57 ± 9 | 83 | 280 | 5 | 39 ± 5 | 2.3 | 7.6 | 50 | 92 ± 3 |
| 4s DPA | 73 | 240 | 0.5 | 62 ± 3 | 13 | 43 | 0.5 | 76 ± 5 | 110 | 380 | 5 | 47 ± 3 | 0.29 | 0.97 | 50 | 100 ± 4 |
| 1,3-DMBA | 750 | 2500 | 5 | 57 ± 3 | 30 | 100 | 20 | 47 ± 6 | 150 | 500 | 20 | 27 ± 3 | 6.0 | 20 | 50 | 98 ± 5 |
| 4-NDPA | 150 | 500 | 0.5 | 43 ± 5 | 30 | 100 | 0.5 | 74 ± 6 | 150 | 500 | 5 | 62 ± 5 | 1.3 | 4.4 | 50 | 107 ± 5 |
| 4-ADPA | 160 | 540 | 0.5 | 106 ± 7 | 10 | 40 | 0.5 | 49 ± 5 | 97 | 320 | 5 | 39 ± 2 | 1.6 | 5.4 | 50 | 75 ± 4 |
| 4-HDPA | 21 | 68 | 0.5 | 99 ± 6 | 5.9 | 20 | 20 | 55 ± 4 | 36 | 120 | 5 | 54 ± 3 | 0.72 | 2.4 | 50 | 97 ± 4 |
| TP 282 | 70 | 230 | n/a[a] | n/a | 2.4 | 8.0 | n/a | n/a | 12 | 38 | n/a | n/a | 0.48 | 1.6 | n/a | n/a |
| TP 274 | 280 | 920 | n/a | n/a | 26 | 87 | n/a | n/a | 690 | 2300 | n/a | n/a | 1.7 | 5.5 | n/a | n/a |

[a] spike recovery cannot be evaluated for TP 282 and TP 274 due to lack of analytical standards.

**Table S5.4** Peak area of the TPs in the blank controls, spike control, and undiluted ozonation mixtures.

| | blank control | spike control | 1-day | 3-day | 7-day |
|---|---|---|---|---|---|
| 6PPD-quinone | ND | 920000 ± 80000 | 68000000 ± 360000 | 73000000 ± 22000 | 68000000 ± 280000 |
| TP 282 | ND | ND | 52000000 ± 400000 | 43000000 ± 11000 | 35000000 ± 4000 |
| 4-ADPA | ND | ND | 36000000 ± 1600000 | 36000000 ± 150000 | 34000000 ± 230000 |
| 4s DPA | ND | 110000 ± 110000 | 24000000 ± 600000 | 21000000 ± 38000 | 23000000 ± 29000 |
| TP 344 | ND | ND | 15000000 ± 210000 | 13000000 ± 64000 | 8800000 ± 8200 |
| TP 546b | ND | 81000 ± 81000 | 11000000 ± 9000 | 9800000 ± 68000 | 12000000 ± 70000 |
| TP 207b | ND | ND | 9800000 ± 36000 | 4400000 ± 1300 | 3100000 ± 1300 |
| TP 546a | ND | ND | 8200000 ± 10000 | 6800000 ± 220000 | 9000000 ± 38000 |
| 1,3-DMBA | ND | 1200000 ± 130000 | 6200000 ± 84000 | 6100000 ± 3300 | 6200000 ± 100000 |
| TP 280a | ND | ND | 5900000 ± 14000 | 6400000 ± 34000 | 4600000 ± 600 |
| TP 312 | ND | 990000 ± 46000 | 5000000 ± 130000 | 4300000 ± 15000 | 3000000 ± 2800 |
| TP 298a | ND | ND | 4600000 ± 22000 | 3500000 ± 21000 | 3300000 ± 30000 |
| TP 298b | ND | ND | 4500000 ± 61000 | 5200000 ± 270000 | 8200000 ± 70000 |
| TP 296 | ND | ND | 4400000 ± 48000 | 4700000 ± 36000 | 4691 ± 23000 |
| TP 280b | ND | 1200000 ± 170000 | 4300000 ± 360000 | 6800000 ± 180000 | 4200000 ± 200000 |
| TP 562 | ND | ND | 4000000 ± 81000 | 2000000 ± 15000 | 1500000 ± 56000 |
| TP 256 | ND | ND | 3900000 ± 23000 | 2600000 ± 7600 | 2300000 ± 11000 |
| TP274 | ND | ND | 3400000 ± 15000 | 2400000 ± 17000 | 2800000 ± 13000 |
| TP 207a | ND | ND | 2700000 ± 2000 | 2700000 ± 2000 | 2800000 ± 5000 |
| 4-NDPA | ND | ND | 800000 ± 18000 | 1500000 ± 200 | 1500000 ± 5400 |

**Table S5.5** Predicted log$K_{ow}$ and p$K_a$ for level 1 and 2 ozonation products. Listed log$K_{ow}$ and p$K_a$ values were for the most relevant species near the mobile phase pH (0.1% formic acid, pH ~2.7).

| Name | Formula | log$K_{ow}$ | | | pK$_a$ | | |
|---|---|---|---|---|---|---|---|
| | | Species | KOWWIN | SPARC | Species | SPARC | Marvin |
| 6PPD | $C_{18}H_{24}N_2$ | 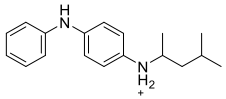 | 2.80 | 2.19 | 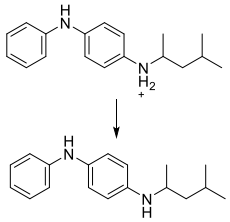 | 5.01 | 6.46 |
| 6PPD-quinone | $C_{18}H_{22}N_2O_2$ | 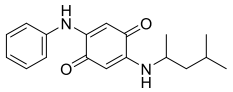 | 3.98 | 1.43 | 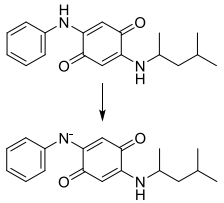 | 10.69 | 11.77 |
| 4s DPA | $C_{12}H_{10}N_2O$ | 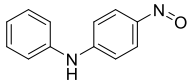 | 3.16 | 3.20 | 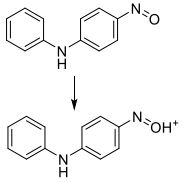 | NA[a] | 2.77 |
| 1,3-DMBA | $C_6H_{15}N$ | 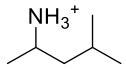 | -1.51 | -1.43 | 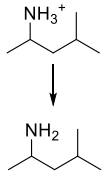 | 10.36 | 10.42 |

| | | | | | | | |
|---|---|---|---|---|---|---|---|
| 4-ADPA | $C_{12}H_{12}N_2$ | 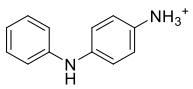 | -0.06 | 0.34 | 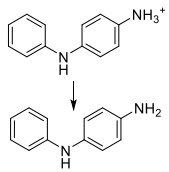 | 4.12 | 5.40 |
| 4-NDPA | $C_{12}H_{10}N_2O_2$ | 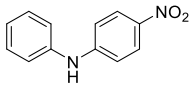 | 3.69 | 4.03 | NA[a] | NA[a] | NA[a] |
| TP 298a | $C_{18}H_{22}N_2O_2$ | 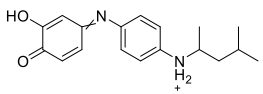 | 0.93 | 0.35 | 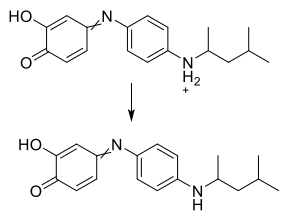 | 4.16 | 4.80 |
| TP 274 | $C_{16}H_{22}N_2O_2$ | 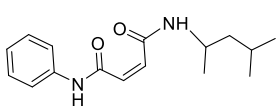 | 3.18 | 2.86 | NA[a] | NA[a] | NA[a] |

[a] No p$K_a$ available in pH 1-14, based on software prediction.

**Table S5.6** Levels of 6PPD and the ozonation TPs in each creek water, roadway runoff, tire leachate sample (ng/L) and tire wear particles before and after ozonation (µg/g).

| Compound | TWP leachate (µg/L) | | | Roadway runoff (µg/L) | | | Creek stormwater (ng/L) | | | | | | TWP methanolic extract (µg/g) | | |
|---|---|---|---|---|---|---|---|---|---|---|---|---|---|---|---|
| | 6/2/19 | 7/2/19 | 7/16/19 | 3/13/19 | 4/8/19 | 6/16/17 | 3/4/21 | 3/18/21 | 10/9/20 | 10/23/20 | 11/03/ | 11/13/20 | non-ozone | air ctrl | ozone |
| 6PPD | 0.37 | <LOQ | 0.066 | <LOQ | N.D. | <LOQ | <LOQ | <LOQ | N.D. | N.D. | N.D. | N.D. | 1300 | 1200 | 550 |
| 6PPD-quinone | 0.23 | 0.33 | 0.18 | 1.3 | 0.91 | 0.38 | <LOQ | <LOQ | N.D. | N.D. | <LOQ | N.D. | 15 | 17 | 36 |
| 4s DPA | 0.049 | <LOQ | <LOQ | 4.7 | 2.5 | 3.8 | <LOQ | N.D. | N.D. | N.D. | N.D. | N.D. | <LOQ | 7.2 | 20 |
| 1,3-DMBA | 2.3 | 1.8 | 1.2 | 17 | 18 | 5.3 | 3.4 | <LOQ | 2.6 | <LOQ | <LOQ | <LOQ | 52 | 40 | 66 |
| 4-NDPA | N.D. | N.D. | N.D. | N.D. | N.D. | N.D. | N.D. | N.D. | N.D. | N.D. | N.D. | N.D. | N.D. | N.D. | 17 |
| 4-ADPA | N.D. | N.D. | N.D. | 2.6 | 2.1 | 1.8 | <LOQ | <LOQ | N.D. | N.D. | N.D. | <LOQ | 7.7 | 9.6 | 23 |
| 4-HDPA | 10 | 7.1 | 5.8 | 1.3 | 0.22 | 0.51 | 0.23 | 0.18 | N.D. | N.D. | N.D. | N.D. | 19 | 24 | 24 |
| TP282 | 0.018 | 0.033 | 0.017 | 5.7 | 3.3 | 1.5 | 2.2 | 1.2 | 0.6 | 1.1 | 0.8 | 1.4 | <LOQ | 11 | 43 |
| TP274 | 1.2 | 1.9 | 1.1 | 23 | 8.5 | 17 | 3.5 | 2.2 | <LOQ | 1.4 | 1.3 | 1.7 | 14 | 15 | 74 |

[a] Variation derived from duplicate injections.
[b] Variation derived from triplicate samples.
[c] Calculated from 6PPD calibration curve.

**Table S5.7** Identification details of 6PPD TPs.

| **Name:** 6PPD | **Formula:** $C_{18}H_{24}N_2$ | **Precursor:** $[M+H]^+$ | **RT:** 6.94 min |
|---|---|---|---|
| **Structure:** 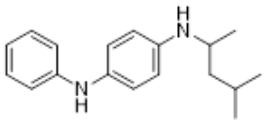 | **Comments:** parent compound | | |

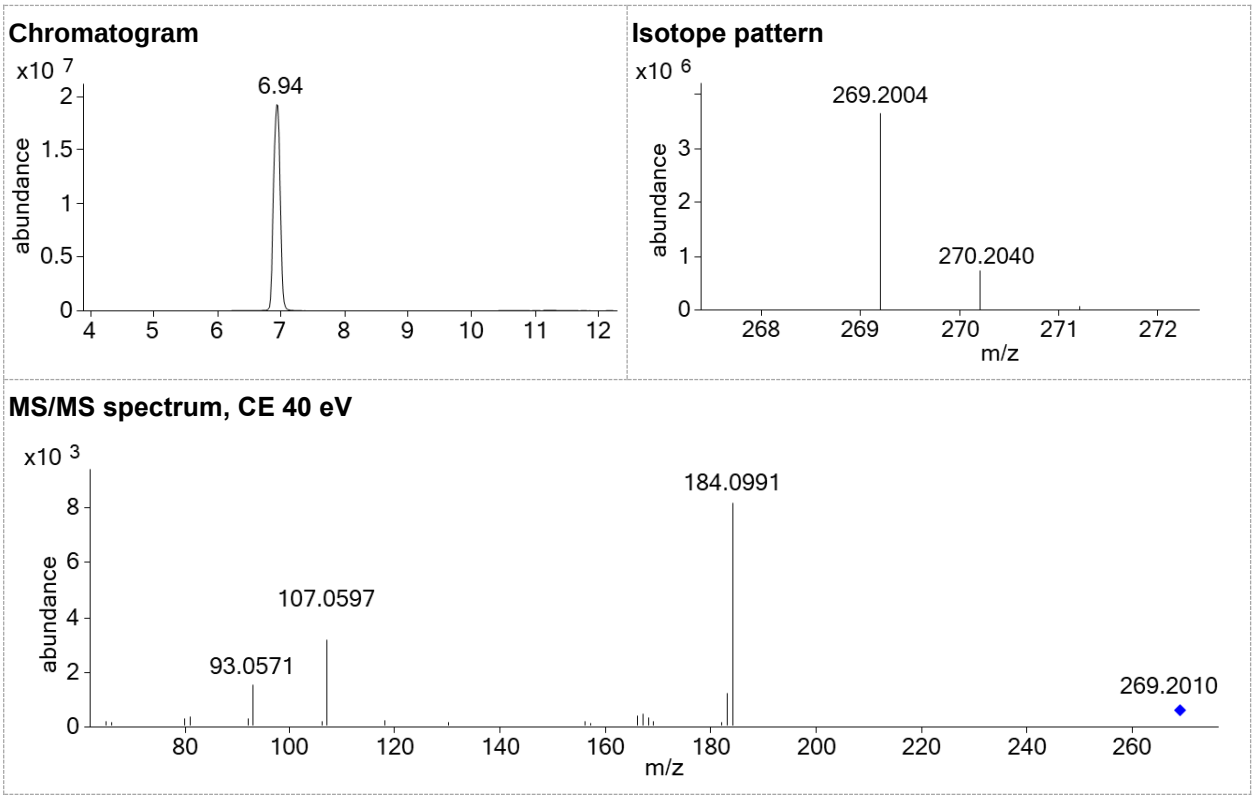

| **Name:** 6PPD-quinone (TP 298c) | **Confidence level:** 1 | **Formula:** $C_{18}H_{22}N_2O_2$ | **RT shift:** + 4.06 min | **Atomic Modification:** - 2H + 2O |
|---|---|---|---|---|
| **Structure:** 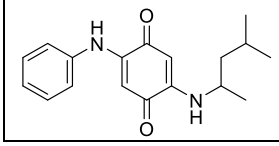 | **Identification:** reference standard | | | |

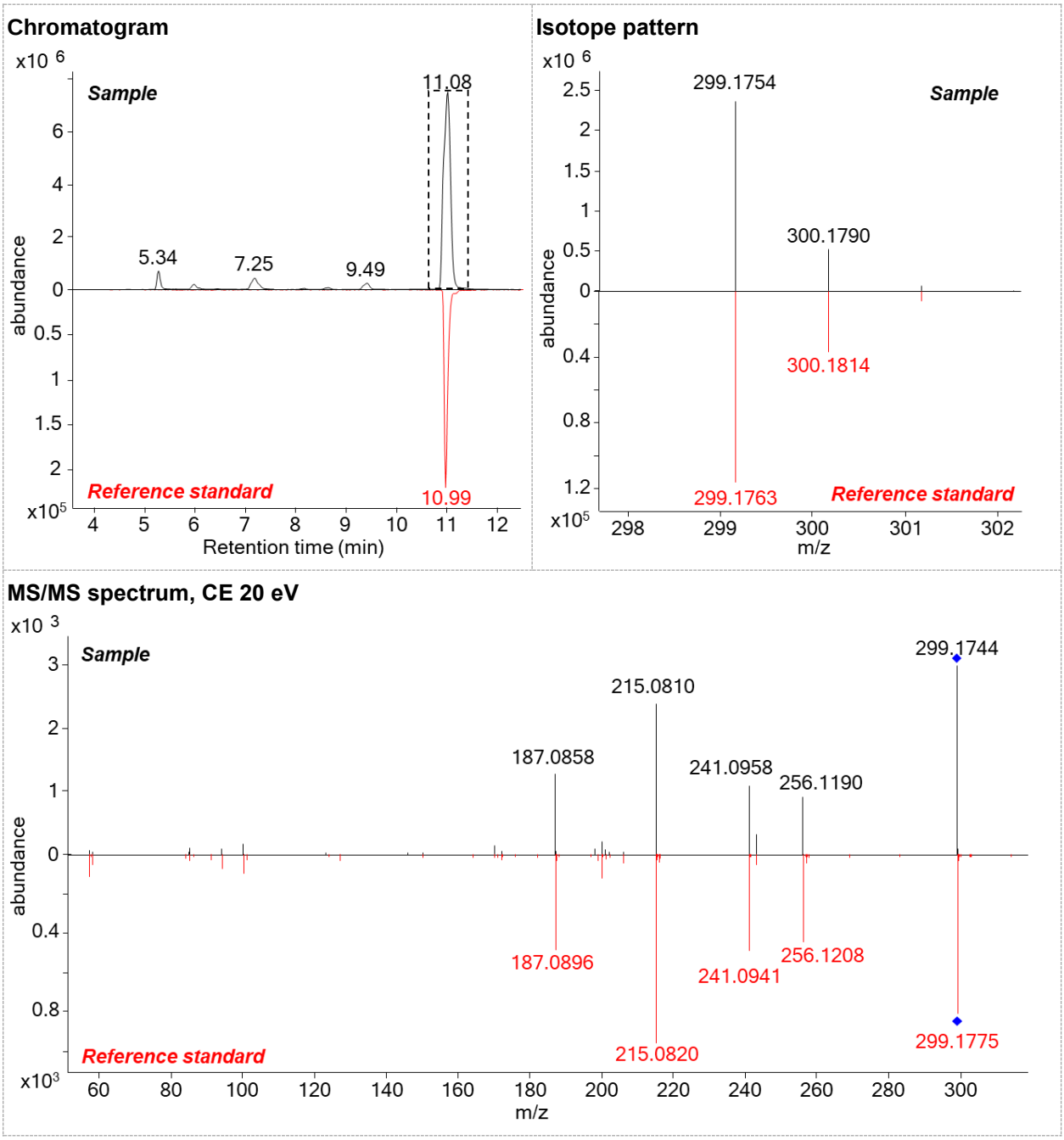

| **Name:** 4s DPA (TP 198) | **Confidence level:** 1 | **Formula:** $C_{12}H_{10}N_2O$ | **RT shift:** + 0.30 min | **Atomic Modification:** - $C_6H_{14}$ + O |
|---|---|---|---|---|
| **Structure:** 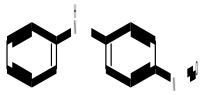 | **Identification:** reference standard | | | |

**Chromatogram**

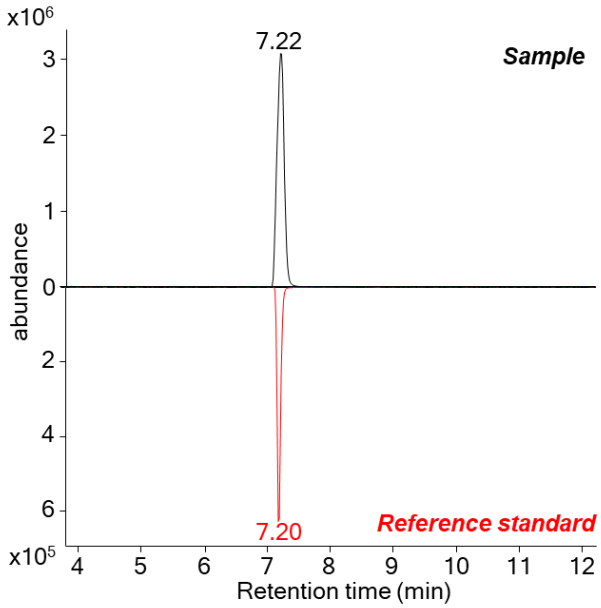


**Isotope pattern**

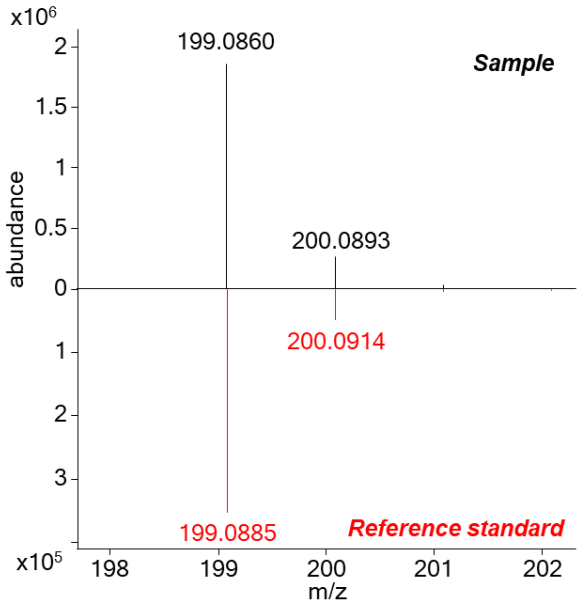


**MS/MS spectrum, CE 40 eV**

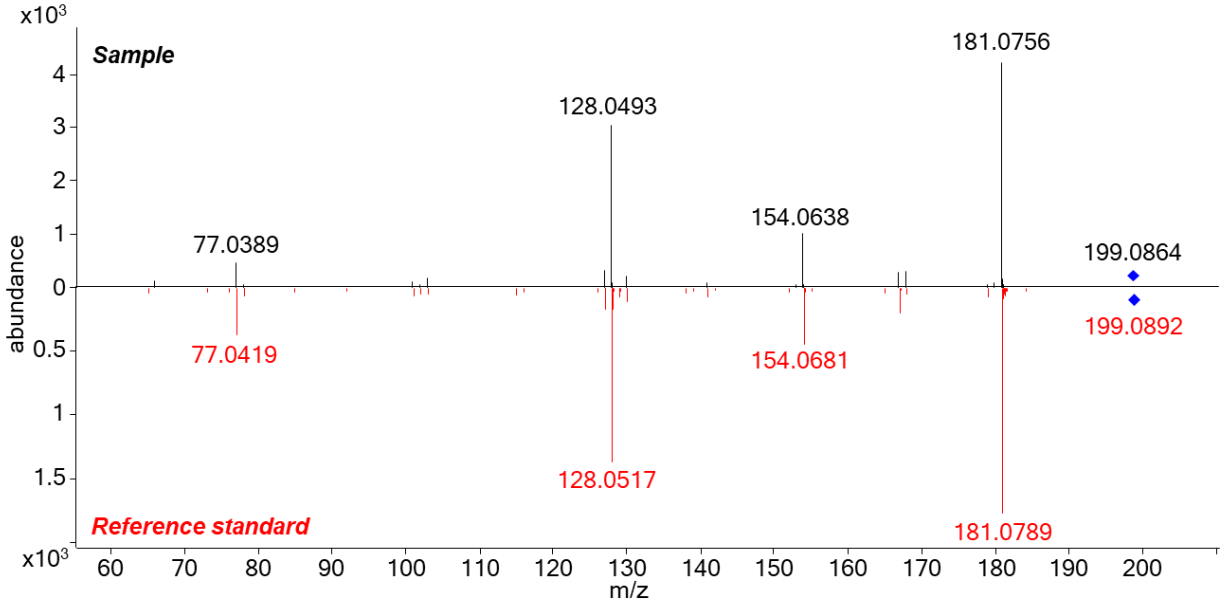

| **Name:** 1,3-DMBA (TP 101) | **Confidence level:** 1 | **Formula:** $C_6H_{15}N$ | **RT shift:** - 3.79 min | **Atomic Modification:** - $C_{12}H_9N$ |
|---|---|---|---|---|
| **Structure:** 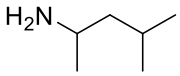 | **Identification:** reference standard | | | |

| **Name:** 4-ADPA (TP 184) | **Confidence level:** 1 | **Formula:** $C_{12}H_{12}N_2$ | **RT shift:** - 2.67 min | **Atomic Modification:** - $C_6H_{12}$ |
|---|---|---|---|---|
| **Structure:** 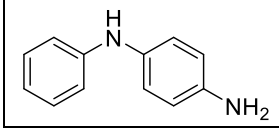 | **Identification:** reference standard | | | |

| **Name:** 4-NDPA (TP 214) | **Confidence level:** 1 | **Formula:** $C_{12}H_{10}N_2O_2$ | **RT shift:** + 1.92 min | **Atomic Modification:** - $C_6H_{14}$ +$O_2$ |
|---|---|---|---|---|
| **Structure:** 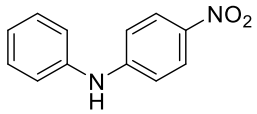 | **Identification:** reference standard | | | |



**Chromatogram**

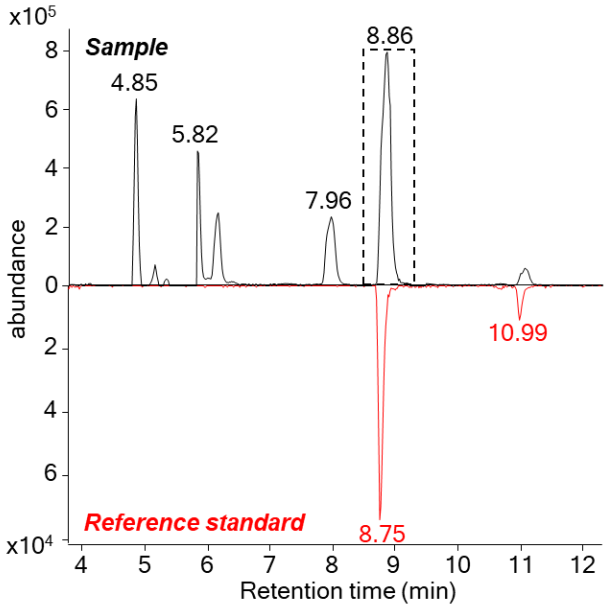


**Isotope pattern**

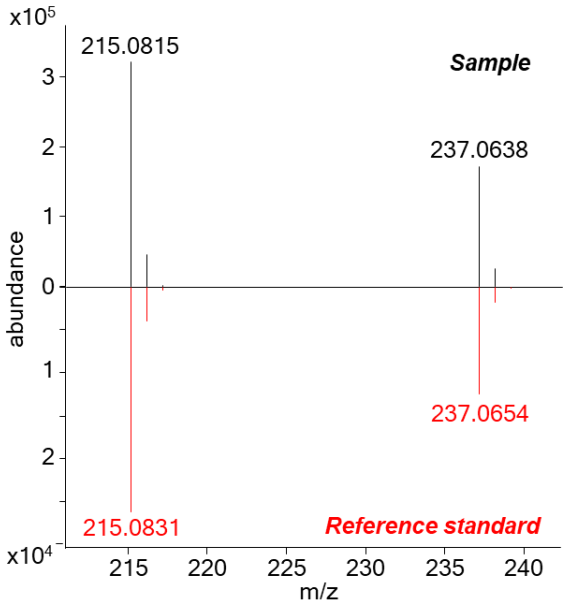


**MS/MS spectrum, CE 20 eV**

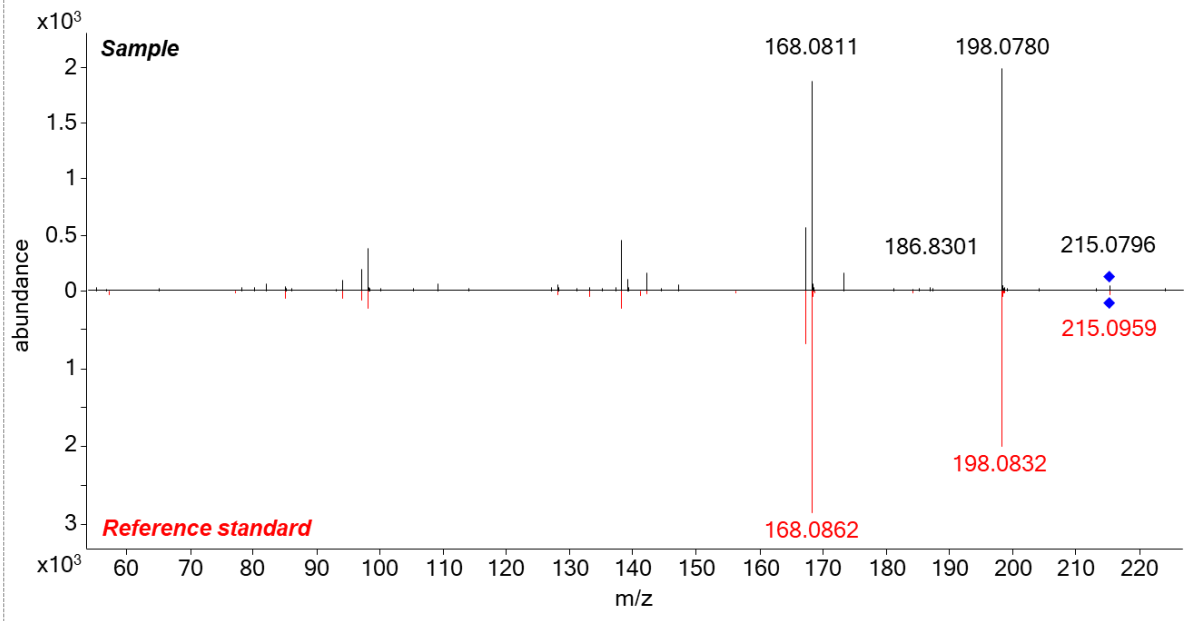

| **Name:** TP 298a | **Confidence level:** 2b | **Formula:** $C_{18}H_{22}N_2O_2$ | **RT shift:** - 1.6 min | **Atomic Modification:** - $H_2$ + $O_2$ |
|---|---|---|---|---|
| **Structure:** 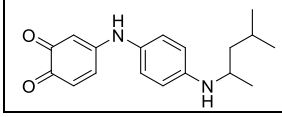 | **Identification:** consecutive CO loss indicates orthoquinone structure. | | | |

**Chromatogram**

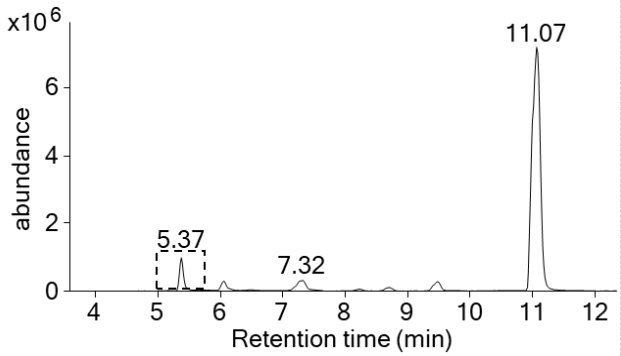


**Isotope pattern**

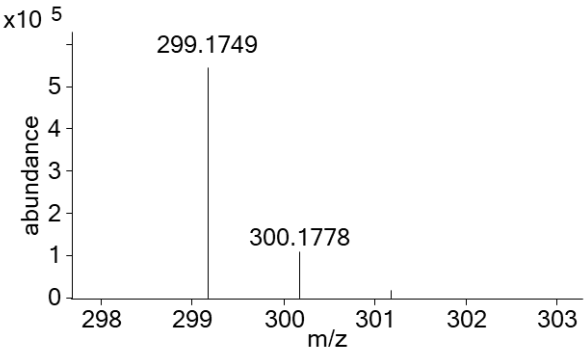


**MS/MS spectrum, CE 40 eV**

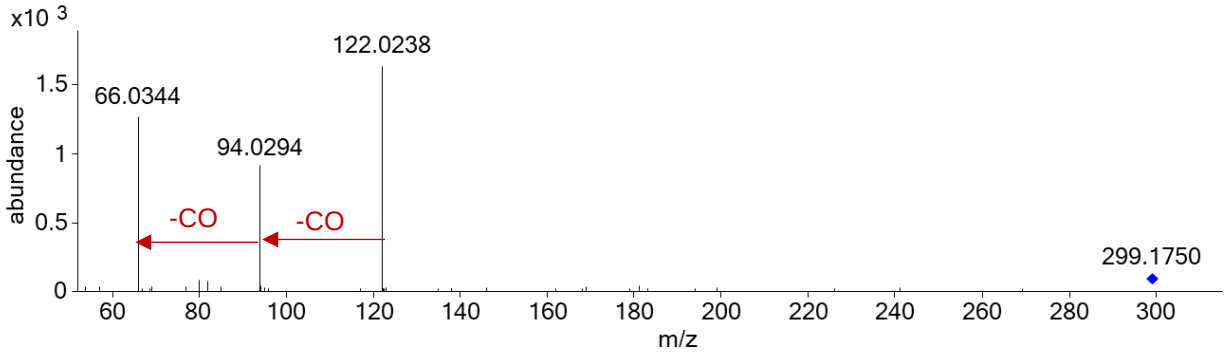

| **Name:** TP 274 | **Confidence level:** 2b | **Formula:** $C_{16}H_{22}N_2O_2$ | **RT shift:** + 3.52 min | **Atomic Modification:** - $C_2H_2$ + $O_2$ |
|---|---|---|---|---|
| **Structure:** 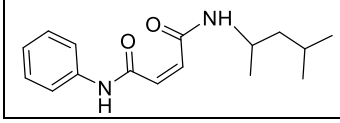 | **Identification:** spectrum pattern | | | |

**Chromatogram**

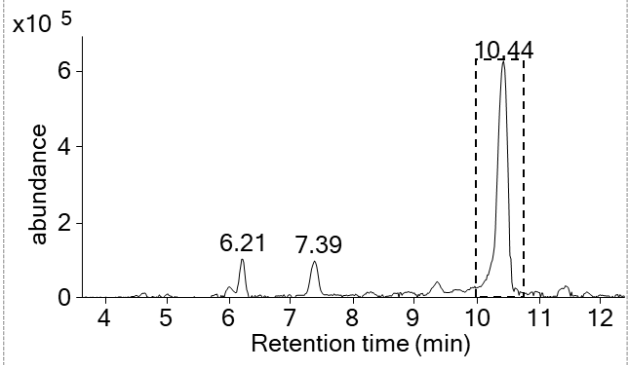


**Isotope pattern**

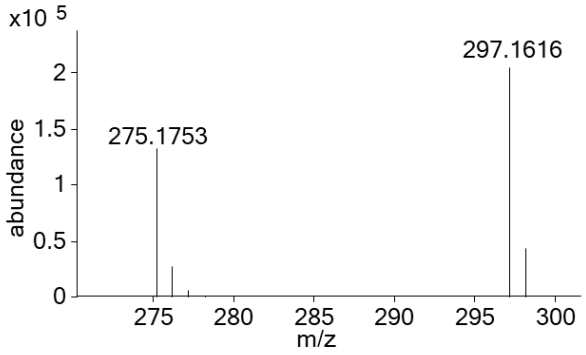


**MS/MS spectrum, CE 10 eV**

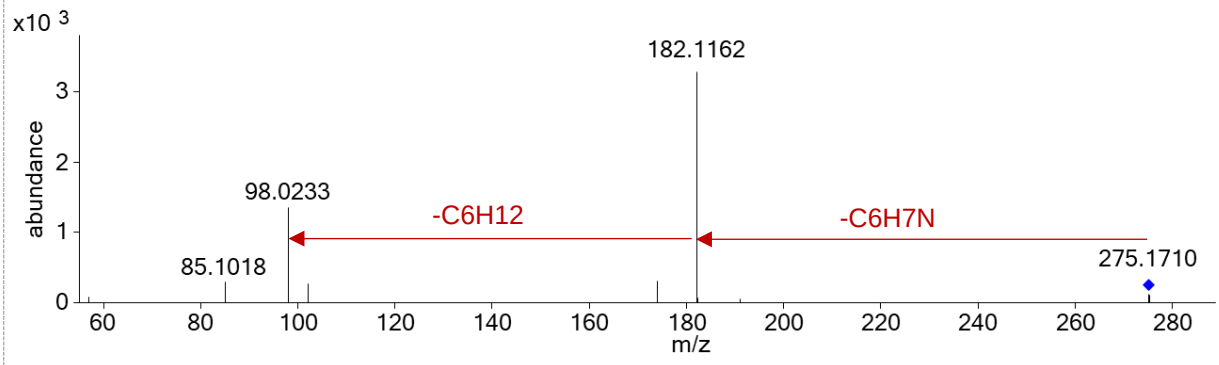

| **Name:** TP 207a | **Confidence level:** 3 | **Formula:** $C_{12}H_{17}NO_2$ | **RT shift:** - 1.90 min | **Atomic Modification:** - C6H7N + $O_2$ |
|---|---|---|---|---|
| **Structure:** 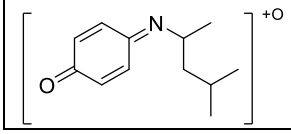 | **Identification:** spectrum pattern | | | |

**Chromatogram**

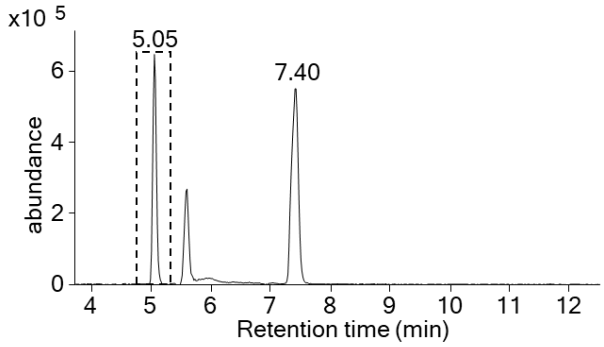


**Isotope pattern**

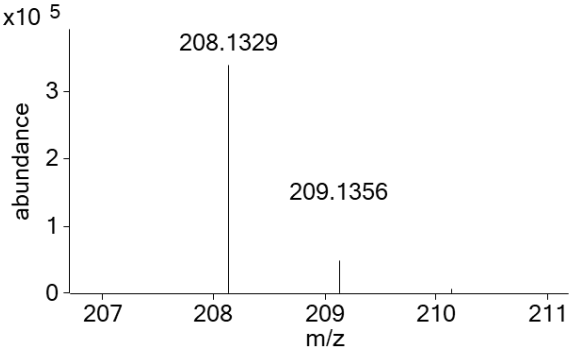


**MS/MS spectrum, CE 10 eV**

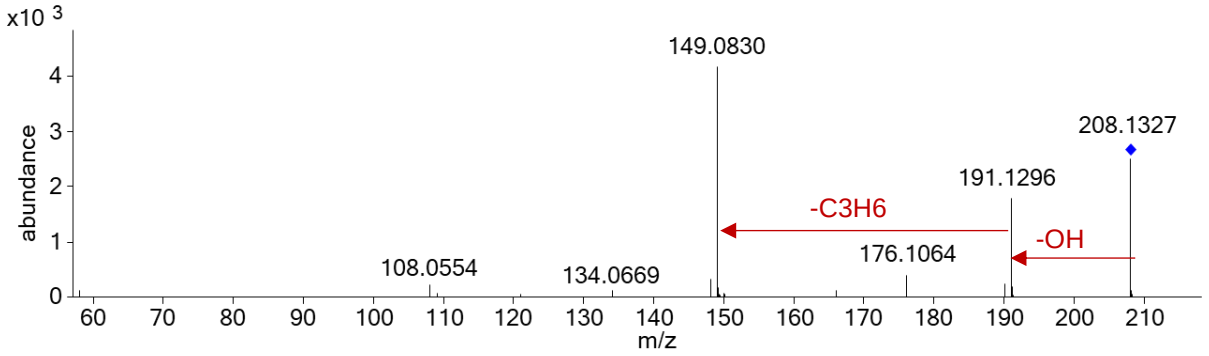

| **Name:** TP 207b | **Confidence level:** 3 | **Formula:** $C_{12}H_{17}NO_2$ | **RT shift:** + 0.47 min | **Atomic Modification:** - C6H7N + $O_2$ |
|---|---|---|---|---|
| **Structure:** 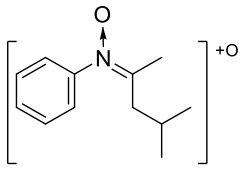 | **Identification:** spectrum pattern | | | |

**Chromatogram**

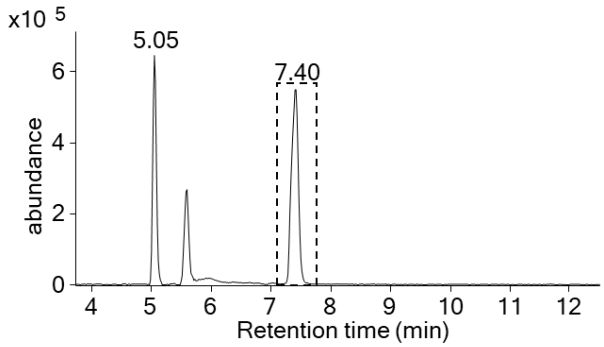


**Isotope pattern**

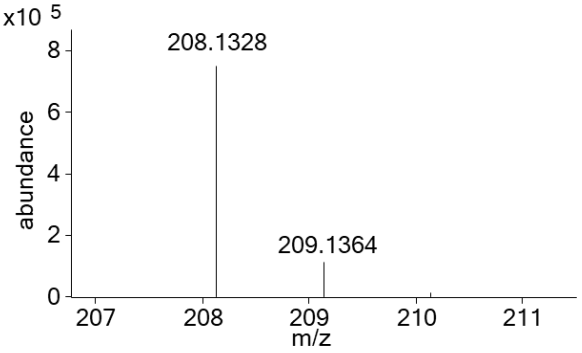


**MS/MS spectrum, CE 10 eV**

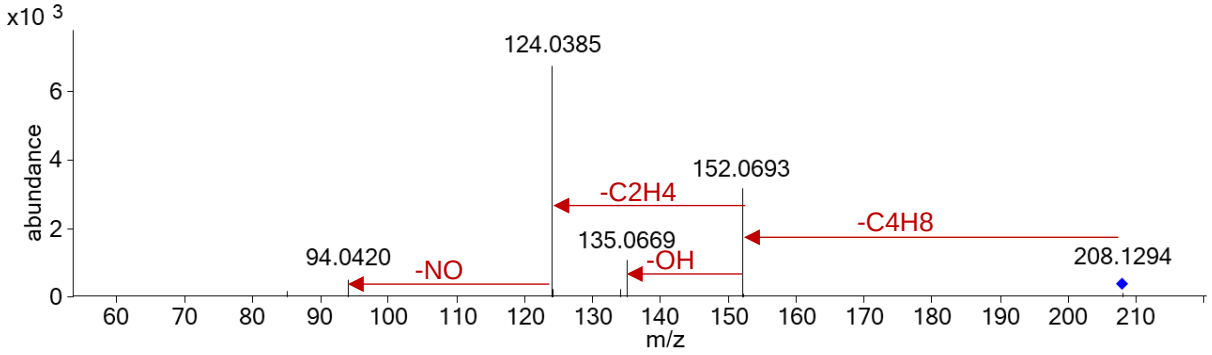

| **Name:** TP 298b | **Confidence level:** 3 | **Formula:** $C_{18}H_{22}N_2O_2$ | **RT shift:** + 0.31 min | **Atomic Modification:** - $H_2$ + $O_2$ |
|---|---|---|---|---|
| **Structure:** 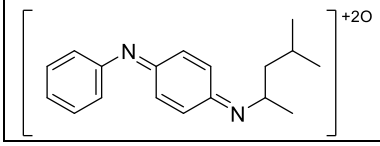 | **Identification:** spectrum pattern (consecutive OH loss indicates orthoquinone structure); literature | | | |

| **Name:** TP 256 | **Confidence level:** 3 | **Formula:** $C_{16}H_{20}N_2O$ | **RT shift:** + 2.58 min | **Atomic Modification:** - $C_2H_4$ + O |
|---|---|---|---|---|
| **Structure:** 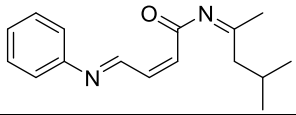 | **Identification:** spectrum pattern | | | |

**Chromatogram**

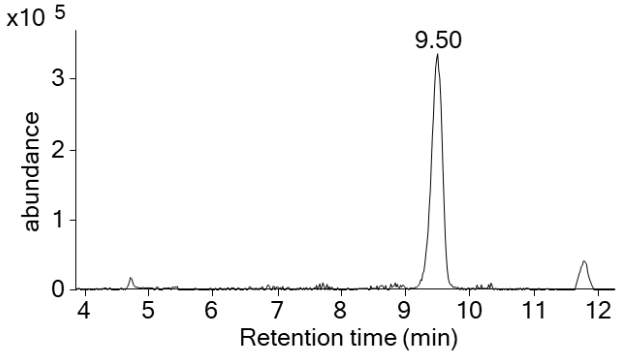


**Isotope pattern**

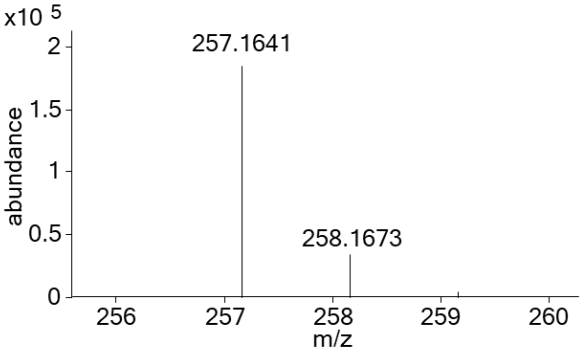


**MS/MS spectrum, CE 40 eV**

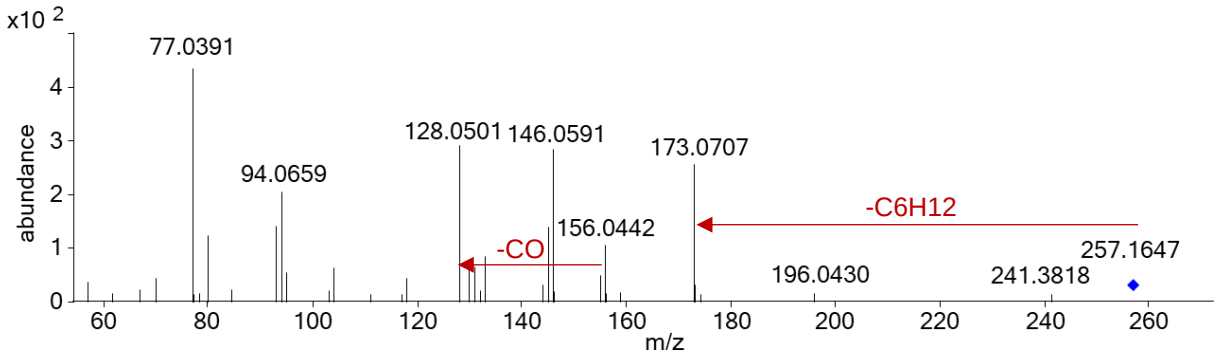

| **Name:** TP 282 | **Confidence level:** 3 | **Formula:** $C_{18}H_{22}N_2O$ | **RT shift:** + 1.6 min | **Atomic Modification:** - 2H + O |
|---|---|---|---|---|
| **Structure:** 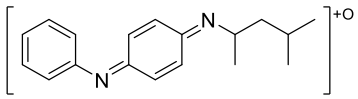 | **Identification:** spectrum pattern, literature | | | |

**Chromatogram**

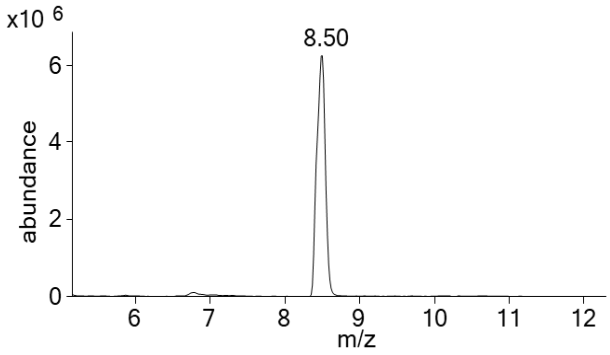


**Isotope pattern**

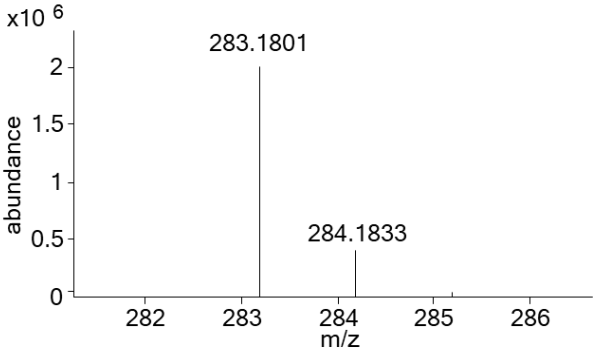


**MS/MS spectrum, CE 20 eV**

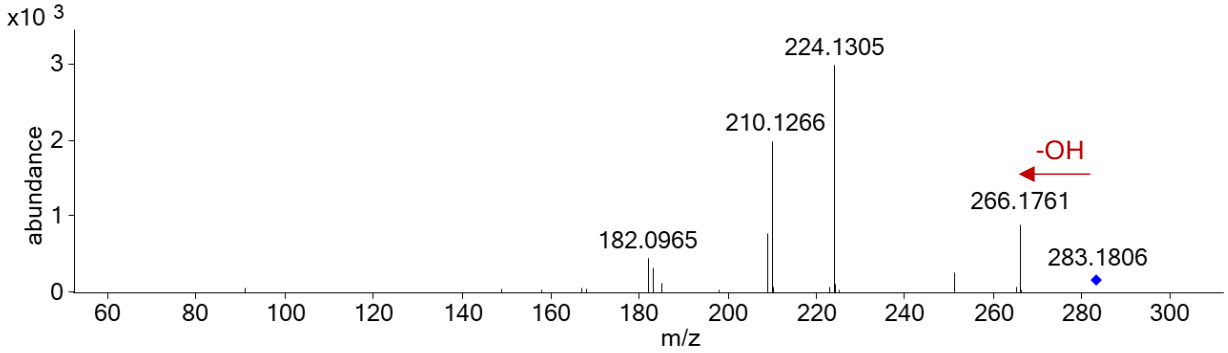

| **Name:** TP 296 | **Confidence level:** 3 | **Formula:** $C_{18}H_{20}N_2O_2$ | **RT shift:** + 3.45 min | **Atomic Modification:** - $H_4$ + $O_2$ |
|---|---|---|---|---|
| **Structure:** 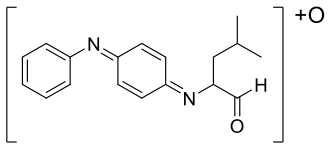  | **Identification:** spectrum pattern | | | |

**Chromatogram**

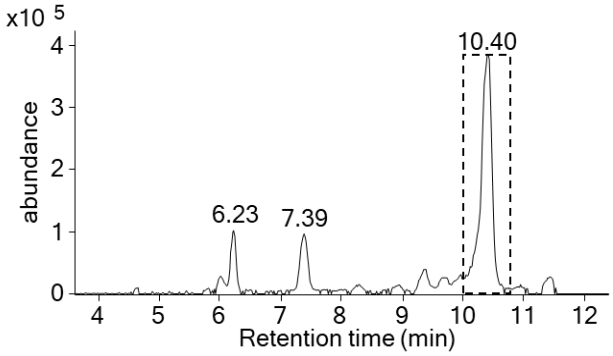


**Isotope pattern**

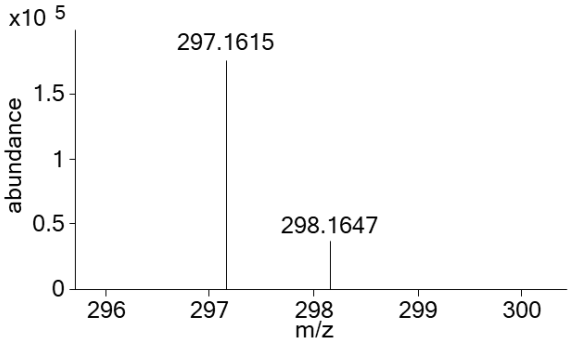


**MS/MS spectrum, CE 40 eV**

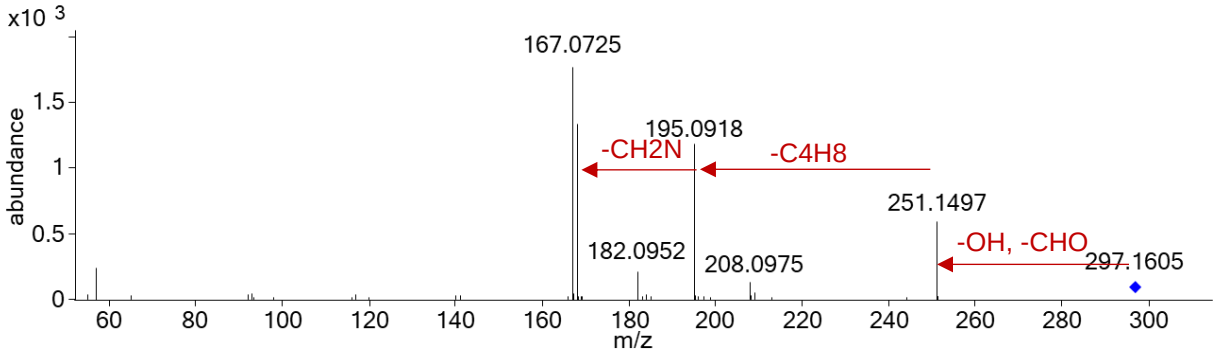

| **Name:** TP 546a | **Confidence level:** 3 | **Formula:** $C_{36}H_{42}N_4O$ | **RT shift:** + 3.63 | **Atomic Modification:** 6PPD × 2 - H6 + O |
|---|---|---|---|---|
| **Structure:** 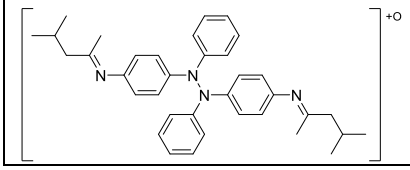 | **Identification:** literature | | | |

**Chromatogram**

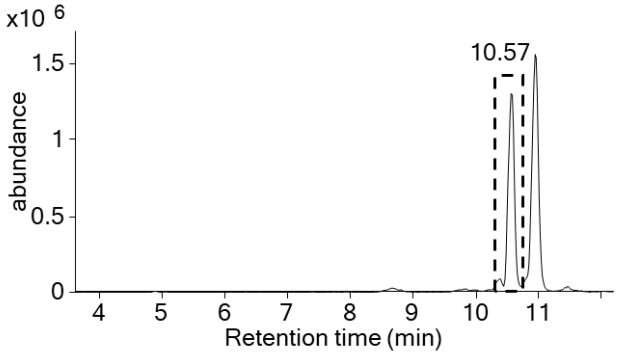


**Isotope pattern**

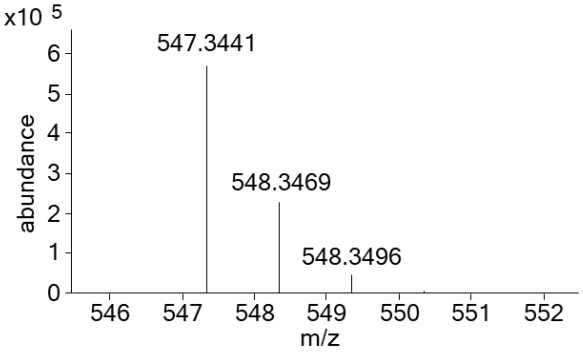


**MS/MS spectrum, CE 40 eV**

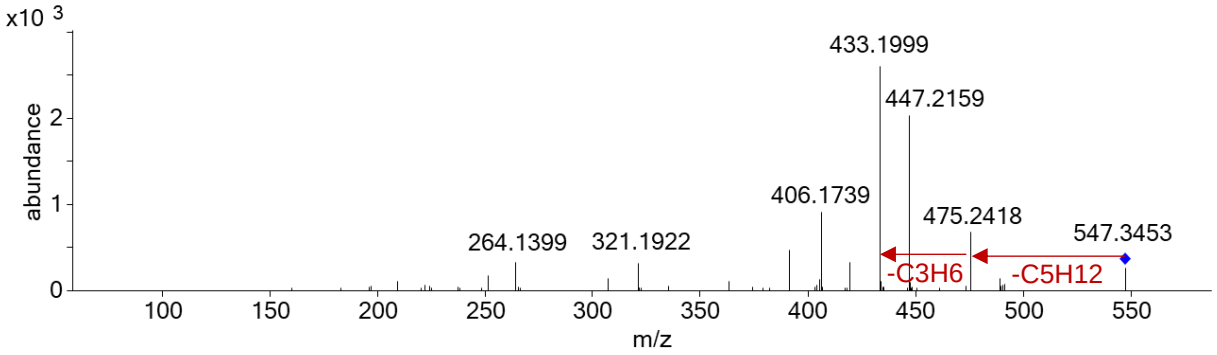

| **Name:** TP 546b | **Confidence level:** 3 | **Formula:** $C_{36}H_{42}N_4O$ | **RT shift:** + 4.00 min | **Atomic Modification:** 6PPD × 2 - H6 + O |
|---|---|---|---|---|
| **Structure:** 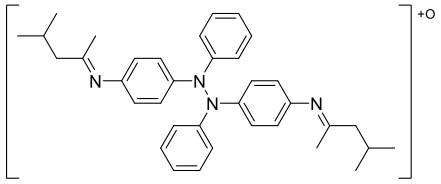 | **Identification:** literature | | | |

**Chromatogram**

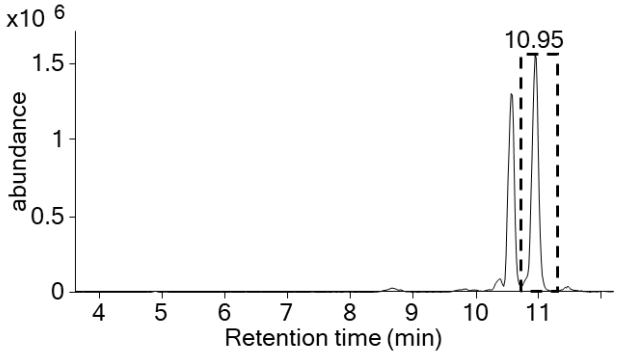


**Isotope pattern**

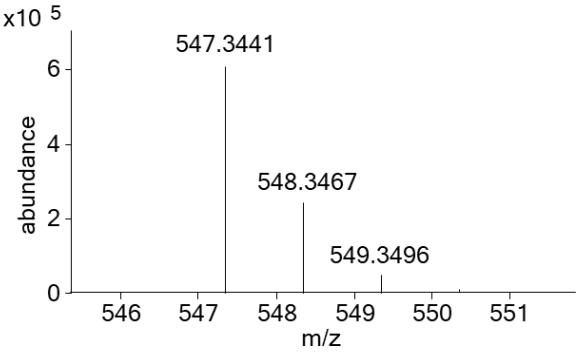


**MS/MS spectrum, CE 40 eV**

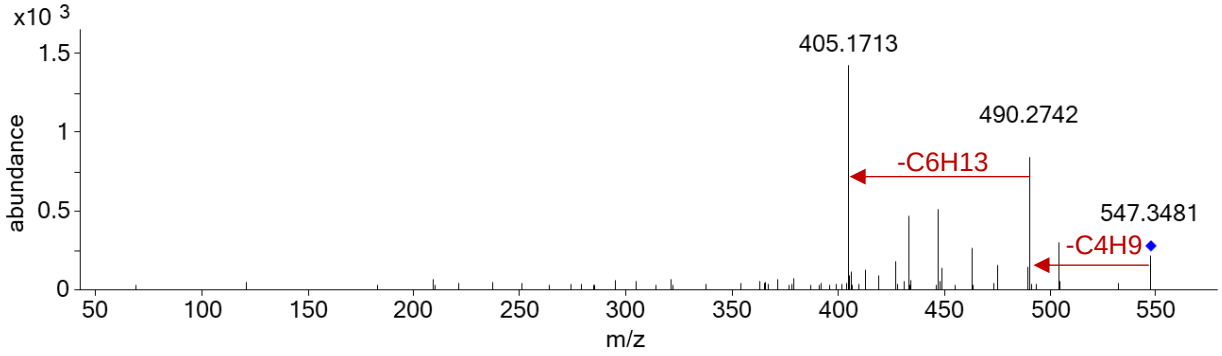

| **Name:** TP 562 | **Confidence level:** 3 | **Formula:** $C_{36}H_{42}N_4O_2$ | **RT shift:** + 8.50 min | **Atomic Modification:** 6PPD × 2 - $H_6$ + $O_2$ |
|---|---|---|---|---|
| **Structure:** 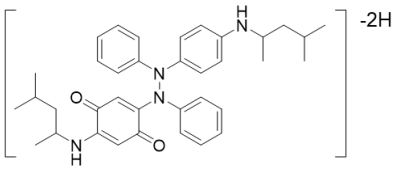  | **Identification:**<br>- spectrum pattern (28 Da neutral loss for CO);<br>- RT difference between TP 546 (6PPD-dimer; 10.59 /10.97 min) and TP 562 (15.44 min) similar to RT difference between 6PPD (6.94 min) and 6PPD-quinone (11.0 min) | | | |

**Chromatogram**

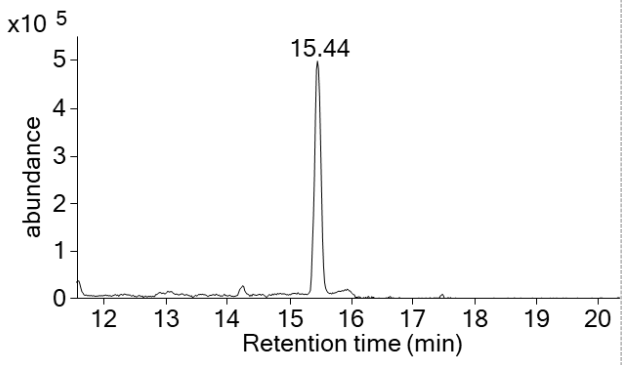


**Isotope pattern**

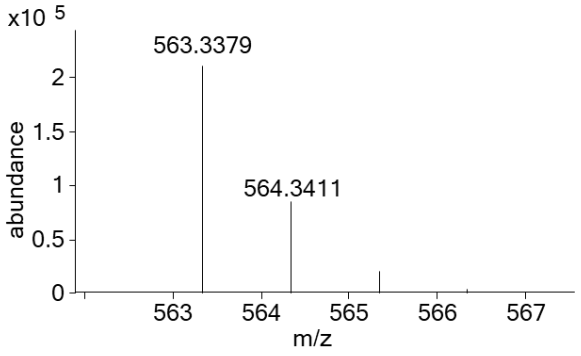


**MS/MS spectrum, CE 40 eV**

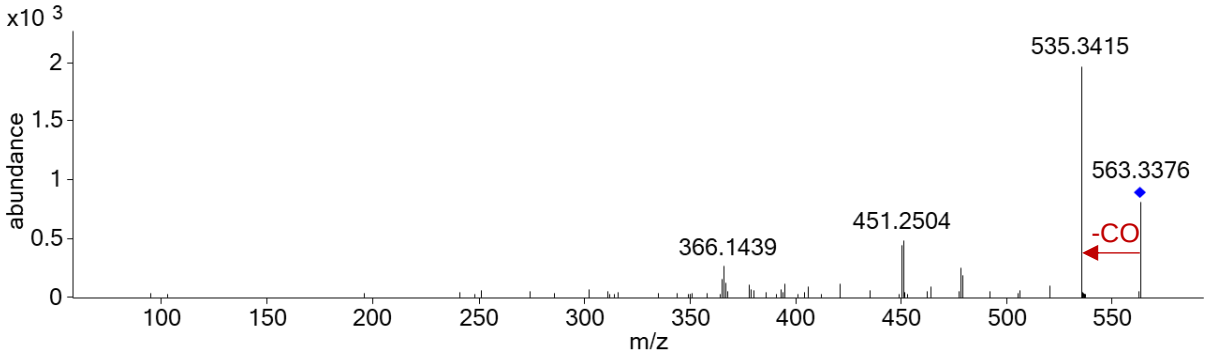

| **Name:** TP 280a | **Confidence level:** 4 | **Formula:** $C_{18}H_{20}N_2O$ | **RT shift:** - 1.09 min | **Atomic Modification:** $-H_4 + O$ |
|---|---|---|---|---|
| **Structure:** no final structure | **Identification:** - | | | |

**Chromatogram**

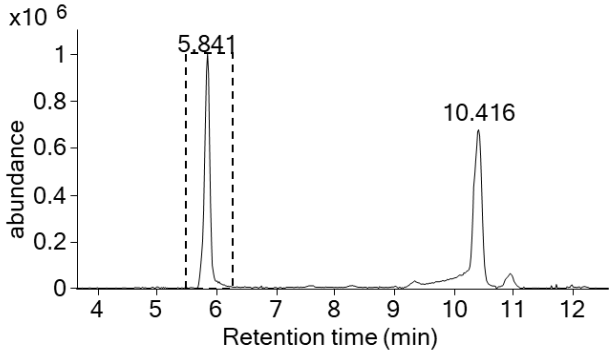


**Isotope pattern**

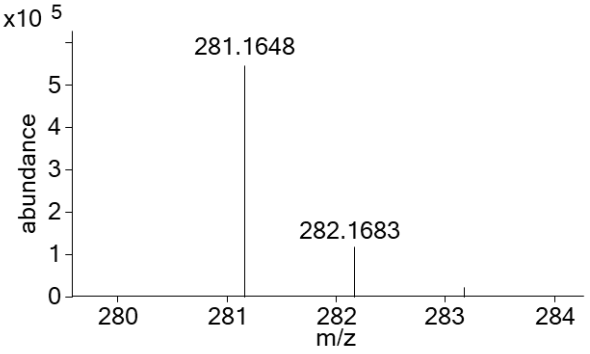


**MS/MS spectrum, CE 20 eV**

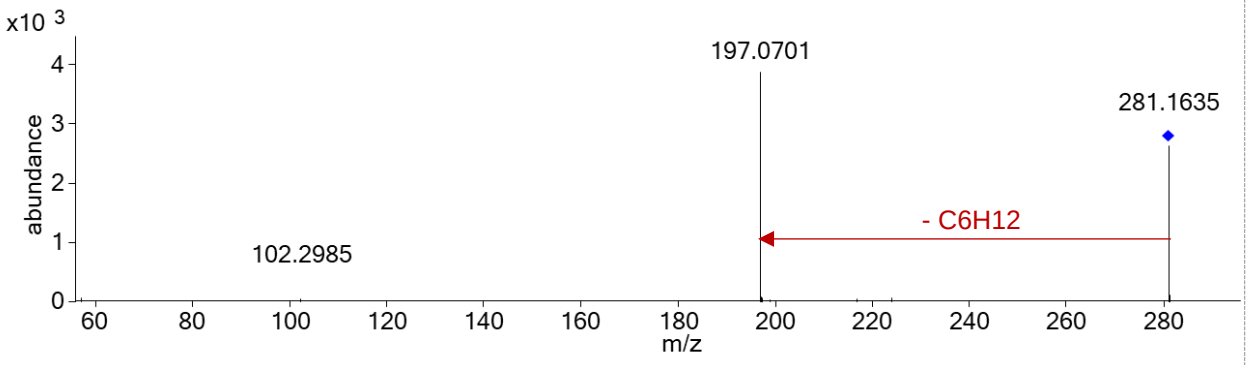

| **Name:** TP 280b | **Confidence level:** 4 | **Formula:** $C_{18}H_{20}N_2O$ | **RT shift:** + 3.50 min | **Atomic Modification:** $-H_4 + O$ |
|---|---|---|---|---|
| **Structure:** no final structure | **Identification:** - | | | |

**Chromatogram**

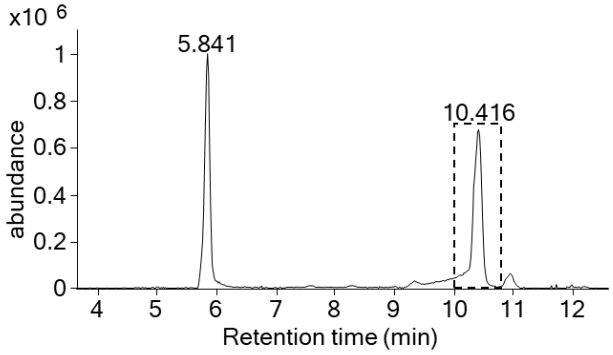


**Isotope pattern**

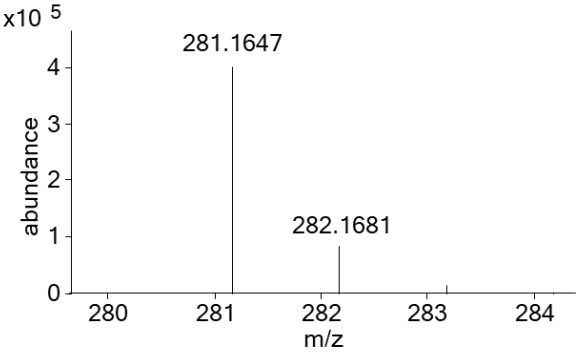


**MS/MS spectrum, CE 20 eV**

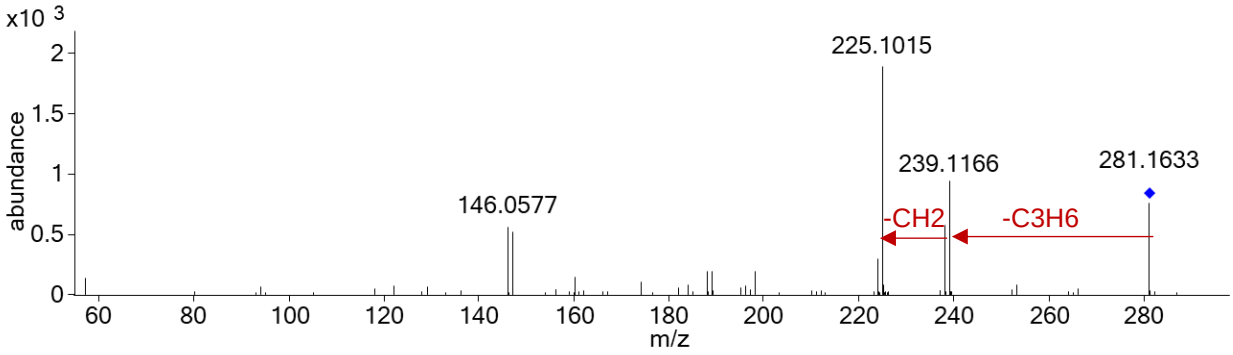

| **Name:** TP 312 | **Confidence level:** 4 | **Formula:** $C_{19}H_{24}N_2O_2$ | **RT shift:** - 1.36 min | **Atomic Modification:** + $CO_2$ |
|---|---|---|---|---|
| **Structure:** no final structure | **Identification:** - | | | |

**Chromatogram**

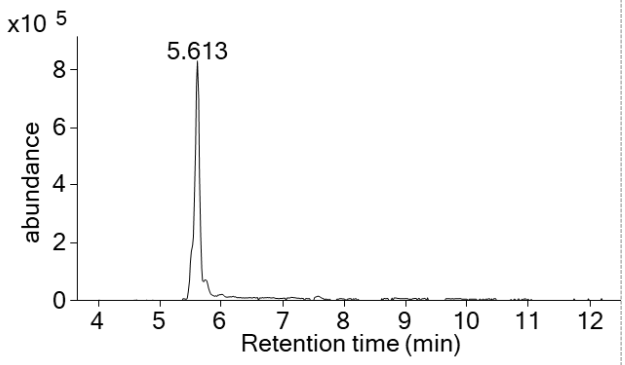


**Isotope pattern**

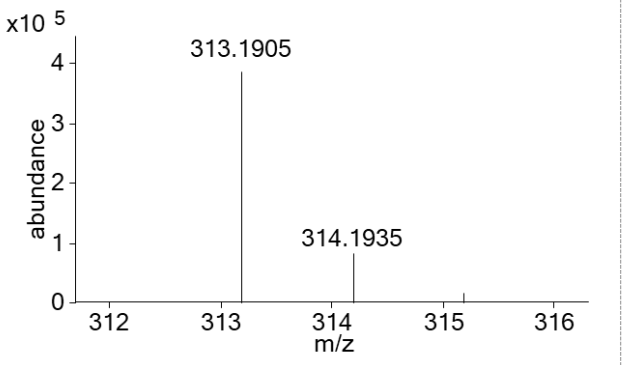


**MS/MS spectrum, CE 20 eV**

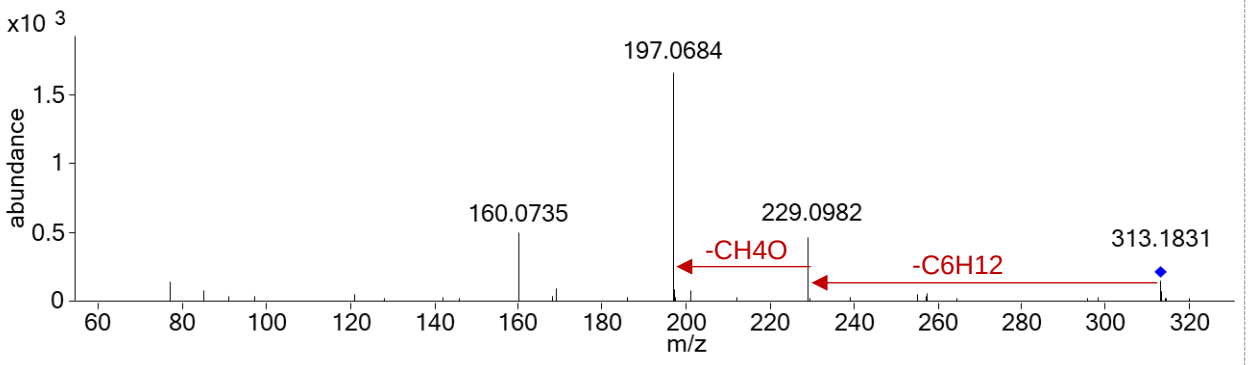

| **Name:** TP 344 | **Confidence level:** 4 | **Formula:** $C_{20}H_{28}N_2O_3$ | **RT shift:** + 7.34 min | **Atomic Modification:** + $C_2H_4O_3$ |
|---|---|---|---|---|
| **Structure:** no final structure | **Identification:** - | | | |

**Chromatogram**

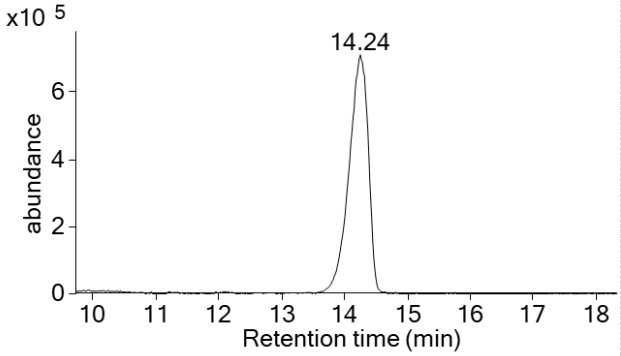


**Isotope pattern**

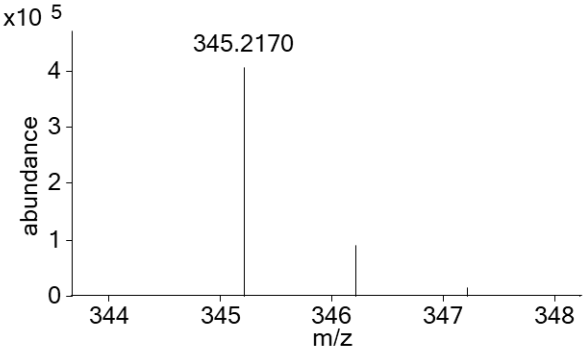


**MS/MS spectrum, CE 20 eV**

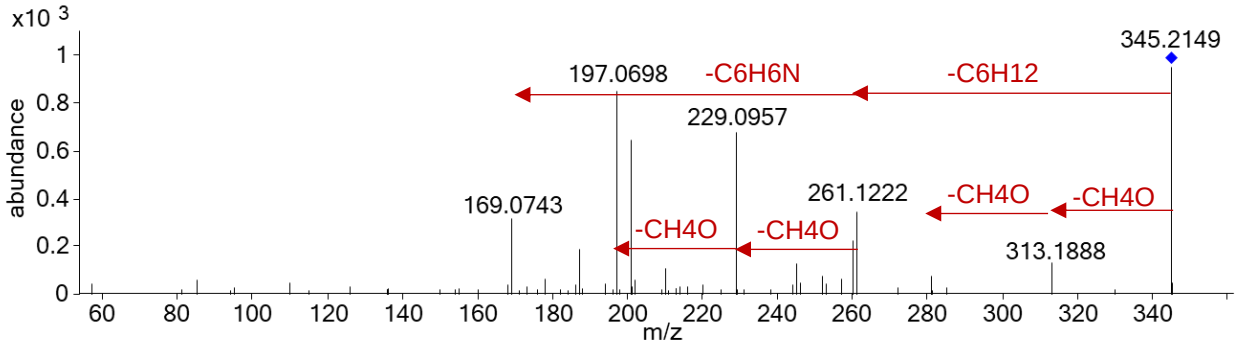

## Reference

Agua, A., Stanton, R., Pirrung, M., 2021. Preparation of 2-((4-Methylpentan-2-Yl)amino)-5-(Phenylamino)cyclohexa-2,5-Diene-1,4-Dione (6PPD-Quinone), an Environmental Hazard for Salmon. ChemRxiv preprint.

Hou, F., Tian, Z., Peter, K.T., Wu, C., Gipe, A.D., Zhao, H., Alegria, E.A., Liu, F., Kolodziej, E.P., 2019. Quantification of Organic Contaminants in Urban Stormwater by Isotope Dilution and Liquid Chromatography-Tandem Mass Spectrometry. Anal. Bioanal. Chem. 411, 7791–7806.

Lattimer, R.P., Hooser, E.R., Layer, R.W., Rhee, C.K., 1983. Mechanisms of Ozonation of N-(1,3-Dimethylbutyl)-N′-Phenyl-p-Phenylenediamine. Rubber Chem. Technol. 56, 431–439.

Pangborn, A.B., Giardello, M.A., Grubbs, R.H., Rosen, R.K., Timmers, F.J., 1996. Safe and Convenient Procedure for Solvent Purification. Organometallics 15, 1518–1520.

# Chapter 6

# General Conclusions

The overall goal of this thesis was to study the environmental transformation of steroid hormone pharmaceuticals and tire rubber antiozonants to identify stable and/or toxic TPs, to study their environmental fate and transport, and to evaluate the potential for TP toxicity. Conclusions for the specific aims are outlined below.

*Aim 1: Targeted quantification of metastable photoproducts of trenbolone and altrenogest and evaluation of their relative sorption behaviors*

A novel and sensitive analytical method was developed for the detection and quantification of metastable trenbolone (TBOH) and altrenogest (ALT) photoproducts in agricultural receiving waters. The method employed C18 solid phase extraction and liquid chromatography-tandem mass spectrometry (LC-MS/MS) analysis. Reference standards for the photoproducts were generated from TBOH or ALT with a solar simulator (~6 hours, >10 half-lives) due to lack of commercial analytical standards. Efficient detection of metastable photoproducts required cold and pH neutral conditions, rapid sample processing, minimal extract storage, and consideration of cationic artifacts. With the above techniques, we achieved method detection limits of 0.034-0.40 ng $L^{-1}$ for parent compounds and 0.16-2.1 ng $L^{-1}$ for photoproducts, sufficient for their detection in agroecosystems. The analytical method was then employed to evaluate the hydrophobicity (octanol-water partitioning) and sorption behaviors of the steroid photoproducts in batch soil-water systems. We demonstrated that the photoproducts exhibited reduced hydrophobicity (log$K_{ow}$ of 1.25-3.25) and sorption affinity (log$K_{oc}$ of 1.92-2.57) relative to the parent structures (log$K_{ow}$ of 2.6-3.74, log$K_{oc}$ of 2.46-2.76). Therefore, traditional runoff

management practices in agroecosystems would be expected to exhibit reduced treatment effectiveness when the photoproducts were considered.

*Aim 2: Identification of biotransformation products of novel progestins with suspect screening and non-targeted analysis.*

We evaluated the biotransformation of ALT and its primary photo-cycloaddition product (ALT-CAP) in agricultural receiving waters and identified the TPs with high-resolution mass spectrometry (HRMS). In a water-sediment suspension microcosm, we showed that ALT-CAP (half-life, 1.6 days) demonstrated ~2-fold faster biotransformation than ALT (half-life, 3.5 days). ALT and ALT-CAP showed similar major transformation pathways, including hydroxylation, dehydrogenation, and isomerization. However, the absolute abundance (based on HRMS peak areas) of the major ALT-CAP TPs was often an order of magnitude higher than that of ALT TPs. This indicated that biotransformation of ALT seemed to produce less abundant and less stable TPs, while ALT-CAP biotransformation tended to produce larger, and more stable TPs with higher potential for retained steroid structures. Therefore, the exposure risks of ALT are prone to underestimation if the formation and subsequent biotransformation products of ALT-CAP are not considered as part of the environmental fate of these compounds.

We then investigated the biotransformation of dienogest (DIE) and drospirenone (DRO) with representative activated sludge batch incubations and identified relevant TPs using HRMS. We showed that DIE exhibited slow biotransformation (16-30 hr half-life). DIE proceeded through a quantitative aromatic dehydrogenation (molar yields ~55%) to form an aromatic TP ~30% estrogenic as 17β-estradiol. DRO experienced more rapid biotransformation (<0.5 hr half-life), and 1,2-dehydrogenation formed the major product (molar yields ~40%) as an anti-mineralocorticoid drug candidate named spirorenone. Lactone ring hydrolysis was another

important biotransformation pathway for DRO (molar yields ~20%) and generated a pharmacologically inactive TP. We also revealed other minor pathways for DIE and DRO included hydroxylation, methoxylation, and 3-keto and C4(5) double bond hydrogenation; distinct bioactivities are plausible for such TPs, including anti-gestagenic activity, anti-gonadotropic activity, and pregnancy inhibition effects. Thus, biotransformation products of DIE and DRO during wastewater treatment should be considered in environmental assessments of synthetic progestins,

*Aim 3: Identification of the primary casual toxicant for coho salmon acute mortality with effect-directed analysis and subsequent environmental fate studies.*

In a large collaborative research project led by Dr. Zhenyu Tian (postdoc scientist of our group), Nina Zhao developed the orthogonal HPLC fractionation steps (C18 – PFP – Phenyl HPLC) in an effect-directed analysis scheme. The orthogonal HPLC fractionation effectively separated out a toxicant acutely lethal to coho salmon from ~600 chemicals in purified aqueous leachate of tire tread wear particles (TWPs). After the coho toxicant was identified as 6PPD-quinone (an ozonation product of a tire antioxidant, 6PPD), this thesis then revealed PPD-quinones formations in four analogue substituted-PPD antioxidants, and confirmed the structures based on retention time and MS/MS spectra match with synthetic PPD-quinone standards (from Dr. Kelly Kim at UWT). Furthermore, this thesis explored other ozonation TPs of 6PPD with HRMS screening, and identified 21 potential TPs with 5 confirmed through reference standards and 11 with likely or probable structures proposed based on MS/MS spectra and literature information. The major 6PPD TPs were then retrospectively screened in archived sample extracts of TWP, TWP leachate, roadway runoff, and creek stormwater. 6PPD TPs showed widespread presence in these sample matrices (ΣTPs: TWP methanolic extracts, 110 ± 7 μg/g; TWP leachate

(0.25 g TWP/L water), 11 ± 2.7 µg/L; roadway runoff, 40 ± 15 µg/L; creek stormwater, 59 ± 20 µg/L).